Localized Corrosion Damage Morphology and Corrosion Electrochemistry for Al-Zn-Mg-Cu Fastener Galvanic Couples in Marine Environments.

A Dissertation

Presented to

the faculty of the School of Engineering and Applied Science

University of Virginia

---

in partial fulfillment

of the requirements for the degree

Doctor of Philosophy

by

Veronica N. Rafla

May

2018

APPROVAL SHEET

The dissertation

is submitted in partial fulfillment of the requirements

for the degree of

Doctor of Philosophy

AUTHOR

The dissertation has been read and approved by the examining committee:

John R. Scully

Advisor

Robert G. Kelly, Chair

David L. Green

James T. Burns

Devin K. Harris

Accepted for the School of Engineering and Applied Science:

Craig H. Benson, Dean, School of Engineering and Applied Science

May

2018

Executive Summary

Aluminum alloy 7050-T7451 (Al-Zn-Mg-Cu) is often used for aerospace applications because it provides an advantageous combination of strength, stress corrosion cracking (SCC) resistance, corrosion resistance, and fracture toughness. Defects in corrosion protection are enhanced at complex joining/fastener locations which trap electrolyte into tight crevices, leading to occluded local environments where a galvanic cell is established between the Al alloy and a steel fastener. While the danger of galvanic corrosion has been recognized, little research has developed an understanding of the physical, metallurgical, and electrochemical factors governing the corrosion damage at the meso- and macro-scale, as well as characterization of the damage morphology between AA7050 and stainless steel. The overall objectives of this work are to (1) investigate the electrochemical, microstructural, and physical factors that govern galvanic corrosion pit morphology development at the macro-, meso-, micro-, and nano-length scales under conditions representative of galvanic coupling between a rivet and plate in an aerospace structure, (2) explore and compare various laboratory-simulated to field damage modes in order to better simulate field damage in fatigue tests, (3) develop an electrochemical-based framework to explain the observed galvanic corrosion morphology developed in environmental conditions simulating a rivet, (4) understand the source and impacts of various cathodic reaction rates when AA7050-T7451 is coupled to stainless steel, and (5) extend these findings to further understand the effect of an inhibitor, such as chromate, on galvanic corrosion damage evolution.

The macro-scale corrosion (i.e., location and number of corrosion sites) was investigated using *in operando* X-ray tomography. X-ray tomography on a simulated fastener of AA7050-T7451 and stainless steel revealed multiple corrosion fissures grew simultaneously over the period of exposure under NaCl and $MgCl_2$ droplets. Fissures did not follow obvious clusters of constituent particles, suggesting the presence of a newly developed strong cathode, such as Cu-replating, and a fixed strong cathode, attributed to the stainless steel rivet. Detailed examination was undertaken to understand the precise macro- and micro-cathodes controlling the galvanic corrosion central to damage between AA 7050-T7451 and Type 316 stainless steel, enabling targeted suppression of

certain cathodes for mitigation of corrosion damage. It was determined that Cu-replating may have a greater contribution to the total cathodic charge than the stainless steel rivet. This was an interesting observation as no corrosion sites grew when the stainless steel was removed before exposure. This suggests that the stainless steel provides the key driving force for AA7050-T7451 localized galvanic corrosion initiation and enables Cu to replate on the surface. Replated-Cu subsequently supports damage evolution.

The meso-scale corrosion (i.e. damage morphologies) of AA7050-T7451 galvanically coupled to stainless steel was investigated using electrochemical methods guided by anodic and cathodic polarization in rivet-specific solutions. This developed a range of relevant potentials and environmental conditions for likely corrosion susceptibility in environments typical around rivets. It was also found that various corrosion damage morphologies can be developed in AA7050-T7451, associated with the galvanic conditions specific to a fastener. For instance, intergranular corrosion was found to prevail in acidic environments and became further intensified with the addition of Al ions in solution. Intragranular corrosion pits were developed in neutral and alkaline NaCl environments. Deep, elongated fissures in grains oriented in the L-direction were often produced in alkaline NaCl environments following the addition of Al ions, which was attributed to Cu-replating on AA7050-T7451. It was found that AA7050-T7451 was more likely to undergo dealloying of Al_2CuMg in alkaline exposure, further promoting Cu to replate The corrosion damage morphologies that were developed in specific cases are significant as they may each affect the fatigue transition differently. Investigation of methods used to study galvanic corrosion were compared to tear-down field damage and other field studies. Zero resistance ammeter resulted in the closest correlation between the simulated fastener corrosion morphology and actual service corrosion from the perspective of damage morphology.

The metallurgical factors and electrochemical framework controlling the path of intergranular and intragranular corrosion were also established in this work. AA7050-T7451 is composed of many different regions with a variety of compositions. This includes the matrix, intermetallic particles, solute-depleted zones, and precipitate-free zones. Each of these regions have different chemical compositions and critical electrochemical potentials. It is rationalized that the difference in critical potential associated with these microstructural regions, combined with E_{couple} within a region accounts for the intergranular corrosion. TEM showed that Cu and Al were often incorporated into the strengthening precipitate, $MgZn_2$. Furthermore, Cu-depletion was often observed in the region adjacent to the grain boundary. It was determined that the window of intergranular corrosion susceptibility decreased with incorporation of Cu and/or Al into the $MgZn_2$. An intergranular corrosion framework was proposed: Cu^{2+} in solution was found to raise the pitting potential of the solute-depleted grain boundary region, closing the window for intergranular corrosion to occur. Cu^{2+} is often found in the micro-chemistry of a corrosion pit. This also suggests that pitting can be attributed to the coarse secondary phases in AA7050-T7451. The corrosion pathway was also determined using EBSD, which showed that unrecrystallized grains containing low-angle boundaries may be more susceptible to intragranular corrosion damage. This was speculated to be attributed to unrecrystallized grains collecting Cu in the precipitates during the over-aging heat treatments of the AA7050 (T7451) with associated Cu-depletion.

The galvanic current interactions under atmospheric conditions were conducted using coupled multi-electrode arrays constructed of AA7050-T7451 coupled to Type 316 stainless steel. It was found that under a NaCl thin films of 70 µm, the net galvanic current density increased by at least one order of magnitude when compared to full immersion kinetics. To investigate the current interactions inside a rivet geometry, a coupled multi-electrode array constructed in a fastener geometry revealed that anodic currents were often higher at the mouth of the crevice and inside the crevice. In many of the exposures, AA7050 net anodic sites were often found to abruptly switch to net cathodic sites. This suggested that dealloyed S-phase (Al_2CuMg) and/or Cu-replating on the surface was the source of the increased cathodic kinetics of AA7050-T7451 electrodes. When AA7050-T7451 was coupled to stainless steel, the AA7050-T7451 electrodes were still significant cathodes supporting ORR. In some cases, AA7050-T7451 electrodes contributed 90% of the total net cathodic reaction. Anodes were dictated by local sites where AA7050 initiated pitting. It is speculated that SS enables initiation, but propagation largely is supported by replated Cu. The CMEAs were also tested under atmospheric wet/dry cycle conditions and resulted in a 4-fold increase in current density, attributed to strong spikes in current on the onset of wetting/drying as the water layer became more concentrated. The cathodic reaction rates under thin films were also studied utilizing an array constructed with an embedded, sintered Ag/AgCl electrode used as both the counter and reference electrode. It was found that cathodic ORR reaction rates increased by at least one order of magnitude in atmospheric thin films or droplet environments as compared to bulk, full immersion conditions. Under droplet conditions, electrodes on the edge of the droplet experienced increased ORR cathodic kinetics when compared to electrodes under the center of the droplet. Under a continuous thin film, AA7050 electrodes exhibited equivalent cathodic kinetics as a function of position. Lastly, the controlling factors in constant potential holds which simulate galvanic couples between Type 316 stainless steel and AA7050-T7451 were investigated and it was found that ORR kinetics of planar and micro-electrodes of pure Cu did not follow mass transport control under Cottrell diffusion kinetics at a constant potential in a droplet.

These findings were extended to further understand the effect of an inhibitor, such as chromate, on galvanic corrosion damage evolution and electrochemistry. Damage morphology studies showed that while the fissure density was reduced with the addition of soluble chromate, aggressive environments created by application of high anodic potentials or galvanic coupling to stainless steel induced deep fissure formation. In one case, fissures were over 37 times deeper in chromate solutions than chromate-free solutions. The growth of corrosion fissures in chromate-containing environments were speculated to be caused by the fully protonated H_2CrO_4 which exists in strongly acidic solutions. Evidence suggests H_2CrO_4 is present in active pits, but does not inhibit corrosion because H_2CrO_4 is not charged and cannot compete with Cl^- and adsorb or interact with the corroding surface. Electrochemical results showed that additions of Na_2CrO_4 reduced cathodic ORR kinetics by one order of magnitude for Type 316 stainless steel and by less than one order of magnitude on Cu. In contrast, additions of Na_2CrO_4 increased the cathodic kinetics of replated Cu on AA7050-T7451, which is detrimental to corrosion inhibition. The addition of chromate was determined to significantly inhibit the corrosion of Al_2CuMg, which minimizes the possible formation of porous Cu-rich phases and Cu-replating on the surface. Therefore, inhibition of Cu^{2+} release through passivation of Al_2CuMg would be a viable route to lower cathodic reaction rates.

This thesis contributed to the scientific understanding of dissimilar, metal-based crevice corrosion in complex precipitation-hardened aerospace alloys, clarified approaches that enabled laboratory simulation of corrosion damage modes seen in the field, helped inform the attributes that can be controlled and regulated in developing new corrosion damage mitigation strategies, investigated the galvanic current interaction under atmospheric conditions, and extended these findings to understand the effect on galvanic corrosion-induced damage morphology of the legacy inhibitor: chromate.

Acknowledgements

Foremost, I would like to thank my advisor, Dr. John Scully, for his guidance and contributions and for providing me the opportunity and endless support to pursue my degree. I will forever be grateful for the mentorship that extended far beyond the technical knowledge he taught me. Thank you, for this rewarding and challenging experience and the countless intangible lessons on how to be a capable researcher. I would also like to thank and acknowledge the members of my thesis committee: Dr. Robert Kelly, Dr. Jimmy Burns, Dr. David Green, and Dr. Devin Harris for their time and assistance with my research. I would also like to thank Dr. Kelly, Dr. Burns, Noelle Co, and Chao Liu for the collaborative research efforts on this project.

I appreciate all the help and support of all the faculty and students in the Materials Science Department who have helped me over the years and specifically the Center for Electrochemical Science and Engineering. The members of CESE has truly provided me with an amazing community of talented researchers that I am forever grateful to have had the opportunity to grow and learn with. Specifically, I would like to thank Brendy C Rincon Troconis, Rebecca Schaller and Andrew King for showing me the ropes and helping me get started.

I truly am thankful for all the amazing friendships that have developed over the last 4.5 years in Charlottesville: Keren Freedy, Rebecca Schaller, Ariel Cohen, Katie Lutton, Kate Quiambao, Lindsey Bloom, Brendy C Rincon Troconis and Ryan Katona. I couldn’t have done it without all of you. Thank you.

Most of all, I would like to thank my family. My mom and dad for continuing to help me grow and provided me endless support over the last few years. I’d also like to thank my sister and brother, Yustina and Andrew for always being there for me no matter what. Thank you to my dog Charlie boy for always being able to put a smile on my face.

Bibliography

The publications that resulted/will result from this dissertation are listed below

1. V. Rafla, A.D. King, S. Glanvill, A. Parsons, A. Davenport, and J.R. Scully, "Operando Observation of Galvanic Corrosion Between Aluminum Alloy 7050-T7451 and 304 Stainless Steel in a Simulated Fastener Arrangement Using X-Ray Tomography," Corrosion 71, 10 (2015): p. 1171-1176.
2. V. Rafla, A. King, S. Glanvill, A. Davenport, and J. Scully, "Operando Assessment of Galvanic Corrosion between Al-Zn-Mg-Cu Alloy and a Stainless Steel Fastener using X-ray Tomography," Corrosion (2017).
3. V. Rafla, A. Davenport, and J.R. Scully, "Determination of Cathodic and Anodic Charge from Operando X-Ray Tomography Observation of Galvanic Corrosion of Aluminum Alloy 7050-T7451 and 304 Stainless Steel in a Simulated Fastener," Corrosion 71, 11 (2015): p. 1300-1303.
4. V. Rafla, P. Khullar, R.G. Kelly, J.R. Scully, “Utilizing a Coupled Mutli-Electrode Array with a Sintered Ag/AgCl Counter/Reference Electrode to Investigate Kinetic Reaction Rates of AA7050-T7451 and Type 316 Stainless Steel Galvanic Couples Under Atmospheric Conditions” Corrosion (2018)
5. V. Rafla, J.R. Scully, “Effect of Soluble Chromate Inhibitor on the Macro and Meso-scale Damage Morphology and Electrochemistry Corrosion Behavior of AA7050-T7451 Coupled to Type 316 Stainless Steel” Corrosion (2018)
6. V. Rafla, J.R. Scully, “Galvanic Couple Current Interactions under Thin Films Assessed with a Coupled Multi-electrode Arrays Constructed of AA7050-T7451 and Type 316 Stainless Steel Arranged in a Fastener Arrangement” Corrosion (2018)
7. V.Rafla, J.R. Scully, “Environmental Factors Effecting the Corrosion Damage Morphology in Simulated Rivet Solutions at the Meso-scale of AA7050-T7451” Corrosion (2018)
8. C. Glover, V. Rafla, M. Hutchison, and J.R. Scully, "Progress in Development of Electrochemical Methods in Corrosion Science and Engineering," STP: Selected Technical Papers: Symposium on Advances in Electrochemical Techniques for Corrosion Monitoring and Laboratory Corrosion Measurements (2018).

Table of Contents

List of Figures

List of Tables

List of Symbols

CMEA	Coupled multi-electrode array
CV	Cyclic voltammetry
D	Diffusion Coefficient
E.W.	Equivalent weight
EAC	Environmentally assisted cracking
EBSD	Electron Backscatter Diffraction
E_{Couple}	Galvanic couple potential
EDS	Energy dispersive spectroscopy
EELS	Electron energy loss spectroscopy
E_{SCE}	Potential measured vs. SCE
F	Faradays Law
GB	Grain boundary
HER	Hydrogen evolution reaction
i	Current density (A/cm^2)
I	Current (Amps)
i_0	Exchange current density
I_{couple}	Galvanic couple current
IGC	Intergranular Corrosion
I_L	limited current density
IMP	Intermetallic particles
I_{net}	Total current density
M	Molar
n	Number of electrons transferred in a reaction
NND	Nearest neighbor distance
OA	Over-aged
OCP	Ppen circuit potential
OES	Optical Emission Spectroscopy,
ORR	Oxygen reduction reaction
PFZ	Precipitate free zones
PI	Pitting index
Q	Quenched

Q	Charge
$Q_{\Delta m}$	Anodic charge density associated with metal dissolution
Q_{H2}	Cathodic charge density associated on the sample of the surface due to hydrogen evolution
S phase	Al_2CuMg
SCC	Stress Corrosion Cracking
SEM	Scanning Electron Microscope
SHT	Solution heat treatment
STEM	Scanning transmission electron microscopy
T	Temperature
t	Time
TEM	Transmission Electron Microscopy
v	Viscosity
WL	Water later thickness
XCT	X-ray computed tomography
β	Al_7Cu_2Fe
δ	Boundary layer thickness
Δm	Mass loss (g)
η	Eta phase $MgZn_2$
ω	Angular frequency

1. Introduction: Background, Significance and Objectives

1.1 Motivation and Overview of Problem

Corrosion damage developed during ground basing combined with operational loading has a harmful effect on long term fatigue life.[1] It was reported in a 2009 U.S. Air Force teardown, based on 711 fatigue damages sites, 80% of these fatigue sites were initiated due to corrosion damage and only 20% due to mechanical damage.[2] Aggressive marine environments enhance the development of corrosion making the corrosion and fatigue interaction tremendously important to the structural integrity of airframes.[3]

Defects in the corrosion protection system are common due to the intense operating conditions. Furthermore, the geometry of fastener holes inherently aids trapping and wicking of the electrolyte into tight crevices typical of these components. An occluded local environment combined with a dissimilar metal establishes a galvanic corrosion cell between the aerospace aluminum component and the steel fastener causing localized corrosion of the aluminum component.[1] The localized corrosion can transition into corrosion fatigue or other damage modes.[4] The corrosion damage enhances the already high inherent stress concentration associated with a fastener hole.[1,5-7]

Although high strength aluminum alloys are widely used in aerospace applications due to their high strength to weight ratio they are prone to localized corrosion due to the formation of micro galvanic couples in the alloy microstructure.[8,9] The localized corrosion can be further exacerbated by galvanic coupling with a more noble material such as stainless steel or other typical fastener materials. [10,11]

While a vast amount of work has been performed regarding the localized corrosion of high strength aluminum alloys there is a lack of literature on the unique factors and environments present in a rivet hole and furthermore how these factors and environments effect the overall damage morphology. [3,10,12-15] Previous work limits our understanding of damage morphologies to a few specific test environments such as Point Judith marine seacoast atmospheric exposures, full immersion in 0.6 M NaCl, EXCO solution [16] and 0.6 M NaCl + H_2O_2,[17] as there has been very little work on crevice and rivet specific environments.

The overall objectives of this work are to (1) investigate the electrochemical, microstructural, and physical factors that govern galvanic corrosion pit morphology development at the macro, meso, micro and nano length scales under conditions representative of galvanic coupling between a rivet and plate in an aerospace structure (2) explore and compare various laboratory simulated damage modes to field damage in order to guide choice of methods to simulate field damage in fatigue tests (3) develop an electrochemical-materials based framework to explain the observed galvanic corrosion morphology developed for various physical geometries (4) understand the source and impacts of various cathodic reaction sites and materials and extend these findings to further understand the effect of an inhibitor such as chromate on galvanic corrosion damage evolution.

1.2 Background

1.2.1 Galvanic Induced Corrosion of Aluminum Alloys

High strength aluminum alloys and stainless steel are widely used in the aerospace industry for fastener applications. Aluminum is one of the more active metals in the galvanic series.[18] Due to aluminum's low electrochemical potential and heterogeneous microstructure, these alloys often undergo significant localized corrosion which is worsened when in contact with a noble material, such as a fastener. The critical issue is galvanic corrosion of passive metals that undergo localized corrosion, such as Al alloys, often triggers pitting and other forms of localized corrosion. When AA7050 is coupled with stainless steel, the aluminum alloy is polarized above various threshold potentials for local corrosion such as intragranular corrosion, crevice corrosion, pitting, and exfoliation corrosion. All these factors need to be addressed at the macro thru nano length scales. Figure 1.1 shows the different forms of localized corrosion in aluminum alloys.[10]

1.2.2 Crevice Corrosion Mechanism in Aluminum Alloys

Many theories on the mechanism of crevice corrosion have been established, however the most established mechanistic theory for aluminum alloys follows the Fontana and Greene model due to its good adaptability to various conditions.[19] Fontana and Greene proposed a basic mechanism of crevice corrosion where initially the anodic dissolution and cathodic reduction reaction processes occur uniformly over the entire metal surface, including the inside of the crevice (stage 1). [19] The oxygen inside the crevice is consumed after some incubation period (stage 2). With the cathodic hydroxide producing reaction stopping inside the crevice, the migration of mobile Cl^- inside the crevice area is required to maintain charge balance as metal (i.e. Al^{3+}) continues to dissolve (stage 3). The resulting metal chlorides hydrolyze in water from insoluble metal hydroxides and free acid. Both the Cl^- and low pH accelerate crevice corrosion, while the reduction reaction cathodically protects the exterior surfaces (stage 4). [19] A summary of the crevice corrosion mechanism is shown in Table 1.1 Crevice corrosion creates a localized anode coupled to a large surface area cathode on the surrounding surfaces. Crevice corrosion grows autocatalytically as more chloride migrates to the crevice, promoting further hydrolysis and consequent acidity. Rosenfeld and Marshakov constructed artificial crevices and measured the corrosion currents that occurred between the Al electrodes. [18] A corrosion current of 160 $\mu A/cm^2$ was observed, with the electrode in the crevice acting as the anode. The solution in the crevice became acidic with a pH of 3.2. This was explained by the hydrolysis of Al^{3+} ions to give $Al(OH)^{2+}$.[10,20] Stoner studied the pH vs time response of a simulated crevice by inserting a pH microelectrode into crevices of AA 2090 machined. He reported that the pH quickly attained a steady state pH value of approximately four.[21]

1.2.3 General Corrosion Overview of Al-Zn-Mg-Cu Alloys

Pitting, intergranular corrosion, and stress corrosion cracking are often exhibited in Al-Cu-Zn-Mg alloys. [10] AA7050-T7451 contains three types of secondary phase particles: strengthening precipitates, dispersoids to control grain size and recrystallization, and coarse constituent particles, which often become aligned in stringers parallel to the rolling axis. Many of these phases play a role in corrosion.[22] [8,10,12,15,22-25] Typically, the strengthening precipitates on grain boundaries and Cu depletion are implicated in intergranular corrosion and intergranular stress corrosion cracking. AA 7050-T7451 alloy contains 2.6 wt. % Cu and the T7451 temper has been overaged to suppress intergranular corrosion and stress corrosion cracking on grain boundaries. Constituent particles are dominant sites for pitting corrosion in the absence of grain boundary (GB) effects resulting from their size and local electrochemical characteristics. [8,26,27] They are also sites for fatigue initiation. [28]

Precipitation hardened aluminum alloys are susceptible to corrosion attack such as pitting, crevice corrosion, intergranular corrosion and stress corrosion cracking.[10] The fundamental cause of pitting corrosion has been attributed to the local breakdown of the passive film that forms on the surface at certain sites, such as constituent particles and solute depleted zones. [29] The presence of a significant amount of second phase constituent particles which are either anodic or cathodic to the matrix is attributed to poor corrosion resistance of these alloys. [18,30] In AA7050-T7451 grain boundary precipitation of the strengthening phase $MgZn_2$- η influences the corrosion behavior by locally depleting Zn, Mg, and Cu, especially in the T6 temper[31], which can enable intergranular corrosion (IGC), intergranular stress corrosion cracking (IGSCC) and exfoliation corrosion [27]. The T74 temper has been overaged to suppress IGC and SCC on grain boundaries[22] [23]. Cu content is important, as the composition of both the bulk matrix and η changes with aging, which decreases the electrochemical potential window between $Mg(Cu)Zn_2$ dissolution and the matrix pitting or repassivation potential; this decreases IGC and exfoliation susceptibility[32]. However, incongruent dissolution of Cu-rich phases may leave a Cu-rich surface that is cathodic to the matrix[33]. This may increase general and local corrosion. [12]

Metallurgical Factors Influencing Aging and Precipitate Strengthening in 7xxx series Al Alloys (Al-Zn-Cu-Mg)

Aluminum alloy 7050 (Al-Zn (6.7% wt) –Cu (2.6% wt)- Mg(2.6% wt) was developed to obtain a combination of strength and fracture toughness resistance greater than that provided by other common high strength alloys such as 7075. [10] AA7050 is precipitate strengthened by the formation of $MgZn_2$- η phase in the reaction sequence[34]:

$$\text{Solid Solution } \alpha \rightarrow \text{Guinier Preston (GP) Zones} \rightarrow \text{Metastable } \eta' \rightarrow \text{Stable } \eta \text{ } MgZn_2$$

Precipitates form by nucleation and growth from a supersaturated solid solution during natural or low temperature aging. The η phase is highly soluble and will readily dissolve into solution during homogenization. In the partially recrystallized and artificially aged microstructure η' is usually found on subgrain boundaries and η on high angle grain boundaries. [35] Temper has a major effect on the microstructure of aluminum alloys. In 7000 series alloys, the T6 temper reaches peak strength but has poor stress corrosion resistance due to a high density of GP zones and η' precipitates that are continuous along the grain boundary. Overaging treatments such as the T73 or T76 temper improve the short transverse stress corrosion cracking resistance by increasing the grain boundary precipitates size and spacing, however, this results in a loss of strength. [36] The T7 (overaged) condition results in an increase in the amount of η equilibrium precipitates on the grain boundaries, the grain boundary precipitates are coarser and more sparsely distributed. [37] The T7451 temper is solution heat-treated, stress-relieved by controlled stretching and artificially overaged between T73 and T76. [38] The T7451 temper proves an advantageous combination of strength, stress corrosion resistance, corrosion resistance and fracture toughness. [39,40]

1.2.4 Effect of Constituent Particles on the Localized Corrosion of AA 7050-T7451

AA7050 contains course constituent particles, strengthening precipitates and dispersoids (Table 1.2). Course constituent particles in the range of 5-30 μm (Al_2CuMg *S*, Al_7Cu_2Fe *β*, and Mg_2Si) form during solidification and are often found in clusters or stringers which become aligned in parallel to the rolling axis. Dispersoids (Al_3Zr) form during homogenization and control recrystallization and grain size and occur at temperatures above the solidus of Al.[41] Dispersoids pin grain boundaries preventing them from growing during solution heat treatment (SHT). Al_3Zr is a noble particle that will not sustain large cathodic currents and may be too small to adversely impact corrosion kinetics.[23] Figure 1.2 shows a schematic of the fastener configuration depicting the micro and nano structure of the bulk alloy showing the $MgZn_2$ phase on the grain boundary and the precipitate depleted zones adjacent to the grain boundaries enabling intergranular corrosion. The course constituent particles can greatly affect the corrosion properties of these alloys. Fe and Si have a strong detrimental influence on fracture toughness and corrosion properties due to the formation of brittle constituents such as S-phase (Al_2CuMg) and –β phase (Al_7Cu_2Fe).

[26,42,43] These constituent particles are often located in the interior of recrystallized grains or on recrystallized grain boundaries and often lead to a particle dealloying mechanism, leading to localized Cu enrichment.[44,45] Dealloying of Al_2CuMg phase will be discussed in detail in Task 3. $MgZn_2$ and Mg_2Si are both active particles with self-dissolution rates, leaving behind a surface cavity. [33,46] $MgZn_2$ greatly effects the corrosion properties of this alloy. $MgZn_2$ is very active with an OCP of -1.4 V SCE in neutral 0.5 M NaCl and a breakdown potential of -1.14 V SCE. [44]

1.2.5 Effect of Temper on the Mechanism of Localized Breakdown in 7xxxSeries

Localized corrosion of Al-Zn-Mg-Cu alloys have been extensively studied, however only in one or two simple salt solutions such as $MgCl_2$ and NaCl. [1,8-10,14,15,25,27,44,47,48] The anodic polarization curve for non-Cu-containing7000-T6 in NaCl exhibits two break down potentials while 7000-T73 only exhibited one break down potential. [14] Maitra and English suggested that for AA7075-T6 the first break down potential (lower E) is due to pitting of the solute enriched grain boundary region and the second breakdown (higher E) to the pitting of the matrix. The single breakdown potential in the T73 temper was attributed to the pitting of the Cu depleted solid solution matrix. [14] It was shown that aging 7xxx series alloys to peak aged T6 condition increased the susceptibility to intergranular corrosion due to the anodic path created by solute enrichment of Zn and Mg near the grain boundaries. [38] Frankel studied the corrosion behavior of Cu-containing AA 7xxx 00-T6, and observed two breakdown potentials in a deaerated NaCl solution. [14,49] However, this behavior has not been extensively investigated specifically for Cu-containing alloys such as AA7050 in the T74 temper.

The effect of temper on localized corrosion of 7xxx series have been studied by understanding matrix solute concentrations of various 7xxx series alloys. [49-51] The pitting potential of AA7055-T6 was around -700 mV SCE which was more noble that that of the overaged alloy which had a pitting potential of -770 mV SCE. [44] In the T73 temper, Cu and Zn have lower matrix concentrations due to a greater amount of precipitation and more Cu incorporation in the precipitates. In the Al matrix, Cu and Zn have the opposite effects on the pitting potential.[37] This decrease in pitting potential for peak aged T6 and overaged T73 was found to be a result of the depletion of Zn content in solid solution which causes the increase in breakdown potential.[49] For 7000 series alloys which contain Cu, it was found that the Cu and Zn ratio controls the pitting potentials.[26] For underaged Cu-containing alloys, the pitting potential was controlled by the Zn content because of the high Zn solute content. [39,44] As stated above. AA7050 is precipitate hardened by $MgZn_2$, which has considerable solid solubility for Cu and Al allowing for $MgZn_2$ to be enriched with Cu or Al resulting in a rise in breakdown potential. In AA7050, intergranular corrosion is often attributed to $MgZn_2$ on grain boundaries and/or Cu depletion. [32,52]

7xxx series alloys exhibit a window of IGC susceptibility as a function of aging time, with resistance to IGC being the lowest in the initial stages of aging and in underaged conditions, with increasing resistance with overaged condition.[53] It has been reported that overaging has a beneficial effect on the susceptibility to exfoliation corrosion by reducing the rate of intergranular corrosion. [53] Intergranular attack of Al-Zn-Mg-Cu alloys were studied by Maitra. [14] The alloys in the T6 temper exhibited two breakdown potentials. The more noble breakdown potential was attributed to the pitting of solid solution matrix and the second break down potential to be attributed to pitting of the solute enriched grain boundary. IGC was observed between the two breakdown potentials in the T6 temper. Electrochemical based mechanisms for IGC are often based on preferential anodic path along the grain boundaries. In the case of AA7000 the case is complex as Cu, Zn, Mg solid solution all change. This active region along the grain boundary is caused by either a solute depleted zone or anodic precipitates. [52]AA7050 has a high Cu content therefore it is important to understand the effect of Cu on the IGC. In Al-Cu alloys, increasing the Cu content in solid solution increases the pitting and repassivaiton potentials of the matrix. [13] Cu depleted at grain boundaries due to diffusion controlled precipitation and growth of Cu-containing grain boundary precipitates can then be the reason for IGC susceptibility because of reduced pitting and repassivation potential at the grain boundary compared to the interior grain matrix. [52] Galvele used this electrochemical framework to study the effect of solute content on pitting potential of Al-Cu alloys. [54] Little and Scully studied the electrochemical framework to explain the intergranular corrosion behavior of Al-Cu-Mg-Ag alloy as a function of aging. They reported improvement in

IGC behavior upon over aging consistent with a decrease in the parameter $(\Delta E(E_{rp}^{matrix} - E_{rp}^{Al})$ with increasing aging time. This correlated with a decrease in global Cu content in solid solution towards the Cu solid solution concentration in equilibrium with grain boundary precipitates. Little and Scully show schematics of the grain boundaries of the matrix, these are shown in Figure 1.3 [52]

It has been proposed that the aging temperature that produces maximum environmental assisted cracking directly depends on the alloy content. AA 7050 was developed as an improvement to AA 7075 because it achieved peak strength at a high temperature of 149˚C. Achieving peak strength was attributed to a higher GP zone solvus in the increase Cu alloy. A higher environmental assisted cracking resistance was attributed to Cu diffusion to grain boundaries and subsequent incorporation into $MgZn_2$ (Cu, Al) It was determined that Cu incorporates into the η when aged above 149°C, but not when aged lower. [27,32,55]

1.2.6 Effect of Cu Content on Microstructure and Corrosion Properties of 7000 series

Cu is distributed in the microstructure in different ways, (1) in the Al matrix (2) hardening precipices (η phase) and (3) Course constituents such as S phase (Al_2CuMg). The effect of Cu content on the microstructure corrosion has been well documented. [27,32,44,45,55,56] A Cu-containing 7000 series alloy will exhibit coarser, more widely spaced particles at grain boundaries as compared to an Al-Zn-Mg alloy. [57] The growth rate of the η phase was shown to be higher in Cu-containing alloys. [58] Cu increases the G.P. zone solvus from 120°C to 160°C resulting in homogeneous precipitated at high aging temperatures (above 149°C) for a Cu content of 1.4 wt.%.[59]

Due to the fact the $MgZn_2$ has a considerable amount of solubility for Cu and Al, it has been observed that the $MgZn_2$ can be enriched in Cu and Al.[32] Meng depicted in Figure 1.4 the composition of η phase precipitates on grain boundaries as a function of alloy Cu content in 7000 series in the T6 temper. [44] However, there has been little work on the electrochemical behavior of this phase and the damage morphology as a result, especially in the T74 temper.

The presence of S phase (Al_2CuMg) is common in AA7050 due to its increase Mg and Cu content. S phase is initially anodic but after dealloying occurs, the Cu remnant turns into a high surface area cathode for oxygen reduction.[60] If the Cu particles become mechanically detached, the Cu particle will dissolve at its corrosion potential in solution and will electrochemically replate on the surface of the bulk aluminum alloy.[33,45,61,62] This phenomenon is known as Cu-replating and can greatly affect the corrosion properties of the alloy[32,63]

1.2.7 Presence of S-phase on High Angle Grain Boundaries

The presence of S-phase (Al_2CuMg) is common in AA7050-T7451 due to its increased Mg and Cu content compared to other 7000 alloys.[55] The presence of S-phase particles may affect environmentally assisted cracking by (1) the removal of Cu from grain boundary regions which may prevent incorporation into grain boundary η precipitates during overaging and may affect the compositions or morphology of the surface film (2) an electrochemical effect by producing galvanic coupling with the matrix material at the crack tip and (3) a mechanical stress concentration at grain boundaries that reduces the more global stress required for fracture.[64] In a chromate environment (2) is not likely to have an effect since both S-phase particles and the matrix are passivated. [65]

1.2.8 Environmental Factors that Effect Damage Morphologies

Literature has shown that galvanically induced localized corrosion in Al alloys can be strongly influenced by environmental parameters such as pH, species and concentration.[66-68] In spite of the understanding that the aircraft environment is complex, most corrosion studies have been conducted in simple test solutions such as moist air or fairly concentrated chloride solutions (NaCl, $MgCl_2$). As discussed above, the depletion of dissolved oxygen in the crevice results in, at first, the formation of a differential aeration cell. Then the metal ions accumulate in the solution inside the crevice as a result of anodic dissolution. Acidification occurs from hydrolysis of metal ions inside the crevice. Chloride ions migrate into the crevice to preserve electroneutrality and the primary cathodic reaction is outside the crevice while hydrogen reduction occurs inside the crevice solution and hydrogen gas evolves. However, Cottis reported variable behavior with pH going acidic near the crevice mouth and alkaline in the deeper region in a crevice of AA 7475. The mechanism of alkalization was deemed unknown.[69] In the case of dissimilar metal crevice corrosion in rivets, the local cathode, SS 316, is functioning as a cathode throughout the length of the crevice. This can affect the pH gradient and differs from conventional crevice corrosion where the cathode is located only or primarily outside the crevice. Preliminary studies by Gilbert Liu show the micro crevice becomes alkaline with a proximate local cathode but local corrosion sites still become acidic locally within the local corrosion site. Therefore, the macro crevice pH rises only to 8 but local acidic sites are still seen at pH 3-4. This is slightly different from cases involving an external cathode which cause larger regions of acidity to develop on the net anode (7050) at the mouth of a crevice. In contrast, an internal cathode involving a dissimilar metal causes the pH to become alkaline. [70]

Solution chemistry changes are important factors to consider as well, as different solution chemistries can lead to different damage modes. Typically, there are two sources contributing to solution chemistry, dissolved metal ions from metal dissolution and anions from the environment such as Cl^-, SO_3^{-2}, SO_4^{-2} or CO_3^{-2}. [68] It is extremely difficult to physically assess the crevice solution in real crevices due to small gap or width and depth. While the exact pH gradient is unknown inside a fastener plate arrangement, it is important to assess the damage morphology first by replicating the solution chemistries that are known. The solution chemistry is known to have Al^{3+} and Cl^- with pH values anywhere from 3-8. [67,68] Therefore, the solutions that need to be considered are NaCl and $MgCl_2$ with additions of HCl, $AlCl_3$ and $NaAlO_2$. This task aims to rigorously build a library of AA 7050-T7451 alloy damage modes over a range of potentials and crevice solutions. Gilbert Liu proposes to better define the solution chemistry using ICP, once these solutions chemistries are established, additional damage mode studies will be conducted in those known environments. [70]

The effects of corrosion on macro potential profiles have all been considered in isolation in Al age hardened alloys but the pertinent combination applicable to this geometry in marine applications have not been considered. It is expected that pitting under mass transport might prevail at high potentials, constituent particle driven micro galvanic anodic attack might prevail at intermediate potentials while cathodic trenching will take over at cathodic potentials. [10,71] These potential effects have not been elucidated in AA 7050-T7451 but likely affect corrosion damage morphology and could ultimately influence the pit to crack transition.[5] This mechanistic understanding of meso scale morphology will be characterized by systematic variation in relevant environmental parameters which will enable prediction for a given set of corrosive environment.

Physical geometry is another crucial factor that can affect the macro current and potential distribution inside a crevice. If the system is under cathodic control, anode to cathode area ratio greatly effects galvanic corrosion. It is known that a larger cathode to anode ratio results in larger corrosion current on the anodic material.[18] Other geometric factors that play an important role is the crevice width and crevice length. Pickering used the scaling law $\frac{L^2}{G}$, where L is the crevice depth and G is the crevice width governed by IR mechanism. [72] The effect of external cathode has been reported to effect the corrosion rate of a galvanic couple as well. Chen showed the size of the external cathode outside of the crevice limits the extent of corrosion inside the crevice. [73] Pryor found that when the distance between the anode and cathode is small compared to the dimension of the electrode, that galvanic corrosion is small due to the limitation of the mass transport and reaction products. [68] However, very few studies have investigated how the gap width can affect the current distribution and furthermore, the damage morphology.

Moreover, many studies have shown the importance of wetting and drying in atmospheric corrosion. [74,75] Mansfeld provided insights into the rates of corrosion during the various parts of the wetting and drying cycle.[76] On a dry metal surface, the RH increases and the corrosion rate initially rises, then decreases to a constant value. On initial wetting, the corrosion rate increases rapidly as accumulated surface salts first dissolve, then the corrosion rate decreases as the surface electrolyte dilutes with continued wetting. During drying, the corrosion increases significantly due to the increase of ionic activity as the surface electrolyte concentrates and also due to the reduced diffusion layer thickness for oxygen transport as the condensed phases becomes thinner. However, eventually once the ionic strength of the electrolyte becomes very high and salts begin to crystalize, the corrosion rate decreases. [77-81] Stratmann experimentally investigated the wet dry cycle of steel and divided the cycle into three steps. During wetting, the anodic dissolution of wetting is mainly balanced by the reduction of the ferric species within the rust layer and very little oxygen is reduced. The second stage, wet stage, is characterized by oxygen reducing as the major cathodic site. At the end of the third stage, drying, the species reduced during the wetting stage and other ferrous compounds produced by the corrosion processes are reoxidized by oxygen. Lastly, the electrolyte film evaporates slowing down the electrochemical corrosion. The corrosion rate and the rust layer modifications were found to be correlated to the number and frequency of the wet dry cycles. [82,83]

Marine environments typically have a high percent of relative humidity. When salts are deposited on a metal surface deliquesce can lead to wetting at a very low % RH. [74,75,84] $MgCl_2$ on the surface of Al can wet at 34 % RH while NaCl requires 77 % RH to achieve deliquesce. [85]. At high % RH the salt concentration equilibrates at a lower salt concentration and a thicker water later due to the significant amount of water in air. At a lower % RH, salts become concentrated but the electrolyte layer is thinner. Variation in the thickness of the electrolyte can affect the current and potential distribution.

1.2.9 Corrosion Fatigue in Aerospace Aluminum Alloys

Interaction of corrosion damage and cyclic loading is an extremely pertinent issue for aerospace structural integrity. Many studies have been conducted to understand the strong deleterious effect of pre-existing corrosion damage on the fatigue behavior of aerospace alloy.[1,3-7,28,29,86-93] In a study by Burns indicated that following a sharp initial degradation that the total fatigue life becomes independent of the corrosion exposure time.[5] The degraded fatigue behavior is attributed to a reduction in the crack formation life as well as the increased crack tip driving forces, which is due to increased local stresses/strains associated with corrosion morphologies. [94-96]It has been elucidated that the effects of internal H pre-charged during the corrosion process on crack propagation was dominated by environmental H production during cycling in a humid environment. Many researchers have proposed different approaches of stress/strain life of corrosion induced fatigue including probability based life predicting approaches[97], linear elastic fracture mechanics based approaches[98,99], pit to crack transition approaches[4,6,88] and total life approaches.[4,88,100] It has been reporting that corrosion fatigue occurs in 4 stages (1) formation of corrosion damage (2) initiation of cracks from corrosion damage (3) small crack growth influenced by local corrosion and microstructure and (4) long crack growth that is described by continuum approaches.[101,102] However, there are several assumptions that have been made inherent to these findings (1) the pit is treated as a crack and therefore crack formation life is not accounted for (2) crack extension occurs around the entire periphery of the pit and (3) interaction between the corrosion progression and fatigue are decoupled.[3,5,28,89]

Studies have been conducted to understand that the corrosion morphology can lead to changes in the mechanisms that govern crack formation.[3-5,29,89,90] Work has been conducted to correlate corrosion features with fatigue crack formation sites. Burns found that the total fatigue life becomes independent on the corrosion exposure times after a sharp initiation derogation.[5] Furthermore, Turnbull analyzed the pit-to-crack transition involving smooth pits in turbine steel and found that the macro scale stress states governed the location of fatigue initiation[103] while Burns reported micro-topographical features associated with the pit in aluminum alloys tend to dominate the location of fatigue initiation sites.[5]

The influence of microstructurally small crack growth rates have reported.[104-106] A stud reported that high initial fatigue crack growth rate is AA 7075-T6 is due to the zone of influence of the pit precursor having locally high plastic strains coupled with subsurface constituent interaction [107]. The growth rate of the microstructurally small crack was found to fluctuate as it moved away from the corrosion damage as it encounters barriers such as grain boundaries and secondary phase particles. While microstructurally small crack complexities have been recognized the effect of the local stress gradient has not been investigated.

1.2.10 Stainless Steel 316 Fasteners

Stainless steel fasteners are often used in the aerospace industry due to their higher resistance to corrosion attributed to the formation of a passive oxide film. In general, corrosion resistance of stainless steel in marine environments is determined by alloying element sand environment. The most beneficial alloying element is chromium and the most harmful factor is chloride ion. The OCP of stainless steel is higher than that of low carbon steel providing a higher driving force for galvanic corrosion with aluminum alloys. [108]

1.2.11 Atmospheric Corrosion of Aerospace Aluminum Alloys

Atmospheric corrosion conditions vary from bulk solution and is one of the most widely spread form of corrosion. [109] As thickness in the electrolyte layer affects (1) mass transport of dissolved oxygen (2) accumulation of corrosion product and (3) the hydration of dissolved metal ions. Therefore the thickness of the electrolyte can have a significant role in atmospheric corrosion. Atmospheric corrosion in general is not a continuous process due to the existence of wet/dry cycles when diurnal changes occur in temperature and relative humidity. Tomashov modeled atmospheric corrosion of metals provided a theory on the dependence of electrolyte layer thickness and the corrosion rate of metals. [110] His theory distinguished the thickness of electrolyte layer on metals in 4 regions (1) dry atmospheric corrosion (WL < 10 nm) (2) humid atmospheric corrosion (10 nm < WL < 1 µm) (3) wet atmospheric corrosion (1µm < WL < 1 mm) and (4) complete immersion (WL > 1mm). He determined the corrosion rate would be the lowest in region 1 as adsorbed water molecules hinders a continuous water layer. In humid conditions the corrosion rate is limited by anodic kinetics and the reduction in WL results in the decrease in corrosion rate due to the lack of water molecules needed for dissolving metal ions. In wet atmospheric conditions, a thinner water layer led to a higher corrosion rate due to increase oxygen transport through the layer. [110]

Electrochemical studies of corrosion in thin film electrolytes have been investigated previously. [111-115] However, there has been a lack of fundamental work due to errors in electrochemical measurements of corrosion rates that arise from the ohmic drop between the reference and working electrodes and ensuring an even current distribution over the working electrolyte. [114,116] Conventional methods using a luggin probe changes the thickness and composition of the electrolyte film. [117]

1.2.12 Corrosion Protection of Heat Treatable Aluminum Alloys

Many methods of corrosion protection of precipitation age hardened have been developed to mitigate the corrosion susceptibility of these alloys. [60,118-127] Passive protection methods involved either thickening a barrier oxide film on the surface of the metal or applying a barrier organic polymer to the metal surface prior to service. Active protection method possess the capability to protect the substrate even after a defect has formed and penetrated the barrier layer. Ionic inhibitors released from coatings and pretreatments is a key approach. Most chemical inhibitors, such as chromate, function by promoting the formation of a passive film or deposit later on the metal surface. The formation of the passivizing film on the surface serves to increase the pitting potential of the material while a passivating film covering constituent particles lower the galvanic driving force between constituent corrosion and the matrix. Other chemical inhibitors such as vanadates function by formation a layer of adsorbed anionic species where reduce the oxygen reduction reaction kinetics and may also displace Cl- ions in the Al matrix which increases the stability of the passive film as well as reduces *S* phase particles. [128] Hexavalent chromates have been reported as one of the most effective chemical species used to mitigation corrosion in aluminum alloys.[60,118,121,123-125,127,129] Chromate is an oxidizing inhibitor and produces a protective film of mixed oxide of chromium and aluminum oxides on the surface of the aluminum inhibitor. Chromate is found to be an anodic and cathodic inhibitor. [125] Hexavalent chromium is commonly incorporated in pretreatments, conversion coatings and as a soluble pigment in organic polymer primers within coating systems where it is actively leached to provide protection by inhibitor transport to a coating defect when it occurs in service. [130] Due to their low weights, high efficacy, and ease of application, hexavalent chromium containing conversion coating or organic polymer paints are the primary active protection method utilized in aerospace application.

1.3 Critical Unresolved Issues

- The effects on corrosion of macro and micro-potential profiles have all been considered in isolation in aluminum alloys but the pertinent combinations applicable to service-like conditions are lacking. It could be expected that pitting under mass transport control might prevail at high potentials while constituent particle driven anodic attack prevails at intermediate potentials and cathodic trenching may take over at cathodic potentials. These effects have not been elucidated but likely affect corrosion damage morphology and the pit to crack transition.

- Constituent phase, grain boundary and matrix electrochemistry has been thoroughly investigated to provide an electrochemical framework for corrosion in precipitation hardened aluminum alloys. These investigations range from IMC rankings to justification for anodic paths on grain boundaries based on favored anodic dissolution rates and threshold potentials, but otherwise cannot be used alone to predict intragranular damage shape evolution affecting the pit to crack transitions.
- Traditional electrochemical methods to assess corrosion under droplets or thin electrolytes have been a challenge due to difficulties associated the ohmic drop between the reference and working electrode and ensuring an even current distribution over the working electrolyte.
- Inhibitor effects on corrosion development when damage moves beyond the surface has only been considered in a few cases.

1.4 Objectives of Research

The overall objectives of this work are to (1) investigate the electrochemical, microstructural, and physical factors that govern galvanic corrosion pit morphology development at the macro, meso, micro and nano length scales under conditions representative of galvanic coupling between a rivet and plate in an aerospace structure (2) explore and compare various laboratory simulated damage modes to field damage in order to guide choice of methods to simulate field damage in fatigue tests (3) develop an electrochemical-materials based framework to explain the observed galvanic corrosion morphology developed for various physical geometries (4) understand the source and impacts of various cathodic reaction sites and materials and (5) extend these findings to further understand the effect of an inhibitor such as chromate on galvanic corrosion damage evolution.

1.5 Thesis Organization

This thesis is organized by these needs, gaps and critical issues pertaining to the localized galvanic corrosion of AA7050-T7451 and Type 316 stainless steel fasteners in marine environments.

Chapter 2 uses *operando* characterization of local galvanic corrosion morphology development using x-ray tomography of a simulated fastener. This chapter examines the macro location and number of damage sites formed along with meso scale galvanic corrosion morphologies that develop under conditions representative of galvanic coupling between a rivet and plate in an aerospace structure. Synchrotron XCT was used to track in 3D in-situ or operando corrosion damage evolution in a simulated rivet geometry. These measurements enabled analysis of corrosion as a function of macro-scale (e.g. rivet geometry) and meso-scale factors (e.g. spacing and size of constituent particles). A combination of electrochemical techniques was used to simulate the damage assessed. As the volume lost to corrosion was tracked and equated to anodic charge, the analysis presented a unique opportunity to quantify which cathode reaction rates were potent to contribute to the damage morphology. A further understanding of the sources of cathodic reactions which account for electrochemical galvanic corrosion damage was discussed in this chapter.

Chapter 3 combines characterizing the macro scale corrosion damage morphology and developing diagnostic lab based galvanic corrosion testing methods and protocols when AA 7050-T7451 is coupled with a stainless steel fastener. This chapter focuses on damage morphology in environments typically observed in crevices and rivets. Different corrosion morphologies are possible depending on the local chemistry, pH, physical and metallurgical factors and potential distribution and chapter 2 will rigorously characterize the macro damage with respect to these factors that may have an effect on the damage morphology. Lab based electrochemical corrosion methods were applied to AA7050-T7451 coupons over a range of relevant potentials and chemical variables to develop a library of damage modes. These methods were also compared to simulated fastener damage in *operando* and service teardown. While this chapter characterizes the damage morphology Chapter 4 will explain it.

Chapter 4 will focus on micro and nano scale factors that affect the corrosion damage progression by examining the various microstructural and nanostructural zones. Differences in corrosion electrochemistry of the different phases and solute depleted zones were rationalized to explain the intergranular and intragranular path. AA7050-T7451 is made up of many different regions with a variety of compositions. This includes the matrix, constituent particles, solute depleted zones and precipitate free zones and each of these regions has a different chemical composition and different critical potentials. This chapter develops an electrochemical framework explaining these various damage modes that occur in rivet specific environments Transmission electron microscopy (TEM) was used to characterize the various zones and phases in the microstructure near the grain boundaries and electron backscatter scanning microscopy (EBSD) to characterize the anodic sites and pathways associated with the damage morphologies observed relative to the microstructure.

In Chapter 5, galvanic current interactions and cathodic and anodic reaction rate measurements under droplets and thin films were conducted using coupled multi-electrode arrays (CMEAs) constructed of AA7050-T7451 and Type 316 stainless steel. The key advantage of the CMEA technique is that multiple electrochemical measurements are taken concurrently and instantaneously, enabling the measurement of real-time local corrosion processes that take place on an electrode surface. Two types of CMEAS were constructed in this work (1) a geometric fastener CMEA and (2) CMEAs in combination with a sintered Ag/AgCl used as both the reference and counter electrodes. This was done in an effort to determine current distribution in an instrument fastener and to develop a method to interrogate ORR cathodic and anodic kinetics under thin films and droplets. The cathode capacity of AA7050-T7451 and Cu-replating was discussed in this chapter.

In Chapter 6, the impact of soluble chromate as an inhibitor in solution on the electrochemical behavior and damage morphology of AA7050-T7451 and Type 316 stainless steel was investigated. Diagnostic full immersion, potentiodynamic, zero resistance ammeter and potentiostatic polarization were utilized in an effort to determine electrochemical behavior and furthermore, characterization of the damage morphology using 2D and 3D methods. The effect of chromate as an inhibitor and differences in damage morphologies observed were discussed in this chapter.

Chapter 7 presents the conclusions and key highlights relevant to utilizing AA7050-T7451 and Type 316 stainless steel in service conditions. Remaining questions and discussion of ongoing and future work are also detailed.

1.6 Research Questions

<u>Chapter 2: Operando Assessment of Corrosion Damage of Galvanic Coupling using XCT</u>

- How can corrosion damage in a rivet hole be characterized in 3D in a non-destructive manner?
- Can the macro scale damage location sites be rationalized and the number of corrosion sites inside a rivet hole using SS 316 and AA7050 be ascertained? Are multiple sites propagating at the same time?
- What cathodic reaction supporting substrates are potent enough to kinetically provide a galvanic driving force when AA7050-T7451 is coupled to SS 316 to provide the cathodic reaction rates and charge that can support the anodic corrosion charge and thereby account for the damage observed?

<u>Chapter 3: Meso-scale Damage Morphologies in Rivet Environments</u>

- What are the meso-scale damage shape evolution and morphologies observed in different environments for AA7050-T7451?
- What is the effect of NaCl compared to $MgCl_2$ on the meso and macro scale corrosion morphology of AA 7050-T7451 when coupled to stainless steel?
- What is the effect of other selected environmental variables such as pH and Al concentration in solution on the macro and meso scale galvanic corrosion of AA7050-T7451 coupled with stainless steel?
- What laboratory simulated electrochemical methods and simulated crevice environments produce damage morphologies that best reproduces field damage modes?

<u>Chapter 4: Micro- and nano-scale Corrosion Effects on Morphology and Pathways</u>

- What does the micro/nano structure of AA7050 in the T7451 entail?
- What micro/nano structural factors govern the development of pits, fissures and IGC in neural, acidic and alkaline environments?
- How can these three damage modes be explained using the electrochemical framework for various microstructural zones of AA7050-T7451 such as intermetallic particles, grain boundary solute zones such as Mg(Al,Cu,Zn) alloys and AA7050-SHT and overaged, with Cu, Zn, Mg solute or depleted zones?
- How does grain orientation and grain boundary angle affect the damage morphology?
- Are recrystallized or unrecrystallized grains favored or correlated to the damage morphologies?

Chapter 5: Atmospheric Corrosion effects on AA7050-T7451 using CMEAs

- How can the effects of atmospheric conditions be considered? Furthermore how doe atmospheric conditions relate to fill immersion techniques?
- What is the effect of atmospheric conditions such as thin films, droplets and wet/dry cycling on galvanic current interactions?
- What is the effect of droplet/thin film geometry on the galvanic corrosion?
- How does Cu-replating effect the ORR cathodic reaction rates?
- How does the galvanic coupling of AA705-T7451 to 316 SS effect the anodic corrosion sites as a function of position?
- What cathode capacity does the AA7050-T7451 hold when coupled to SS 316?
- How can this information be used to guide mitigation strategies?

Chapter 6: Effect of Chromate on Galvanic Corrosion Electrochemistry and Damage

- What is the effect of chromate inhibitor on the galvanic corrosion of AA7050-T7451?
- What is the resulting damage morphology when using chromate as an inhibitor on AA7050-T7451?
- What is the effect of chromate on Cu-replating, 316 SS and other possible cathodic reactions?
- What is the effect of chromate on pitting potential of AA7050-T7451?

1.7 Tables

Table 1.1 Summary of crevice corrosion stages 2-4 for the inside and outside of a crevice

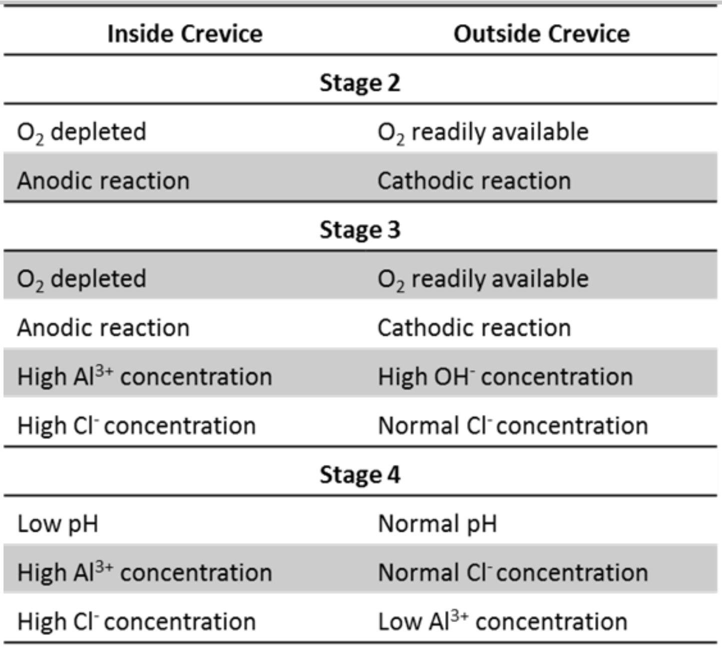

Inside Crevice	Outside Crevice
Stage 2	
O_2 depleted	O_2 readily available
Anodic reaction	Cathodic reaction
Stage 3	
O_2 depleted	O_2 readily available
Anodic reaction	Cathodic reaction
High Al^{3+} concentration	High OH^- concentration
High Cl^- concentration	Normal Cl^- concentration
Stage 4	
Low pH	Normal pH
High Al^{3+} concentration	Normal Cl^- concentration
High Cl^- concentration	Low Al^{3+} concentration

Table 1.2. Secondary phases found in AA7050 and the OCP values and electrochemical effects.

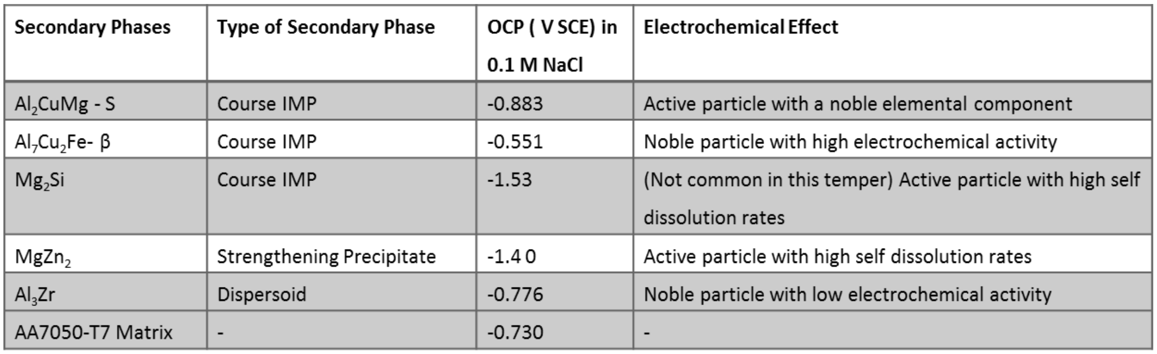

Secondary Phases	Type of Secondary Phase	OCP (V SCE) in 0.1 M NaCl	Electrochemical Effect
Al_2CuMg - S	Course IMP	-0.883	Active particle with a noble elemental component
Al_7Cu_2Fe- β	Course IMP	-0.551	Noble particle with high electrochemical activity
Mg_2Si	Course IMP	-1.53	(Not common in this temper) Active particle with high self dissolution rates
$MgZn_2$	Strengthening Precipitate	-1.4 0	Active particle with high self dissolution rates
Al_3Zr	Dispersoid	-0.776	Noble particle with low electrochemical activity
AA7050-T7 Matrix	-	-0.730	-

1.8 Figures

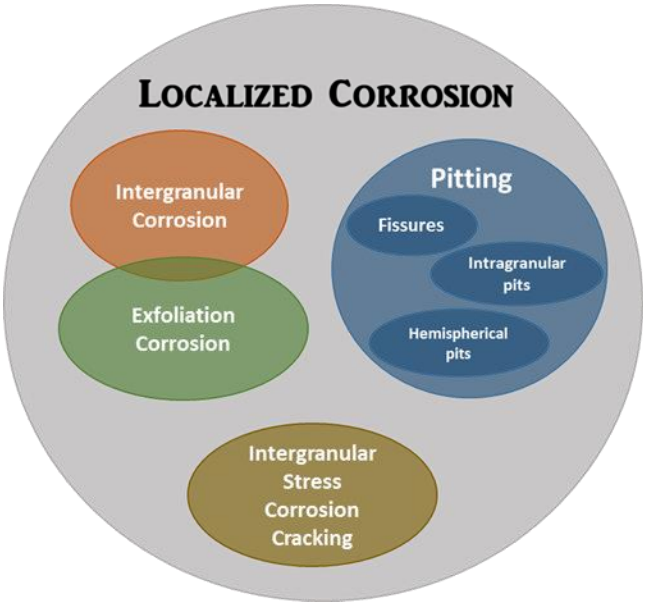

Figure 1.1. Venn diagram showing the different forms of localized corrosion observed in this work.

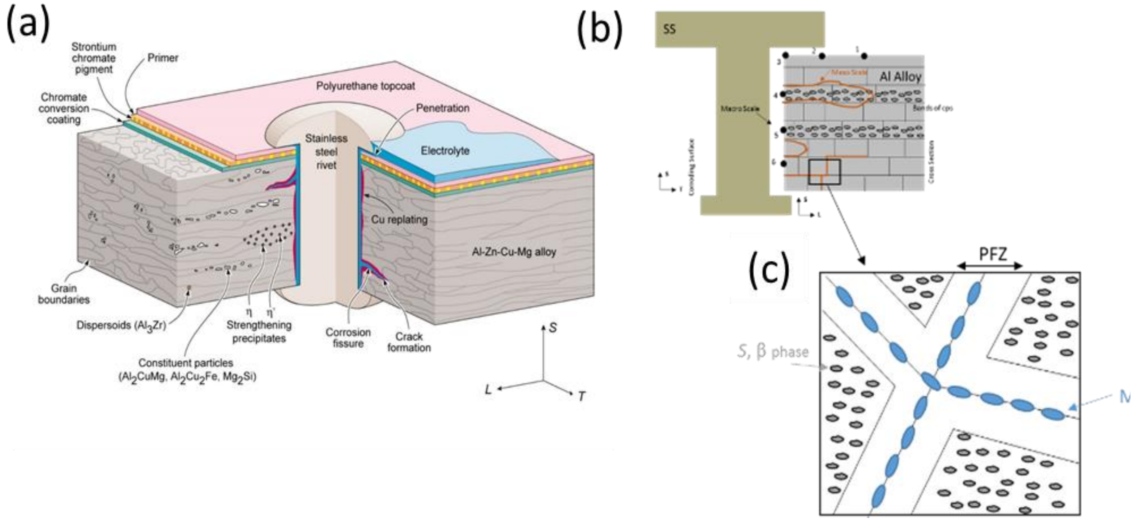

Figure 1.2. Schematic showing (a) fastener configuration of AA7050 coupled to SS 316 (b) macro and meso scale corrosion (c) micro and nano scale microstructure of AA7050-T7451, including the constituent particles, η phase and the precipitate free zone (PFZ).

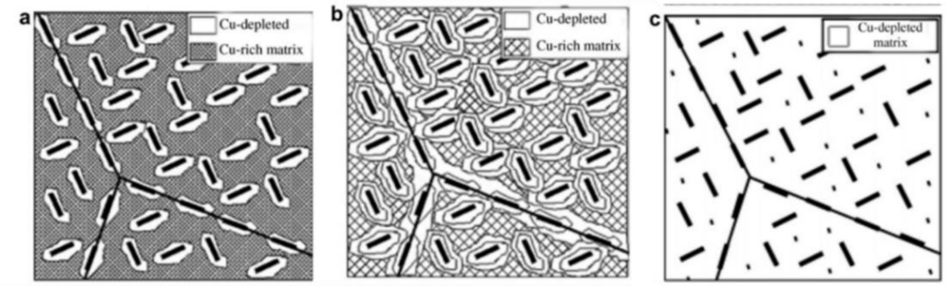

Figure 1.3. Schematic of solute depletion around plate-shaped Cu-bearing precipitates along grain boundaries and in the matrix. (a) Shows an under-aged condition where the boundary has the heaviest concentration difference between Cu-depleted zones and the supersaturated matrix (highest Cu in matrix). (b) Represents a peak-aged or slightly over-aged condition where the Cu depletion zones around Cu-containing precipitates begin to overlap with each other not only at the boundaries but also in the matrix (lower Cu in matrix). This leads to an overall lowering of the global Cu content in solid solution in the matrix. (c) Represents a schematic of the Cu-depleted matrix that would be associated with an extremely over-aged condition (lowest Cu in matrix). The preferential Cu depleted path along grain boundaries is eliminated. With the long aging times more nanoscale precipitates will form although not accurately depicted. (Figure taken from Little and Scully.

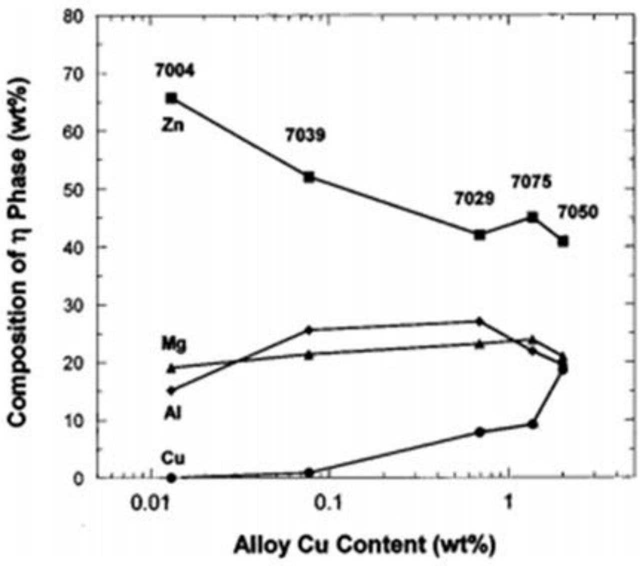

Figure 1.4. Composition of $MgZn_2$ η phase precipitate on grain boundaries as a function of alloy Cu content in 7000 series T6 of various 7xxx alloys

2 Operando Assessment of Galvanic Corrosion between Al-Zn-Mg-Cu Alloy and a Stainless Steel Fastener Using X-ray Tomography

Three Manuscripts based on this Chapter have been published:

1. V.N. Rafla, A.D. King, S. Glanvill, A. Davenport, and J.R. Scully, "Operando Assessment of Galvanic Corrosion Between Al-Zn-Mg-Cu Alloy and a Stainless Steel Fastener Using X-ray Tomography," Corrosion (2017).
2. V. Rafla, A.D. King, S. Glanvill, A. Parsons, A.J. Davenport, and J.R. Scully, "Operando Observation of Galvanic Corrosion between AA7050-T7451 and 304 Stainless Steel in a Simulated Fastener Arrangement using X-ray Tomography," Corrosion (2015).
3. V. Rafla, A. Davenport, and J.R. Scully, "Determination of Cathodic and Anodic Charge from Operando X-Ray Tomography Observation of Galvanic Corrosion of Aluminum Alloy 7050-T7451

2.1 Abstract

Operando X-ray tomography was used to study the galvanic corrosion between aluminum alloy 7050-T7451 and 304 stainless steel using a simulated fastener covered with droplets of either 4 M NaCl or 2 M $MgCl_2$. The simulated rivet was an X-ray transparent cylindrical 1 mm pin with a 250 µm diameter rivet hole in the center. The rivet hole was embedded with a 500 µm, in length, stainless steel wire. The rivet hole formed an alkaline crevice between the stainless steel and AA 7050-T7451 owing to the proximity of anodic and cathodic sites. The X-ray tomography indicated that multiple corrosion fissures propagated over the galvanic couple potential range at all depths examined suggesting the presence of multiple strong proximate cathodes. The volume loss was converted to anodic charge using Faraday's Law. The cathodic reactions occurring at a high enough rate to support the growth of these fissures were found to be the stainless steel fastener, Cu-replating on the AA 7050-T7451 surface and dealloyed S phase. Moreover, removal of the stainless steel fastener stifled fissure growth. The damage morphology assessed with X-ray tomography was compared to laboratory produced accelerated exposures as well as field data and were found to have similar morphologies.

2.2 Introduction

Al alloy 7050 (Al-Zn (6.7% wt)-Cu (2.6% wt)- Mg(2.6% wt) was developed to obtain a combination of strength and fracture toughness resistance greater than that provided by other common high strength alloys such as 7075.[10] AA 7050-T7451 is precipitate strengthened by the formation of $MgZn_2$-η phase in the reaction sequence.[14,32,34,44,47]

Solid Solution α → Guinier Preston (GP) Zones → Metastable η' →Stable η $MgZn_2$

Precipitates form by nucleation and growth from a supersaturated solid solution during natural or low temperature aging. The η phase is highly soluble in the matrix and will readily dissolve during homogenization.[3] In the partially recrystallized and artificially aged microstructure, η and η' are usually found on high angle and subgrain boundaries, respectively.[35,38,131] Tempering has a significant effect on the microstructure of Al alloys.[37-39] In 7xxx series alloys, the T6 temper reaches peak strength, but possesses poor stress corrosion cracking (SCC) resistance, due to a high density of GP zones and the formation of η' precipitates along grain boundaries. Overaging treatments, such as the T73 and T76 tempers, improve the short transverse SCC resistance by increasing grain boundary precipitate size, spacing, and by modifying their composition. However, these tempers result in a loss of strength.[36] Aging can also effect the Cu content in these Al alloys. Overaging can result in higher Cu content on grain boundary precipitates such as η, producing a Cu-depleted zone which can facilitate intergranular corrosion (IGC) and SCC.[27] The T7 (overaged) condition results in an increase in the amount, coarseness and distribution of η precipitates on the grain boundaries.[37] The T7451 temper is achieved by solution heat-treating, stress-relieving through controlled stretching, and artificially overaging the alloy between T73 and T76.[38] The T7451 temper provides an advantageous combination of strength, SCC, general corrosion resistance and fracture toughness.[39,40]

AA 7050-T7451 contains coarse constituent particles, strengthening precipitates and dispersoids. Coarse constituent particles in the range of 5-30 µm in diameter (S-Al_2CuMg, β-Al_7Cu_2Fe, and Mg_2Si) form during solidification and are often found in clusters or stringers aligned parallel to the rolling axis. Dispersoids (Al_3Zr) form during homogenization, control recrystallization and occur at temperatures above the Al-solidus.[41] Dispersoids pin grain boundaries, preventing them from growing during solution heat treatment (SHT). Additionally, they act as a noble particle that will not sustain large cathodic currents and may be too small to adversely impact corrosion kinetics.[23] Contrastingly, coarse constituent particles can greatly influence the corrosion properties of these alloys. Alloying with Fe and Si can have strong detrimental influences on fracture toughness and corrosion properties due to the formation of brittle constituents such as S-Al_2CuMg and β-Al_7Cu_2Fe.[26,42,43] These constituent particles are often located in recrystallized grains or at their grain boundaries and can lead to dealloying of the particle leading to localized Cu enrichment.[44,45] $MgZn_2$ and Mg_2Si are both active particles with high self-dissolution rates which leave behind surface cavities.[33,46] $MgZn_2$ greatly affects the corrosion properties of AA 7050-T7451 as the IMP is very active: the open circuit potential (OCP) is -1.4 V SCE and the breakdown potential is -1.14 V SCE in neutral 0.5 M NaCl.[44]

The effect of Cu content on the microstructure corrosion has been well documented.[27,32,44,45,55,56] Cu is distributed throughout the microstructure in different ways: (1) in the Al matrix, (2) in hardening precipitates (η phase), and (3) in coarse constituent particles such as S-Al_2CuMg. A Cu-containing 7xxx series alloy will exhibit coarser, more widely spaced η particles at grain boundaries as compared to an Al-Zn-Mg alloy.[57] The growth rate of the η phase was shown to be higher in Cu-containing alloys.[58] Cu increases the GP zone solvus from 120°C to 160°C, resulting in homogeneous precipitation at aging temperatures above 149˚C for a Cu content of 1.4 wt%.[59] It has been observed that $MgZn_2$ can become enriched with highly soluble Cu and Al, locally depleting the matrix of Zn, Mg, and Cu. In particular, the T6 temper[31], was found to increase the corrosion potential by about 250 mV with 17 at % Cu enrichment in η phase.[27,32.] The presence of S-Al_2CuMg is common in AA 7050-T7451 due to its increased Mg and Cu content. *S* is initially anodic to the AA 7050-T7451 matrix but, after dealloying occurs, the Cu remnants become high surface area cathodes for oxygen reduction.[60]

Cu-replating on the surface of the Al alloy can greatly impact corrosion properties of the alloy substrate.[18,30,32,63] Cu may become oxidized and made available for plating by a number of pathways. For instance, if Cu particles become mechanically detached, they can dissolve at their own corrosion potential in solution and electrochemically replate on the alloy surface.[33,45,61,62] The alloy Cu content is important since the composition of the bulk matrix, depleted zones, and η precipitates change with aging time. This decreases the electrochemical potential window between $Mg(Cu)Zn_2$ dissolution and the matrix pitting potential. This decrease in the potential window decreases IGC and exfoliation susceptibility.[32] Overall, Cu plays a complex role, lowering IGSCC susceptibility while raising that for general corrosion. Moreover, Cu's effect on fissure growth is unclear. Dissolution of Cu-rich phases may leave a Cu-rich surface that is cathodic to the matrix[33], increasing general and local corrosion by providing a site that supports fissure growth.[12] As such, 7xxx series Al alloys are typically protected with a multifaceted coating system. [123,132]

Defects in the corrosion protection system are common due to the harsh-environment operating conditions of aircraft applications. This is enhanced at complex joining/fastener locations that trap electrolyte into tight crevices. The geometry leads to occluded local environment formations where a galvanic cell is established between an Al alloy plate and a high strength steel fastener.[12] While the danger of galvanic corrosion has been recognized, little work has been done to assess the extent of corrosion damage and to characterize the damage morphology of AA 7050-T7451 and stainless steel at rivet sites.[11,133] Significant previous work has investigated the localized corrosion of high strength Al alloys and developed an electrochemical framework for IGC attack. However, there is a dearth of literature concerning the unique factors and environments present in a rivet hole and how they can influence the overall damage morphology.[3,10,12-15] Previous work is limited to the study of damage morphologies in only a few specific test environments, namely: Point Judith marine seacoast atmospheric exposures[134], full immersion in 0.6 M NaCl[15], EXCO solution[16] and 0.6 M NaCl + H_2O_2.[17] There have been very few detailed investigations into crevice and rivet environments formed in marine atmosphere solutions.

Literature has shown that galvanically induced localized corrosion in Al alloys can be strongly influenced by environmental parameters such as pH, chemical species, and concentration.[66-68] The depletion of dissolved oxygen inside a crevice initially results in the formation of a differential aeration cell. Metal ions accumulate in the crevice solution as a result of anodic dissolution, and acidification follows with their subsequent hydrolysis. Then, a corresponding migration of chloride ions into the crevice occurs in order to preserve electroneutrality. The primary cathodic reaction occurs outside the crevice while hydrogen gas reduction evolves inside the crevice solution.[19,20] Cottis reported variable behavior where the pH appeared acidic near the crevice mouth and alkaline in the deeper region of a crevice on AA 7475.[126] The mechanism of alkalization was deemed unknown. However, it can be speculated that, as the anode and cathode lack anodic and cathodic separation, there is greater OH^- production by the cathodic reaction than H^+ by hydrolysis. In the case of crevice corrosion in dissimilar metal rivets, the local cathode supports cathodic reactions throughout crevice lengths. This can affect the pH gradient and differs from conventional crevice corrosion where the cathode is located only (or primarily) outside the crevice.

A final important aspect of crevice corrosion in a rivet hole is the damage morphology. Corrosion damage in an Al crevice is typically assessed by metallographic cross section and imaging. However, this process is destructive and time consuming. Moreover, using this process, it may be difficult to assess whether damage sites existed simultaneously or initiated separately. The pathway of damage sites relative to the microstructure is also not well-discerned using this method. The corrosion volume and oxidation charge can be determined from the area fraction, enabling qualitative investigation of cathodes. Synchrotron X-ray computed tomography (XCT) is a non-destructive technique which enables three-dimensional (3D) analysis of microstructural defects and corrosion damage volume at the micrometer length scale.[89,91,135-140] The technique is based on the differences in absorption coefficients of the materials along the path of transmission X-ray beams through the sample. The absorption coefficient is correlated to atomic number, enabling easy differentiation of different materials and phases.[141] Three-dimensional analysis is generated by acquiring many 2D micrographs while rotating 180˚ to create a 3D volume.[91]

While laboratory XCT has been used previously to study IGC rates in Al alloys,[91,136,142] the resolution was not high enough to characterize corrosion propagation paths.[143] In recent years, there have been studies using synchrotron radiation XCT to investigate localized corrosion.[91,144] Knight previously used synchrotron XCT to examine IGC of bare Al alloys 7050 and 2024, with no dissimilar metal couple, in service-like conditions and showed that the growth of one fissure was constrained by that of another fissure.[142] Ghahari also utilized XCT to investigate pitting corrosion in stainless steel under different applied currents and potentials,[145] while Davenport correlated the distribution of Y in a Mg alloy with corrosion propagation.[146] These studies have been contributory in demonstrating the effectiveness of XCT to analyze corrosion morphology. However, XCT has rarely been applied to the galvanic corrosion damage assessment between an Al alloy and stainless steel in a tight crevice.

2.2.1 Objective

The objective of this study was to examine the macro location and number of damage sites formed and the meso scale galvanic corrosion morphologies that develop under conditions representative of galvanic coupling between a rivet and plate in an aerospace structure. Synchrotron XCT was used to track corrosion damage evolution in a simulated rivet geometry in 3D *in-situ* or *operando*. These measurements enabled analysis of corrosion as a function of macro-scale (e.g. rivet geometry) and meso-scale factors (e.g. spacing and size of constituent particles). A combination of electrochemical techniques was used to simulate the damage assessed. The volume lost to corrosion was tracked and equated to anodic charge presenting a unique opportunity to quantify the key cathodic reaction rates and identify which and, to what extent, contributed to the damage morphology. As such, a further understanding of the sources of cathodic reactions that account for electrochemical galvanic corrosion damage is obtained. Subsequent studies on inhibiting cathodic sites might be guided by these findings.

2.2.2 Hypothesis

Previous work on bare AA7050 with no stainless steel fasteners showed that the growth of corrosion fissures were by limited to one corrosion fissure growing at a time.[142] Based on preliminary results, it is hypothesized that when AA7050-T7451 is coupled with Type 316 stainless steel corrosion will not be cathodically limited and multiple sites may propagate over the time of the exposure. Moreover, it is hypothesized that cu-replating may be a primary cathode in the presence of a SS fastener, supplying sites for ORR to occur readily.

2.3 Experimental Methods

2.3.1 Materials

The material used in this study was machined from Al-Zn-Mg-Cu alloy plate (AA 7050-T74511) 50 mm in thickness from the LT surface with the rivet hole in the LT plane and long axis parallel to the S orientation. A stainless steel 304 wire was embedded into the plate, simulating a rivet. A 3D rivet schematic with grain structure and orientation is shown in Figure 2.1. The microstructure of AA 7050-T7451 has elongated grains in both the longitudinal (L) and long transverse (T) direction and are thinned in the short transverse (S) forming pancake-like microstructure. The grains range from 22-1250 µm, 15-265 µm, and 12-112 µm in the L, T and S directions, respectively. Aspect ratio, width over length, was determined to be 0.07, 0.51 and 1.41in the L, T and S directions, respectively.

Stainless steel 304 was used in the *operando* XCT exposures and stainless steel 316 was used in the pH measurement studies and cathodic reaction rate studies conducted in the laboratory. The cathodic reaction rates of stainless steel 304 and 316 are found to be nearly identical. The composition of these materials are shown in Table 2.1.

2.3.2 Material Characterization

The grain structure, particle size and spacing of AA 7050-T7451 was analyzed and is discussed below. Particle analysis was conducted using micrographs obtained with a JEOL JSM-6700F scanning electron microscope (SEM). These images had sufficient contrast to allow constituent particles to be distinguishable. The threshold was adjusted so that the particles appeared black and the background appeared white. ImageJ[147] was used to calculate the size of the particle. The grain structure of the alloy was revealed by exposing samples to Keller's etchant which was made up of 190 mL DI water, 5 mL nitric acid, 3 mL hydrochloric acid and 2 mL of hydrofluoric acid. The samples were etched for 25 seconds to reveal the grain structure of the alloy in the SL, TS and LT orientations.

2.3.3 Simulated Fastener Geometry and Corrosion Conditions

The X-ray fastener geometry was a 1 mm diameter cylindrical AA 7050-T7451 pin with a 250 µm rivet hole embedded with a 304 stainless steel wire. The rivet hole was 500 µm deep. The gaps between the stainless steel wire and the AA 7050-T7451 varied from 1 µm to 50 µm, depending on the 360° location and the tilt of the pin. The area ratio inside the hole of AA 7050-T7451 to stainless steel was 0.89:0.87. The entire pin was encapsulated with a plastic tube that contained filter paper with saturated potassium sulfate (K_2SO_4) controlling the relative humidity to approximately 98%. The plastic was sealed with an Al stopper at the top. A schematic of the simulated fastener is shown in Figure 2.2. Two pin samples with two different solutions were tested *in operando*, a 0.4 µL droplet of 4.0 M NaCl or 2.0 M $MgCl_2$ were placed on the surface on the pin. The electrolyte concentrations of the droplet on the surface of the pin equilibrated to the droplet's equilibrium concentration of 0.5 M NaCl and 0.5 M $MgCl_2$ at 98% RH.

2.3.4 Electrochemical Polarization of the Constituent Phases of AA 7050-T7451 Coupled to Stainless Steel and pH Measurements inside the Crevice

Potentiodynamic and potentiostatic polarization were conducted in simulated rivet environments to observe the anodic and cathodic electrochemical behavior of AA 7050-T7451, the constituent phases of the alloy (Al_2CuMg, Al_7Cu_2Fe, $MgZn_2$), stainless steel 316, pure Cu and Cu-replated on AA 7050-T7451. The solutions used were simulated rivet solutions of 0.5 M NaCl, pH 5.5; 0.5 M $MgCl_2$, pH 5; and 0.5 M NaCl + $NaAlO_2$, pH 8. These environments were chosen to best represent different regions in a macro-crevice where acidified pH may not exist because of the lack of anode and cathode separation. Electrochemical testing was performed using a three-electrode cell with a platinum mesh counter electrode and a saturated calomel reference electrode (SCE). Hydrogen gas was collected using an electrolyte filled burette with an inverted funnel attached centered over the sample. The samples were exposed through a 1 cm^2 washer. Selected experiments were deaerated using nitrogen for 1 hour prior to testing and through the duration of the test. OCP was measured for 30 minutes prior to each test to ensure equilibrium at the surface had been established. Scan rates of 1 mV/second were utilized for potentiodynamic polarization. A rotating disk electrode (RDE) was used to match the diffusion boundary layer thickness to the water layer thickness for some cathodic polarization experiments. The experimental current density was area corrected using the entire rivet geometry. All electrochemical tests were conducted three times to ensure statically reliable results. The average standard deviation of E_{corr} and I_{corr} were all found to be within +/- 5%.

pH measurements inside a simulated crevice were conducted. Type 316 stainless steel bolt was fixed into a 6.35 mm thick AA7050-T7451 plate. The cathode to anode ratio was approximately 1:1. The fastener was cross-sectioned and attached with a plastic plate with set screws into the AA 7050-T7451 cross-section. This enabled the plastic to be removed quickly after exposure and the pH to be measured inside the rivet hole. The sample was immersed in 4 M NaCl for 62 hours following the same test protocol of the simulated rivets. After the conclusion of the exposure, the plastic was removed and universal pH indicator and pH paper was used to determine the pH inside the rivet hole, in cross-section, with the stainless steel 316 bolt present.

2.3.5 Synchrotron X-ray Tomography at Diamond Light Source

XCT measurements were performed at the Diamond Manchester Imaging Branchline (I13-2) at Diamond Light Source, U.K., on an actively corroding sample. The X-ray transparent AA 7050-T7451 cylinders were exposed under NaCl or $MgCl_2$ droplets for various exposure times. The droplet covered the entire top of the pin and wicked into the crevice between the AA 7050-T7451 hole and stainless steel rivet. Measurements were performed using a pink beam with a spread of energies between 6.6 keV and 20 keV, with a primary peak at 8.3 keV and a PCO edge detector with a 100 μm CdWO4 scintillator, a 2x relay optic, and a 4x objective, giving an effective pixel size of ~812 nm. All of the XCT scans were performed at high resolution, taking 3,600 projections (radiographs) over 180° with continuous motion of the stage, giving a data collection time of approximately 7 minutes. Twenty dark scans (no beam) and 30 flat scans (full beam without sample) were taken for background subtraction and normalization of the image.[*] The camera was checked with the dark field scans (images without the beam). The shutter was closed for balance of exposure times. The specs used for this *operando* X-ray tomography experiment enabled resolution of 0.8 µm allowing local pitting attack to be monitored with time and depth.

2.3.6 Faraday's Law to Determine Charge

Volume loss from corrosion can be used to calculate the anodic charge associated with the fissure damage. The anodic charge associated with corrosion damage, Q_A (C), can be determined using Equation 2.1:

$$Q_A = \frac{V_{XCT} F \rho}{EW} \qquad \text{Equation 2.1}$$

Where V_{XCT} is the volume loss from corrosion, found by the XCT (cm^3), F is Faraday's constant[18], 96,500 (coul/cm^3), ρ is the density of AA 7050-T7451 (2.83 g/cm^2), and EW is the equivalent weight of AA 7050-T7451. The EW was 9.77 g/equiv assuming congruent dissolution and 9.54 g/equivalent assuming incongruent dissolution. Incongruent dissolution refers to the circumstance when Cu does not dissolve with the Al, Zn and Mg equally.

Hydrogen gas was collected using an inverted burette filled with solution. The H_2 collected for select exposures was converted cathodic charge using the ideal gas law and Faraday's law using Equation 2.2.

$$Q_{H2} = \frac{zPVF}{ART} = \frac{ZnF}{A} \qquad \text{Equation 2.2}$$

---

[*] The flat scan is an image taken without the sample in view, allowing any defects on the camera or scintillator, or non-uniformities in the incident X-ray beam to be used to divide the image and remove any artifacts.

Where z is 2 for H_2 evolution, P is the pressure inside the burette (1 atm), V is the volume of gas in the burette (cm^2), A is the area of the electrode (cm^2), R is the ideal gas constant, and T is temperature.

The cathodic charge, $Q_{i\,net\,cathodic}$, can be determined using the integrated signal of the current as a function of time transient at each potential using Equation 2.3.

$$Q_{cathodic}(C) = i_c(E_{couple})\,A\,t \qquad \text{Equation 2.3}$$

Where $i_c(E_{couple})$ is the cathodic current at E_{couple}, the galvanic couple potential. E_{couple} was derived from finite element analysis (FEA) reported elsewhere.[148]

Area of Corrosion Fissures and Shape Descriptors Utilizing Image Processing

The corroded area from the XCT was quantified using contrast analysis. At each slice the image was individually adjusted. Ring artifacts were subtracted at each slice as they appeared in different locations throughout the slices. This was necessary to ensure the contrasted area was physical damage and not artifacts. Each fissure was then individualized per 10. There were 470 and 380 slices in the 4 M NaCl and 2 M $MgCl_2$, respectively.

Shape descriptors were calculated to geometrically describe the corrosion fissures in the 4 M NaCl case. The applicable shape descriptors were form factor and aspect ratio. Form factor reflects the smoothness of the corrosion fissure. A value close to one indicates a smooth and round shape and a value close to zero indicates an elongated shape. The form factor and aspect ratio were calculated using Equation 2.4 and Equation 2.5.[149] The aspect ratio is defined using the largest diameter and the smallest diameter orthogonal to it. Form factor and aspect ratio were determined and analyzed using ImageJ.[147,149]

$$Form\ Factor\colon\ \frac{4\pi A}{perimeter^2} \qquad \text{Equation 2.4}$$

$$Aspect\ Ratio: \frac{\max diameter}{\min diameter}$$ Equation 2.5

2.3.7 Methods for Replating Cu Study on AA7050-T7451

Two methods of emulating Cu deposition were used to study the cathodic effect of Cu-replating on AA7050-T7451. The first method was to plate Cu from solution onto the surface of AA7050-T7451 by cathodic polarization at E=-1.0V SCE. The electrolyte used was 0.2 M $CuSO_4$ + 0.5 M H_2SO_4 pH 1.6. This produced a thin layer (50 µm) of Cu on the surface. The second method was enabling Cu to replate by exposing samples to NaCl solution over 48 hours allowing *S* phase to dealloy. The solutions used was 0.5 M NaCl + HCl at pH 3, 0.5 M NaCl + $NaAlO_2$ at pH 8 and 0.1 M $CuSO_4$ at pH 3.3. This enabled S-phase to dealloy and redeposit on the surface. All methods were subsequently studied with cathodic polarization in 0.5 M NaCl + $NaAlO_2$ and cyclic voltammetry in deaerated borate buffer.

2.3.8 Rotating Disc Electrode

Cathodic kinetics of Type 316 stainless steel and pure Cu were studied using a rotating disc electrode. A three-electrode setup with an ASR rotator (supplied by Pine Research Instrumentation, Inc., Durham, NC) with the electrode facing downward, saturated calomel reference electrode (SCE) and a platinum-niobium mesh as the counter electrode was used. The experiments were performed at a scan rate of 1 mV/s with the RDE at various rotation speeds ranging from 0 to 3000 RPM. The electrode rotates during experiments inducing a flux of analyte to the electrode. Equating the Levish equation (Equation 2.6) to the limiting current density (i_L) (Equation 2.7) enables varying the rotation speed as a function of boundary layer thickness.

$$i_L = 0.62nFD^{2/3}\omega^{1/2}v^{-1/6}C$$ Equation 2.6

$$i_L = \frac{NFDC}{\delta}$$ Equation 2.7

Where n is number of electrons transferred for ORR, F is Faradays constant, D is the O_2 diffusion coefficient, C is the O_2 bulk concentration, δ is the boundary water layer thickness, ω is the angular frequency and v is the kinematic viscosity.

2.4 Results

2.4.1 Constituent Particle Analysis on AA 7050-T7451 Plate

Confirmed by electron dispersive spectroscopy (EDS) analysis, AA 7050-T7451 has three types of coarse constituent particles; Al_7Cu_2Fe, $MgSi_2$ and Al_2CuMg. [9] One micrograph from each plane from the middle of the plate (~25 mm) can be observed in Figure 2.3. The bright white spots are the constituent particles. The constituent particles are observed to be aligned in stringers parallel to the L direction. It was observed that the size and distribution of the constituent particles varied with plate depth and with plate orientation (Figure 2.4). On the LT surface the average particle size was 2.6 µm, 3.3 µm at eighth-thickness, 3.8 µm at quarter-thickness and finally 3.4 µm at mid-plate thickness. At mid-plate the average diameter of the particles were 2 µm. The measured number of particles per 1 mm^2 on the surface was 290, 503, and 424 on the LT, LS and TS planes, respectively. At mid-plate, the observed number of particles per 1 mm^2 was 246, 350, and 292 on the LT, LS and TS planes, respectively. For all three orientations the number of constituent particles per 1 mm^2 had a decreasing trend until quarter thickness then changed to an increasing trend at the mid-plate depth. The mean particle diameter increased from the surface to the quarter plate depth then a decrease in particle size was observed at the mid-plate depth. At the surface the mean particle diameter was 2.6 µm, 2.3 µm, and 2.6 µm at the LT, LS and TS planes, respectively. At the mid-plate depth, the mean particle diameter was 3.3 µm, 2.8 µm and 3.1 µm at the LT, LS and TS planes, respectively. The cumulative size distribution show that the microstructure is heterogeneous, which agrees with previous findings.[9]

2.4.2 Real Time Tracking of AA 7050-T7451 Corrosion Fissure Growth as a Function of Droplet Solution using X-ray Tomography

A typical horizontal slice through an X-ray tomogram for the sample exposed to 4 M NaCl and a secondary electron image of the LT surface are shown in Figure 2.5. This shows a horizontal section viewed from the top of the cylindrical AA 7050-T7451 test piece. The large grey disk is the AA 7050-T7451. The bright blocky and round particles are Mg, Fe and Cu rich constituent particles and the large central white circle is the stainless steel wire. The circular bands to the lower right of the stainless steel are reconstruction artifacts. The dark corrosion fissures were observed in AA 7050-T7451 around the rivet-hole and extended from 1 to 500 µm in depth. The corrosion damage in both the 4 M NaCl and 2 M $MgCl_2$ were identified by phase contrast and verified using SEM. The fissures are seen to be intragranular and the relationship to grain structure is shown below.

After 62 h, four separate fissures were observed in the 4 M NaCl exposure; one at the mouth of the rivet, one at the middle of the rivet, and two at the bottom of the rivet. The first fissure was located 1.1 µm deep, with respect to crevice depth, the second fissure was located 22.7 µm deep, the third fissure was located 286.5 µm deep and the last fissure was located 159.0 µm deep. Figure 2.6 shows one of the 4 fissures growing over time for the 4 M NaCl exposure at ~82.1 µm into the rivet hole.

In the 2 M $MgCl_2$ exposure, three fissures were observed after 60 h, one was seen at the rivet mouth and two at the bottom of the rivet. In the 2 M $MgCl_2$ exposure the first fissure was located 13.1 µm deep, the second fissure was located 105.3 µm deep and the last fissure was located 251.0 µm deep into the 500 µm rivet hole. Figure 2.7 shows one of the three fissures growing over time in the 2 M $MgCl_2$ exposure at ~258.5 µm into the rivet hole.

The two exposures were reconstructed in 3D using Avizo Fire software enabling 3D differentiation of the corrosion damage over time. The four fissures in the 4 M NaCl exposure and the three fissures in $MgCl_2$ exposure can be observed in a 3D reconstruction in Figure 2.8 and Figure 2.9. The 3D reconstruction shows the simulated rivet with a transparent AA 7050-T7451 matrix where the blue cylinder is the stainless steel 304 wire and the red 3D regions around the wire are the corrosion fissures. The samples were exposed for 62 h under the 4 M NaCl exposure and 60 h under the 2 M $MgCl_2$ exposure. The 62 and 60 h damage morphologies can be observed in relation to the constituent particles, which are shown in green (Figure 2.10). It can be observed that the first fissure (top of the pin) was the largest fissure in the 4 M NaCl exposure while the second fissure (middle of the pin) was the largest in 2 M $MgCl_2$. Both exposures had corrosion sites located at the top and bottom of the simulated rivet with no relationship with respect to the constituent particles in the 4 M NaCl exposure.

In the 4 M NaCl exposure, the corrosion fissures did not obviously follow bands of IMP clusters. The fissures corroded intragranually. Multiple fissures developed over the same time period in both 4 M NaCl and 2 M $MgCl_2$ exposures (Figure 2.11). The first corrosion fissure initiated after 12 h in the NaCl exposure and after 4 h in the $MgCl_2$ exposure. The fissure area was tracked with time and depth for each sample. The 2D area of corrosion as a function of depth and time can be observed in Figure 2.12 for the 4 M NaCl exposure and in Figure 2.13 for the 2 M $MgCl_2$ exposure. The 4 M NaCl exposure contained more damaged volume than 2 M $MgCl_2$ exposure. The 2D area of coarse constituent particles at each slice for each exposure was determined using the threshold method. The constituent particle area on each slice was determined as a function of rivet depth for the 62 h 4 M NaCl exposure and the 60 h 2 M $MgCl_2$ exposure. The area fraction of the constituent particles observed was about 0.4% area fraction of AA 7050-T7451 pin for the 4 M NaCl exposure and about 0.15% area fraction of AA 7050-T7451 pin for the $MgCl_2$ exposure. The area fraction of constituent particles varied due to the changing consistent particle area fraction with plate thickness.

As a control, laboratory XCT was utilized to study a simulated fastener without the stainless steel wire present and also with the use of a cylindrical plastic 250 µm pin crevice former. These simulated fasteners had the same geometry and were exposed to a 0.4 µL droplet of 4 M NaCl and 2 M $MgCl_2$ in a desiccator at 98% RH for 62 h and 60 h. These samples were used as a control to compare to the *operando* simulated fasteners with stainless steel. In the *operando* exposures, it was unclear whether corrosion damage occurred due to constituent particles, crevice corrosion, or the stainless steel. The control samples showed no damage in any of the exposures on the surface and through the entire 500 µm rivet hole. This indicated the corrosion was due to the stainless steel fastener which also becomes a driving force for Cu-replating to initiate.

There were 4 corrosion sites in the 4 M NaCl exposure, one on the surface and the other 3 in the lower half of the rivet producing fissure type damage. The 2 M $MgCl_2$ case had 3 corrosion sites, one on the surface and two at the bottom of the rivet. Damage was in the form of fissures somewhat aligned with the L direction bands of constituent particles.

Recall that intragranular fissures were observed in Figure 2.5 and Figure 2.10. Electron backscatter diffraction (EBSD) was conducted on the *operando* XCT samples to reveal the grain structure. Figure 2.14 shows the grain structure of the 4 M NaCl surface and Figure 2.15 shows the grain structure of the 2 M $MgCl_2$ surface with their corresponding SEM image and XCT surface images. The grain structure is dissimilar for each exposure. In the 4 M NaCl exposure, the grains are pancake-shaped while in the 2 M $MgCl_2$ exposure the grains are thinner and longer. These grain structures produced slightly different damage morphologies. In the 4 M NaCl exposure, the damage was in the form of round-like corrosion fissures, while in the 2 M $MgCl_2$ exposure the damage was in the form of elongated corrosion fissures that followed the grain shape.

The samples were also characterized in cross-section using a focused ion beam and polishing techniques at the Analytical Instrumentation Facility at North Carolina State University. The first fissure (Figure 2.5) was cross-sectioned in the 4 M NaCl exposure. The cross-section revealed the fissure was 105 µm deep. The 4 M NaCl pin was cross-sectioned approximately 300 µm from the edge of the pin. Fissure 3, at the bottom of the 2 M $MgCl_2$ exposure, was also cross-sectioned. A depth of 260 µm from the top LT plane was examined. The 2 M $MgCl_2$ pin was cross-sectioned approximately 370 µm from the edge of the pin. The corrosion fissure was found to be 94 µm in depth. The 4 M NaCl exposure cross-section is shown in Figure 2.16.. Figure 2.17 shows the EDS map in cross-section. It can be observed that the secondary phases were rich in Cu, Mg and Fe. EBSD was conducted on the cross-section on the sample exposed to 4 M NaCl to determine grain structure (Figure 2.18). The grain structure revealed grains on the order of 100 µm. Furthermore, grains appeared as deformed-free recrystallized gains. The cross-sectional analysis verified the XCT

2.4.3 Anodic Charge to Produce the Corrosion Damage Observed in AA 7050-T7451 Crevice

The volume loss from corrosion in the *operando* exposures was calculated for various exposure times. The volume loss was an important parameter to determine, enabling analysis of the required anodic charge to produce the observed damage. The volume and charge as a function of time for the 4 M NaCl and 2 M $MgCl_2$ can be observed in Figure 2.19. This was calculated using Faraday's law. In the 4 M NaCl exposure, the first fissure had the largest volume loss and the second fissure had the smallest volume loss. In the 2 M $MgCl_2$ exposure the first fissure had the smallest volume loss and the second fissure had the largest volume loss. The total anodic charge is the sum of the anodic charge for all the individual fissures. The total anodic charge was 14 mC and 9 mC for the 2 M $MgCl_2$ exposure, assuming congruent dissolution with all elements dissolving as the same time.

2.4.4 Shape Descriptors of Corrosion Fissures in the 4 M NaCl Exposure

The form factor gave indication of smoothness and circularity of the corrosion fissures. Circularity is defined when all the points on a surface of revolution are the same distance away from a common axis or center point.[149] Form factor and aspect ratio of the fissures in the 4 M NaCl exposure varying with depth can be observed in Figure 2.20. The first fissure was the least circular fissure of the four fissure while the second fissure had the highest form factor indicating a smoother shape. The average form factor was 0.15, which indicated that the cross-section of the corrosion fissures varied from an ideal circle. The form factor varies with surface irregularities but not with elongation and the aspect ratio has the opposite shape attributes. The aspect ratio describes length/breadth of the corrosion fissure. This indicates that the size of the fissure will not change the numerical value of aspect ratio. The average aspect ratio of the four corrosion fissures in the 4 M NaCl exposure was 2.45. The second and third fissures had the lowest aspect ratio. This means that the major axis of the corrosion fissure was larger than the minor axis, indicating that these corrosion fissures were more elongated than the first and fourth corrosion fissures.

2.4.5 Cathodic Reactions Rates of Cu-replating on AA7050-T7451

Figure 2.21 shows the SL surface of AA7050-T7451 after a ZRA measurement in 0.5 M NaCl + $NaAlO_2$ compared with laboratory Cu plating methods. The image shows dark gold remnants which are believed to be Cu, (b)-(e) show the surface after each of the methods described above to emulate Cu redepositing on the surface. After the Cu was replated on the surface, cathodic polarization and cyclic voltammetry were used to evaluate the cathodic kinetics and to confirm the presence of Cu on the surface, respectively. Figure 2.22 shows the cathodic polarization of AA7050-T7451, pure Cu and AA7050-T7451 after a 100 h ZRA exposure compared with specimens subject to the Cu plating methods discussed above. The OCP of AA7050-T7451 with replated Cu was slightly ennobled and the polarization curves indicate that the cathodic kinetics are similar to that of high purity Cu, except in the case of method 3, 48 h at OCP in 0.1 M $CuSO_4$. The i_L for ORR on pure Cu, AA7050-T7451 after 100 h ZRA exposure in 0.5 M NaCl + $NaAlO_2$ pH 8 and AA7050-T7451 after Cu plating by cathodic polarization were 5.3 x 10^{-5} A/cm^2, 6.2 x 10^{-5} A/cm^2 and 6.3 x 10^{-5} A/cm^2, respectively. Figure 2.23 shows the cyclic voltammetry (CV) scans in deaerated borate buffer for AA7050-T7451, pure Cu, and one sample from each of the Cu-replating methods described. The pure Cu CV curve had two peaks at E= -0.42 V and E=-0.18 V. These peak locations were used as an indication of Cu on the surface to assess the surface coverage relative to each coupon. All the AA7050-T7451 coupons showed coverage of Cu on the surface, with the exception of the exposure in 0.5 M NaCl + HCl. In this case, the surface appeared to be pitted with no apparent discoloration.

2.4.6 Cathodic Kinetics of the Differences in Diffusion Boundary Layer Thickness using the Rotating Disk Electrode

RDE was use to understand the effect of thin film ORR cathodic kinetics in simulated rivet environments. The effect of scan rate on the cathodic kinetics of Type 316 stainless for δ= 30 µm and δ= 100 µm can be observed in Figure 2.24 and Figure 2.25, respectively. It was found that with δ=30 µm, scan rate influenced ORR kinetics. However with δ=100 µm cathodic kinetics were not affected. The effect of OCP time was also studied in Figure 2.26 and Figure 2.27 for δ=30 µm and δ=100 µm on Type 316 stainless steel. Prior to cathodic polarization the time the specimen was left at OCP was varied between 0 h and 2h. For δ = 30 µm, it was found that OCP time had an effect on cathodic kinetics. Cathodic kinetics measured after longer OCP hold times were reduced compared to those measured after shorter OCP hold times. The OCP was ennobled by 150 mV after 2 h at OCP compared to no time at OCP. For δ= 100 µm, the cathodic kinetics were not affected. However, OCP followed the same trend as that measured at δ= 30 µm. After 2 h of OCP time prior to testing, a steady potential value was not reached. This can be attributed to the RDE stirring the solution resulting in difficulty in establishing equilibrium at the surface of the electrode.

Cathodic polarization utilizing the RDE was compared to quiescent environments of Type 316 stainless at δ=200,100, 30 and δ=10 µm (Figure 2.28). Cathodic polarization was conducted in simulated rivet solutions of 0.5 M NaCl, 0.5 M NaCl + $NaAlO_2$ at pH 10 and at pH 8 and 0.5 M NaCl + $AlCl_3$ at pH 2 and at pH 1. In neutral and alkaline environments the cathodic kinetics of Type 316 stainless steel increased. In acidic environments only a marginal increase was observed in ORR kinetics. In most cases, the OCP of Type 316 stainless was ennobled using the RDE. As expected, i_L decreased with increasing δ. Similar results were obtained on pure Cu. However, on pure Cu (Figure 2.29), while cathodic kinetics increased, the OCP was lowered.

Potentiostatic polarization at E=-0.7 V SCE on Type 316 stainless in 0.5 M NaCl + $NaAlO_2$ over 62 hours was conducted with δ values of 100 µm, 10 µm and 8 µm and compared to quiescent environment (Figure 2.30) . After 62 hours, the net cathodic charge density was 77.4 C/cm^2, 473 C/cm^2 and 600 C/cm^2. In a quiescent environment, the charge density was 3 C/cm^2. This indicated that, with a boundary layer thickness of 100 µm and 10 µm, cathodic current density was 25 times and 157 times, respectively. Figure 2.31 shows a stepped cathodic potentiostatic test demonstrating that a change in rotation speed instantaneously increased the current density.

A summary of RDE on Type 316 stainless steel, pure Cu and replated Cu compared to full immersion quiescent environment in 0.5 M NaCl can be observed in Figure 2.32. The dark green line is data obtain from previous work by Policastro[150] on 304 steel under a droplet of NaCl. The increase in current density agrees well with RDE data. In this work RDE data enabled an understanding of the increased current density associated in atmospheric conditions. Furthermore, RDE was used to understand cathodic reaction rates of the simulated fastener exposures.

2.4.7 Sources of Substrates Supporting Fast Cathodic Reactions

In a separate study, the pH gradient inside a dissimilar metal couple of AA 7050-T7451 and a stainless steel 316 bolt was measured. The pH was found to be between 7 and 8 at the top of the rivet hole and around 5-6 near the bottom of the rivet hole. No acidic sites were found.[†] These results guided the environments chosen for the cathodic reaction rate studies.

Cathodic polarization studies were desired to provide an indication of the different possible cathodes and their reaction rates. Cathodic and anodic polarization of AA 7050-T7451, pure aluminum, pure Cu, stainless steel 316, Al_7Cu_2Fe, Al_2CuMg and emulated Cu-replating on AA 7050-T7451 were characterized with respect to cathodic kinetics in 0.5 M NaCl + NaAlO2, pH 8. Pure Cu and stainless steel 316 were measured to the electrolyte film using a RDE with the intent to match to a diffusion boundary layer thickness of 100 µm. The cathodic and anodic polarization curves are shown in Figure 2.33. Type 316 stainless steel, pure Cu, Cu-replated on AA 7050-T7451 and, to a lesser extent, Cu-containing Constituent particles all contribute to the pertinent cathodic current.

Potentiostatic polarization was conducted at E=-0.77 V SCE for the stainless steel 316 and E= -0.80 V SCE for the Cu-replated on AA 7050-T7451. The experimental current density was area corrected using the rivet geometry. These potentials were chosen using FEA conducted on the simulated pin geometry to represent the galvanic couple potential distribution in a galvanic couple, $E_{couple,}$ extracted from current and potential distribution.[70] The FEA model showed no IR drop through the 500 µm rivet hole. The FEA model determined that the galvanic couple potential distribution was consistent with typical galvanic couple potentials observed utilizing zero resistance ammeter measurements and overlying anodic and cathodic polarization curves. The environments that simulated inside the crevice were deaerated stagnant solutions to simulate the restriction of oxygen diffusion into a crevice and a confided space area without flow. The pin was simulated utilizing cathodic reaction studies open to air using RDE with δ=100 µm. The current was converted to cathodic charge by integrating the current and normalizing it to the assumed wetted area of the simulated pin. The cathodic current density and cathodic charge density with respect to time can be observed in Figure 2.34.

[†] However, this does not preclude very local acidic sites as this did not test local fissure acidity. Local fissures were assessed by H_2 collection.

The cathodic charge has three components; (1) the charge associated with the macro stainless steel rivet, (2) the charge associated with Cu-replated on the surface, and the dealloyed S phase, and (3) the charge associated with the HER. The cathodic charge was obtained from potentiostatic and RDE exposures over 62 hours. The charge associated with HER was found to be 0.27 mC, the charge associated with the macro stainless steel rivet was found to be 11 mC and the charge associated with replated Cu and the dealloyed S phase was found to be 17 mC. The cathodic charge for each of the contributing cathodic reactions are shown in Figure 2.35. The total cathodic charge for the environments considered was found to be 28 mC over 62 h, meaning the estimated cathodic charge was greater than the anodic charge, $Q_C > Q_A$. Charge calculations enabled a comparison of anodic charge from XCT to the cathodic charge, which will be discussed in the next section.

2.5 Discussion

2.5.1 Corrosion Fissure Path and Morphology Comparison between 4 M NaCl and 2 M $MgCl_2$ Exposure

The key results of these rivet galvanic couples were: (1) multiple fissures were extended in size and length over the period of exposure, albeit the instantaneous corrosion rate could not be verified to be non-zero at the same time instant and (2) fissures did not follow obvious clusters of constituent particles in the 4 M NaCl exposure. This was interpreted to be due to the presence of one or more strong cathodes associated with sites, other than constituent particles.

While both exposures had the same chloride concentration, the damage morphologies in the simulated rivet varied between exposures. The cross section (Figure 2.6), 3D reconstructions (Figure 2.8) and shape descriptors (Figure 2.20) of the 4 M NaCl exposure showed the fissure to have a more circular shape that did not seem to follow bands of constituent particles. However the 2 M $MgCl_2$ exposure was observed to have more elongated corrosion fissures that followed bands of constituent particles in the rolling direction (Figure 2.9). The EBSD on the simulated pin surface showed a different grain structure for the two exposures (Figure 2.14 and Figure 2.15). 4 M NaCl simulated rivet came from the surface of the AA 7050-T7451 plate while the 2 M $MgCl_2$ simulated rivet was cut from the middle of the AA 7050-T7451 block with 50 cm thickness. The grain structure of the AA 7050-T7451 may be similar to the fissure morphology, in both cases, as might be expected for intragranular corrosion. However, the corrosion fissures were not cathodically limited to one corrosion site at a time. Fissures were able to grow through the entire depth of the 500 µm-deep rivet hole due to the presence of several strong cathodic sites.

2.5.2 Favored Cathodic Sites when AA 7050-T7451 is Coupled with Stainless Steel 316

When stainless steel is coupled with AA 7050-T7451 there are multiple cathodic reactions occurring. There are 4 key cathodic contributor sites (1) Cu-replating on the surface of AA 7050-T7451 (2) dealloyed S phase (3) the stainless steel rivet, inside the crevice as well as externally above the crevice, and (4) a local hydrogen evolution reaction, which is a cathodic reaction local to a fissure, that may be an acidic site. In the simulated fastener plate system, multiple corrosion fissures grew simultaneously over the period of exposure (Figure 2.12 and Figure 2.13). The question remains as to the governing cathodes that supports a high number of fissures. Previous work has shown that, with no stainless steel present, the corrosion fissures are stunted by the growth of another fissure as the same cathodic site.[142] This indicated that the corrosion rate was cathodically limited. In these exposures the corrosion fissures did not follow obvious clusters of constituent particles suggesting the presence of the stainless steel rivet and a newly developed strong cathode, such as replated Cu, were important. However, corrosion may be dominated by the cathodic reaction occurring on the stainless steel dissimilar metal, since the removal of this pin resulted in suppression of corrosion.

Pure aluminum and Al-Cu-Zn-Mg alloys are viable substrates for cathodic reactions supporting local corrosion.[151-154] However, the low exchange current density on Al, and the insulating oxide film, limits electron transfer reaction on aluminum alloys. [8] Cu-replating significantly enhances the cathodic reactions supporting local corrosion. [33,153] There are two sources of Cu in AA 7050-T7451, (1) Cu in solid solution and (2) Cu present in precipitated and constituent particles, such as S phase. Cu-replating occurs on the surface of many Cu-containing alloys during corrosion. [45] This is a result of dealloying of Cu-containing second phase particles in the matrix as well as the release of Cu in solid solution. [52,60]

The cathodic polarization scans in Figure 2.33 in 0.5 M NaCl + $NaAlO_2$ at pH 8 showed the different cathodic reaction rates of various possible cathodes within the galvanic couple range, which was determined by various zero resistance ammeter exposures as well as FEA modeling. The cathodic reaction rate at potential E= 0.9 V vs SCE of the stainless steel 316 and Cu-replating on AA 7050-T7451 were $3\text{x}10^{-5}$ and $5\text{x}10^{-5}$ A/cm^2, respectively. When the RDE was used to simulate a 100 µm electrolyte layer, the current density increased by 2 orders of magnitude. The RDE reaction rate was comparable to previous work conducted by Policastro[150] on polarization under droplets of 0.6M NaCl at 80% RH on UNS S13800. This type of analysis indicated that, under full immersion and thin film conditions, the stainless steel 316 and replated Cu have a significant effect on the cathodic kinetics when AA 7050-T7451 is coupled with stainless steel 316 and an even larger significance under thin film conditions.

The anodic charge, calculated based on the volume of X-ray tomography, enabled a comparison study of the cathodic charge, Q_c, associated with the cumulated net cathodic charge determined from the stainless steel and other sources at the galvanic couple potential determined by the FEA modeling. The cathodic charge for each of the contributing cathodic reactions can be seen in Figure 2.35. The total cathodic charge for the environment considered was found to be greater than the anodic charge, $Q_C > Q_A$. The simulated pin geometry was considered in various crevice environments to study the various cathodic contributors. The cathodic current has four important contributors: the stainless steel above the crevice, the stainless steel inside the crevice, hydrogen evolution in an acidified fissure, and any replated Cu or dealloyed S phase (Equation 2.8). In addition, each of these locations has a specific solution chemistry. This study aimed to determine the cathodic charge associated with each of these cathodic contributors or reactions.

$$\sum Q_{anode\,(XCT)} = \sum Q_{cathode} = \sum Q_{copper\ replated} + \sum Q_{dealloyed\ S\ phase} + \sum Q_{remote\ macro\ cathode\ (SS)} + \sum Q_{H2} \qquad \text{Equation 2.8}$$

Where $\sum Q_{anode\,(XCT)}$ is the anodic charge associated with volume loss as a result of corrosion found using XCT, $\sum Q_{cathode}$ is the cumulated net cathodic charge, $Q_{copper\,replated}$ is the cathodic charge associated with Cu plating on the surface on AA 7050-T7451 and $\sum Q_{dealloyed\,S\,phase}$ is the cathodic charge associated with dealloyed S phase leaving behind a cathodic particle to the bulk matrix, $\sum Q_{remote\,macro\,cathode\,(SS)}$ refers to the cathodic charge of the macro stainless steel wire and $\sum Q_{H2}$ is the associated charge from the local hydrogen evolution reaction.

The cathodic charge that has the biggest contribution in these environments was the charge associated with Cu-replating on the surface and dealloyed S-phase, followed by the charge associated with the stainless steel 316 macro rivet with the hydrogen evolution reaction contributing less than 10% of the overall cathodic charge. However, the X-ray tomography control samples, with no stainless steel 316 wire, showed no corrosion sites which may suggest that the stainless steel rivet is needed for the initiation of Cu-replating.

As stated above, a need exists to examine environments typical of crevices. Various conditions were explored. All surface (above crevice) environments were examined using RDE and ambient aeration to simulate a thin water layer and all (inside) crevice environments were deaerated to simulate oxygen depletion inside a crevice. Once the potentiostatic library in various environments was complete, the rivet simulated by a pin geometry was considered in various pH gradients and environments. The most realistic environment that was considered was the mouth of the crevice in an alkaline pH and the inside of the crevice was considered to be neutral. Therefore, pH 9 RDE data was used on the surface and deaerated pH 7 and pH 5.5 data used for inside the rivet hole.

This type of analysis enabled a study on which precise macro and micro cathodes control the galvanic corrosion between AA 7050-T7451 and stainless steel 316 central to damage, this guides future studies based on targeted suppression of certain cathodes to mitigate corrosion damage. It was observed that the Cu-replating had a greater contribution to the total cathodic charge than the stainless steel rivet. This was an interesting observation as no corrosion sites grew when the stainless steel was removed. This may indicate that the stainless steel provides the key driving force for Cu to replate on the surface which in turn is the key cathodic reaction site.

2.6 Conclusions

- XCT enabled the operando 3D visualization of hidden corrosion damage at the micrometer scale and enabled investigation of how the corrosion initiates and grows in an AA7050 model galvanic couple between an AA7050 plate and a stainless steel rivet.
- XCT enables the study of the distribution and size of coarse constituent particles, but not nm-sized precipitates, prior to attack and can be used to understand such microstructural features as local cathodes and link to the subsequent damage modes observed.
- The corrosion of AA 7050-T7451 was not observed to be cathodically limited to one fissure in a simulated fastener as multiple fissures grew over the same time period of 62 hours for the NaCl exposure and 60 hours for the $MgCl_2$ exposure.
- Cathodic polarization scans of selected phases present in AA 7050-T7451, as well as stainless steel 316, were investigated and compared to the galvanic couple range from E_{couple} experiments. The main contributors to the cathodic currents over the galvanic potential range were the stainless steel and AA 7050-T7451 with replated Cu. Cathodic reaction rates were quantified and the replated Cu was found to be the strongest cathodic contributor.

2.7 Tables

Table 2.1. Nominal composition of AA 7050-T7451 and stainless steel 304 in wt. % used in this study.

Material	**Mg**	**Zn**	**Cu**	**Zr**	**Fe**	**Al**			
AA 7050-T7451	2.2	6.1	2.2	0.11	0.08	Bal.			
	C	Mn	Si	P	S	Cr	Ni	N	Fe
Stainless Steel 304	0.08	1.67	0.76	0.0045	0.030	18.6	9.1	0.10	Bal.
Stainless Steel 316	0.05	1.37	0.43	0.031	0.027	18.2	8.16	0.06	Bal.

2.8 Figures

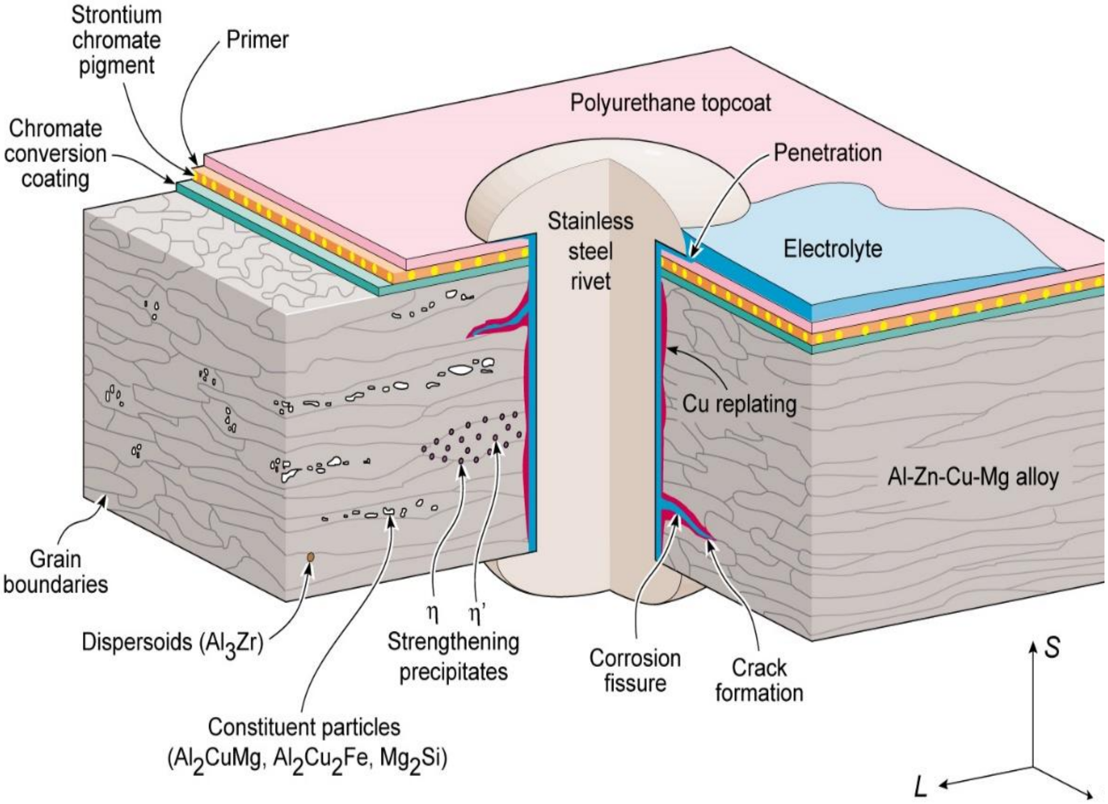

Figure 2.1. Schematic of stainless steel rivet in an AA 7050-T7451 plate describing the microstructure and orientation of a rivet hole.

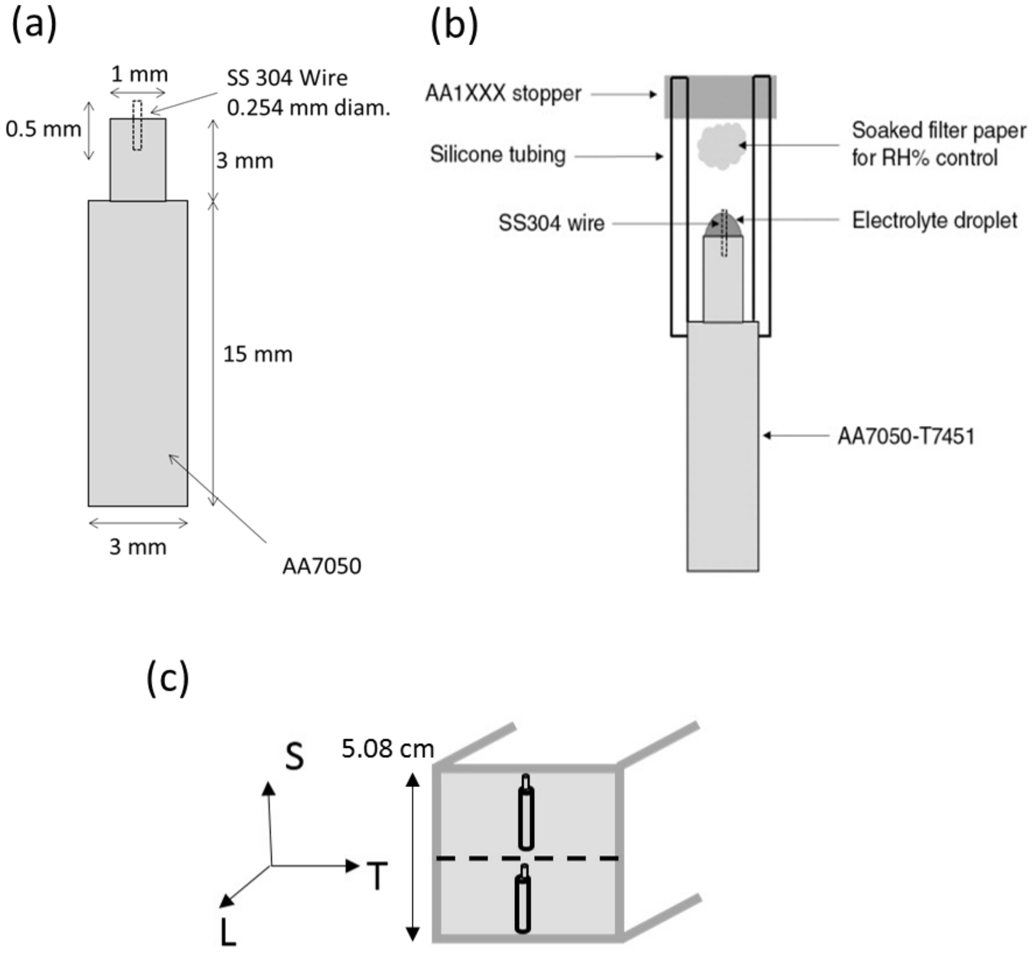

Figure 2.2. (a) Schematic of simulated rivet geometry consisting of an AA 7050-T7451 pin and stainless steel wire. (b) Experimental set up of a simulated rivet encapsulated with the Si tubing capped with the AA1xxx stopper. The soaked filter paper was used to control the RH. (c) Schematic showing the location where the samples came from relative to the LT plane, with the long axis in the S orientation.

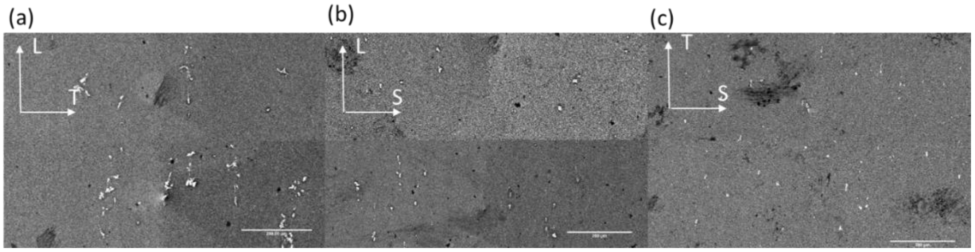

Figure 2.3. Scanning electron micrographs showing the constituent particles (bright white) in the (a) LT plane (b) LS plane and (c) TS plane.

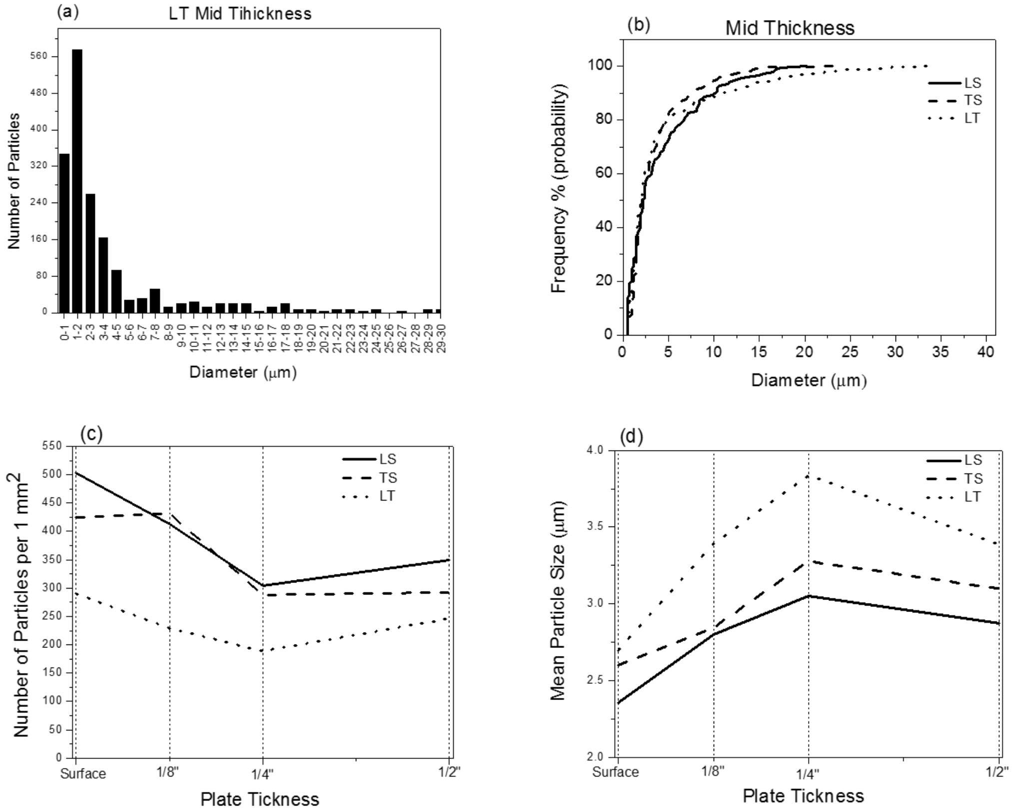

Figure 2.4. Particle analysis results of AA 7050-T7451 showing (a) Number of particles per 1 mm2 as a function of particle diameter at mid-plate thickness on the LT plane (b) Cumulative probability as a function of particle diameter in LT, SL and TS planes at mid-plate thickness (c) Number of particles per 1 mm^2 as a function of plate thickness and plate orientation and (d) Average particle size as a function of plate thickness and plate orientation.

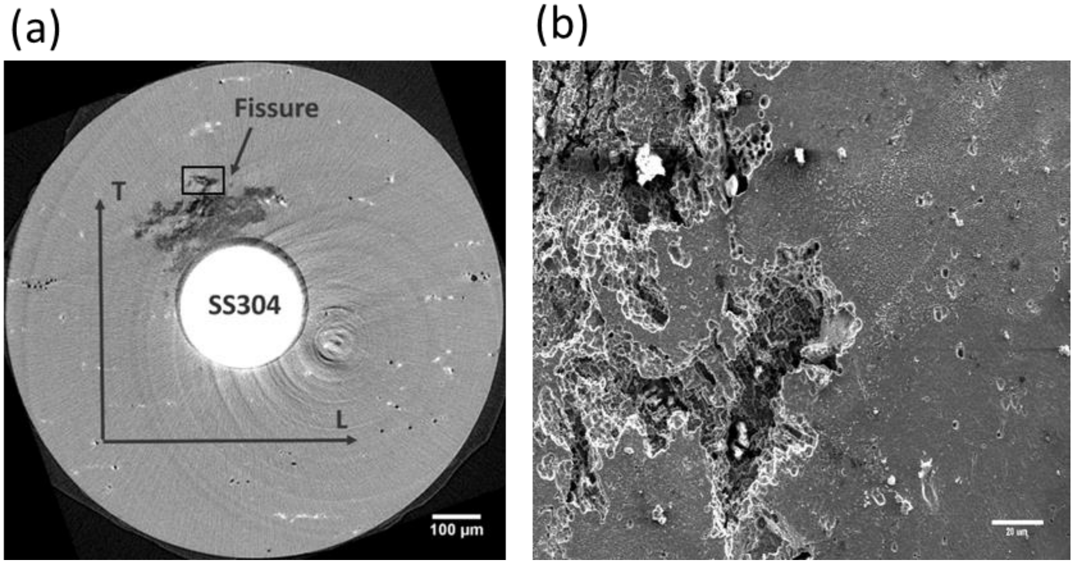

Figure 2.5 (a) X-ray tomography of a selected 2D vertical projection at a depth of 84 μm after 62 h of the NaCl exposure. The light gray area is the AA 7050-T7451 matrix and the white circle in the center is the stainless steel. The corrosion is indicated by the dark gray fissures. The constituent particles are the bright white circular particles in the AA 7050-T7451 matrix. (b) Secondary electron image of the polished LT plane showing the fissure on the surface of the AA 7050-T7451 indicated by the box in (a).

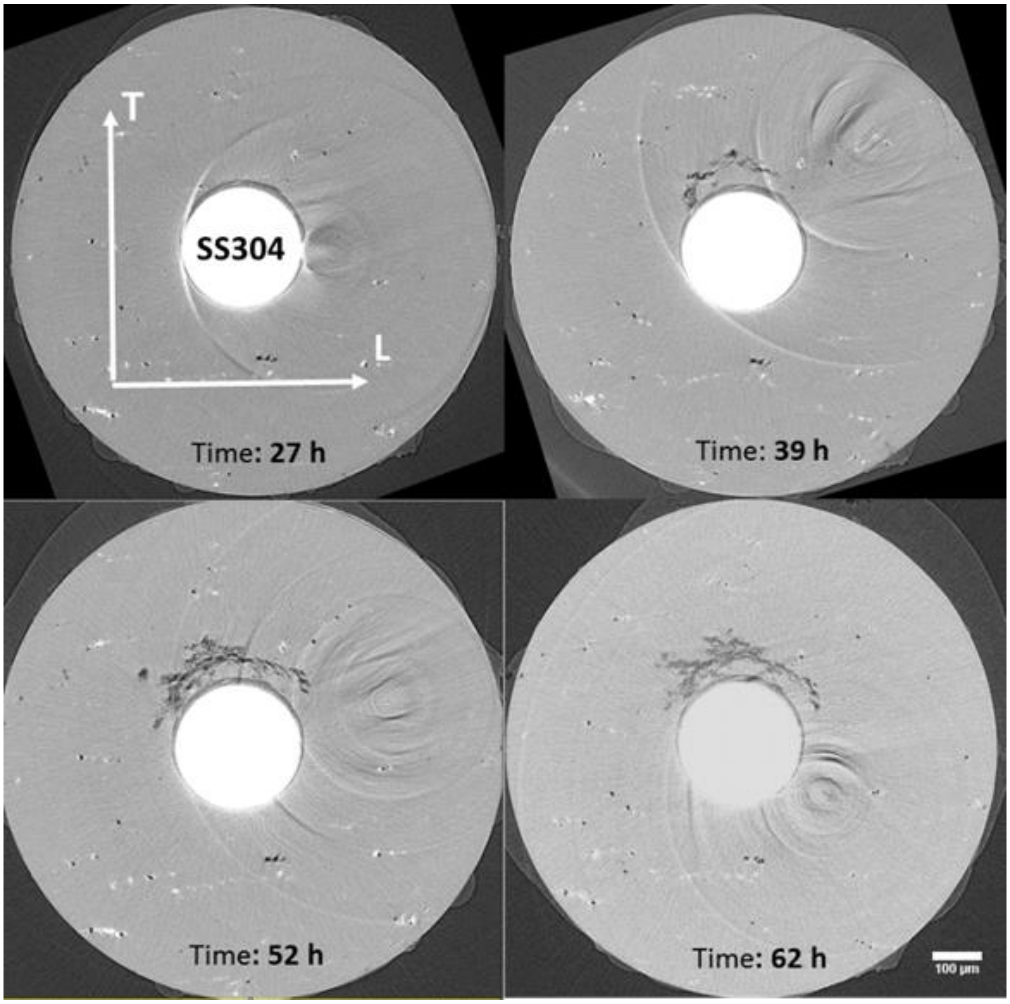

Figure 2.6. The development of one of the four corrosion fissures (fissure 1) in the 4 M NaCl solution after 27 h, 39 h, 52 h and 62 h of exposure 82.1 µm into the rivet. The small black dots are voids in the material in the as-received condition

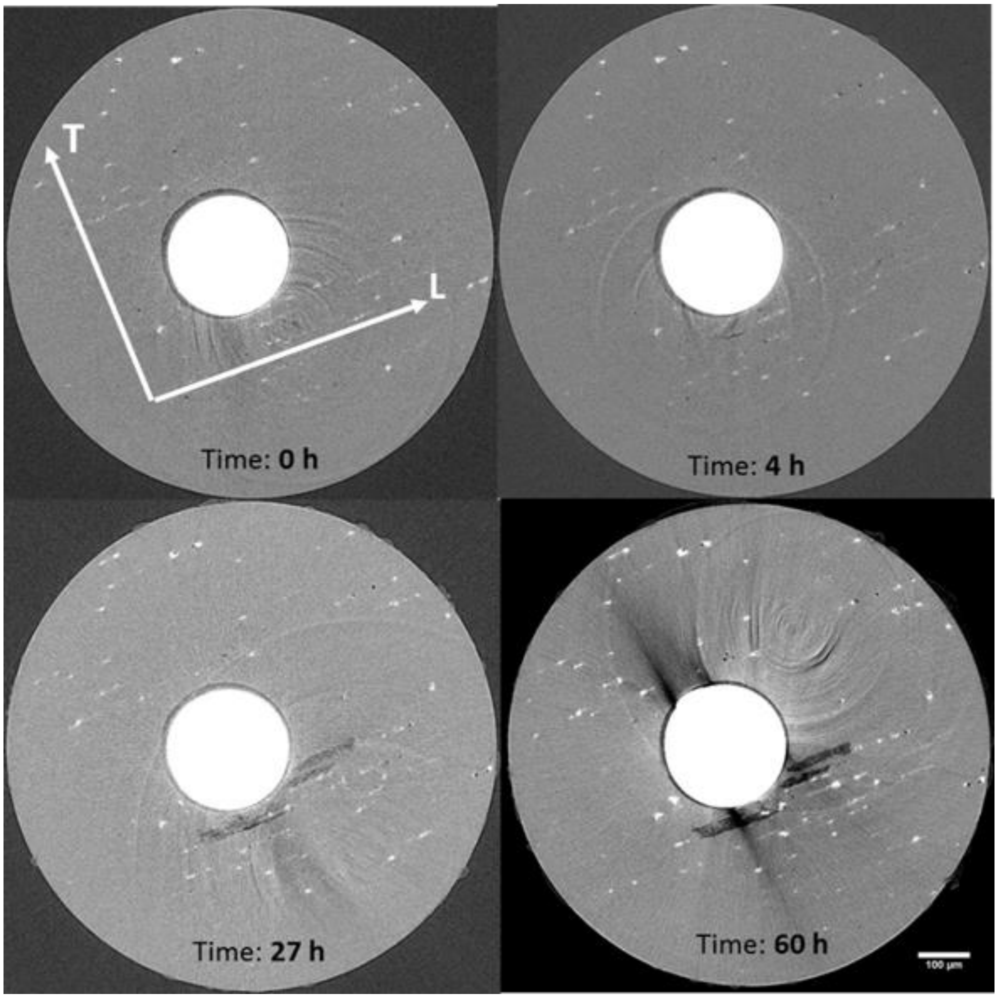

Figure 2.7. The development of one (fissure 2) of the three corrosion fissures in the 2 M MgCl2 solution after 0 h, 4 h, 27 h and 60 h of exposure 258.5 µm into the river. The small black dots are voids in the material in the as-received conditions.

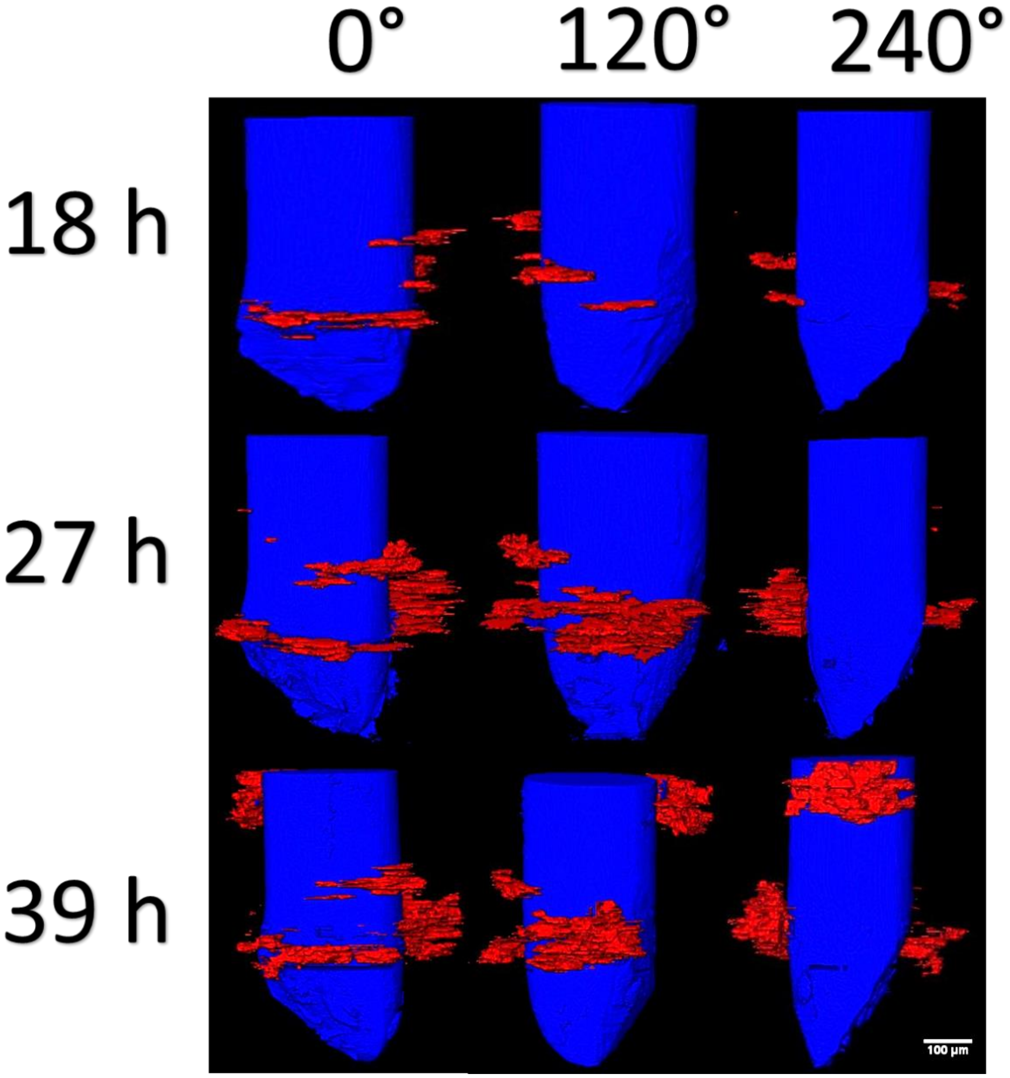

Figure 2.8. 3D reconstruction of simulated fastener of AA 7050-T7451 and stainless steel 304 under a droplet of 4 M NaCl exposure after 18 h, 27 h and 39 h showing the 4 fissures growing with time.

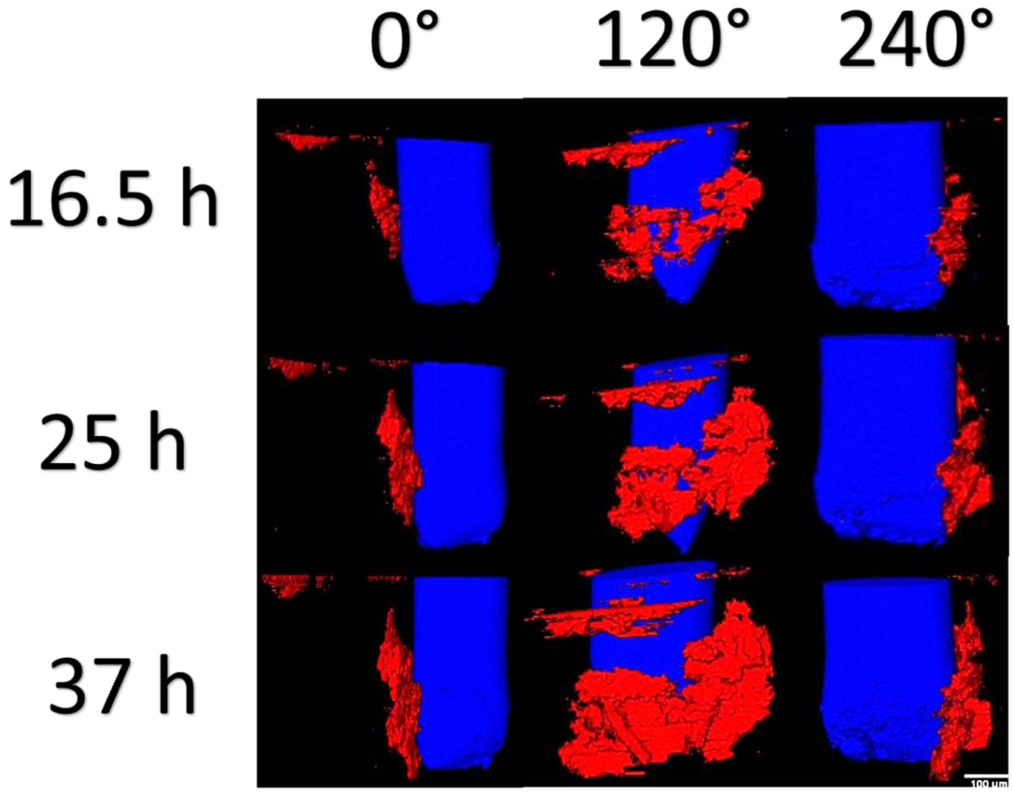

Figure 2.9. 3D reconstruction of simulated fastener of AA 7050-T7451 and stainless steel 304 under a droplet of 2 M $MgCl_2$ exposure after 16.5 h, 25 h and 37 h showing the 3 fissures growing with time.

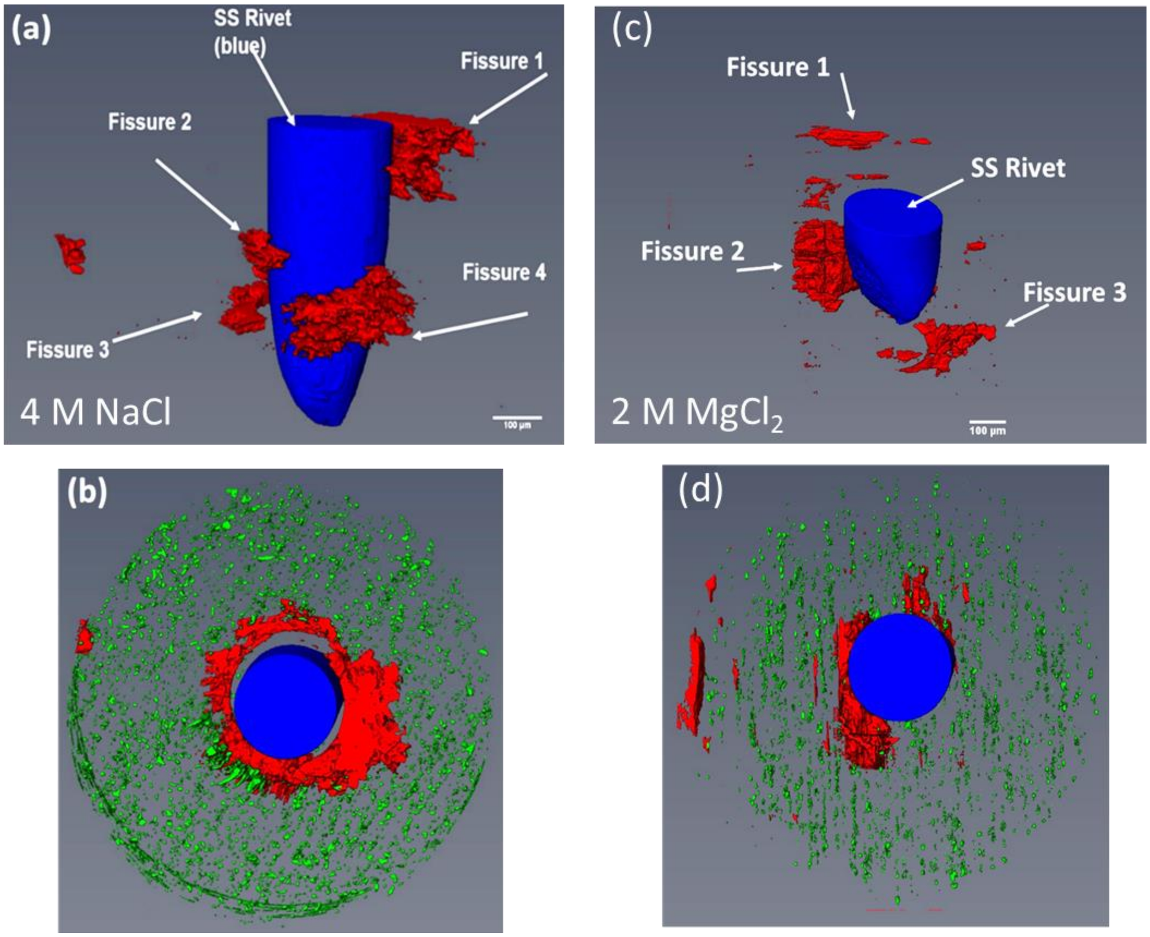

Figure 2.10. The reconstructed 3D representation of corrosion damage for the (a) 4 M NaCl droplet exposure after 62 h with the AA 7050-T7451 transparent showing the stainless steel rivet (blue) and the 3D-shaped volume (red) representing the corrosion damage in the form of fissures. (b) The location of the CPs (green) in relation with the stainless steel and fissures in the 4 M NaCl exposure (c) 2 M $MgCl_2$ droplet exposure after 60 h with the AA 7050-T7451 transparent and (d) The location of the CPs (green) in relation with the stainless steel and fissures in the 2 M $MgCl_2$ exposure.

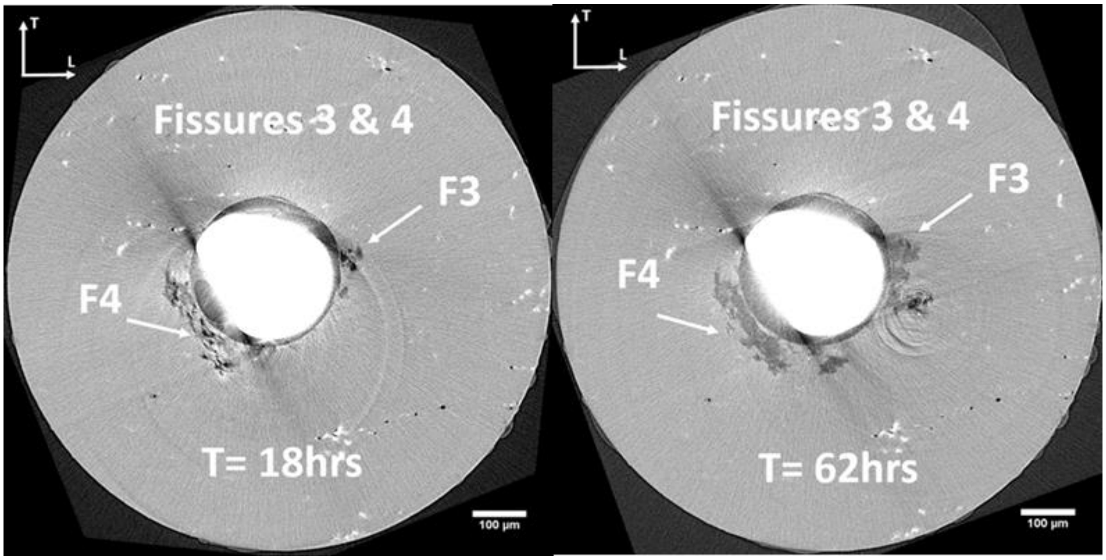

Figure 2.11. X-ray tomography slices showing the development of fissure 3 and 4 growing at the simultaneously after 18 and 62 hours 518 µm into the rivet in the 4 M NaCl exposure.

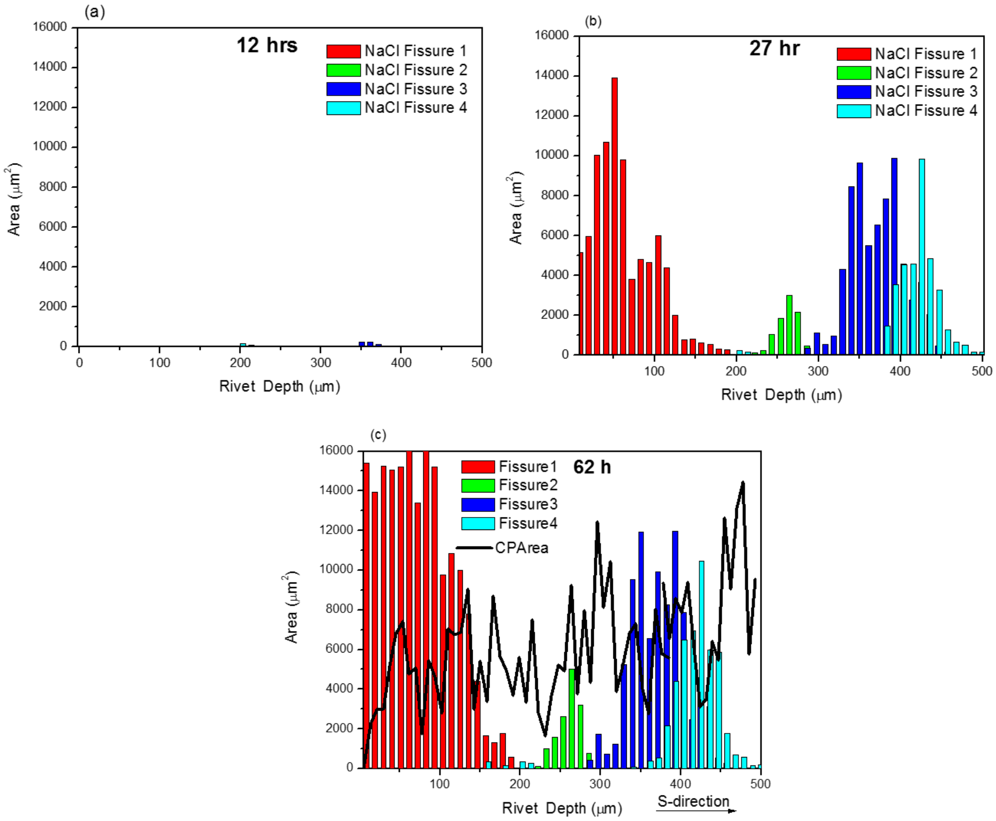

Figure 2.12. Corrosion fissure area bars for the 4 fissures observed in AA 7050-T7451 in the 4 M NaCl exposure after (a) 12 h (b) 27 and (c) 62 hours of exposure as a function of rivet depth. The various colors represent the different corrosion fissures. (c) includes the constituent particle area (black line) obtained through thickness.

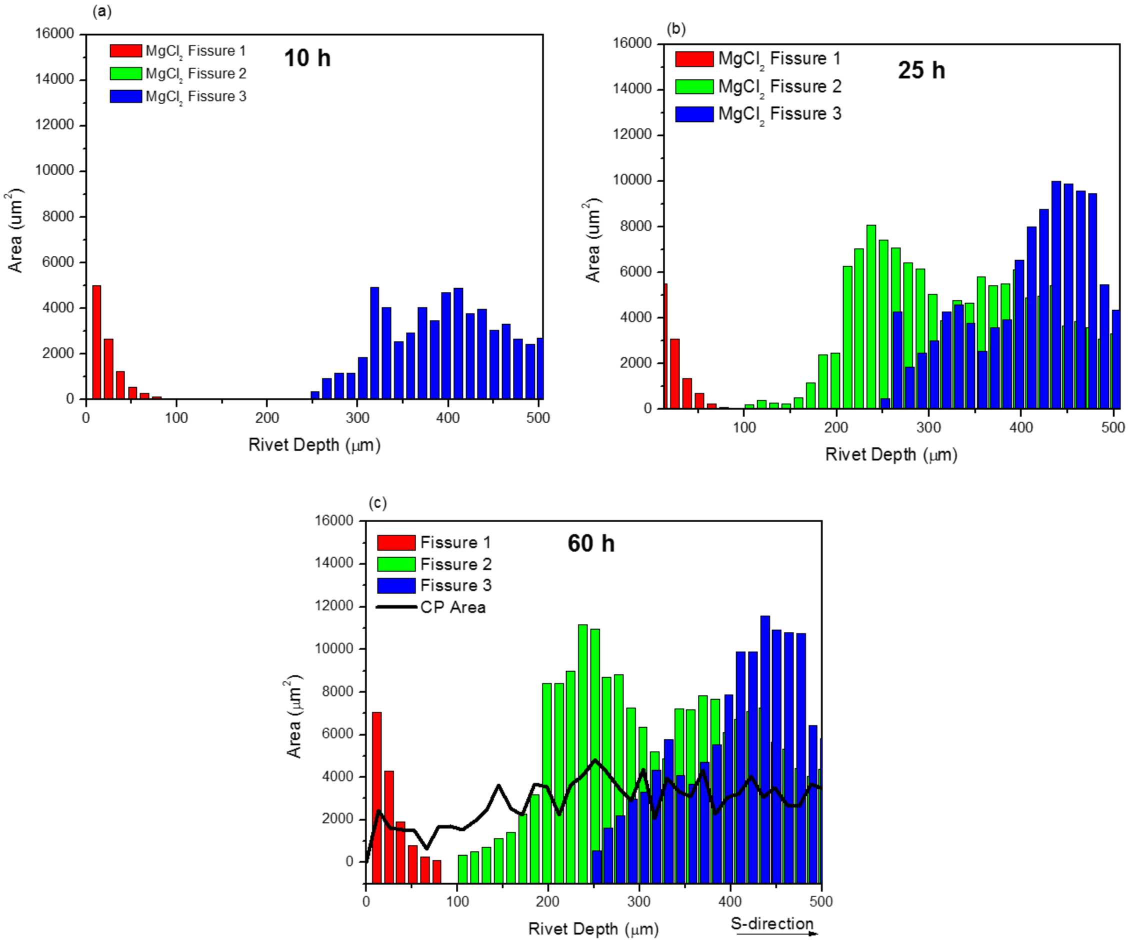

Figure 2.13. Corrosion fissure area bars for the 3 fissures observed in AA 7050-T7451 in the 2 M $MgCl_2$ exposure after (a) 10 h (b) 25 h and (c) 60 hours of exposure as a function of rivet depth. The various colors represent the different corrosion fissures. (c) includes the constituent particle area (black line) obtained through thickness.

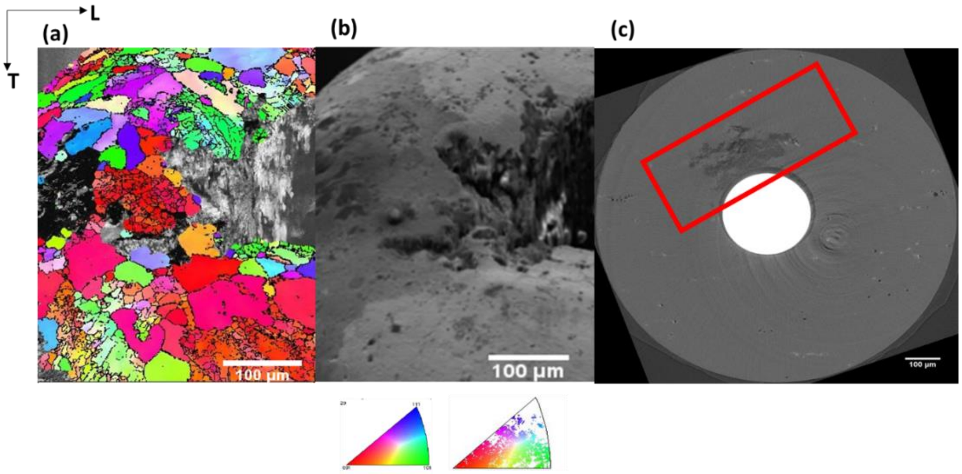

Figure 2.14. (a) Electron backscatter diffraction map of X-ray tomography exposed pin of AA 7050-T7451 with a stainless steel wire in the center after 62 h of exposure to a 0.4 µL droplet of 4 M NaCl on the surface. (b) Scanning electron image of mapped area (c) X-ray tomography corresponding slice on surface.

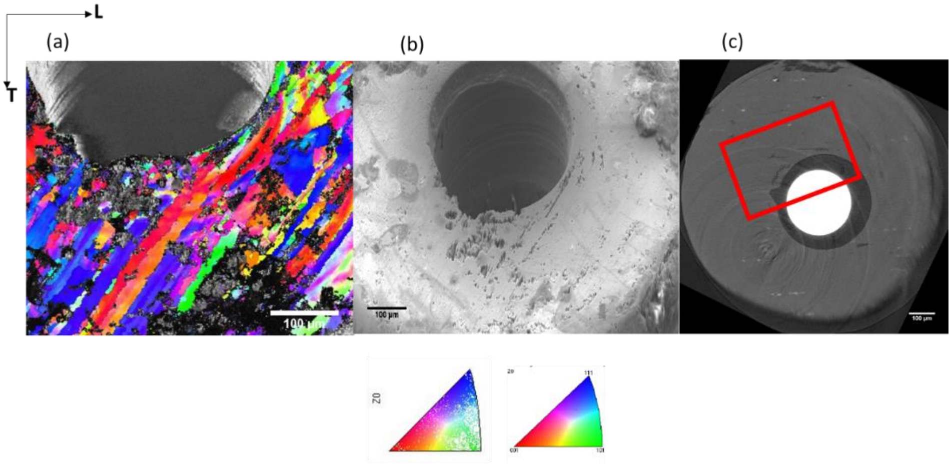

Figure 2.15. (a) Electron backscatter diffraction map of X-ray tomography exposed pin of AA 7050-T7451 with a stainless steel wire in the center after 60 h of exposure to a 0.4 µL droplet of 2 M $MgCl_2$ on the surface. (b) Scanning electron image of mapped area (c) X-ray tomography corresponding slice on surface.

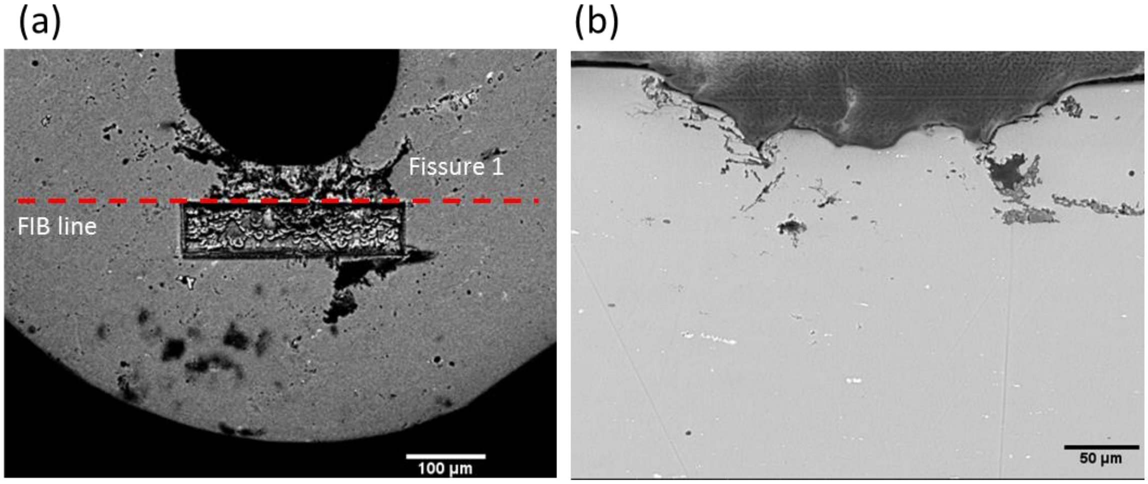

Figure 2.16. (a) Scanning electron micrograph in backscatter mode, showing the LT surface of the 4 M NaCl pin. The red dotted line indicates the focus ion beam (FIB) line that was used as a guide to cross-section. (b) Cross-section of fissure one in the 4 M NaCl exposure, showing the fissure was 105 µm deep.

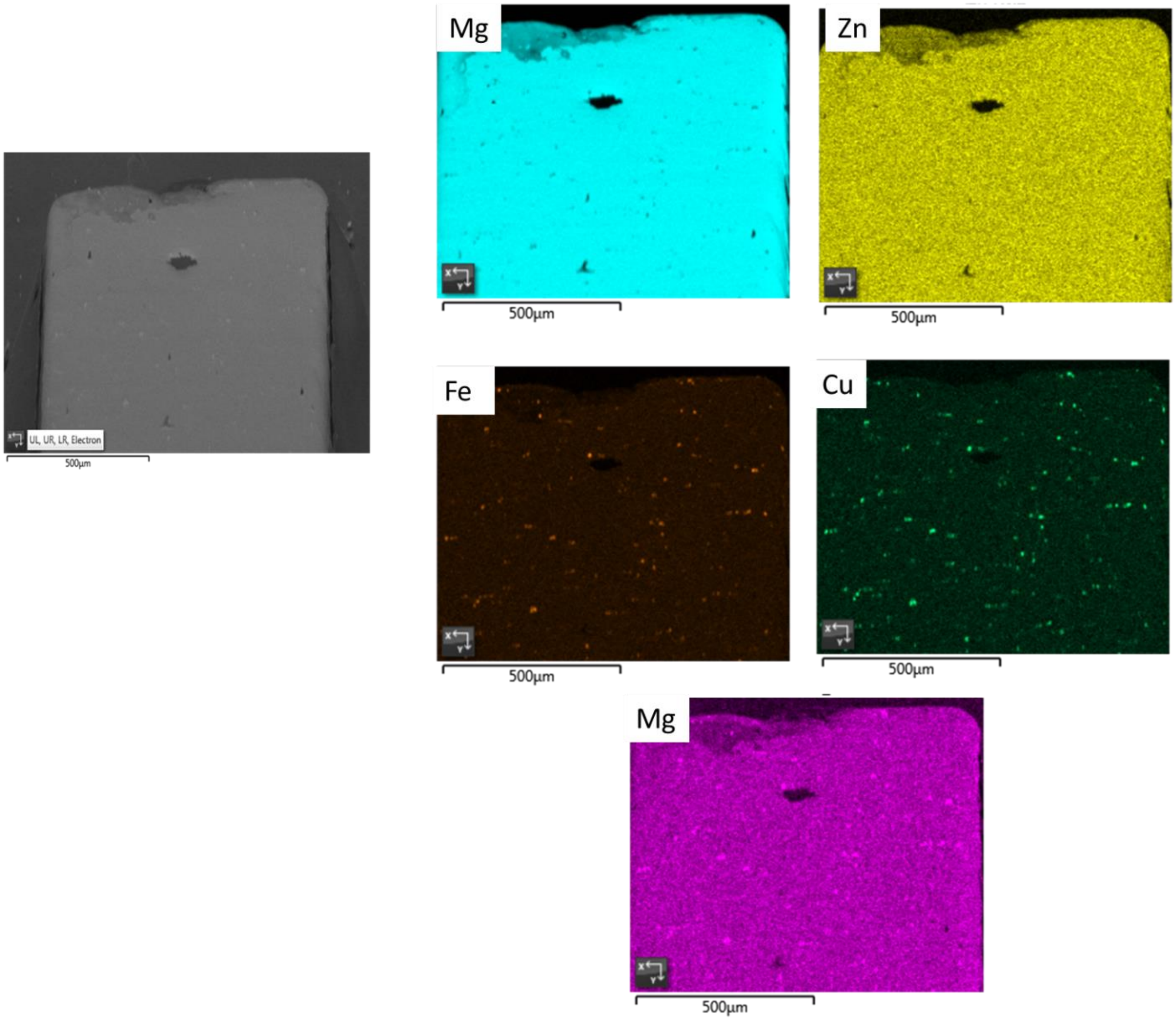

Figure 2.17. Secondary electron micrograph of cross-section of AA7050-T7451 after operando XCT exposure in 4 M NaCl and corresponding EDS composition maps for Mg, Zn, Fe Cu and Mg.

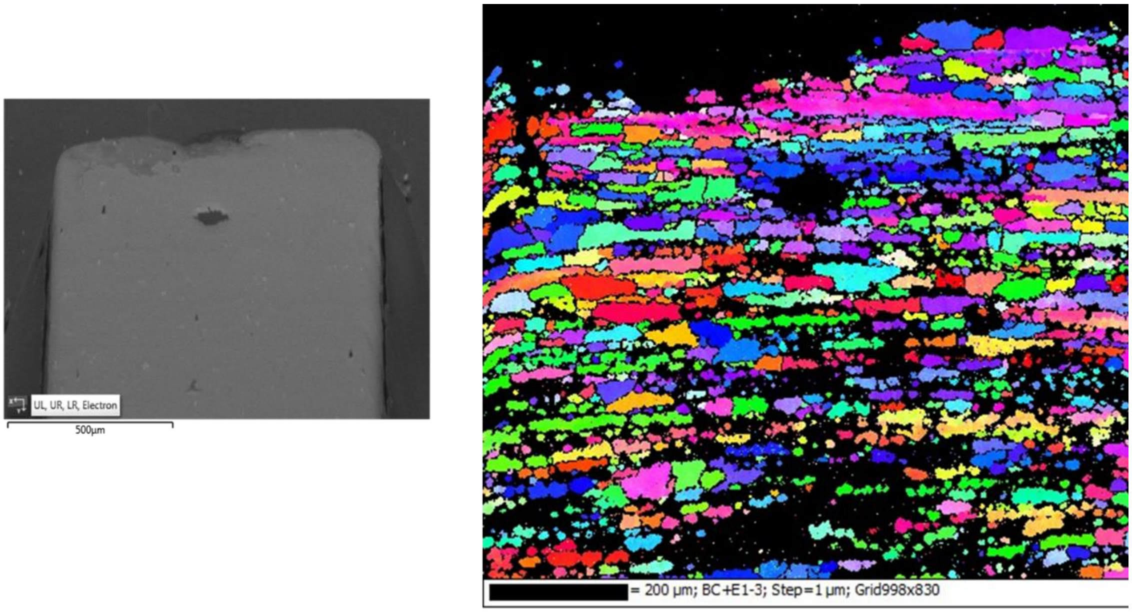

Figure 2.18. EBSD map in cross-section of AA7050-T7451 after exposure to a droplet of 4 M NaCl corresponding to the operando XCT results.

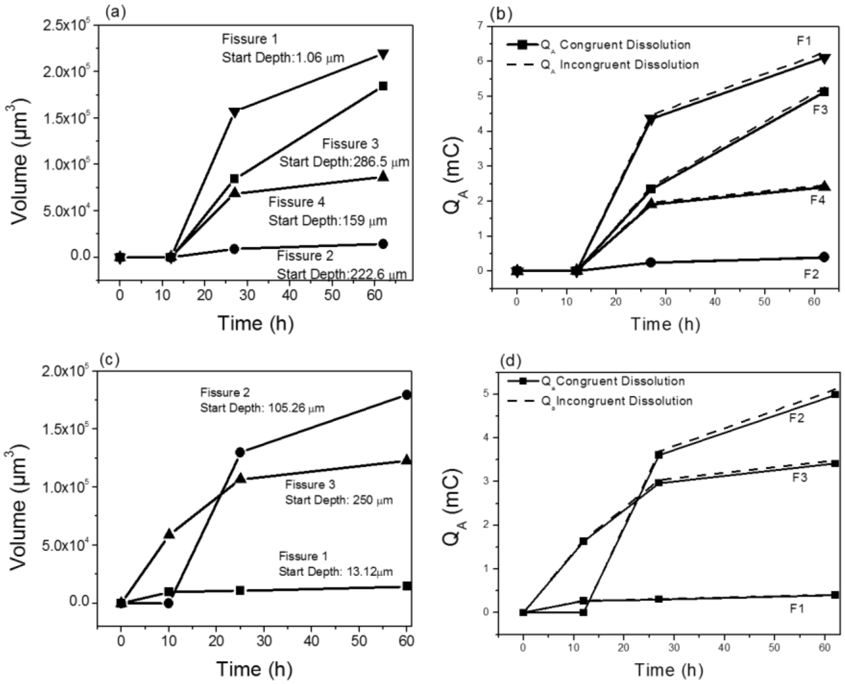

Figure 2.19.(a) Volume of damage lost from the three fissures observed in the 4 M NaCl exposure (b) Associated anodic charge for each of the fissures that were observed calculated with incongruent dissolution, Cu not dissolving, and congruent dissolution for 4 M NaCl. (c) Volume of damage lost from the three fissures observed in the 2 M $MgCl_2$ exposure (d) Associated anodic charge for each of the fissures that were observed calculated with incongruent dissolution, Cu not dissolving, and congruent dissolution for 2 M $MgCl_2$.

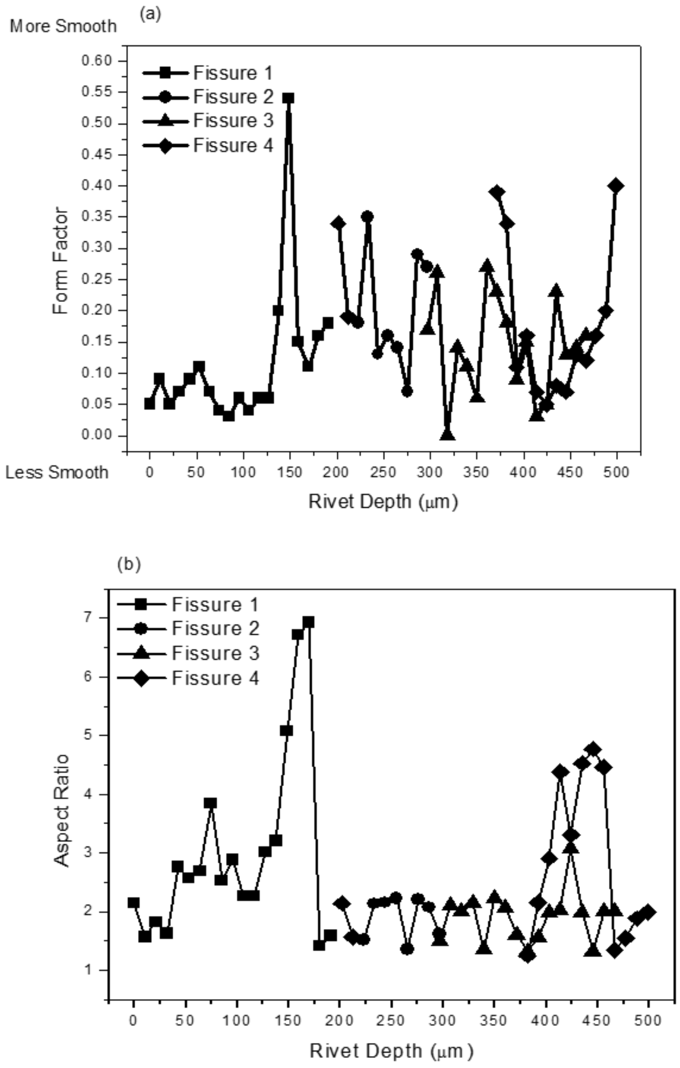

Figure 2.20. (a) Shape factor and (b) aspect factor for the 4 M NaCl exposure as a function of rivet depth after 62 hours of exposure.

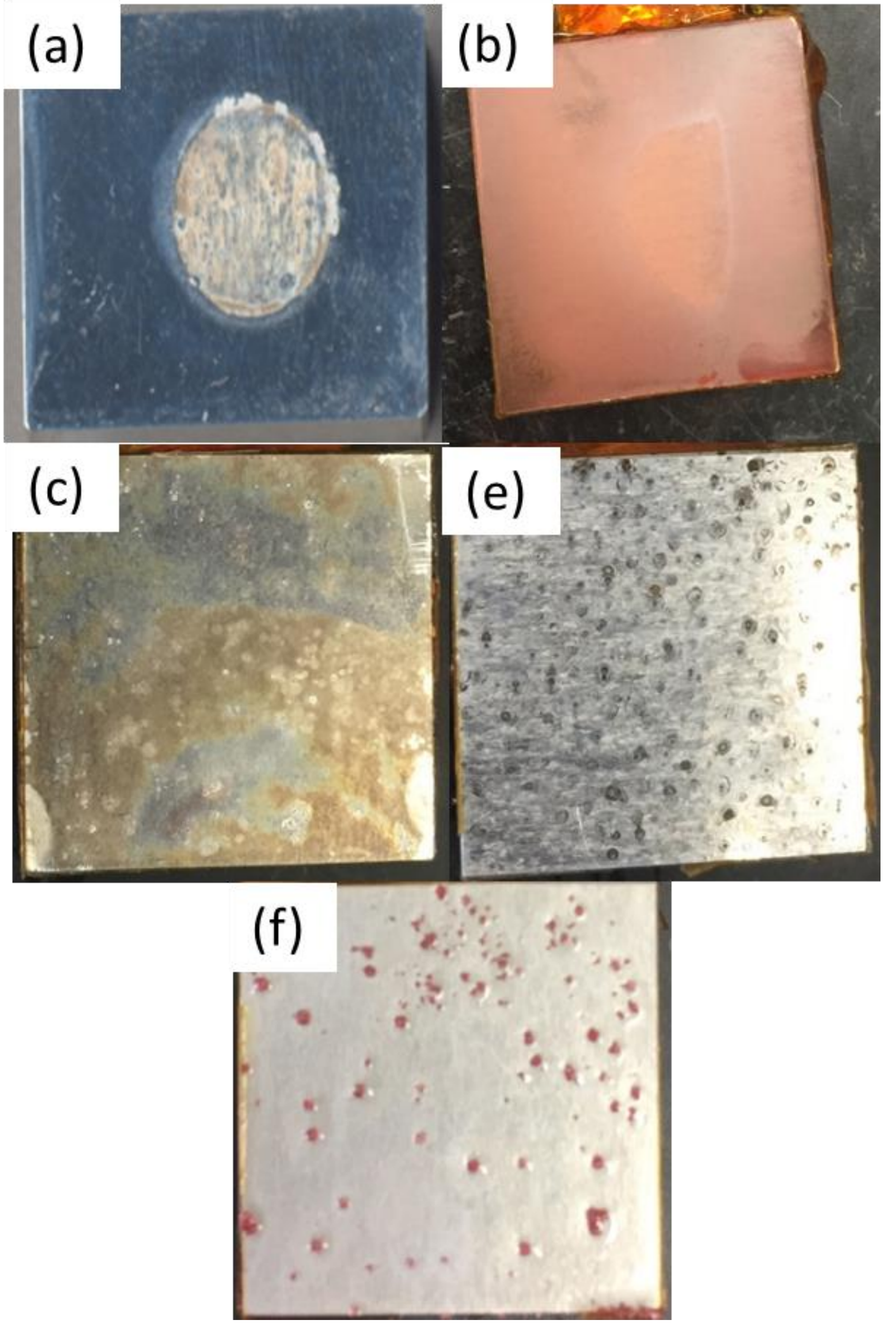

Figure 2.21. Images of Cu-replated after (a) 100 h ZRA exposure in 0.5 M NaCl + $NaAlO_2$ after 100 h (b) Cu-replating using potentiostatic deposition at E=-1.0 V SCE in 0.2 M $CuSO_4$+0.5M H_2SO_4 pH: ~1.6 (c) Cu plating by potentiostatically holding for 600 sec in 0.1 M $CuSO_4$+H_2SO_4 pH: ~3 (d) 48 h OCP in 0.5 M NaCl + $NaAlO_2$ pH: 8 (e) OCP for 48 0.5 M NaCl + HCl pH:3 (f) 48 h OCP in 0.1 M $CuSO_4$ pH: 3.3

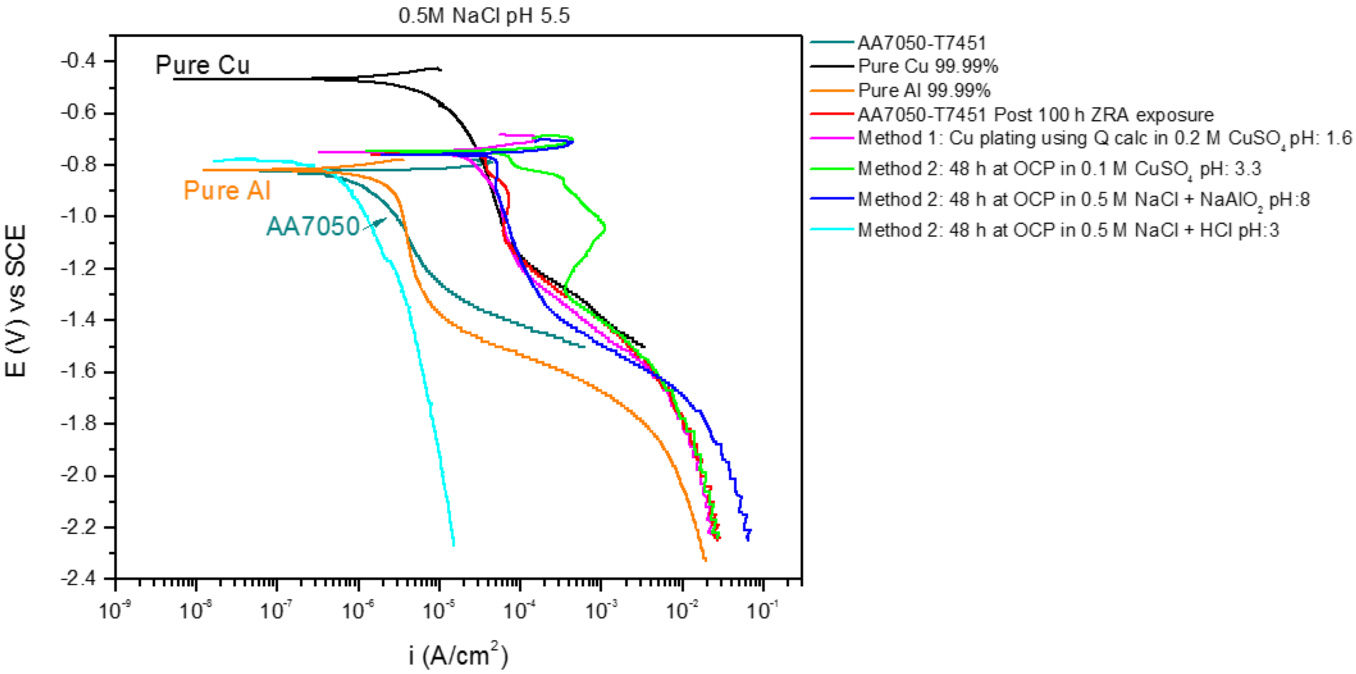

Figure 2.22. Cathodic polarization on AA7050-T7451, pure Cu and the various Cu-replating methods in 0.5 M NaCl + NaAlO$_2$ pH 8.

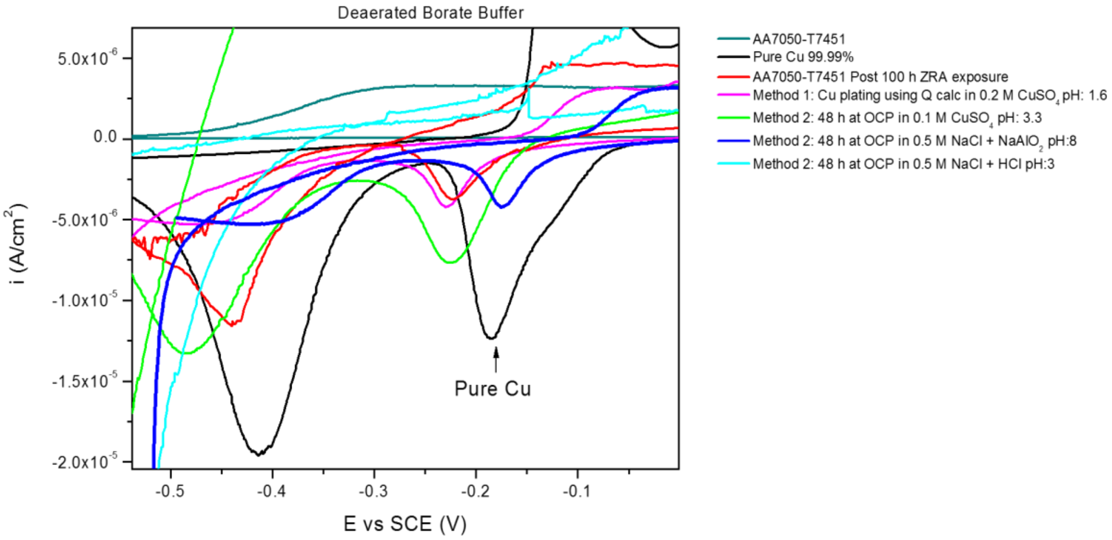

Figure 2.23. Cyclic voltammetry scan from -2 V to +2 V on AA7050-T7451, pure Cu, and the various the Cu-replating methods in deaerated borate buffer.

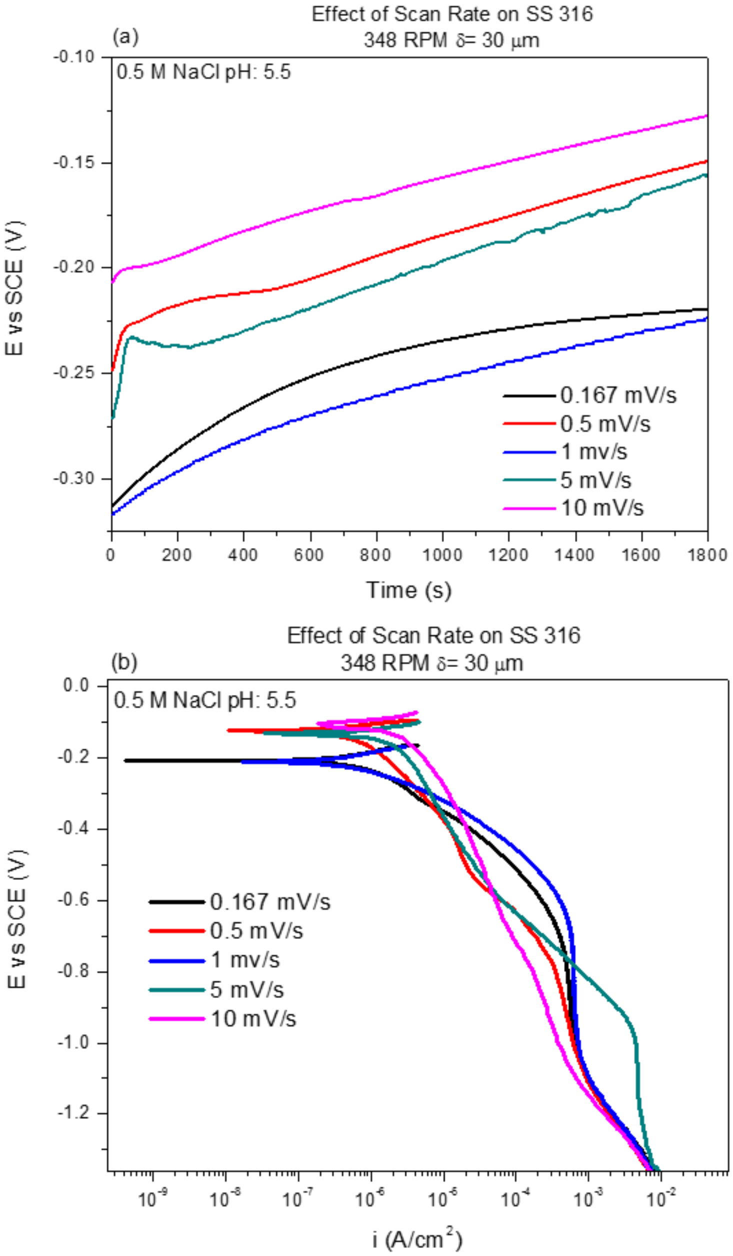

Figure 2.24. (a) OCP and (b) Cathodic polarization using a Type 316 stainless steel RDE in 0.5 M NaCl varying the polarization scan rate from 0.167 mV/s to 10 mV/s at δ=30 µm.

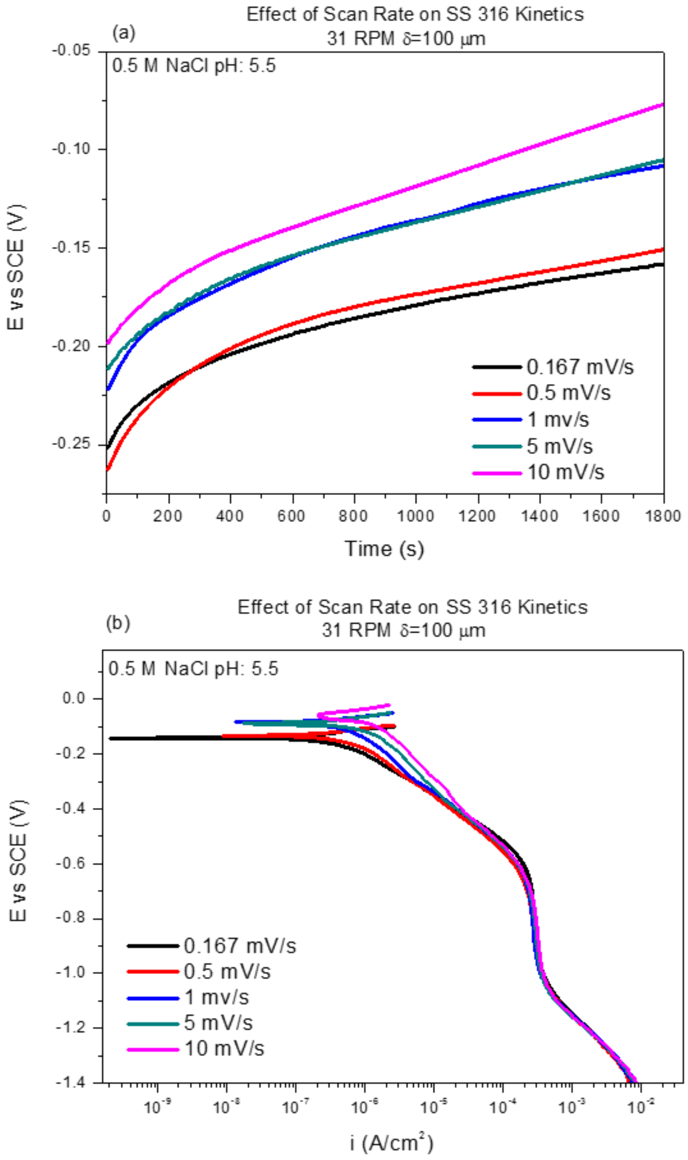

Figure 2.25. (a) OCP and (b) Cathodic polarization using a Type 316 stainless steel RDE in 0.5 M NaCl varying the polarization scan rate from 0.167 mV/s to 10 mV/s at δ=100 µm.

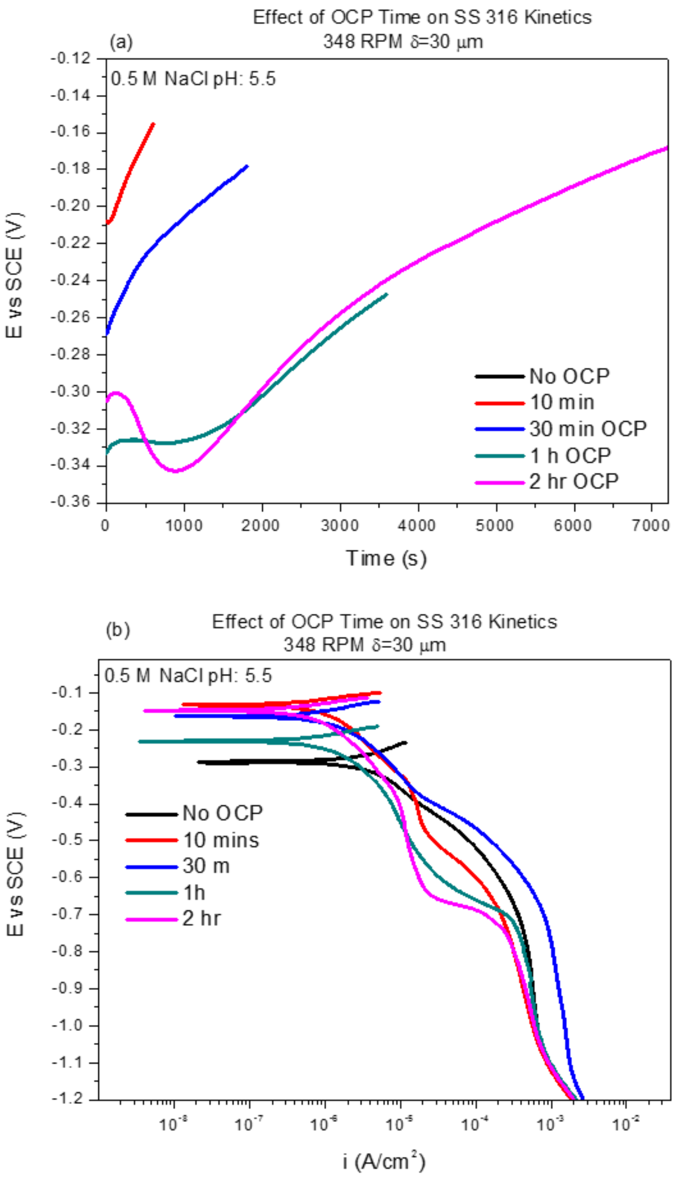

Figure 2.26. (a) OCP and (b) Cathodic polarization using a Type 316 stainless steel RDE in 0.5 M NaCl varying the OCP time from 0 h to 2 h δ=30 µm.

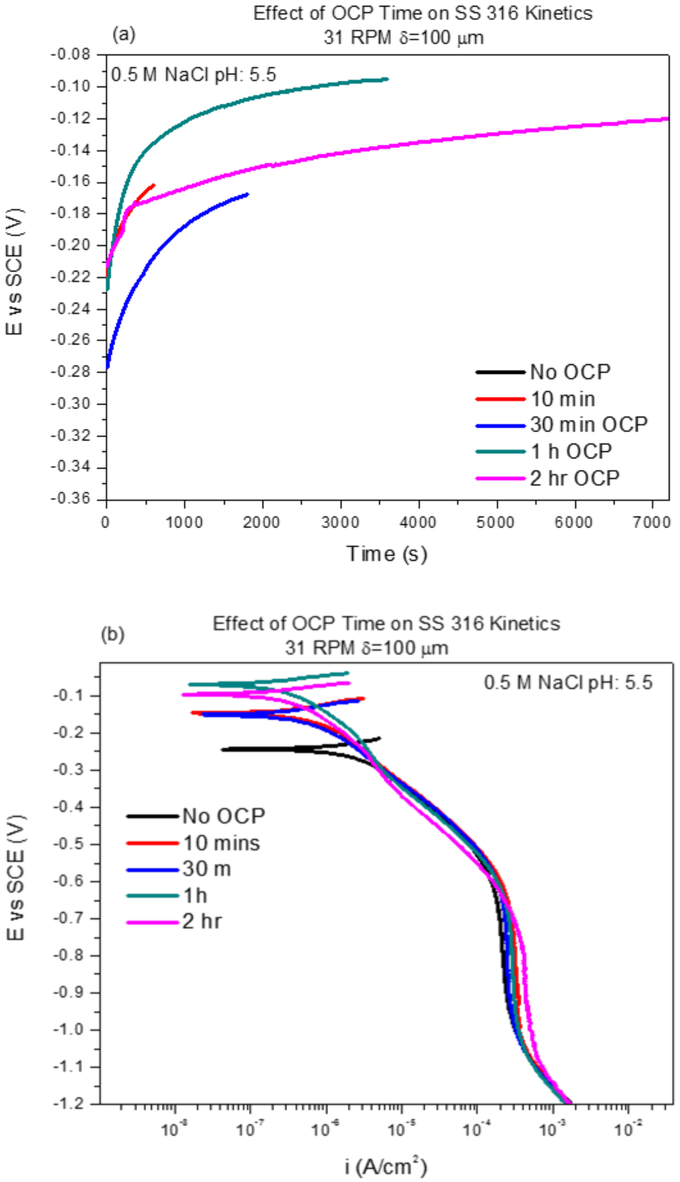

Figure 2.27. (a) OCP and (b) Cathodic polarization using a Type 316 stainless steel RDE in 0.5 M NaCl varying the OCP time from 0 h to 2 h δ=100 μm.

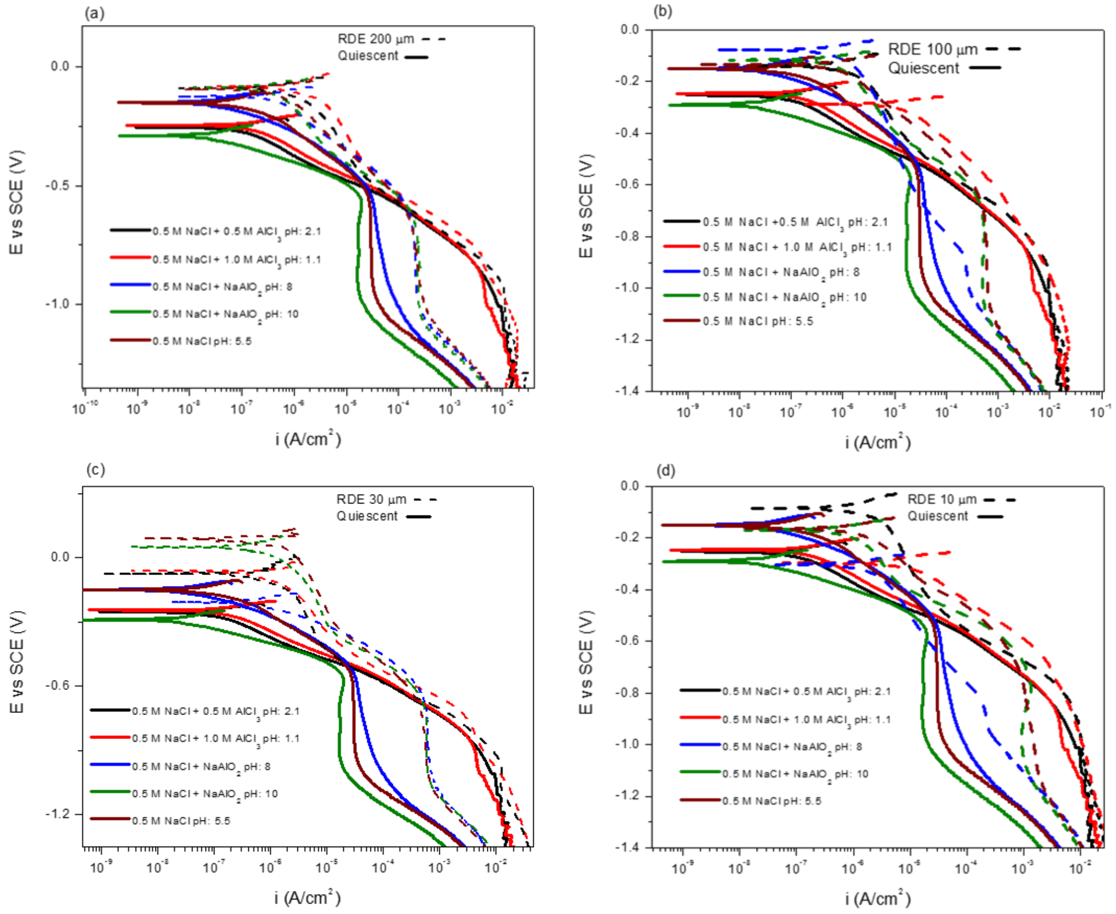

Figure 2.28. Cathodic polarization on Type 316 stainless steel using the RDE in rivet solutions of 0.5 M NaCl, 0.5 M NaCl + $NaAlO_2$ at pH 10 and at pH 8 and 0.5 M NaCl + $AlCl_3$ at pH pH 2 and at pH 1 corresponding to (a) δ=200 μm (b) δ=100 μm (c) δ=30 μm and (d) δ=10 μm.

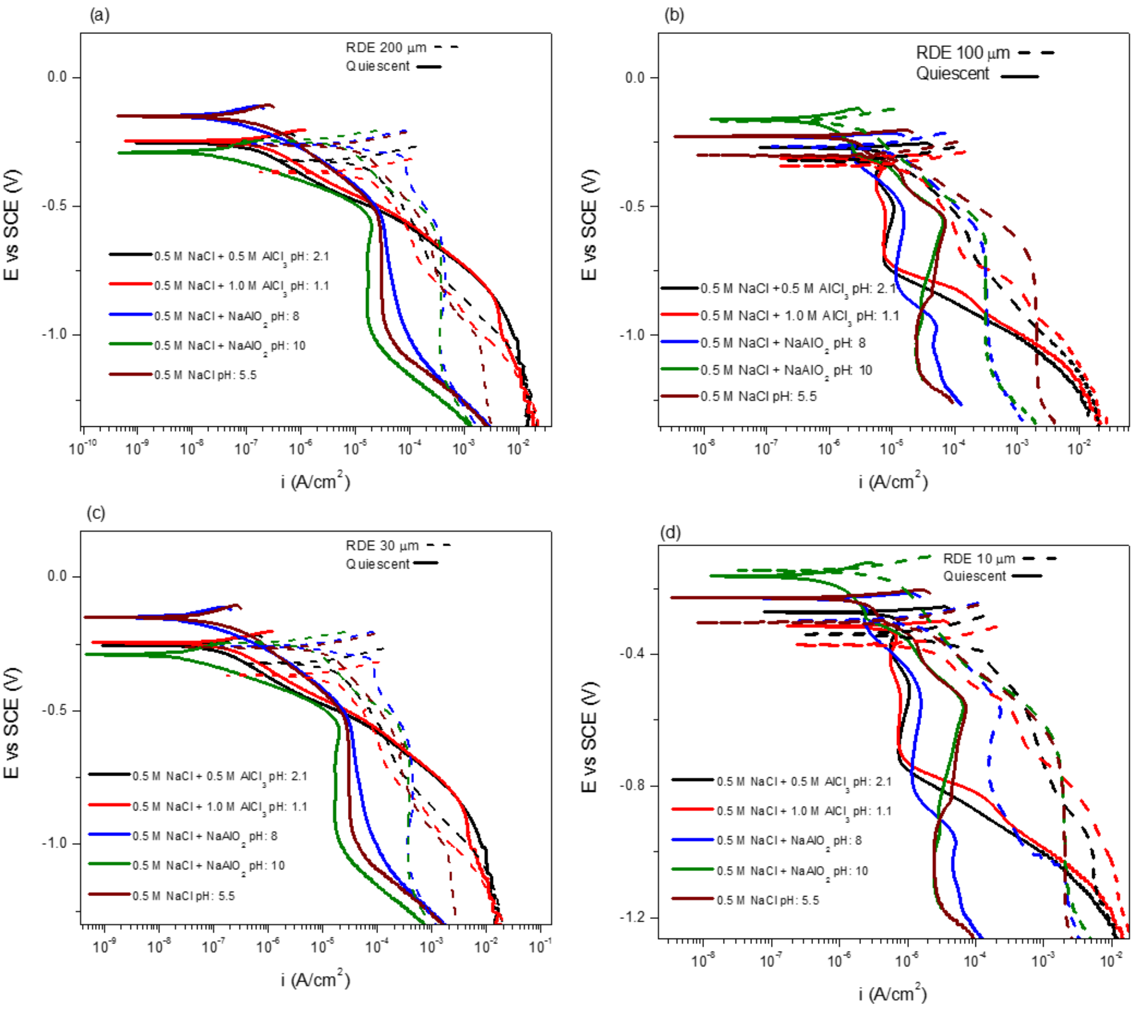

Figure 2.29. Cathodic polarization on Cu using the RDE in rivet solutions of 0.5 M NaCl, 0.5 M NaCl + $NaAlO_2$ at pH 10 and at pH 8 and 0.5 M NaCl + $AlCl_3$ at pH pH 2 and at pH 1 corresponding to (a) δ=200 µm (b) δ=100 µm (c) δ=30 µm and (d) δ=10 µm.

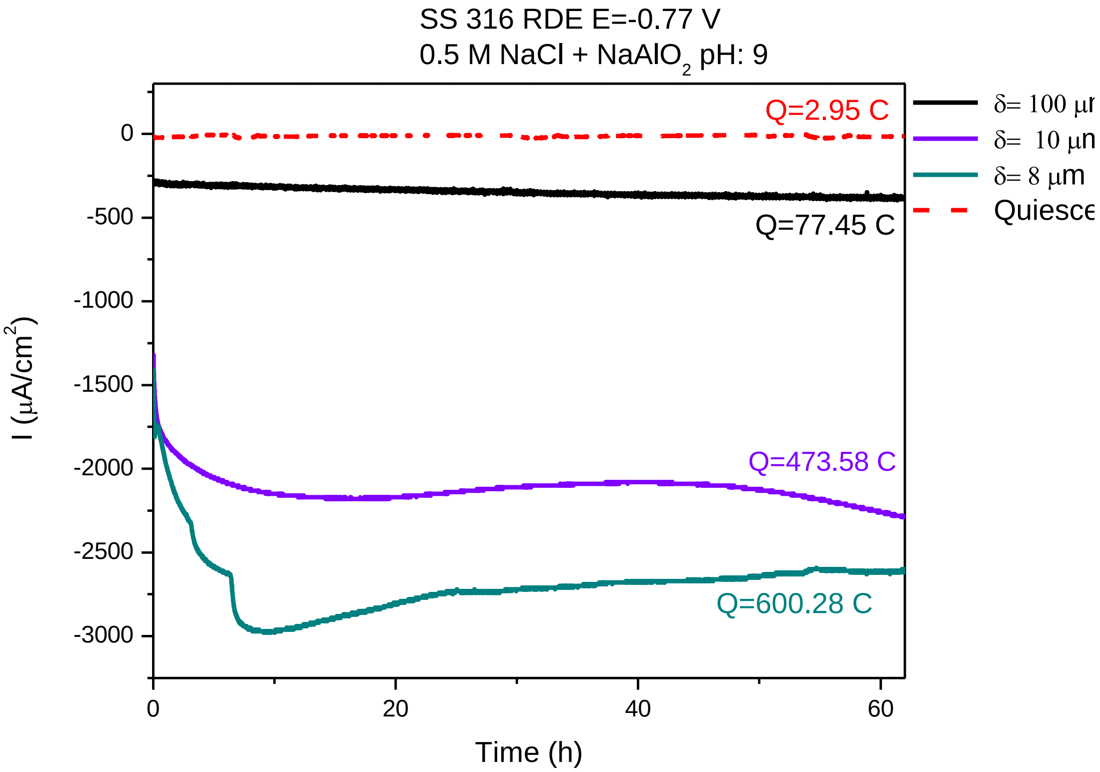

Figure 2.30. Potentiostatic cathodic polarization, E=-0.77 V on Type 316 stainless in 0.5 M NaCl + $NaAlO_2$ at pH 8 for δ=8 μm, 10 μm and 100 μm compared to quiescent conditions.

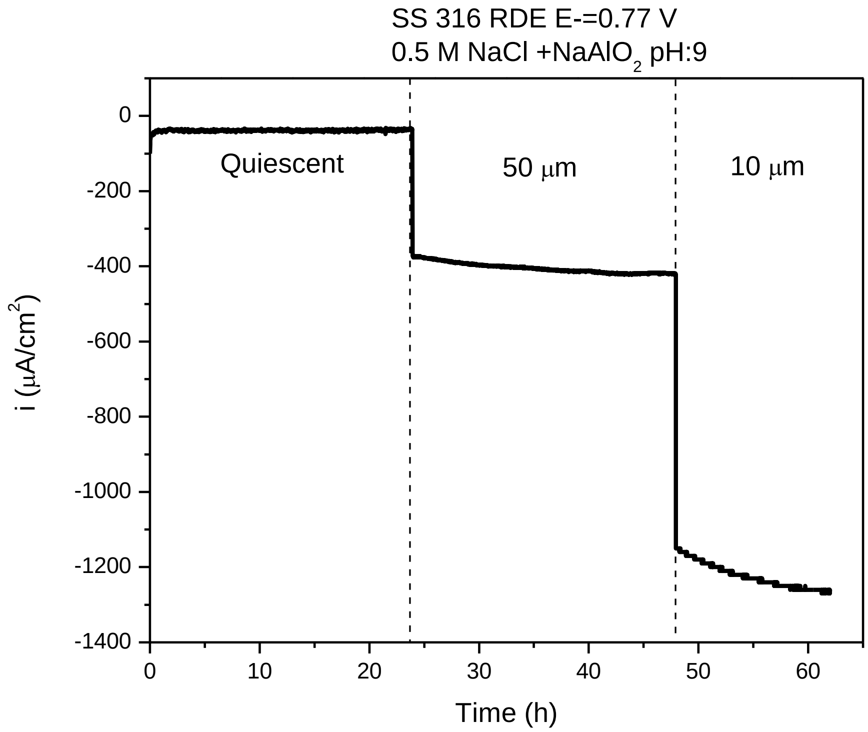

Figure 2.31. Potentiostatic, E=-0.77 V , cathodic polarization over 60 hours continuously changing the boundary layer thickness on Type 316 stainless in 0.5 M NaCl + $NaAlO_2$ at pH 8 at δ=8 µm, 10 µm and 100 µm compared to quiescent conditions.

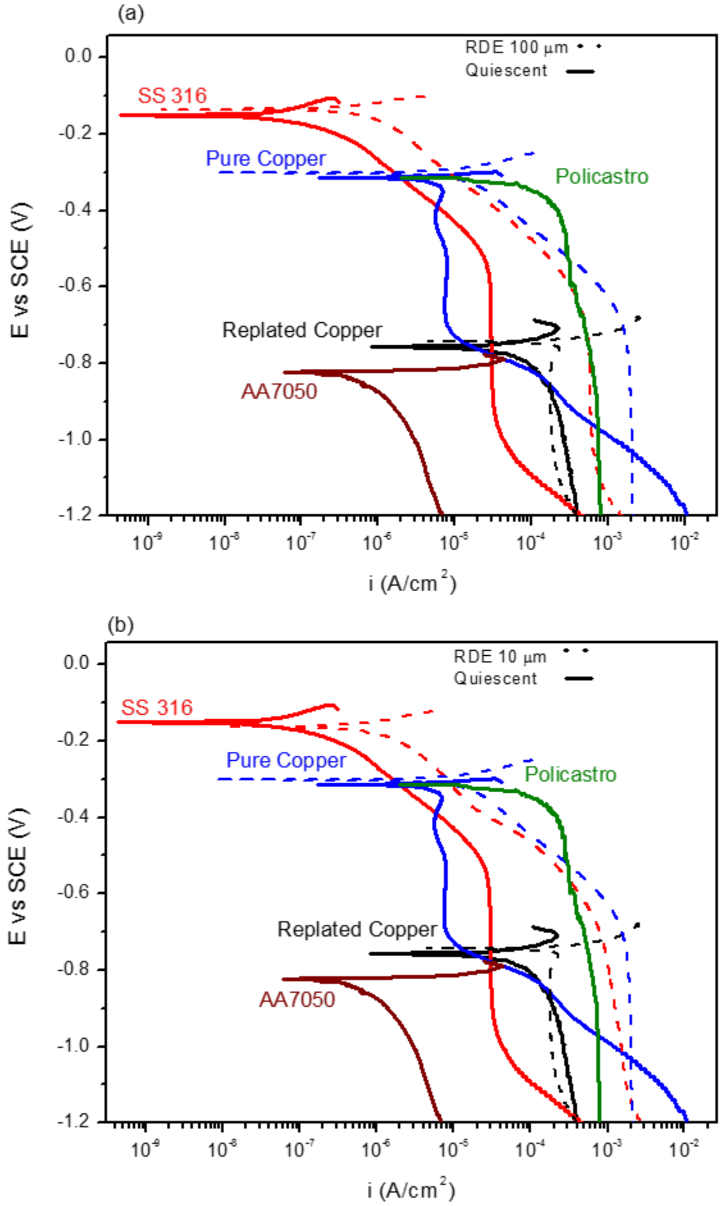

Figure 2.32. Comparison cathodic polarization plots of possible cathode on Type 316 stainless steel, pure, Cu, replated Cu, AA7050-T7451 in 0.5 M NaCl at (a) δ=100 µm and (b) 10 µm.

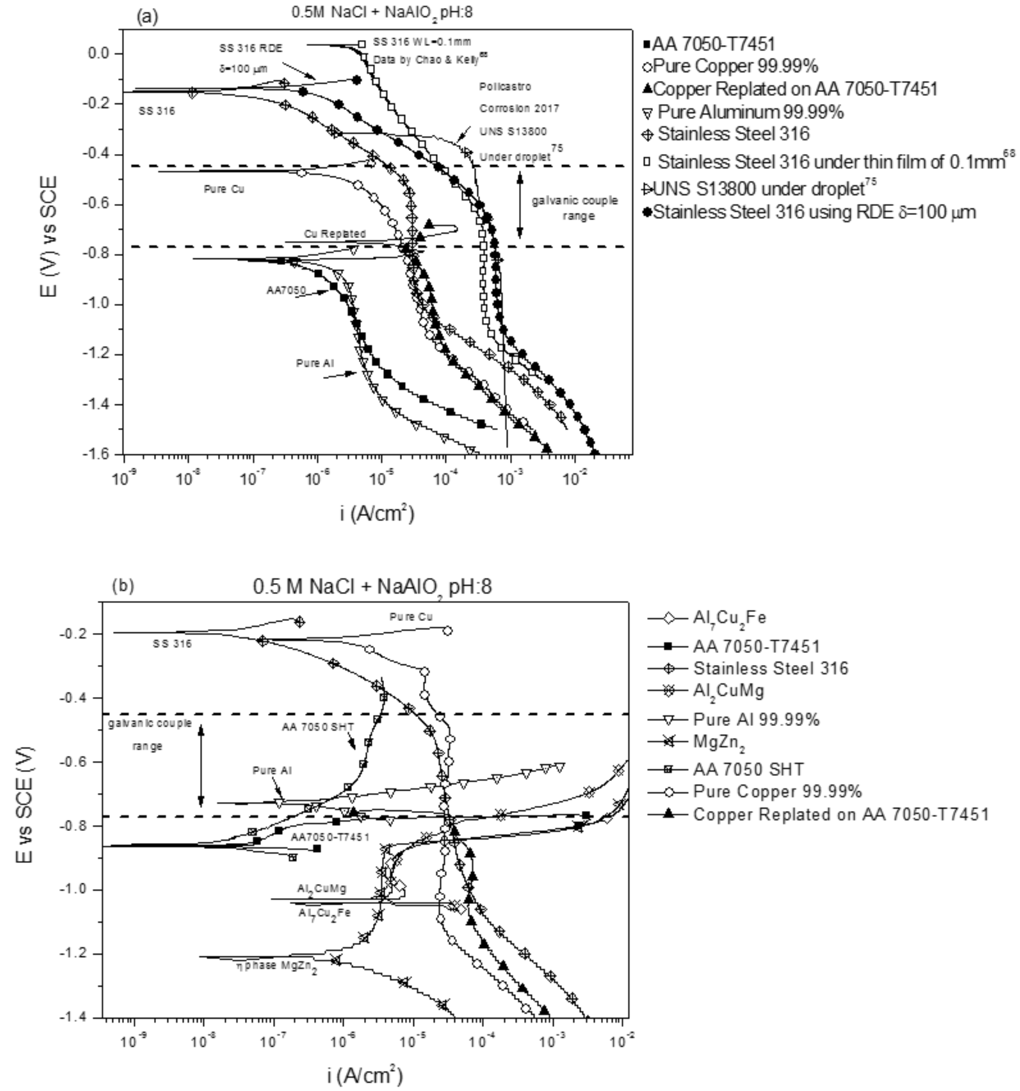

Figure 2.33. E-log i polarization behavior of the different phases in AA 7050-T7451, pure Cu, pure aluminum and stainless steel 316 in (a) in 0.5 M NaCl + $NaAlO_2$ pH 8 and (b) Cathodic and anodic polarization of the cathodic reactions occurring on various phases and surfaces when AA 7050-T7451 is coupled with stainless steel 316 0.5 M NaCl + $NaAlO_2$ pH 8.

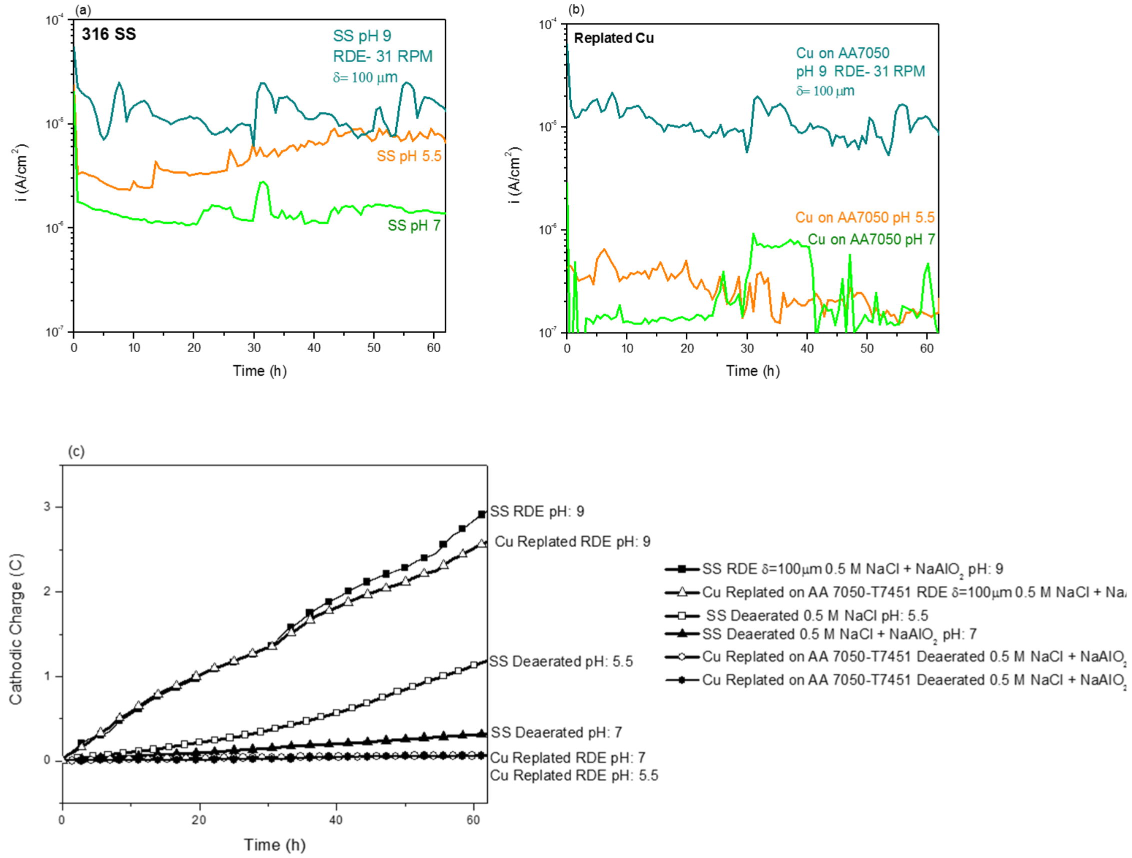

Figure 2.34. a) Cathodic current density from potentiostatic polarization on stainless steel 316 at E=-0.77 V conducted on a planer electrode of area 0.78 cm^2.(b) Cathodic current density from potentiostatic polarization on Cu-replated on AA 7050-T7451 at E=-0.80 V conducted on a planer electrode of area 0.78 cm^2 and (b) Cathodic charge density from potentiostatic polarization on stainless steel 316 and Cu-replated on AA 7050 for 62 hours.

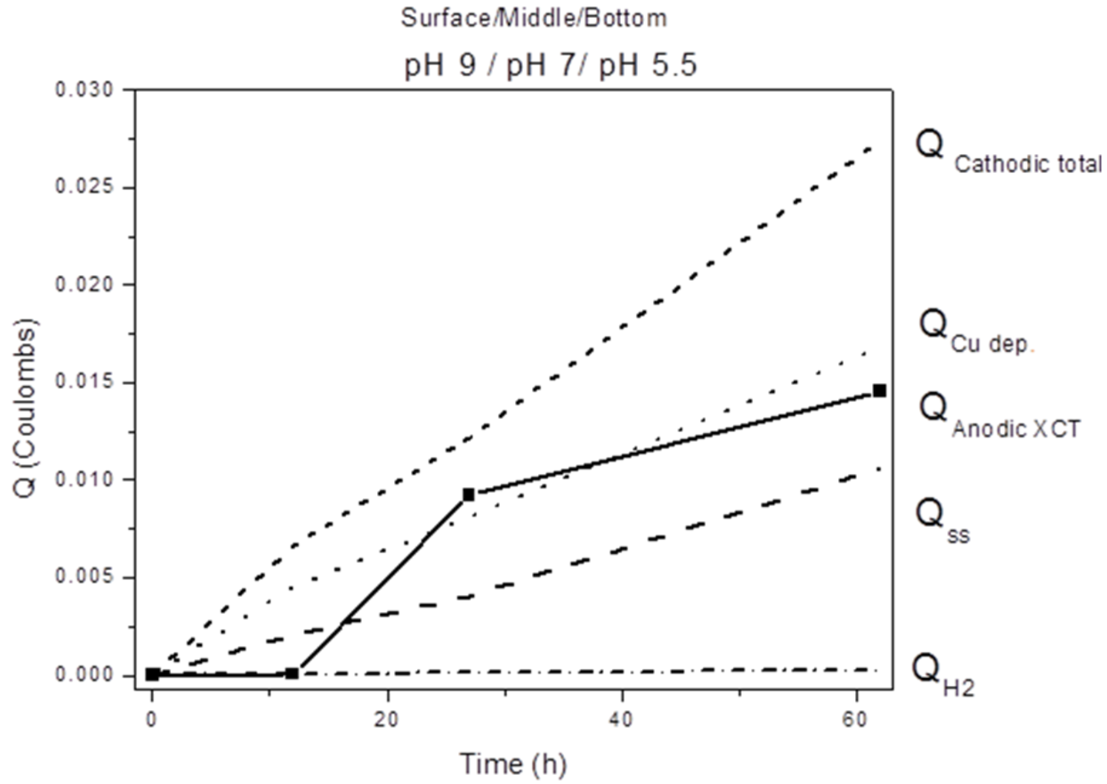

Figure 2.35. Charge over time for the different cathodic types of cathode sites which may contribute to fissure corrosion. The total anodic charge observed from the volume lost from all 4 fissures as a result of the XCT exposures is shown in red and the total cathodic charge the sum of all the contributors is shown in blue. This represents a gradient pH thorough the crevice where the pH turned alkaline pH of 9 at the surface followed by a region of pH 7 and finally pH 5.5 near the bottom of the crevice. The charge was calculated by using a known electrode area to get current density followed by multiplying by the rivet geometry and converting to charge.

3 Environmental Factors Affecting the Corrosion Damage Morphology in Simulated Rivet Solutions at the Meso-scale of AA7050-T7451

3.1 Abstract

The corrosion electrochemistry and damage morphology of AA7050-T7451 was studied in simulated rivet environments. Simulated rivet solutions consisted of 0.5 M NaCl with additions of $AlCl_3$ and $NaAlO_2$ adjusted to different pH values representative of different regions in a dissimilar metal galvanic couple crevice of AA7050-T7451 and Type 316 stainless steel. Firstly, guided electrochemical tests of anodic and cathodic potentiodynamic polarization was used to develop a range of relevant potentials and corrosion susceptibility in rivet solutions when AA7050-T7451 is coupled to Type 316 stainless steel. Potentiodynamic polarization showed that acidic environments had fast hydrogen evolution reaction that dominated over the oxygen reduction reactions. Environments with additions of $AlCl_3$ and $NaAlO_2$ were found to lower the galvanic couple potential and increase the galvanic coupling current. Secondly, lab based electrochemical corrosion methods (zero resistance ammeter, potentiostatic, and galvanostatic) on AA7050-T7451 coupled to Type 316 stainless steel over the range of relevant potentials and chemical variables was conducted to develop a library of damage modes. Environmental, and therefore corrosion electrochemical-material combinations were considered in accompanying lab studies which produced severe morphologies and were compared to the field data and other rescaled rivet studies. It was observed that in 0.5 M NaCl at pH 5.5 and $MgCl_2$ at pH 5 rounded-hemispherical pits formed. However in alkaline environments with additions of Al ions, the damage morphology was deep corrosion fissures (200 μm) in the L-direction. In acidic environments, the damage was a combination of corrosion pits and fissures with networks of intergranular corrosion. The differences in damage morphology based on environment is an imperative observation as it was also shown that the pH may vary in different regions of a rivet-hole. The damage morphologies observed after 504 h zero resistance ammeter exposures were found to have the closest correlation in damage morphology when compared with tear-down data from the Center for Aircraft Structural Life Extension Program.

3.2 Introduction

Aluminum alloy 7050-T7451 (Al-Zn-Mg-Cu) is often used for aerospace applications because it provides an advantageous combination of strength, stress corrosion cracking (SCC) resistance, corrosion resistance, and fracture toughness.[12,13] Although high strength aluminum alloys are widely used in aerospace applications due to their high strength to weight ratio they are prone to localized corrosion due to the formation of micro-galvanic couples in the alloy microstructure. [8,9] The localized corrosion can be further be exacerbated by galvanic coupling with a more noble material such as stainless steel or other typical fastener materials. [10,11] Defects in corrosion protection are enhanced at complex joining/fastener locations which trap electrolyte into tight crevices leading to occluded local environments where a galvanic cell is established between the aluminum alloy and a steel fastener. [12] Furthermore, the geometry of a fastener results in chemical and environmental changes at the mouth of a fastener from inside the fastener. Therefore, it is important to characterize the damage morphology of AA7050-T7451 in these relevant environmental and chemical environments. While the danger of galvanic corrosion has been recognized, little research has been developed to understand the physical, metallurgical and environmental factors governing the corrosion damage at the meso-scale between AA7050 and stainless steel.[11,133] Moreover, there is little understanding of laboratory approaches that produce damage morphologies comparable to those observed in service.

While a vast amount of work has been performed regarding the localized corrosion of high strength aluminum alloys there is a lack of literature on the unique factors and environments present in a rivet hole and furthermore how these factors and environments effect the overall damage morphology. [3,10,12-15] Previous work limits our understanding of damage morphologies to a few specific test environments such as Point Judith marine seacoast atmospheric exposures, full immersion in 0.6 M NaCl, EXCO solution, [16] and 0.6 M NaCl + H_2O_2,[17] as there has been very little work on crevice and rivet specific environments with galvanic coupling between Type 316 stainless steel fasteners. Literature has shown that galvanically induced localized corrosion in Al alloys can be strongly influenced by environmental parameters such as pH, species, and concentration.[66-68]

3.2.1 pH Change inside a Crevice

The depletion of dissolved oxygen in the crevice results in, at first, the formation of a differential aeration cell. Metal ions then accumulate in the solution inside the crevice as a result of anodic dissolution. Acidification occurs from hydrolysis of metal ions inside the crevice. Chloride ions migrate into the crevice to preserve electroneutrality and the primary cathodic reaction is outside the crevice while hydrogen reduction occurs inside the crevice solution and hydrogen gas evolves. However, Cottis reported variable behavior with pH going acidic near the crevice mouth and alkaline in the deeper region in a crevice of AA 7475. The mechanism of alkalization was deemed unknown.[69] In the case of dissimilar metal crevice corrosion in rivets, the local cathode (Type 316 stainless steel), is functioning as a cathode throughout the length of the crevice. This can affect the pH gradient and differs from conventional crevice corrosion where the cathode is located only or primarily outside the crevice. Preliminary studies show the micro crevice becomes alkaline with a proximate cathode but local corrosion sites still become acidic within the corrosion site. [155] Therefore, the macro crevice pH rises only to 8 but local acidic sites are still seen at pH 3-4. This is slightly different from cases involving an external cathode which cause larger regions of acidity to develop on the net anode (7050) at the mouth of a crevice. In contrast, an internal cathode involving a dissimilar metal causes the pH to become alkaline.[70] Furthermore, Kelly and Stewart studied the pH inside a crevice of stainless steels utilizing computational modeling and found that pH continued to fall due to Cr^{3+} hydrolysis. The position of minimum pH was found to move deeper into the crevice with time, but the differences in pH between the mouth, the minimum point and the base of the crevice were observed to be small (< 0.5 pH units).[156]

3.2.2 Effect of Solution Chemistry

The effect of cations on crack growth behavior in Al-Zn-Mg-Cu was studied by Speidel. [157] It was reported that the only cations that have an effect on crack growth behavior were Hg^+ and H^+[157] in aqueous Cl^-. However, Sotoudeh reported that aluminum salts in the pH range 3 to 4 enhance aluminum corrosion in comparison to NaCl solutions of the same pH.[158] It was noted that this effect was not restricted to $AlCl_3$ solutions. Sotoudeh also found that it is the nature of aluminum salts rather than the pH of solution produced by the hydrolysis of the aluminum cation. Thus, aluminum sulfate solutions were non-corrosive and aluminum nitrate solution accelerated corrosion. This result emphasized the chemical nature of the process as opposed to strictly physical or electrochemical approaches. This suggested that there may be some role of Al ions in solution on the corrosion kinetics.

The propensity of an anion to form soluble Al-complexes and activate the aluminum surface has been implicated in the ability of a particular salt to promote corrosion and environmental cracking. Le stated that the local corrosion is viewed as serving two functions of stress corrosion cracks: (1) its pH is such as to keep the aluminum surface active and (2) it provides the anions required to form soluble complexes with aluminum to effect one necessary step in the corrosion process. [159] Soluble Al-complexes can form in the presence of iodine, bromide, and chloride which may promote localized corrosion and thus can influence crack propagation and initiation. [10,160]However it was also found that fluoride, sulfate, nitrate, and chromate either passivate or inhibit corrosion processes by forming stable and/or insoluble complexes with Al.[132,159]

3.2.3 Corrosion Morphologies in Aluminum Alloys

Many heat treatable aluminum alloys are susceptible to exfoliation corrosion since they often have highly directional grain structures and can be subject to intergranular corrosion. Resistance to exfoliation corrosion of these alloy is improved by artificial aging treatments. [29,53,161,162] The EXCO immersion test (ASTM G34) was developed using alloys 7075 and 7178. However, when the high solute AA7050 was introduced it was found that the degree of correlation was different between the tests in the accelerated EXCO method and other seacoast exposures. Lifka designed a modified EXCO solution containing 600 mg/L of aluminum, 4.0 M chloride and 0.6 M nitrate at pH 3.2. The modified EXCO was named ANCIT (aluminum-nitrate-chlorine-immersion test) and was found to be more reliable in predicting exfoliation performance in natural environment such as seacoast atmosphere and of distinguishing between various commercial tempers of 7050 and 7150.[162] Virtanen studied the influence of temper and surface morphology on the exfoliation behavior of Al-Zn-Mg-Cu alloys in ANCIT. There was almost no distinct differences between the tempers T6 and T76, even though the latter is slightly less susceptible to exfoliation. Alloys of the AA7010 system exhibited, in general, a much higher resistance to exfoliation than alloys of the AA7349 system. This behavior was concluded to be due to the higher Zn content of AA7349, and thus the higher concentration of active grain boundary precipitates.[53] In EXCO solution, 7xxx series Al alloys were found to undergo intergranular dissolution induced damage, which is localized intergranular corrosion that results in exfoliation corrosion by subsequent grain lift-up when precipitation of the corrosion products occurs. [163]

In another study, the corrosion damage morphology of Al alloys in 57% NaCl + 10 ml/L H_2O_2 were investigated. Al-Zn-Mg-Cu OA alloys were found to undergo total IGC damage over the entire specimen. The IGC damage morphology was characterized in different forms of intergranular corrosion. The first form (crystallographic IGC) was caused by the formation of corrosion active areas at high-angle boundaries of recrystallized grains at certain stages of recrystallization. The second form (structure-decomposition IGC) was associated with the formation of corrosion active areas in close proximity to incoherent or partly coherent phase particles located at grain boundaries. [164]

3.2.4 Aluminum Alloy Field and Tear-Down Data

In a study by Young, AA2024-T3 plates with Type 316 stainless steel fasteners were exposed in Daytona, Florida at the Battelle site.[11] Assemblies were placed on a wooden exposure rack at a 45˚ angle 100 meters from shore. The average temperature fluctuated between 18-28˚C and time of wet hours ranged from 200-420 hours per months. According to Battelle, the average salinity was between 26-35 parts per thousand which is classified as Class III water.[165] Samples were exposed for 6, 12, 18 and 24 months. Figure 3.1 shows the surface and cross-section of the field exposures. When exposed with the stainless steel fastener, corrosion pits and IGC penetrated to depths of 150 µm after 6 months exposure. At 12 months exposure, the corrosion advanced to depths of 220 µm and the IGC advanced to 250 µm. After the 24 month exposure, corrosion pits measured 270 µm, IGC 230 µm, and SCC 750 µm, respectively. The deepest penetration depths after 24 months exposure were found to be 850 µm throughout the 24 months of exposure. The SS fastener remained passive and did not exhibit damage.[11]

Teardown data from a United States air force aircraft was provided by The Center for Aircraft Structural Life Extension program as a comparison tool. The damage morphology observed in the data was localized corrosion such as exfoliation, IGC, IGSCC, pitting and fissures. Details such as alloy, temper, and location of damage were undisclosed, however, most USAF aircrafts are built using 2xxx or 7xxx series alloys. Figure 3.2 and Figure 3.3 show two different fastener-hole configurations that experienced corrosion damage under operational conditions. In the damage that occurred in Figure 3.2, the corrosion damage was located away from the hole-bore with no cracks seen inside the bore. Two cracks were observed on the section surface. Intergranular cracks initiated from the mechanical damage on the surface and extended through the thickness while branching along grain boundaries. The cracks were approximately 812 µm in length. Figure 3.3 shows a different corrosion site where microscopy found corrosive attack throughout the bore, this is indicated in red in (b). The polished surfaces showed corrosion extending up to the cut sections. Teardown data was provided as a useful comparison measure to laboratory based exposure tests.

3.2.5 Objective

The objective of this work was two-fold. Firstly, guided electrochemical testing using anodic and cathodic potentiodynamic polarization developed a range of relevant potentials of corrosion susceptibility of AA7050-T7451 coupled to Type 316 stainless steel. These tests were conducted in simulated rivet environments, NaCl with $AlCl_3$ or $NaAlO_2$ at acidic and alkaline pH levels. This will give indication on the effect of simulated rivet environments on the galvanic couple potential and current. Secondly, lab based electrochemical corrosion methods on AA7050-T7451 coupled to Type 316 stainless steel over the range of relevant potentials set by the anodic and cathodic potentiodynamic polarization will be conducted. This task will develop a library of damage modes in environments and chemical variables that are often observed when AA7050-T7451 and Type 316 are coupled. Environmental and therefore corrosion electrochemical-material combinations were considered in accompanying lab studies which can produce severe morphologies and be compared to the field data and other rescaled rivet studies. This chapter will characterize the corrosion damage morphologies that may be induced in fasteners when AA7050-T7451 is coupled to SS.

3.2.6 Hypothesis

Based on preliminary results it is hypothesized that environmental factors such as Al^{3+} ions in solutions will affect the damage morphology of AA7050-T745 at potentials that are relevant to galvanic coupling to Type 316 stainless steel. Furthermore, it is hypothesized that dealloying and Cu-replating may occur more readily in alkaline environments than in acidic environments.

3.3 Experimental Methods

3.3.1 Materials

The material used in this study was machined from Al-Zn-Mg-Cu alloy plate of 50 mm thickness provided by Alcoa. The microstructure has elongated grains in both the longitudinal (L) and long transverse (T) direction and are thinned in the short transverse (S) forming pancake-like microstructure. The grains in the L direction ranged from 22-1250 µm in length, while the grains in the T and S directions ranged from 15-265 µm and 12-112 µm, respectively. The microstructure in shown in 3D in Figure 3.4. The Type 316 stainless steel coupons used for this work were machined from a 3.2 mm thick plate provided by McMaster Carr.

Coupons were freshly ground with successive finer grit SiC abrasive paper (LECO wet/dry 600, 800, 1200 grit) using water lubrication. To prevent corrosion during polishing, final polishing was conducted without water in a 1:3 mixture of glycerol (Fisher Chemical, Certified ACS, ≥99.5 %) to denatured ethanol (UltraPure, ACS/USP grade, 190 proof). Alumina powders (Electron Microscopy Sciences 3.0 µm Al_2O_3, 1.0 µm Type DX α-Al_2O_3, and 0.05 µm Type DX γ-Al_2O_3) were mixed with the glycerol/ethanol lubricant to make slurries. Residual polishing compound was removed using a clean polishing pad saturated in ethanol prior to ultrasonication in ethanol for 30 seconds, and blown dry with clean, compressed air. Samples were etched with Keller's etch to reveal the grain size and microstructure in select exposures.

3.3.2 pH Gradient Measurements

As discussed above, the pH inside a dissimilar metal differs at the mouth of the crevice from the inside of the crevice. Therefore, it is important to understand the pH gradient inside a crevice when A7050-T7451 is coupled with Type 316 stainless steel to assess lab based corrosion damage morphologies. pH measurements inside a rivet were conducted using a Type 316 stainless steel screw inside a 6.35 mm thick plate of AA7050-T7451. The cathode to anode ratio was masked to be approximately 1:1. The fastener was cross-sectioned and attached with a plastic plate with set screws into the AA7050-T7451 cross-section. This enabled the plastic to be removed quickly after exposure and the pH to be measured inside the rivet hole. The sample was immersed in 4 M NaCl for 62 hours. After the conclusion of the exposure the plastic was removed and universal pH indicator and pH paper was used to determine the pH inside the rivet hole, in cross-section, with the Type 316 stainless steel screw present.

3.3.3 Electrochemical Methods

All testing, unless noted otherwise, was performed using a three electrode flat cell with a platinum mesh counter electrode and a saturated calomel reference electrode (SCE). Hydrogen was collected using an electrolyte filled burette with an inverted funnel attached centered over the sample. The area exposed was 1 cm^2. Samples were cleaned in dilute nitric acid as according to ASTM standard G-1 to remove corrosion products for determination of mass loss. All experimental procedures were conducted after 30 minutes at open circuit potential. Anodic and cathodic potentiodynamic polarization was conducted with a scan rate of 1 mV/s.

Cathodic and anodic potentiodynamic polarization was used to (1) understand the effect of environmental conditions on the galvanic couple potential and current and (2) yield electrochemical guidance for inducing lab damage morphologies. One these guidelines and potential/current ranges were established three different electrochemical methods were used to induce various damage morphologies, potentiostatic polarization, galvanostatic polarization, zero resistance ammeter (ZRA), immersion based exposures. Relevant potentials and current ranges were chosen based anodic and cathodic potentiodynamic scans and FEA studies.[148] Solutions that were studied include 0.5 M NaCl at pH 5.5, 0.5 M $MgCl_2$ at pH 5 as well as simulated fastener solutions of 0.5 M NaCl + $AlCl_3$ at pH 3 and 0.5 M NaCl + $NaAlO_2$ at pH 8.

3.3.3.1 Potentiodynamic Polarization to Establish Galvanic Corrosion Susceptibility Potential and Current Range in Rivet Environments to Further Guide Producible Electrochemical Lab Methods

Potentiodynamic polarization was conducted on AA7050-T7451 and Type 316 stainless steel in various environments to understand the effect on the galvanic couple potential and current contributions. The effects of NaCl concentration (0.001 M NaCl, 0.01 M NaCl, 0.1 M NaCl, 1.0 M NaCl and 5 M NaCl), effects of pH level (0.5 M NaCl + NaOH at pH 9,7 and 0.5 M NaCl + HCl at pH 3), effects of MgCl2 concentration (0.01 M MgCl2, 0.1 M MgCl2 and 2.0 M MgCl2), and the effect of rivet environments (0.5 M NaCl + AlCl3 at pH 3 and 0.5 M NaCl + NaAlO2 at pH 8) were investigated. The effect of isolated Al ions were also studied by conducting potentiodynamic polarization in various concentrations of HCl (0.5 M NaCl at pH 2 and 3), various concentrations of AlCl3, (0.5 M NaCl + 0.5 M AlCl3, 0.5 M NaCl + 1.0 M $AlCl_3$, and 0.5 M NaCl + 3.0 M $AlCl_3$) and various concentrations of $AlCl_3$ keeping the chloride concentration constant (0.485 M NaCl + 0.005 M $AlCl_3$, 0.35 M NaCl + 0.05 M $AlCl_3$, and 0.167M $AlCl_3$).

3.3.3.2 Zero Resistance Ammeter to Produce Laboratory Corrosion Morphologies to Compare with Field Data

Zero resistance ammeter[‡] was used to measure the galvanic coupling current between Type 316 stainless steel and AA7050-T7451. The tests were conducted using a flat cell with planar electrodes where SL AA7050-T7451 exposed, was the working electrode (anode) and Type 316 stainless steel was the counter electrode (cathode).

The galvanic corrosion of AA7050-T7451 coupled to Type 316 stainless steel was investigated via ZRA exposures in solutions that best simulated the rivet environment. These solutions were 0.5 M NaCl at pH 5.5, 0.5 M $MgCl_2$ at pH and solutions of 0.5 M NaCl + $AlCl_3$ at

---

[‡] Zero resistance ammeter is a current to voltage converted that produces a voltage output proportional to the current flowing between its input terminals while imposing a zero voltage drop to the external circuit.

pH 3 and 0.5 M NaCl + $NaAlO_2$ at pH 8. The samples were in tested for 504 h with 1:1 anode to cathode ratio.

In addition, the effect of Al ions on the damage morphology was investigated by conducting ZRA between AA7050-T7451 and Type 316 stainless steel in 0.5 M NaCl with varying amounts of $AlCl_3$ keeping the chloride concentration constant (0.5 M NaCl) for 144 h with 1:1 anode to cathode ratio.

The effect of anode to cathode ratio was studied vie ZRA. Anode to cathode ratios of 1:1, 1:2 and 1:5 were studied by increasing the exposed area of Type 316 stainless steel in the flat cell in 0.5 M NaCl at pH 5.5 over 504 h.

3.3.3.3 Potentiostatic and Galvanostatic Polarization to Produce Laboratory Corrosion Morphologies to Compare with Field Data

Constant Potential

The environments that were studied using potentiostatic polarization were 0.5 M NaCl, 0.5 M $MgCl_2$, 0.5 M NaCl + $AlCl_3$, and 0.5 M NaCl + $NaAlO_2$. These solutions were adjusted to various pH values ranging from 3-9. The surfaces that were exposed were TS and LS, these orientations were important to study because of the geometry of a rivet-hole. Applied potentials near the galvanic couple potential (-0.65, -0.70, -0.73 and -0.76 V SCE) were chosen and applied over 24, 72, 100 and 144 hours in simulated rivet solutions.

Constant Current

In a separate set of experiments, applied galvanic current values were guided by FEA modeling work from a simulated crevice of AA7050-T7451 and Type 316 stainless steel.[155] The model predicted current distributions for anode to cathode ratios of 1:1, 1:4, 1:6 and 1:8 for a simulated a crevice of AA7050-T7451 coupled with Type 316 stainless steel both at the mouth and middle of the crevice. The galvanic currents the model predicted were applied to AA7050-T7451 planar coupons polished to 1200 grit for 100 h. The exposures that simulated the center of the crevice were tested in 0.5 M NaCl + $AlCl_3$ at pH 4. Exposures that simulated the mouth of the crevice were tested in 0.5 M NaCl + $NaAlO_2$ at pH 8. Table 3.1 shows the test matrix and applied currents for the various environments. Samples in the SL orientation and TS orientation were investigated. The galvanic couple crevice design and current distribution can be seen in Figure 3.5.

3.3.3.4 Aluminum-Nitrate-Chloride Immersion Test (ANCIT) Exposures

Due to the elongated grain structure AA7050 may be susceptible to exfoliation corrosion. ANCIT was used as a constant immersion exfoliation corrosion test on AA7050-T7451. ANCIT solution was composed of 5.4 g/L aluminum chloride hexahydrate ($AlCl_3$-$6H_2O$), 4 M sodium chloride (NaCl) and 0.6 M potassium nitrate (KNO_3). The pH of the solution was approximately 2.9. [162] Coupons of AA7050-T7451 in the SL, TS and LT orientations were machoned into 20 mm x 20 mm x 20 mm cubes. Samples were masked with polyimide film to provide a volume to metal surface area of approximately 236 mL/in^2. AA7050-T7451 was exposed to ANCIT for 96 h. Results were interpreted using qualitative visual assessment following ASTM G34-01[16] where N: shows no appreciable attack where the surface may be discolored or etched, but no evidence of pitting or exfoliation. P: Pitting-Discrete pits, sometimes with a tendency for undermining and slight lifting of metal at the pit edges and lastly, EA through ED: Exfoliation where ED is the most severe.

3.4 Faraday's Law Methods and Mass Loss

Using electrochemical measurements and gravimetric mass loss, the rates of corrosion may be calculated from Faraday's Law. Methods for converting corrosion current density values to either mass loss rates or charge density in this work was conducted using ASTM G102-89. These methods aided in producing more consistent corrosion rate analysis from electrochemical results obtained.

Under anodic polarization the total charge associated with anodic dissolution is theoretically described by Equation 3.1.

$$\boldsymbol{Q_{\Delta m} = Q_{H2} + Q_{i\ net\ anodic}} \qquad \text{Equation 3.1}$$

Where $Q_{\Delta m}$ is the anodic charge density associated with metal dissolution which can be determined from gravimetric mass loss after cleaning, Q_{H2} is the cathodic charge density associated on the sample of the surface due to hydrogen evolution that is not reflected in $Q_{i\ net\ anodic}$, $Q_{i\ net\ anodic}$ is the net anodic charge density monitored by the potentiostat. $Q_{\Delta m}$ was calculated using the gravimetric mass loss from exposure using Equation 3.2.

$$Q_{\Delta m} = \frac{\Delta m * F}{E. * A} \qquad \text{Equation 3.2}$$

Where EW is the equivalent weight of AA7050, n the number of e^- transferred, Δm is change in mass, F is Faradays constant and A is the area of the electrode

Equivalent weight of AA7050 (Al-Zn-Mg-Cu), given Equation 3.3, was calculated according to ASTM G102. Assuming incongruent dissolution (Cu not dissolving) EW was 9.54 g/equiv. Assuming congruent dissolution (Al,Zn,Mg and Cu all dissolve) the E.W. was 9.77 g/equiv. In this equation f_{i},, n_{i},, a_i are mass fraction, number of electrons exchanged to complete a given half-cell and atomic weight of the ith alloying element, respectively.

$$E.W. = \sum \frac{a_i}{f_i n_i} \qquad \text{Equation 3.3}$$

The hydrogen collected for select exposures was converted to the corresponding cathodic charge density using the ideal gas law and Faraday's law using Equation 3.4

$$Q_{H2} = \frac{zPVF}{ART} \qquad \text{Equation 3.4}$$

Where z is 2 for hydrogen evolution, P is the pressure inside the burette (1 atm), V is the volume of gas in the burette, F is Faraday's constant, A is the exposed area of the electrode, R is the ideal gas constant and T is temperature.

The net charge density from the measured current was determined by integrating the current density over time at each potential.

The pitting index (PI) was calculated using Equation 3.5 where p is the deepest pit penetration obtained from metallography and d is the average penetration from mass loss divided by the total exposed area. PI gave indication to the severity of pitting observed.

$$\mathrm{PI} = \frac{\mathrm{p}}{\mathrm{d}} \qquad \text{Equation 3.5}$$

3.5 Results

3.5.1 Assessment of pH Gradient inside a Rivet

The pH inside a rivet of a cross-sectioned Type 316 stainless steel round-head screw into an AA7050-T7451 plate was measured. The pH was found to be between 7 and 8 at the top of the rivet hole and between 5 and 6 near the bottom of the rivet hole. No macro acidic sites were found. These results guided the pH environments chosen for the damage morphology studies. Figure 3.6 show the test piece and the corresponding result in pH gradient after exposure where the blue/green indicates alkaline pH and the yellow indicates neutral pH. Therefore, NaCl solutions where adjusted to pH values of 3-8. Although no acidic sites were observed here, local corrosion sites may become acidic and therefore, understanding the effect this may have on the corrosion damage morphology is important.

3.5.2 Determination of Galvanic Couple Potential and Current in Various Rivet Environments

3.5.2.1 Effect of Chloride Concentration, pH and Rivet Environments on the Galvanic Couple Potential and Current of AA7050-T7451 and Type 316 Stainless Steel

Anodic polarization on AA7050-T7451 and cathodic polarization on Type 316 stainless steel was conducted in various electrolytes discussed above, including simulated rivet solutions with additions of Al ions. The pH levels were adjusted to assess possible galvanic couple potentials representative of different regions in a fastener geometry. Figure 3.7 shows the effects of (a) NaCl concentration (b) pH, (c) $MgCl_2$ concentration, and (d) rivet environment on the galvanic couple potential and current. The galvanic couple potential (E_{couple}) depended on the Cl^- concentration. The pitting potential of AA7050-T7451 decreased with increasing Cl^-. ORR was increased on Type 316 stainless steel as Cl^- increased. In 0.001 M NaCl, E_{couple} was -0.44 V SCE while in 5 M NaCl E_{couple} was -0.77 V SCE. The effect of pH can be observed in (b) where polarization was conducted in 0.5 M NaCl + NaOH at pH 9 and 7 and 0.5 M NaCl + HCl at pH 3 as well as 0.5 M NaCl unadjusted for pH. Anodic kinetics were not affected by pH. This was expected as pH does not affect the pitting potential. However, the cathodic kinetics increased with the addition of HCl due to HER dominating cathodic kinetics. The galvanic couple potential for 0.5 M NaCl unadjusted for pH was -0.69 V SCE and with the addition of NaOH at pH 7 and 9 and HCl at pH 3, E_{couple} was -0.68, -0.69 and -0.72 V SCE, respectively. Due to the effect of acidity on cathodic kinetics, the contribution of current due to the galvanic couple (I_{couple}) in unadjusted 0.5 M NaCl was 2.8×10^{-5} A/cm^2 and with the addition of NaOH at pH 7 and 9 and HCl at pH 3 I_{couple} was 3.5×10^{-5}, $6.9 \times 10^{-}5$, and 4.3×10^{-4} A/cm^2, respectively. The effect of $MgCl_2$ can be observed in (c) where E_{couple} in 0.01 M $MgCl_2$ was -0.59 V SCE and in 2.0 M $MgCl_2$, -0.78 V SCE. The anodic kinetics increased with increasing Cl^- concentration. The effect of rivet environments, (solutions with additions of $NaAlO_2$ or $AlCl_3$ adjusted at different pH levels) can be observed in (d). The galvanic couple potential decreased with additions of $NaAlO_2$. This was due to an increase in ORR kinetics on Type 316 stainless steel at pH 7 and 9 compared to pH 5. With the addition of $AlCl_3$, the galvanic couple potential decreased to E_{couple}=-0.71 V SCE and the galvanic couple current increased by an order of magnitude where I_{couple}=4.8×10^{-4} A/cm^2 as a result of HER. Both the anodic and cathodic kinetics were increased with the addition of $AlCl_3$.

3.5.2.2 Effect of Al ions on the Anodic and Cathodic Kinetics of AA7050-T7451 and Type 316 Stainless Steel and on Galvanic Couple Potential

Cathodic and anodic potentiodynamic polarization was conducted on AA7050-T7451 and Type 316 stainless steel to understand the effect of Al ions on corrosion kinetics. These experiments were conducted in solutions with a varying amount of $AlCl_3$ and were compared to solutions without $AlCl_3$ and to solutions containing HCl. Figure 3.8 shows the anodic and cathodic polarization showing the effect of (a) HCl concentration, (b) $AlCl_3$ concentration and (c) Al ions in solution at equivalent pH. The anodic and cathodic kinetics were increased with the addition of HCl. However, the ORR cathodic reaction were affected the most. The cathodic reaction rate was increased by one order of magnitude from 0.5 M NaCl at pH 5 to 0.5 M NaCl + HCl at pH 3. Plot (b) shows as the concentration of $AlCl_3$ increases, anodic kinetics are slightly amplified and cathodic reactions are greatly increased. Plot (c) shows the effect of Al ions. The chloride concentration was held constant at 0.5 M Cl with the addition of various amounts of Al ions. The addition of $AlCl_3$ reduced the pH to approximately 3 and increased both the anodic and cathodic kinetics. In the solution with 0.005 M $AlCl_3$, E_{couple} was -0.71 V SCE and I_{couple} was 1.6 x 10^{-4} A/cm^2. In contrast, in the solution with 0.167 M $AlCl_3$, E_{couple} was -0.70 V SCE and I_{couple} was 4.7 x 10^{-4} A/cm^2. In general, the use of $AlCl_3$, instead of NaCl, increased cathodic kinetics. This was observed as HER dominated the ORR kinetics. Cathodic kinetics increased with the addition of HCl and further increased with the addition of Al. This was an important observation Al ions are often found in solution

3.5.2.3 Effect of Anode to Cathode Ratio on the Galvanic Couple Potential and Current of AA7050-T7451 Coupled to Type 316 Stainless Steel

The effect of cathode area (Type 316 SS) on the galvanic couple potential can be observed in Figure 3.9. Polarization was conducted in 0.5 M NaCl at pH 5.5, 0.5 M NaCl + $NaAlO_2$ at pH 8, and 0.5 M NaCl + $AlCl_3$ at pH 3. In all solutions, the current density increased with increasing cathode area. In 0.5 M NaCl at pH 5.5 for anode to cathode ratio of 1:1 I_{couple}=3.5 x 10^{-5} A/cm^2 and for 1:10, I_{couple}=2.9 x 10^{-4} A/cm^2. This trend was observed for 0.5 M NaCl + $NaAlO_2$ pH 8 and 0.5 M NaCl + $AlCl_3$ pH 3.

3.5.2.4 Summary: Effect of Solution Chemistry on Galvanic Couple Potential and Current

Figure 3.10 shows a compilation of the effects of environmental conditions on the galvanic potential and the contribution of current due to the galvanic couple potential. The environments that produced the highest I_{couple} can be observed on the lower right side of the plot. The shaded region shows the potential range for where severe galvanic corrosion may occur when AA7050-

T7451 is coupled with Type 316 stainless steel. Solutions with $AlCl_3$ and HCl can be found in bottom right side, denoting more negative potentials and high current densities. Solutions with higher Cl^- and $NaAlO_2$ additions can be found in the bottom middle of the plots. Lastly, solutions with low Cl^- and no additions of $NaAlO_2$ or $AlCl_3$ can be observed at the top/middle right, denoting high galvanic couple potentials and lower current densities.

1.1.1 Electrochemical Laboratory Tests to Assess Damage Morphologies and Duplicate Field Data in Simulated Rivet Environments

3.5.2.5 Zero Resistance Ammeter to Study the Effect of Simulated Rivet Solutions on the Damage Morphology of AA7050-T7451 Coupled to Type 316 Stainless Steel

Zero resistance ammeter (ZRA) laboratory testing was used to monitor both galvanic current and galvanic potential over time when AA7050-T7451 was coupled to Type 316 stainless steel. The electrolytes considered were 0.5 $MgCl_2$ (pH 5), 0.5 M NaCl + $AlCl_3$ (pH 3), 0.5 M NaCl + $NaAlO_2$ (pH 8), and 0.5 M NaCl (pH 5) and were exposed for 504 h. Figure 3.11 shows the measured galvanic potentials and current densities in these solutions. The simulated rivet solutions of 0.5 M NaCl + $NaAlO_2$ at pH 8 had the highest current density while the 0.5 M $MgCl_2$ had the lowest current density. The galvanic couple potential range was between -0.72 and -0.86 V SCE. Over the 504 h exposure, the galvanic potential showed breakdown events. The charge density after 504 h, in 0.5 M NaCl and 0.5 M $MgCl_2$ were 22 and 8 C/cm^2, respectively. In simulated rivet solutions of 0.5 M NaCl + $NaAlO_2$ (pH 8) and 0.5 M NaCl + $AlCl_3$ (pH 3) the charge density was 76 and 27 C/cm^2, respectively. After exposure and before cleaning the surface, replated-Cu could be observed on AA7050-T7451 on the sample exposed to 0.5 M NaCl + $NaAlO_2$ (pH 8) and to a lesser extent 0.5 M NaCl and $MgCl_2$. Cyclic voltammetry conformed these results and will be discussed in another section.

Scanning electron microscopy (SEM) on the surface and optical microscopy in cross-section of AA7050-T7451 are shown in Figure 3.12 and Figure 3.13. The surface micrographs showed that in NaCl + $AlCl_3$ (pH 3), IGC surrounding round pits prevailed, while only pitting prevailed in 0.5 M NaCl and 0.5 M $MgCl_2$. This was an interesting finding as the T7451 temper has been overaged to suppress IGC. Interestingly, 0.5 M NaCl + $NaAlO_2$ (pH 8) produced narrow, deeper, and elongated pitting. With the addition of $NaAlO_2$ the pit density increased and pits coalesced into wide pits in the L and T directions. In 0.5 M $MgCl_2$ and 0.5 M NaCl discrete pitting was observed. Pitting index calculations supported this notion. In 0.5 M NaCl + $NaAlO_2$ (pH 8), the PI was 61 indicating severe pitting and little attack away from pits. The cross-sectioned micrographs showed that the 0.5 M NaCl + $AlCl_3$ (pH 3) and 0.5 M NaCl + $NaAlO_2$ (pH 8) produced the deepest maximum pit depths of 177 and 157 μm after 504 hours, respectively. Table 3.2 shows the data summary as well as the damage modes produced in each of the environments.

3.5.2.6 Effect of Constant Potential Exposures in Simulated Rivet Environments on the Damage Morphology on AA7050-T7451

Figure 3.14 shows the current density, charge density, and cross-sectional maximum corrosion depth over 144 hours for potentials near the galvanic couple potential in 0.5 M NaCl at pH 5.5 and 0.5 M NaCl + $NaAlO_2$ at pH 8 with the TS orientation exposed. The solution with additions of $NaAlO_2$ at pH 8 produced higher current densities and deeper corrosion pits than in unadjusted 0.5 M NaCl at pH 5.5. Microscopy of each exposure showed that -0.65 and -0.70 V SCE produced uniform corrosion while -0.73 and -0.76 induced localized corrosion in the form of fissures or pits that grow intragranually. The pits that's formed in 0.5 M NaCl + $NaAlO_2$ at pH 8 were deeper and elongated in the L orientation. This can also be observed by looking at the pitting index of the exposures. The PI for -0.65 and -0.70 V SCE was around 1 suggesting uniform corrosion while for -0.73 and -0.76 V SCE the PI was around 20-80 indicating severe localized corrosion. Cross-sections for each of the exposures in both 0.5 M NaCl at pH 5.5 and 0.5 M NaCl + $NaAlO_2$ after 144 hours can be seen in Figure 3.15. No damage morphology differences were observed in the TS and SL orientations.

At -0.73 V SCE, the damage morphology appeared to be isolated pitting corrosion with different morphologies. Figure 3.16 shows the cross-sectional micrographs in the simulated rivet solutions of 0.5 M NaCl at pH 5.5, 0.5 M NaCl + $NaAlO_2$ at pH 8, 0.5 M at $MgCl_2$, and 0.5 M NaCl + $AlCl_3$ at pH 3. At the pitting potential, 0.5 M NaCl and $MgCl_2$ produced discrete pits that were round in shape. 0.5 M NaCl + $NaAlO_2$ produced larger elongated pits and the environment with $AlCl_3$ produced IGC

Table 3.3 shows the reported post-exposure pH, total charge density, charge associated with mass loss, average damage length from metallography, charge associated with hydrogen evolution and pitting index for the -0.73 V SCE exposure in the simulated crevice environments. It can be noted that the pH increased over time and that hydrogen evolution only contributed around 4 C/cm^2 or 23% of the total charge. In the acidic environment, HER contributed over 30% of the total charge. The potential -0.73 V SCE proved to be an important potential as it is near the pitting potential of AA7050-T7451 and produces deep fissures that may have an effect on fatigue life. Figure 3.16 shows the cross-sectional micrographs from the potentiostatic polarization in 0.5 M NaCl at pH 5.5 and 0.5 M NaCl + $NaAlO_2$ at pH 8 after 144 hours at -0.65, -0.70, -0.73, and -0.76 V SCE. The corrosion fissures that formed in 0.5 M NaCl at pH 5.5 were round pits approximately 199 µm in diameter and 111 µm in length while the corrosion fissure that formed in 0.5 M NaCl + $NaAlO_2$ at pH 8 were approximately 17 µm in diameter and 195 µm in length. The IGC that formed in the $AlCl_3$ acidic solution was 120 µm in depth and between 5-20 µm in width.

3.5.2.7 Constant Current Exposures in Simulated Rivet Environments

Galvanostatic exposures were conducted on AA7050-T7451 planar electrodes. The selected currents were based off an FEA model which simulated a crevice galvanic couple where current values were calculated as a function of (1) location, inside of the crevice or mouth of crevice (2) various anode to cathode ratios (Figure 3.5). Currents that simulated the mouth of the crevice were tested in pH 8 solutions and currents that simulated the inside of the crevice were tested in pH 4 solutions.

Figure 3.17 shows the galvanic potential over 100 hours, in 0.5 M NaCl + $AlCl_3$ at pH 4 and in 0.5 M NaCl + $NaAlO_2$ at pH 8 for AA7050-T7451. In the alkaline environment, simulating the mouth of the crevice, the potential remained fairly constant between -0.76 - 0.71 V SCE, while for the acidic solution, the potential decreased approximately 20 mV over the 100 hour exposure. No orientation dependence was found between TS and SL exposed surfaces. It was also observed that the alkaline 1:1 area ratio exposure had a more negative galvanic potential than the larger anode to cathode ratios. The exposed surfaces of each sample were imaged using SEM and were cross-sectioned to discern damage morphologies. Figure 3.18 and Figure 3.19 show the surface damage morphology and the corresponding cross-sectional micrographs of AA7050-T7451 SL simulating a rivet galvanic couple with Type 316 stainless steel with anode to cathode ratio of (a) 1:1 (b) 1:4 (c) 1:6, and (d) 1:8 in 0.5 M NaCl + $NaAlO_2$ at pH 8, and 0.5 NaCl + $AlCl_3$ at pH 4, respectively. Figure 3.20 and Figure 3.21 show the AA7050-T7451 exposures in the TS orientation. In 0.5 M NaCl + $AlCl_3$ at pH 4 (simulating regions inside the crevice), the damage morphologies were observed to be IGC with pitting corrosion. This was an interesting finding as the T7451 temper has been overaged to suppress IGC. All simulated anode to cathode ratios in the 0.5 M NaCl + $AlCl_3$ at pH 4 exposures revealed deep elongated fissures plus IGC. In the 0.5 M NaCl + $NaAlO_2$ at pH 8, the cross-sectional analysis revealed elongated fissure damage in the simulated 1:1 and 1:4 and uniform corrosion with deep fissures in the 1:6 and 1:8 samples with more cathode area.

Table 4 shows the charge analysis and overall summary for these exposures. The charge associated with mass loss in 0.5 M NaCl + $AlCl_3$ at pH 4 increased from 9.8 to 69.2 C/cm^2 with 8 times more cathodic area while in the alkaline solution, it increased from 6.8 to 218 C/cm^2 over 100 hours. Overall, more corrosion damage occurred in the 0.5 M NaCl + $NaAlO_2$ at pH 8 exposures. As observed above, replated-Cu was observed in the 0.5 M NaCl + $NaAlO_2$ environments. Furthermore, in the alkaline environment, on average, HER contributed 30% to the total anodic charge. In contrast, in the acidic environment, on average, HER contributed over 50% to the total anodic charge. In both cases, HER increased with increasing cathode size.

3.5.2.8 Effect of Cathode Size on the Damage Morphology of AA7050-T7451

AA7050-T7451 was coupled to Type 316 stainless steel for 504 h via ZRA in 0.5 M NaCl with various anode to cathode (Al:SS) ratios of 1:1, 1:2 and 1:5. The galvanic potential and current is plotted in Figure 3.22. The galvanic potential ranged from -0.72 to -0.82 V SCE for all ratios. A larger exposed cathodic area did not have an effect on the galvanic potential, although, breakdown events were observed throughout the exposure. The galvanic current, I_{couple}, increased with increasing stainless steel area. I_{couple} was approximately 9 times larger for the 1:5 case and 3 times larger for the 1:2 case compared to the 1:1 case. After exposure, the damage morphology on AA7050-T7451 was analyzed using SEM on the surface and optical microscopy in cross-section. These micrographs can be observed in Figure 3.23. The damage morphology in the 1:1 exposure revealed small rounded pits. The pit density and pit width increased for anode to cathode ratios of 1:2 and 1:5. In the 1:5 case, the pits coalesced together to form even wider pits. Figure 3.24 shows a cross-sectional micrograph of the entire exposed sample. This enables comparison in pit density and pit shape where the pits get wider and deeper with increasing stainless steel area. It is important to note that the area of visible Cu-replated on the surface of AA7050-T7451 increased with increasing cathode areas. The exposure results can be summarized in Table 3.5.

3.5.2.9 Exfoliation Corrosion Assessment using ANCIT

AA7050-T7451 in all three orientations were tested following the ANCIT testing protocol described above. AA7050-T7451 was resistant to classic exfoliation. Corrosion damage appeared to be exfoliation corrosion with pitting. The LT-plane surface experienced the most exfoliation with an ASTM P rating. The average corrosion fissures was L=80.9 µm (Figure 3.25). The cross-section shows parts of the grain being lifted up in the L direction. The SL-plane did not undergo exfoliation with an ASTM rating of P. However the average corrosion fissure was L= 137.0 µm (Figure 3.26). The TS-plane experienced some exfoliation corrosion with the ASTM rating of EA+P and the deepest corrosion fissures, L=161.0 µm (Figure 3.27). Table 3.6 shows a summary of these findings where the visual rating and average corrosion fissure length are shown.

3.5.2.10 Effect of Al ions in Solution on the Damage Morphology of AA7050-T7451 when Coupled to Type 316 Stainless Steel

The effect of Al ions in solution on damage morphology of AA7050-T7451 was investigated using ZRA technique for 144 h. Figure 3.28 shows the ZRA measured (a) galvanic potential (b) galvanic current density and (c) anodic charge over 144 hours. In general, E_{couple} made was more negative with increasing amounts of Al ions. This means E_{pit} dropped faster than i_L^{H+} increases. The (b) galvanic current density and (c) anodic charge had a strong dependence on Al ions. The anodic charge over 144 hours in 0.5 M NaCl, 0.0485 M NaCl + 0.005 $AlCl_3$, 0.35 M

NaCl + 0.05 $AlCl_3$, and 0.167 M $AlCl_3$ was 17, 37, 52, and 76 C/cm^2. This demonstrated that there was a 4-fold increase in charge density from 0.5 M NaCl to 0.167 M $AlCl_3$. Surface SEM analysis showed pitting corrosion in 0.5 M NaCl and IGC for $AlCl_3$ environments. Interestingly, the more Al ions, the deeper the IGC grew. The damage depth increased by 18 times in the exposure with only 0.0485 M NaCl + 0.0005 $AlCl_3$ relative to 0.167 $AlCl_3$. This suggests a strong dependence on Al ions in solution and IGC damage (Figure 3.29).

3.6 Discussion

3.6.1 Effect of Environmental Conditions on the Damage Morphology of AA7050-T7451

In this work, three different corrosion morphologies were observed, hemispherical pits, intragranular deep corrosion fissures propagating in the L-orientation and intergranular corrosion. These various damage morphologies prevailed at different electrode potentials and environments. At potentials -0.73 V, and -0.76 V IGC occurs in $AlCl_3$ and pitting occurs in NaCl and $NaAlO_2$. At electrode potentials -0.65-0.73 V. uniform corrosion occurred. It was observed that in 0.5 M NaCl at pH 5.5 and $MgCl_2$ at pH 5, rounded-hemispherical pits formed. However in alkaline environments with additions of Al ions the damage morphology was observed to be deep corrosion fissures (200 μm) in the L-direction. In acidic environments, the damage was observed to be a combination of corrosion pits and fissures with networks of intergranular corrosion. The differences in damage morphology based on environment is an important observation as it was also shown that the pH may vary in different regions of a rivet hole. It was shown that the pH is likely to become alkaline (pH 8-9) at the mouth of the rivet and become neutral (pH 4-5) inside the rivet. However, acidic sites may still occur local to a corrosion fissure. The solution inside the crevice also changes as Al ions are dissolved into solution. All of these factors have been shown to impact the type of corrosion damage morphology observed in the AA7050-T7451.

For AA7050 damage either forms fissures along constituent particle bands switching to a form of anodic dissolution, transitions to intergranular corrosion within tight fissures with the right chemistry and grain boundary susceptibility, or at high anodic potentials, developed as widespread hemispherical pits. It is important to understand that the sub-meso-scale and shape of the corrosion damage may vary from hemispherical shapes to complex fissures with intergranular penetrations dependent on the electrochemical conditions and the environmental conditions, specifically, simulated rivet environments.

Al-Zn-Mg-Cu alloys can exhibit a window of intergranular corrosion as a function of aging time. Aging of an alloy leads to an increase in the number of precipitates and or an increase in the volume fraction of the precipices in the alloy. In AA7050 diffusion controlled precipitation is the cause for local and global solute depletion. The depletion of Cu at the grain boundaries would make them more susceptible to preferential localized corrosion if Cu-content remained higher in the matrix. Furthermore, in acidic environment it was shown in Figure 3.7 and Figure 3.9 that such extensive hydrogen evolution was occurring that HER dominated ORR kinetics. This increase in HER can result in attack on the passive film on AA7050-T7451, leading to faster corrosion rates. It has been previously shown that for binary Al-Cu alloys with precipitates, the E_{pit} of the Cu-depleted regions near the grain boundaries are about 100 mV lower than the E_{pit} of the solid solution. Therefore the breakdown of the passivation layer will occur more rapidly in the Cu-depleted regions, leading to the extensive pitting along grain boundaries.[42,54] This mechanism can be used to describe the IGC corrosion observed here and will be further investigated in Chapter 4.

Micro-galvanic couples between AA7050-T7451 and *S* phase (Al_2CuMg) and β (Al_7Cu_2Fe) particles are often attributed to pitting on this alloy. AA7050-T7451 often contains 20-30% coverage of Al_2CuMg and Al_7Cu_2Fe. It has been demonstrated that the crevice between the particle and the matrix can act as pit nucleation sites. [71] S-phase dissolution is often complicated due to the polarity of *S* phase compared to AA7050. It is known that in chloride solution bulk Al_2CuMg exhibits an OCP potential of -0.920 V which is negative to AA7050 suggesting that *S* phase is active to the alloy. However, corrosion morphology studies of pitting in AA7050-T7451 show that pitting can occur in the matrix phase at the boundary of these particles. Moreover, *S* phase is known to undergo dealloying. When the Al and Mg dissolve, it leaves a Cu-rich remnant that can be an effective local cathode capable of inducing matrix pitting, provided that hydrous corrosion products does not limit reduction reactions by electronic insulation or by restricted diffusion of cathodic reactants. After exposures in NaCl pH 5 and in $NaAlO_2$ pH 8 the surface of AA7050-T7451 was often visibly covered with Cu. $NaAlO_2$ pH 8 exposures often contained more Cu-replating. CVs from Chapter 2 confirmed that Cu was on the surface of AA7050-T7451. The CV of pure Cu, AA7050-T7451 polished and AA7050 post 504 h exposure in 0.5 M NaCl compared to 0.5 M NaCl + $NaAlO_2$ pH 8 are shown in Figure 3.30. It can be seen that pure Cu exhibits two peaks. The area under the peak of the sample exposed to 504 h in 0.5 M NaCl + $NaAlO_2$ pH 8 was larger than the sample exposed in only 0.5 M NaCl indicated a larger surface coverage of Cu on the samples exposed to 0.5 M NaCl + $NaAlO_2$ pH 8. The surface of AA7050-T7451 with replated-Cu has been proposed to facilitate reduction reactions on Al oxide surfaces by enabling direct electronic conduction or electron conduction by tunneling. This phenomenon can be attributed to the deep corrosion fissures observed in AA7050-T7451 in Figure 3.15 and Figure 3.19. While this work characterizes the damage morphologies, Chapter 4 will use electrochemical framework to understand from the microstructural view point why these damage morphologies differ in different environments.

3.6.2 Laboratory Induced Damage Methods as Compared to Tear-down and Field Data

Figure 3.2 and Figure 3.3 show two different fastener-hole configurations that experienced corrosion damage under operational conditions. In the damage that occurred in Figure 3.2 the corrosion damage was located away from the hole bore with no cracks seen inside the bore. Two cracks were observed on the section surface. Intergranular cracks initiated from the mechanical damage on the surface and extended through the thickness while branching along grain boundaries. The cracks were approximately 812 µm in length. Figure 3.3 shows a different corrosion site were microscopy found corrosive attack throughout the bore, this is indicated in red in (b). The polished surfaces showed corrosion extending up to the cut sections. Tear-down data was provided as a useful comparison measure to laboratory based exposure tests. Figure 3.31 shows the tear-down data relative to laboratory ZRA for 144 h in 0.485 M NaCl + $NaAlO_2$ pH 8 around a faying surface. The tear-down data showed surface exfoliation and intergranular stress corrosion cracking. Failure analysis reported that 37% of metal corrosion thickness was lost as a result. Figure 3.32 shows a comparison of corrosion damage morphology between the work conducted here, operando XCT from Chapter 2[139,166,167] exposures and teardown data. From the damage morphology and corrosion pit depth standpoint the ZRA test method exhibited in 0.5 M NaCl for 504 h had the closest correlations to teardown data. The simulated fastener results in Chapter 2 also resembled the ZRA and tear down data. 504 h exposures produced damage depths that were similar to corrosion pits formed in service-like conditions.

3.7 Conclusions

- The galvanic couple potential (E_{couple}) is heavily dependent on the Cl^- concentration. The pitting potential of AA7050-T7451 decreased with increasing Cl^-. The ORR cathodic kinetics were increased on Type 316 stainless steel as Cl^- increased. The galvanic couple potential decreased with additions of $NaAlO_2$. This was due to an increase in ORR kinetics on Type 316 stainless steel at pH 7 and 9 compared to pH 5. With the addition of $AlCl_3$, the galvanic couple potential decreased and the galvanic couple current increased by an order of magnitude as HER began to dominate ORR. Increasing the area of Type 316 stainless steel resulted in an increase on the galvanic current density.
- Three different corrosion morphologies were observed, corrosion hemispherical pits, intragranular deep corrosion fissures propagating in the L-orientation and intergranular corrosion. These various damage morphologies prevailed at different electrode potentials and environments. AA7050-T745 was found to be resistant to exfoliation corrosion.
- In 0.5 M NaCl at pH 5.5 and $MgCl_2$ at pH 5 rounded-hemispherical pits formed. In alkaline environments with additions of Al ions the damage morphology was observed to be deep corrosion fissures (200 μm) in the L-direction. In acidic environments, the damage was observed to be a combination of corrosion pits and fissures with networks of intergranular corrosion. The differences in damage morphology based on environment is an imperative observation as it was also shown that the pH may vary in different regions of a rivet-hole.
- A strong dependence of Al ions in solution and IGC damage depth was observed. The damage depth increased by 18 times in the exposure with only 0.0485 M NaCl + 0.0005 $AlCl_3$ relative to 0.167 $AlCl_3$.

- Samples exposed to $NaAlO_2$ at pH 8 often visibly contained more surface coverage of Cu-replated. Cyclic voltammetry confirmed that there was a higher surface coverage of Cu on samples exposed in 0.5 M NaCl + $NaAlO_2$ pH 8 relative to samples exposed to 0.5 M NaCl. Replated-Cu can facilitate reduction reactions on Al oxide surfaces by enabling direct electronic conduction or electron conduction by tunneling. The deep corrosion fissures observed in this environment can be attributed to more replated-Cu
- The laboratory method that induced damage morphologies that presented the closest correlation to tear-down data and the simulated rivet in Chapter 2 was zero resistance ammeter for 504 h in 0.5 M NaCl.

3.8 Tables

Table 3.1. Galvanic currents applied to AA7050-T7451 to simulate galvanic corrosion with various anode to cathode ratios in the chemistry associated with the center and mouth of the FEA crevice.

	1:1	**1:4**	**1:6**	**1:8**
Center 0.5M NaCl + $AlCl_3$ pH: 4	0.01 mA/cm^2	0.04 mA/cm^2	0.04 mA/cm^2	0.05 mA/cm^2
Mouth 0.5M NaCl + $NaAlO_2$ pH:8	0.01 mA/cm^2	0.21 mA/cm^2	0.41 mA/cm^2	0.57 mA/cm^2

Table 3.2. ZRA exposure data summary for AA7050-T7451 coupled with Type 316 stainless Steel in 0.5 $MgCl_2$ at pH 5, 0.5 M NaCl + $AlCl_3$ at pH 3, 0.5 M NaCl + $NaAlO_2$ at pH 8 and 0.5 M NaCl at pH 5 over 504 hours. Q_{net} is the charge consumed from by the potentiostat, $Q_{\Delta m}$ is the anodic charge consumed from metal dissolution determined from gravimetric mass loss, average L is the average corrosion fissure length determined by sectioning and PI is the pitting index.

Environment	**Post pH**	**Q_{net} (C/cm^2)**	**$Q_{\Delta m}$ (C/cm^2)**	**Average L (µm)**	**PI**	**Damage Morphology**
0.5 M NaCl pH 5	6.6	22.6	19.8	142	11	Large pits, clustered together, round and long pits
0.5M NaCl + $NaAlO_2$ pH 8	7.5	76.0	39.6	133	61	Highest pit density, large and very close pits, many pits cluster together to form one large deeper pit
0.5 M $MgCl_2$ pH 5	5.3	7.7	9.9	139	15	Least amount of pitting damage, small discrete rounded pits
0.5 M NaCl + $AlCl_3$ pH 3	4.5	27.2	19.8	160	42	IGC + large pitting seen

Table 3.3. Reported values for potentiostatic polarization at E=-0.73 V SCE in simulated crevice environments after144 h of exposure. TS surface exposed. Q_{net} is the charge consumed from by the potentiostat, $Q_{\Delta m}$ is the anodic charge consumed from metal dissolution determined from gravimetric mass loss, Q_{H2} is the charge associated with HER, average L is the average corrosion fissure length determined by sectioning and PI is the pitting index.

E=-0.730 V SCE for 144 h							
Solution	Post pH	Q_{net} (C/cm^2)	Q_{H2} (C/cm^2)	Q_{net} + Q_{H2} (C/cm^2)	$Q_{\Delta m}$ (C/cm^2)	Average L (µm)	PI
0.5 M NaCl pH 5.5	7.6	37.7	1.74	39.5	48.9	162	26.3
0.5 M NaCl + $NaAlO_2$ pH 8	6.86	55.5	4.94	60.5	106.0	181	62.1
0.5 M $MgCl_2$ pH 5	5.1	40.8	7.95	48.7	57.3	145	31.5
0.5 M NaCl + $AlCl_3$ pH 3	4.70	38.0	11.5	49.5	45.6	175	52.6

Table 3.4. Galvanostatic charge and Faraday mass loss analysis for 0.5 M NaCl + AlCl3 pH: 4 and 0.5 M NaCl + NaAlO2 pH 8 over 100 h. iapplied is the applied current, Qnet is the charge consumed from by the potentiostat, QΔm is the anodic charge consumed from metal dissolution determined from gravimetric mass loss, QH2 is the charge associated with HER, average L is the average corrosion fissure length determined by sectioning and PI is the pitting index.

Mouth of Crevice SL: 0.5 M NaCl + NaAlO$_2$ pH 8								
Simulated Ratio	**$i_{applied}$ (mA/cm^2)**	**Q_{net} (C/cm^2)**	**Q_{H2} (C/cm^2)**	**$Q_{\Delta m}$ (C/cm^2)**	**Q_{net} + Q_{H2} (C/cm^2)**	**Average L (μm)**	**PI**	**Damage Mode**
1:1	0.012	4.32	3.21	6.82	7.5	53.6	31.7	Only 3-4 pits
1:4	0.214	77.0	21.2	109.0	98.2	30.5	1.01	High pit density
1:6	0.409	147.0	20.5	168.0	168.0	49.1	0.921	Deep pits, fissure damage
1:8	0.571	206.0	21.9	218.0	228.0	45.4	0.531	Fissure damage
Inside Crevice SL: 0.5 M NaCl + AlCl$_3$ pH 4								
1:1	0.012	4.32	4.91	9.88	9.2	23.7	14.0	Only a few pits
1:4	0.039	14.0	6.61	39.5	20.6	223.0	4.26	Only a few pits + IGC
1:6	0.043	15.5	21.6	59.7	37.1	72.5	11.9	Few deep pits and + IGC
1:8	0.047	16.9	25.2	69.2	42.1	113.9	17.2	Deep pits + IGC
Mouth of Crevice TS: 0.5 M NaCl + NaAlO$_2$ pH 8								
Simulated Ratio	**$i_{applied}$ (mA/cm^2)**	**Q_{net} (C/cm^2)**	**Q_{H2} (C/cm2**	**$Q_{\Delta m}$ (C/cm^2)**	**Q_{net} + Q_{H2} (C/cm2)**	**Average L (μm)**	**PI**	**Damage Mode**
1:1	0.012	4.32	3.6	9.72	7.92	77.28	45.7	3-4 pits
1:4	0.214	77.0	22.6	98.4	99.6	133.0	4.39	Many deep pits
1:6	0.409	147.2	25.3	168.0	173.0	267.0	4.62	High pit density + uniform corrosion
1:8	0.571	205.5	25.1	258.0	231.0	210.0	2.60	Fissure like damage
Inside Crevice TS: 0.5 M NaCl + AlCl$_3$ pH 3								
1:1	0.012	4.32	5.18	9.80	9.42	92.2	54.6	3-4 pits
1:4	0.039	14.0	8.65	37.4	22.6	94.4	17.1	High wide pit density
1:6	0.043	15.5	22.6	59.5	38.1	106.7	17.6	High pit density
1:8	0.047	16.9	25.1	69.1	42.0	118.9	17.9	High pit density

Table 3.5. Effect of anode to cathode ratio. ZRA exposure summary after 504 h in 0.5 M NaCl pH 5.5 with anode to cathode ratio of 1:1. 1:2 and 1:5. Q_{net} is the charge consumed from by the potentiostat, $Q_{\Delta m}$ is the anodic charge consumed from metal dissolution determined from gravimetric mass loss, average L is the average corrosion fissure length determined by sectioning and PI is the pitting index.

Anode:Cathode Ratio	**Post pH**	**Q_{net} (C/cm^2)**	**$Q_{\Delta m}$ (C/cm^2)**	**Average L (µm)**	**PI**	**Damage Morphology**
1:1	5.34	13.5	19.8	142	11	Large pits, clustered together, round and long pits
1:2	5.24	24.7	34.27	169	42	Large round pits, Cu-replating
1:5	4.32	68.2	110.35	236	68	High pit density, Cu-replating

Table 3.6. ANCIT exposure of AA7050-T7451 after 96 h exposure

Orientation	**Visual Rating**	**Average L (µm)**
LT	EB + Pitting	80.95
SL	EA + Pitting	137.27
TS	EB + Pitting	161.47

Table 3.7. ZRA exposure data summary for AA7050-T7451 coupled with Type 316 stainless steel 0.5 M NaCl pH 5.5, 0.0485 M NaCl + 0.0005 M $AlCl_3$ pH 3.8, 0.35 M NaCl + 0.05 M $AlCl_3$ pH 3.2 and 0.167 M $AlCl_3$ pH 2.8 after 144 hours. Q_{net} is the charge consumed from by the potentiostat, $Q_{\Delta m}$ is the anodic charge consumed from metal dissolution determined from gravimetric mass loss, average L is the average corrosion fissure length determined by sectioning and PI is the pitting index.

Environment	**Post pH**	**Q_{net} (C/cm^2)**	**$Q_{\Delta m}$ (C/cm^2)**	**Average L (μm)**	**PI**	**Damage Morphology**
0.5 M NaCl pH 5.66	5.34	16.53	16.60	53.3	21.3	Pitting
0.485 M NaCl +0.005 $AlCl_3$ pH 3.8	4.24	37.07	51.9	120	36.5	IGC
0.35 M NaCl + 0.05 M $AlCl_3$ pH 3.2	3.58	52.12	80.73	600	42.6	IGC
0.167 $AlCl_3$ pH 2.8	3.31	76.05	76.67	900	62.1	Deep IGC

3.9 Figures

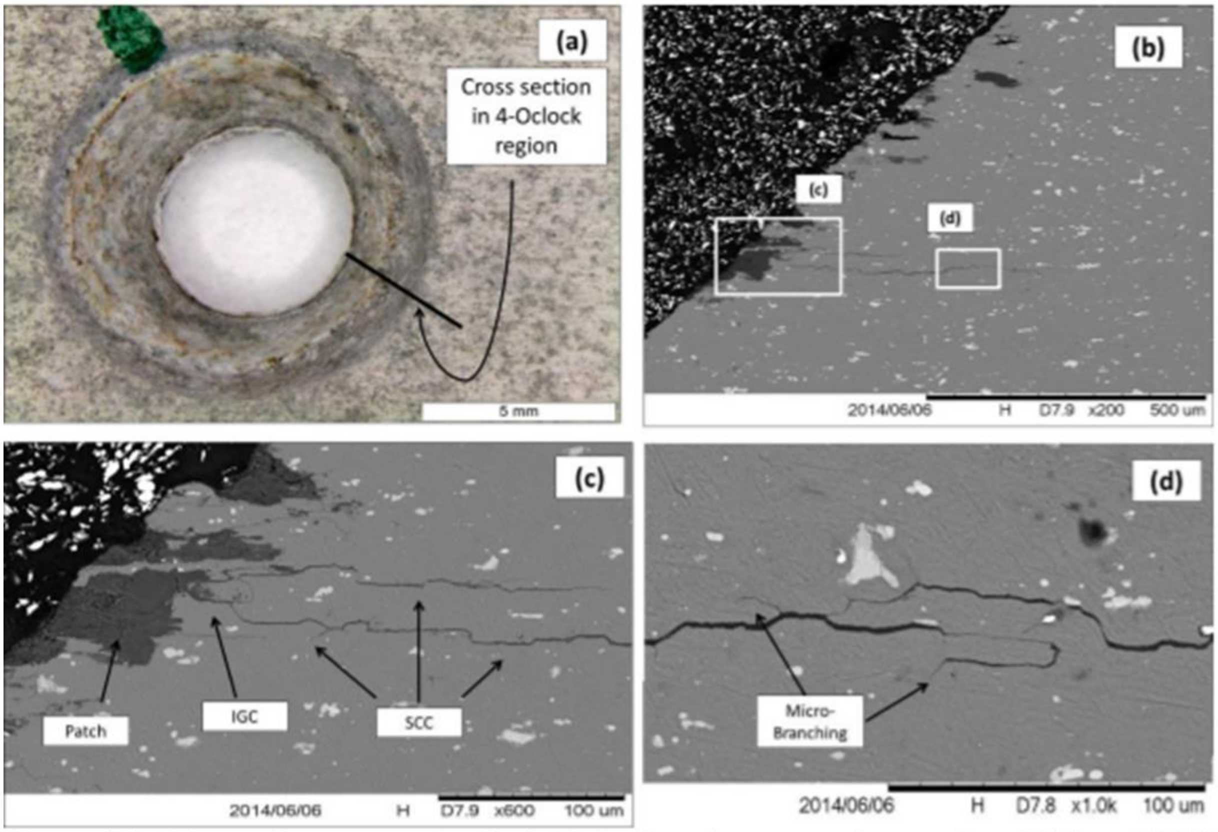

Figure 4.4: 24 month cross section in 4 O'clock region: corrosion patches, IGC and SCC are viewed. Cracks follow the grain boundaries with micro-branching.

Figure 3.1. Surface and cross-section of AA2024-T3 with a Type 316 stainless steel fasteners after 24 months of exposure in Daytona, Florida. This work was conducted by Young. [11]

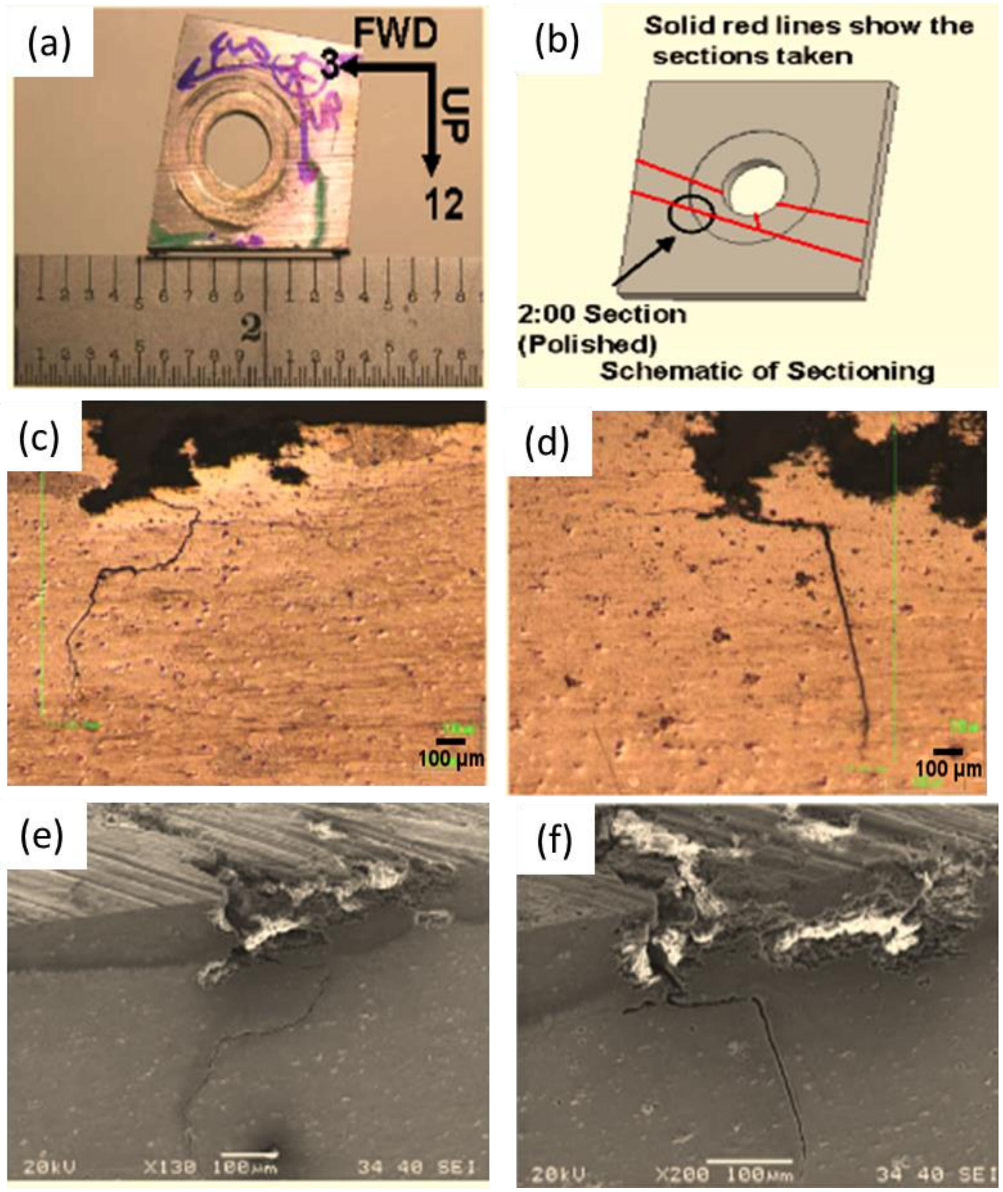

Figure 3.2. CAStLE teardown data showing (a) a picture of the fastener part that was corroded (b) a schematic of the fastener part showing in red where the piece was sectioned. (c) and (d) sectioned optical micrographs of the corrosion damage (e) and (f) sectioned electron micrographs of the corrosion damage.

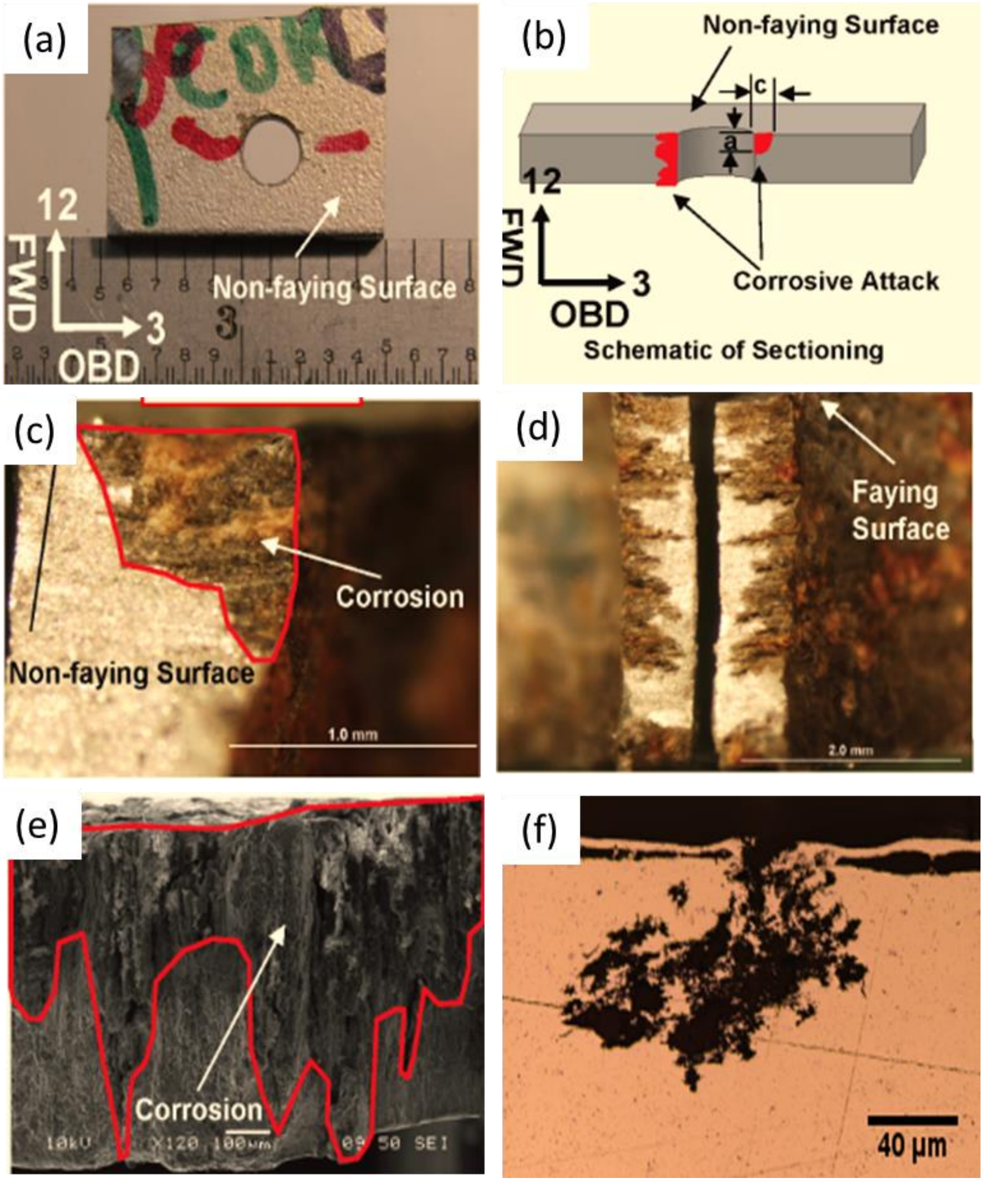

Figure 3.3. CAStLE teardown data showing (a) a picture of the fastener part that was corroded (b) a schematic of the fastener part showing in red where corrosion occurred (c) and (d) optical micrographs showing the surface of the part (e) Electron micrograph in cross-section (f) optical micrograph of the corrosion damage in cross-section.

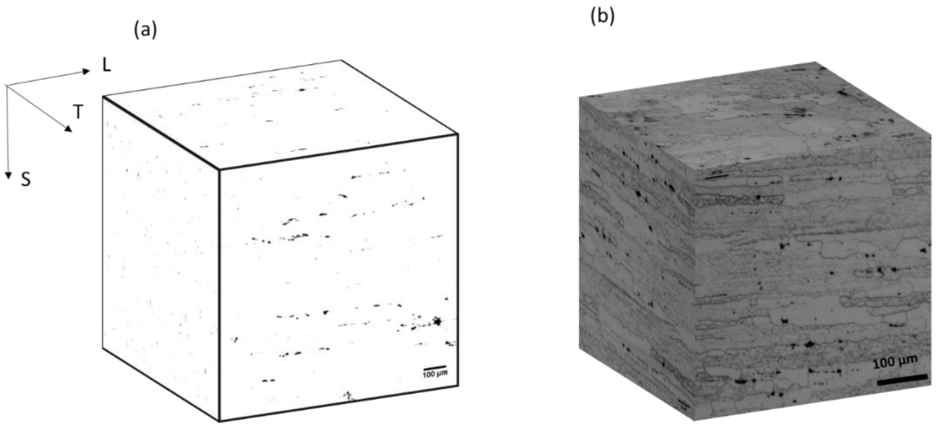

Figure 3.4. 3D microstructural cubes of AA7050-T7451 showing (a) constituent particles (black dots) and (b) after exposure to Keller's etch for 30 s revealing elongated grains in the rolling direction (L).

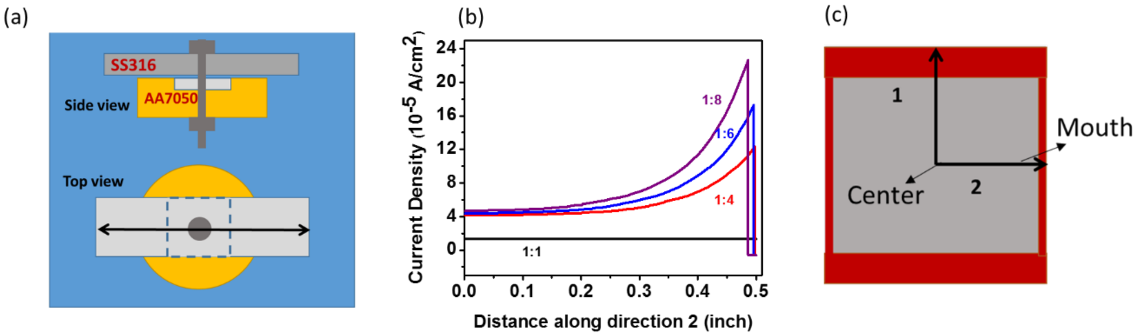

Figure 3.5. (a) FEA galvanic couple crevice of AA7050-T7451 (b) resulting FEA current over distance for AA7050-T7451 electrodes shown in (c) The exposures that simulated the center of the crevice were exposed in 0.5 M NaCl + $AlCl_3$ at pH 4 while exposures that simulated the mouth of the crevice were exposed in 0.5 M NaCl + $NaAlO_2$ at pH 8.

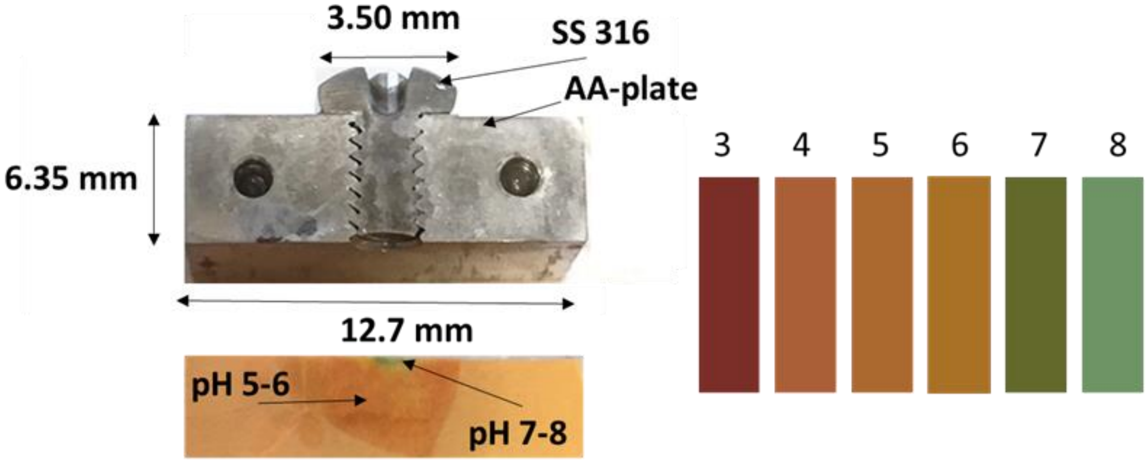

Figure 3.6. Cross-sectioned Type 316 stainless steel screw in an AA7050-T7451 SL plate with the corresponding pH paper after a full immersion exposure in 4 M NaCl for 62 hours. The rivet mouth was at pH 7-8 while inside the rivet was observed to be at pH 7-8.

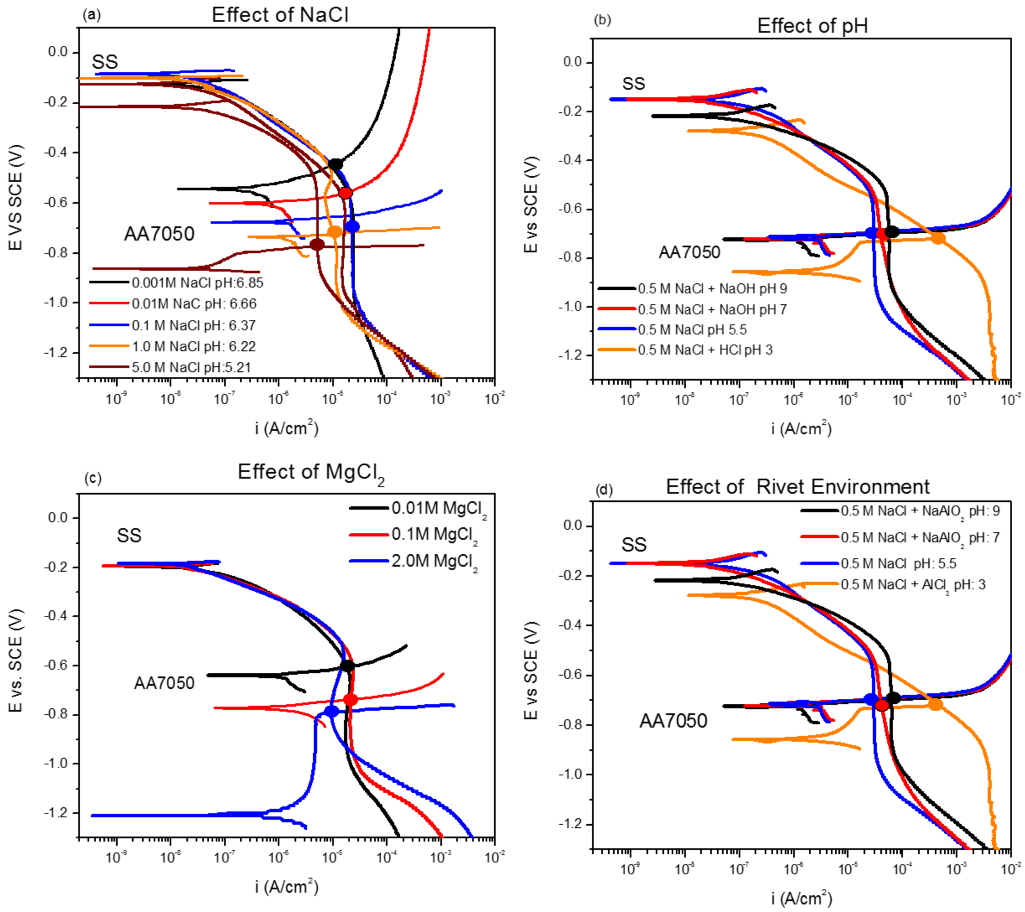

Figure 3.7. Cathodic polarization on Type 316 stainless steel and anodic polarization on AA7050-T7451 showing the effect of (a) concentration of NaCl (b) pH and environment (c) $MgCl_2$ (d) various rivet environments.

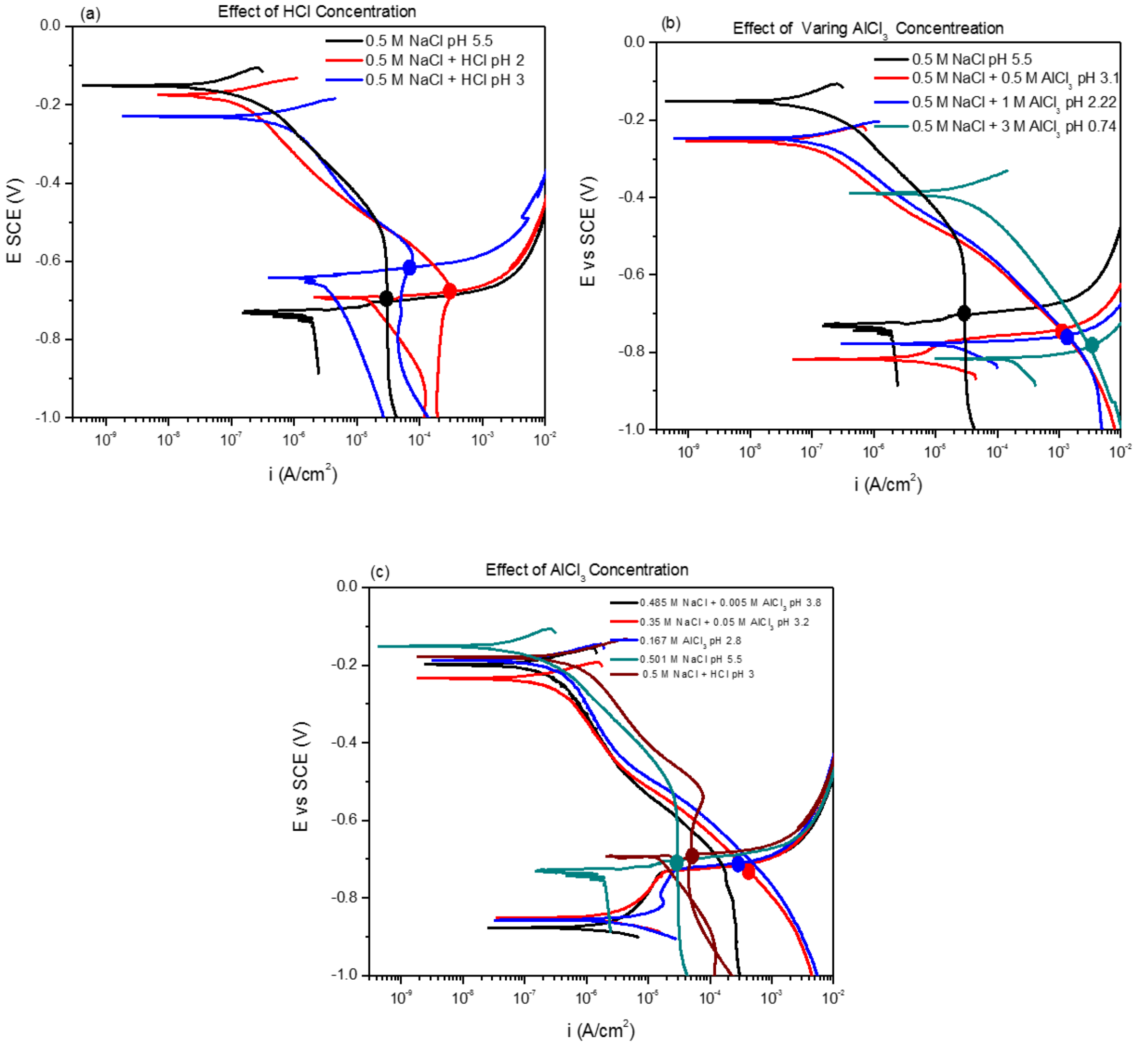

Figure 3.8. Cathodic and Anodic polarization investigating the effect of $AlCl_3$ where shows the effect of (a) HCl concentration (b) varying $AlCl_3$ concentrations and (c) Al ions.

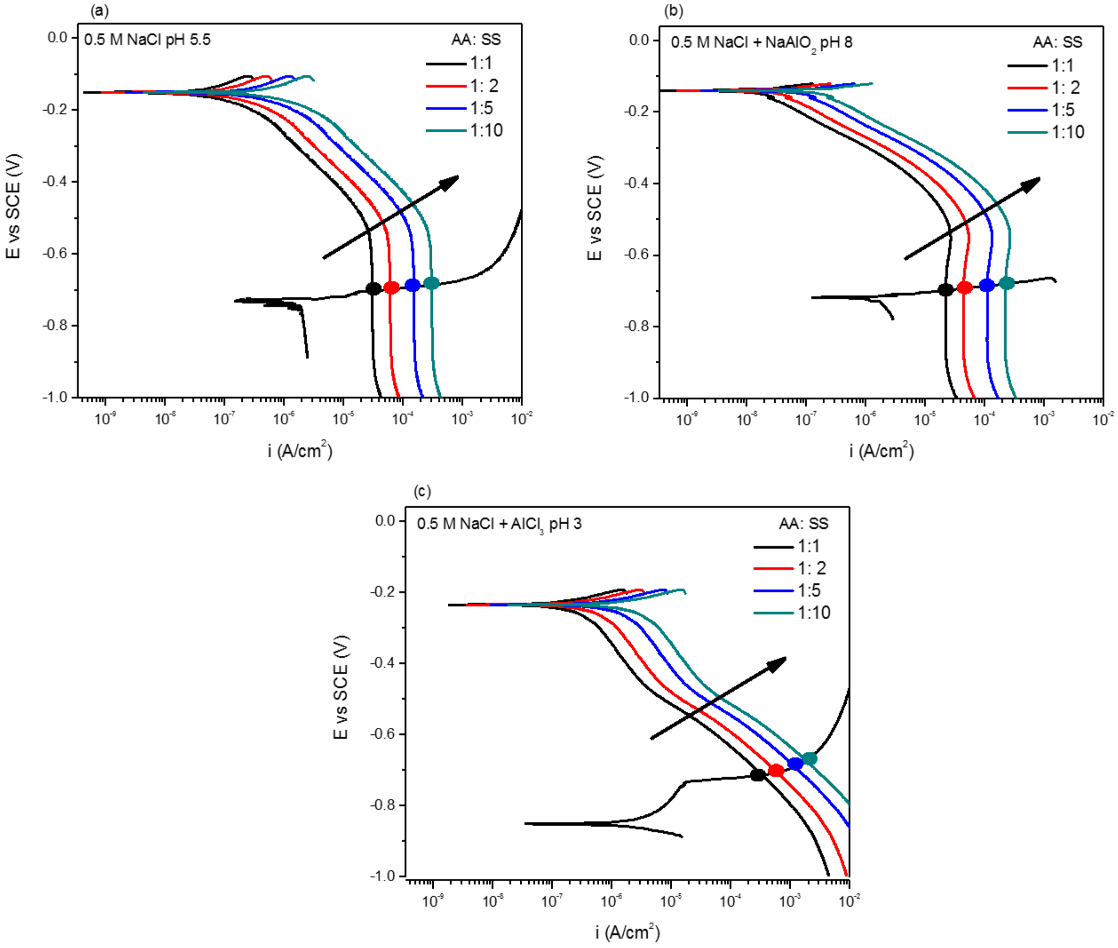

Figure 3.9. Anodic potentiodynamic polarization of AA7050-T7451and cathodic potentiodynamic polarization on Type 316 stainless steel for increasing cathode area in (a) 0.5 M NaCl at pH 5.5 (b) 0.5 M NaCl + NaAlO2 at pH 8 and (c) 0.5 M NaCl + AlCl3 at pH 3.

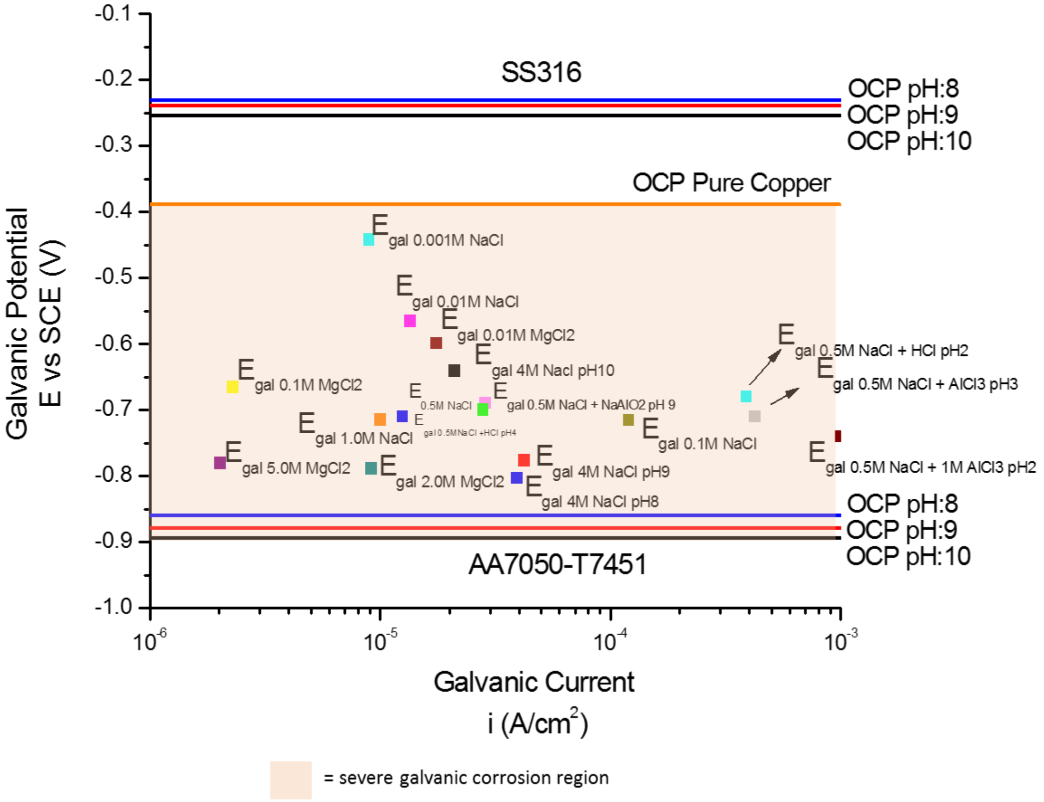

Figure 3.10. Galvanic couple potential and corresponding galvanic current summary plot extracted from polarization data showing the range where severe galvanic corrosion may occur when AA7050-T7451 is coupled to Type 316 stainless steel.

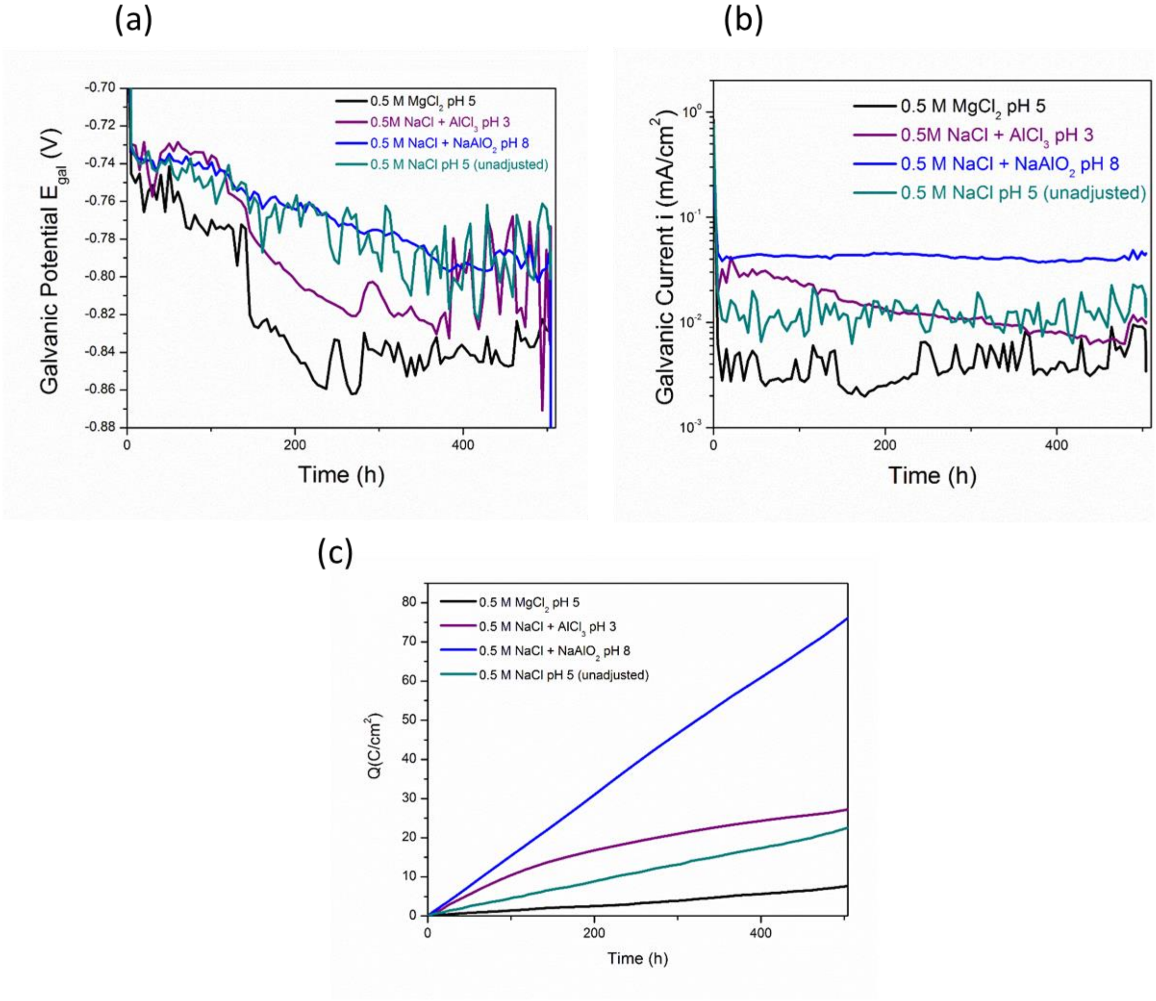

Figure 3.11. Galvanic couple (a) potential (b) current and (c) charge density of AA7050-T7451 coupled with Type 316 stainless steel obtained via zero resistance ammeter for 504 h in simulated crevice solutions.

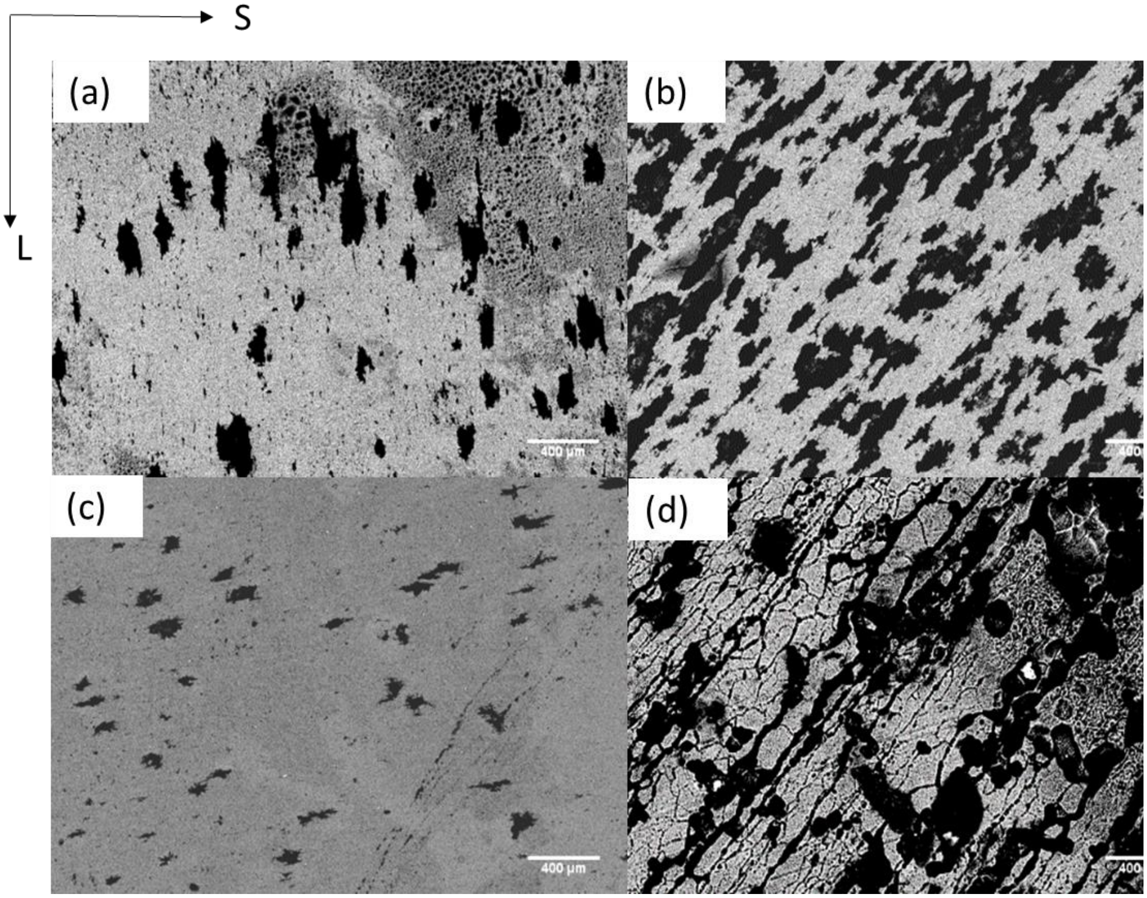

Figure 3.12. Surface damage morphology of AA7050-T7451 coupled with Type 316 stainless steel for 504 h in (a) 0.5 M NaCl (b) 0.5 M NaCl + $NaAlO_2$ (c) 0.5 $MgCl_2$ and (d) 0.5 M NaCl + $AlCl_3$.

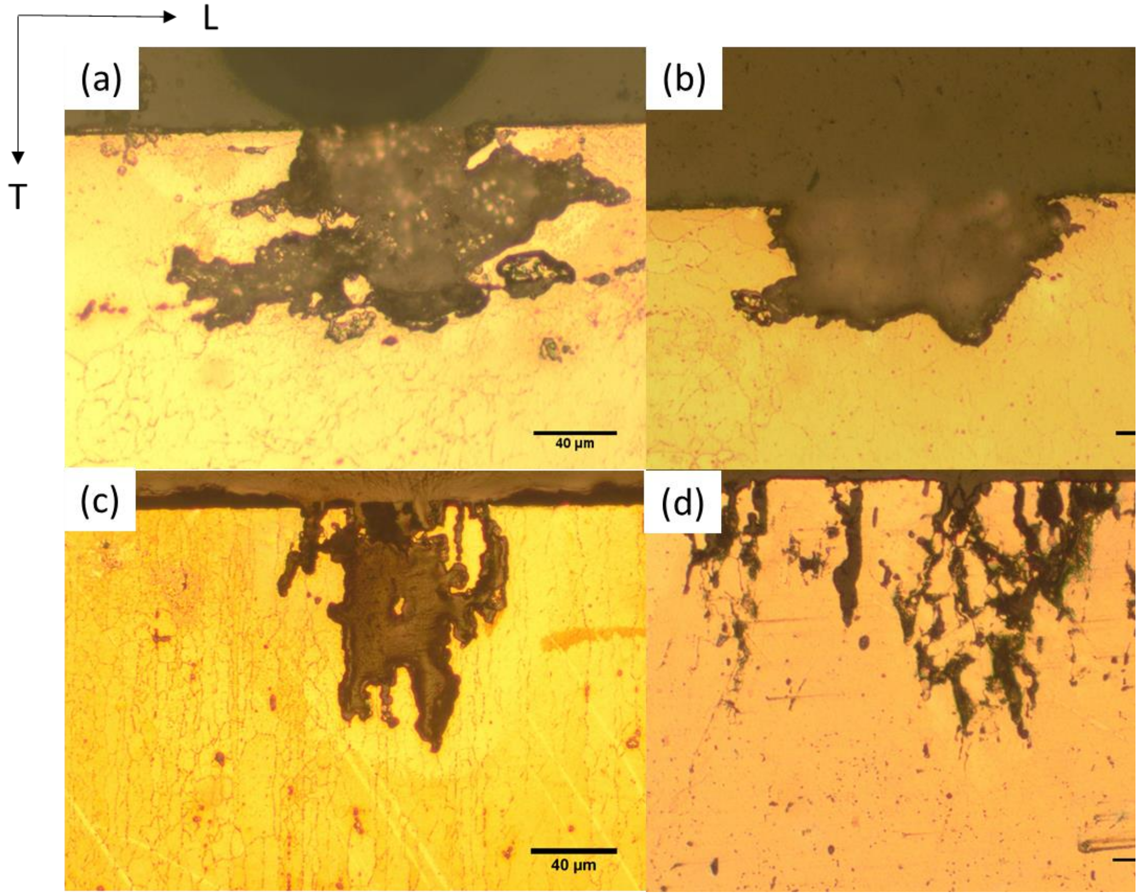

Figure 3.13. Cross-section damage morphology of AA7050-T7451 coupled with Type 316 stainless steel for 504 h in (a) 0.5 M NaCl (b) 0.5 M NaCl + $NaAlO_2$ (c) 0.5 $MgCl_2$ and (d) 0.5 M NaCl + $AlCl_3$.

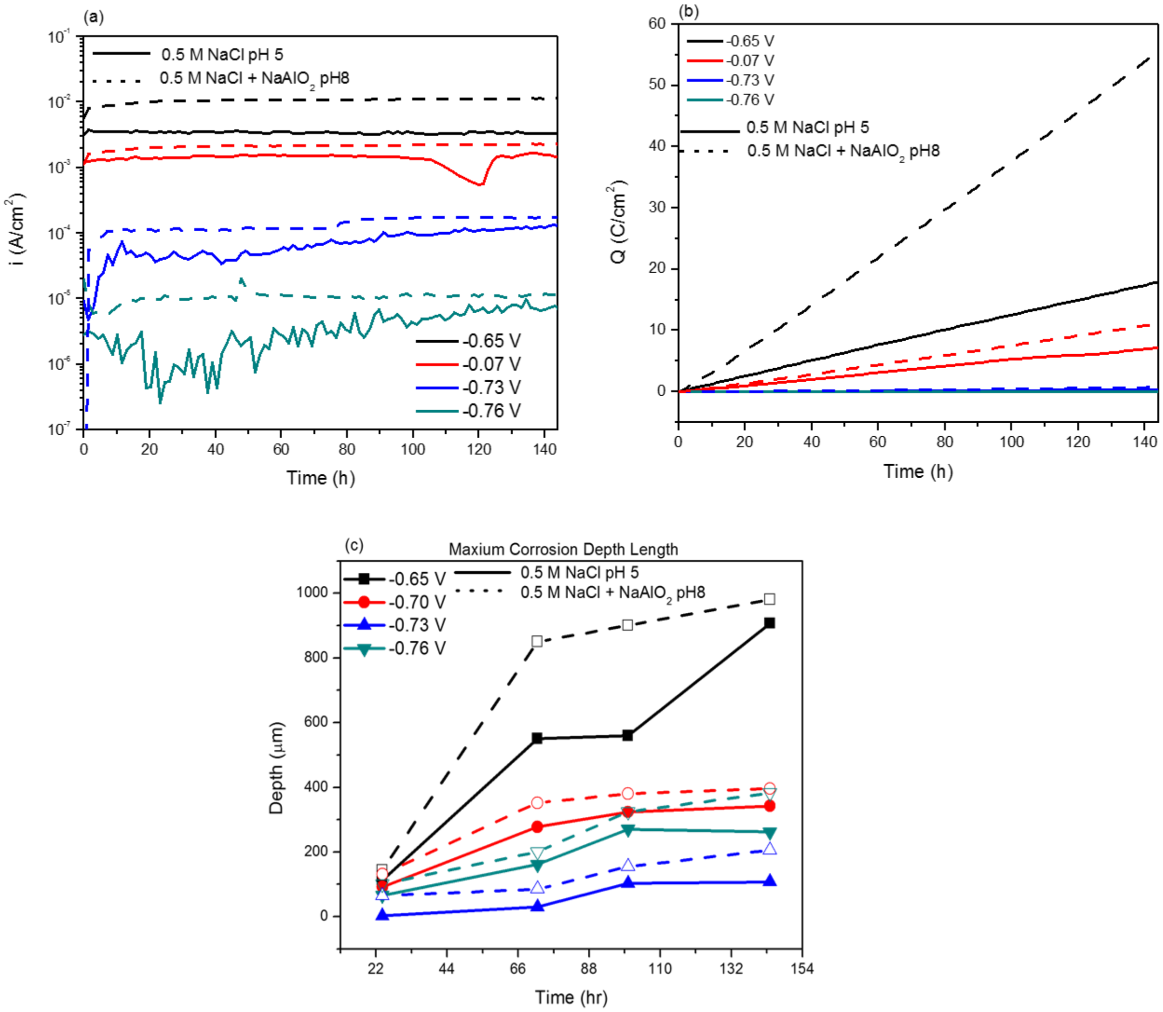

Figure 3.14. Potentiostatic polarization at pertinent galvanic couple potentials of AA7050-T7451 coupled with Type 316 stainless steel in simulated crevice solutions of 0.5 M NaCl pH 5.5 (solid line) and 0.5 M NaCl + NaAlO2 pH 8 (dotted line) showing (a) current density over 144 h and (b) charge density over 144 h and (c) corrosion fissure depth after 24, 72, 100 and 144 hours.

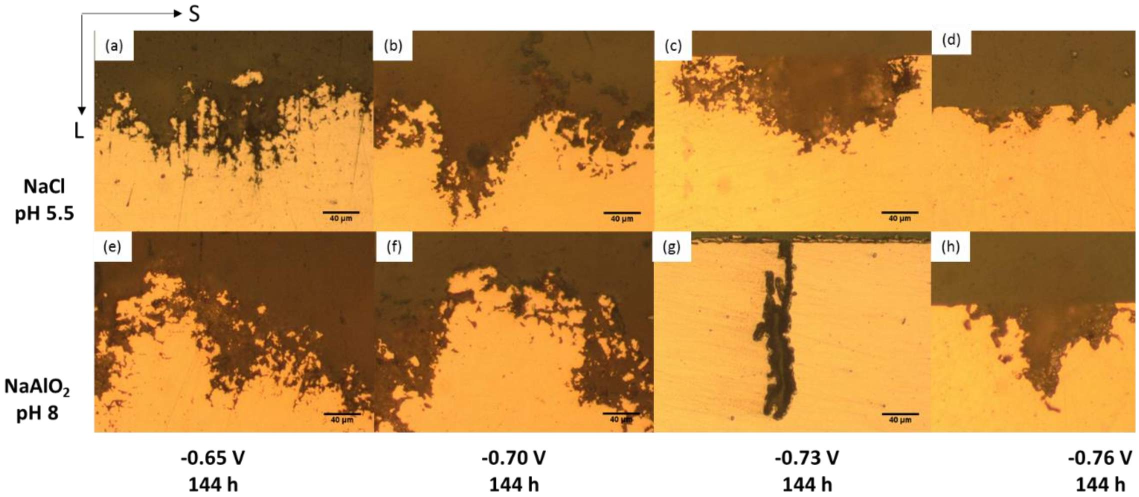

Figure 3.15. Cross-sectional corrosion damage morphologies of AA7050-T7451 in 0.5 M NaCl + $NaAlO_2$ pH 8 (a)-(d) and 0.5 M NaCl unadjusted pH 5.5 (e)-(h) after potentiostatic polarization at -0.65, -0.70, -0.73 and -0.76 V SCE after 144 h showing the different damage morphology produced.

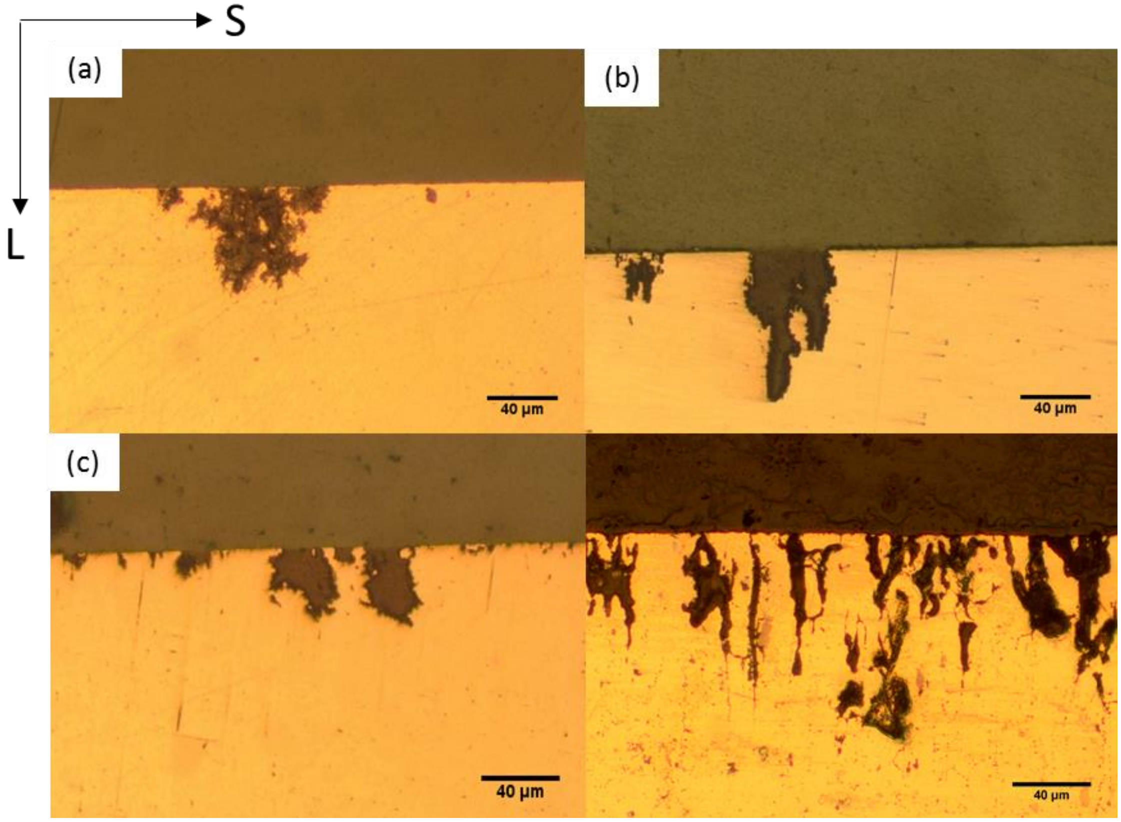

Figure 3.16. Cross-sectional corrosion damage morphologies of AA7050-T7451 at E=-0.73 V SCE after 72 h in (a) 0.5 M NaCl pH 5.5 (b) 0.5 M NaCl + $NaAlO_2$ pH 8 (c) 0.5 M MgCl2 pH 5 and (d) 0.5 M NaCl + $AlCl_3$ pH 3.

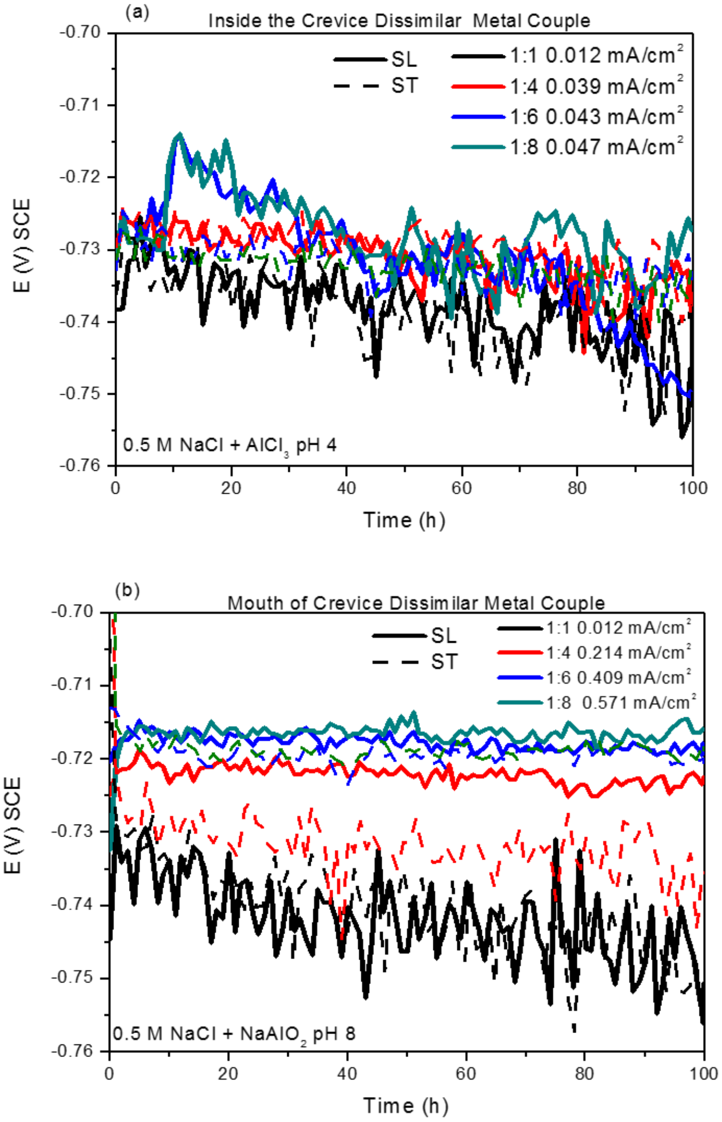

Figure 3.17 Galvanic couple potential of AA7050-T7451 coupled with Type 316 stainless steel obtained by galvanostatic polarization for various anode to cathode areas in simulated crevice solutions of 0.5 M NaCl + $AlCl_3$ at pH 4 and 0.5 M NaCl + $NaAlO_2$ at pH 8 simulated typical current values at the (a) inside the crevice of a dissimilar metal crevice and (b) mouth of the crevice of a dissimilar metal couple. SL orientations are shown in solid lines and ST orientations are shown in dashed lines.

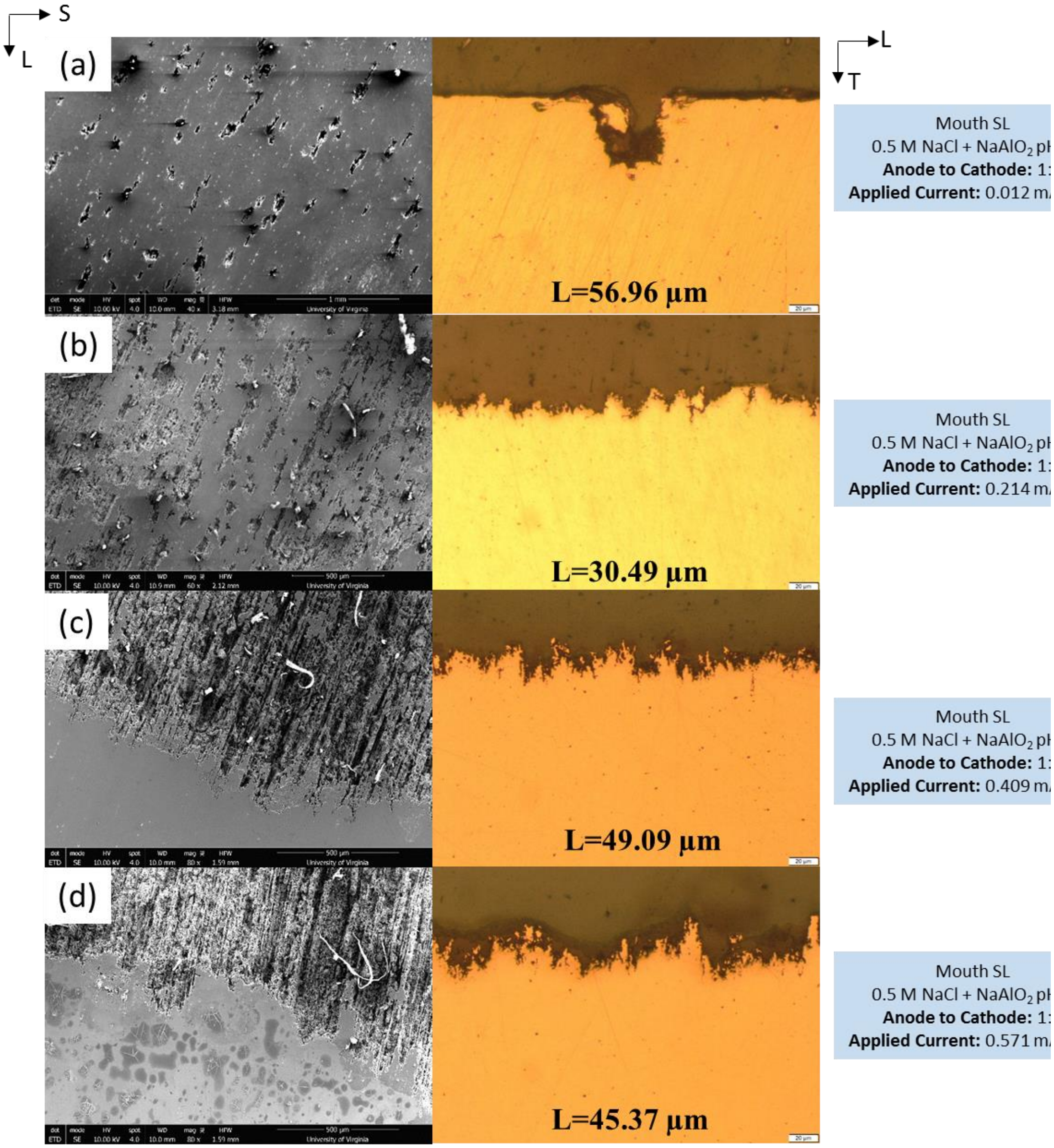

Figure 3.18. Surface and cross-sectional corrosion damage morphologies after 100 h of galvanostatic polarization and currents that simulated a galvanic couple between AA7050-T7451 SL and Type 316 stainless steel at the mouth in a crevice in 0.5 M NaCl + NaAlO$_2$ at pH 8 with anode to cathode ratio of (1) 1:1 (0.012 mA/cm^2) (b) 1:4 (0.214 mA/cm^2) (c) 1:6 (0.409 mA/cm^2) and (d) 1:8 (0.571 mA/cm^2).

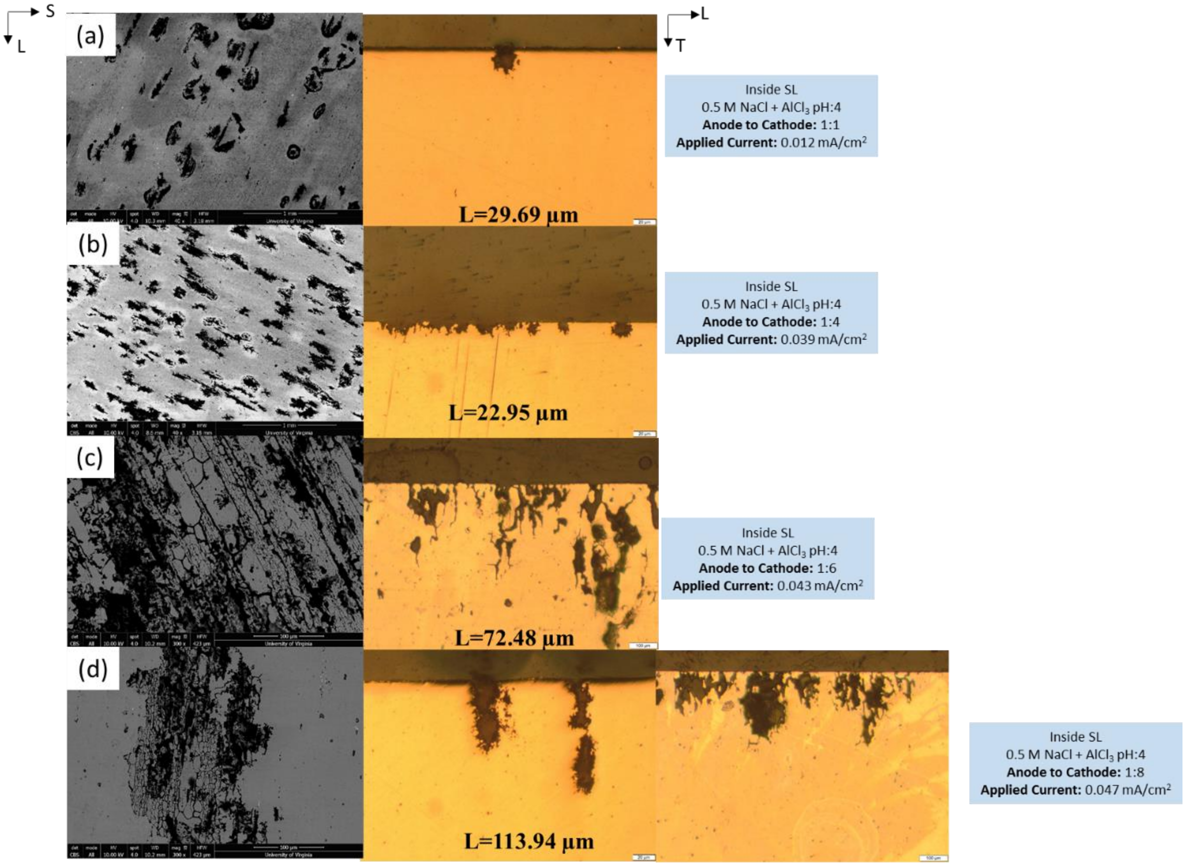

Figure 3.19. Surface and cross-sectional corrosion damage morphologies after 100 h of galvanostatic polarization and currents that simulated a galvanic couple between AA7050-T7451 SL and Type 316 stainless steel inside the crevice in 0.5 M NaCl + $AlCl_3$ at pH 4 with anode to cathode ratio of (1) 1:1 (0.012 mA/cm^2) (b) 1:4 (0.039 mA/cm^2) (c) 1:6 (0.043mA/cm^2) and (d) 1:8 (0.047 mA/cm^2).

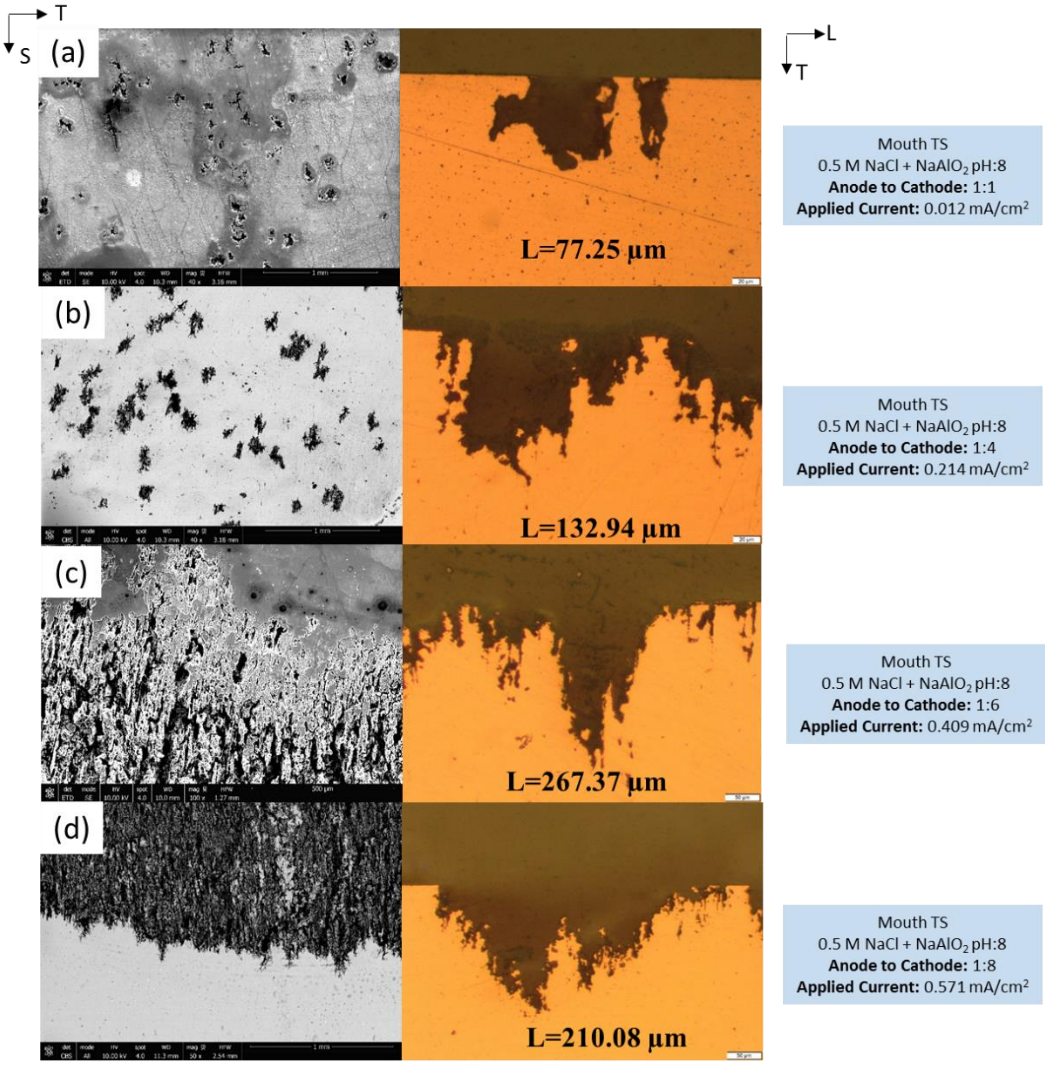

Figure 3.20. Surface and cross-sectional corrosion damage morphologies after 100 h of galvanostatic polarization and currents that simulated a galvanic couple between AA7050-T7451 TS and Type 316 stainless steel at the mouth in a crevice in 0.5 M NaCl + NaAlO2 pH 8 with anode to cathode ratio of (1) 1:1 (0.012 mA/cm2) (b) 1:4 (0.214 mA/cm2) (c) 1:6 (0.409 mA/cm2) and (d) 1:8 (0.571 mA/cm2).

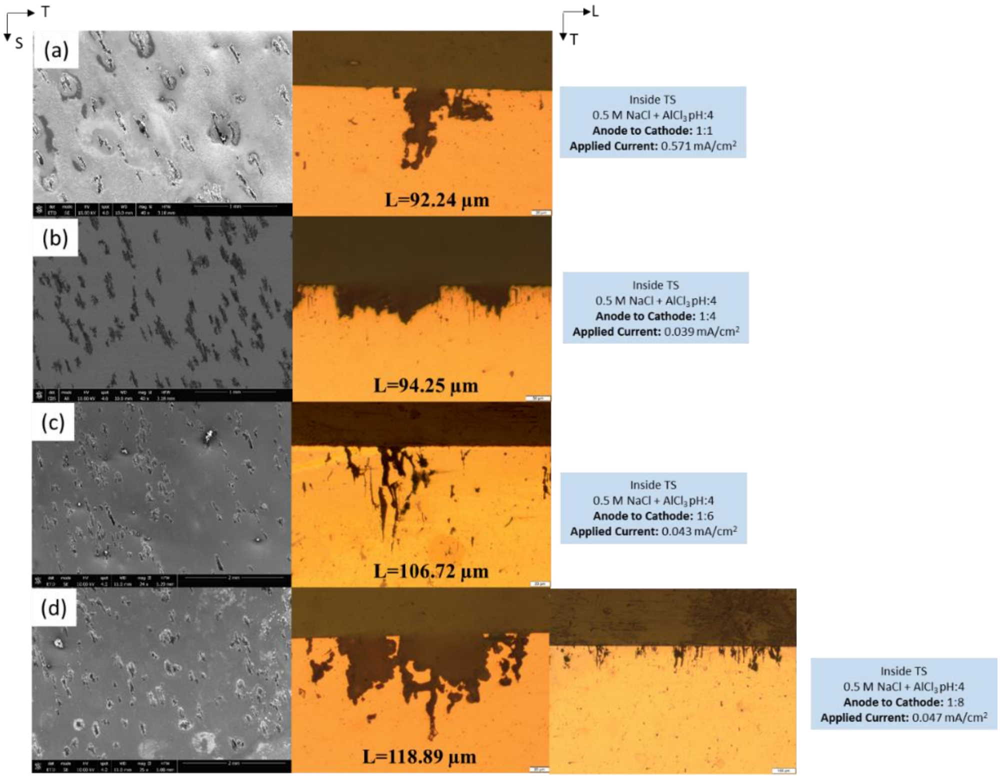

Figure 3.21. Surface and cross-sectional corrosion damage morphologies after 100 h of galvanostatic polarization and currents that simulated a galvanic couple between AA7050-T7451 TS and Type 316 stainless steel inside the crevice in 0.5 M NaCl + $AlCl_3$ pH 4 with anode to cathode ratio of (1) 1:1 (0.012 mA/cm$_2$) (b) 1:4 (0.039 mA/cm$_2$) (c) 1:6 (0.043mA/cm2) and (d) 1:8 (0.047 mA/cm$_2$).

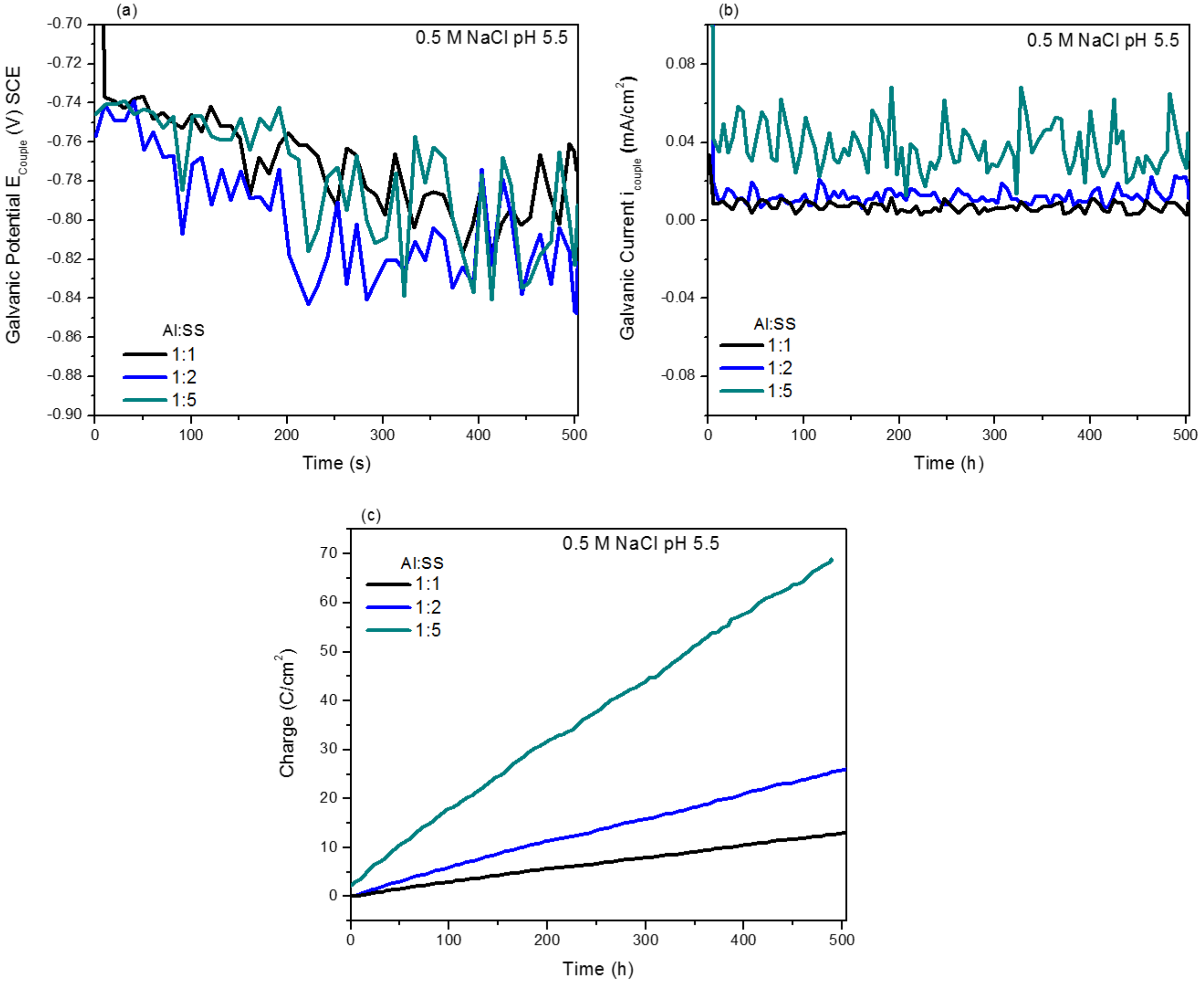

Figure 3.22. Galvanic couple (a) potential and (b) current density and (c) charge density of AA7050-T7451 coupled with Type 316 stainless steel obtained utilizing zero resistance ammeter for 504 h in 0.5 M NaCl at pH 5.5 with increasing area of stainless steel, anode to cathode ratios of 1:1, 1:2 and 1:5.

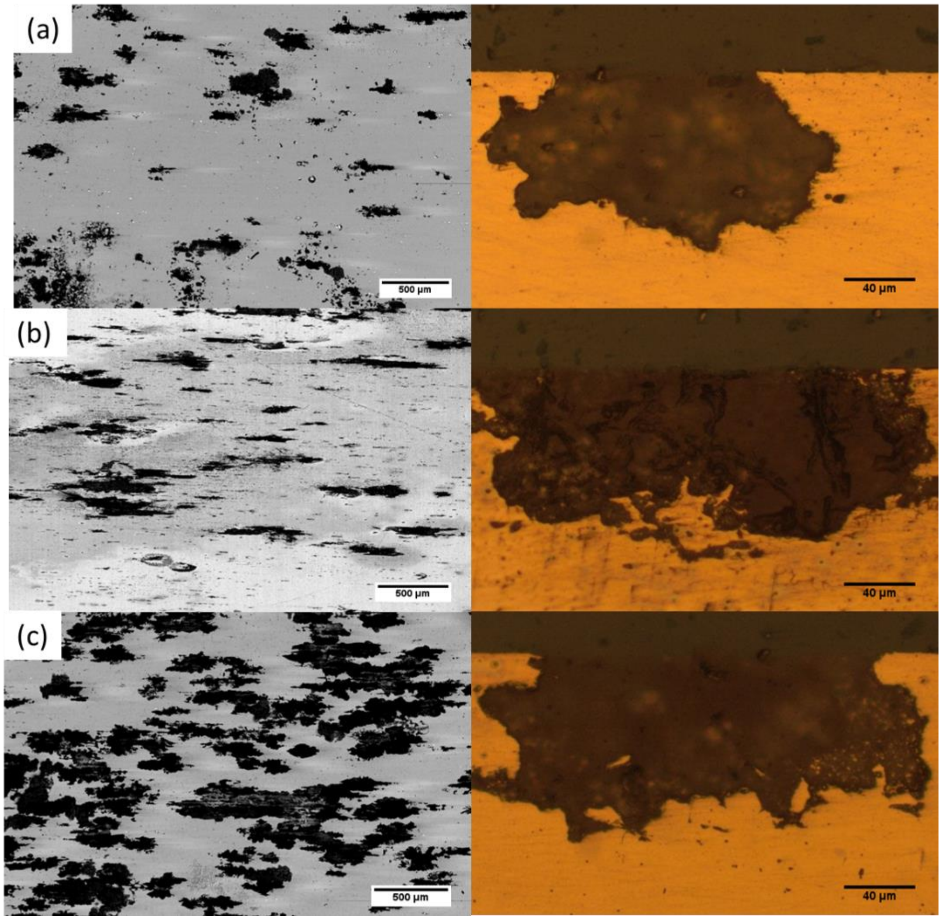

Figure 3.23. Surface and cross-sectional corrosion damage morphologies after 504 h of AA7050-T7451 was coupled with Type 316 stainless steel through ZRA in 0.5 M NaCl at pH 5.5 with anode to cathode ratio of (a) 1:1 (b) 1:2 (c) 1:5

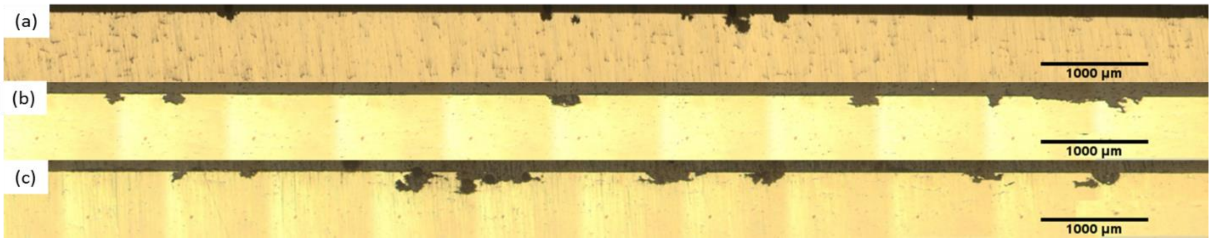

Figure 3.24. Cross-sectional micrograph of AA7050-T7451 coupled with Type 316 stainless steel through ZRA in 0.5 M NaCl at pH 5.5 after 504 h with anode to cathode ratio of (a) 1:1 (b) 1:2 and (c) 1:5

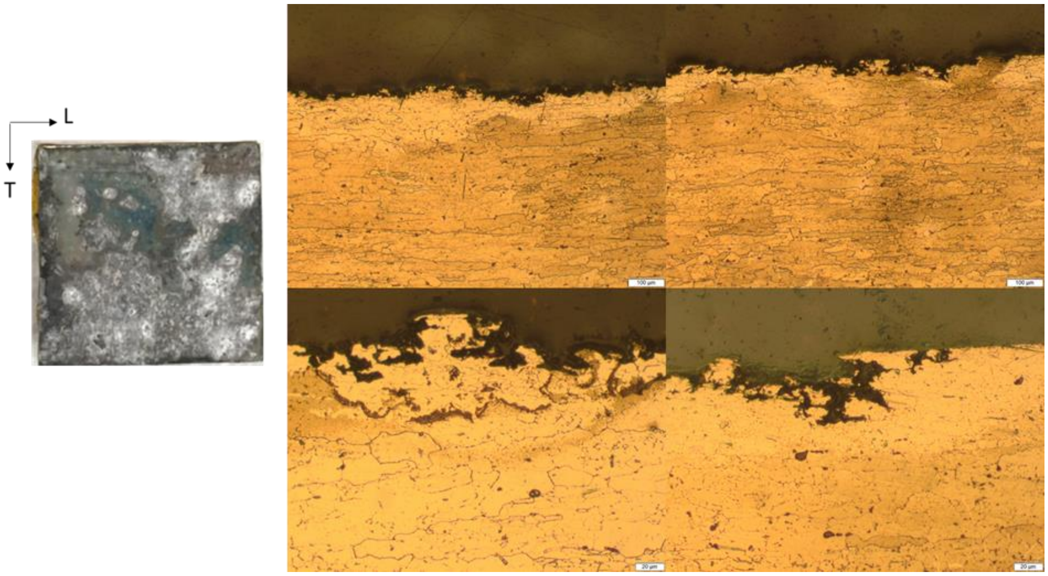

Figure 3.25. AA7050-T7451 LT after 96 h of exposure in full immersion ANCIT (aluminum-nitrate-chloride-test) showing the surface and cross-section characterization

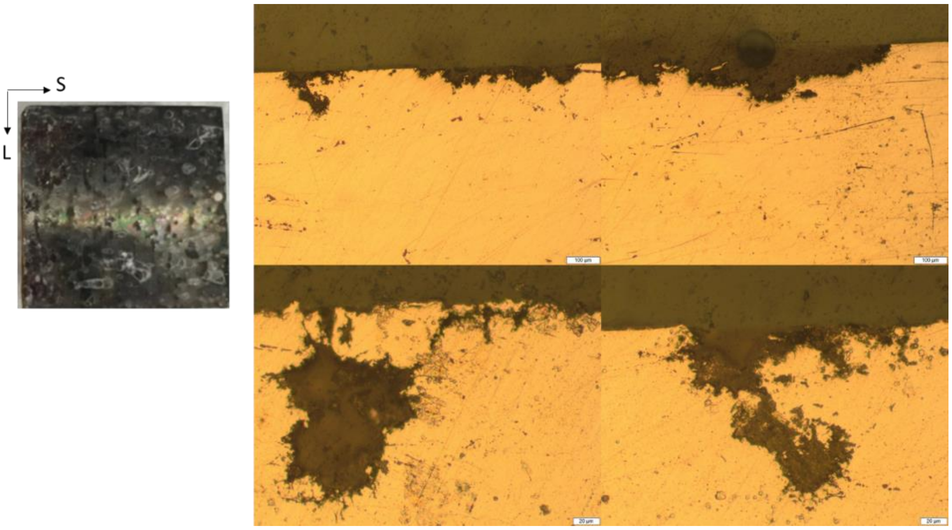

Figure 3.26. AA7050-T7451 SL after 96 h of exposure in full immersion ANCIT (aluminum-nitrate-chloride-test) showing the surface and cross-section characterization

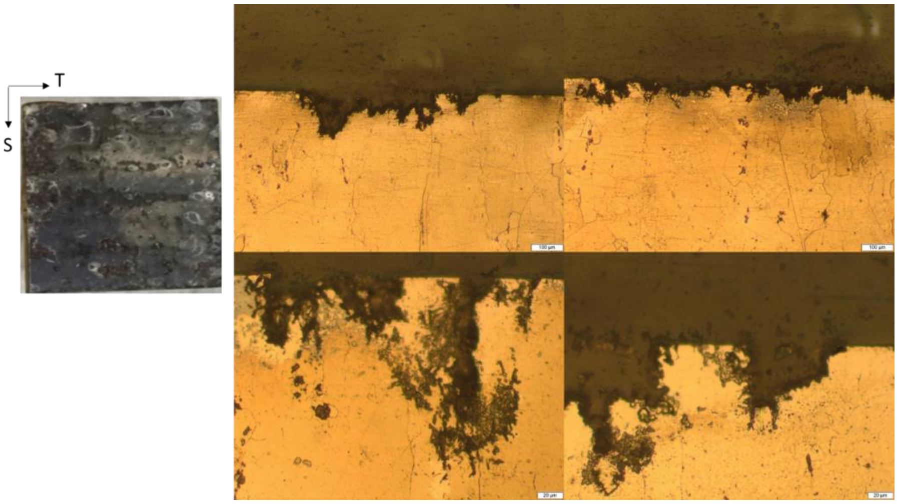

Figure 3.27. AA7050-T7451 SL after 96 h of exposure in full immersion ANCIT (aluminum-nitrate-chloride-test) showing the surface and cross-section characterization

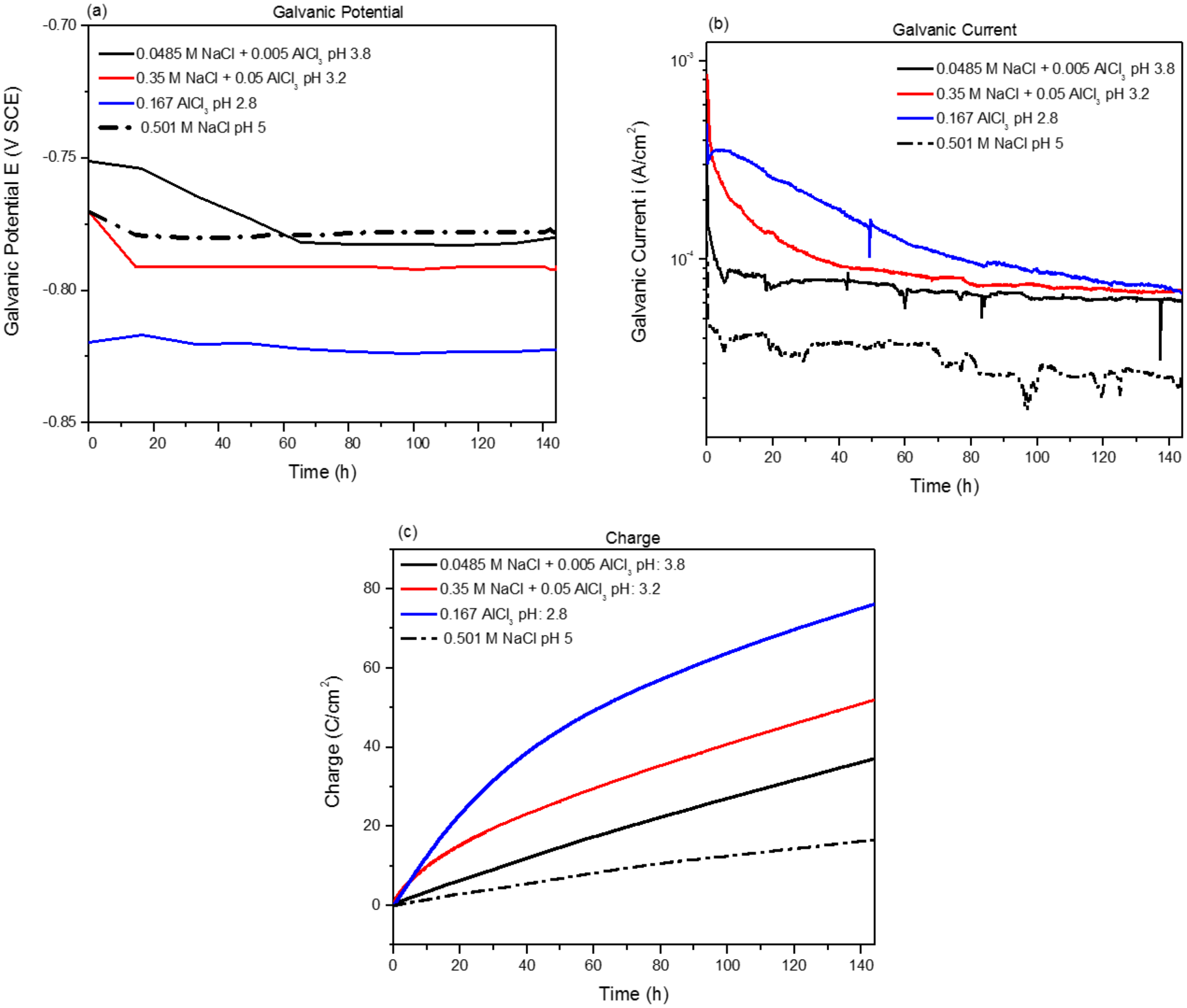

Figure 3.28. Galvanic couple (a) potential and (b) current (c) anodic charge over 144 h of AA7050-T7451 coupled with Type 316 stainless steel obtained using zero resistance ammeter in 0.5 M NaCl at pH 5, 0.167 M $AlCl_3$ at pH 2.8, 0.35 m NaCl + 0.05 M $AlCl_3$ at pH 3.2 and 0.0485 M NaCl + 0.005 M $AlCl_3$ at pH 3.8.

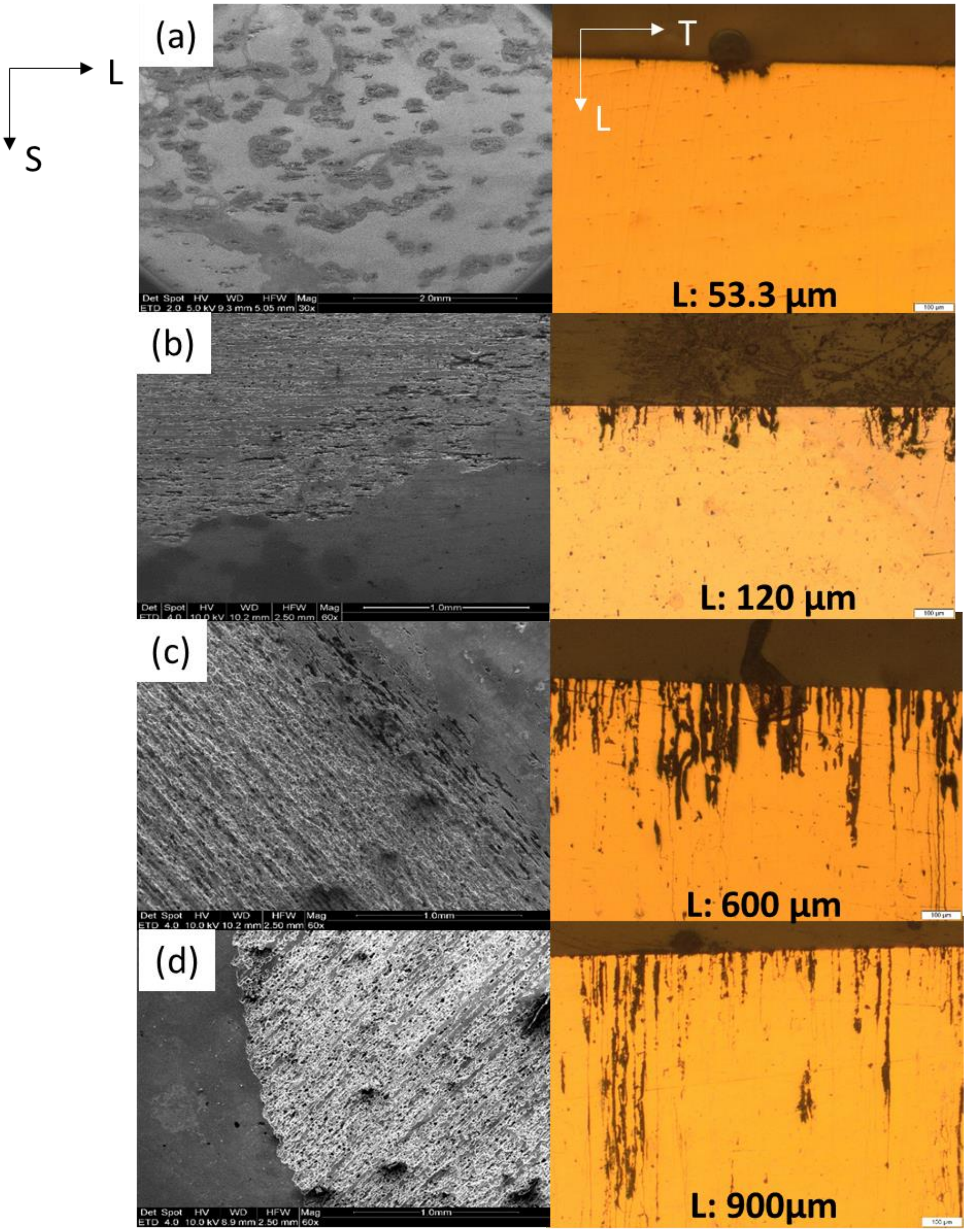

Figure 3.29. SEM micrograph of surface and optical micrograph of cross-section after ZRA exposure for 144 hours in (a) 0.5 M NaCl at pH 5.5 (b) 0.0485 M NaCl + 0.0005 M $AlCl_3$ at pH 3.8, 0.35 M NaCl + 0.05 M $AlCl_3$ at pH 3.2 and 0.167 M $AlCl_3$ at pH 2.8

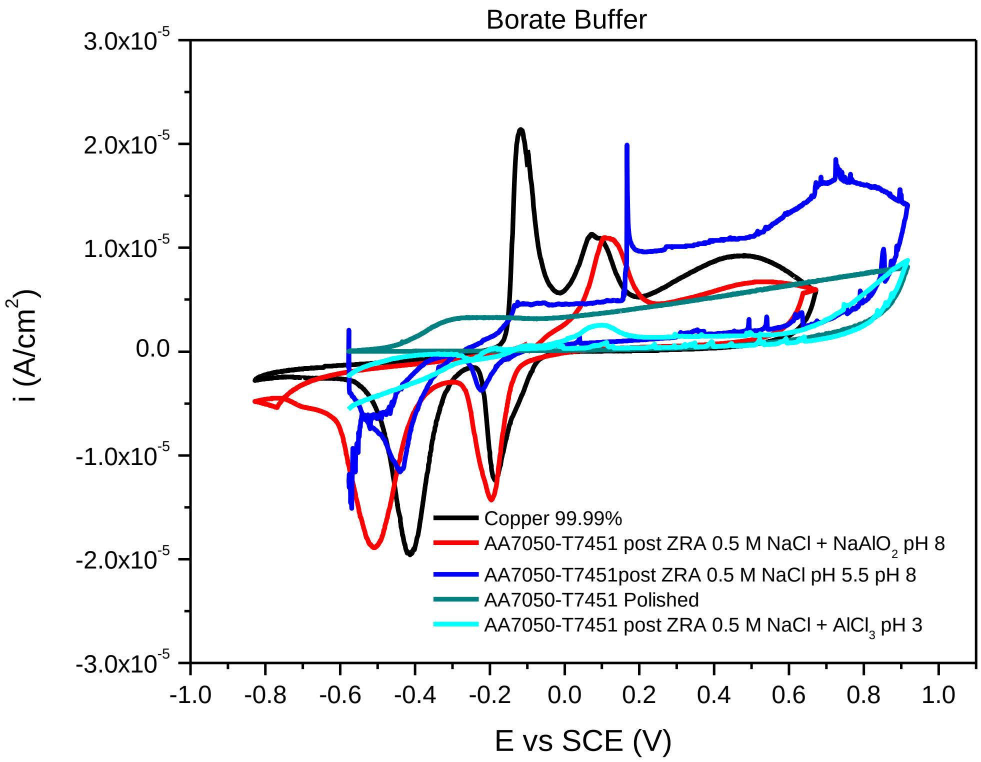

Figure 3.30. Cyclic voltammogram of pure Cu, AA7050-T7451 compared to AA7050-T7451 after exposure in 504 h in 0.5 M NaCl, 0.5 M NaCl + $NaAlO_2$ pH 8, and 0.5 M NaCl + $AlCl_3$ pH 3 in deaerated, pH 8.4 borate buffer

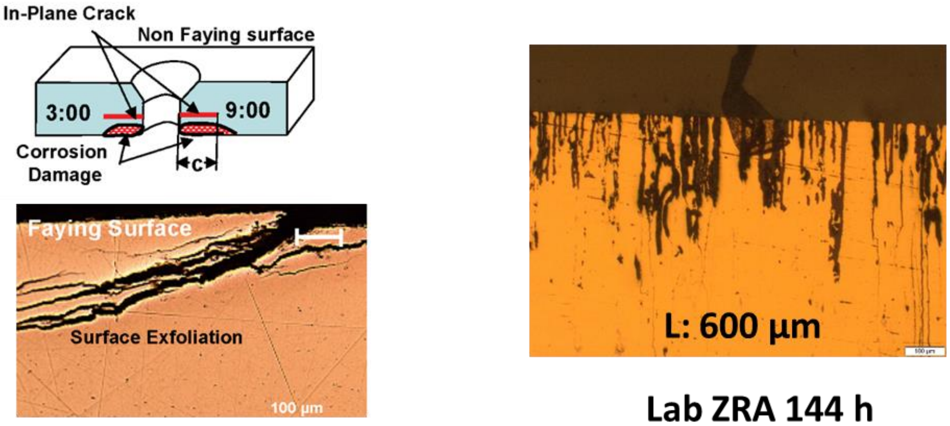

Tear-down data

Lab ZRA 144 h
0.485 M NaCl + 0.005 M $AlCl_3$ pH: 3.8

Figure 3.31. Tear down data showing surface exfoliation and IGC compared to laboratory ZRA testing for 144 h in 0.485 M NaCl + 0.005 M $AlCl_3$ pH 3.8.

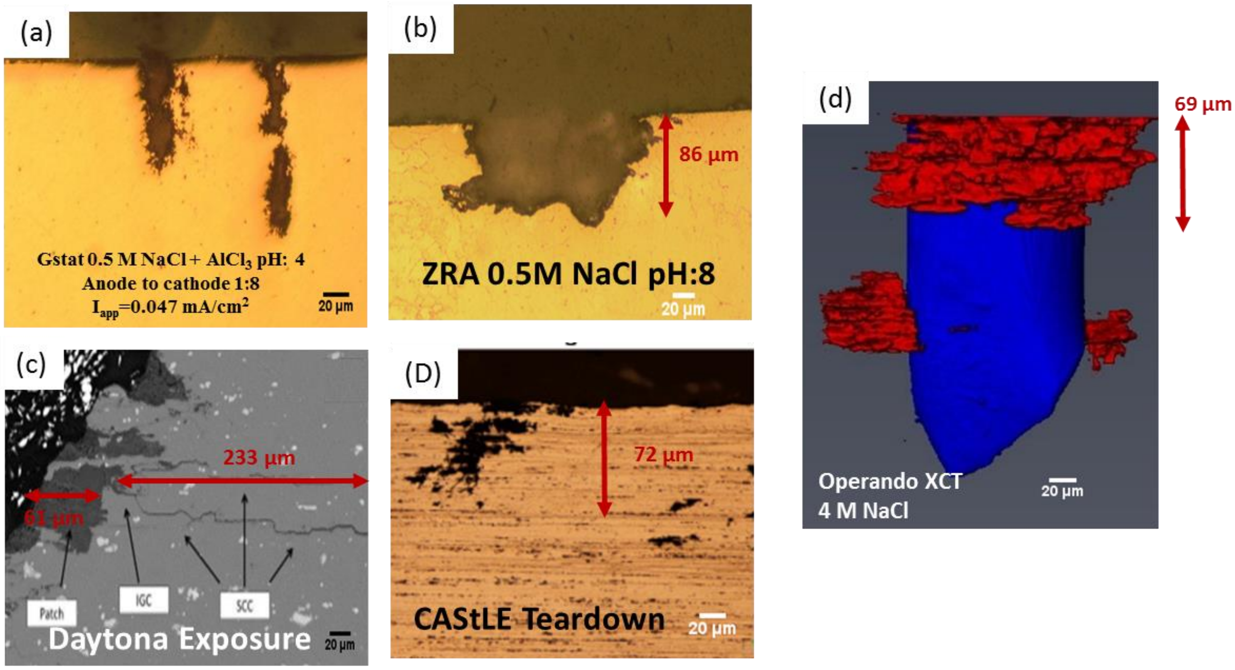

Figure 3.32. Lab vs field vs tear down comparison showing (a) optical micrograph on AA7050-T7451 after galvanostatic polarization laboratory testing for 100 h at i=0.047 mA/cm^2 (b) Optical micrograph of AA7050-T7451 after laboratory zero resistant ammeter testing for 504 h. AA7050-T7451 was coupled with Type 316 stainless steel with a 1:1 anode to cathode ratio (c) AA2024-T3 plate coupled with a Type 316 stainless steel fastener after 24 months of exposure in Daytona, Florida (d) CAStLE tear down optical micrograph of unknown Al alloy and SS fastener (d) Operando XCT 3D reconstruction of AA7050-T7451 simulated fastener of Type 316 stainless steel after exposure for 62 to hours under a droplet of 4 M NaCl at 98% RH.

4 Micro and Nano-scale Understanding of Localized Corrosion of AA7050-T7451 in Rivet Environments

4.1 Abstract

In this work, the microstructure of AA7050-T7451 was studied to provide an understanding, from the electrochemical-microstructure view point, of the corrosion damage morphologies and paths observed in previous work shown in Chapter 3. The AA7050-T7451 exhibits an improvement in resistance to intergranular corrosion (IGC) with increasing aging time, implying that a change in the metallurgical factors governing the susceptibility of the IGC occurs. While the heterogeneous microstructure of age hardened AA7050-T7451 is desirable to optimize mechanical properties, the solute depleted zone (SDZ) and the second phase particles render the alloy susceptible to localized corrosion using a traditional electrochemical framework for attack. It was determined that in the T74 over-aged heat treatment, η-phase $MgZn_2$ often becomes enriched with Cu and/or Al improving its corrosion resistance but also leaving a solute depleted zone adjacent to the grain boundary and depleting the matrix of the Cu. Therefore, different zones of the alloy, with compositions as determined by transmission electron microscopy (TEM), were obtained and electrochemically tested to speculate on the preferential paths of corrosion given the different possible rivet environments. The electrochemical window of susceptibility for preferential attack can be attributed to the difference in pitting potentials between the bulk matrix and the Cu-depleted zone and the $Mg(ZnCuAl)_2$ phases. The enrichment of Cu and/or Al in η grain boundary phase was found to increase the pitting potential, closing the potential difference window between the matrix and the η phase $Mg(ZnCuAl)_2$ for corrosion. However, the solute depleted zone, adjacent to the grain boundary η phase, can also often lead to corrosion damage due to the difference in potential between bulk alloy and the solute depleted regions. In AA7050-T7451 it was found that IGCFS occurs most in acidic $AlCl_3$. The reason for IGC can be speculated to be the due to the lack of Cu^{2+} in solution in $AlCl_3$ environment, as result from the absence of replated Cu. In this case, the pitting potential of the solute depleted zones (Al-Zn-Mg-Zr and Pure Al) were raised within 5 mV below the matrix. This closes the window of IGC susceptibility and suggests that in neutral or

alkaline environments, corrosion damage can be attributed to pitting of course constituent particles. The IGC corrosion observed in $AlCl_3$ environments can be attributed to difference in pitting potential between AA7050-T7451 the Cu-depleted and solute depleted zone. Furthermore, electron backscatter diffraction (EBSD) was conducted in cross-section around fissures and pits to elucidate a corrosion pathway. It was found that possible pathway may be attributed to sub-Grain boundaries within deformed grains of the partially recrystallized alloy preferentially attacked.

4.2 Introduction and Background

4.2.1 Evolution of AA7050 Composition

AA7050 is strengthened by the formation of hardening precipitates in the reaction sequence: [9,34,168]

Solid solution→GP zones→ semicoherent η'→ incoherent η

In the partially recrystallized and artificially aged microstructure, η' is typically located on sub-grain boundaries and interiors and η is found on high angle boundaries. [38] The levels of Mg, Zn and Cu in AA7050 were optimized for higher stress corrosion cracking (SCC) resistance from the previous legacy alloy AA 7075. Higher levels of Zn or Cu produce detrimental phases and higher or lower Mg reduces the environmental resistance. [157] Gruhl reported that SCC resistance was highest for Zn/Mg ratio in the range of 2.7-3.0 for the bulk alloy. [169]

Maximum strengthening occurs in the peak-aged (T6) condition that consists of primarily η′ precipitates. The microstructure also consists of precipitate free zones (PFZ) that are often observed adjacent to Grain boundaries. These depleted regions are weak and are preferred sites for stress concentration leading to cracking, particularly the propagation of stress corrosion cracks. [170]

AA7050 is alloyed with 0.08-0.15 wt% Zr. Zr forms Al_3Zr dispersoids, 18-25 nm in diameter, during homogenization. [35,41,59] Dispersoids control grain size and suppress recrystallization during solution heat treatment. Zr-containing alloys are less quench-sensitive than alloys containing Mn or Cr which can be attributed to the increased coherence of the dispersoid-matrix interface resulting in an increase in SCC.[171]

Fe and Si have a strong detrimental influence on fracture toughness, attributed to the formation of coarse constituent particles including Al_7CuFe, Mg_2Si, and Al_2CuMg. These constituent particles are often located in the interior of recrystallized grains or on recrystallized grain boundaries suggesting an influence on the degree of recrystallization. [9,22-24] The presence of *S* phase Al_2CuMg is common in AA7050 due to the high Cu and Mg content. The potential to form

S phase is fixed by alloy composition and the amount formed may be minimized by optimal thermal processing such as proper homogenization, high temperature solution treatment, and slow heating rate to solution temperature.[23,27,42,44,55]

4.2.2 Effect of Cu on Fatigue and Corrosion Behavior

AA7050 contains 2.2% Cu, AA7075 contains 1.6% Cu, and AA7079 contains 0.6% Cu. In AA7050-T7451, Cu is distributed in the microstructure in different ways, (1) in the Al matrix (2) hardening precipices (η phase), and (3) course constituents such as *S* phase (Al_2CuMg).

The degree of recrystallization on fatigue resistance of 7xxx series aluminum alloys has been reported to increase with increasing Cu content from 0.01 to 2.1%, regardless of the test environment. [172] Furthermore, it was determined that the cyclic strain hardening exponent increased with increasing Cu content as does the cyclic strain resistance of the alloys. This was attributed to the increase in Cu content resulting in less shearable precipitates which increases the geometrically necessary dislocation density.[173,174]

The effect of Cu content on the microstructure corrosion has been well-documented. [27,32,44,45,55,56] A Cu-containing 7xxx series alloy will exhibit coarser, more widely spaced particles at grain boundaries compared to an Al-Zn-Mg alloy. [57] The growth rate of the η phase was shown to be higher in Cu-containing alloys. [58] Cu increases the GP zone solvus from 120°C to 160°C resulting in homogeneous precipitation at high aging temperatures (above 149°C) for a Cu content of 1.4 wt.%.[59] Increasing the Cu content in solid solution increases the pitting potential associated with the alloy matrix. Cu depletion at grain boundaries due to diffusion-controlled precipitation and growth of Cu-containing grain boundaries precipitates can lead to intergranular corrosion (IGC) susceptibility. [27] However, in the over-aged (OA) heat treatments, the susceptibility could be eliminated over time because the pitting potential of the Cu-bearing matrix would be lowered to the pitting potential of the grain boundaries due to the depletion of global Cu solute from the matrix during extensive precipitation and nucleation and growth. [13]

Due to the fact the $MgZn_2$ has a considerable amount of solubility for Cu and Al, it has been observed that the $MgZn_2$ can be enriched in Cu and Al.[32] Meng depicted the composition of η phase precipitates on grain boundaries as a function of alloy Cu content in 7000 series in the T6 temper. [44] However, there has been little work on the electrochemical behavior of this phase and the damage morphology as a result, specifically in the T74 temper.

The presence of *S* phase (Al_2CuMg) is common in AA7050 due to its increased Mg and Cu content. *S* phase is initially anodic, but after dealloying of Mg and Al occurs, the Cu remnant becomes a high-surface area cathode for oxygen reduction.[60] If the Cu particles become mechanically detached, the Cu particle will dissolve at its corrosion potential in solution and will electrochemically replate on the surface of the bulk aluminum alloy.[33,45,61,62] This phenomenon is known as Cu-replating and can greatly affect the overall corrosion properties of the alloy[32,63]

4.2.3 Effect of Heat Treatments on Corrosion Behavior

Localized corrosion of Al-Zn-Mg-Cu alloys have been extensively studied.[31-38] However, previous studies have been primarily in one or two simple salt solutions such as $MgCl_2$ and NaCl. [1,8-10,14,15,25,27,44,47,48] The anodic polarization curve for non-Cu-containing 7xxx-T6 in NaCl exhibits two break down potentials while 7xxx-T73 only exhibited one break down potential. [14] Maitra and English suggested that for AA7075-T6 the first break down potential (lower E) is due to pitting of the solute-enriched grain boundary region and the second breakdown (higher E) to the pitting of the matrix. The single breakdown potential in the T73 temper was attributed to the pitting of the Cu-depleted solid solution matrix. [14] It was shown that aging 7xxx series alloys to peak-aged T6 condition increased the susceptibility to IGC due to the anodic path created by solute enrichment of Zn and Mg near the grain boundaries. [38] Frankel studied the corrosion behavior of Cu-containing AA 7xxx-T6, and observed two breakdown potentials in a deaerated NaCl solution. [14,49] He attributed the first breakdown potential to transient dissolution due to attack of the fine hardening particles and the surrounding solid solution in a thin surface layer. The second breakdown potential was associated with both intergranular and selective grain attack. However, this behavior has not been extensively investigated specifically for Cu-containing alloys such as AA7050 in the T74 temper.

The effect of temper on localized corrosion of 7xxx series have been studied by understanding matrix solute concentrations of various 7xxx series alloys. [49-51] The pitting potential of AA7055-T6 was around -700 mV SCE which was more noble that that of the over-aged alloy which had a pitting potential of -770 mV SCE. [44] In the T73 temper, Cu and Zn have lower matrix concentrations due to a greater amount of precipitation and more Cu incorporation in the precipitates. In the Al matrix, Cu and Zn have the opposite effects on the pitting potential.[37] The decrease in pitting potential for peak-aged T6 and over-aged T73 can be attributed to the depletion of Zn content in solid solution which results in an increase in breakdown potential.[49] For 7xxx series alloys which contain Cu, it was found that the Cu to Zn ratio controls the pitting potentials in different tempers.[26] For underaged alloys, the Zn matrix content controls the pitting potential because of high Zn solute content, while the effect of Cu in solid solution is not obvious. During over-aging from the T6 peak-aged to T7 over-aged tempers, a decrease in Cu content leads to a decrease in pitting potential, even though the Zn solute content continues to decrease. This is due to a low Zn concentration during the over-aged condition. [15] As stated above, AA7050 is precipitate-hardened by $MgZn_2$, which has considerable solid solubility for Cu and Al allowing for $MgZn_2$ to be enriched with Cu or Al resulting in increased breakdown potential. In AA7050, IGC is often attributed to $MgZn_2$ on grain boundaries and/or Cu depletion from the Al matrix. [32,52]

7xxx series alloys exhibit a window of IGC susceptibility as a function of aging time, with resistance to IGC being the lowest in the initial stages of aging and in underaged conditions and with increasing resistance in the over-aged condition.[53] It has been reported that over-aging has a beneficial effect on the susceptibility to exfoliation corrosion by reducing the rate of IGC. [53] Intergranular attack of Al-Zn-Mg-Cu alloys were studied by Maitra. [14] The alloys in the T6 temper exhibited two breakdown potentials; the more noble breakdown potential was attributed to the pitting of solid solution matrix and the second break down potential was attributed to pitting of the solute-enriched grain boundary. IGC was observed between the two breakdown potentials in the

T6 temper. Electrochemical-based mechanisms for IGC are often based on preferential anodic paths along the grain boundaries established due to differences in electrochemical composition reactivity. In the case of AA7xxx, the case is complex because Cu, Zn, Mg solid solution composition all change. This active region along the grain boundaries is caused by either a solute depleted zone or anodic precipitates. [52]AA7050 has a high Cu content, therefore it is important to understand the effect of Cu on the IGC. In Al-Cu alloys, increasing the Cu content in solid solution increases the pitting and repassivaiton potentials of the matrix. [13] Cu-depletion at grain boundaries, due to diffusion controlled precipitation and growth of Cu-containing grain boundary precipitates, is responsible for IGC susceptibility because of reduced pitting and repassivation potential at a grain boundary zone compared to the interior grain matrix. [52] Galvele used this electrochemical framework to study the effect of solute content on pitting potential of Al-Cu alloys. [54] Little and Scully studied the electrochemical framework to explain the IGC behavior of Al-Cu-Mg-Ag alloy as a function of aging. They reported improvement in IGC behavior upon over-aging consistent with a decrease in the parameter $\Delta E(E_{rp}^{matrix} - E_{rp}^{Al})$ with increasing aging time. [52] This correlated with a decrease in global Cu content in solid solution towards the Cu solid solution concentration in equilibrium with grain boundary precipitates.[52]

It has been proposed that the aging temperature that produces maximum environmental assisted cracking directly depends on the alloy content. AA7050 was developed as an improvement to AA7075 because it achieved peak strength at a high temperature of 149˚C. [58] Achieving peak strength was attributed to a higher GP zone solvus in the alloy with increased Cu content. A higher environmental assisted cracking resistance was attributed to Cu diffusion to grain boundaries and subsequent incorporation into $Mg(ZnCuAl)_2$. It was determined that Cu incorporates into the η when aged above 149°C, but not when aged at lower temperatures. [27,32,55]

4.2.4 Fracture Paths in Aluminum Alloys

In 7xxx series, ductile fracture of the partially recrystallized microstructure typically involves transgranular voids of varying size intermixed with regions of grain boundary fracture.[175] This can be attributed to many reasons: (1) intergranular decohesion along high-angle grain boundaries due to dislocation pile up, typically on recrystallized grains, (2) decohesion and fracture of brittle constituent particles, and (3) transgranular fracture governed by interactions of dislocations with precipitates in the grain interior.[176-180] Typically SCC fracture path studies focus on fully recrystallized Al-Mg-Zn alloys only containing high-angle boundaries and equiaxed grains. [169,181] However, SCC fracture in partially recrystallized alloys may involve several boundary types including (1) two recrystallized grains, (2) one recrystallized-one unrecrystallized grain, (3) two unrecrystallized grains, and (4) two sub-grains. It has been reported that a low degree of misorientation, such as sub-grain boundaries, were much more resistant to cracking than boundaries with a high degree of misorientation. [182] While IGC and grain structure have been well correlated and discussed, little work has been conducted on relating the grain structure to the localized corrosion behavior. [1,4,5,87,88,93,107]

4.3 Objective

The objective of this chapter is to provide an understanding of the corrosion damage morphologies observed in previous work in Chapter 3 from the electrochemical-microstructure view point and relate this to underlying microstructure, environment, and electrochemical corrosion properties at the nanoscale. While the heterogeneous microstructure of AA7050 is desirable to optimize mechanical properties, the solute depleted zone and the second phase particles, particularly those aligned on grain boundaries, render the alloy susceptible to localized corrosion. The different zones in the microstructure coupled with various crevice environments can cause distinctively different dissolution paths. The goal of this chapter is to develop an electrochemical framework to explain preferential paths of galvanic corrosion given the different plausible environments due to the crevice arrangement. This requires that microstructure path and environment both be defined. This necessitates that model analogs to microstructural zones be tested and a framework to rationalize path be established. In previous work conducted in Chapter 3, it was observed that different damages modes prevailed in AA7050-T7451. These include pitting, fissures, and IGC. This work aims to link the micro and nano-structures in various relevant environments with an electrochemical framework for each of the three damage modes to rationalize the observed paths. In this work, the three prominent damage morphologies, pitting, fissures, and IGC will be explained based upon the electrochemical behavior of the T74 temper zones and phases in comparison to model alloys representing the various aspects of the microstructure present in the T7451 condition.

4.3.1 Hypothesis

AA7050-T7451 has been specially heat treated to suppress SCC and IGC. However, in Chapter 3, IGC was observed in acidic environments. Based on preliminary results it is hypothesized that the intergranular corrosion mechanism in AA7050-T7451 can be attributed to enrichment of Cu and/or Al into the grain boundary precipitate $MgZn_2$, forming a solute depleted region adjacent to the grain boundary.

4.4 Experimental Methods

4.4.1 Grain Structure and Particle Analysis of AA7050-T7451

Particle analysis was conducted on AA7050-T7451 using micrographs obtained with a JEOL JSM-6700F scanning electron microscope (SEM). These images had sufficient contrast to allow constituent particles to be distinguishable. The threshold was adjusted so that the particles appeared black and the background appeared white. ImageJ[147] was used to calculate the size of the particle size, Feret length, standard deviation, minimum and maximum diameter, area fraction, and nearest neighbor distance (NND). AA7050-T7451 was cross-sectioned into four specimens at the surface, eighth, quarter, and half of the plate for the LT, SL, and TS planes. Figure 4.1 shows the cross-sectioned area and the naming convention used to indicate each sample and depth. Electron backscatter diffraction (EBSD) and energy dispersive spectroscopy (EDS) was conducted on AA7050-T7451 at the surface, quarter, and half-plate thickness on the LT plane.

4.4.2 Transmission Electron Microscopy

Transmission electron microscopy (TEM) was utilized to study the grain boundary nano-chemistry of AA7050 in the T7451 temper. Dr. Helge Heinrich (UVa) conducted TEM and scanning transmission electron microscopy (STEM) using the FEI Titan equipped electron energy loss spectroscopy (EELS) and EDS with a resolution of 0.135 nm for STEM and 0.205 nm for TEM. TEM was used as a tool to relate the various zones and phases in microstructure to localized corrosion type damage in different environments and furthermore determine the compositions of these different phases.

4.4.3 Materials and Model Alloys

Six model alloys were obtained in this work including, Al-Zn-Mg-Zr (Cu-free), $MgZn_2$, $Mg(ZnCu)_2$, $Mg(ZnCuAl)_2$, Al 99.999% and AA7050 solution heat treated (SHT) at 475°C for 4 h and water quenched. The compositions of these alloys can be found in Table 4.1. The compositions were determined from TEM results and will be discussed in the results section.

The Al-Zn-Mg-Zr was cast at the Kroehling Advanced Materials Foundry, Virginia Tech Foundry Institute for Research and Education. The molten alloys were cooled in a sand mold where a thermocouple was used to determine cooling rates. Optical emission spectroscopy (OES) was used to determine final composition. The sample was analyzed using SEM and EDS under three heat treatments: (1) as-cast, (2) SHT at 475°C for 4 h water quenched, and (3) over-aged for 156 h at 120°C. Figure 4.2 shows a schematic of the heat treatments utilized in the Cu-free Al-Zn-Mg-Zr alloy. Grain structure and particle analysis of over-aged Al-Zn-Mg-Zr were compared to AA7050-T7451.

The galvanic corrosion behavior of the Cu-free Al-Zn-Mg-Zr alloy was studied via ZRA to measure the galvanic coupling current between Type 316 stainless steel and Al-Zn-Mg-Zr. The tests were conducted using a flat cell with planar electrodes where Al-Zn-Mg-Zr was the working electrode (anode) and Type 316 stainless steel was the counter electrode (cathode). The solutions investigated were 0.5 M NaCl at pH 5.5, 0.5 M $MgCl_2$ at pH 5, as well as solutions of 0.5 M NaCl + $AlCl_3$ at pH 3 and 0.5 M NaCl + $NaAlO_2$ at pH 8. The samples were tested for 504 h with 1:1 anode to cathode ratio

The $MgZn_2$, $Mg(ZnCu)_2$ and $Mg(ZnCuAl)_2$ were obtained from Kurt J. Lesker Company and were in the form of 3-6 mm pellets. $Mg(ZnCuAl)_2$ alloys were sealed under vacuum in a quartz tube and heat treated at the solid solution temperature 650°C for 4 h. The alloys were analyzed using SEM and EDS in the as-cast and SHT/Q conditions. The pure aluminum (99.999%) was obtained from McMaster-Carr.

4.4.4 Anodic Polarization to Establish Electrochemical Framework

Anodic potentiodynamic testing was conducted on AA7050-T7451 and the model alloys in deaerated solution. After 30 minutes at OCP the working electrode specimens were polarized to 1.2 V above OCP. The scan rate was 1.0 mV/s. All electrochemical tests were conducted with a computer-controlled Gamry potentiostat and the standard 3-electrode configuration consisting of a working, reference and platinum mesh counter electrode. Nitrogen was bubbled through the flat cell for 1 h prior to test and through the remainder of the test. Unless otherwise noted, just prior to testing specimens were wet-ground to 1200 grit, ultrasonically cleaned for 5 minutes in methanol or reagent-grade alcohol (95 % ethanol + 5 % methanol), rinsed with high purity water, and blown dry with compressed lab air.

AA7050-T7451 and the model alloys were tested in simulated rivet environments including 0.5 M NaCl at pH 5.5, 0.5 M $MgCl_2$ at pH 5 and simulated fastener solutions of 0.5 M NaCl + $AlCl_3$ at pH 3 and 0.5 M NaCl + $NaAlO_2$ at pH 8. In select experiments, Cu^{2+} ions were added to 0.5 M NaCl to simulate the micro-chemistry solution in the case of Al_2CuMg dealloying.

The electrochemical behavior can be determined by the potential window (ΔE) between the pitting potential of the matrix and the solute depleted zones and the $Mg(ZnCuAl)_2$ phases that are assumed to reside at the grain boundary.[§] ΔE analysis in various environments can explain which type of damage is expected. Figure 4.3 shows a hypothetical E vs log i plots for two cases. In (a), the pitting potential of η + Cu phase is much lower than that of the AA7050 Cu-depleted zone; this window or, ΔE, indicates the window where IGC can occur. In the second case (b) all

---

[§] An assumption that the galvanic couple potential has a finite probability to reside between E_{max} and E_{matrix}

the zones have similar pitting potentials resulting in minimal ΔE, indicating very minimal IGC. This type of analysis is needed for the different zones, phases, and environment to rationalize corrosion path based on an electrochemical framework.

4.4.5 Electron Backscatter Diffraction Surrounding Pits and Fissures

EBSD is a microstructural characterization technique that provides information on crystal orientation, grain size, substructure analysis, and grain boundary characterization as well as recrystallization fractions. EBSD was chosen as a useful technique to elucidate more information on corrosion propagation path and preferred grain orientation. EBSD was conducted using the Quanta 650 FEI SEM equipped with an EBSD detector. The step size used to obtain the EBSD maps was 1 µm. EBSD was conducted in cross-section around the pits and fissures that were produced. EBSD was used to determine if certain grains were corroding faster than others as well as to determine if there was a preferred granular path.

4.5 Results

4.5.1 Particle Analysis

The microstructure of the AA7050-T7451 substrate plays an important role in governing the corrosion morphology. An SEM micrograph of a typical section on the TS plane of AA7050-T7451 is shown in Figure 4.4. The bright white spots are coarse constituent particles that were verified to be β- Al_7Cu_2Fe and *S*-Al_2CuMg. Particle analysis was important to provide some understanding of the nature of the alloy used in this work. To decipher the chemical composition of these constituent particles, EDS maps were conducted at 400 times (Figure 4.5), 800 times (Figure 4.6) and 1000 times magnification (Figure 4.7). The elemental maps showed Cu, Mg and Fe rich particles which were depleted of Al. Areas with bright colored contrast indicated high elemental content in that area. The majority of these particles were found to have high amounts of Cu. Constituent particles that were found in this analysis were verified to be β- Al_7Cu_2Fe, *S*-Al_2CuMg and small amounts of Mg_2Si. The constituent particles were observed to be aligned in stringers parallel to the L-direction in the plate.

The spacing and size distribution of these particles is important, as it will determined the distribution of anodes and cathodes under a water layer formed in environmental exposures, and subsequently played a large role in determining the morphology of attack of the alloy. Spacing and size distribution of AA7050-T7451 was analyzed as a function of orientation and plate thickness. SEM micrographs on the LT plane with the corresponding threshold image can be observed in Figure 4.8. In the SEM micrographs the constituent particles can be distinguished by the bright white particles and in the threshold image constituent particles are indicated in black. The LS and TS planes can be observed in Figure 4.9 and Figure 4.10, respectively. SEM micrographs were taken from the surface, eighth, quarter and half plate thickness for each plate orientation. On the LT plane, constituent particles covered 2.7% on the surface and 5.7% at half-plate thickness. On the LT surface, with the S-direction parallel to thickness, the average particle size was 2.6 µm at the surface, 3.3 µm at eighth thickness, 3.8 µm at quarter thickness, and finally 3.4 µm at half plate thickness. At half plate thickness the average diameter of the particles were about 2 µm. On the LS plane 6.3% of the surface contained constituent particles while 3.1% contained particles in the half plate thickness. Lastly, on the TS plane, 4.1% of the surface contained constituent particles while 2.9% contained particles in the half plate thickness.

The measured number of particles per 1 mm^2 on the surface was 290 on the LT plane, 503 on the LS plane, and 424 on the TS plane. At half plate depth, the observed number of particles per 1 mm^2 was 246 on the LT plane, 350 on the LS plane and 292 on the TS plane. Furthermore, Feret diameter of the particles were analyzed in bins for the surface and half plate thickness by number of particles. Figure 4.11 showed that at the surface, most of the particles are between zero and three microns in Feret diameter and contrastingly, Figure 4.12 showed at half plate thickness, while the majority of the particles are between zero and three microns in Feret diameter, there appears to larger particles between 7 and 25 µm. For all three orientations, the number of constituent particles per 1 mm^2 had a decreasing trend until quarter thickness then switched to an increasing trend at the half plate depth. The mean particle diameter increased from the surface to the quarter plate depth, then a decrease in particle size was observed at the half plate thickness.

At the surface of the plate, the mean particle diameter was 2.6 µm on the LT plane, 2.3 µm on the LS plane, and 2.6 µm on the TS plane. At the half plate depth the mean particle diameter was 3.3 µm on the LT plane, 2.8 µm on the LS plane and 3.1 µm on the TS plane. The LT plane had the largest constituent particles followed by TS plane. The cumulative size distribution showed that the microstructure is heterogeneous, which agrees with previous findings (Figure 4.13)[9]

Furthermore the averaged nearest neighbor distance (NND) on the LT, LS, and TS planes were observed to be 17, 16, and 19 µm. However, at the surface of the plate on the LT, LS, and TS planes the NND was observed to be 9, 11, and 19 µm. The statistics for the particle analysis study can be found in Table 4.2 for the LT plane, Table 4.3 for the LS plane and lastly, Table 4.4 for the TS plane. Particle analysis summary plots can be observed in Figure 4.14.

The grain structure as a function of plate thickness can be found in Figure 4.15. On the surface of the plate, the average grain length in the L-direction was 78 µm. Grains appeared to be small but elongated. At the quarter and half plate thicknesses many grains became longer and wider surrounding smaller grains. The average grain length at the quarter and half plate thicknesses was 593 µm and 680 µm, respectively. Cu EDS maps were collected on the EBSD maps to determine Cu-containing particle distribution as a function of plate thickness. Figure 4.16 shows the EDS elemental maps for Cu at the surface, quarter, and half plate thickness. At the surface of the plate, the Cu-containing constituent particles were aligned in stringers parallel to the L-direction. Furthermore, Cu was well-distributed in the bulk matrix. At the quarter and half plate thicknesses, the Cu-containing particles increased in size and decreased in location density. Furthermore, the Cu in the bulk matrix became less distributed at the half plate thickness.

Particle analysis enabled the correlation between constituent particles versus plate thickness data and corrosion results to interpret whether changes in corrosion damage morphology were linked to depth-dependent electrochemical conditions or microstructural variation. Moreover, particle analysis ensured that the area chosen for corrosion studies statically captured the top end (95%) distribution of the largest constituent particles.

4.5.2 Transmission Electron Microscopy and AA7050-T7451 Microstructural Zones

TEM revealed lenticular Mg-Zn-Cu rich precipitates at the grain boundaries of AA7050-T7451. The particles had a typical size of 20 nm thickness and 40-80 nm width. The grain boundary precipitates can be observed in Figure 4.17. Tilt series scanning transmission electron microscopy determined that approximately 20-25% of the total grain boundary area was covered with these precipitates. The particle density at the grain boundaries was found to be approximately 8×10^{13} m^{-2}. Figure 4.18 shows (a) a grain boundary in AA7050-T7451 and (b) the associated EDS line scan. The intensity (c) is plotted vs position which gives an indication of where precipitates were located. The bright spots (precipitates) correspond to higher intensity. On this particular grain boundary, the EDS line scan showed atomic % compositions for Zn, Mg, Cu and Al. A precipitate free zone of approximately 20 nm was located at the grain boundary, and a sharp increase in Cu composition was observed. The line profile shows depletion of Al, Zn, Mg and Cu for approximately 25 nm adjacent to the grain boundary. A key result is that there appears be slightly less Cu in the region adjacent to the grain boundary followed by a sharp increase in the compositions for Cu, Zn, Mg and Al when the precipitate is reached. Two more grain boundaries on the same sample can be observed in Figure 4.19 and Figure 4.20. These grain boundaries show a depletion of Al at the grain boundary. However, an increase in composition for Cu, Mg and Zn, was observed. A line scan was conducted in-between precipices in Figure 4.21. It can be observed that along the grain boundary in between predicates compositions of Zn Mg and Cu all increased. Figure 4.22 shows a STEM micrograph with the corresponding EELS profile for Cu. The EELS shows relative composition with respect to position. A Cu-depleted zone on both sides of the precipitate can be observed here. The EELS profile was an average of composition in the box indicated in (a) and (b). Lastly, Figure 4.23 shows a comprehensive color map showing the composition of Cu, Zn, Al and Mg. A Cu-depleted zone was confirmed with these maps by examining the EDS data from points near the grain boundary which showed less than 1% of Cu in those regions and furthermore no enrichment of Al on the grain boundary precipitates.

In summary, the TEM study showed a Cu-depleted zone and Cu and Al enriched $MgZn_2$ precipitates. The depletion of Cu may explain IGC observed in previous work in Chapter 3 on

AA7050-T7451. Three zones in the microstructure were observed: (1) two types of solute depleted zones. Depletion of Cu only, and depletion of Cu, Zn and Mg, (2) the grain boundary precipitates $Mg(ZnCuAl)_2 - \eta$ in various compositions, and (3) the bulk T74 alloy composition.

Based on these results, model materials to these zones were acquired. Pure Al was used to simulate regions which are solute depleted in Mg, Zn and Cu. A model alloy of Al-Zn-Mg-Zr over-aged was used to simulate the region in the microstructure which is only depleted in Cu. The Al-Zn-Mg-Zr also gave a microscale understanding of the effect of Cu on the macro and meso-scale corrosion behavior. $Mg(ZnCuAl)_2 - \eta$ model alloys will simulate the grain boundary precipitates were enriched with Cu and/or Al. AA7050-SHT/Q, quenched and stored in a refrigerator was used to simulated regions where all the Al, Cu, Mg and Zn were in solid solution. The compositions of these alloys were selected based on these TEM and EELS results. The compositions of the model alloy analogs are listed in Table 4.1.

4.5.3 Al-Zn-Mg-Zr Cu-free Model Alloy and the Effect of Cu on Corrosion Behavior and Morphology

Microstructural assessment and anodic polarization behavior of Cu-free alloy (Al-Zn-Mg-Zr)

Al-Zn-Mg-Zr model alloys were tested under three treatments (Figure 4.2): as-cast, SHT/Q, and OA. EDS maps of the Al-Zn-Mg-Zr as-cast, SHT/Q and OA can be observed in Figure 4.24-Figure 4.26, respectively. The as-cast sample contained $MgZn_2$ second phase particles and dendritic regions which were depleted of Al, Mg, Zn, and Zr. The Al-Zn-Mg-Zr alloy in solid solution contained very few constituent particles, however, dendritic regions were depleted in Zr. After the alloy was over-aged for 156 h the sample contained some second phase particles that were enriched with Mg and had little to no depletion or segregation of Zr. Particle analysis was conducted on these alloys and the corresponding threshold micrographs can be observed in Figure 4.27. The second phase particles are indicated in black. The average particle size for the as-cast, SHT/Q, and Al-Zn-Mg-Zr OA were 22, 6, and 19 µm, respectively. Furthermore, the area fraction for the as-cast, SHT/Q, and OA heat treatments were 3.1%, 0.3% and 0.2%, respectively.

EBSD maps were conducted on the Al-Zn-Mg-Zr as-cast, SHT/Q, and OA. The grain structure of these alloys can be seen in Figure 4.28. All three alloys contained pancake-shaped grains. The OA alloy had the largest grain size. The average grain size area for as-cast, SHT/Q, and OA alloys were 63, 35 and 183 µm, respectively compared to AA7050-T7451 which had an average grain size of 0.17 µm. The results for the particle analysis on Al-Zn-Mg-Zr alloy are found in Table 4.5. Summary bar graphs (Figure 4.29) show that the Al-Zn-Mg-Zr OA had the largest grain size, which was over 150 times larger than AA7050-T7451. Furthermore, the average particle size in the OA Al-Zn-Mg-Zr alloy was approximately three times larger than AA7050-T7451. The SHT/Q alloy contained particles that were approximately four times smaller than the OA alloy. Lastly, the average aspect ratio, ratio of width to height, of the OA Al-Zn-Mg-Zr alloy was 2 compared to AA7050-T7451which had an aspect ratio of 8. The larger aspect ratio of the grains indicated the elongated shaped grains vs the rounder, shorter shaped grains.

Anodic potentiodynamic polarization was conducted on Al-Zn-Mg-Zr as-cast, SHT/Q and OA alloys in 0.6 M NaCl at pH 5.5. The OCP and polarization can be observed in Figure 4.30. The OCP was -1.02 V SCE for the as-cast alloy and -1.12 V SCE for the SHT/Q and OA alloys. Anodic polarization indicted two breakdown potentials for the Al-Zn-Mg-Zr SHT/Q and OA samples. The OCP of OA Al-Zn-Mg-Zr alloy was 40 mV lower than the OCP of AA7050-T7451.

Assessment of the damage morphology of Cu-free (Al-Zn-Mg-Zr) relative to AA7050-T7451

To understand the effects of Cu on the damage morphology, Al-Zn-Mg-Zr OA was coupled to Type 316 stainless steel in various simulated rivet solutions for 504 h and measured via ZRA. The ZRA measured galvanic couple potential and current over 504 h can be seen in Figure 4.31. The galvanic couple potential was lowered by 130 mV in Al-Zn-Mg-Zr OA as compared to AA7050-T7451. The galvanic couple potential of the Cu-free model alloy in 0.5 M NaCl, 0.5 M NaCl + $AlCl_3$ at pH 3, 0.5 M NaCl + $NaAlO_2$ at pH 8 and 0.5 M $MgCl_2$ were -0.92, -0.97, -0.90, and -0.93 V SCE, respectively. Furthermore, the current densities of Al-Zn-Mg-Zr were found to be higher in all four rivet solutions. The highest current densities occurred in 0.5 M NaCl + $AlCl_3$ pH 3 followed by 0.5 M $MgCl_2$ pH 5, 0.5 M NaCl + $NaAlO_2$ pH 8, and 0.5 M NaCl pH 5.5. The surface damage morphologies can be observed in Figure 4.32. The Cu-free Al-Zn-Mg-Zr alloy produced hemispherical pits while the Cu-containing AA7050-T7451 alloy, produced wider pits that often coalesced and formed larger pits. Furthermore, Al-Zn-Mg-Zr alloys were observed to have a lower pit density than AA7050-T7451. The cross-sectional optical micrographs can be observed in Figure 4.33. Average damage length for 0.5 M NaCl + $AlCl_3$ at pH 3, 0.5 M $MgCl_2$ at pH 5, 0.5 M NaCl + $NaAlO_2$ at pH 8 and 0.5 M NaCl at pH 5.5 were 439, 21, 185, and 175 µm, respectively.

4.5.4 Assessment of Model Alloys to Simulate Grain Boundary Precipitates $Mg(ZnCuAl)_2$

Microstructural Analysis of $Mg(ZnCuAl)_2$

The microstructure of $Mg(ZnCuAl)_2$ and $Mg(ZnCu)_2$ grain boundary model alloys were verified using EDS to ensure uniform compositions. Figure 4.34 and Figure 4.35 show the EDS elemental composition maps for $Mg(ZnCu)_2$ and $Mg(ZnCuAl)_2$, respectively. The microstructure of $Mg(ZnCu)_2$ and $Mg(ZnCuAl)_2$ both contained segregation in dendritic regions. Moreover, $Mg(ZnCuAl)_2$ contained much more segregation than $Mg(ZnCu)_2$. The microstructure of $Mg(ZnCuAl)_2$ also contained many pores and cracks. $Mg(ZnCu)_2$ and $Mg(ZnCuAl)_2$ alloys were heat treated at the solid solution temperature and water quenched. Figure 4.36 and Figure 4.37 show the EDS elemental composition maps for SHT/Q $Mg(ZnCu)_2$ and $Mg(ZnCuAl)_2$. EDS maps show uniform composition for both SHT/Q $Mg(ZnCu)_2$ and $Mg(ZnCuAl)_2$ with the exception of minor Al segregation in the $Mg(ZnCuAl)_2$ alloy. These alloys were used to simulate the grain boundary matrix.

Measured OCP and cyclic anodic potentiodynamic polarization of $MgZn_2$, $Mg(ZnCu)_2$, and $Mg(ZnCuAl)_2$ in 0.6 M NaCl at pH 5.5 are shown in Figure 4.38. The measured OCP of $MgZn_2$, $Mg(ZnCu)_2$ and $Mg(ZnCuAl)_2$ were -1.09, -0.87 and -0.99 V SCE, respectively. The addition of Cu into $MgZn_2$ ennobled the OCP. Furthermore, the pitting potential of $MgZn_2$, $Mg(ZnCu)_2$ and $Mg(ZnCuAl)_2$ were -1.05, 0.85, and -0.95 V SCE, respectively. Therefore, the addition of Cu into $MgZn_2$ increased the OCP and pitting potential by about 20% and the addition of Cu and Al into $MgZn_2$ increased the OCP and pitting potential by 10%.

4.5.5 Electrochemical Framework of AA7050-T7451 and Constituent Phases

Anodic potentiodynamic polarization of AA7050-T7451 and constituent phases including pure Al, AA7050 SHT/Q, $MgZn_2$, $Mg(ZnCuAl)_2$, and the Cu-free Al-Zn-Mg-Zr OA alloy in simulated rivet environments of: (a) 0.5 M NaCl at pH 5 (b) 0.5 M $MgCl_2$ at pH 5, (c) 0.5 M NaCl + 0.5 M $AlCl_3$ at pH 3, and (d) 0.5 M NaCl+ $NaAlO_2$ at pH 8 are shown in Figure 4.39. ΔE, the window for corrosion susceptibly is defined as the difference in pitting potential of the η-$MgZn_2$ phase and the bulk AA7050-T7451 matrix. The operating premise is that a large ΔE between the grain boundaries and the AA7050-T7451 matrix produces conditions that may lead to IGC. Of course, this functions under the assumption that E_{gal} of the grain boundary phase is somewhere between $E_{matrix} + E_{MgZn2.}$

The window of susceptibly, ΔE, was 0.28, 0.34 0.38 and 0.14 V SCE in 0.5 M NaCl, 0.5 M $MgCl_2$, 0.5 M NaCl + 0.5 M $AlCl_3$ at pH 3, and 0.5 M NaCl+ $NaAlO_2$ pH 8, respectively. Therefore, ΔE was largest in 0.5 M NaCl + $AlCl_3$ pH and the smallest in 0.5 M NaCl + $NaAlO_2$ pH 8. However, these results did not explain why IGC was not observed in neutral NaCl and $MgCl_2$. The results found in this study may infer that the IGC likely occurs as a result of the micro-chemistry local to a corrosion site. These results will be explained in the discussion of the chapter with analysis in environments that simulate the micro-chemistry of Cu^{2+} ions in solution.

4.5.6 Electron Backscatter Diffraction to Elucidate Corrosion Propagation Pathway

EBSD was conducted on many AA7050-T7451 coupons exhibiting different damage modes to establish the fissure path and its relationship to the grain structure. An EBSD map around a pit formed on the surface of AA7050-T7451 is shown in Figure 4.40. In this exposure, AA7050-T7451 LT was polarized at the galvanic couple potential (-0.73 V SCE) for 24 h in 0.5 M NaCl + $NaAlO_2$ at pH 8. The EBSD map revealed that the corrosion pits were elongated in the L-direction.

Figure 4.41 shows an EBSD map in cross-section around two fissures on AA7050-T7451 TS plane and the corresponding backscatter electron micrograph at low magnification. This coupon was exposed for 100 h in 0.5 N NaCl + $NaAlO_2$ pH 8 at the anodic potential -0.73 V SCE. The EBSD map revealed elongated grains in the L-direction with many sub-grain boundaries surrounding the corrosion fissures. The grains appeared to be less than 20 µm in width and typically 300-900 µm in length. While this EBSD map provides a low magnification overview of the grain structure, little information on recrystallization can be obtained. Figure 4.42 shows and EBSD map in cross-section around two fissures on a separate sample exposed in the same environments at a higher magnification. The EBSD also shows elongated grains in the L direction containing both sub- grain boundaries and recrystallized grains. Recrystallized grains have been marked with an R on the EBSD maps. Moreover, the grains at higher magnification reveal color gradients within grains, indicating deformed unrecrystallized grains surrounding one side of the fissure.

EBSD was conducted on AA7050-T7451 in cross-section after potentiostatic polarization (-0.73 V SCE) in 0.5 M NaCl + $AlCl_3$ at pH 3. This environment produced IGC (Figure 4.43). The IGC corrosion propagated along the grain boundaries and in certain cases resulted in grain fallout. Unrecrystallized grains can be characterized as the grains that contain a color gradient. The recrystallized grain have been marked with an R in the EBSD maps. It can be observed here that corrosion was favored in unrecrystallized grains as the recrystallized grains often were not corroded around the IGC regions.

Figure 4.44 shows an EBSD map in cross section around a deep fissure that was formed after galvanostatic testing at 0.047 mA/cm^2 for 100 h in 0.5 M NaCl + $AlCl_3$ pH 4, with the SL plane exposed. The EBSD map revealed that the grains near the two fissures were unrecrystallized grains that contained many sub-grains surrounded by low-angle grain boundaries. Undamaged deformation-free recrystallized grains were observed near the surface of the sample.

Figure 4.45 shows an EBSD map at higher magnification around a fissure after potentiostatic testing at the anodic potential E=-0.73 V SCE for 72 h in 0.5 M NaCl pH 5, with the

SL plane exposed. The right side of the pit revealed large high angle grain boundaries while the left side of the pit showed large deformed grains with many sub-grain boundaries.

Figure 4.46 shows a cross section around a pit that was exposed to the LT plane but cross-sectioned perpendicular to the T direction, showing pancake shaped grains. The sample was coupled to Type 316 stainless steel for 504 h in 0.5 M NaCl pH 5.5 via ZRA (1:1). One part of the pit (left side) revealed larger recrystallized sub-grain free grains while the other side contains deformed low-angle sub-grain boundaries.

Figure 4.47 shows an EBSD map around a corrosion pit in cross-section formed on AA7050-T7451 TS coupled with Type 316 stainless steel after 144 h in 0.5 M NaCl pH 5 via ZRA. The EBSD map revealed elongated deformed unrecrystallized grains surrounding the corrosion fissure and recrystallized deformation free grains near the undamaged surface. The EBSD map revealed that the large recrystallized grains were in the (001) orientation on the face of the cross-section.

Lastly, Figure 4.48 shows an EBSD map around a fissure in cross-section that formed in AA7050-T7451 TS plane after 100 h of potentiostatic polarization at the galvanic couple potential (-0.730 V SCE) in 0.5 M NaCl + $NaAlO_2$ at pH 8. The elongated fissure was completely surrounded by large grains that contained many sub-grains with the exception of a recrystallized grain near the mouth of the fissure. Furthermore, the fissures appeared to follow the shape of the grain, indicating whole grain fallout. The map revealed grains that were unrecrystallized containing sub- grain boundaries, prominently surrounding the damaged regions of the sample.

In summary, the EBSD maps conducted in cross-section revealed some whole grain fallout. Furthermore it can be speculated that unrecrystallized grans contained more corrosion damage. This can be speculatively explained as grains that have not been recrystallized collect more Cu in precipitates upon over-aging leading to preferential attack on the unrecrystallized grains.

4.6 Discussion

4.6.1 Al-Zn-Mg-Zr, Cu-free Model Alloy, Corrosion Behavior as Compared to AA7050-T7451

The effect of alloyed Cu on the microstructure and furthermore, the corrosion behavior was studied in this work. The OA Al-Zn-Mg-Zr alloy was shown to reduce the number of constituent particles as compared to AA7050-T74 (Figure 4.27). Anodic potentiodynamic polarization of Al-Zn-Mg-Zr possessed lower OCP and pitting potentials relative to AA7050-T7451 (Figure 4.30). This was expected, as Cu is more noble than Al, Zn and Mg. The anodic polarization indicated multiple breakdown potentials likely attributed to Zn-rich bands observed in the microstructure (Figure 4.24). The pitting potential of AA7050-T7451 and Al-Zn-Mg-Zr as a function of chloride concentration can be observed in Figure 4.49. This potential difference between AA7050-T77451 and Al-Zn-Mg-Zr OA creates a potential window between the matrix and solute depleted zone for corrosion to occur in AA7050-T7451. The effect of Cu on the damage morphology of Al alloys coupled to Type 316 stainless steel was studied via ZRA in simulated rivet environments. The galvanic corrosion rate was shown to be higher in Al-Zn-Mg-Zr than AA7050-T7451 (Figure 4.31). However, interestingly the damage morphology was shown to be less severe (Figure 4.32). AA7050-T7451 contains Cu-rich constituent particles which are cathodic to the matrix which can result in pitting initiation sites due to the electrochemical activity of the secondary phase compared to the bulk matrix. Furthermore, when AA7050-T7451 is coupled to Type 316 stainless steel there is a larger driving force for Cu to replate on the surface, leaving a high surface area of Cu supporting high cathodic reaction rates and therefore, more damage to the Al alloy. While Cu increases the pitting potential of AA7050-T7451 when in solid solution, Cu is detrimental to the overall corrosion behavior of AA7050-T7451 which can be attributed to the secondary phase Al_2CuMg.

4.6.2 Predicting Damage Electrochemical Framework of AA7050-T451 in Simulated Rivet Environments

4.6.2.1 Case study: Grain Boundary Precipitation Control Electrochemical Framework

Diffusion controlled precipitation is the cause for the local and global solute depletion that takes place in these heat-treatable alloys. In a solution heat-treated and quenched alloy with little to no precipitation there is little difference in the solute level between the matrix and the boundaries and globally Cu is depleted from the matrix. However, the difference in solute levels increases after aging and diffusion controlled precipitation and growth since Cu is accumulated by the precipitates at the grain boundaries. Therefore, due to mass balance, the Cu must be depleted from the matrix. TEM showed that $MgZn_2$ phase often becomes enriched with Cu and or Al as shown in Figure 4.19. Figure 4.50 shows the electrochemical framework for the case of $MgZn_2$ enriched with Cu and/or Al. The difference in pitting potential between the matrix and $MgZn_2$ was 0.38 V SCE. If only Cu was incorporated then it was $\Delta E=0.32$ V. When Cu and Al are both incorporated into $MgZn_2$ the window of susceptibility decreased to 0.29 V. However, this led to a region that was depleted in Cu near the grain boundary. Figure 4.51 shows the electrochemical framework for this case. The difference in pitting potential between the matrix in SHT/Q and the Cu depleted region Al-Zn-Mg-Zr, analog was 0.26 V. In contrast, Figure 4.52 shows that the potential window of susceptibility for IGC was reduced between $Mg(ZnCuAl)_2$ and the Cu-depleted zone. Therefore, IGC is more likely to occur in a condition where IGC occurs at the gain boundary at the Cu-depleted region near the grain boundary. The corrosion damage susceptibility can therefore be determined under the premise $E_{pit}^{GB} < E_{applied} < E_{pit}^{matrix}$.

Another factor besides pH is the Cl^- concentration in a crevice. Figure 4.53 shows a plot of the pitting potential as a function of the chloride concentration for the matrix and the possible grain boundary precipitates or regions. This potential differences between the matrix and the possible grain boundary regions show window of susceptibility as a function of chloride concentration. ΔE between various zones is preserved over all Cl^- concentrations tested.

In summary, Figure 4.54 show anodic and cathodic potentiodynamic polarization on the different phases in 0.5 M NaCl + $NaAlO_2$ at pH 8. Coarse precipitates, such as Al_7Cu_2Fe, Al_2CuMg and the fine grain boundary precipitates $MgZn_2$ are all anodic and actively dissolve in aqueous environments relative to the AA7050-T7451 matrix. Theses precipitates could also be the reason for preferential corrosion of the grain boundaries, rom dissolution of the anodic particles or localized corrosion adjacent to cathodic dealloyed *S*phase particle. This work presents a mechanisms for IGC in environments when Cu^{2+} ions are not readily in solution. The solute depleted regions adjacent to the grain boundary due to enrichment of grain boundary precipitates is attributed to IGC. However, this does not account for intragranular corrosion seen. Intragranular corrosion can be attributed to the coarse constituent phases such as Al_7Cu_2Fe, Al_2CuMg.

4.6.2.2 Electrochemical Framework in Rivet Solutions

Figure 4.39 showed the electrochemical behavior of AA7050-T7451 and the analog model alloys representing different zones and phases in the alloy. In rivet environments, ΔE between AA7050-T7451 and $MgZn_2$ was the largest in the 0.5 M NaCl + 0.5 M $AlCl_3$ at pH 3 and the smallest in 0.5 M NaCl + $NaAlO_2$ at pH 8 (Figure 4.39). In previous work shown in Chapter 3, it was observed that in 0.5 M NaCl + 0.5 M $AlCl_3$ at pH 3 the damage morphology was focused IGC. In 0.5 M NaCl + $NaAlO_2$ at pH 8, the damage morphology was categorized as deep intragranular fissures which was more severe than in environments of 0.5 M NaCl or 0.5 M $MgCl_2$. The IGC that prevailed in acidic environments may not be completely explained by the difference in pitting potentials of grain boundary precipitates and the AA7050-T7451 matrix as done in classic IGC framework. Interestingly, ΔE between the matrix and $MgZn_2$ decreases with the incorporation of Cu and/or Al into the $MgZn_{2.}$ Cu incorporated into $MgZn(Cu)_2$ decreased ΔE. Furthermore, incorporation of Cu and Al into $Mg(ZnCuAl)_2$ decreased ΔE to 0.250 V. However, previous work in Chapter 3 showed that Cu-replating on the surface occurs more readily in 0.5 M NaCl + $NaAlO_2$ at pH 8 than in 0.5 M NaCl at pH 5. In 0.5 M NaCl + $NaAlO_2$ at pH 8, $MgZn_2$ exhibits a higher pitting potential, closing the window of corrosion susceptibility (Figure 4.39). This passive window was not observed in $Mg(ZnCuAl)_{2.}$

The electrochemical framework considered here did not explain why IGC corrosion is often observed in $AlCl_3$ environments only. However, a key result from Chapters 2 and 3 showed that Cu relating is more likely to occur in alkaline and neutral environments. Hence, more Cu^{2+} can be found in the micro-chemistry of pits in situations where Al_2CuMg is dealloyed. Figure 4.55 shows the electrochemical framework in an environment where the Cu^{2+} ions are in solution. In this case, the pitting potential of the solute depleted zones (Al-Zn-Mg-Zr and pure Al) were raised within 5 mV below the matrix. This closes the window of IGC susceptibility and suggests that in neutral or alkaline environments corrosion damage can be attributed to pitting of course constituent particles. The IGC corrosion observed in $AlCl_3$ environments can be attributed to difference in pitting potential between AA7050-T7451 the Cu-depleted zone and other solute depleted zones. Figure 4.56 shows the pitting potential of AA7050-T7451as a function of the chloride concentration for the matrix and the solute depleted zone analog (Al-Zn-Mg-Zr). The potential differences between the matrix and the possible grain boundary regions show window of IGC susceptibility as a function of chloride concentration. It is seen that ΔE between is preserved over all Cl^- concentrations tested. This IGC framework may also be supported by the literature. Frenkel et all found that dissolution kinetics of the pure Al was ennobled in the presence of Cu^{2+} ions by nearly 200 mV. [27]

4.6.3 AA7050-T7451 Corrosion Propagation and Pathway

It is known that in face centered cubic Al, the degree of plastic deformation in individual grains is highly dependent on the grain orientation when the metal is subjected to low strain during alloy fabrication. [183] This implies that plastic deformation occurs in certain grains leading to the formation of dense dislocation bands in the deformed grains. The EBSD maps in this work showed trends that revealed there may be a correlation between unrecrystallized sub-grain boundaries and corrosion damage sites (Figures 39- 46). Typically localized corrosion occurs on particular grains in heat-treatable aluminum alloys which are artificially aged to obtain designed mechanical properties. Prior to aging, the extruded ingot is solution heat-treated to obtain a super-saturated solution. Additionally, in order to restrict excessive precipitation of η or *S* at the grain boundaries the T7451 temper is stress relieved by stretching to increase dislocations within a grain interior promoting the precipitation of the secondary phase within grain interiors during subsequent aging. [5] At low or medium strains, all the grains experience different degrees of plastic deformation. Grains with a large Schmid factor experiences more plastic deformation than grains with a lower Schmid factor. [184] This results in a higher dislocation density in selected grains. Furthermore, higher dislocation density results in an increase in the number of η and *S* phase. It was shown that the corrosion potentials of $MgZn_2$ and Al_2CuMg are -1.22 V SCE and -1.02 V SCE in 0.5 M NaCl + $NaAlO_2$ pH 8, respectively. The corrosion potential of the matrix is higher than that of these phases. Due to Cu-depletion in these phases we speculate that the grains containing a higher volume fraction of *S* and η become more susceptible to corrosion than other grains due to Cu-depletion. Recall that Cu-depletion from the matrix lowers corrosion resistance. Once the corrosion propagates, the network of corrosion paths can restrict dilution of the fissure with the bulk solution to the corrosion sites leading to a buildup of Cl^- and H^+ resulting in continuous corrosion propagation. In the EBSD maps shown in Figure 4.41-4.42, sub-grain boundaries within deformed unrecrystallized grains may be preferentially attacked. It also may be speculated that the local plastic deformation near sub-grain boundaries plays a more decisive role in corrosion propagation along the boundaries compared to the presence of secondary phase precipitates at the boundaries. In summary, EBSD showed that unrecrystallized grain containing low-angle boundaries may be more susceptible to corrosion damage. This may be attributed unrecrystallized grains that collected greater Cu in the precipitates upon the over-aging heat treatment (T7451). This may also be a function of the plate thickness shown in Figure 4.16.

4.7 Conclusions

- AA7050-T7451 grain structure varied with plate thickness. On the surface of the plate, the average grain length in the L direction was 78 µm. Grains appeared to be small but elongated. At the quarter and half plate thicknesses, many grains became longer and wider surrounding smaller grains. The average grain length at the quarter and half plate thicknesses was found to be 593 µm and 680 µm, respectively.

- At the surface of the plate the Cu-containing constituent particle were aligned in stringers parallel to the L direction. Cu was well-distributed in the bulk matrix. At the quarter and half plate thicknesses the Cu-containing particles increased in size and decreased in location density.
- Particle analysis showed that the constituent particles can be described as random through thickness of the plate. Particle analysis enabled the correlation between constituent particles versus plate thickness data and corrosion results to interpret whether changes in corrosion damage morphology are linked to depth-dependent electrochemical conditions or microstructure variation.
- TEM study showed a Cu depleted zones, Zn-Mg-Cu depleted zones, and Cu and Al enriched in $MgZn_2$. Three zones in the microstructure were observed (1) the solute depleted zones (2) the grain boundary precipitates $Mg(ZnCuAl)_2 - \eta$ in various compositions, and (3) the bulk T74 alloy composition.
- The addition of Cu into $MgZn_2$ increased the OCP and pitting potential of this phase by about 20% and the addition of Cu and Al into $MgZn_2$ increased the OCP and pitting potential by 10%.
- Electrochemical framework showed that IGC is more likely to occur in a condition where Cu^{2+} is found in the micro-chemistry of a fissure. IGC occurs in the Cu and solute depleted regions near the grain boundary. The corrosion damage susceptibility can therefore be determined under the premise $E_{pit}^{GB} < E_{applied} < E_{pit}^{matrix}$.
- An IGC framework was proposed as Cu^{2+} in solution was found to raise the pitting potential of the solute depleted grain boundary region closing the window for IGC to occur. This suggests that pitting can be attributed to the course secondary phases in AA7050-T7451
- EBSD showed that unrecrystallized grains containing low-angle boundaries may be more susceptible to intragranular corrosion damage. This may be attributed to unrecrystallized grains

collecting Cu in the precipitates upon the over-aging heat treatment of the AA7050 (T7451) with associated Cu depletion.

4.8 Tables

Table 4.1. Composition of model alloys and constituent components in weight %

Model Alloy	**Composition**
AA 7050-T7451	Al (87.5%), Zn (6.7%), Mg (2.6%), Cu (2.6), Zr (0.2%)
Al-Zn-Mg-Zr (Cu-free 7000)	Al (93.1%), Zn (5.5%), Mg (1.2%), Zr (0.2%)
η-$MgZn_2$	Mg (33.3%), Zn (66.7%)
$MgZn_2Cu$	Mg (11.1%), Zn (59.8%), Cu (29.1%)
$MgZn_2CuAl$	Mg (9.9%), Zn (53.2%), Cu (25.9%), Al (11%)
Pure Al	Al (99.999%)
AA 7050 solid solution (SHT) (475˚C 4 h)	Al (87.5%), Zn (6.7%), Mg (2.6%), Cu (2.6), Zr (0.2%)

Table 4.2. Summary of particle analysis conducted on AA7050-T7451 on the LT plane. Where NND is nearest neighbor distance.

AA7050 LT Plane						
Specimen	**Mean Particle Area (μm^2)**	**Mean Feret Length (µm)**	**Min Diameter (µm)**	**Max Diameter (µm)**	**Area Fraction (%)**	**Mean NND (µm)**
Surface	3.35	2.39	0.22	49.0	2.7	9.32
Eighth	10.5	4.17	0.12	86.5	5.2	17.9
Quarter	11.7	4.05	0.21	147.0	3.6	25.3
Half	13.5	4.63	0.32	191.0	5.2	17.6

Table 4.3. Summary of particle analysis conducted on AA7050-T7451 on the LS plane. Where NND is nearest neighbor distance.

AA7050 LS Plane						
Specimen	**Mean Particle Area (µm^2)**	**Mean Feret Length (µm)**	**Min Diameter (µm)**	**Max Diameter (µm)**	**Area Fraction (%)**	**Mean NND (µm)**
Surface	2.48	3.65	0.22	129.0	6.3	11.2
Eighth	4.95	3.13	0.21	60.5	3.4	13.5
Half	5.86	2.26	0.11	128.0	3.1	19.1
Quarter	12.0	4.13	0.21	123.0	3.5	22.2

Table 4.4. Summary of particle analysis conducted on AA7050-T7451 on the TS plane. Where NND is nearest neighbor distance.

AA7050 TS Plane						
Specimen	**Mean Particle Area (µm^2)**	**Mean Feret Length (µm)**	**Min Diameter (µm)**	**Max Diameter (µm)**	**Area Fraction (%)**	**Mean NND (µm)**
Surface	10.6	4.46	0.22	64.1	4.1	18.7
Eighth	3.69	2.54	0.22	40.73	2.8	13.5
Quarter	7.26	3.68	0.33	49.1	3.1	13.2
Half	10.9	4.53	0.21	63.79	2.9	29.2

Table 4.5. Summary of particle analysis conducted Al-Zn-Mg-Zr Cu-free model alloy compared with AA7050-T7451

Alloy	**Average Particle Size (µm)**	**Area Fraction (%)**	**Average Particle Perimeter (µm)**	**Number of Particles**	**Average Grain Area (mm)**
As-cast	22.0	3.24	14.7	277	63.8
SHT 475 °C	6.25	0.34	7.94	72	35.7
OA 120°C	19.8	0.25	15.3	190	183
AA7050-T7451	4.86	2.64	8.72	586	1.7 x 10^{-4}

4.9 Figures

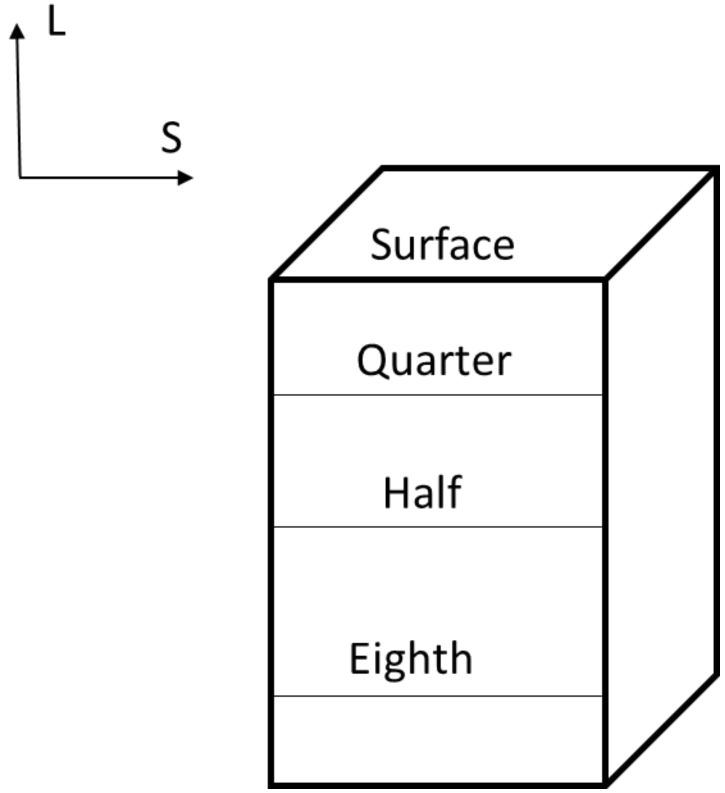

Figure 4.1. (a) Schematic of the AA7050-T7451 plate and corresponding specimen cross-sections and name designations for particle analysis studies.

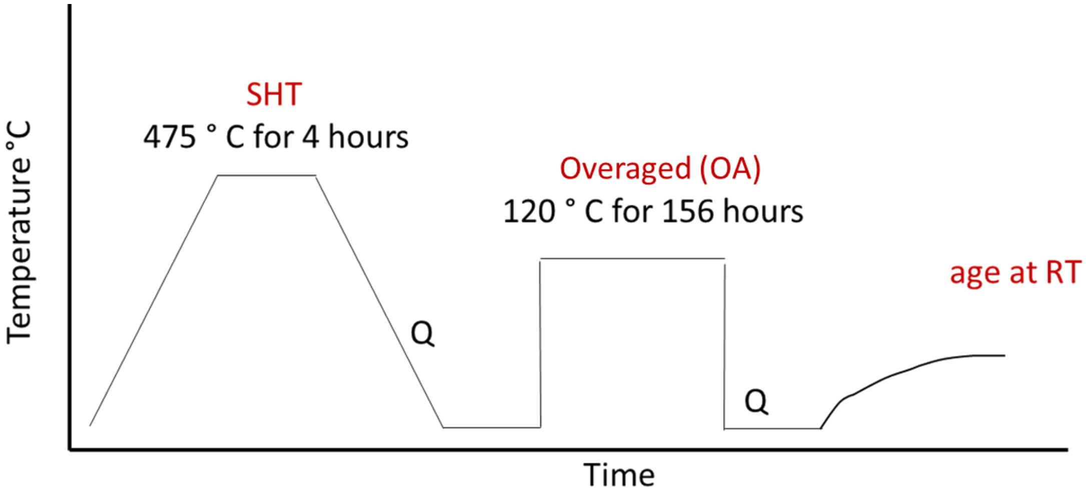

Figure 4.2. Heat-treatment schematic for Al-Zn-Mg-Zr Cu-free model alloy showing the solution heat treatment and the over-aged treatment used in this study.

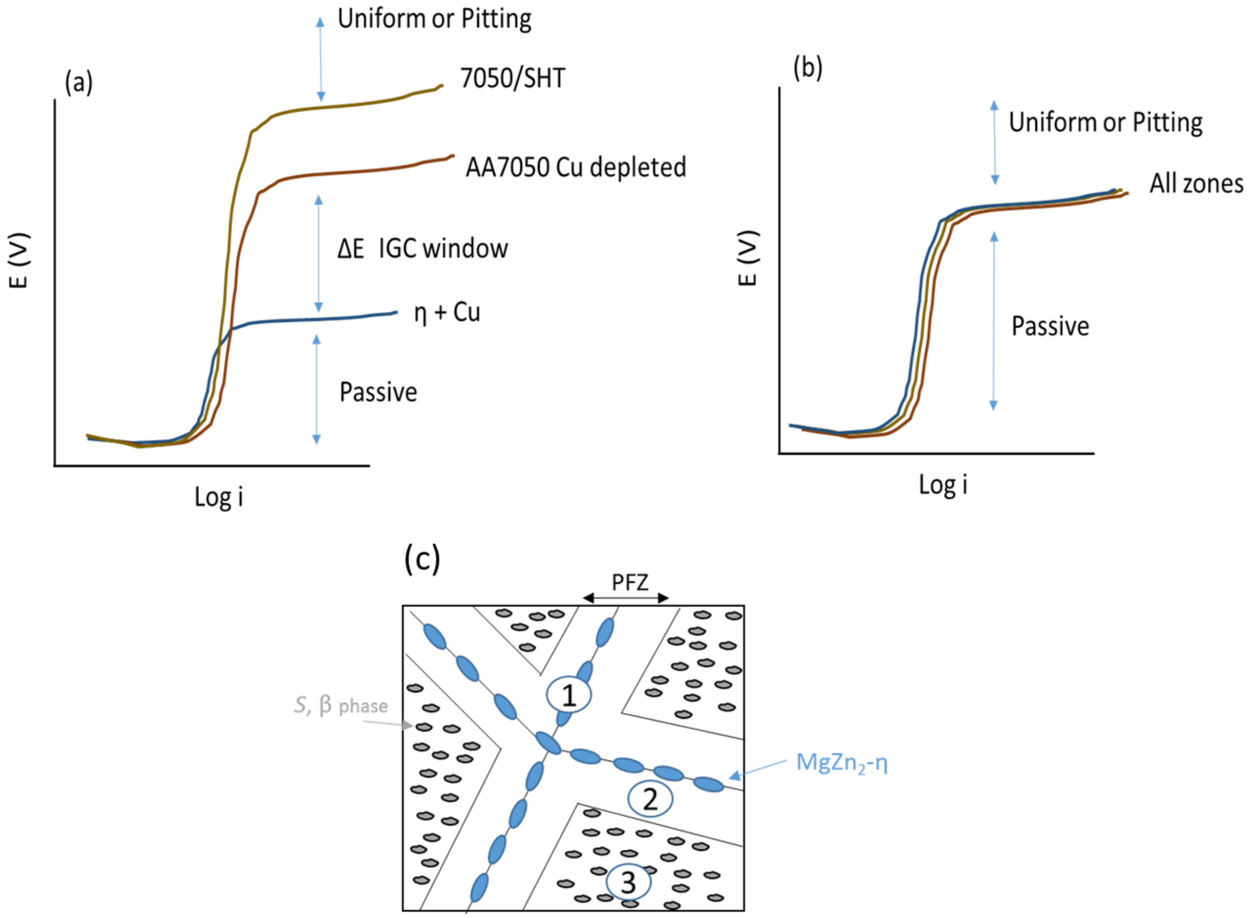

Figure 4.3. Hypothetical E vs log i showing (a) large ΔE window suggesting IGC will prevail from a perspective of a potential window of susceptibility and (b) no Δ E window indicating that uniform or pitting corrosion will prevail. (c) Schematic of a grain boundary region in AA7050-T7451 showing zone 1 at the grain boundary precipitate, zone 2 the area adjacent to the grain boundary and zone 3 which is the bulk matrix.

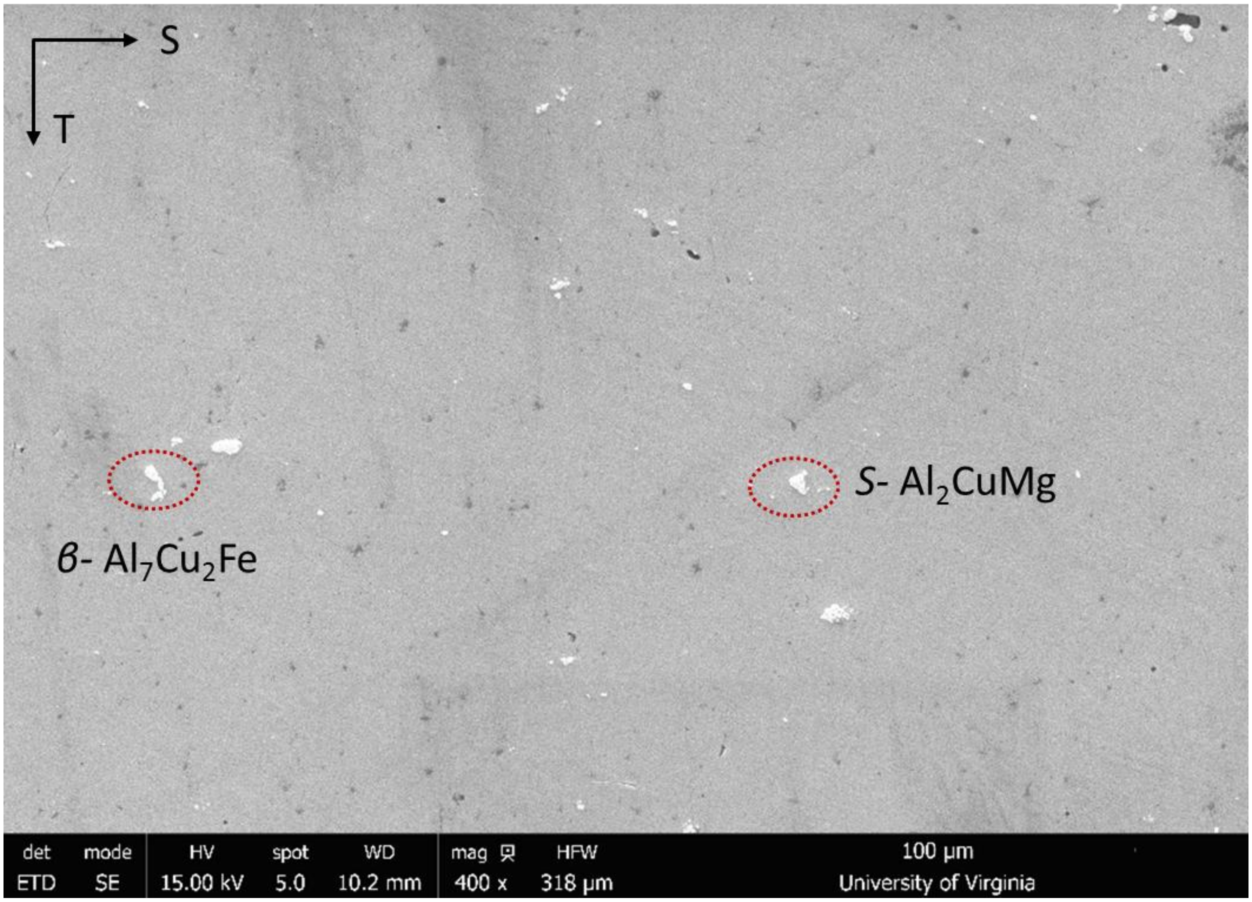

Figure 4.4. Scanning electron micrograph of a typical section of AA7050-T7451 in the TS plane showing the course constituent particles β (Al_7Cu_2Fe) and *S* (Al_2CuMg) are indicated by the bright white particles in the matrix.

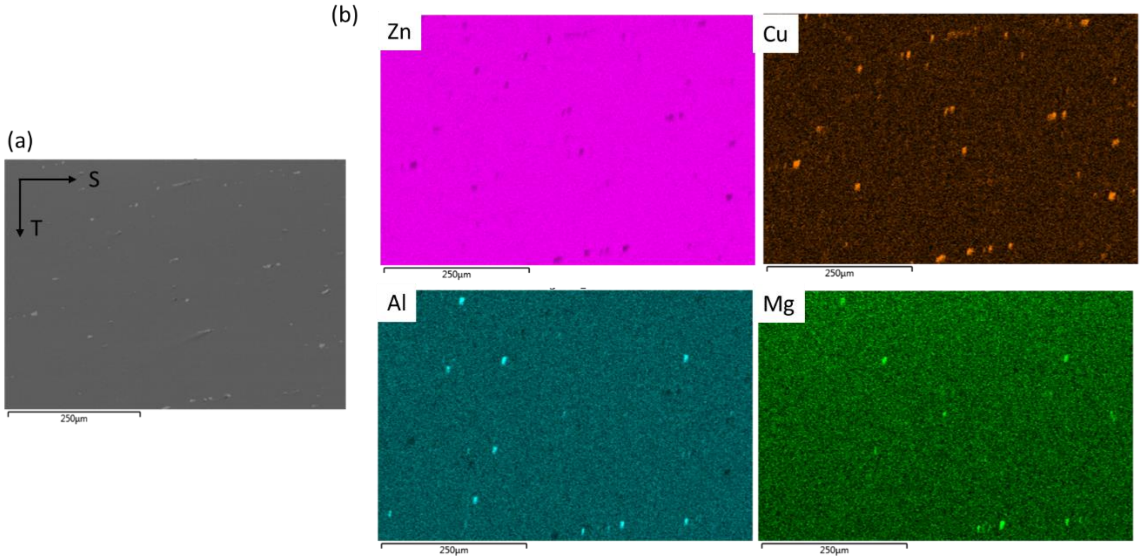

Figure 4.5. (a) Secondary electron micrograph of AA7050-T7451 plate on the TS surface (b) EDS elemental composition maps of the entire field of the AA7050-T7451 matrix of the of Zn, Cu, Al and Mg at 400 times magnification.

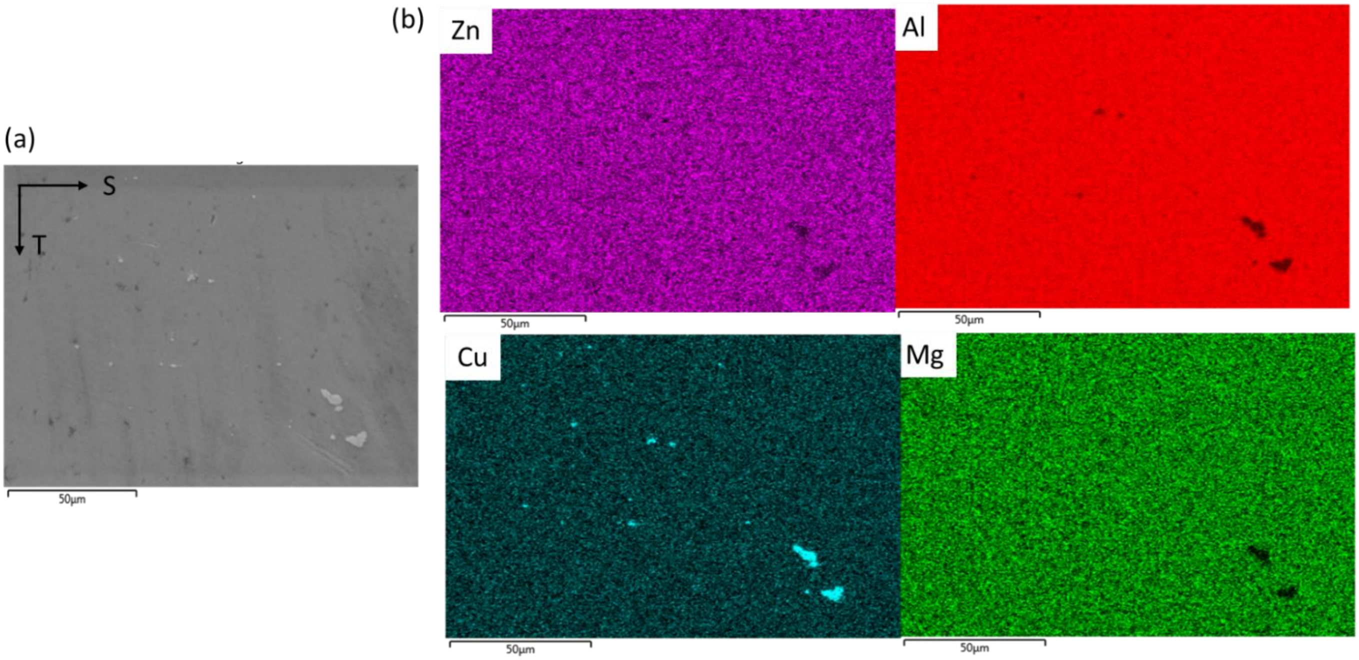

Figure 4.6. (a) Secondary electron micrograph of AA7050-T7451 plate on the TS surface (b) EDS elemental composition maps of the entire field of the AA7050-T7451 matrix of the of Zn, Cu, Al and Mg at 800 times magnification.

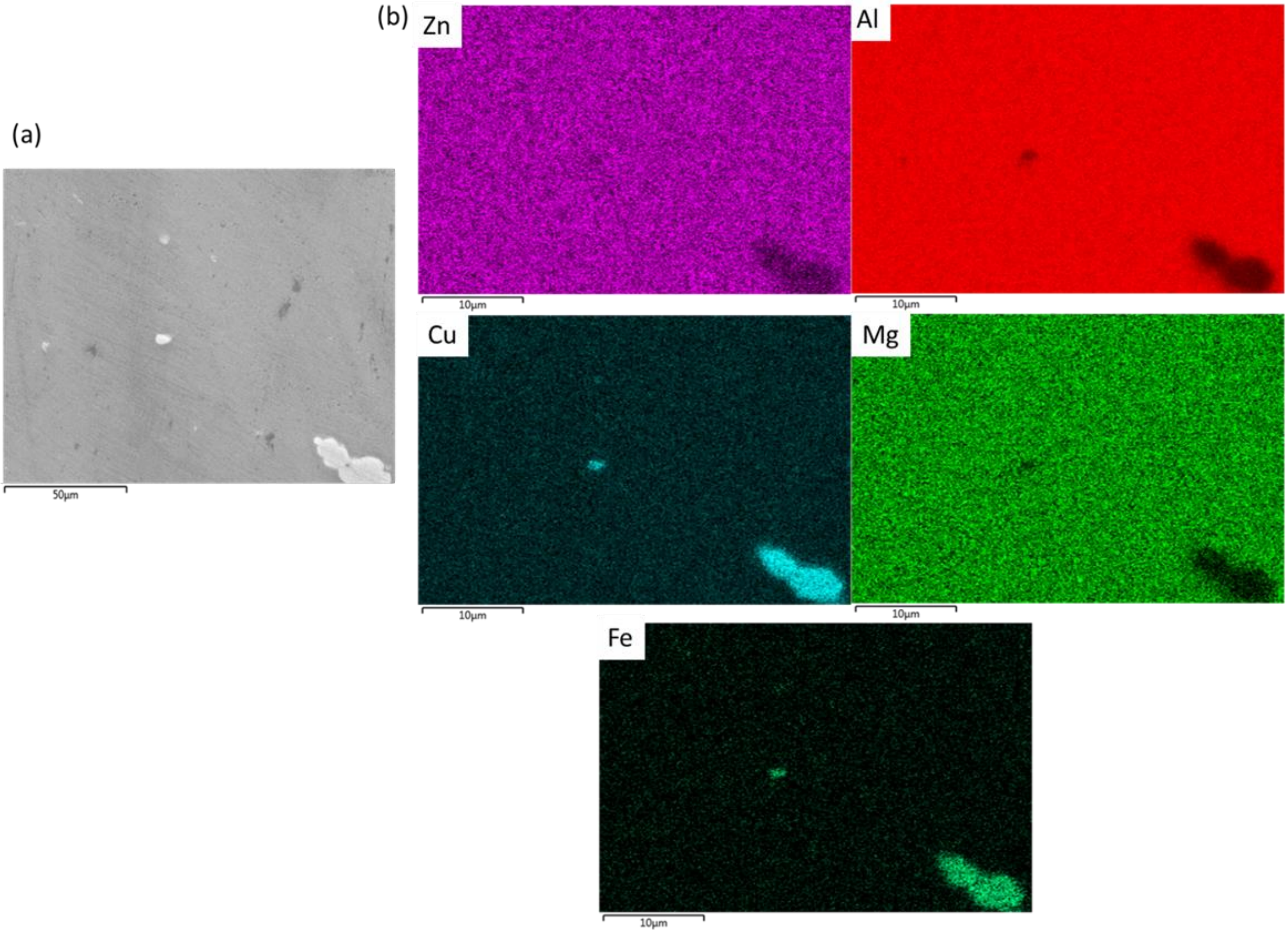

Figure 4.7. (a) Secondary electron micrograph of AA7050-T7451 plate on the TS surface (b) EDS elemental composition maps of the entire field of the AA7050-T7451 matrix of the of Zn, Cu, Al and Mg at 1000 times magnification.

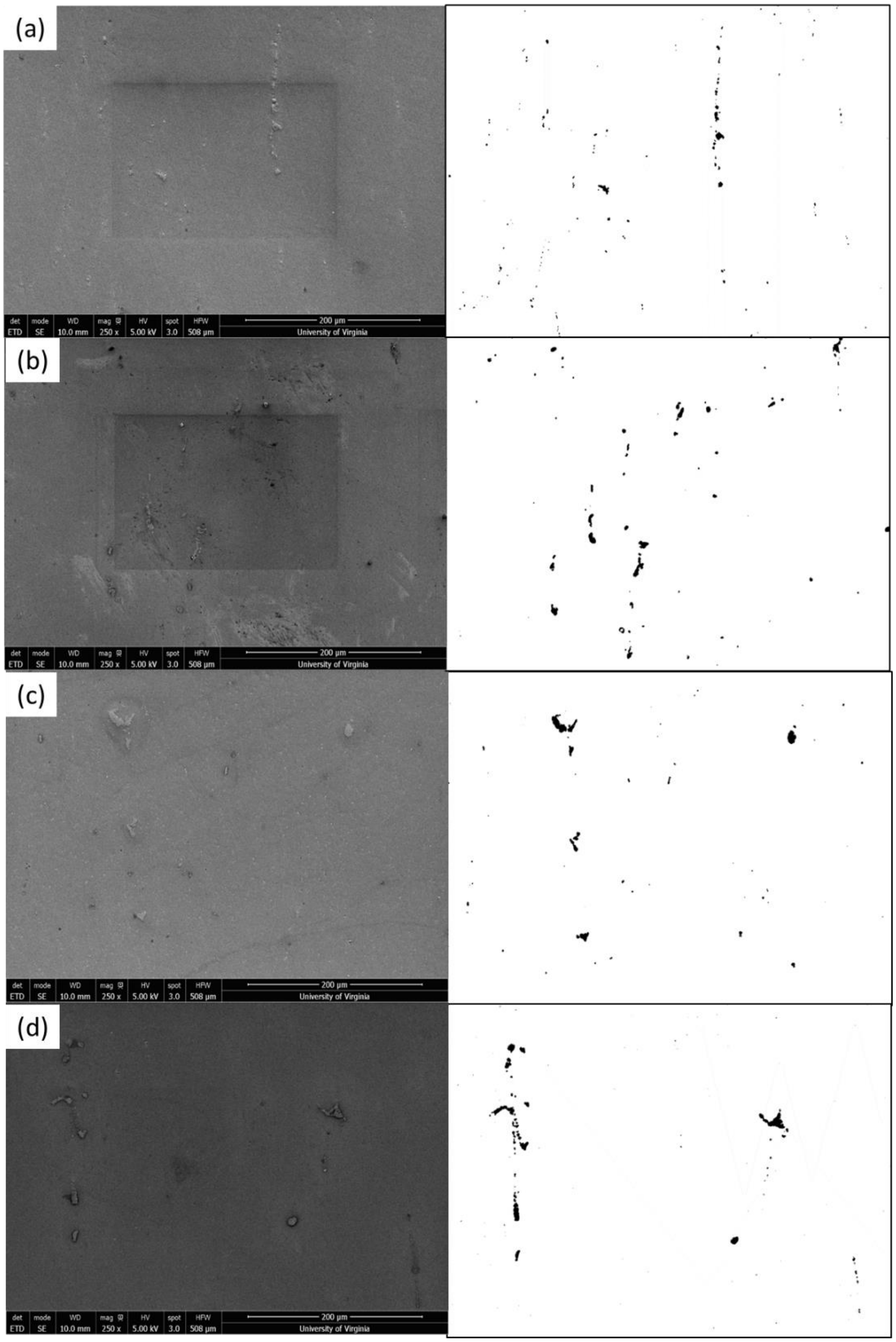

Figure 4.8. Secondary electron micrograph indicating the constituent particles as bright white spots and the corresponding threshold image indicating the constituent particles in black of AA7050-T7451 on the LT plane for (a) surface (b) eighth (c) quarter (d) half plate thickness.

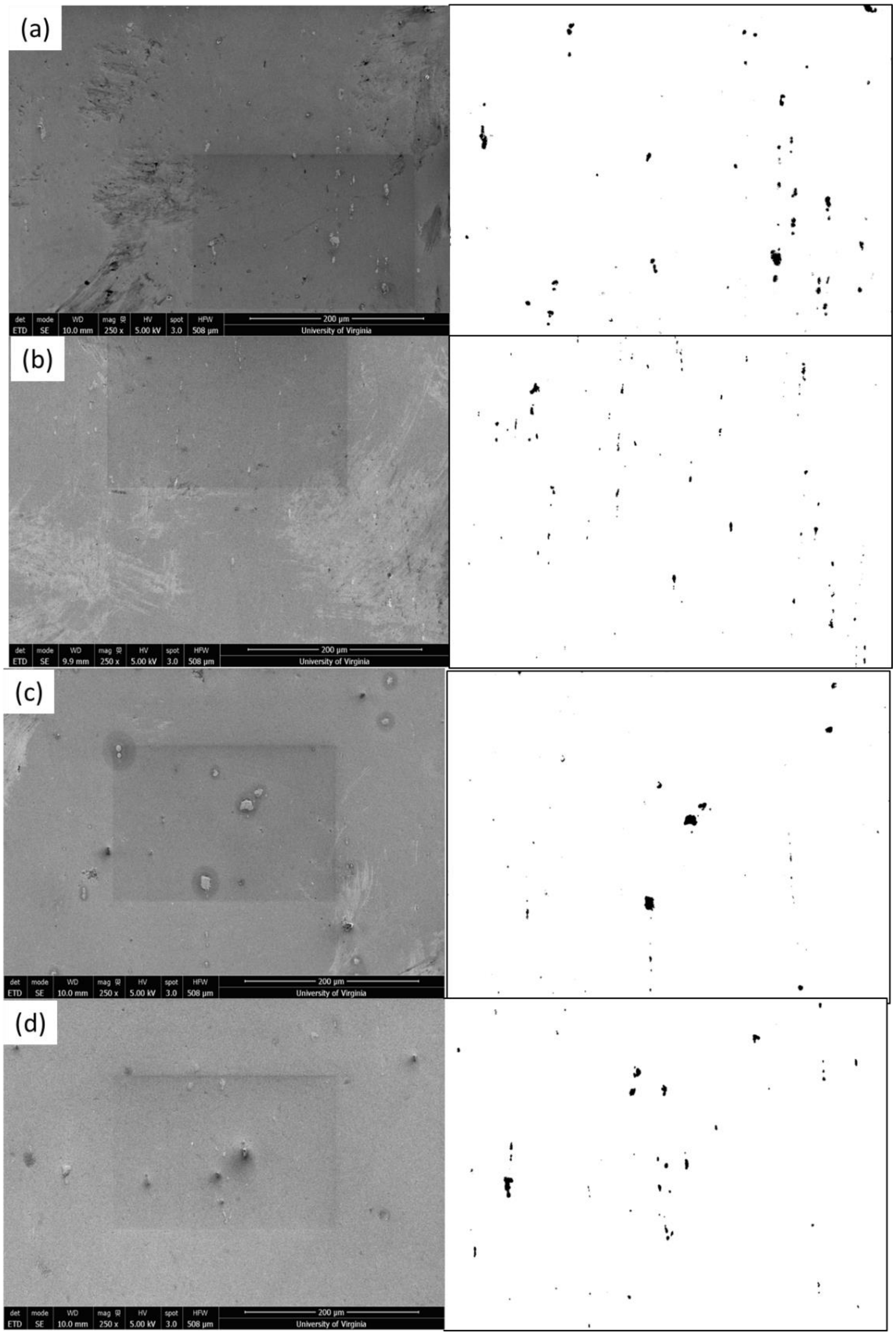

Figure 4.9. Secondary electron micrograph indicating the constituent particles as bright white spots and the corresponding threshold image indicating the constituent particles in black of AA7050-T7451 on the LS plane for (a) surface (b) eighth (c) quarter (d) half plate thickness.

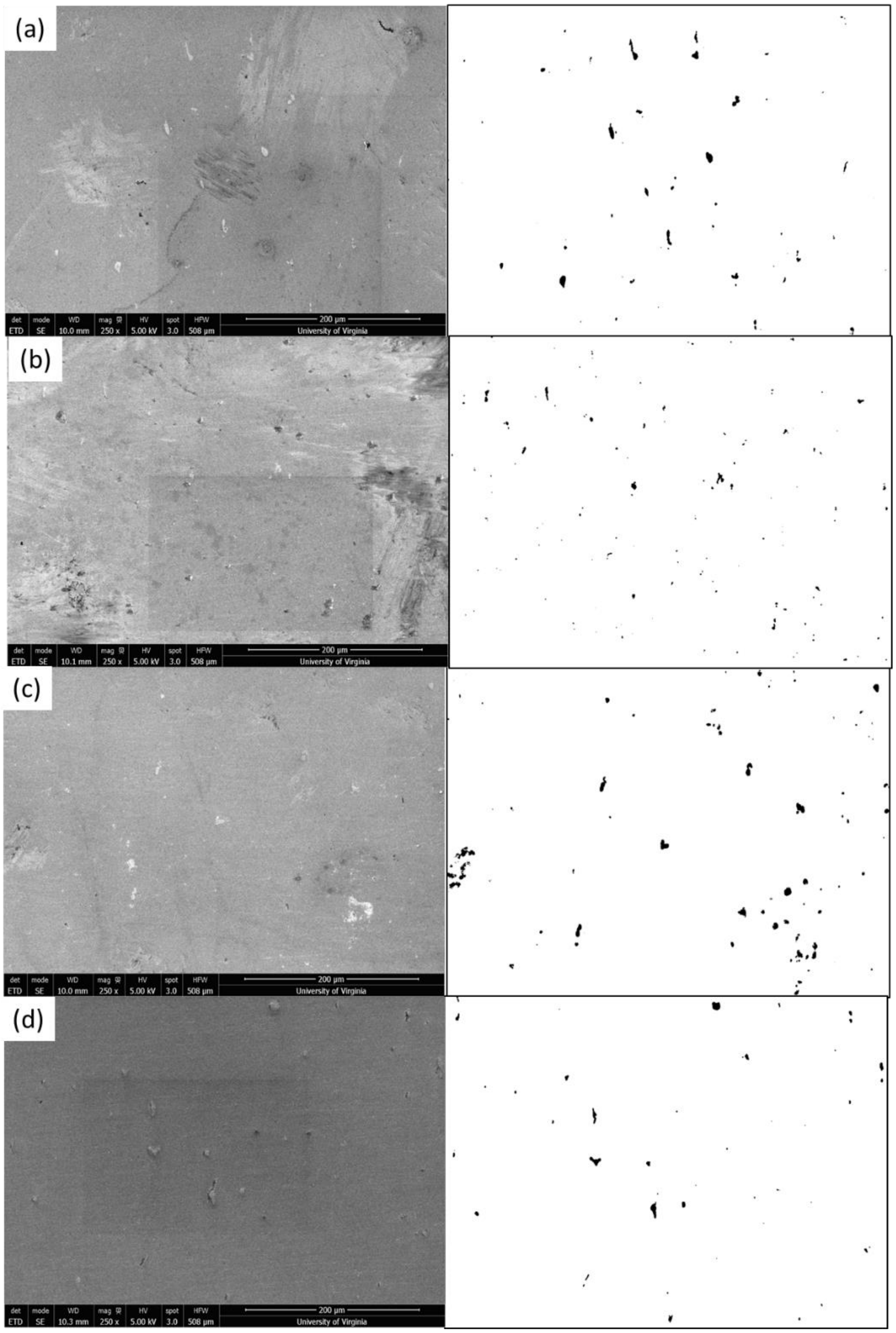

Figure 4.10. Secondary electron micrograph indicating the constituent particles as bright white spots and the corresponding threshold image indicating the constituent particles in black of AA7050-T7451 on the TS plane (a) surface (b) eighth (c) quarter (d) half plate thickness.

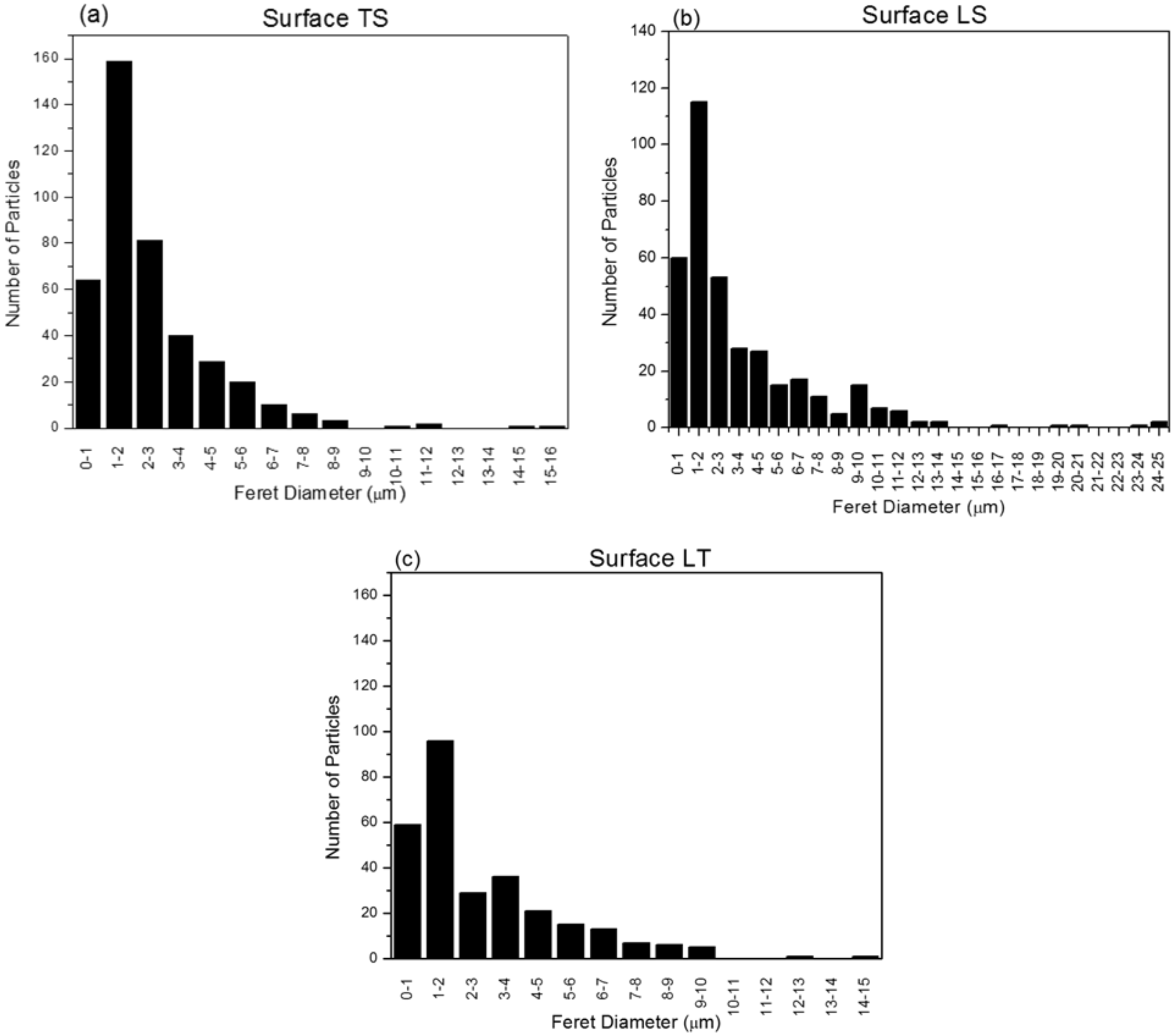

Figure 4.11. Number of particles per 1 mm^2 area of AA7050-T7451 separated in Feret diameter bins on the surface specimens on the (a) TS (b) LS and (c) LT planes.

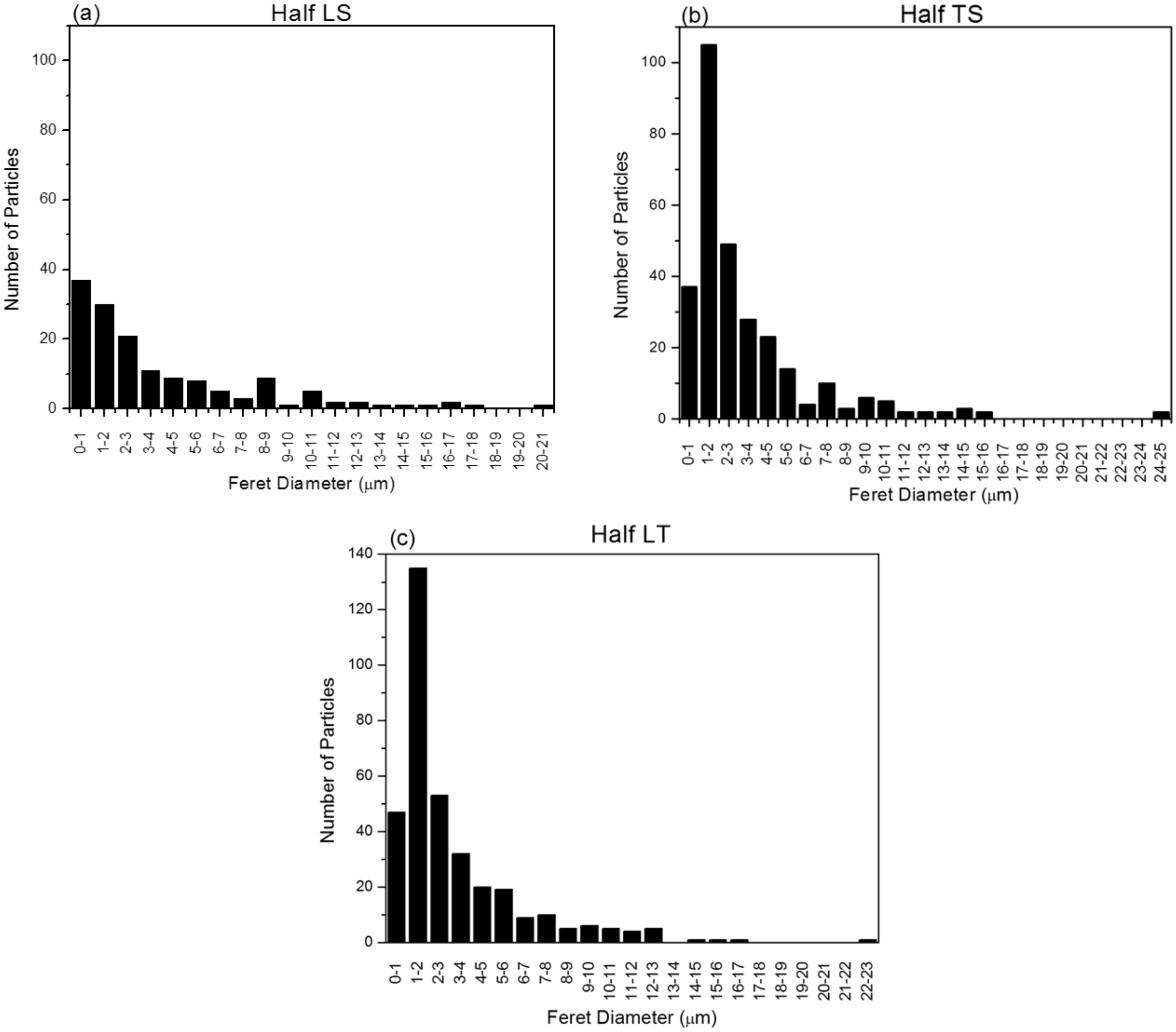

Figure 4.12. Number of particles per 1 mm^2 area of AA7050-T7451 separated in Feret diameter bins at the half plate thickness specimens on the (a) TS (b) LS and (c) LT planes.

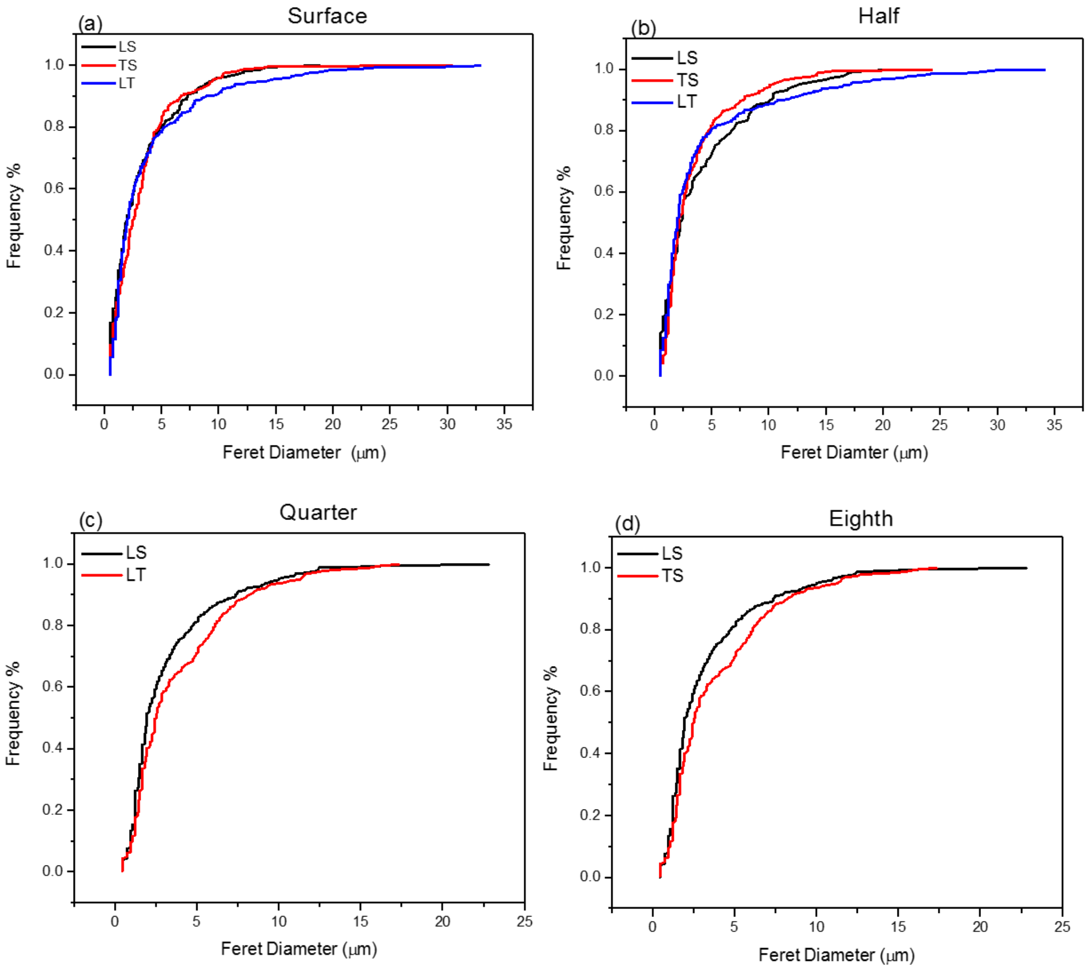

Figure 4.13. Cumulative frequency plots of Feret diameter as a function of plate thickness and plate orientation of the constituent particles for (a) surface (b) half (c) quarter and (d) eighth plate thicknesses.

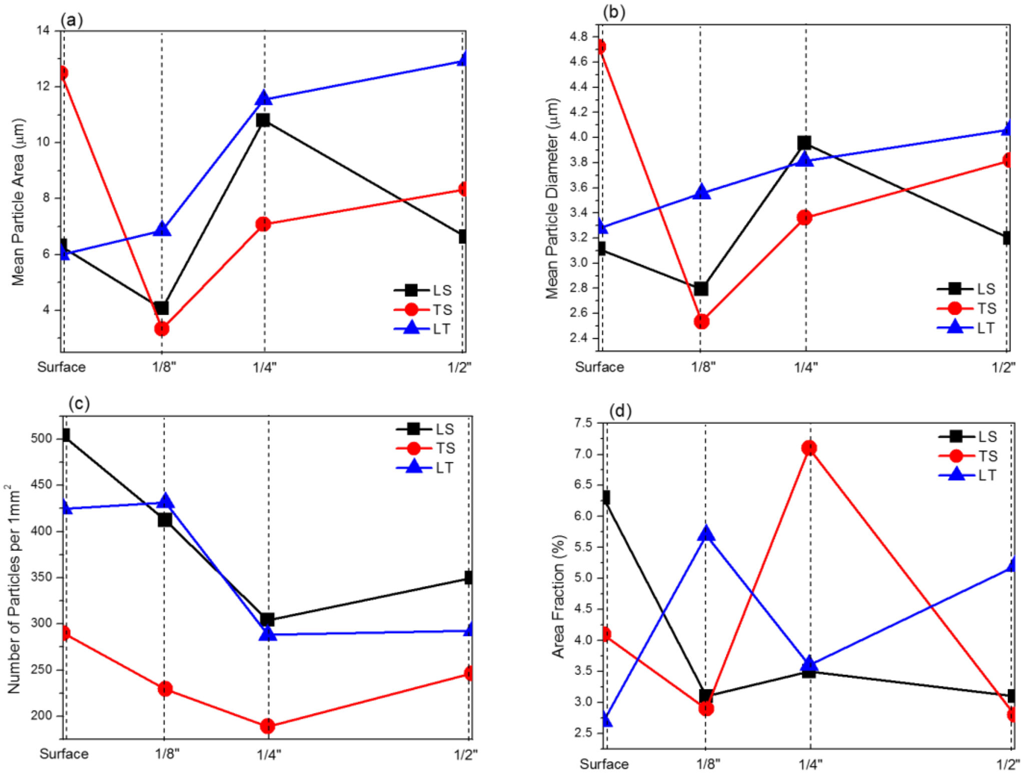

Figure 4.14. Summary of constituent particle analysis of AA7050-T7451 as a function of plate thickness and (a) mean particle area (b) mean particle diameter (c) number of particles per 1 mm^2 and (d) area fraction

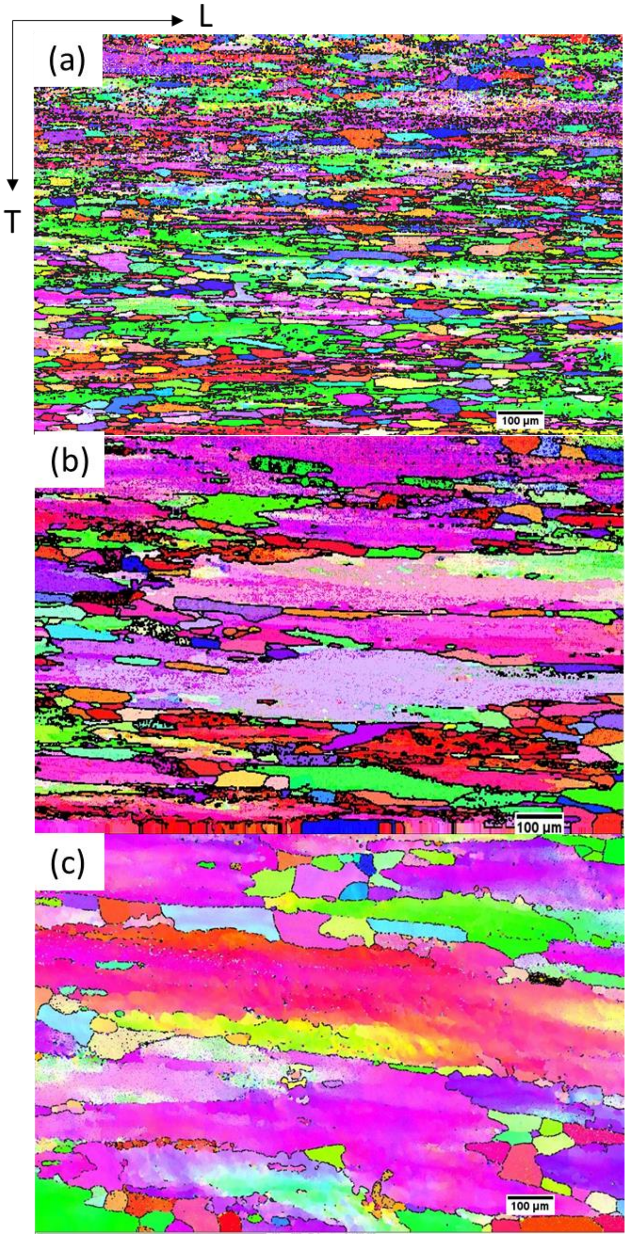

Figure 4.15. EBSD maps of AA7050-T7451 on the LT plane at the (a) surface of the plate (b) quarter thickness of plate and (c) half thickness of plate.

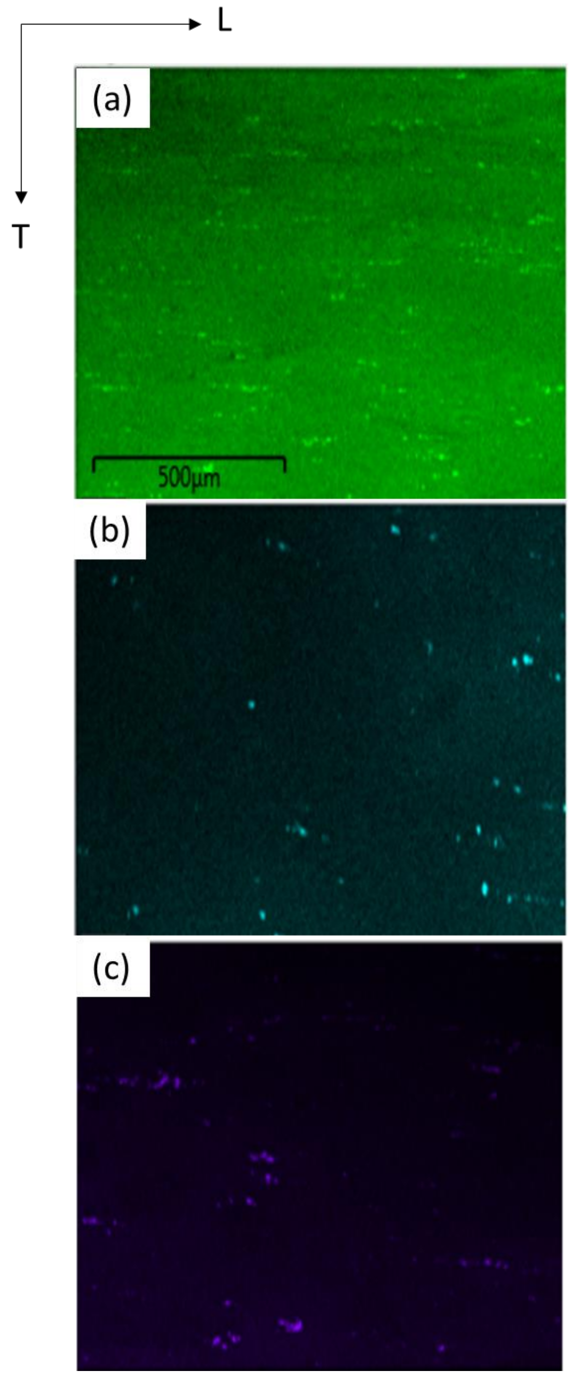

Figure 4.16. EDS elemental Cu map of AA7050-T7451 on the LT plane at the (a) surface of the plate (b) quarter thickness of plate and (c) half thickness of plate.

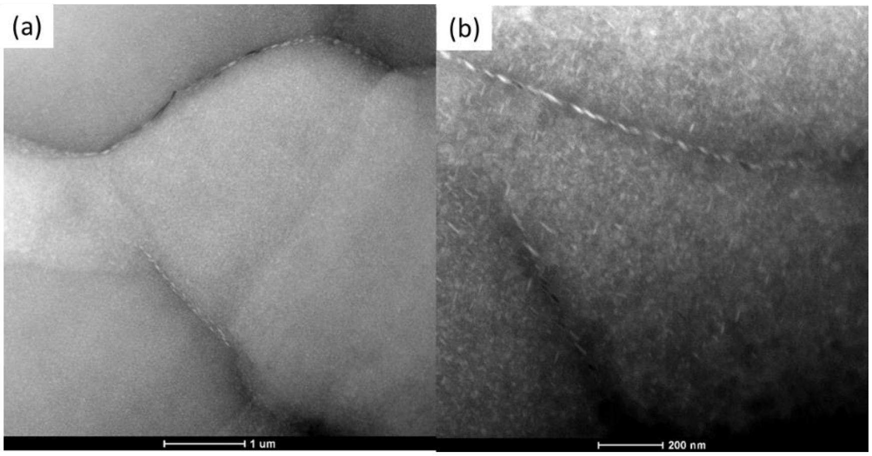

Figure 4.17. High-angle annular dark-field detector in scanning transmission electron microscopy on the grain boundaries of AA7050-T7451 in the SL orientation at (a) 1 μm scale and (b) 200 nm scale.

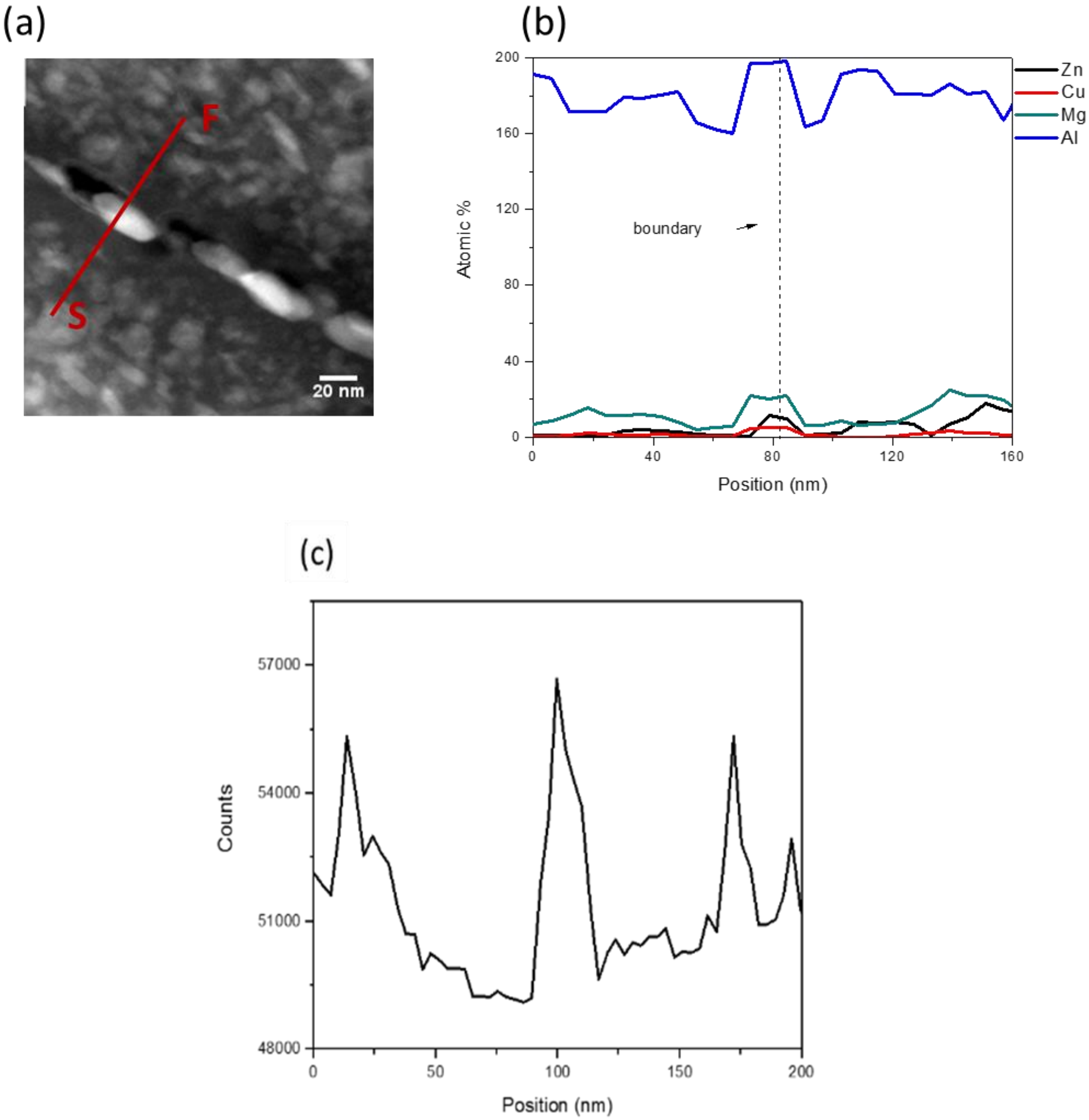

Figure 4.18. (a) High-angle annular dark-field detector in scanning transmission electron microscopy image along a grain boundary in AA7050-T7451, where the bright white spots are grain boundary precipitates. (b) corresponding EDS line profile across the grain boundary in atomic % vs position (c) counts vs position for the line scan. Higher counts indicate a precipitate.

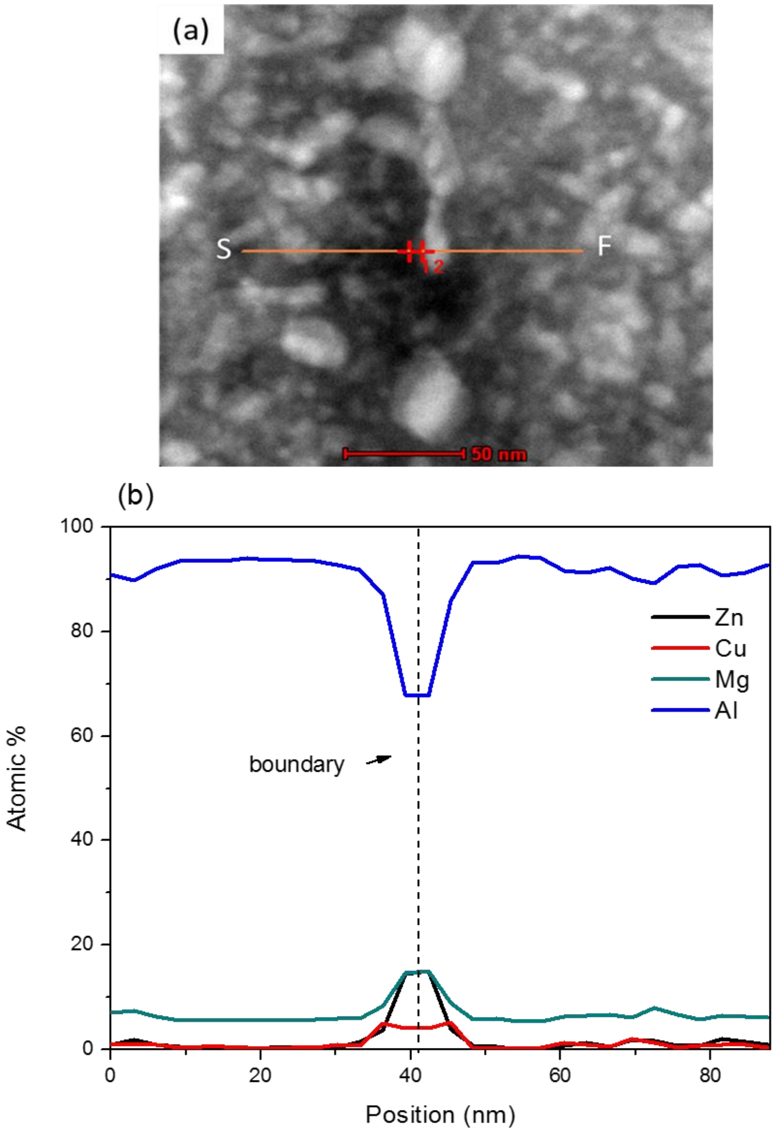

Figure 4.19. (a) High-angle annular dark-field detector in scanning transmission electron micrograph along a grain boundary in AA7050-T7451, where the bright white spots are grain boundary precipitates. (b) corresponding EDS line profile across the grain boundary in atomic % vs position.

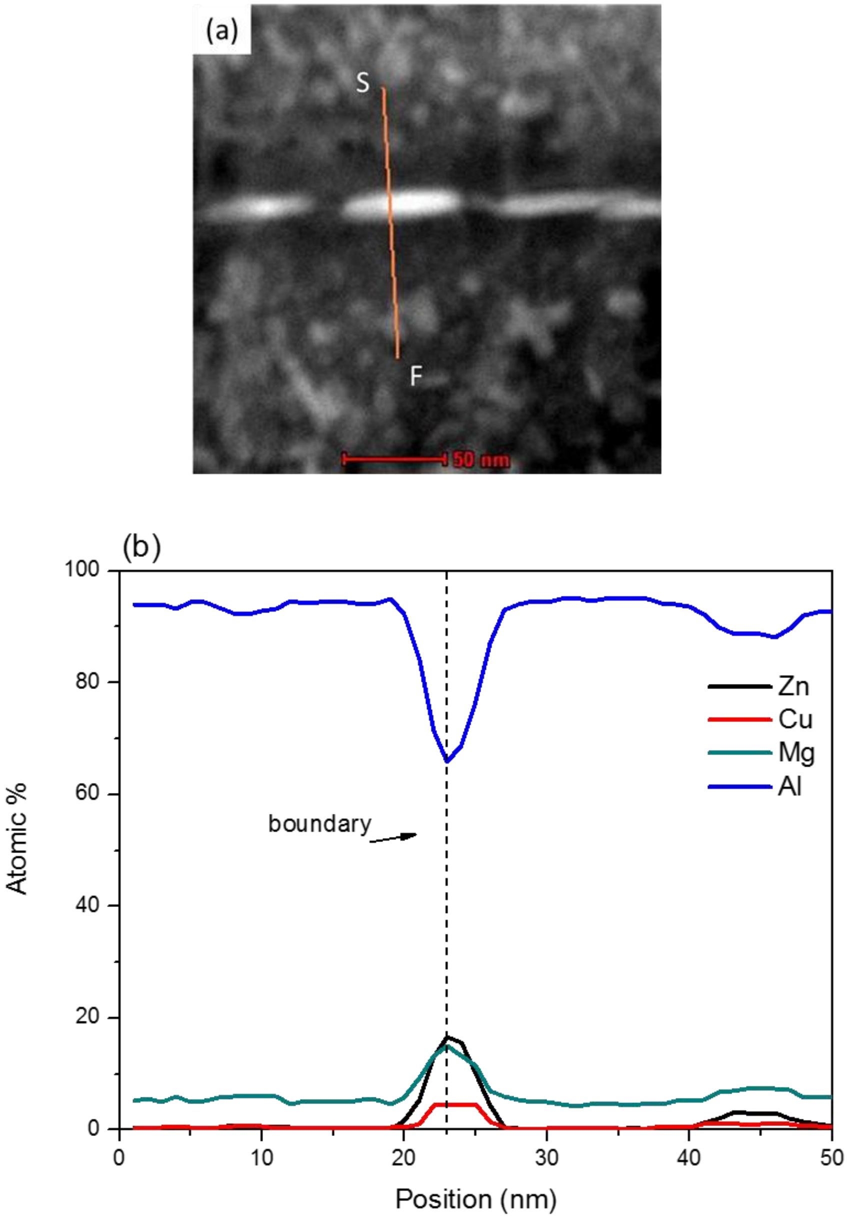

Figure 4.20. (a) High-angle annular dark-field detector in scanning transmission electron micrograph along a grain boundary in AA7050-T7451, where the bright white spots are grain boundary precipitates. (b) Corresponding EDS line profile across the grain boundary in atomic % vs position

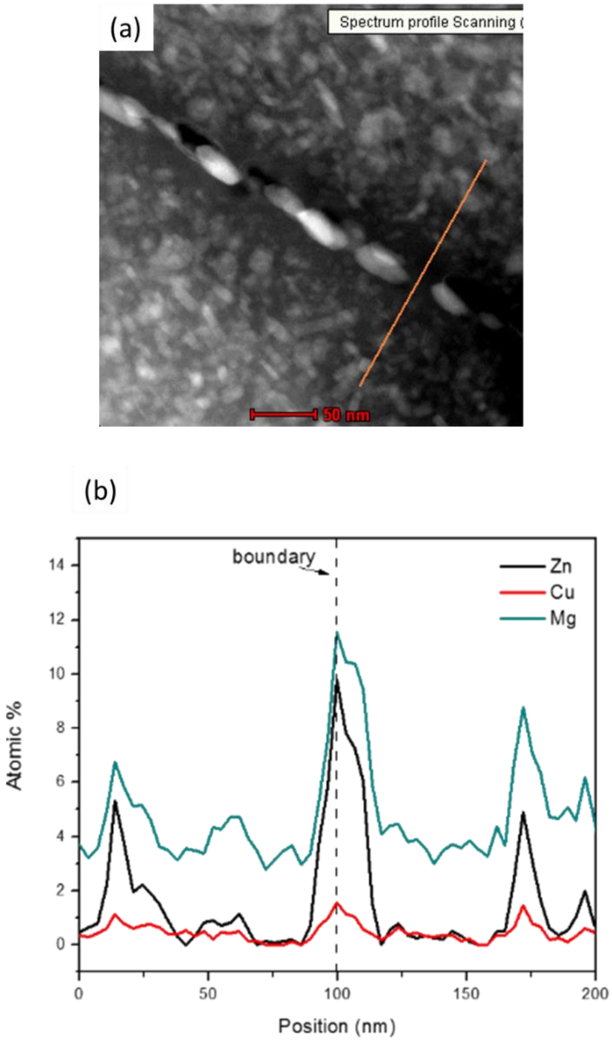

Figure 4.21 (a) High-angle annular dark-field detector in scanning transmission electron micrograph along a grain boundary in AA7050-T7451, where the bright white spots are grain boundary precipitates. (b) Corresponding EDS line profile across the grain boundary in atomic % vs position. This map specially shows a line scan in-between precipitates.

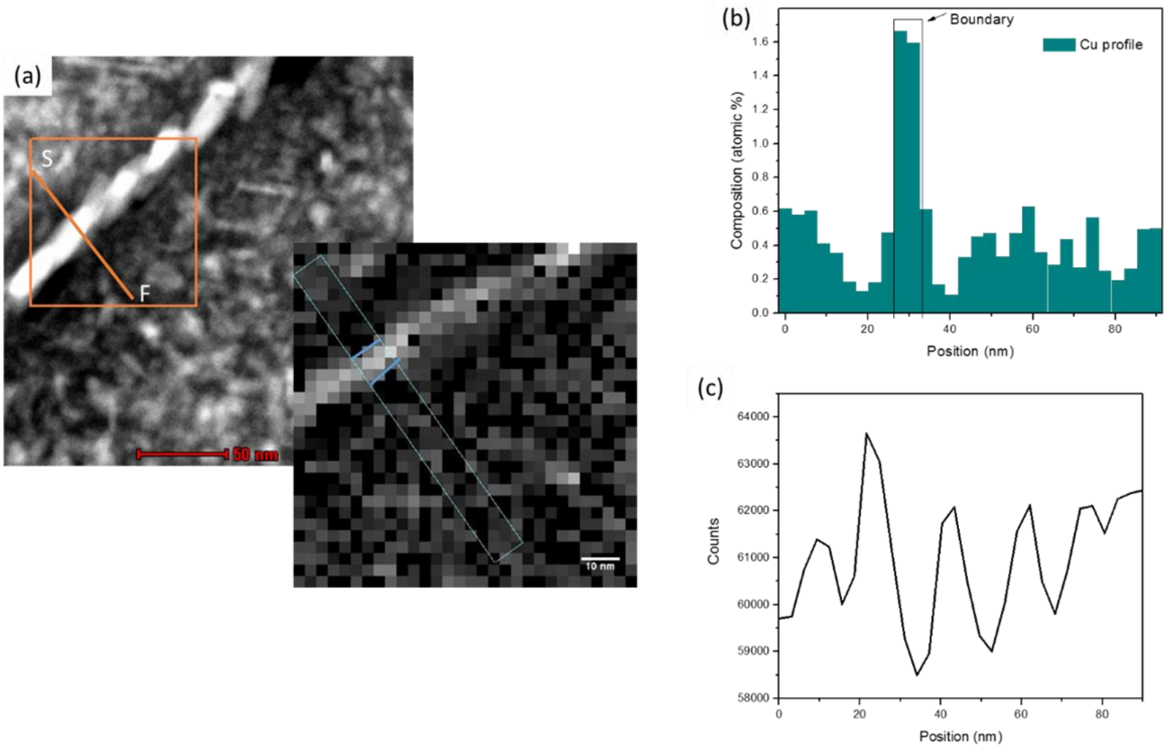

Figure 4.22. (a) High-angle annular dark-field detector in scanning transmission electron microscopy micrograph showing area of line scan on AA7050-T7451 grain boundary (b) EELS profile of Cu showing relative composition over position. (c) Counts vs position for the line scan. Higher counts indicate a precipitate. The line scan runs from S to F on the orange line.

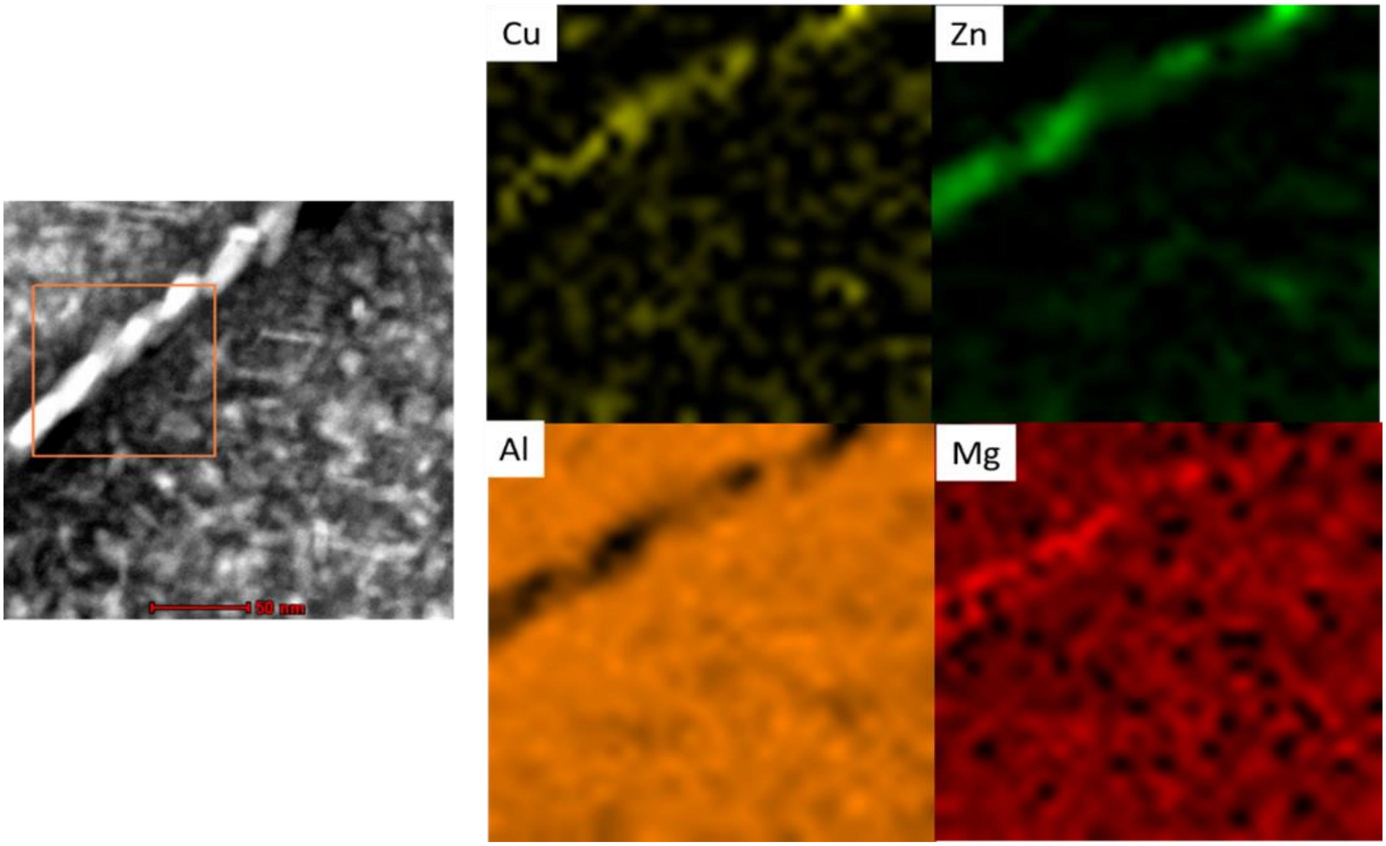

Figure 4.23. High-angle annular dark-field detector in scanning transmission electron microscopy EDS map for Cu, Zn, Al, and Mg in the grain boundary region of AA7050-T7451. The brighter regions in each map indicate a higher concentration of that specific element in the area of focus.

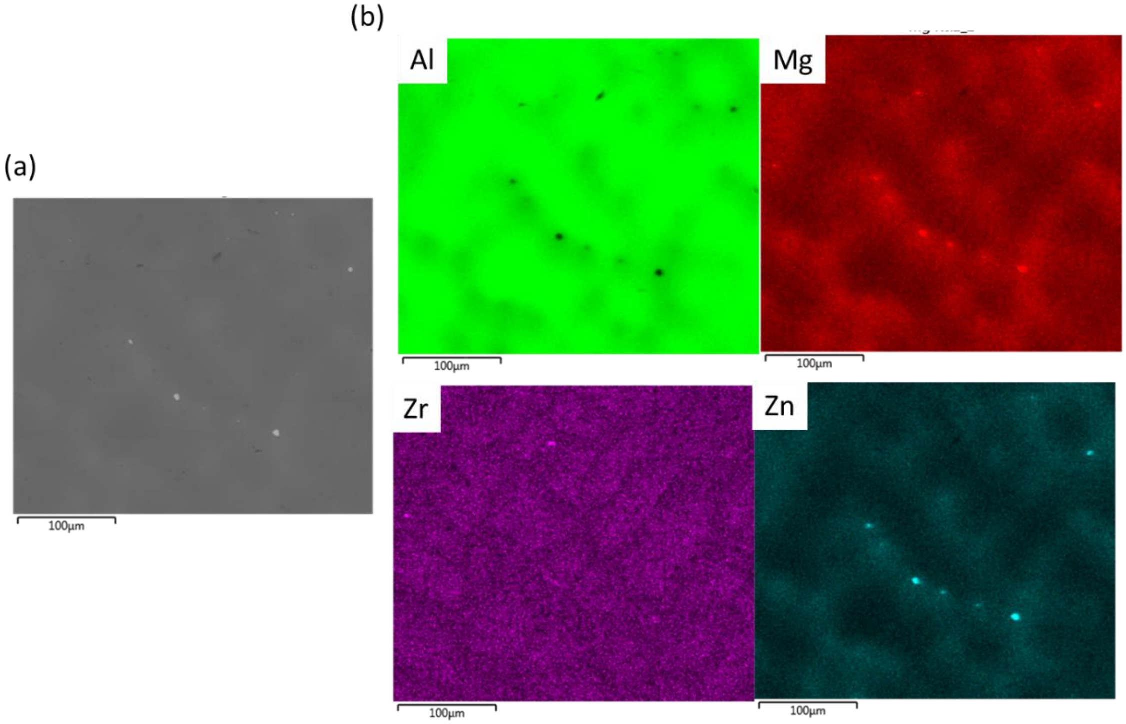

Figure 4.24. (a) Secondary electron micrograph of as-cast Al-Zn-Mg-Zr model alloy (b) EDS map of entire field of view within Al-Zn-Mg-Zr model alloy showing elemental composition maps of Al, Mg, Zr, and Zn.

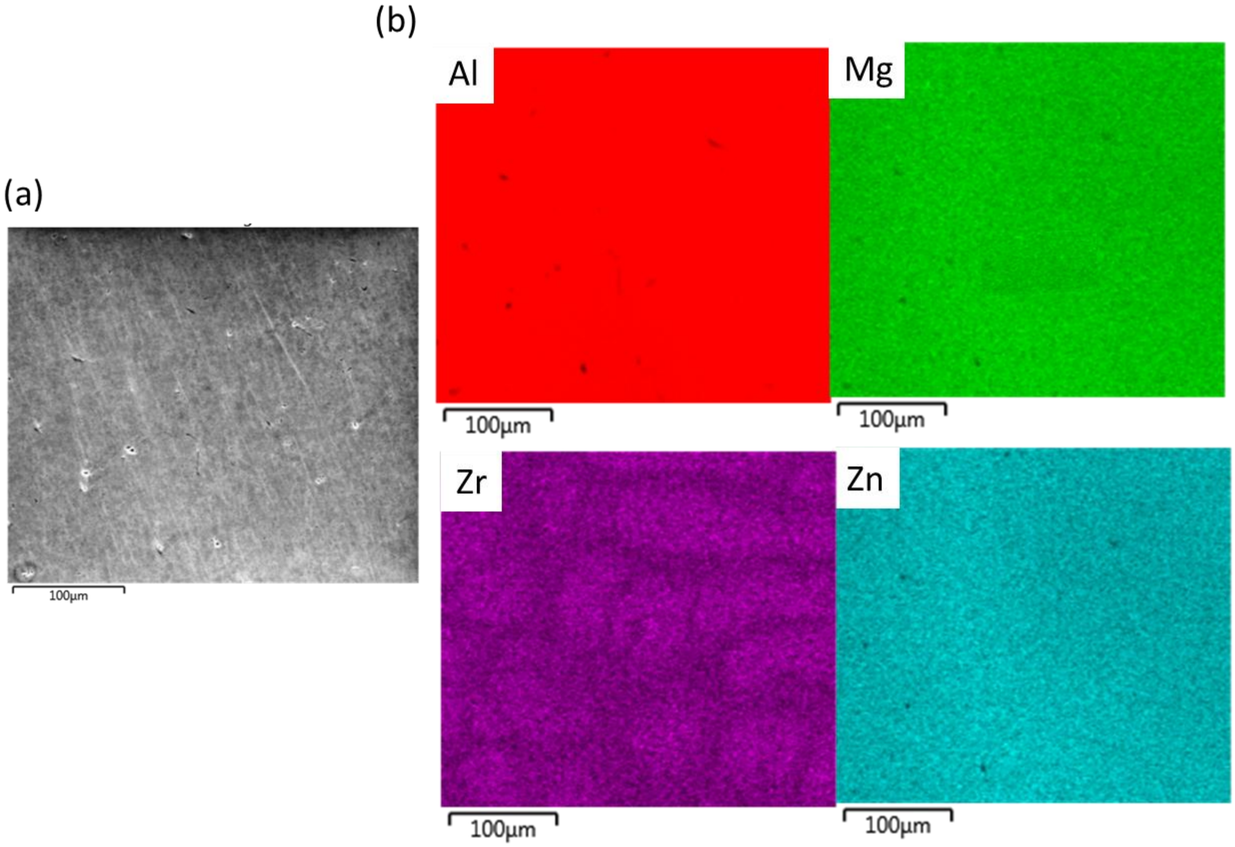

Figure 4.25. (a) Secondary electron micrograph of SHT/Q Al-Zn-Mg-Zr model alloy (b) EDS map of entire field of view within Al-Zn-Mg-Zr SHT/Q model alloy showing elemental composition maps of Al, Mg, Zr, and Zn.

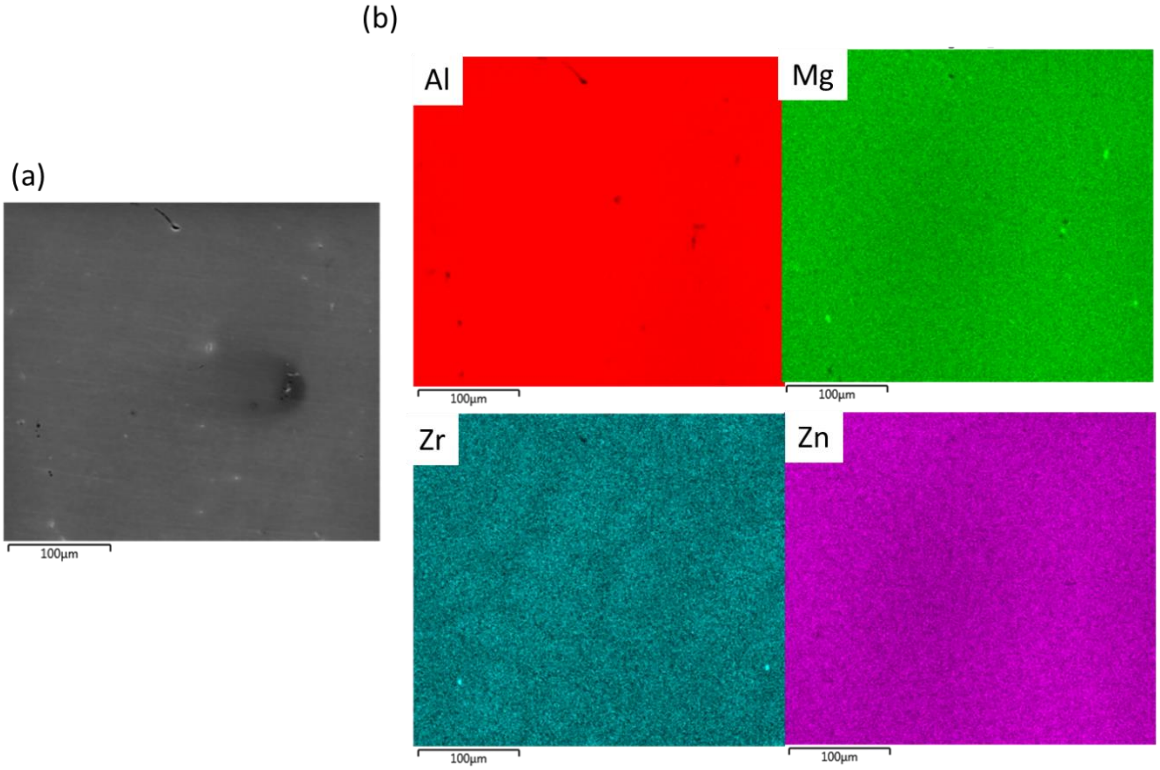

Figure 4.26. (a) Secondary electron micrograph of over-aged Al-Zn-Mg-Zr model alloy (b)) EDS map of entire field of view within Al-Zn-Mg-Zr OA model alloy showing elemental composition maps of Al, Mg, Zr, and Zn.

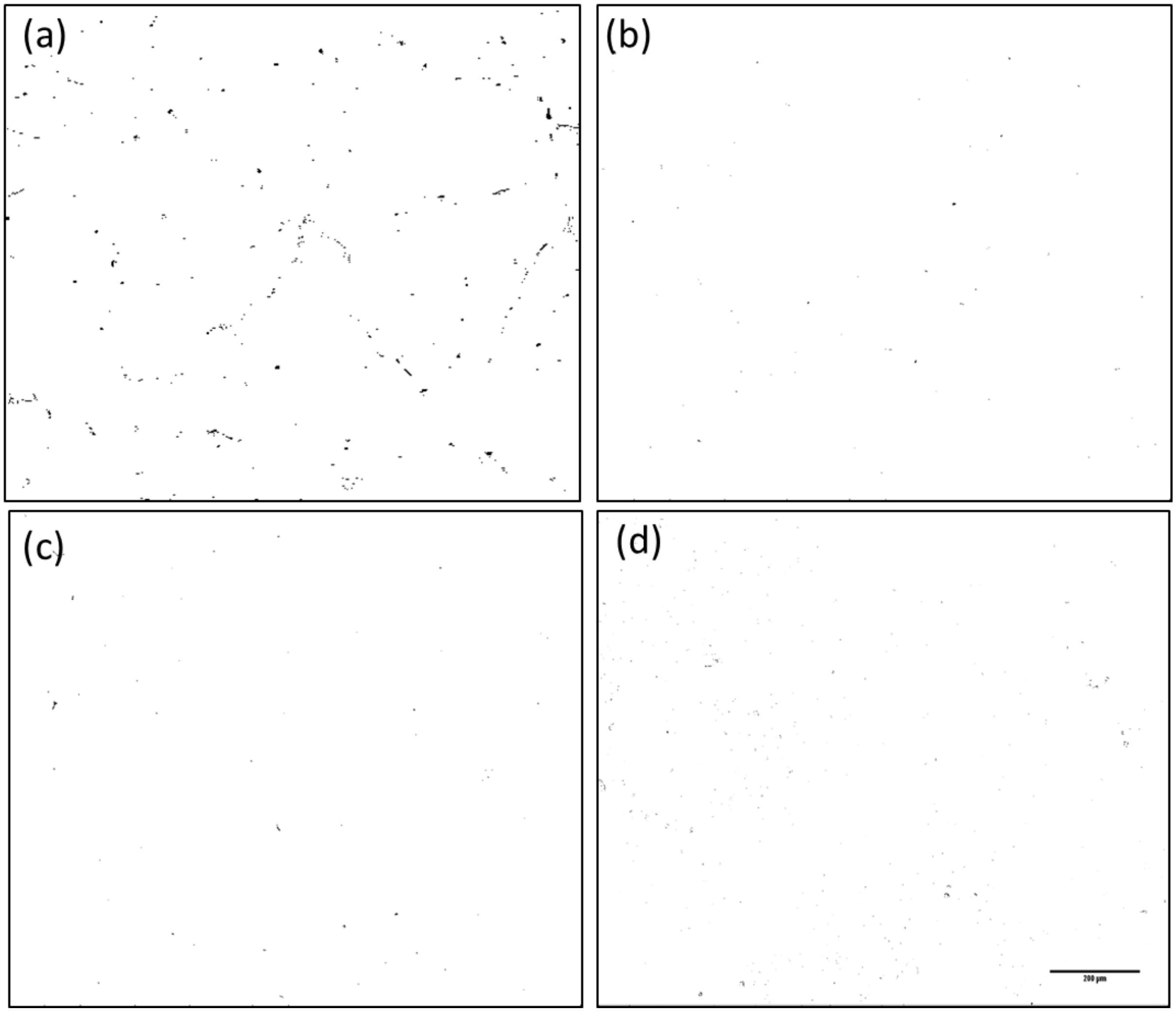

Figure 4.27. Threshold image obtained from BSE micrograph of Al-Zn-Mg-Zr Cu-free model alloy for the (a) as-received (b) solution heat treatment (SHT/Q) (c) over-aged sample and (d) AA7050-T7451.

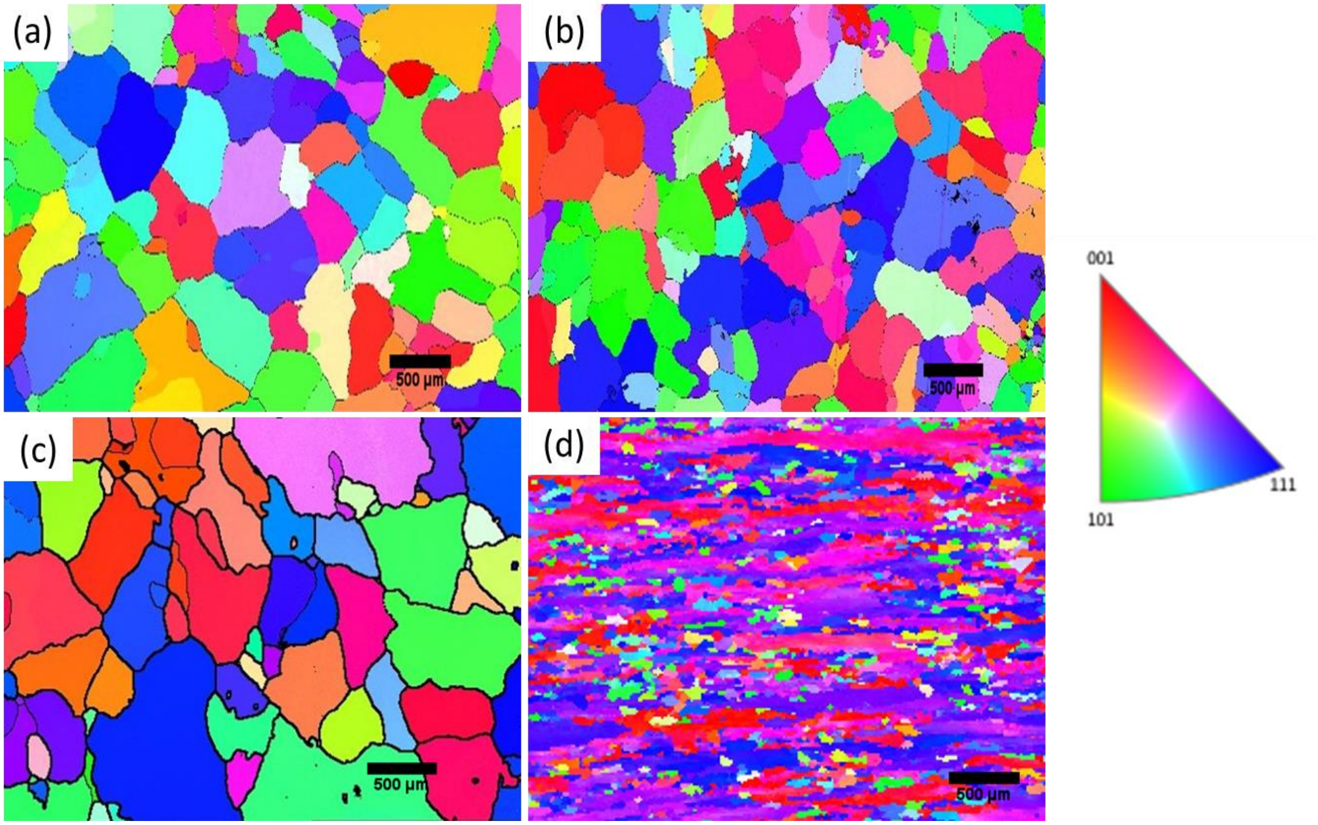

Figure 4.28. EBSD map of Al-Zn-Mg-Zr Cu-free model alloy for the (a) as-cast (b) solution heat treatment (SHT/Q) (c) over-aged sample compared to (d) AA7050-T7451.

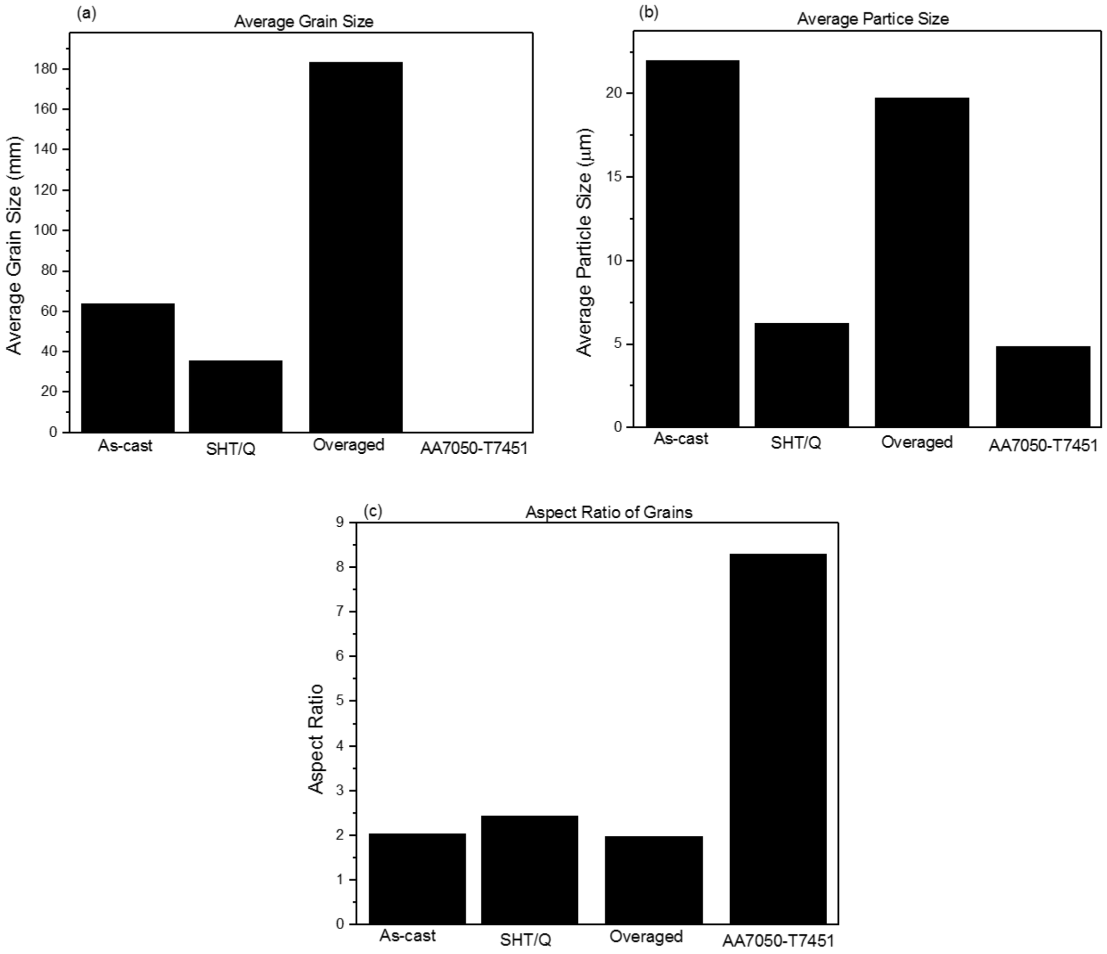

Figure 4.29. Bar plots showing (a) average grain size (b) average particle size and (c) aspect ratio of the Al-Zn-Mg-Zr Cu-free alloy as-cast, SHT/Q and over-aged samples compared with (d) AA7050-T7451.

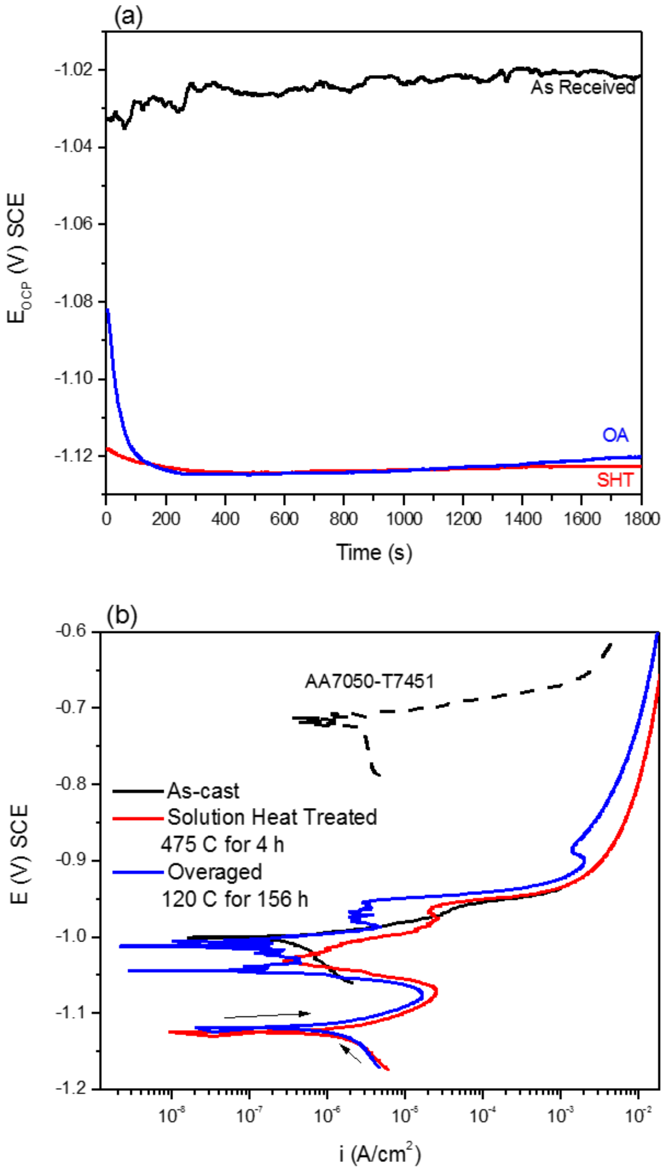

Figure 4.30. Electrochemistry on Al-Zn-Mg-Zr Cu-free model alloy in the as-cast, SHT/Q and over-aged heat treatments in 0.6 M NaCl pH 5.5 (a) OCP over 1800 s (b) anodic potentiodynamic polarization.

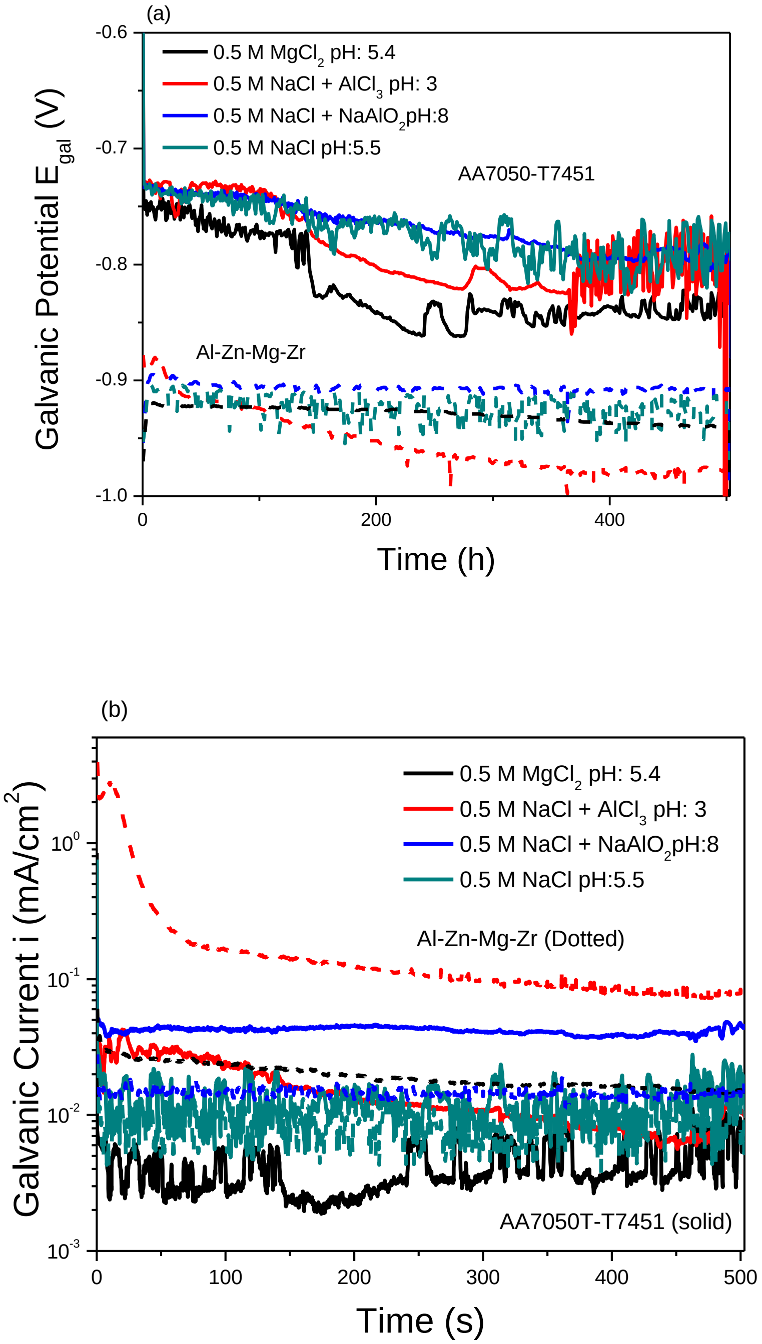

Figure 4.31. Galvanic couple (a) potential and (b) current density for Al-Zn-Mg-Zr over-aged coupled with Type 316 stainless steel obtained using zero resistance ammeter over 504 h in simulated crevice solution.

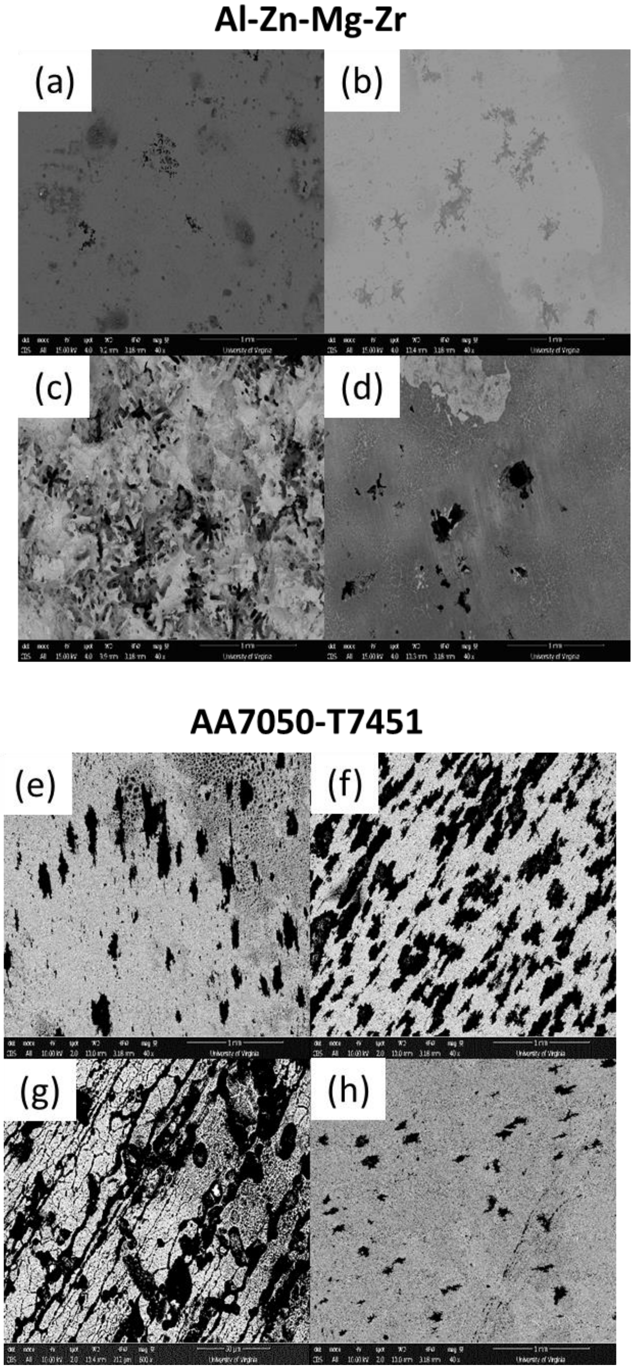

Figure 4.32. SEM surface damage morphology of Al-Zn-Mg-Zr alloy (a)-(d) as compared to AA7050-T7451 (e)-(h) after 504 h exposure in simulated rivet solutions of (a)(e) 0.5 M NaCl pH 5.5 (b)(f) 0.5 M NaCl + NaAlO2 pH 8 (c)(g) 0.5 M NaCl + AlCl3 pH 3 (d)(h) 0.5 M MgCl2 pH 5.4.

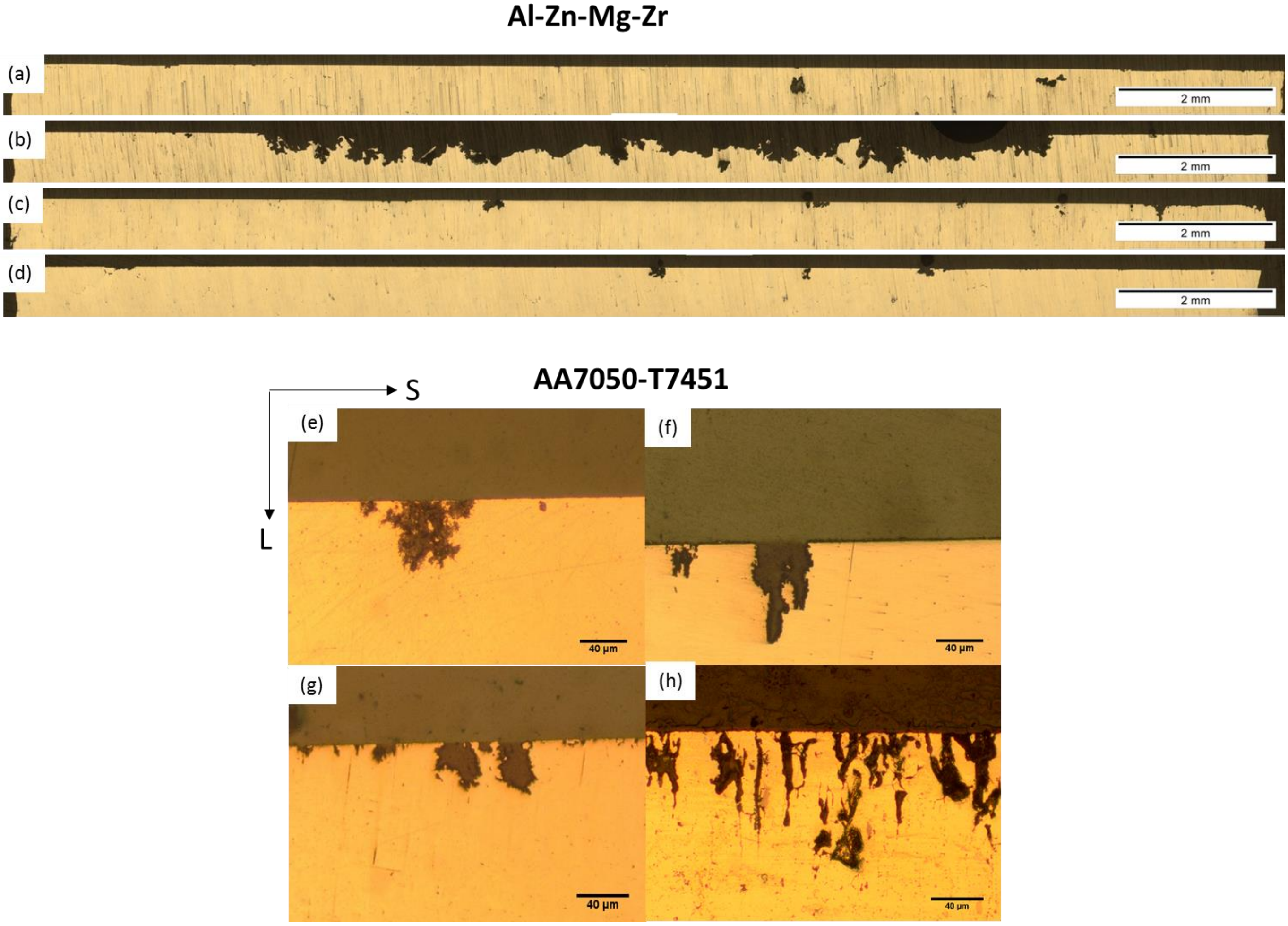

Figure 4.33. Cross-sectional corrosion damage morphologies of Al-Zn-Mg-Zr coupled Type 316 stainless steel via ZRA for 504 h in (a) 0.5 M MgCl2 (b) 0.5 M NaCl + AlCl3 pH 3 (c) 0.5 M NaCl + NaAlO2 pH 8 (d) 0.5 M NaCl pH 5 compared to AA7050-T7451 in (e) 0.5 M MgCl2 (f) 0.5 M NaCl + AlCl3 pH 3 (g) 0.5 M NaCl + NaAlO2 pH 8 (h) 0.5 M NaCl pH 5

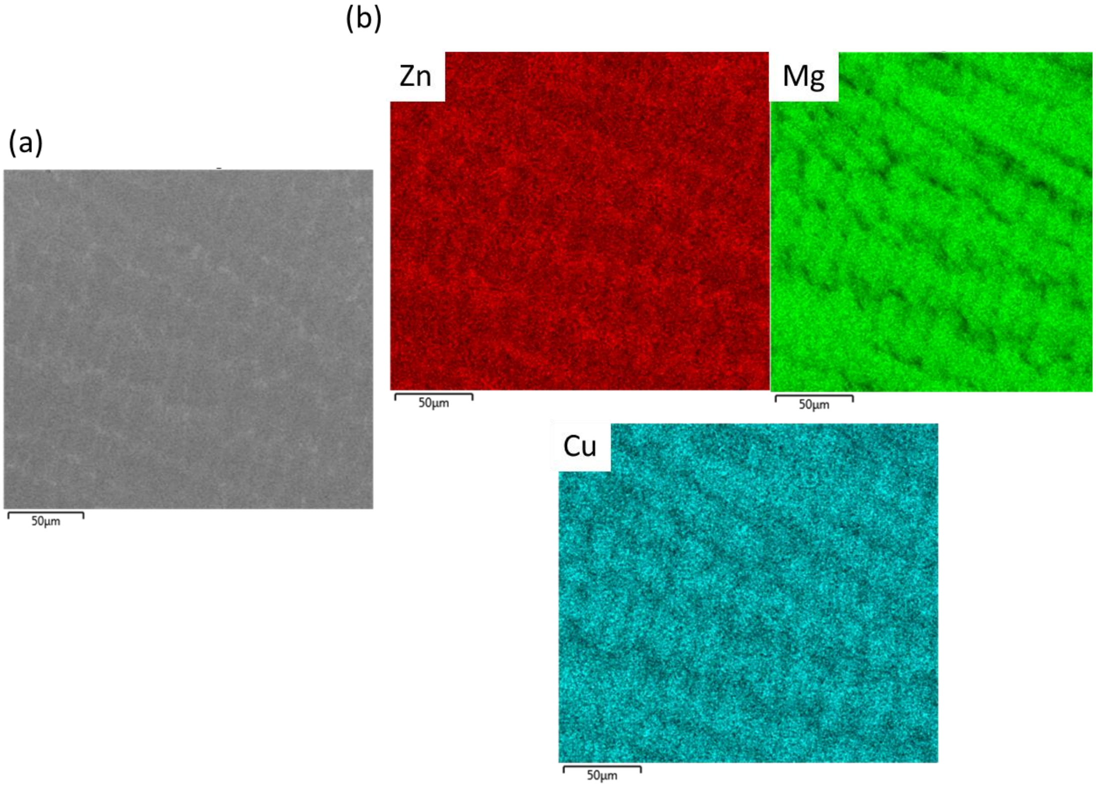

Figure 4.34. (a) Secondary electron micrograph of as-cast Mg(ZnCu)2 (b) EDS analysis entire field of view within Mg(ZnCu)2 showing elemental composition maps of Zn, Mg and Cu.

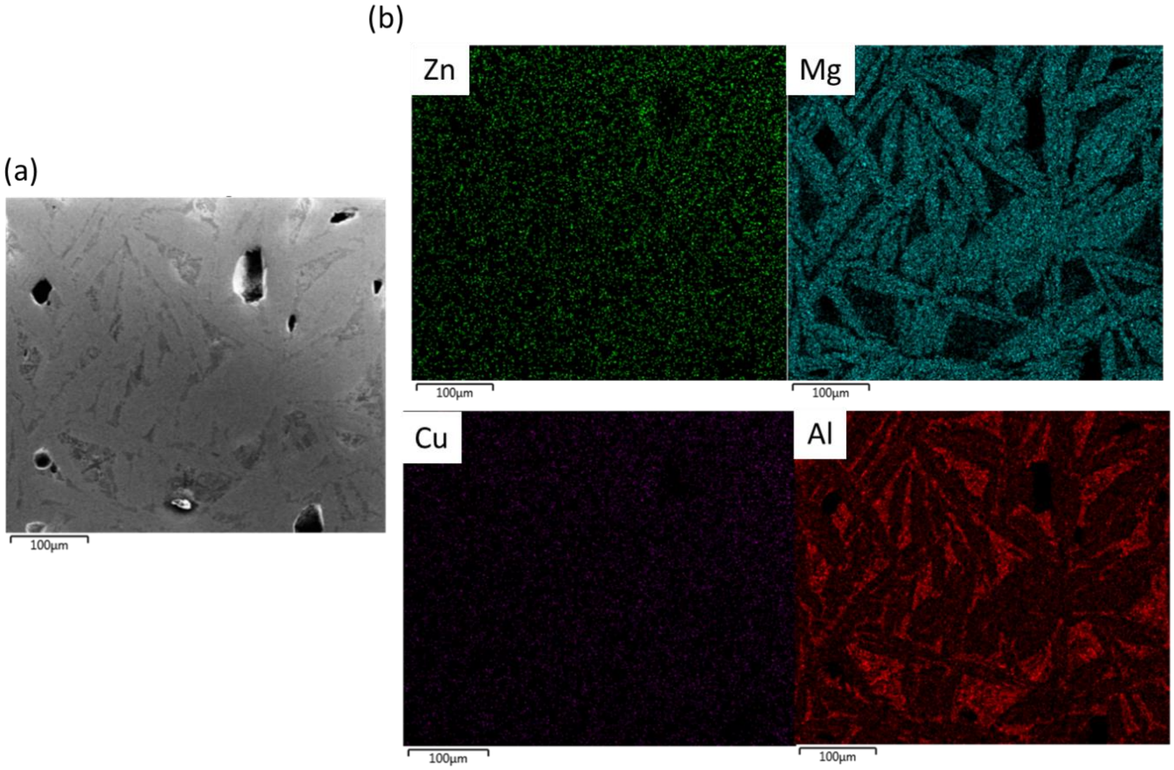

Figure 4.35. (a) Secondary electron micrograph of as-cast Mg(ZnCuAl)2 (b) EDS analysis of entire field of view within Mg(ZnCuAl)2 showing elemental composition maps of Zn, Mg, Cu and Al.

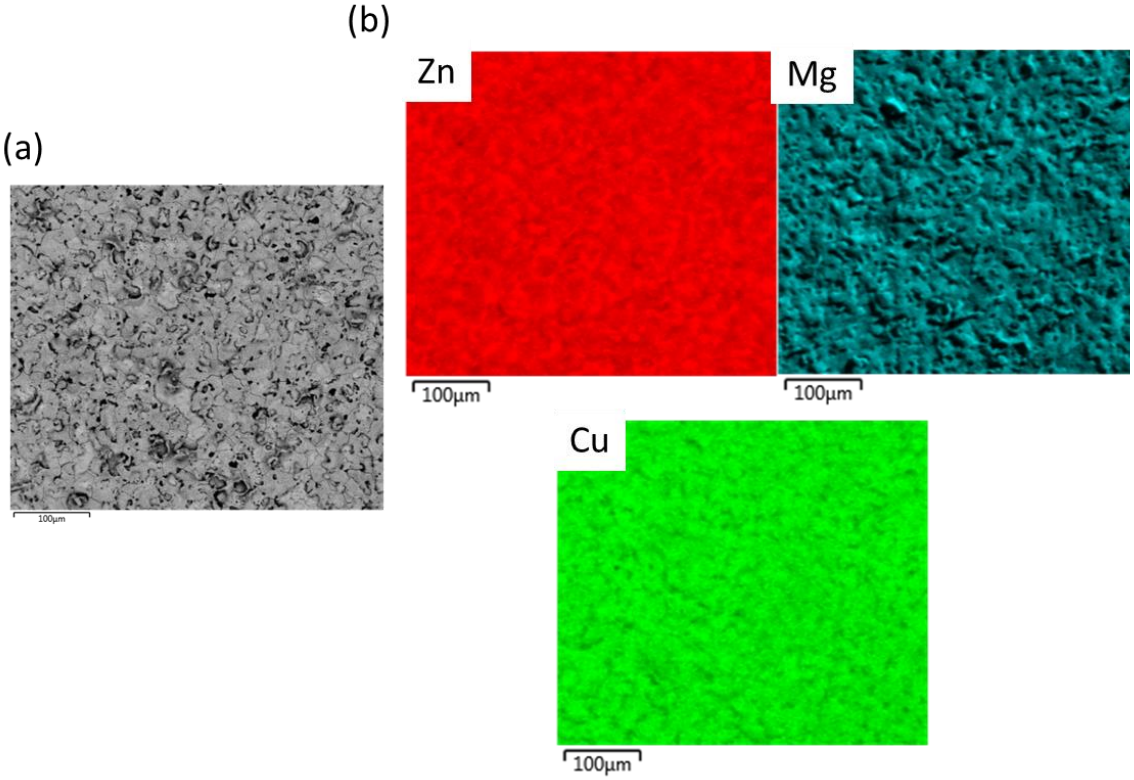

Figure 4.36. (a) Secondary electron micrograph of SHT/Q Mg(ZnCu)2 (b) EDS analysis of entire field of view within Mg(ZnCu)2 showing elemental composition maps of Zn, Mg and Cu.

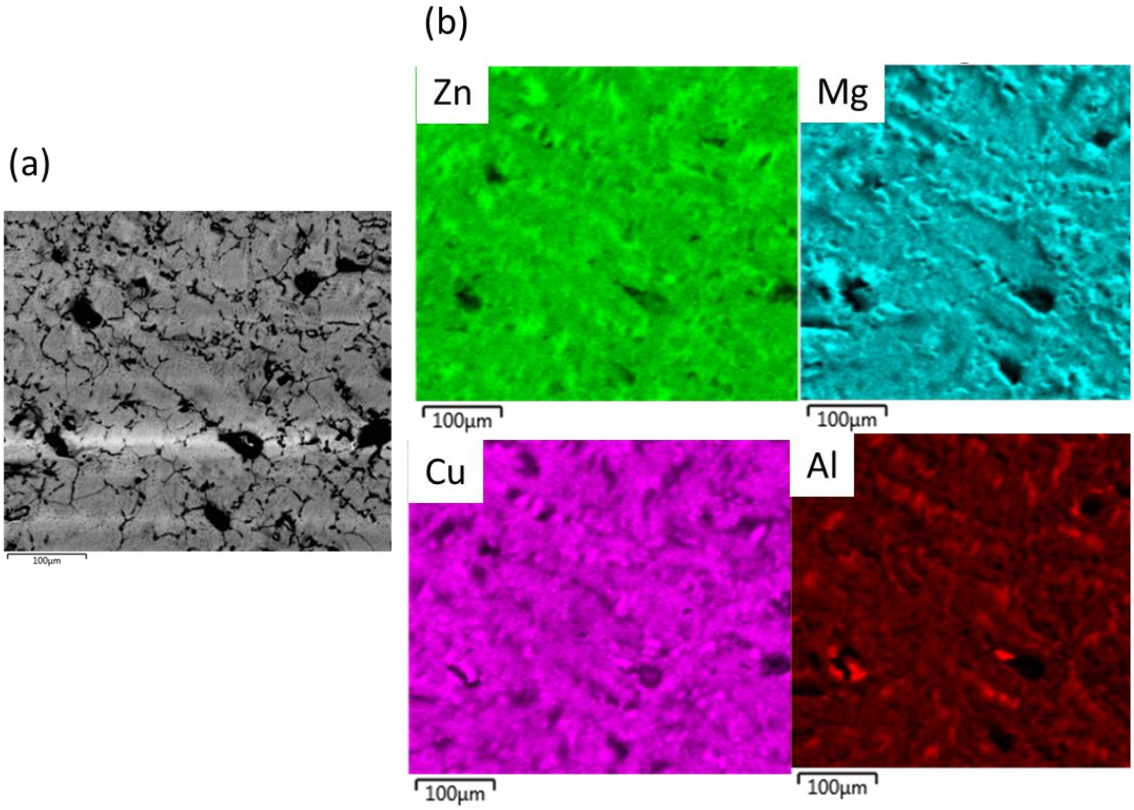

Figure 4.37. (a) Secondary electron micrograph of SHT/Q Mg(ZnCuAl)2 (b) EDS analysis of entire field of view within SHT/Q Mg(ZnCuAl)2 showing elemental composition maps of Zn, Mg, Cu and Al.

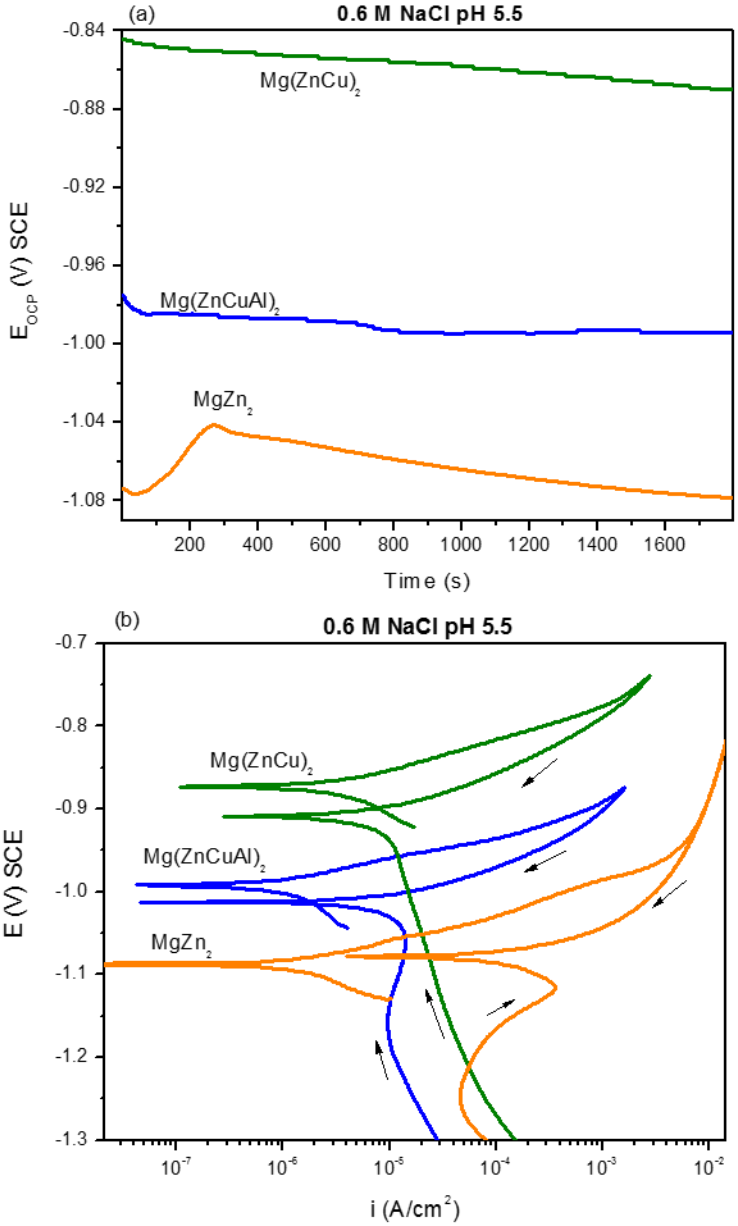

Figure 4.38. (a) OCP of Mg(ZnCuAl)$_2$ model alloys over 1800 s in 0.6 M NaCl (b) Cyclic anodic potentiodynamic polarization of Mg(ZnCuAl)$_2$ in 0.6 M NaCl.

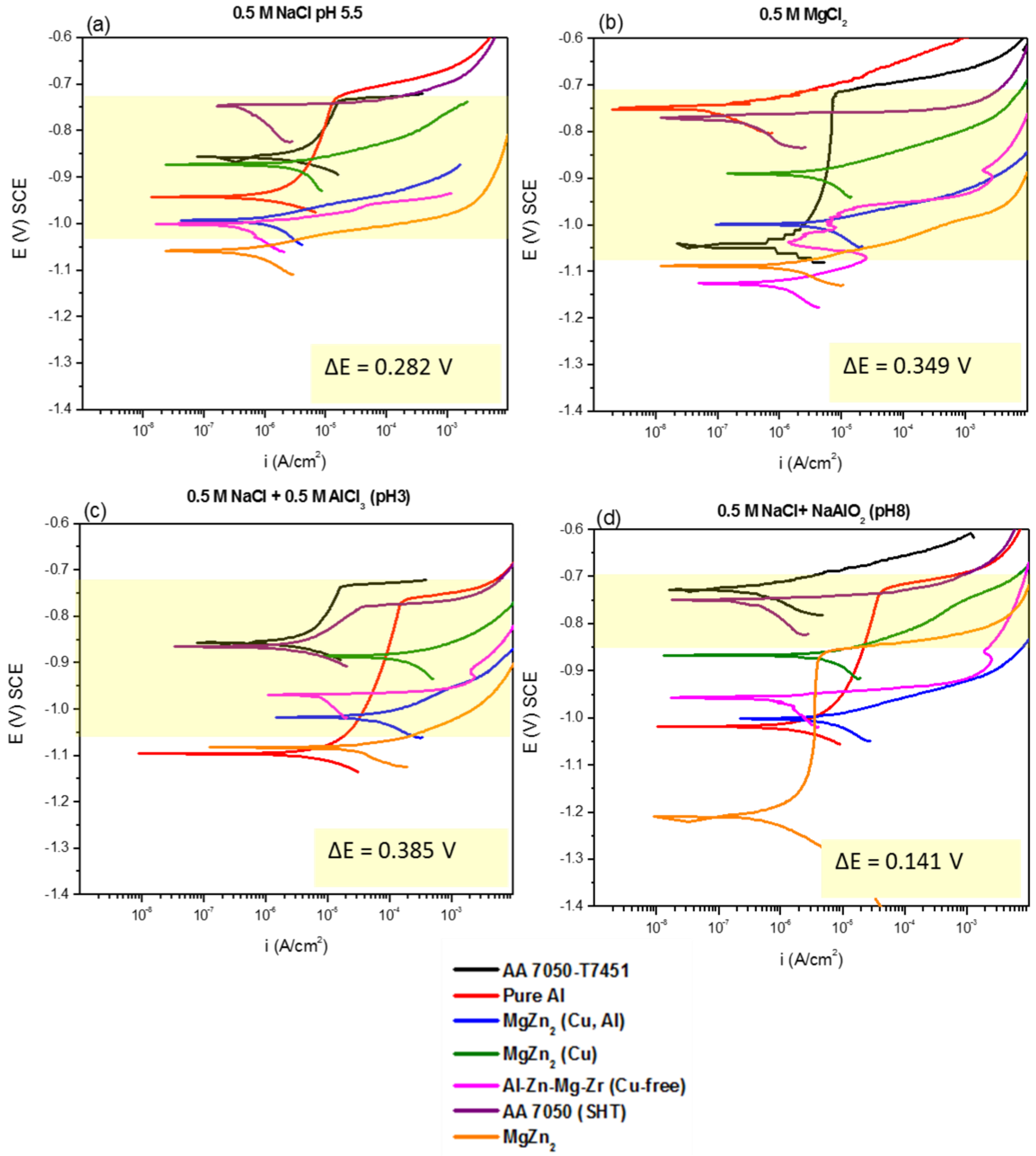

Figure 4.39. Anodic polarization scans of different phases in AA7050-T7451 including pure Al, AA7050 SHT/Q at 477°C for 4 h, MgZn2, Mg(ZnCuAl)$_2$ and the Cu-free Al-Zn-Mg-Zr alloy in (a) 0.5 M NaCl pH 5 (b) 0.5 M MgCl$_2$ pH 5(c) 0.5 M NaCl + 0.5 M AlCl$_3$ pH 3 and (d) 0.5 M NaCl+ NaAlO$_2$ pH 8. The highlighted regions show the window for IGC susceptibility, ΔE, between the AA7050-T7451 matrix and the MgZn$_2$. The assumption is that IR drop between SS and/or Cu can place a galvanic couple potential somewhere in the range of ΔE.

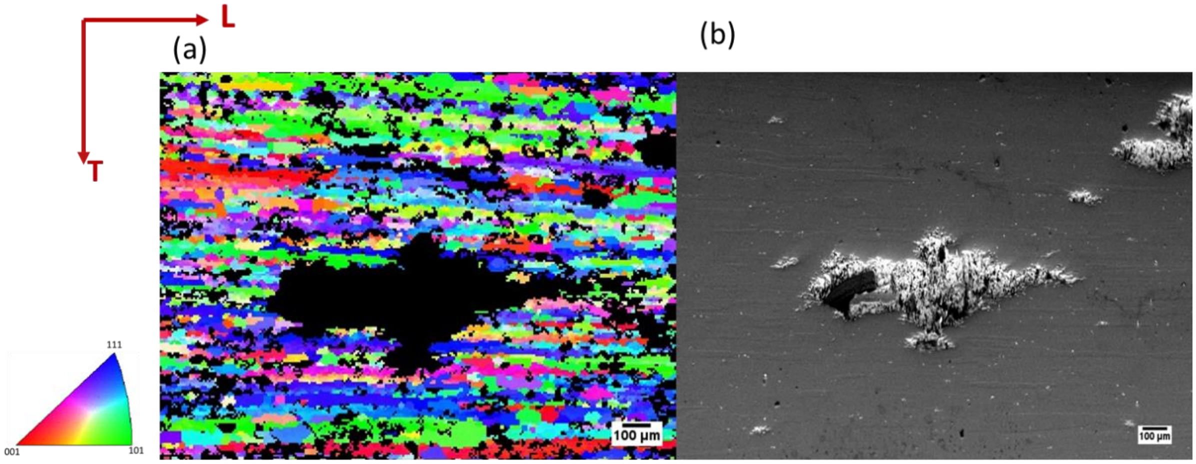

Figure 4.40. (a) EBSD map around a corrosion pit on the surface of AA7050-T7451 LT plane after 24 h of potentiostatic polarization at -0.73 V SCE in 0.5 M NaCl + $NaAlO_2$ pH 8 (b) Secondary electron micrograph of the fissure.

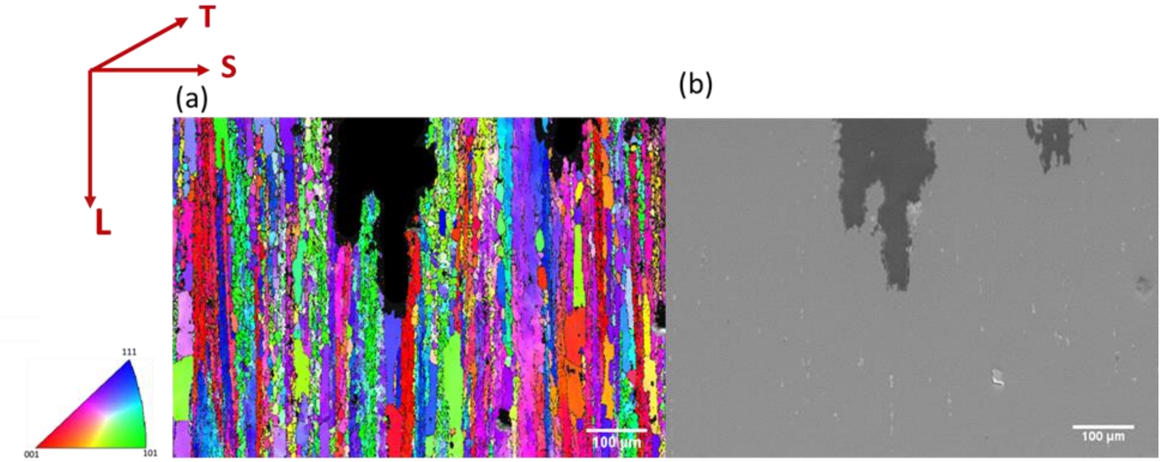

Figure 4.41. (a) EBSD map around a fissure in cross-section that formed in AA7050-T7451 TS plane after 100 h of potentiostatic polarization to -0.73 V SCE in 0.5 M NaCl + $NaAlO_2$ pH 8 (b) Secondary electron micrograph of the fissure.

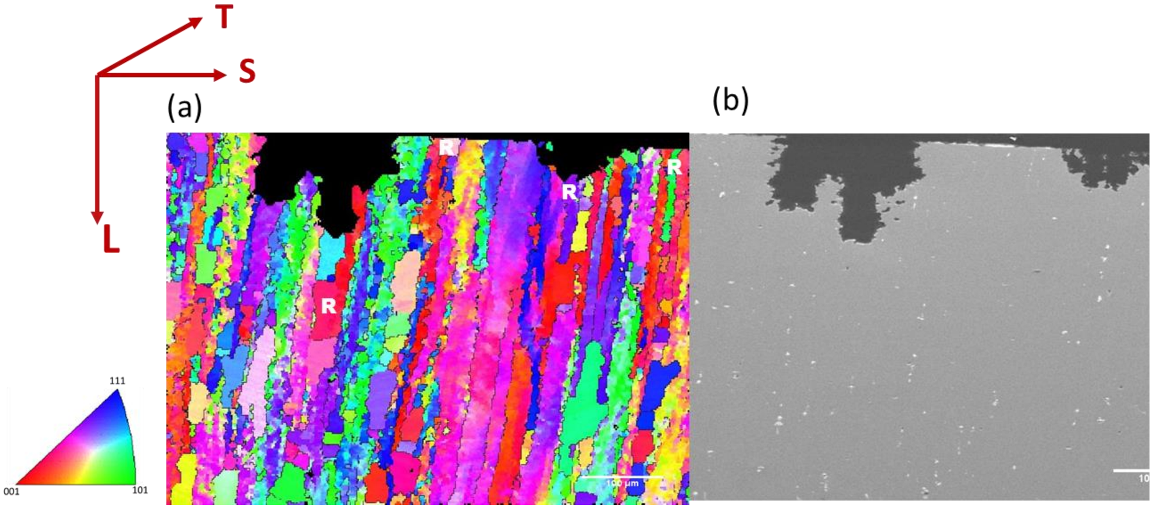

Figure 4.42. a) EBSD map around a fissure in cross-section that formed in AA7050-T7451 TS plane after 100 h of potentiostatic polarization to -0.73 V SCE in 0.5 M NaCl + $NaAlO_2$ pH 8 (b) Secondary electron micrograph of the fissure.

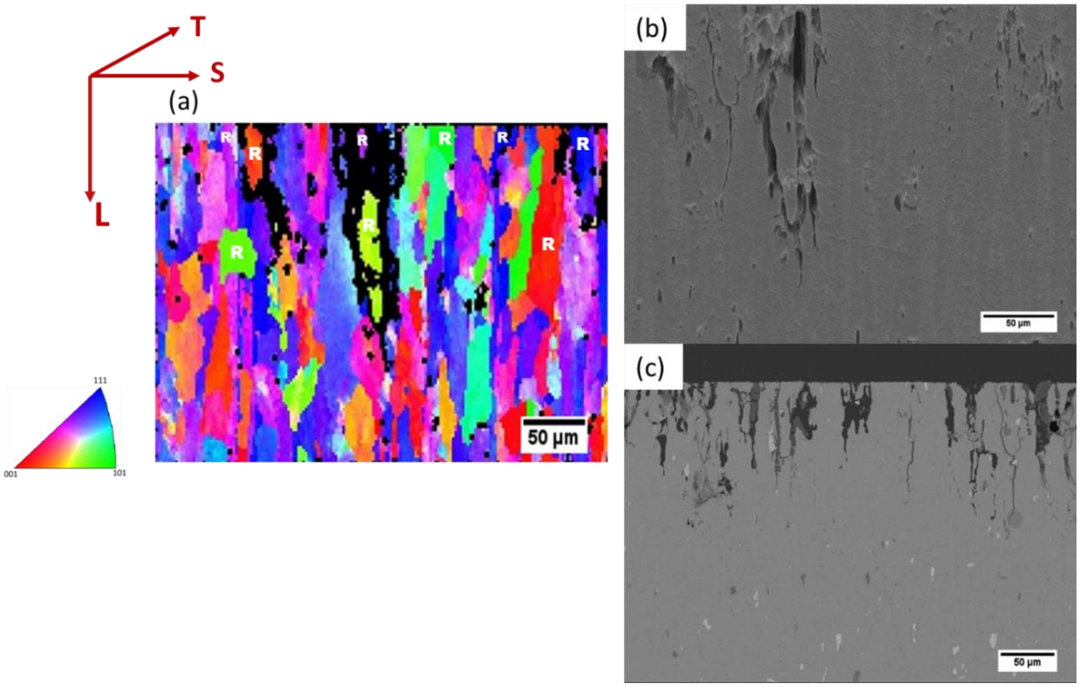

Figure 4.43. (a) EBSD map around a fissure in cross-section that formed in AA7050-T7451 TS plane after 72 h of potentiostatic polarization to -0.73 V SCE in 0.5 M NaCl + $AlCl_3$ pH 3 (b) Secondary electron micrograph of the fissure (c) low-mag micrograph of the IGC.

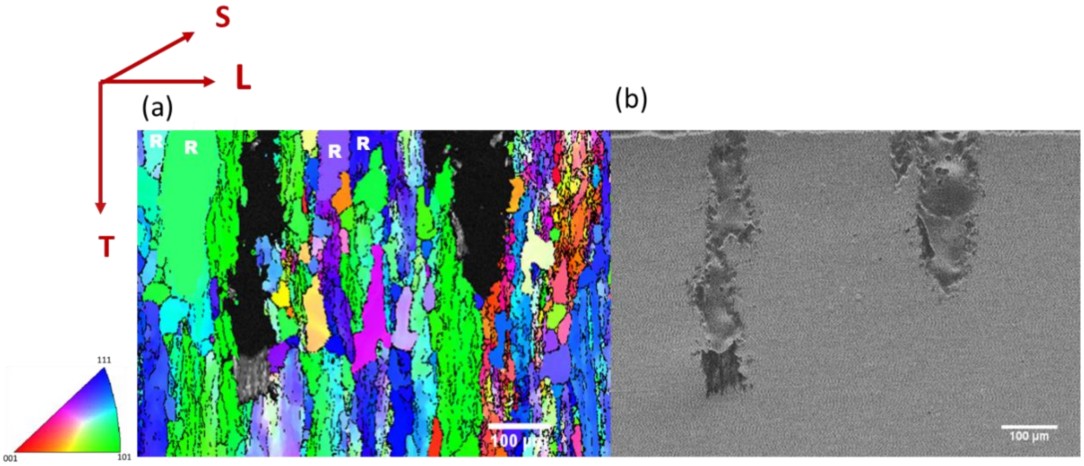

Figure 4.44. a) EBSD map around fissure in cross-section that formed in AA7050-T7451 SL plane after 100 h of galvanostatic polarization at 0.047 mA/cm2 in 0.5 M NaCl + $AlCl_3$ pH 4 (b) Secondary electron micrograph of the fissure.

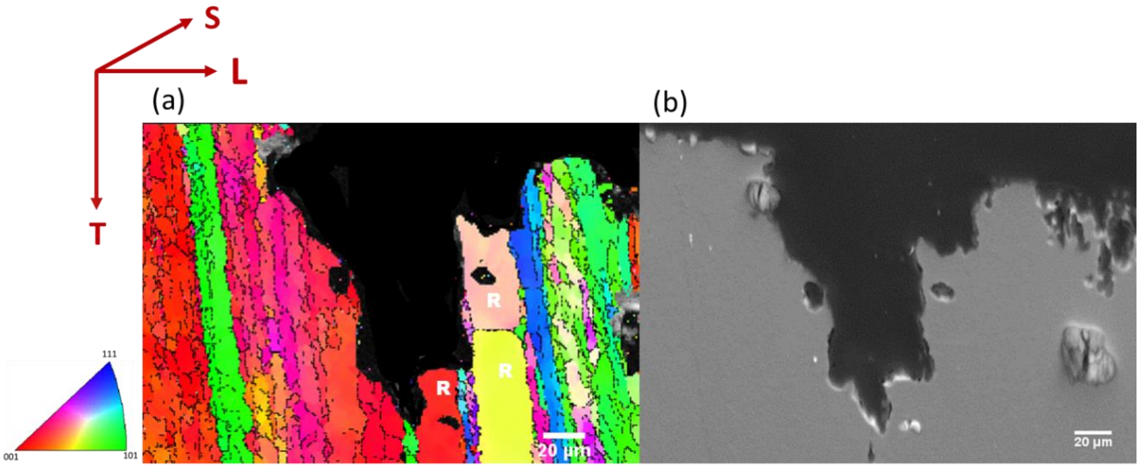

Figure 4.45. a) EBSD map around fissure in cross-section that formed in AA7050-T7451 SL plane after 72 h of potentiostatic polarization to E=- 0.73 V SCE in 0.5 M NaCl pH 5.5 (b) Secondary electron micrograph of the fissure.

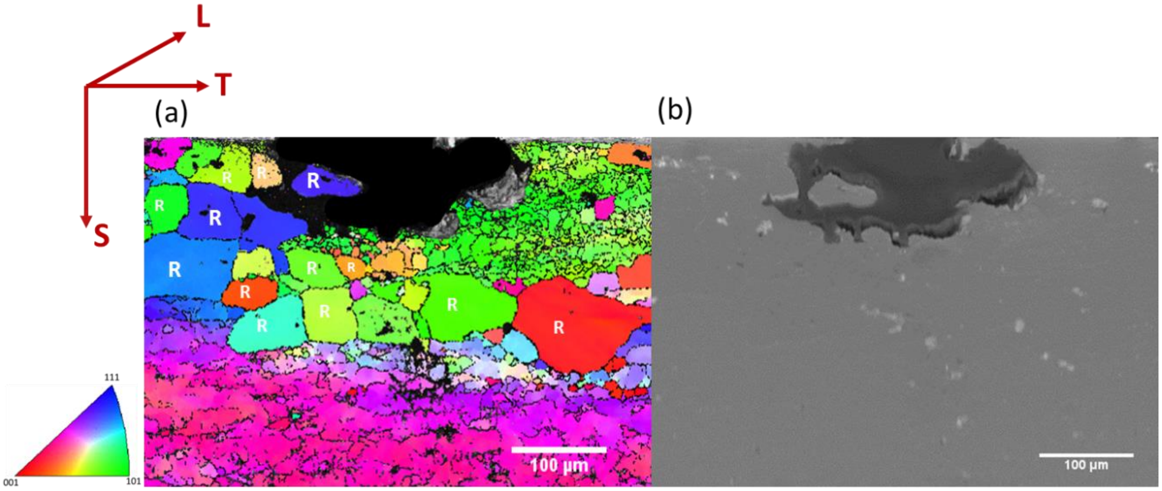

Figure 4.46. (a) EBSD map around fissure in cross-section formed in AA7050-T7451 LT after 504 h coupled with Type 316 stainless steel in 0.5 M NaCl pH:5 (b) Secondary electron micrograph of the fissure.

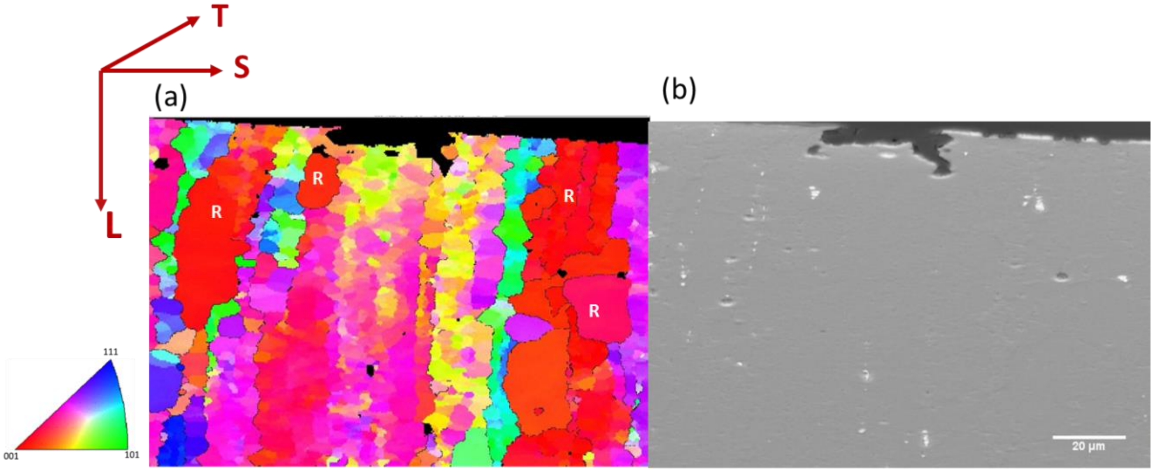

Figure 4.47. (a) EBSD map around fissure in cross-section formed in AA7050-T7451 TS after 144 h coupled with Type 316 stainless steel in 0.5 M NaCl pH 5 (b) Secondary electron micrograph of the fissure.

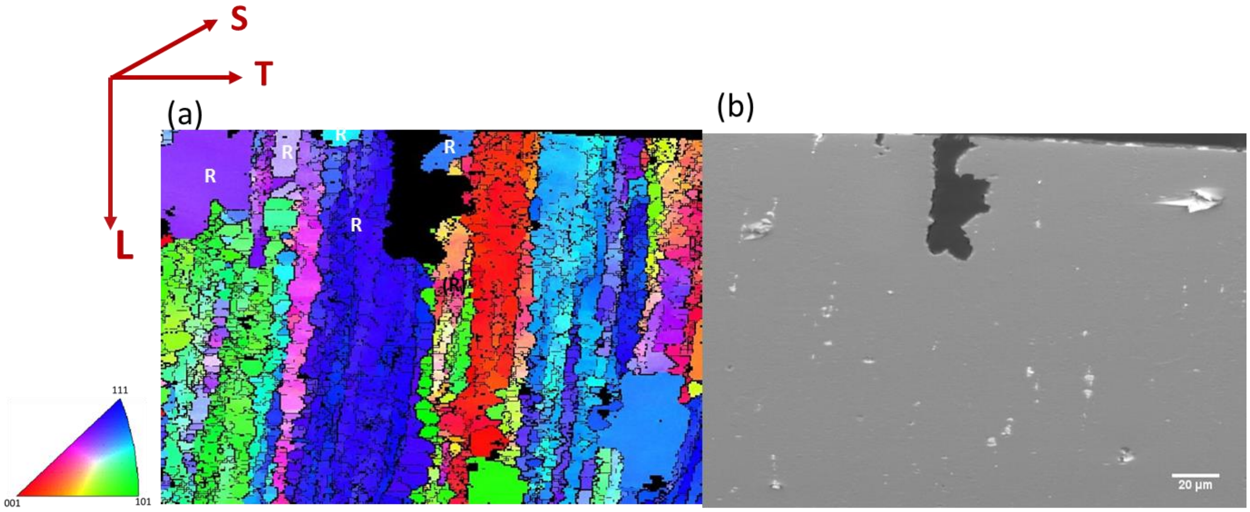

Figure 4.48. (a) EBSD map around a fissure in cross-section that formed in AA7050-T7451 TS plane after 100 h of potentiostatic polarization at E=-0.730 V SCE in 0.5 M NaCl + $NaAlO_2$ pH 8 (b) Secondary electron micrograph of the fissure.

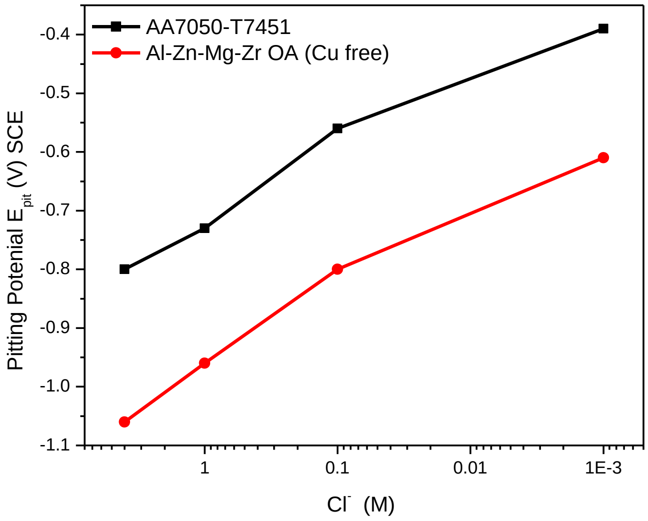

Figure 4.49. Pitting potential as a function of chloride concentration of AA7050-T7451 and the Cu depleted zone analog Al-Zn-Mg-Zr. The difference in potential reveals the potential window for IGC susceptibility.

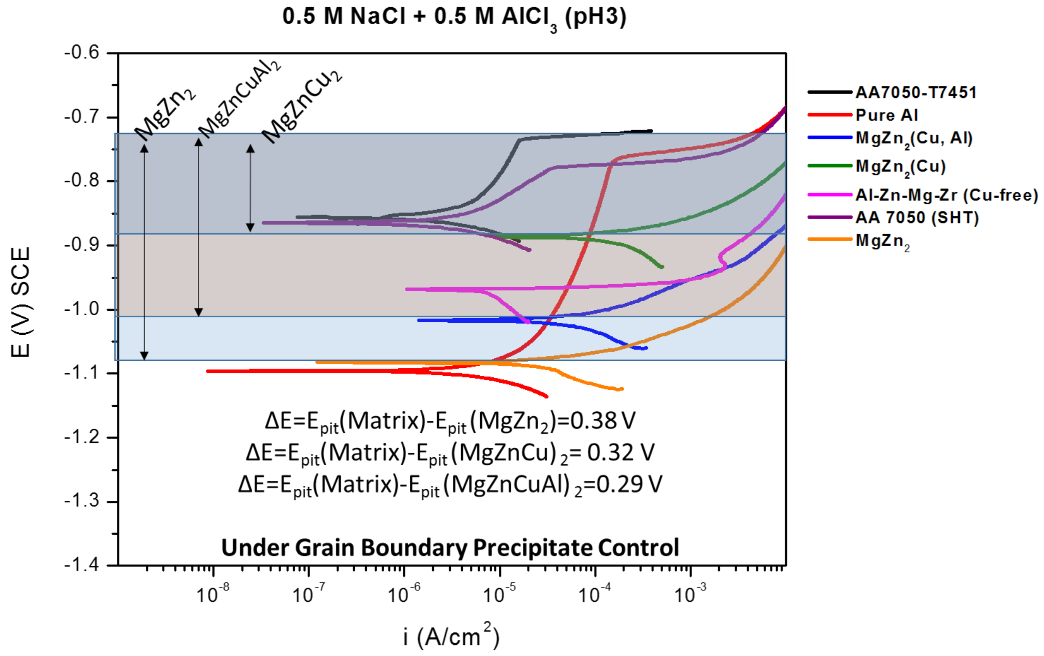

Figure 4.50. Anodic polarization scans of different phases in AA7050-T7451 including pure Al, AA7050 SHT/Q, MgZn2, Mg(ZnCuAl)$_2$ and the Cu-free Al-Zn-Mg-Zr alloy in 0.5 M NaCl + 0.5 M AlCl$_3$ pH 8. The highlighted regions show the window for IGC susceptibility, ΔE, between the AA7050-T7451 matrix and MgZn$_2$, Mg(ZnCu)$_2$ and Mg(ZnCuAl)$_2$.

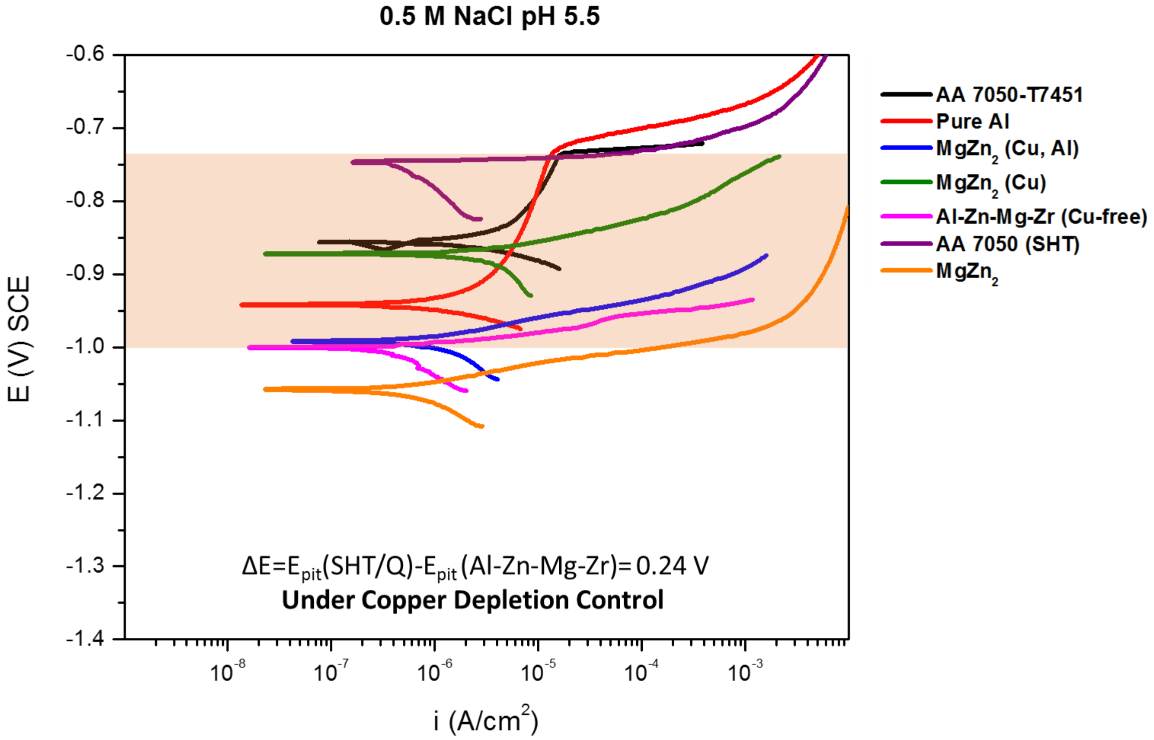

Figure 4.51. Anodic polarization scans of different phases in AA7050-T7451 including pure Al, AA7050 SHT/Q, $MgZn_2$, $Mg(ZnCuAl)_2$ and the Cu-free Al-Zn-Mg-Zr alloy in 0.5 M NaCl. The highlighted region shows the window for IGC susceptibility, ΔE, between the AA7050 SHT/Q matrix and the analog for maximum Cu depletion, Al-Zn-Mg-Zr.

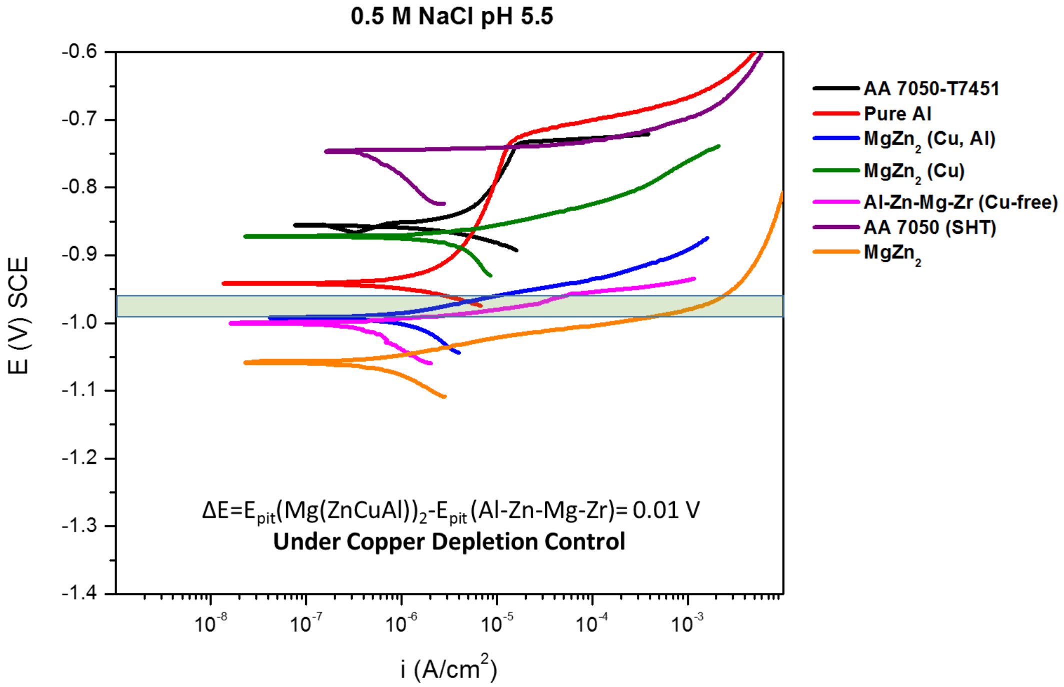

Figure 4.52. Anodic polarization scans of different phases in AA7050-T7451 including pure Al, AA7050 SHT/Q, $MgZn_2$, $Mg(ZnCuAl)_2$ and the Cu-free Al-Zn-Mg-Zr alloy in 0.5 M NaCl + 0.5 M $AlCl_3$ pH 8. The highlighted regions show the window for IGC susceptibility, ΔE, between the $Mg(ZnCuAl)_2$ and the Cu depleted analog, AL-Zn-Mg-Zr.

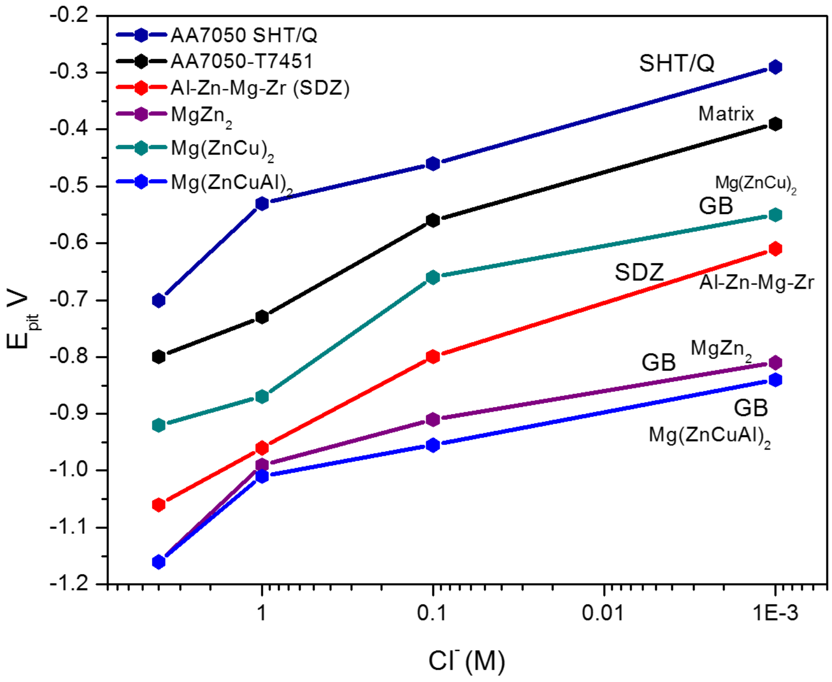

Figure 4.53. Pitting potential as a function of chloride concentration (pH 5.5) of the matrix and grain boundary analogs including AA7050-T7451, AA7050 SHT/Q, Al-Zn-Mg-Zr, $MgZn_2$ $Mg(ZnCu)_2$ and $Mg(ZnCuAl)_2$. The difference in potential between the matrix reveals the potential window for IGC susceptibility.

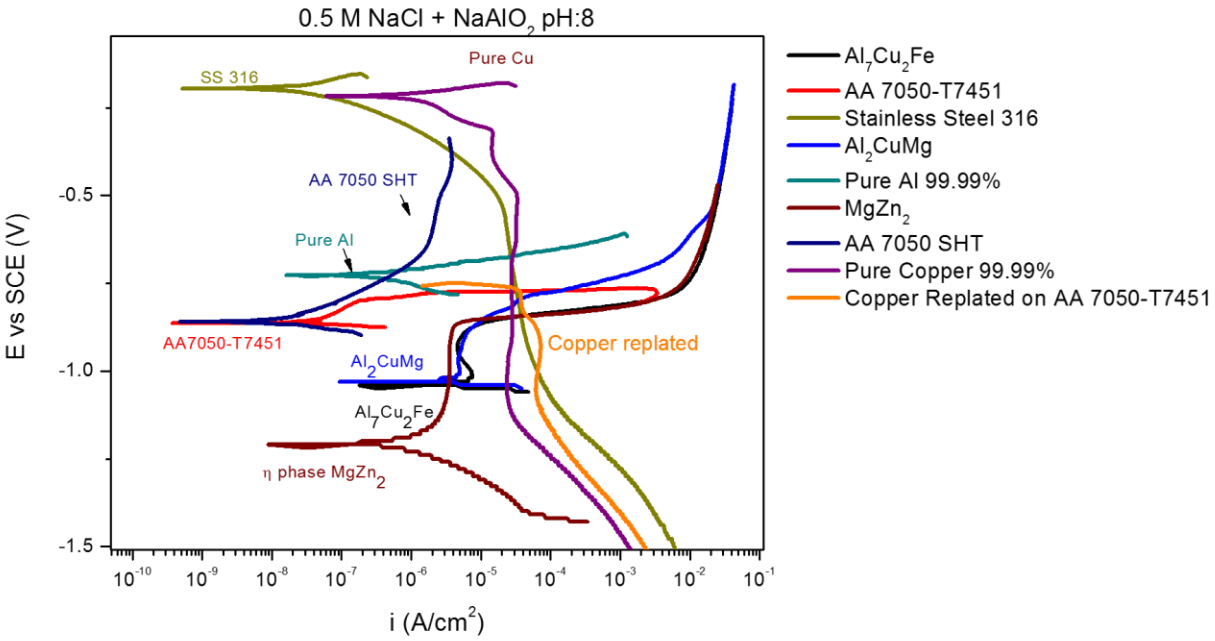

Figure 4.54. E-log i polarization behavior of AA 7050-T7451 coupled with Type 316 stainless steel and the different secondary phases including the different grain boundary region analogs.

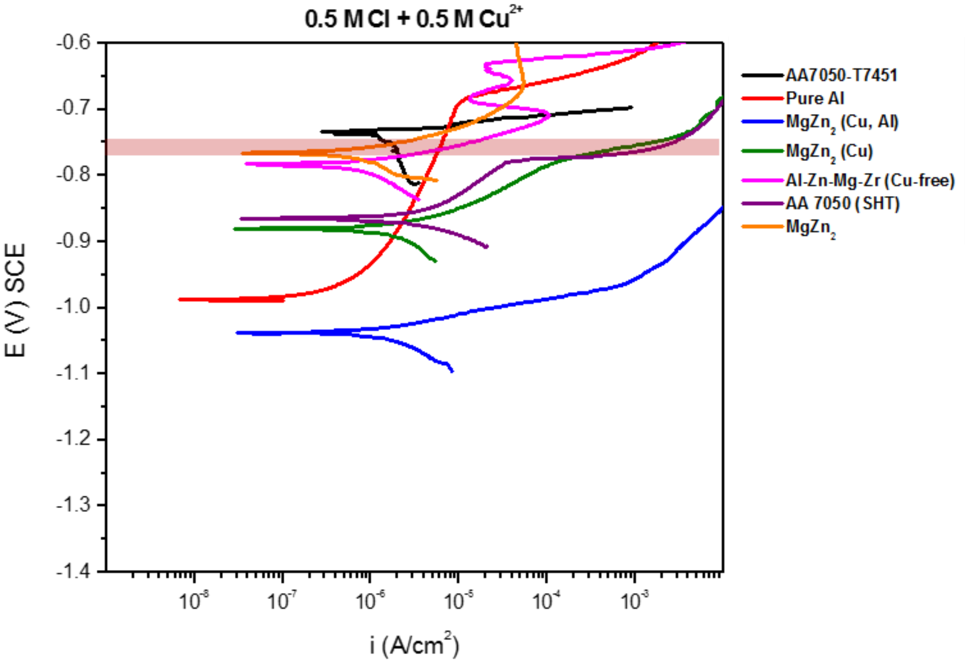

Figure 4.55. Anodic polarization scans of different phases in AA7050-T7451 including pure Al, AA7050 SHT/Q, $MgZn_2$, $Mg(ZnCuAl)_2$ and the Cu-free Al-Zn-Mg-Zr alloy in 0.5 M NaCl + 0.5 M Cu^{2+}. The highlighted regions show the window for IGC susceptibility, ΔE, between the AA7050-T7451 matrix and Al-Zn-Mg-Zr

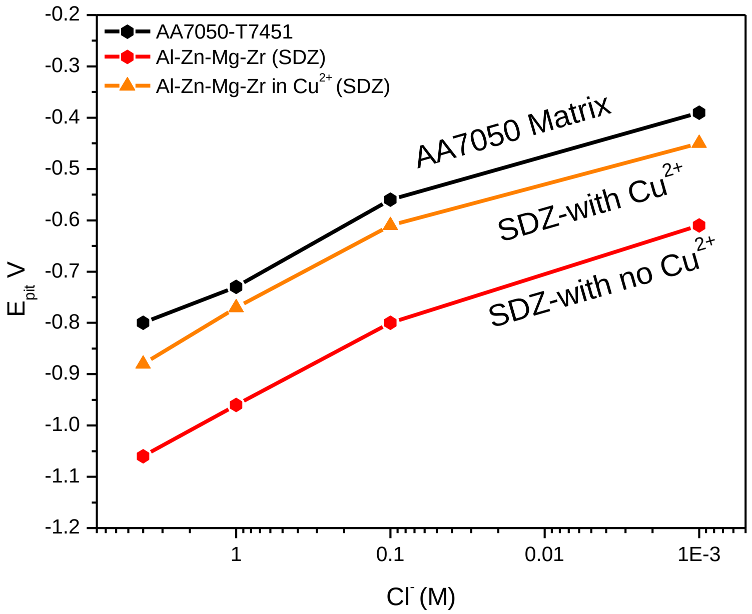

Figure 4.56. Pitting potential as a function of chloride concentration (pH 5.5) of the matrix and the Cu-depleted zone (Al-Zn-Mg-Ze). The difference in potential between the matrix reveals the potential window for IGC susceptibility.

5 Cathodic and Anodic Reaction Rate Measurements under Droplets and Thin Films with the use of Coupled Multi-electrode Arrays Constructed of AA7050-T7451 and Type 316 Stainless Steel

5.1 Abstract

Dissimilar metal coupled multi-electrode arrays (CMEAS) of AA7050-T7451 and Type 316 stainless steel were constructed to investigate galvanic coupling behavior under atmospheric conditions, represented by thin electrolyte films and wet/dry cycling. CMEAs in simple geometry provided baseline measurements. Furthermore, it was found that often pitting often occurred at random positions in the galvanic couple (i.e. not the closest position to stainless steel), this indicated that pitting corrosion in AA7050 can be attributed to heterogeneous microstructure. A CMEA arranged in a fastener geometry showed that corrosion current kinetics increased by over one order of magnitude under a static 70 µm thin film of NaCl relative to full immersion. Moreover, anodic currents were higher at the mouth of the fastener and deep inside the fastener. It was determined that under thin film conditions, the fastener geometry increased the net galvanic current density 10-fold.

The cathodic and anodic kinetics of AA7050-T7451 and Type 316 stainless steel were investigated under thin electrolyte films and droplets utilizing CMEAs consisting of 20 individual close packed electrodes coupled together to simulate a planar surface. The CMEA was embedded in an AA7050 panel in combination with a sintered Ag/AgCl electrode functioning as both the RE and CE. This CMEA enabled cathodic and anodic kinetics to be investigated as a function of material position, time and electrolyte shape. It was determined that cathodic kinetics increased by 4-fold under a 70 µm thin electrolyte film and 0.4 µL droplet (height=70 µm). Under droplet conditions, the AA7050 electrodes on the edge of the droplet experienced increased oxygen reduction cathodic kinetics compared to electrodes under the center of the droplet. Under a thin (70 µm) continuous film of electrolyte, all electrodes exhibited equal oxygen reduction cathodic kinetics as a function of position. In contrast, AA7050 anode sites formed randomly or at sites speculated to contain coarse constituent particles

Lastly, dissimilar metal galvanic CMEAs enabled understanding of galvanic corrosion rates under atmospheric conditions. Zero resistance ammeter for 24 hours showed that after 8 hours of exposure under a 70 µm thin film, increased kinetics were observed as localized corrosion initiation on AA7050-T7451 occurred. Selected preferential anodes were observed. This phenomenon was attributed to Cu-replating on the surface accompanied by distinct anodes observed switching polarity from anodic sites to cathodic sites. In this case, AA7050-T7451 electrodes contributed over 50% of the total net cathodic currents when coupled to Type 316 stainless steel.

Cyclic wet/dry exposures on the CMEA under 70 films increased the anodic charge density by one order of magnitude relative to exposures under constant 98% RH. During the wet/dry cycle, sharp current increases were observed on the onset of wetting and drying, which can be attributed to the high Cl-concentration of the droplet as the RH drops below 98%.

5.2 Introduction

7000 series aluminum alloys are widely used in the aerospace application due to their combination of high fracture toughness and resistance to stress corrosion cracking. [1,15,53,185,186]AA7050-T7451 is a precipitation-hardenable Al-Zn-Mg-Cu alloy that is susceptible to pitting, intergranular corrosion (IGC), and stress corrosion cracking (SCC). [26,37,40,42,124,139,140,142,168,186-188] The increased Cu contented in this alloy provides a good balance of strength and SCC resistance. [9] The T74 temper represents an overaging treatment designed to suppress IGC and SCC on grain boundaries.[4,5,12] AA7050-T7451 is often used in aerospace applications with Type 316 stainless steel fasteners, usually with a corrosion protection system in place. Unfortuntely, defects in corrosion protection are often enhanced at complex joining/fastener locations which trap electrolyte into tight crevices. This trapping of solution leads to occluded local environments where a galvanic cell is established between the aluminum alloy and a steel fastener causing acceleration of corrosion on AA7050-T7451.

AA7050-T7451 contains three types of second-phase particles: constituents, dispersoids, and strengthening precipitates. [9] The coarse constituent particles are Al_7Cu_2Fe β phase and Al_2CuMg S phase. These constituent particles form during solidification and are not dissolved during other processing steps. Constituent particles are found in clusters or stringers that often become aligned in parallel to the rolling axis. The strengthening precipitate is $MgZn_2$ and is active to the Al alloy matrix. [38] IGC is often attributed to heterogeneously nucleated $MgZn_2$ on grain boundaries and/or proximate Cu depletion. Grain boundary precipitation of η influences the corrosion behavior by locally depleting Zn, Mg, and Cu, enabling IGC or exfoliation corrosion. [13,22,23,38,64,189] Cu-rich intermetallic particles play a role in the local corrosion electrochemistry. Incongruent dissolution of Cu-rich phases may leave a Cu-rich surface that is cathodic to the matrix. [44] The presence of S phase (Al_2CuMg) is common in AA7050 due to the increased Mg and Cu alloy's content. [26] S phase is initially anodic but after dealloying occurs, the copper remnant turns into a high surface area cathode for oxygen reduction. [33,55] If the copper particles become mechanically detached, the copper particle will dissolve at its corrosion potential in solution and the copper ions so created will electrochemically replate on the surface of the bulk aluminum alloy. [45] This copper replating phenomenon can greatly affect the subsequent corrosion properties of the alloy. [27,31-33,45,55,56] The alloy Cu content is important, as the composition of both the matrix and $MgZn_2$ changes with aging, closing the potential window between $Mg(Cu)Zn_2$ and the matrix; this decreases IGC and exfoliation susceptibility. [13,52]

Aerospace applications structures typically experience atmospheric conditions. Atmospheric corrosion involves thin, discontinuous electrolytes and deliquescing conditions that differ from bulk full immersion electrolyte behavior[114,190-197]. When an aerospace metal is exposed in a marine environment, a thin layer of electrolyte forms on the top surface of the material due to the splash, rain water, and salt-enabled deliquescence, creating an ionic path between cathodic sites and anodic sites needed for the occurrence of corrosion. Atmospheric corrosion behavior differs from full immersion corrosion behavior in three main ways. Firstly, unlike bulk electrolyte environments atmospheric corrosion is not a continuous process due to the existence of wet/dry cycles attributed diurnal changes in relative humidity and temperature. Secondly, in atmospheric conditions the limited volume of electrolyte available leads to an accumulation of dissolved species leading to dramatic changes in the chemistry of solution. Lastly, in atmospheric corrosion conditions, specifically in variable humidity conditions, the electrolyte layer thickness and composition do not remain constant which may impact the mass-transfer limited electrochemical kinetics of the metal. These differences often can lead to an increase in corrosion kinetics by at least one order of magnitude.[192,194,196]

Conventional full immersion experimental techniques cannot be readily used to study atmospheric corrosion due to the challenges of placing reference electrode (RE) and counter electrodes (CE) into a thin film or droplet. Different approaches have been conducted to study atmospheric corrosion, including the use of the scanning Kelvin Probe to examine surface potentials under thin films [74,198], use of a Pt wire as CE [199], or a conventional SCE over a single working electrode [200]. Cao designed a experimental cell arrangement where the working electrode was inserted in the center of a Teflon cylinder fixed in the cell. The electrochemical cell was put on a horizontal stage allowing adjustment according to the water level. A Pt needle was used as the CE and a SCE as the RE. [201] Lyons developed a three-electrode cell by embedding the electrodes in an epoxy a well to submerge the reference electrode. [202] Policastro designed a dual electrode where a Pt wire counter electrode and a fritted Ag/AgCl reference electrode were inserted into a pulled pipette. [203] However, in all cases as the electrolyte layer thinned the current distribution across the working electrode became less uniform due to the location of the counter electrode. While a Pt electrode as the CE is valuable in full immersion environments, the reaction at the CE may alter the chemistry and pH of the droplet or thin film by producing O_2 and H^+ or OH^-, depending upon the direction of the polarization. These approaches also experience irregular ohmic drop due to the position of the reference electrode. While Liu obtained a correlation between the dependence of the cathodic current delivery capacity of the electrolyte film thickness using a rotating disk electrode,[204] there has still been an absence of literature on the current distribution under thin film and droplet exposures.

In other studies, open circuit corrosion has been studied in the atmosphere with coupled microelectrode arrays (CMEAs).[205-208] CMEAs are assortments of electrically isolated electrodes that are coupled together through zero resistance ammeters (ZRAs). This forms a galvanically coupled electrode surface that is designed to closely simulate a planar electrode surface but allows current behavior to be mapped and monitored over time in various environments or conditions. CMEAs can be designed to satisfy specific corrosion problems to replicate common real-life configurations in terms of material, geometry, physical arrangement and environment including thin film and full immersion conditions. CMEAs can be built with either nominally identical electrodes, to simulate large planar electrodes, or a combination of different electrode materials to simulate complex alloys with non-uniform composition and structure. The key advantage of the CMEA technique is that multiple electrochemical measurements are taken concurrently and instantaneously, enabling the measurement of real-time local corrosion processes that take place on an electrode surface. Budiansky demonstrated that far-spaced configurations, in contrast to close-packed configurations, can be optimized for high-throughput experiments capable of elucidating the statistical distributions of flaws under different variables and their effect on corrosion processes. [208] CMEAs have also been used to investigate the spreading of intergranular corrosion (IGC) by cooperative interactions where CMEAs were constructed from sensitized 304 stainless steel to understand the origins of persistent interactions in localized corrosion sites. [209] It was interesting to note that while IGC was limited to isolated electrodes, chemical and electric fields coupled across electrodes. King utilized CMEAs to study the effect of immersion conditions on the ‘galvanic throwing power’ of a magnesium-rich primer system for AA2024-T351 substrates. [206] Firstly, he was able to demonstrate that, for continuous, thin (500 µm microns) electrolyte layers, throwing power can extended across an entire 6 mm array. Secondly, for tortuous electrolyte geometries (resulting from drying or isolated droplet formation due to low initial salt deposition density), throwing power is limited by the reduction in length of ionically conductive pathways. Moreover, galvanic interaction just before drying increases significantly at the galvanic interface due to the highly concentration Cl at humilities just above the efflorescence RH. [206] Budiansky built an artificial crevice made from a 316 stainless steel CMEA and monitored the current through each individual electrode within the crevice. They were able to demonstrate for the first time that, in conditions where the potential inside and outside are equal, and pitting corrosion resistance is modest, corrosion initiates on the outside in a region adjacent to the crevice mouth and subsequently progresses inside. [208,209]

The foremost drawback of the technique is the use of model materials and the matching of micro-structural length scales with the length scale of the electrodes. The most valuable and key advantage of this technique is the capability for temporal and spatial measurements of electrochemical processes concurrently and instantaneously enabling the measurement of real-time processes that take place on an electrode surface. However in previous work mention above, CMEAs cannot be polarized without dealing with the need of both a reference and counter electrode that does not alter the environmental and operate at a very high surface/volume ratio.

Khullar presented the feasibility of using a sintered Ag/AgCl electrode as a combined RE and CE or polarization measurements in thin film solutions. [196] Supply of cathodic current from the AgCl CE results in the reduction of AgCl to Ag according to Equation 5.1:

$$AgCl + e^- \leftrightarrow Ag + Cl^- \qquad \text{Equation 5.1}$$

Each coulomb of AgCl provides 1 coulomb of electrons, but releases one coulomb of Cl^- into solution. Khullar showed that in the case of anodic polarization using a 12 mm diameter Ag/AgCl disc (area=113 mm^2) under a 0.254 mm thick solution layer, the concentration of chloride in the layer increased by less than 1%.[196] Commercially available Ag/AgCl electrodes can be used to preform polarization of WE without changing the pH of the electrolyte and with minimal ohmic drop. [196] Sintered Ag/AgCl electrodes have been shown to function up to currents of 1 mA with a relatively small polarization of approximately 10 mV, allowing them to be used simultaneously as RE and CE.

While CMEAs have been previously used to study corrosion behavior[206-208,210] they have been limited to ZRA measurements when conducting atmospheric studies due to difficulties positing and placing the RE as discussed above. In this work, two CMEAs were constructed of AA7050-T7451 and Type 316 stainless steel in combination with an embedded sintered Ag/AgCl electrode functioning as both the CE and RE in order to measure cathodic reaction rates under droplets and thin electrolyte films under various atmospheric conditions. This technique enabled assessment of atmospheric conditions under thin films and droplets with minimal ohmic resistance or alternation of solution chemistry. Current measurements taken concurrently and instantaneously enabled the measurement of real-time local corrosion processes that took place on the electrode surface. Additionally, an understanding of local current distribution and kinetic ORR rates on a simulated planar electrode as a function of electrode position and electrolyte thickness and geometry was developed

5.3 Objectives

In this work, CMEAs were utilized in different geometries to elucidate (1) galvanic current interactions of AA7050-T7451 and Type 316 stainless steel under thin films, droplets and atmospheric wet/dry cycles with different geometric arrays (2) current interactions on AA7050-T7451 under thin films and droplets with no galvanic couple (3) cathodic and anodic reaction rates under thin films using an sintered Ag/AgCl as the RE/CE in combination with CMEAs. CMEAs enabled assessment of atmospheric conditions under thin films and droplets with minimal ohmic resistance or alternation of solution chemistry. Current measurements taken concurrently and instantaneously facilitated the measurement of real-time local corrosion processes that take place on an electrode surface. Additionally, an understanding of local current interactions and kinetic ORR rates on simulated planar electrodes as a function of electrode position and electrolyte thickness and geometry can be developed.

5.4 Hypothesis

Based on preliminary results, it is hypothesized that under atmospheric conditions, the ORR cathodic reaction rates will increase due to faster diffusion rates of O_2 in a thin electrolyte layer. Furthermore, it is hypothesized that when AA7050-T7451 is coupled to Type 316 stainless steel, in atmospheric and full immersion conditions, AA7050-T7451 is able to provide strong cathodic reactions due to *S* phase (Al_2CuMg) and Cu-replating.

5.5 Experimental Methods

5.5.1 Materials

The material used in this study was machined from Al-Zn-Mg-Cu plate of 50 mm thickness provided by Alcoa. The microstructure has elongated grains in both the longitudinal (L) and long transverse (T) direction that are thinned in the short transverse (S), forming pancake-like grains. The grains in the L direction ranged from 22-1250 µm in length, while the grains in the T and S directions ranged from 15-265 µm and 12-112 µm, respectively. The 250 µm wire for the CMEA assembly was obtained from Ames Laboratory. The wire was drawn from a rod machined from the bulk plate of AA7050-T7451. Energy dispersive spectroscopy analysis was conducted on the AA7050-T7451 wire to ensure no microstructural changes occurred in the process (Figure 5.1). The Type 316 stainless steel wires (diameter 250 µm) used for this work was obtained from California Fine Wire Company. The Type 316 stainless steel wires were insulated with heavy polyamide. The compositions of AA7050-T7451 and Type 316 stainless steel can be found in Table 5.1. Between exposures CMEAs were freshly ground with successively finer grit SiC abrasive paper (LECO wet/dry 600, 800, 1200 grit) using water lubrication.

5.5.2 CMEA to Study Galvanic Current Interactions of AA7050-T7451 and Type 316 Stainless Steel

Two CMEAs were constructed in different geometries to understand the galvanic current interactions when AA7050-T7451 was coupled to Type 316 stainless steel. The first CMEA was constructed using an AA7050-T7451 rectangular panel (2.7 mm x 10.5 mm) with twenty holes (0.25 mm) spaced 0.15 mm apart. 6 AA7050-T7451 and 6 Type 316 stainless steel electrodes (diameter 0.25 mm) were embedded in the AA panel. Each individual electrode was coated with insulating varnish allowing electrodes to contact each other and the panel while ensuring electrical isolation. The AA panel of flush mounted electrodes was embedded in EpoThin epoxy. Figure 5.2 shows a schematic of this CMEA which is referred to as the flat galvanic CMEA. The second CMEA was constructed in a simulated fastener geometry where 22 AA7050 electrodes were embedded in an AA panel and 20 Type 316 stainless steel electrodes were embedded in a stainless steel panel and arranged in a fastener geometry. The CMEA simulated a fastener where the gap between the AA7050-T7451 and Type 316 stainless steel could be adjusted using plastic set screws in the epoxy in combination with shims of 100 µm or 500µm to set the gap. Thin films were placed on the AA7050-T7451 fastener mouth and wicked inside the fastener hole. In all cases, electrodes were separately addressable and constructed from electrically isolated wires of 0.25 mm diameter with a spacing of 0.15 mm. This CMEA is referred to as the geometric galvanic fastener CMEA. Figure 5.3 shows a schematic of the geometric fastener CMEA described.

The two CMEAs described were tested in 70 µm thin films of 0.6 M NaCl or 4 M NaCl. The metal panel was used in this study due to the high and more realistic wettability of Al and its oxides compared to epoxy. The equilibrium concentration of 0.6 M NaCl at 98% RH remains 0.6 M NaCl. At 95% RH the equilibrium concentration of 0.6 M NaCl is 1.4 M NaCl.

5.5.3 CMEA to Investigate Cathodic and Anodic Reaction Rates of AA7050-T7451 and Type 316 Stainless Steel under Thin films

Two other CMEAs were constructed with a sintered Ag/AgCl electrode to interrogate cathodic and anodic reaction rates under atmospheric conditions on selected CMEA electrodes. The first CMEA in this study was constructed using AA7050-T7451 rectangular panel (4.5 mm x 5.5 mm) with twenty holes (0.27 mm) surrounding one larger hole in the center (1 mm). Twenty

AA7050-T7451 wires with 0.25 mm diameter (area=0.004 mm), provided by AMES laboratory, were embedded in the drilled panel. A sintered Ag/AgCl electrode with 0.8 mm diameter was embedded in the larger hole in the center of the panel. Electrodes were spaced 0.125 mm apart and each individual flush mounted wire was coated with insulating varnish allowing electrodes to contact each other while ensuring electrical isolation. The panel of flush mounted electrodes was embedded in EpoThin epoxy. The second CMEA was constructed geometrically identical, however, half the AA7050-T7451 wires were replaced with ten Type 316 stainless steel electrodes to simulate a galvanic couple between the two metals. The metal panel was used in this study due to the high and more realistic wettability of Al and its oxides compared to epoxy. A schematic and optical micrograph of the CMEAs can be observed in in Figure 5.4.

The reusable 0.8 mm sintered Ag/AgCl electrodes were purchased from BioMed Products Inc. The charge capacity of the 0.8 mm diameter Ag/AgCl electrode was approximately 12 coulombs (C) determined by cathodic polarization scans of the Ag/AgCl electrode. The CMEAs that were constructed with a sintered Ag/AgCl were conducted only in 0.6 M NaCl to ensure the chloride concentration and potential was reproducible.

5.5.4 CMEA Exposure testing

CMEA exposures were conducted in a controlled relative humidly (RH) chamber set to 98% RH (Figure 5.5). The ribbon cable connections were made to the MMA901B via a feed through the wall cabinet. The RH controlled cabinet was instrumented with a RH and temperature logger and was controlled via the flow of humid air into the chamber. The humid air was produced using a humidifier filled with deionized water. Two electrolyte geometries were examined: droplets and thin films. Droplets were placed on the CMEA using a controlled area masked with polyamide tape and a micropipette to place a droplet of controlled volume on the surface. This enabled the height of the droplet to be estimated. Thin films were adjusted using plasma cleaning to increase wettability and polyamide tape to ensure a thin continuous layer of electrolyte. Wet/dry cycling was also conducted in the controlled relative humidly (RH) chamber. The wet/dry cycle was a 24 h exposure of 30 minutes at 95% RH and 3.5 hours at 30% RH. Wet/dry cycles were tested at 30°C or 50°C. In one case, a longer 48 h wet/dry cycle was conducted. The cycle was 4 hours at 25% RH and 8 hours at 95% RH at a temperature of 50°C.

Figure 5.6 shows a plot of salt concentration as a function of relative humidity for NaCl. The initial electrolyte concentration and RH used were chosen to avoid size change of the electrolyte droplet deposited on the material surface. At 98% RH the equilibrium salt concentration for NaCl is 0.6 M NaCl.

5.5.5 Electrochemical Methods

A Scribner Associates (Pinehurst, NC) model MMA910B multi-electrode analyzer was used to provide a graphical interface and data acquisition of each microelectrode current. The MMA 910B is capable of galvanically coupling and measuring up to 100 working electrode current channels and contains an individual zero resistance ammeter (ZRA) on each current channel with a measureable current range of 3.3 nA to 100 µA per channel. The minimum total current limit of the MMA 910B is approximately 1×10^{-9} A and the maximum is 2×10^{-4} A. Due to the cross-sectional area of the flush-mounted microelectrodes the minimum and maximum measured current densities are 2×10^{-6} A/cm^2 and 2×10^{-1} A/cm^2 for each electrode. In each color map, dark red indicates an anodic current $\geq 1 \times 10^{-5}$ A/cm^2 and dark blue indicates a cathodic current of $\leq -1 \times 10^{-5}$ A/cm^2. Microelectrodes which are freely corroding pass a net current of zero and are color coded white.

A Gamry Reference 600 potentiostat was used to conduct the cathodic and anodic potentiodynamic polarization on the CMEAs with a scan rate of 1 mV/s, utilizing the sintered Ag/AgCl electrode as both the CE and RE. In many cases, cathodic polarization was conducted on a single AA7050-T7451 electrode after exposures. Immediately after a ZRA exposures, the CMEA was disconnected from the MMA and one single AA7050-T7451 electrode, showing fast cathodic kinetics relative to other electrodes, was connected to the Gamry Reference 600. Cathodic potentiodynamic polarization was conducted on the electrode at 5 mV/s in order to interrogate the electrode for cathodic kinetics.

5.5.6 Cottrell Diffusion and ORR Theory Experimental Methods

To gain insight on cathodic reactions in atmospheric droplets. A study on the ORR kinetics under full immersion and thin films was conducted on a 99.99% pure Cu single wire (250 µm) embedded in Cu button (diameter 1 cm^2) with a sintered Ag/AgCl (diameter 0.8 mm) electrode placed into the center of the button and flush mounted with epoxy. A schematic of the Cu single electode setup can be observed in Figure 5.7. In this set of experiments, OCP stepped to a cathodic constant potential at -0.8 V SCE was conducted under full immersion and under 0.4 µL droplet of 0.6 M NaCl. The constant potential was in the ORR regime of Cu. These results was compared to Cottrell diffusion for planar and micro-electrodes cathodic current density.

The expression for the current time dependence at constant potential of a planar electrode in full immersion can be derived from Fick's second law of diffusion. The expression is given in Equation 5.2.

$$j = nF(\frac{D}{\pi})^{0.5}\ x\ \frac{C_{bulk}}{t^{0.5}} \qquad \text{Equation 5.2}$$

Where j is the flux of electroactive material at the surface (A/cm^2), n is the number of electrons transferred in ORR (4), D is the diffusion coefficient of O_2 (10^{-5} or 10^{-6} cm^2/s), C_{bulk} is the bulk concentration of O_2 (8 ppm), and t is time (seconds). Under the circumstances where the solution is valid j vs t $^{1/2}$ will be linear during constant potential holds. The slope of this line enables the determination of diffusion coefficient D.

Micro-electrodes transfer from linear to spherical diffusion at increasing time of measurements. The diffusion layer thickness δ, for a curved surface in which the radius of curvature, r_0 is much larger than δ can be calculated using Equation 5.2. However, if the radius of curvature decreases the diffusion equation for a spherical geometry must be given by:

$$j = nFDC_{bulk}\left[\left(\frac{1}{\pi D t^{0.5}}\right) + \frac{1}{r_0}\right] \qquad \text{Equation 5.3}$$

These equations were used to assess controlling factors in constant potential holds which simulate galvanic couples between Type 316 stainless steel and AA7050-T7451.

5.6 Results

5.6.1 Galvanic Current Interactions under Thin Electrolyte NaCl Films in a Geometrically Flat Galvanic Couple between AA7050-T7451 and Type 316 Stainless Steel

The flat geometric CMEA, shown in Figure 5.2, provided a reference point for a geometrically simple galvanic couple between AA7050-T7451 and Type 316 stainless steel. The flat geometric CMEA consisted of 6 AA7050-T7451 electrodes and 6 Type 316 stainless steel electrodes. The CMEA was exposed to different atmospheric conditions to understand the effect of (a) water layer thickness (2) chloride concentration (3) wet/dry cycling at 30°C (4) wet/dry cycling at 50°C and (5) 48 hour wet/dry cycling at 50°C.

The ZRA net galvanic current density for the flat geometric CMEA in 0.6 M NaCl full immersion can be observed in Figure 5.8. Two strong AA7050 anodes prevailed over the 24 hour exposure A5 and A6. These two electrodes were positioned closest to the stainless steel electrodes. However, in other identical exposures, this was not always the case. 100% of the net anodic charge was contributed from A5 and A6. The rest of the other AA7050 electrodes had a net cathodic current. Figure 5.9 shows the color maps after every 10,000 s in the exposure. Initially, all AA7050 electrodes were red (indicating anodic current) and all the Type 316 stainless steel electrodes were blue (indicated cathodic current). After 20,000 s, electrodes A1-A4 switched from net anodic to net cathodic behavior. The total net anodic charge density over the 24 h exposure was 0.89 C/cm^2. The cathodic charge density was equal but opposite in sign. In Chapter 3, ZRA corrosion measurements (Pt mesh and SCE) on planar electrodes of AA7050-T7451 coupled to Type 316 stainless for 24 h in 0.6 M NaCl showed that the net anodic charge density was 0.84 C/cm^2.

Figure 5.10 shows the ZRA net galvanic current density over a 24 h exposure under a 70 µm continuous thin film of 0.6 M NaCl at 98% RH. It can be observed that two anodes prevailed throughout the 24 hour exposure, A4 and A5. The charge density A4 and A5 was 16.3 C/cm^2 and 0.8 C/cm^2. Electrode A4 accounted for 95% of the total net anodic current observed. The cathodic electrodes all maintained analogous current values through the 24 h exposure. The color maps in Figure 5.11 show that at the start of the exposure all AA7050 electrodes where initially anodic (red). However, by 10,000 s four of the six AA7050 electrodes switched from anodic to cathodic current (blue). Therefore, by the end of the 24 exposure under a 70 µm thin film, 85% of the electrodes were supporting ORR sustaining the two anodic sites. The total net anodic charge density over the 24 h exposure was 16.2 C/cm^2. The cathodic charge density was equal but opposite in sign. Under a 70 µm thin film, the charge density was increased by over one order of magnitude when compared to full immersion conditions. In fact the current density increased 15-fold.

To examine to effect of chloride concentration, a 24 h exposure under a 70 µm continuous thin film of 4 M NaCl at 98% RH was conducted. 3 anodic sites prevailed throughout the 24 hour exposure, A2, A3, and A5 (Figure 5.12). A3 was the strongest anodic site accounting for 87% of the total net anodic current. After about 20 hours, the anodic current of electrode A3 was reduced while the anodic current of A5 increased. Interestingly, AA7050 electrode A2 sharply switched from anodic current to the strongest cathodic current for the remaining 8 hours. The net charge density of A2 after the 24 h exposure was -1.27 C/cm^2. AA7050 electrodes contributed approximately 20% of the total net cathodic current density. Figure 5.13 shows the color map after every 10,000 s. After 50,000 s, A2 switched from a red anodic site to the strongest blue, cathodic site. The total net anodic charge density over the 24 h exposure was 19 C/cm^2. The cathodic charge density was equal but opposite in sign. The 4 M NaCl exposure exhibited a faster corrosion rate by 18% over the 0.6 M NaCl exposure, furthermore, Cu-replating occurred due to this increase in corrosion rate.

Figure 5.14 shows the net ZRA current under a 24 h exposure under a thicker film of 500 µm of 0.6 M NaCl at 98% RH. During the 24 hour exposure, three anodic sites prevailed, A2, A6, and A4. The net anodic charge density of A2, A6, and A4 were 1.47 C, 2.10, and 9.3 C/cm^2, respectively. After 4 hours of exposure, the anodic current density of A6 and A2 diminished to near zero and A4 increased and remained the dominant anodic site for the remaining 20 h. Under the 500 µm thin film, 50% of the AA7050 electrodes were anodic sites. The total net anodic charge density over the 24 h exposure was 11.9 C/cm^2. Figure 5.15 shows the color maps over the 24 hour exposure. Initially currents were minimal but increased within the first 3 hours of exposure. The cathodic charge density was equal but opposite in sign. The exposure under a 500 µm thin film experienced a lower charge density by 4.3 C/cm^2 relative to the exposure under a 70 µm thin film.

5.6.2 Galvanic Current Interaction during Wet/Dry Cycling under Thin Electrolyte NaCl Films in a Geometrically Flat Galvanic Couple between AA7050-T7451 and Type 316 Stainless Steel

The first cycle was operated at 30 minutes near 95% RH followed by 3.5 hours near 30% RH for 24 h. The cycle was operated at 30°C, which is slightly above room temperature. The flat geometric CMEA was exposed to a 70 µm thin film. Figure 5.16 shows the net ZRA current density over the 24 hour exposure. The yellow shading indicated periods of drying. Part (b) shows the same plot without the RH% cycle data. Under cyclic conditions, current spikes occurred during periods of wetting. A6 was the strongest anodic contributor, providing 61% of the anodic net current. Other strong anodic sites include A2 and A5. Under cyclic conditions only 1 of the 6 AA7050 electrodes had a negative net current over the duration of the 24 h, A1. Figure 5.17 shows the color maps in relation to the wet/dry cycle. Stronger currents are depicted in darker colors. It can be observed here that the strongest currents occurred on the onset of wetting. This can be attributed to higher concentrations of Cl$^-$ when the RH was below 98%. The anodic charge associated with the wet/dry cycling at 30°C after 24 h was 37.1 C/cm^2. This was over twice as high as the exposure under a 70 µm thin film at 98% RH with no cycling.

Figure 5.18 shows the ZRA current measurements for the same wet/dry cycle but with a higher chloride concentrated 70 µm thin film of 4 M NaCl. 5 anodic sites prevailed over the 24 h cycle test. The strongest anodic site, A5 contributed less than 50% of the total anodic charge. A1, A5 and A6 contributed the rest of the anodic current. AA7050 electrode A5 experienced the most intense current spikes. Interestingly, A3 switched between anodic and cathodic currents throughout the exposure. Initially, A3 was anodic and switched polarity during the first dry cycle after 30 minutes, and became a cathodic site for the next 15 hours. On the onset of the wet cycle, A3 became an anodic site and continued to get stronger during wetting/drying cycles. Currents were more aggressive on the onset of wetting and on the onset of drying (Figure 5.19). The total net anodic charge density over the 24 h exposure was 48.1 C/cm^2. The cathodic charge density was equal but opposite in sign. The anodic charge density was 50% more than in the 98% RH 4 M NaCl 70 µm exposure.

A 24 h wet/dry cycle of 30 minutes near 95% RH followed by 3.5 hours near 30% RH for 24 h at 50°C was conducted on the flat CMEA (Figure 5.20). Five anodic sites prevailed over the exposure. A2 was the strongest anode supplying 39% of the anodic current. Anodic and cathodic current spikes were observed immediately at the end of dry cycle as the RH began climbing to the wet cycle. Interestingly, the strongest cathode was AA7050 electrode A1 supplying 90% of the total net cathodic charge. The cathodic current of A1 became more negative during wetting periods supplying the cathodic reaction for anodic sites A2-A6. Figure 5.21 shows the color maps relative to the wet/dry cycles. It can be observed that at 4 hours, as the dry cycle ended and the RH began to climb A1 was a strong cathodic site (blue) supplying the current for A2, A3 and A4 and A5 which were all dark red indicating strong anodic sites. While the six stainless steel electrodes were also cathodic sites, the SS electrodes only supplied 10% of the total cathodic current. The total anodic charge over 24 h for the 0.6 M NaCl 70 µm thin film wet/dry cycle was 46.7 C/cm^2.

The last wet/dry cycle exposure on the flat geometric array was a 48 h wet/dry cycle at 50°C. In this cycle test, wet/dry cycles were longer with 4 hours near 20% RH and 6 hours near 95% RH. Figure 5.22 shows the net ZRA current measured for this exposure. Under the 70 µm thin film of 0.6 M NaCl, five anodic sites prevailed. The strongest anodic sites were A5 and A6 which contributed 36% and 41% of the total net anodic current. As observed in previous exposures, current spikes occurred as the dry cycling ended and the wet cycle began. After 12 hours of exposure AA7050 electrode A1 became the strongest cathodic site and remained the primary cathode until 28 hours, supplying over 90% of the cathodic current. After 28 hours a decrease in anodic and cathodic current for the remainder of the 48 hours was observed. Figure 5.23 shows the color maps correlating with the wet/dry cycles. This further suggested that the strongest currents occurred between 12 and 24 hours as AA7050 electrode A1 switched polarity from an anodic site to a primary cathodic site.

5.6.3 Current Interactions under Thin Film Electrolytes in a Dissimilar Metal Fastener Geometry

The CMEA arranged in a fastener geometry shown in Figure 5.3, was exposed under thin films of various thicknesses and other atmospheric conditions such as wet/dry cycling. As a reference point, Figure 5.24 shows a 10,000 s exposure in 0.6 M NaCl full immersion with a 100 µm gap between the AA7050-T7451 and Type 316 stainless steel. It can be observed that AA7050 electrode A11 was the dominant anodic site throughout the exposure. A11 was located inside the crevice near the mouth. Figure 5.25 shows the color maps at different scales allowing the electrode with the highest currents to be distinguished. It can be observed that in this exposure, higher currents were observed at the mouth of the fastener and at the bottom of the fastener. The dominant cathode was observed at the bottom of the Type 316 stainless steel fastener. The middle region of the crevice had the slowest kinetics. The net anodic charge density over the 10,000 s was 0.71 C/cm^2.

Figure 5.26 shows the ZRA current measurements over 10,000 s under a 70 µm thin film of 0.6 M NaCl with a 100 µm gap between the AA7050-T7451 and Type 316 stainless steel. Under a thin film, many more anodic and cathodic sites were active than in full immersion. The strongest anodic AA7050 sites were A8 and A22. A8 corresponds with the electrode at the edge of the mouth of the fastener and A22 corresponds to the last electrode in the bottom of the crevice. The stainless steel rivet had the highest cathodic currents inside the fastener. In general, currents were higher at the mouth and at the bottom of the crevice (Figure 5.27). The highest anodic and cathodic currents were seen at the edge of mouth of the fastener. The net anodic charge density over the 10,000 s was 7.12 C/cm^2. The anodic charge density was higher by one order of magnitude under a thin film than in full immersion. Moreover, the fastener geometry resulted in currents 4 times higher than in the geometric flat array.

The CMEA arranged in a fastener geometry was also exposed under a thicker film of height 500 µm (Figure 5.28). In this exposure, the highest anodic currents were observed on AA7050 electrodes A2, A4, A7, A9, A10, and A11. These electrodes were located at the mouth of the crevice (Figure 5.29). These anodic sites were supported by three strong cathodic sites inside the crevice. The net anodic charge density over the 10,000 s was 5.9 C/cm^2. Overall, lower currents were observed under 500 µm than in under a 70 µm thin film of 0.6 M NaCl.

Figure 5.30 shows the ZRA measured current over 10,000 s under a 70 µm thin film, however, the gap was set to 500 µm. In this exposure, the highest anodic currents were observed on AA7050 electrodes A1, A2, A6, A7 and A8, initially. Interestingly, after 4000 s A22, located at the bottom of the crevice began to increase in anodic current. This was due to AA7050 electrode A2 switching from a strong anodic site to a strong cathodic site. This can be likely attributed to S-phase dealloying or Cu-replating on the surface. The mouth of the crevice had the highest anodic currents (Figure 5.31). Moreover, AA7050 electrodes inside the crevice were mostly cathodic sites. This may be attributed to restricted access of O_2 inside the crevice. The net anodic charge density over the 10,000 s was 5.6 C/cm^2. Overall, lower currents were observed with a larger gap of 500 µm when compared to the exposure with a gap of ~100 µm.

The fastener array was also exposed for a longer period of time, 24 h, under an initially 70 µm thin film at 98% RH. The gap between AA7050 and Type 316 stainless steel was 100 µm. Figure 5.32 shows that initially, A1-A6, located at the top of the fastener, and A20-22, located at the bottom of the fastener, all had the highest anodic currents. A17 and A20 had the highest anodic currents throughout the exposure. For the first 8 hours, the highest anodic currents were observed at the top and bottom of the fastener. However, after 8 hours, the mouth of the fastener became slightly cathodic and the electrodes inside the fastener became stronger anodic sites. Figure 5.33 shows that the dominant cathode was S17. However, most of the Type 316 stainless steel electrodes had comparable cathodic currents. The net anodic charge density over the 24 h exposure was 59.12 C/cm^2. The net anodic charge of the fastener geometry was 3.5 times larger than the flat geometric CMEA exposure under the same conditions.

The CMEA arranged in a fastener geometry was exposed under 24 h wet/dry cycle, with a 70 µm thin film of 0.6 M NaCl. The cycle test was operated at 30 minutes near 95% RH followed by 3.5 hours near 30% RH for 24 h at 30°C, which is slightly above room temperature. ZRA current measurements can be observed in Figure 5.34. Current increase was observed during wet cycles. A1 was the dominant anode throughout the exposure. The highest currents were observed at the bottom of the fastener (Figure 5.35). During the wet/dry cycles many polarity switches were observed. Electrodes at the mouth of the electrode often switched from anodic sites to cathodic sites (Figure 5.36) throughout the cycle. The net anodic charge density over the 24 h was 72.4 C/cm^2. The net anodic charge of the cyclic environment was slightly larger than the same exposure under constant 98% RH.

5.6.4 CMEA Charge Analysis Comparison for the Geometrically Flat CMEA and the CMEA Arranged in a Fastener Geometry under Various Atmospheric Conditions Compared to Full Immersion

The geometrically flat CMEA was tested under seven atmospheric conditions and compared to full immersion on both the CMEA and a planar three electrode flat cell setup (Pt mesh and SCE). Figure 5.37 shows a comparison of the net anodic charge density from each exposure. The charge density for the geometric flat CMEA was determined over 24 hour exposure, unless noted otherwise. Under full immersion (0.6 M NaCl) conditions, the net anodic charge density on the geometrically flat CMEA was 0.89 C/cm^2. Under full immersion, on planar electrodes of galvanically coupled AA7050-T7451 and Type 316 stainless steel in a flat cell, the net anodic current was 0.84 C/cm^2. This shows good agreement. Under a 70 µm thin film at 98% RH, the anodic charge density was 16.2 C/cm^2. Furthermore, under a 70 µm thin film of 4 M NaCl the charge density was 19.1 C/cm^2. This shows that under thin films, the galvanic corrosion rate was increased by over one order of magnitude. Under a thicker thin film, 500 µm, (0.6 M NaCl) the net anodic charge density was 11.9 C/cm^2, denoting that under a thicker film the corrosion rate was reduced by nearly 25% compared to a 70 µm thin film. However, under a 500 µm thin film, the corrosion rate was less than one magnitude higher than full immersion. Under cyclic wet/dry environments the corrosion rate nearly doubled compared to thin film exposure at constant RH. After a wet/dry cyclic exposure (0.6 M NaCl) at 30°C and 50°C the charge density was 37.1 C/cm^2 and 46.7 C/cm^2. After a wet/dry cyclic exposure under 70 µm thin film of 4 M NaCl the charge density was 48.2 C/cm^2. Lastly, a 48 h wet/dry cycle at 50 °C with longer wet/dry period had a charge density of 158 C/cm^2.

The CMEA arranged in a fastener geometry was exposed to four atmospheric conditions for 10,000 s and compared to full immersion on both the CMEA and a planar three electrode flat cell setup. The CMEA was also exposed to 24 h exposures at constant 98% RH and cyclic environments. Figure 5.38 shows the charge density summary plots for the fastener 10,000 s exposure. Under full immersion conditions, 0.6 M NaCl, the net anodic charge density was 0.71 C/cm^2. For comparison purposes, the charge density after 10,000 s on the geometric flat CMEA under a 70 µm thin film was extrapolated from the 24 h exposure from Figure 5.10. The charge density over 10,000 s for the flat geometric CMEA was 1.87 C/cm^2. Under the same conditions, the fastener type CMEA had a charge density of 7.1 C/cm^2. This shows the fastener geometry contributed to an increase in corrosion rate by almost 4-fold. Under a thicker film of 500 µm, the charge density was slightly lower than the 70 µm exposure, 5.9 C/cm^2. For all other exposures, the gap between AA7050-T7451 and Type 316 stainless was approximately 100 µm. With a larger gap, 500 µm, the charge density was 5.6 C/cm^2. This was 1.5 C/cm^2 less than the exposure with a gap of 100 µm.

5.7 Cathodic and Anodic Reaction Rate Measurements under Droplets and Thin Films on AA7050-T7451 Coupled with Type 316 Stainless Steel under Atmospheric Conditions Utilizing a Coupled Mutli-Electrode Array with a Sintered Ag/AgCl Counter/Reference Electrode

CMEA consisting of only 20 AA7050-T7451 and sintered Ag/AgCl as RE/CE

Given the effect of film thickness and cycling, it was of great interest to explore cathodic reactions in thin films. In this work, two CMEAs were constructed of AA7050-T7451 and Type 316 stainless steel in combination with an embedded sintered Ag/AgCl electrode functioning as both the CE and RE was utilized to measure cathodic reaction rates under droplets and thin electrolyte films under various atmospheric conditions. This technique enabled assessment of atmospheric conditions under thin films and droplets with minimal ohmic resistance or alternation of solution chemistry. Current measurements taken concurrently and instantaneously will enable the measurement of real-time local corrosion processes that take place on an electrode surface. Additionally, an understanding of local current interactions and kinetic ORR rates on a simulated planar electrode as a function of electrode position and electrolyte thickness and geometry can be developed.

Two CMEAs were constructed for this study. The first CMEA in this study was constructed using AA7050-T7451 rectangular panel with twenty holes surrounding one larger hole in the center. Twenty AA7050-T7451 wires with 0.25 mm diameter were embedded in the drilled panel. A sintered Ag/AgCl electrode with 0.8 mm diameter was embedded in the larger hole in the center of the panel. The second CMEA was constructed geometrically identical, however, half the AA7050-T7451 wires were replaced with 10 Type 316 stainless steel wires to simulate a galvanic couple between the two metals. A schematic and optical micrograph of the CMEAs can be observed in in Figure 5.4.

Figure 5.39 shows cathodic polarization of AA7050-T7451 in a full immersion conventional 3 electrode system using SCE as the RE and a Pt mesh as the CE compared with a single electrode on the 20 electrode AA7050-T7451 CMEA under full immersion conditions using Ag/AgCl (converted to SCE). The results were nominally identical between Pt as a CE and Ag/AgCl as a RE/CE in full immersion. The primary cathodic reaction was ORR.

Cathodic polarization on a single electrode on the CMEA consisting of 20 AA7050-T7451 electrodes under droplet and thin film conditions was conducted. Figure 5.40 shows cathodic polarization on the CMEA under a droplet (height 70 µm) and Figure 5.41 shows the CMEA under a 70 µm continuous thin film using Ag/AgCl at different electrode positions at the edge and center of the CMEA. The atmospheric corrosion environments under a 70 µm thin film and 70 µm droplet both showed increased ORR cathodic kinetics compared to the full immersion conditions. However, differences in ORR kinetics were observed between droplet and thin film conditions. Under the 70 µm droplet the electrodes near the edge of the droplet (1 and 20), indicated by the triangle symbols, had higher ORR cathodic reaction rate than the electrodes positioned near the middle of the droplet. Under a continuous, level electrolyte layer with 70 µm height, cathodic kinetics increased by one order of magnitude, no spatial effects could be seen. The electrodes on the edge of the thin film and near the middle of the thin film had similar cathodic reaction rates.

The OCP decreased 60 mV from full immersion conditions to both thin film and droplet conditions.

Cathodic constant potential polarization at (-1.0 V vs SCE) under a 70 µm thin film for 10,000 s can be observed in Figure 5.42. Current decay occurred over the 10,000 s exposure. All electrodes had current density within +/- 1x10^{-5} A/cm^2 of each other. The dotted line corresponds to the full immersion exposure. The average current densities at 1.0 V SCE for the CMEA of only AA7050 electrodes and the full immersion exposures were -2.62 x 10^{-5} A/cm^2 and -3.69 x 10^{-6} A/cm^2. This shows that under a 70 µm thin film, the current density was increased by an order of magnitude.

The ZRA current was monitored for 10,000 s under a 0.6 M NaCl 70 µm thin film at 98% RH on the CMEA consisting of 20 AA7050-T7451 electrodes (Figure 5.43). During the ZRA measurements no CE/RE was used. The sintered Ag/AgCl RE/CE was only used after the ZRA exposure to interrogate cathodic kinetics of a single electode showing faster ORR kinetics than other AA7050-T7451 electrodes. Under the thin film, three anodic sites formed, A5, A7, and A11. Figure 5.44 shows the color maps for the exposure showing the location of the anodic sites (red) and cathodic sites (blue). Of the 20 AA7050 electrodes, only 3 electrodes had a positive net charge density, while the 17 other electrodes had a negative charge density supporting ORR. Immediately after the 10,000 s exposure, AA7050-T7451 electrode A15 was connected to a potentiostat and cathodic polarization was conducted. The cathodic region of the ZRA exposure showing A15, and the cathodic polarization can be observed in Figure 5.45. After the 10,000 s exposure, the OCP was made more negative by 80 mV and cathodic kinetics were increased by less than an order of magnitude.

Galvanic couple CMEA consisting of only 10 AA7050-T7451 and 10 Type 316 stainless steel and sintered Ag/AgCl as RE/CE

The galvanic couple potential under a 70 µm thin film was determined by overlaying potentiodynamic polarization of AA7050-T7451 (anodic) and Type 316 stainless steel (cathodic) using the dissimilar galvanic couple CMEA consisting of an AA7050-T7451 panel with 10 embedded AA7050-T7451 electrodes, 10 Type 316 stainless steel electrodes and a sintered Ag/AgCl electrode functioning as the RE and CE. Figure 5.46 shows the measured OCP and cathodic and anodic potentiodynamic polarization in full immersion and under a 70 µm thin film of 0.6 M NaCl. Under thin film conditions, the OCP of stainless steel was not changed, however, the E_{OCP} of AA7050-T7451 was lowered by 80 mV. Thin film conditions affected both the galvanic couple potential and current. The galvanic couple potential was made more negative from -0.69 to -0.80 V SCE from full immersion to thin film conditions. Furthermore, the galvanic couple current was increased from 2.9×10^{-5} to 1.9×10^{-4} A/cm^2 in the change from full immersion to thin film conditions (height 70 µm).

A 24 hour ZRA measurement of the galvanic couple CMEA was conducted under a 70 µm thin film. The results of the ZRA exposure are shown in Figure 5.47. Part (a) shows the current density over the 24 h exposure. The solid lines indicate AA7050-T7451 electrodes and dashed lines indicated Type 316 stainless steel electrodes. It can be observed that 4 anodic sites dominated over the exposure (A6, A3, A2 and A7). This was not surprising as corrosion is highly localized on AA7050. [47,188] After approximately 8 hours of exposure an increase in anodic kinetics and cathodic kinetics was observed. Furthermore, Figure 5.48 illustrates an expanded region focusing on the cathodic electrodes after the increase in kinetics observed after 8 h. It can be seen that 5 AA7050-T7451 electrodes (A1, A4, A8, A9, A10), shown in bold colored lines, experienced a polarity switch from net anodic to net cathodic currents. Immediately after the 24 h exposure Al electrode 1 was disconnected from the CMEA and cathodic polarization was conducted. Al electrode 1 is distinguished in red. Figure 5.48 shows the cathodic polarization of Al electrode 1 after the 24 h ZRA exposure compared to cathodic polarization conducted on Al electrode 1 pre-exposure and with AA7050-T7451 under full immersion conditions. Cathodic kinetics at -1.1 V SCE in full immersion, under a 70 µm thin film pre-exposure and post-exposure were 4.8×10^{-6} A/cm^2, 6.3×10^{-5} A/cm^2, and 1.9×10^{-3} A/cm^2, respectively. Cathodic kinetics increased by over one order of magnitude after ZRA exposure and the OCP was reduced by 8 mV. Figure 5.49 shows the color maps as a function of time. The red indicates positive current (anodic) and the blue indicates negative current (cathodic) and white indicates zero net current (freely corroding). The color map shows the polarity switch between the five Al electrodes (A1, A4, A8, A9, and A10) as well as the spatial distribution of the strong anodic sites (A6, A3, A2 and A7). To ensure validity the total of the net cathodic current passing through each AA7050-T7451 microelectrode was found to be equal in magnitude and opposite in sign to the total anodic current passing through the galvanically coupled Al microelectrode confirming that the interaction between the microelectrodes was in accordance with mixed potential theory and that measured currents were above the detection limit. The net anodic charge density over the 24 h exposure was +16.6 C/cm^2 and the net cathodic charge density over the 24 hour exposure was -16.7 C/cm^2. This shows that the stainless steel polarized the AA7050-T7451 to increase the corrosion rate by 14-fold when compared to same exposure with only AA7050-T7451 shown above.

The galvanic CMEA consisting of 10 AA7050 electrodes and 10 Type 316 stainless steel electrodes was tested under cyclic atmospheric conditions. The cycle testing was operated at 30 minutes near 95% RH followed by 3.5 hours near 30% RH for 24 h at 30°C. Figure 5.50 shows the net ZRA measured current density. Current spikes were observed on the onset of wetting. The dominant anodic sites were A3, A4, A7, and A8. The charge density of AA7050 electrodes A8 and A3 were 17.7 C/cm^2 and 14.3 C/cm^2. This accounted for 32% and 18% of the net anodic current. 100% of the ten Type 316 stainless steel electrodes had a net cathodic current and 30% of the ten AA7050-electodes also had a net cathodic current (A2, A5 and A9). The AA7050 electrodes contributed approximately 5% of the net cathodic current. Figure 5.51 shows the color maps in correlation with the wet/dry cycles. It can be observed that during drying periods, corrosion rates were reduced while in wet periods corrosion rates were increased. Furthermore it can be observed that after 18 hours AA7050 A3 switched from a strong anodic site (12.6 h) to a cathodic site (21.8 h). Immediately after the 24 h ZRA exposure, a cathodic scan on A3 was conducted. Figure 5.52 shows the cathodic polarization of Al electrode A3 after the 24 h ZRA exposure compared to the cathodic polarization conducted on Al electrode 3 pre-exposure and with

AA7050-T7451 under full immersion conditions. The OCP was unchanged and cathodic kinetics were increased by less than an hour of magnitude.

5.7.1 Theoretical and Experimental Oxygen Reduction Kinetics on Cu

Under constant cathodic potential polarization in the ORR regime (-0.8 V SCE) of a planar Cu electrode in full immersion 0.6 M NaCl, the current density experienced a current decay within 30 s (Figure 5.53). The current decayed quickly for a short time and tends to a limiting value with increasing time. This can be explained by the oxygen concentration profile in bulk solution. Initially, concentration of O_2 is high. However, as time increases the concentration near the electrode surface is consumed and the current decreases. For a planar Cu electrode the time dependence can be observed in Figure 5.53 compared to the theoretical current decay from Equation 5.2. The experimental current density of a planar electrode approached a steady value of 1.5×10^{-4} A/cm^2, which can be compared to the theoretical current density of 1.2×10^{-4} A/cm^2 for the diffusion coefficient 10^{-5} cm^2/s.

Figure 5.54 shows the current density and time dependence of the single Cu microelectrode under full immersion and droplet conditions compared to theoretical current density for spherical diffusion given by Equation 5.3. Under cathodic constant potential polarization in the ORR regime (-0.8 V SCE) of a Cu micro-electrode in 0.6 M NaCl, the current density experienced a current decay. At sufficiently short times, the thickness of the diffusion layer that was depleted of reactant was much smaller than the electrode radius and the spherical electrode appeared to be planar. The mass transport process is dominated by linear diffusion to the electrode surface. At longer times, the spherical character of the electrode becomes important and the mass transport process is dominated by spherical diffusion. Under a 70 µm droplet of 0.6 M NaCl no current decay was observed. The current density immediately approached a steady current value of 1×10^{-3} A/cm^2, this was approximately double the current density relative to full immersion single electrode exposure given a theoretical oxygen diffusion rate of D=10^{-6} cm^2/s (Figure 5.54).

5.8 Discussion

5.8.1 Accelerated Corrosion Rates during Wet/Dry Cycling

Figure 5.21 and Figure 5.50 showed the RH cycle CMEA exposure for the geometrically flat CMEA and the CMEA arranged in a faster arrangement. The equilibrium concentration of NaCl solution varies with ambient RH. [191] After drying, the NaCl on the surface of the CMEA deliquesces over time and forms an electrolyte layer or droplet of equilibrium concentration. Figure 5.55 shows the salt concentration and water layer thickness as a function of one wet to dry cycle used in this work. As the RH in an exposure environment changes, the equilibrium salt concentration and water layer thickness change as well. NaCl deliquesces at 75% RH, therefore under 75% RH no galvanic coupling should occur. However, Schindelholtz showed evidence that corrosion may occur down to 33% RH in NaCl solutions. [211] In this work, cycling increasing the corrosion rate by over two orders of magnitude. During the wet to dry cycle, it was observed in Figure 5.55 that the salt concentration was as high at 6.3 M, assuming NaCl deliquesces at 75% RH. This concentration could be even higher if the droplet stayed wet to 33% RH. Through-out the exposure, the water layer thickness varied from 0.1 µm to 8 µm. The combination of the increase in salt concentration and resulting thin water layers led to increased corrosion rates.

5.8.2 Cathode Capacity of AA7050-T7451 when Galvanically Coupled with Type 316 Stainless Steel

In many of the CMEA exposures (Figure 5.12, Figure 5.30 and Figure 5.34) anodic sites were often found to abruptly switch to cathodic sites. This suggested that dealloyed S-phase (Al_2CuMg) and/or increased replated-Cu on the surface was the cause of the increased cathodic kinetics of AA7050-T7451 electrodes. When AA7050-T7451 was coupled to stainless steel, the AA7050-T7451 electrodes were still significant cathodes supporting ORR. For instance, after a 24 h exposure under 70 µm thin film of 0.6 M NaCl, 66% of the AA7050-T7451 electrodes were cathodic sites contributing to over 10% of the total cathodic reactions (Figure 5.9). In cyclic exposures as shown in Figure 5.22, after two wet/dry cycles (24 h) AA7050-T7451 A1 sharply switched from an anodic site to a the strongest cathodic sites. In this exposure, while only one AA7050-T7451 had a net cathodic current, A1 contributed 60% of the total net cathodic reaction. This enabled the support and growth of corrosion fissures. In many other exposures, Figure 5.20

and Figure 5.22 AA7050-T7451 electrode contributed over 90% of the cathodic current. This is consistent with previous work shown in Chapter 2.

5.8.3 Using a Sintered Ag/AgCl Electrode Functioning as the Reference and Counter Electrodes in Combination with CMEAs

The CMEA setup with the sintered AgCl electrode avoided alteration of the solution chemistry and definition of the electrolyte later thickness. Furthermore the use of a sintered Ag/AgCl electrode had minimal effect on the solution composition.[196] Utilizing this setup of CMEA with a sintered Ag/AgCl electrode as a reference and counter electrode enables many corrosion based applications. While only a few techniques were discussed here, CMEAs enable analysis using electrochemical impedance spectroscopy, galvanostatic polarization, and anodic and cathodic potentiostatic polarization under droplets and thin films of various thicknesses and different atmospheric conditions such as wet/dry cycling. This work is unique in that it allows local identification of spatial current interactions under thin film and droplet atmospheric conditions with minimal ohmic drop and distortion of electrolyte shape while also minimizing changes in the droplet chemistry, which would not be present naturally, by elimination of reactions occurring on the counter electrode. While Pt electrodes are typically used as CE, issues arise with this setup. Pt as a CE in aqueous chloride solution produces O_2 and H^+ from HER during cathodic polarization of the WE, and H_2 and OH^- during anodic polarization of the WE. For sufficiently small currents a sintered Ag/AgCl electrode can serve as a RE and CE attributed to the fact that the potential would not be altered significantly in a non-polarizable electrode. Therefore, it can supply significant currents with minimal polarization. Figure 5.39 shows minimal difference in polarization between a planar electrode of AA7050-T7451 using Pt mesh and SCE and a single wire array with an Ag/AgCl as both the RE and CE.

5.8.4 Oxygen Reduction Kinetics of Thin Films versus Droplets on AA7050-T7451

On AA7050-T7451 the primary cathodic reaction over the potential range from -1.0 V to -1.4 V SCE was ORR (Figure 5.40 and Figure 5.41). Corrosion under thin films is regulated by the electrolyte layer thickness due to the impact of the water layer thickness and O_2 concentration on both diffusional kinetics at the cathode and ohmic drop in solution between the anode and cathode.

[204] In Figure 5.40, under the 70 µm droplet condition the cathodic reaction rates were shown to be higher at the edges of the droplet than in the center of the droplet. This can be attributed to a thinning of the droplet around the edges resulting in O_2 diffusing into the regions with a shorter diffusion distance. This result can be substantiated by cathodic polarization conducted under a continuous layer of 70 µm (Figure 5.41). Figure 5.41 shows little variation in ORR cathodic reaction rates as a function of electrode position. This indicated that the uniform water layer enabled ORR to occur relatively uniformly with position. Previous reports with thin film electrolytes have suggested that ORR rates increased until the electrolyte film thickness decreased to 10 µm to 30 µm, at which point oxygen transfer across the air/electrolyte interface becomes slower than oxygen transport through the electrolyte[75,150]

5.8.5 Implications for Galvanic Corrosion of AA7050-T7451 and Type 316 Stainless Steel Under Thin Film Conditions

From a galvanic corrosion perspective, AA7050-T7451 displayed flattened Tafel regions in the full immersion and thin film conditions (Figure 5.46). At -0.8 V or E_{gal}, ORR current density was mass transport limited. This suggests that AA7050-T7451 corrosion is under cathodic control in a galvanic couple. The difference in 100 mV in the OCP of AA7050-T7451 from full immersion to thin film affected the galvanic corrosion by shifting the galvanic potential in the negative direction. Cathodic polarization of Type 316 stainless steel transitioned to ORR at approximately -0.6 V SCE. Under the thin film conditions it was observed that Type 316 stainless steel exhibits flatter Tafel slopes and furthermore, reaches the onset of diffusion limitation at more positive potentials. Under atmospheric conditions the increase in ORR kinetics on Type 316 stainless steel can explain the 4-fold increase in galvanic corrosion rates from full immersion to thin film environments.

Figure 5.47 and Figure 5.48 showed the dominant anodic and cathodic sites and furthermore, sites that switched from anodes to cathodes. This could be an indication of S-phase (Al_2CuMg) initially an anodic site switching to a cathodic hotspot after dealloying of the Al and Mg leaving behind a cathodic high surface area remnant which as discussed above may replate on the surface of the alloy. [33] Specifically, it was observed that around 8 hours, an increase in cathodic/anodic kinetics occurred. After 8 hours, Al switched from net anodic site to a net cathodic site. This could be attributed to Cu dissolving into solution and electrochemically plating on the surface of the electrode. The ZRA exposure also enabled a better spatial description of pitting sites such as electrodes A3 and A6 which showed the highest anodic behavior throughout the entire exposure. The CMEA exposure under the thin film condition illustrated an important point that the AA7050-T7451 is a significant cathode. After 12 h of exposure under a 70 µm thin film 40% of the AA7050-T7451 were producing cathodic reaction rates which could suggest a role of Cu in localized corrosion on AA7050-T7451. In previous work it was shown that growth of corrosion fissures in a rivet hole were not cathodically limited based on inventory of cathodic reaction changes compared to anodic charge. (Chapter 2). This was speculated to be attributed to ORR occurring on the stainless steel rivet and the presence of another strong a cathode, which was speculated to be replated-Cu on the surface. [139,167,188] Furthermore, in Chapter 3, CVs showed the Cu was on the surface of AA7050-T7451 post exposures (Figure 3.30). In this work, instantaneous local current measurements illustrated agreement that Cu-replating on the surface resulted in initial anodic regions to become cathodic ORR hotspots supporting the growth of anodic corrosion sites such as A3, A6 and A7 in Figure 5.48.

5.8.6 Modeling Kinetics of ORR of Cu-rich constituents with the use of Pure Cu

Corrosion of AA7050-T7451 can occur in bulk solutions or under droplets and in humid air. The electrolyte layer can vary from a few µm to over 500 µm. The corrosion of AA7050-T7451 is controlled by the capacity of the secondary phases and replated-Cu sites to support the oxygen reduction reaction. [64] In AA7050-T7451, S phase (Al_2CuMg) is a noteworthy phase because it forms spatially separate micrometer-scale constituent particles that become enriched with Cu on their surfaces due to dealloying. Therefore, the general corrosion rate of AA7050 and the successive extent of damage depend on kinetics of ORR at the Cu-enriched particles. Cu-replating on the surface of AA7050 affects the corrosion in two ways. First, the OCP of the electrode is ennobled and secondly, ORR is raised towards the theoretical limit of a homogenous Cu electrode.[154,212] The OCP AA7050-T7451 is under a mixed kinetic regime for ORR. In previous work, it was shown that activation controlled current density on an electrode that was partially covered with an inactive layer such as the Al-Al_2O_3 alloy matrix, is proportional to the current density on an uncovered active cathodic site treated as homogenous electrodes and to the surface coverage of the active sites.[154] However, in the mass transfer limited region, the diffusion limited current density on a partially inactive surface is different from a homogenous surface resulting in nonlinear diffusion. Furthermore, the cathodic reaction rate depends on the diffusional boundary layer thickness relative to the size and spacing of the active sites distributed across the surface. Theoretically, in a truly stagnant electrolyte, the diffusion boundary layer thickness grows to infinity as the limiting current density would approach a negligible value. In a real system, the limiting current density could never approach zero due to natural occurring convection and a finite boundary layer thickness. At very small boundary layer thickness, the diffusion current density is independent of the boundary layer thickness because the rate limiting step is the transport of oxygen through to the electrolyte. [82] Microelectrodes allow very little current to pass and there is a transition from linear to spherical diffusion at increasing time of measurements. This diffusion profile enables enhanced transport rates to the electrode by the onset of stationary diffusion at long times.

Figure 5.53 showed current over time at a constant cathodic potential in the ORR regime of Cu (-0.8 V). Theoretical current densities and experimental current densities exhibited similar values and the current decay was fast. The time dependence plot, i vs $t^{1/2}$, shows a linear tendency indicating the current response is controlled by diffusion with the intercept at zero. Therefore, the current is expected to decay to zero at long times for planar electrodes. Figure 5.43 demonstrates that the microelectrodes showed improved mass transport properties and facilitated the measurements of higher exchange current densities and electron transfer rate constants. The current density under a droplet experienced a higher mass transport limiting current density and did not show a current decay at short times. The time dependence plot, i vs $t^{1/2}$, shows a linear trend under immersion also suggesting the current response is controlled by diffusion. However, for a spherical electrode, the intercepts are not at zero as in the planar electrode. For a microelectrode the intercepts are equal to the steady state current. The time dependence under a

70 µm droplet was not linear implying that the current response was not limited by classical diffusion under a thin layer of electrolyte.

The theoretical current approximations are given for mass transport diffusion only. Therefore, discrepancies between experimental responses compared to theoretical responses are expected because of natural convection such as vibration, or thermal gradients. Moreover, at extremely shortened times the experimental data will be affected by the charging of the double layer. The data showed that electrodes such as Cu sites or *S* phase supported fast cathodic reactions that do not decay with time. This may be obvious but it is an important finding that active Cu sites under droplets grow quickly and do not decay with time as seen in microelectrode behavior. This implies that corrosion could occur at linear damage accumulation rates if controlled by the cathode.

5.9 Conclusions

- Two galvanic dissimilar metal CMEAs were constructed with AA7050-T7451 and Type 316 stainless steel electrodes to determine galvanic current interaction under atmospheric conditions. A flat geometric CMEA showed that under a 70 µm thin film of 0.6 M NaCl corrosion kinetics were increased by at least one order of magnitude when compared to full immersion kinetics.
- Water layer thickness of 500 µm reduced corrosion kinetics as relative to the 70 µm thin film.
- Wet/dry cycling resulting in a 4 fold increase in current density. Cyclic exposures increased corrosion kinetics due to strong spikes in current on the onset of wetting/drying as the water layer was more concentrated.
- The CMEA arranged in a fastener geometry showed higher currents on the mouth of the crevice and deep inside the crevice. The net anodic charge of the fastener geometry was 3.5 times larger than the flat geometric CMEA exposure under the same conditions.
- Two novel CMEAs, one consisting of 20 microelectrodes of AA7050-T7451 and the second consisting of 10 microelectrodes of AA7050-T7451 and 10 microelectrodes of Type 316 stainless steel both embedded into an Al panel with a sintered Ag/AgCl electrode as the counter

and reference electrodes were utilized to develop an understanding of atmospheric corrosion under droplets and thin films. The CMEAs enabled measurements of cathodic and anodic kinetics as a function of position, time and electrolyte shape. The Ag/AgCl electrode is a preferred non-polarizable electrode which can function as a reference electrode and counter electrode. It was found that cathodic ORR reaction rates increased by at least one order of magnitude in atmospheric thin film or droplet environments as compared to bulk full immersion conditions. Furthermore, under droplet conditions it was observed the electrodes on the edge of the droplet had increased cathodic kinetics as compared to electrodes under the center of the droplet while a thin continuous film exhibited equal cathodic kinetics as a function of position. Anodes were dictated by local sites where AA7050 initiated pitting or micro galvanic coupling .

- In many of the CMEA exposures, AA7050 anodic sites were often found to abruptly switch to cathodic sites. This suggested that that dealloyed S-phase (Al_2CuMg) and/or Cu-replating on the surface was the cause of the increased cathodic kinetics of AA7050-T7451 electrodes. It was observed that when AA7050-T7451 was coupled to stainless steel, the AA7050-T7451 electrodes were still significant cathodes supporting ORR. In some cases AA7050-T7451 electrodes contributed 90% of the total net cathodic reaction. This enables the support and growth of corrosion fissures.
- Cyclic wet/dry exposures on the CMEA under a 70 µm thin film increased the anodic charge density by one order of magnitude relative to the exposure under constant 98% RH. During the wet/dry cycle, sharp current increases were observed on the onset of wetting attribute to the high Cl^- concentration of the droplet.
- The controlling factors in constant potential holds under droplets, which simulate galvanic couples between Type 316 stainless steel and AA7050-T7451 at a fixed galvanic couple potential were investigated using a single Cu micro-electrode. It was shown that simulated Cu-rich sites supported fast cathodic reactions that did not decay with time implying that corrosion could occur at linear damage accumulation rates if controlled by the cathode.

5.10 Tables

Table 5.1 Nominal composition of AA 7050-T7451 and Type 316 stainless steel wires in wt. % used in this study.

Material	**Mg**	**Zn**	**Cu**	**Zr**	**Fe**	**Al**			
AA 7050-T7451	2.2	6.1	2.2	0.11	0.08	Bal.			
	C	**Mn**	**Si**	**P**	**S**	**Cr**	**Ni**	**N**	**Fe**
316 Stainless Steel	0.05	1.37	0.43	0.031	0.027	18.2	8.16	0.06	Bal.

5.11 Figures

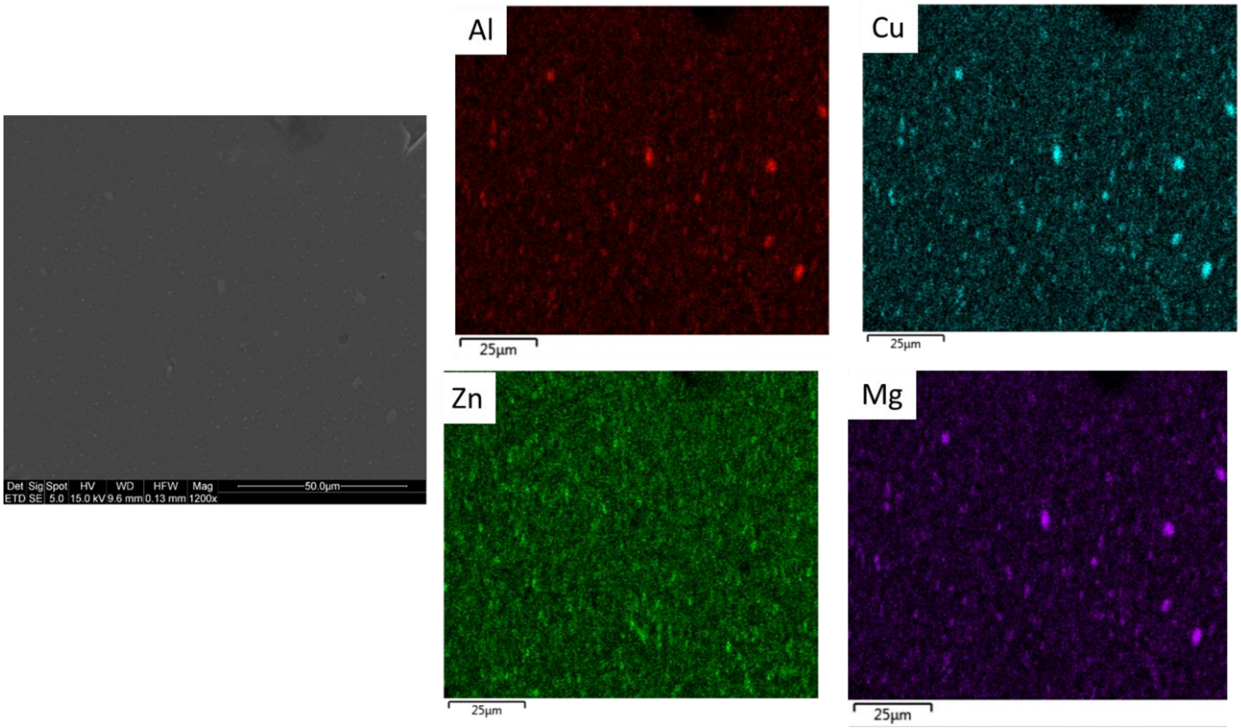

Figure 5.1. Secondary electron micrograph on AA7050-T7451 wire (250 µm) showing the Al, Cu, Zn and Mg EDS map profiles.

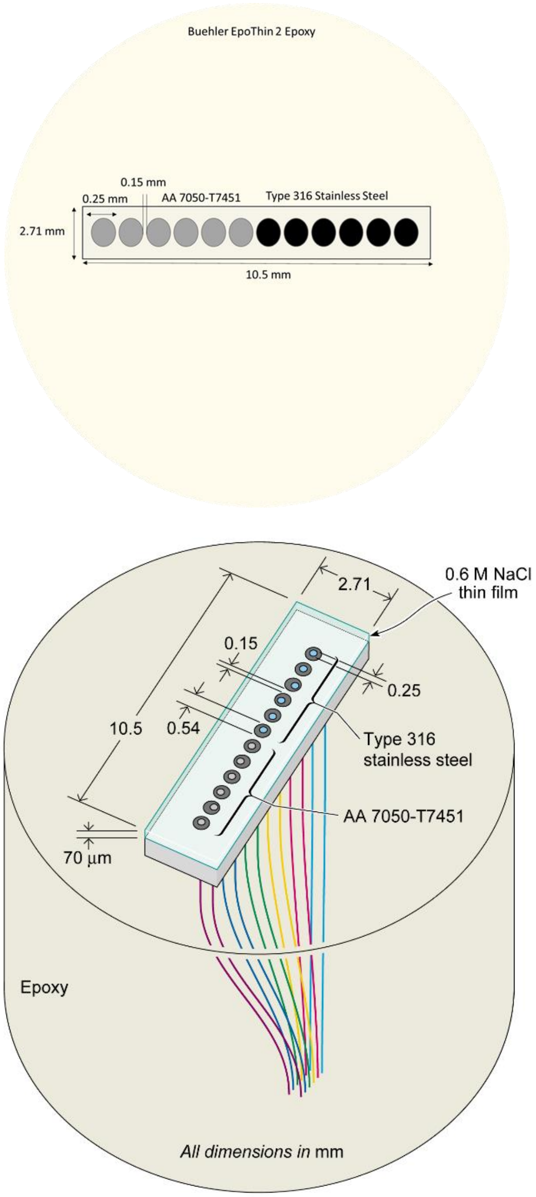

Figure 5.2. CMEA schematic of the flat galvanic geometric CMEA where 6 AA7050 electrodes (right) and 6 Type 316 stainless steel electrodes (left) were embedded in an AA7050-T7451 panel in a flat arrangement.

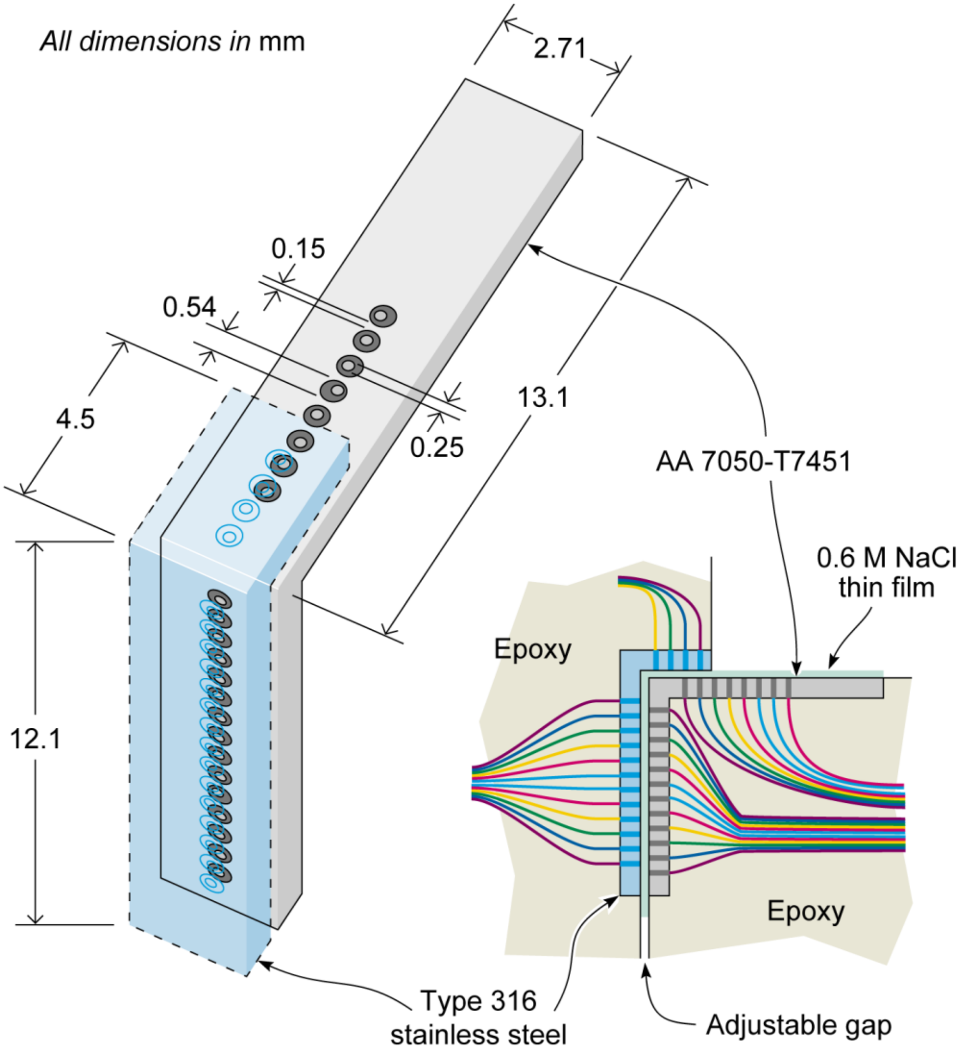

Figure 5.3. (a) Schematic of the CMEA arranged in a fastener geometry where 22 AA7050 electrodes were embedded in an AA7050 panel and 20 SS 316 electrodes were embedded in an Type 316 stainless steel panel and arranged in a geometry representing a fastener with an adjustable gap between the rivet and 7050-T7451 plate where the separately addressable electrodes in each panel are facing (note: the electrodes in the schematic have been deliberately rotated by 90˚ so that each electrode can be seen). (b) 2D schematic showing the CMEA arranged in a fastener geometry. The thin film electrolyte was deposited only on the AA7050-T7451 mouth.

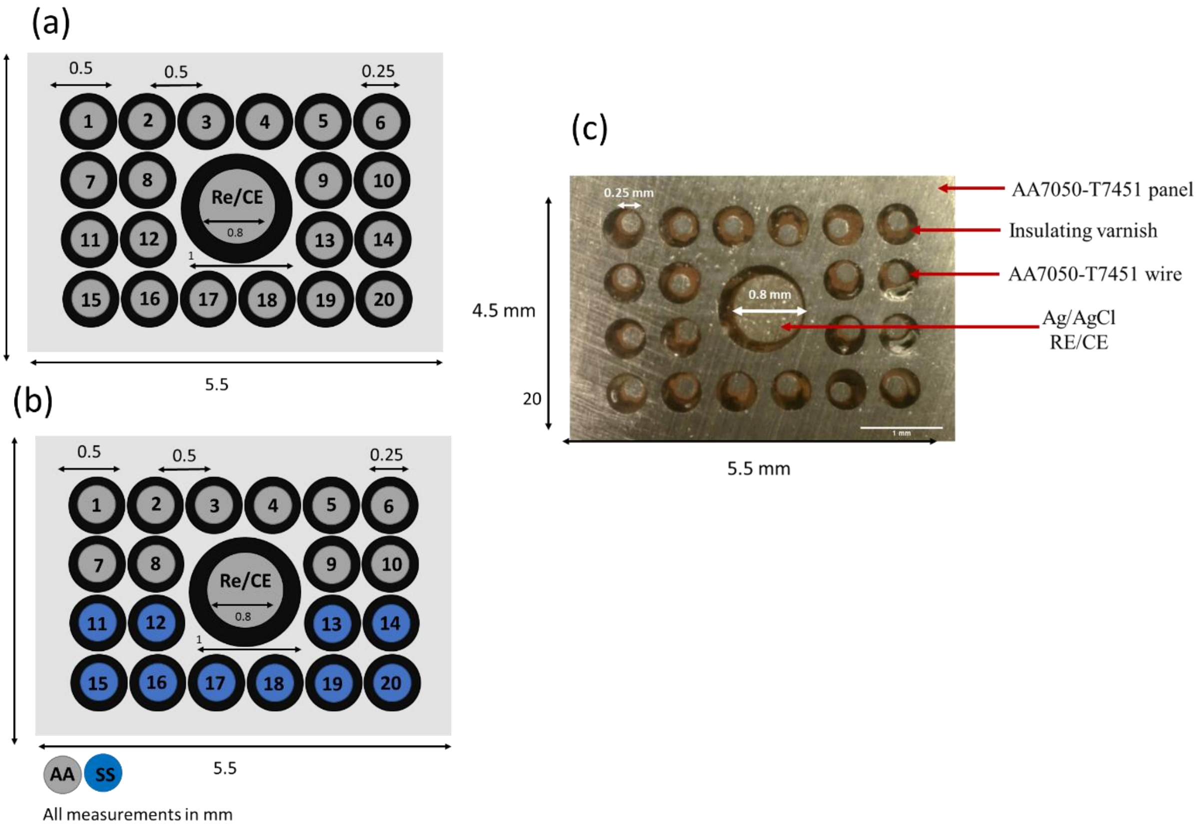

Figure 5.4. Schematic of the two CMEAs consisting of (a) an AA7050-T7451 panel with 20 embedded AA7050-T7451 electrodes (WE) and a sintered Ag/AgCl electrode used as the RE and CE (b) an AA7050-T7451 panel with 10 embedded AA7050-T7451, 10 Type 316 stainless steel wires and a sintered Ag/AgCl electrode used as the RE and CE (c) Optical micrograph showing the CMEA consisting of only AA7050-T7451 electrodes.

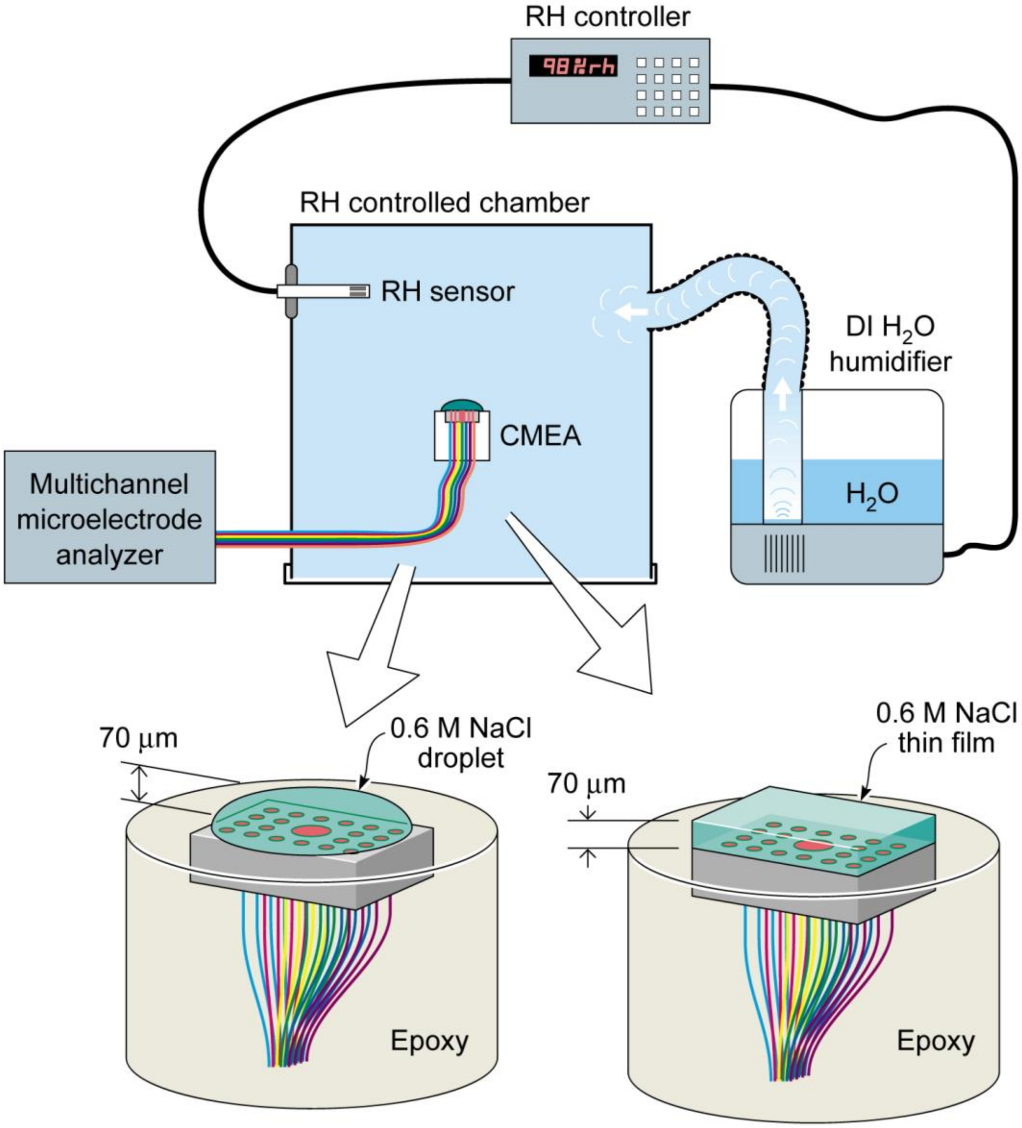

Figure 5.5. Schematic of the controlled relative humidity cabinet setup used to environmentally expose the CMEAs.

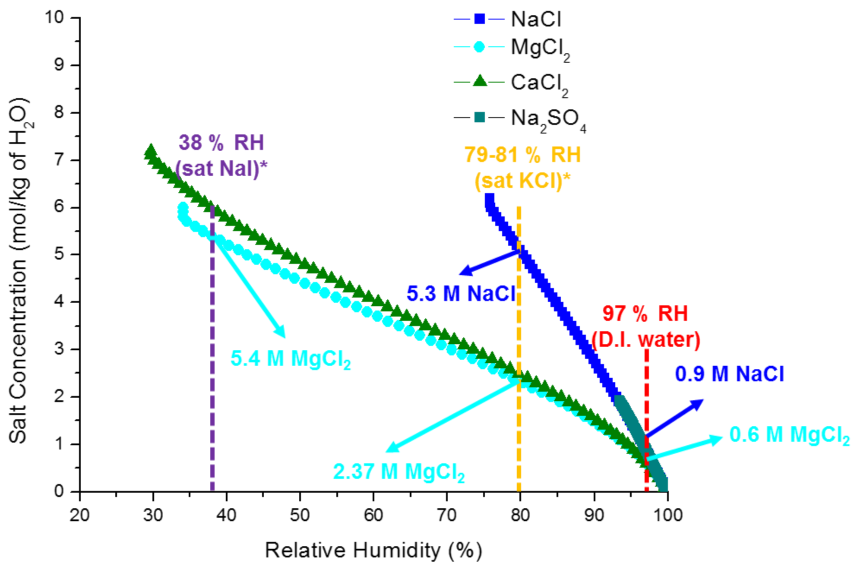

Figure 5.6. Salt concentration as a function of relative humidity for NaCl, $MgCl_2$, $CaCl_2$ and Na_2SO_4. The initial electrolyte concentration and RH used were chosen to avoid size change of the electrolyte droplet deposited on the material surface. (Plot obtained from R. Schaller)

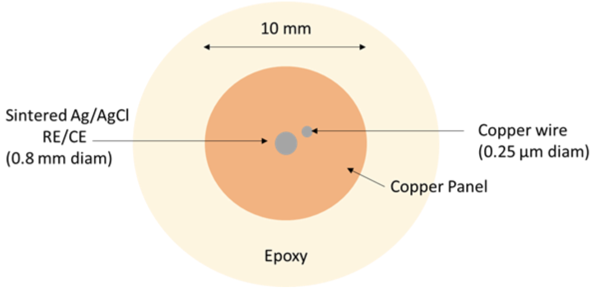

Figure 5.7. Single wire Cu electrode (WE) and sintered Ag/AgCl (CE/RE) embedded into a 99.99% pure Cu button and flush mounted in epoxy.

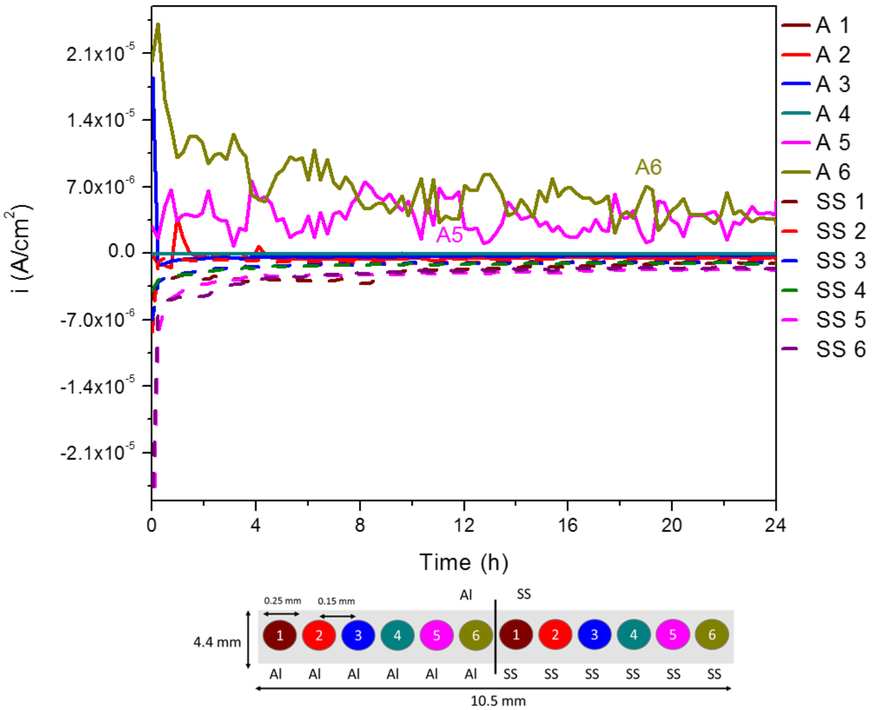

Electrode	Q (C/cm^2)
A 1	-0.0041
A 2	-0.037
A 3	-0.029
A 4	-0.0031
A 5	0.33
A 6	0.59
SS 1	-0.16
SS 2	-0.078
SS 3	-0.11
SS 4	-0.11
SS 5	-0.21
SS 6	-0.19
$\sum Q_a = \sum Q_c$	0.89=-0.89

Figure 5.8. Net ZRA galvanic current density recorded over 24 hours for the flat galvanic geometric array where solid lines represent the current for AA7050 electrodes and dotted lines represent the Type 316 stainless steel electrodes. The key at the bottom shows the position of each wire in the array. The CMEA was in full immersion 0.6 M NaCl.

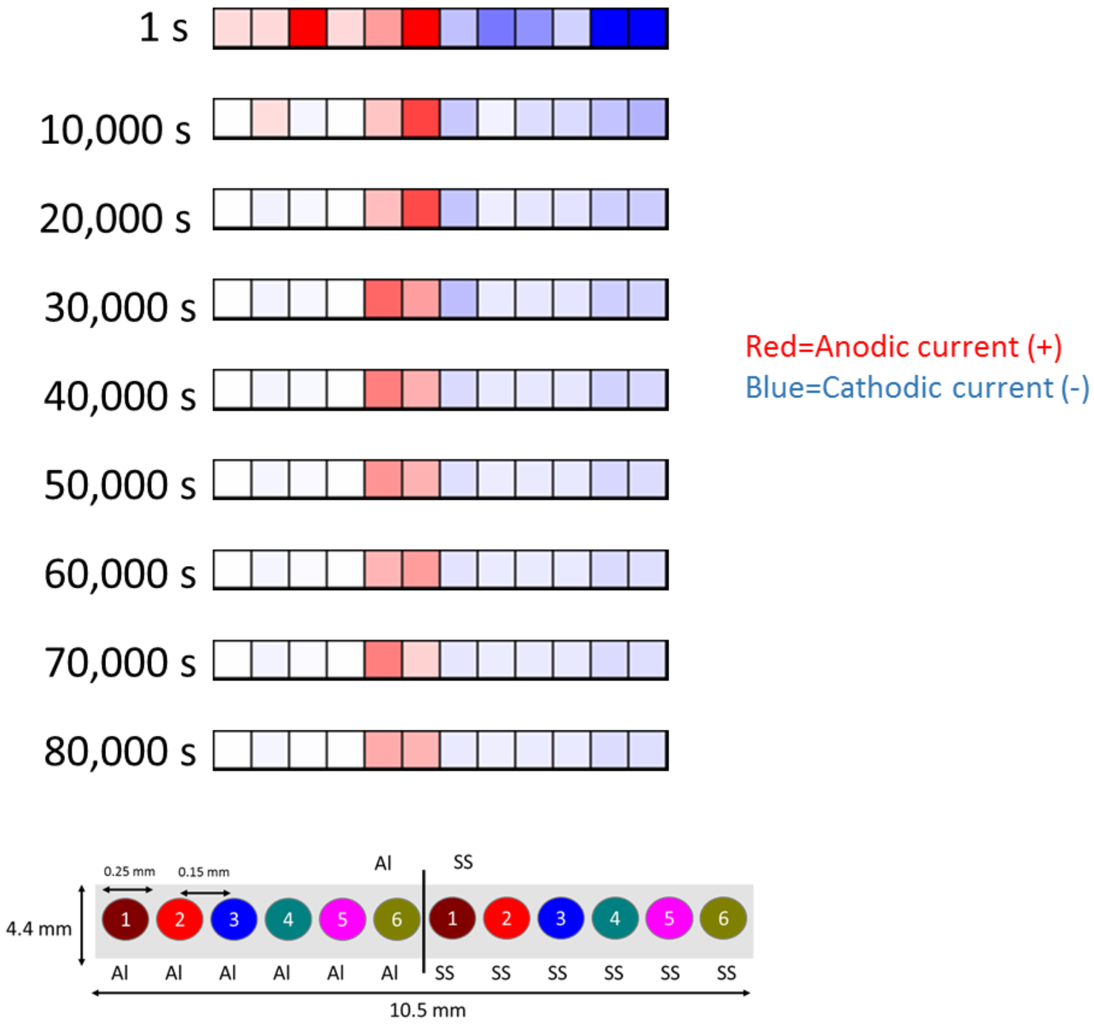

Figure 5.9. Color maps of the flat galvanic geometric CMEA over the 24 h exposure in full immersion. Red indicates positive values (net anodic current), blue indicates negative values (net cathodic curent) evident of galvanic coupling and white indicates zero current (electrodes with a net galvanic current close to zero). The key at the bottom shows the position of each wire in the array.

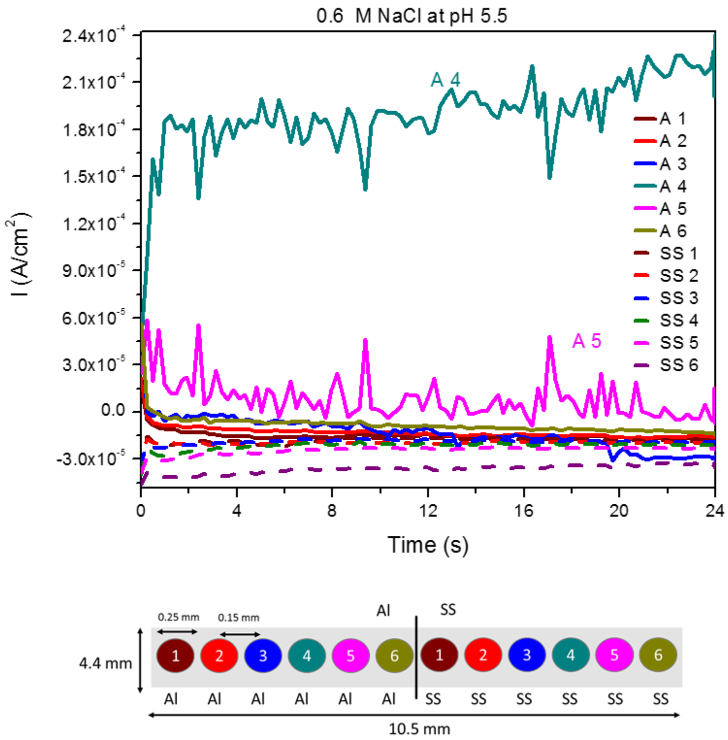

Electrode	Q (C/cm^2)
A 1	-1.31
A 2	-1.14
A 3	-1.18
A 4	15.52
A 5	0.82
A 6	-0.74
SS 1	-1.55
SS 2	-1.68
SS 3	-1.62
SS 4	-1.85
SS 5	-2.091
SS 6	-3.13
$\sum Q_a=\sum Q_c$	16.29=-16.32

Figure 5.10. Net ZRA galvanic current density recorded over 24 hours for the flat galvanic geometric array where solid lines represent the current for AA7050 electrodes and dotted lines represent the Type 316 stainless steel electrodes. The key at the bottom shows the position of each wire in the array. The CMEA was exposed to a 0.6 M NaCl 70 µm thin film at 98 %RH at 23°C.

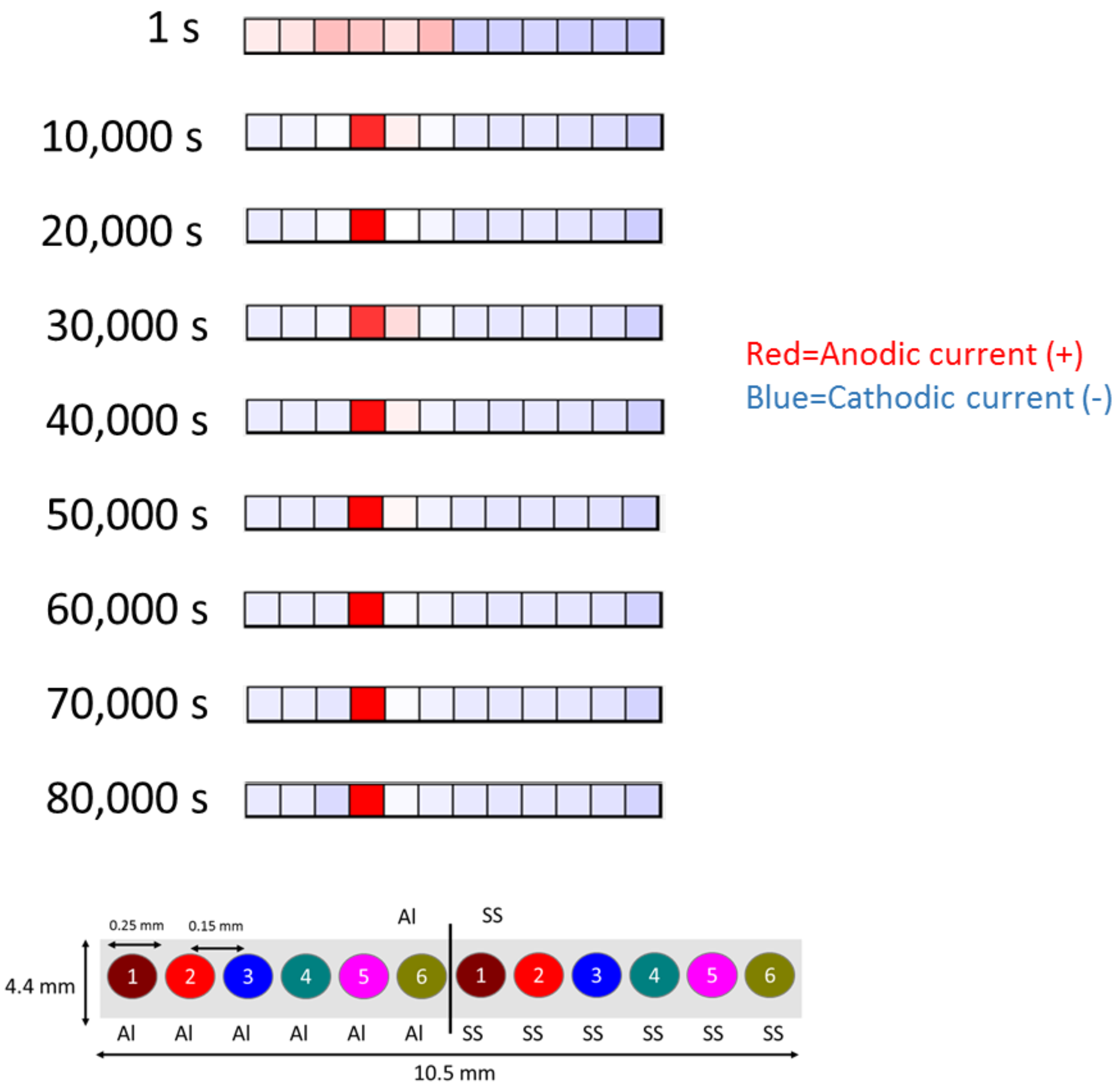

Figure 5.11. Color maps of the flat galvanic geometric CMEA over the 24 h exposure under a 0.6 M NaCl 70 µm thin film at 98% RH at 23°C. Red indicates positive values (net anodic current), blue indicates negative values (net cathodic current) evident of galvanic coupling and white indicates zero current (electrodes with a net galvanic current close to zero). The key at the bottom shows the position of each wire in the array.

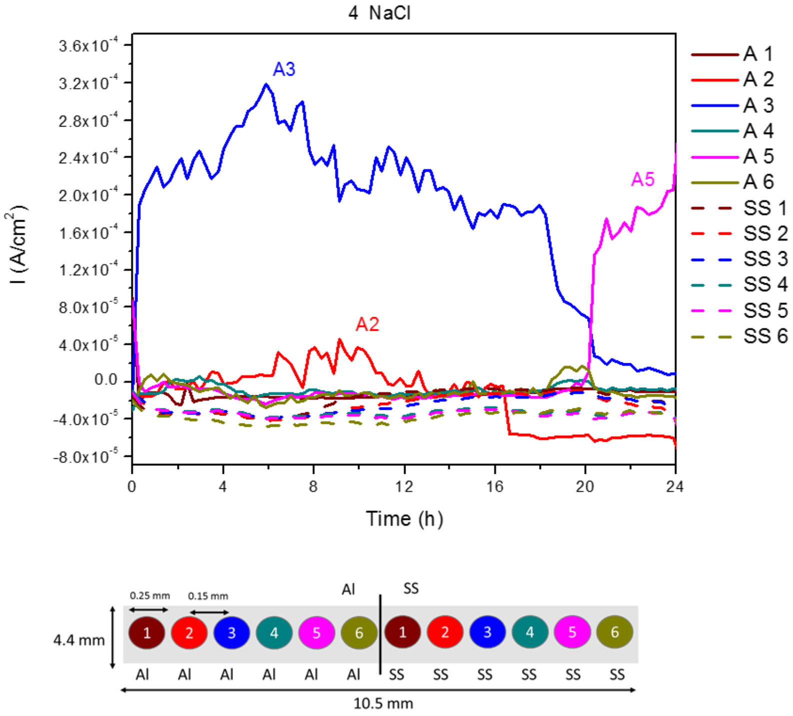

Electrode	Q (C/cm^2)
A 1	-1.091
A 2	-1.27
A 3	16.65
A 4	-0.75
A 5	2.48
A 6	-0.92
SS 1	-1.72
SS 2	-2.11
SS 3	-2.14
SS 4	-2.79
SS 5	-2.94
SS 6	-3.27
$\sum Q_a=\sum Q_c$	19.21=-19.11

Figure 5.12. Net ZRA galvanic current density recorded over 24 hours for the flat galvanic geometric array where solid lines represent the current for AA7050 electrodes and dotted lines represent the Type 316 stainless steel electrodes. The key at the bottom shows the position of each wire in the array. The CMEA was exposed to a 4.0 M NaCl 70 µm thin film at 98 % RH at 23°C.

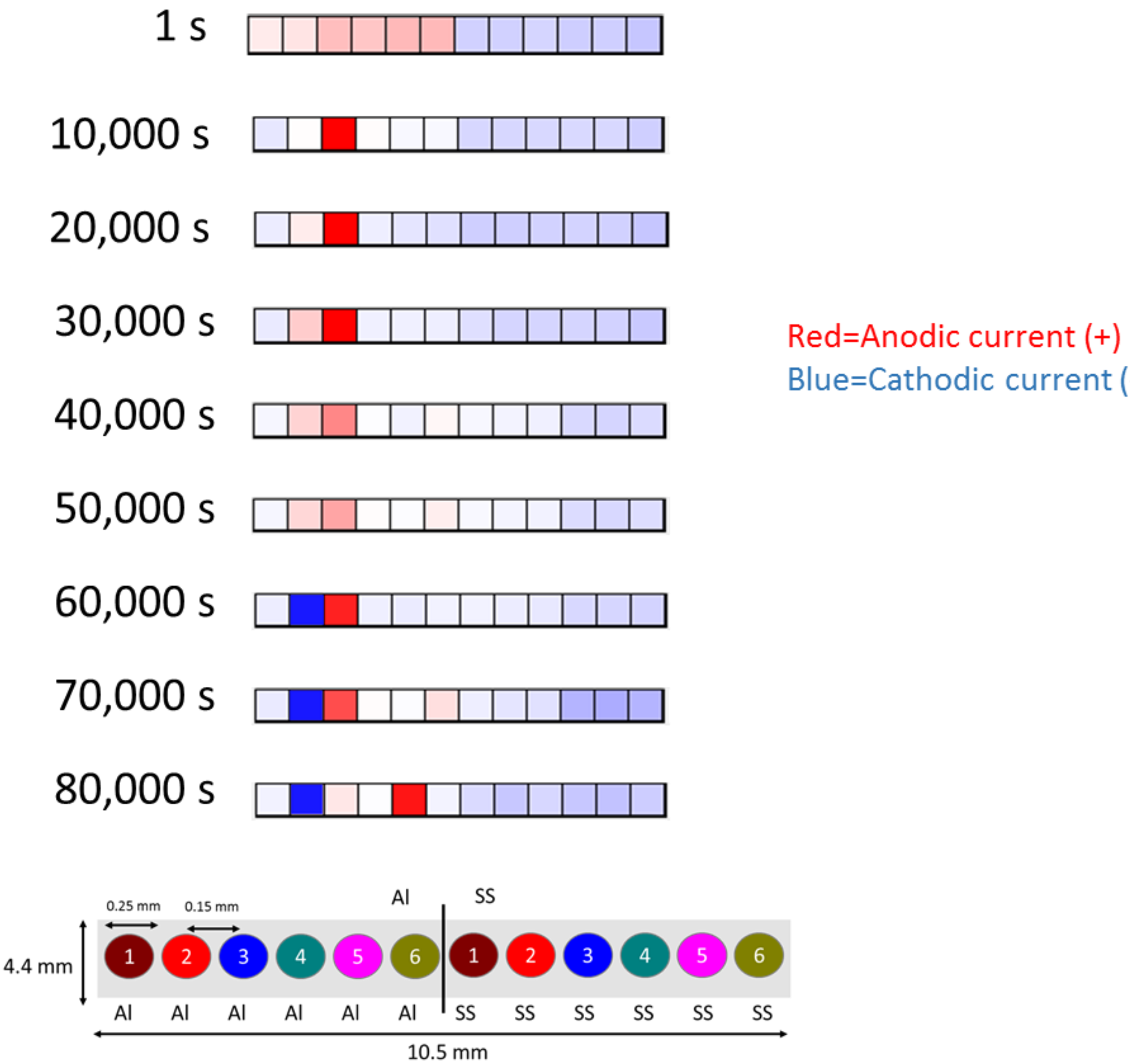

Figure 5.13. Color maps of the flat galvanic geometric CMEA over the 24 h exposure under a 4.0 M NaCl 70 µm thin film at 98% RH at 23°C. Red indicates positive values (net anodic current), blue indicates negative values (net cathodic current) evident of galvanic coupling and white indicates zero current (electrodes with a net galvanic current close to zero). The key at the bottom shows the position of each wire in the array.

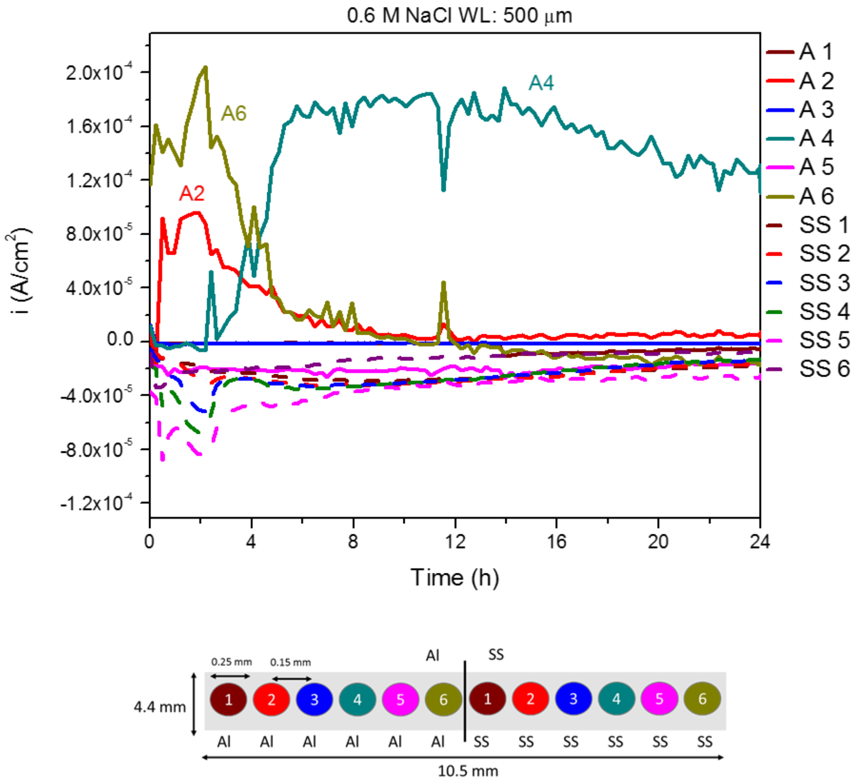

Electrode	Q (C/cm^2)
A 1	-0.33
A 2	1.47
A 3	-0.11
A 4	9.31
A 5	-1.76
A 6	2.12
SS 1	-2.041
SS 2	-1.18
SS 3	-1.21
SS 4	-1.95
SS 5	-2.044
SS 6	-1.054
$\sum Q_a = \sum Q_c$	11.91=-11.75

Figure 5.14. Net ZRA galvanic current density recorded over 24 hours for the flat galvanic geometric array where solid lines represent the current for AA7050 electrodes and dotted lines represent the Type 316 stainless steel electrodes. The key at the bottom shows the position of each wire in the array. The CMEA was exposed to a 0.6 M NaCl 500 µm thin film at 98% RH at 23°C.

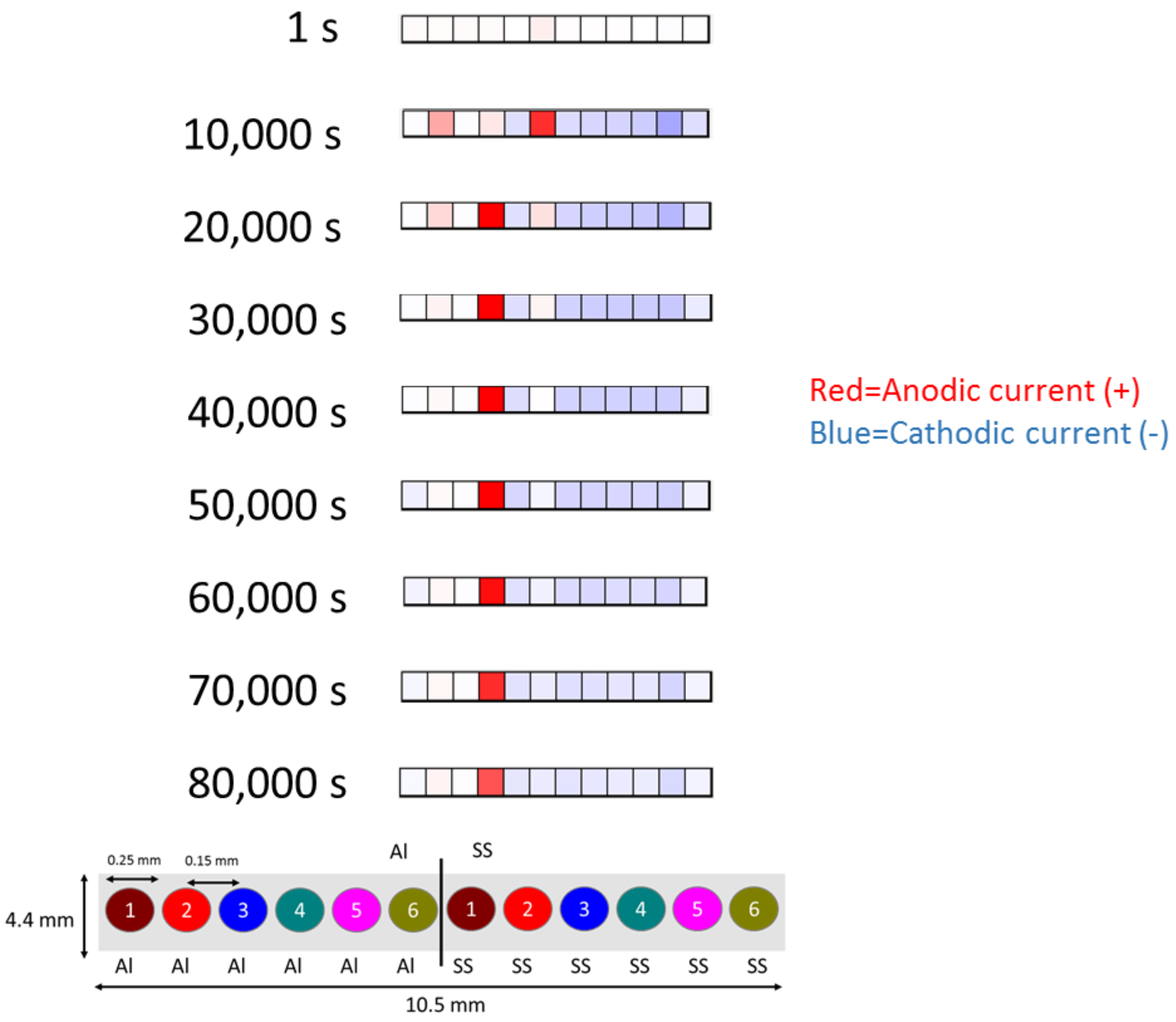

Figure 5.15. Color maps of the galvanic geometric CMEA over the 24 h exposure under a 0.6 M NaCl 500 μm thin film at 98 % RH at 23°C. Red indicates positive values (net anodic current), blue indicates negative values (net cathodic current) evident of galvanic coupling and white indicates zero current (electrodes with a net galvanic current close to zero). The key at the bottom shows the position of each wire in the array.

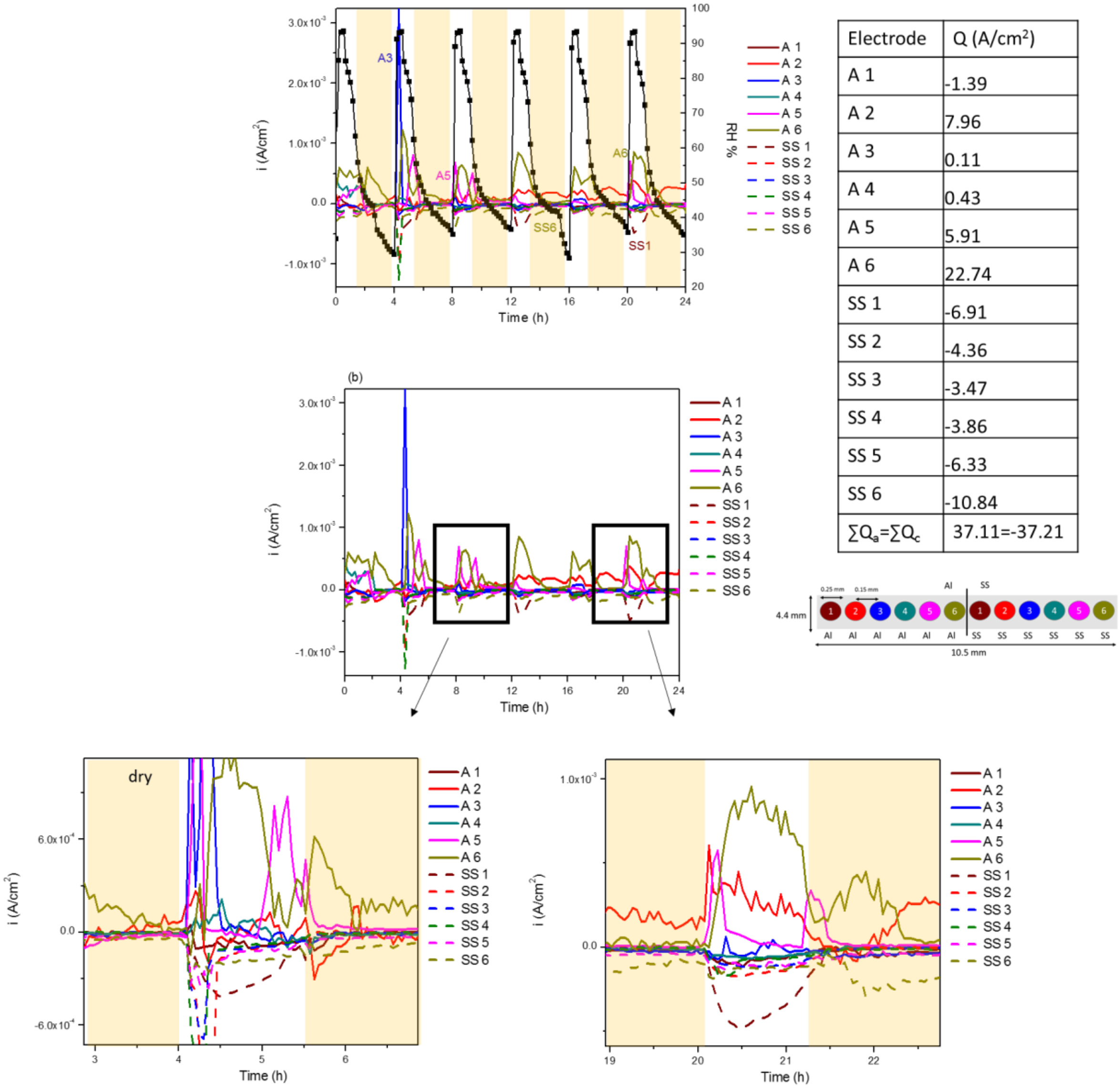

Electrode	Q (A/cm^2)
A 1	-1.39
A 2	7.96
A 3	0.11
A 4	0.43
A 5	5.91
A 6	22.74
SS 1	-6.91
SS 2	-4.36
SS 3	-3.47
SS 4	-3.86
SS 5	-6.33
SS 6	-10.84
$\sum Q_a=\sum Q_c$	37.11=-37.21

Figure 5.16. (a) Net ZRA galvanic current density recorded over time for the flat galvanic geometric array where solid lines represent the current for AA7050 electrodes and dotted lines represent the Type 316 stainless steel electrodes. (b) CMEA net current density without the RH cycle data. The key at the bottom shows the position of each wire in the array. The CMEA was exposed to a 0.6 M NaCl 70 µm thin film for 24 hours under a wet/dry cycle at 30°C. The cycle was 30 minutes at 95% RH and 3.5 hours at 30% RH.

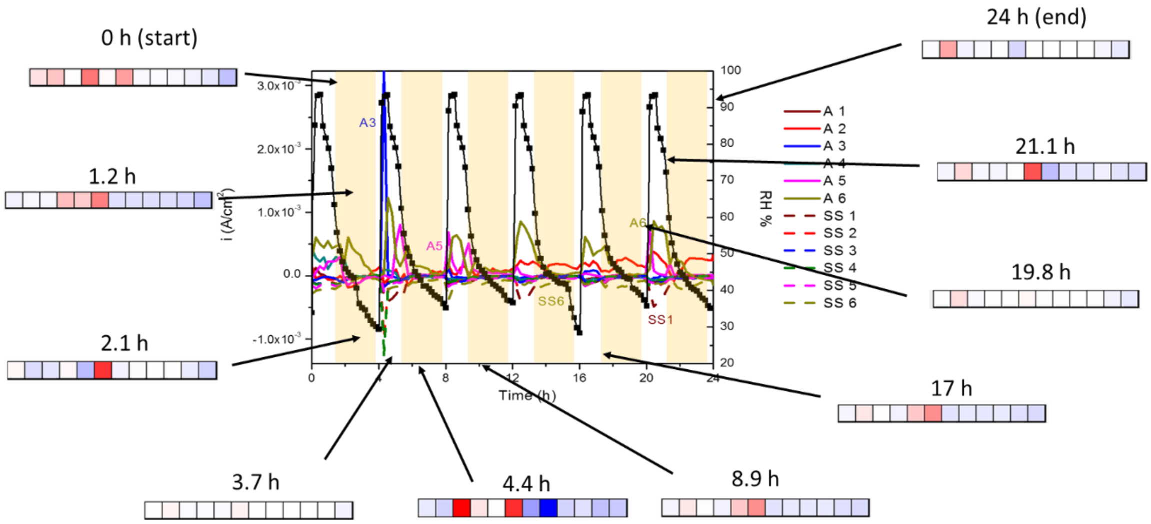

Figure 5.17. Net ZRA galvanic current density over time for the flat galvanic geometric array and the corresponding color maps. The CMEA was exposed to a 0.6 M NaCl 70 µm thin film for 24 hours under a wet/dry cycle at 30°C. The cycle was 30 minutes at 95% RH and 3.5 hours at 30% RH. Red indicates positive values (net anodic current), blue indicates negative values (net cathodic current) evident of galvanic coupling and white indicates zero current (electrodes with a net galvanic current close to zero).

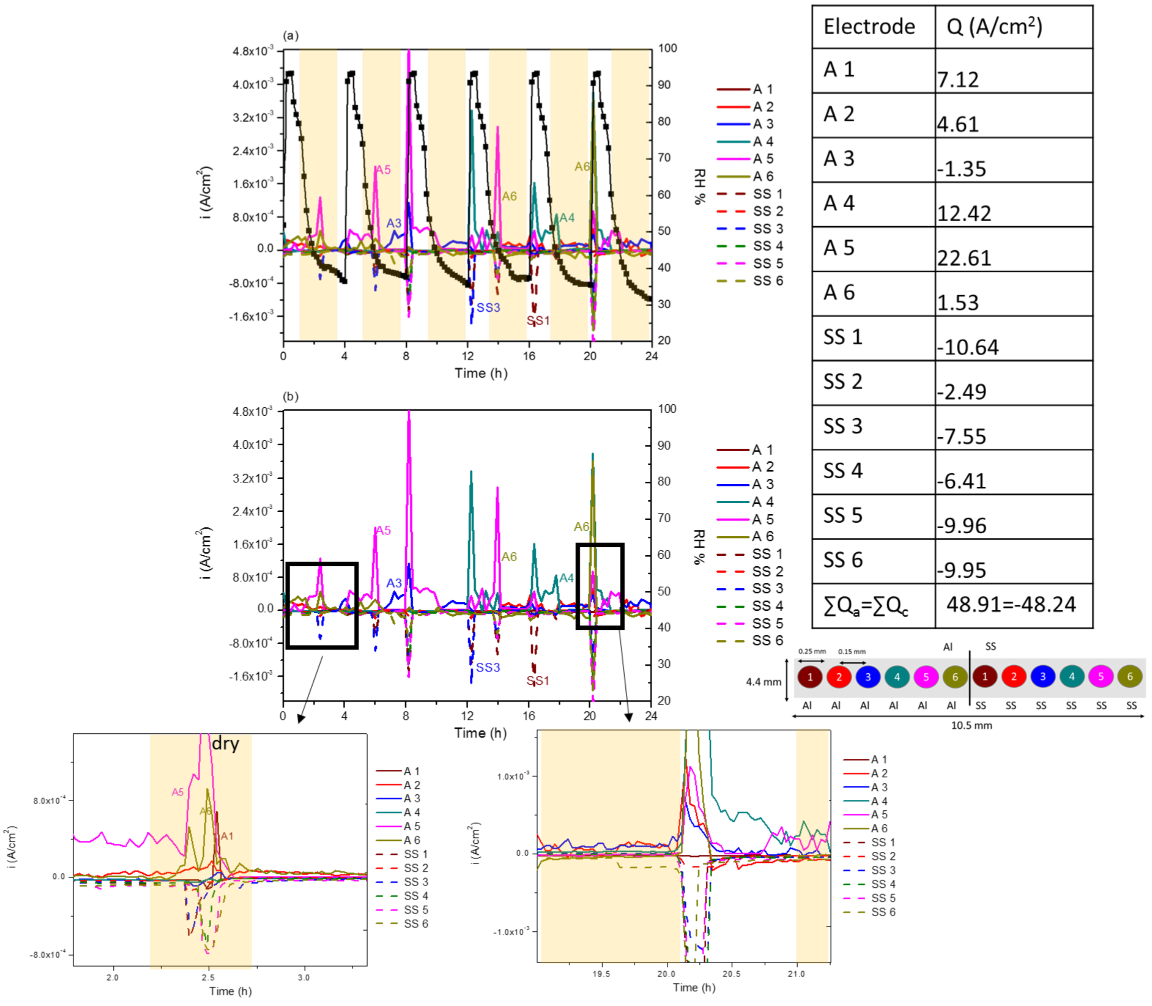

Electrode	Q (A/cm^2)
A 1	7.12
A 2	4.61
A 3	-1.35
A 4	12.42
A 5	22.61
A 6	1.53
SS 1	-10.64
SS 2	-2.49
SS 3	-7.55
SS 4	-6.41
SS 5	-9.96
SS 6	-9.95
$\sum Q_a = \sum Q_c$	48.91=-48.24

Figure 5.18. (a) Net ZRA galvanic current density over time for the flat galvanic geometric array where solid lines represent the current for AA7050 electrodes and dotted lines represent the Type 316 stainless steel electrodes. (b) CMEA net current density without the RH cycle data. The key at the bottom shows the position of each wire in the array. The CMEA was exposed to a 4.0 M NaCl 70 µm thin film for 24 hours under a wet/dry cycle at 30°C. The cycle was 30 minutes at 95% RH and 3.5 hours at 30% RH.

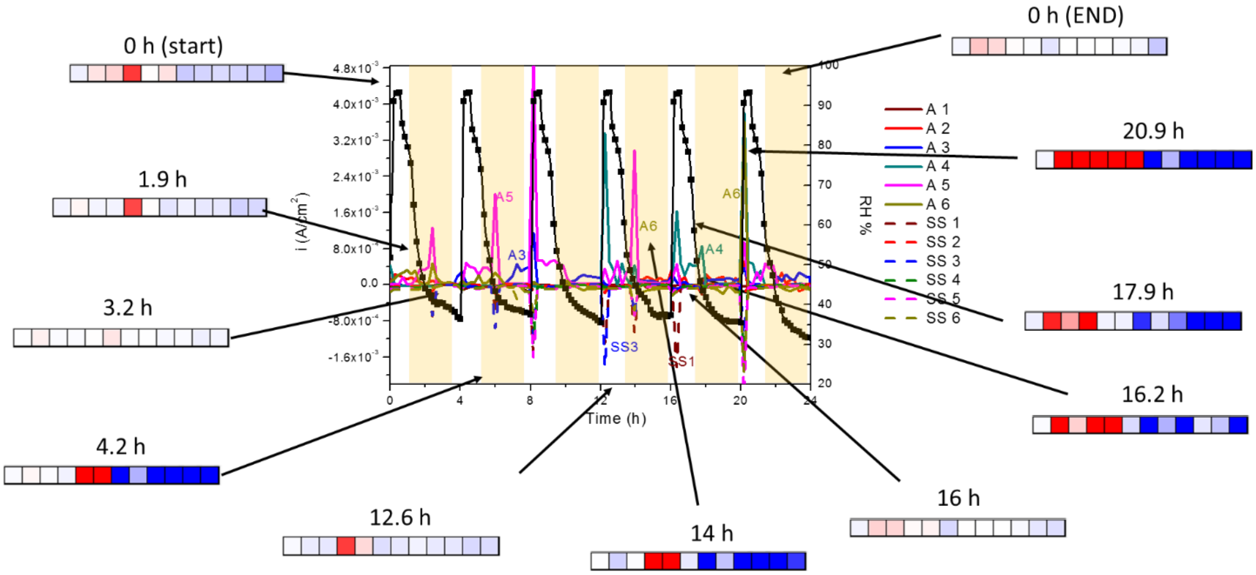

Figure 5.19. Net ZRA galvanic current density recorded over time for the flat galvanic geometric array and the corresponding color maps. The CMEA was exposed to a 4.0 M NaCl 70 µm thin film for 24 hours under a wet/dry cycle at 30°C. The cycle was 30 minutes at 95% RH and 3.5 hours at 30% RH. Red indicates positive values (net anodic current), blue indicates negative values (net cathodic current) evident of galvanic coupling and white indicates zero current (electrodes with a net galvanic current close to zero).

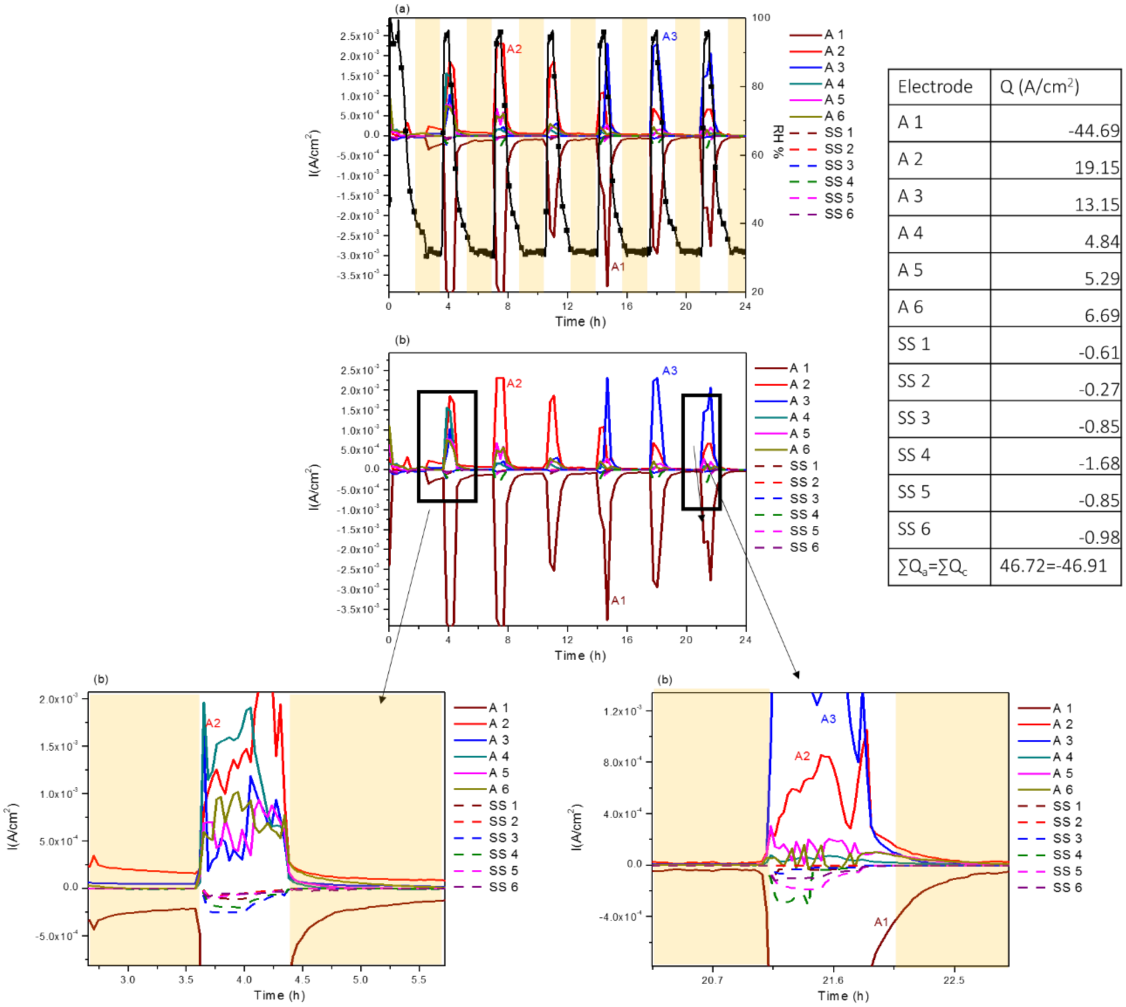

Electrode	Q (A/cm^2)
A 1	-44.69
A 2	19.15
A 3	13.15
A 4	4.84
A 5	5.29
A 6	6.69
SS 1	-0.61
SS 2	-0.27
SS 3	-0.85
SS 4	-1.68
SS 5	-0.85
SS 6	-0.98
$\sum Q_a=\sum Q_c$	46.72=-46.91

Figure 5.20. (a) Net ZRA galvanic current density recorded over time for the flat galvanic geometric array where solid lines represent the current for AA7050 electrodes and dotted lines represent the Type 316 stainless steel electrodes. (b) CMEA net current density without the RH cycle data. The key at the bottom shows the position of each wire in the array. The CMEA was exposed to a 0.6 M NaCl 70 µm thin film for 24 hours under a wet/dry cycle at 50°C. The cycle was 30 minutes at 95% RH and 3 hours at 50% RH at a higher temperature of 50°C.

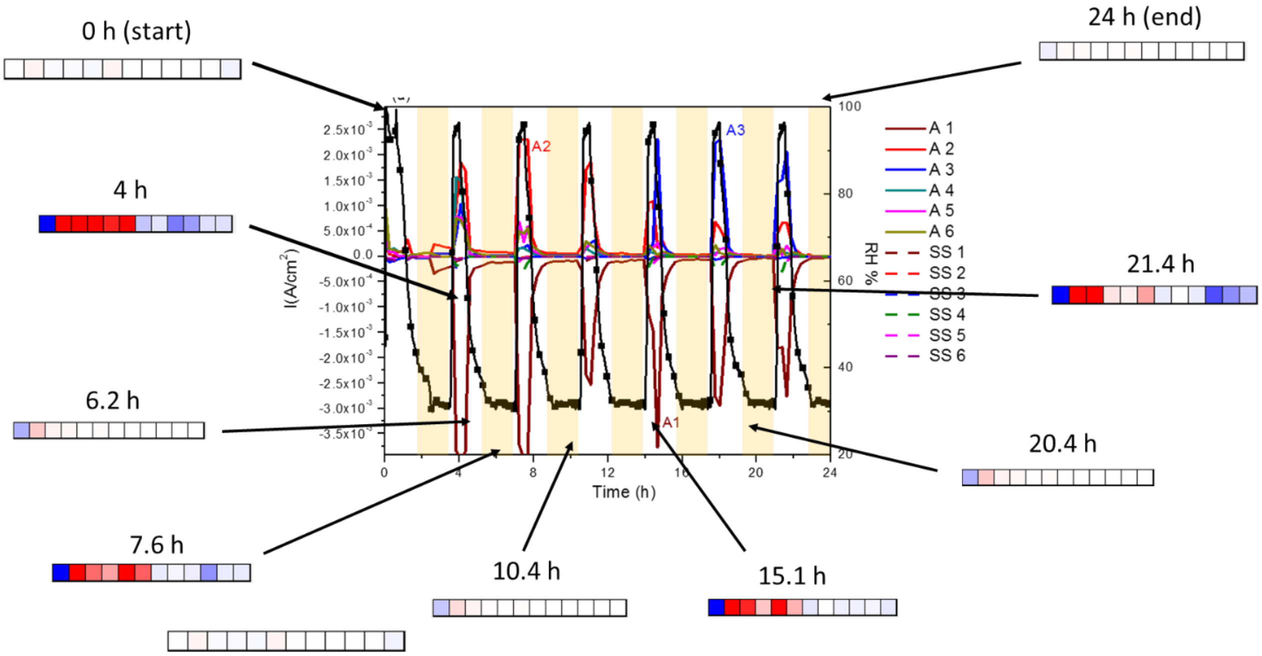

Figure 5.21. Net CMEA current recorded over time for the flat galvanic geometric array and the corresponding color maps. The CMEA was exposed to a 0.6 M NaCl 70 µm thin film for 24 hours under a wet/dry cycle at 50°C. The cycle was 30 minutes at 95% RH and 3.5 hours at 30% RH. Red indicates positive values (net anodic current), blue indicates negative values (net cathodic current) evident of galvanic coupling and white indicates zero current (electrodes with a net galvanic current close to zero).

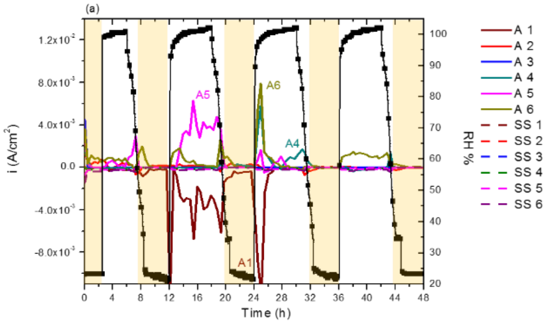

Electrode	Q (C/cm²)
A 1	-92.41
A 2	6.52
A 3	0.45
A 4	28.31
A 5	57.22
A 6	65.24
SS 1	-8.96
SS 2	-8.76
SS 3	-8.24
SS 4	-9.08
SS 5	-11.75
SS 6	-16.95
$\sum Q_a = \sum Q_c$	158.27=-158.62

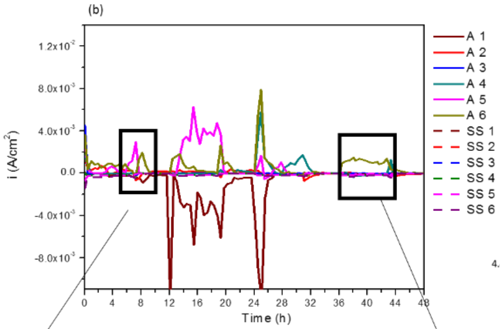

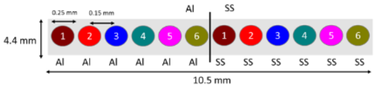

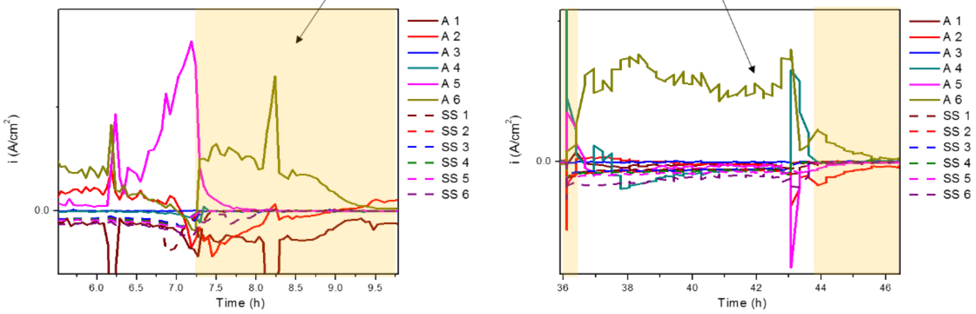

Figure 5.22. (a) Net ZRA galvanic current density recorded over time for the flat galvanic geometric array where solid lines represent the current for AA7050 electrodes and dotted lines represent the Type 316 stainless steel electrodes. b) CMEA net current density without the RH cycle data. The key at the bottom shows the position of each wire in the array. The CMEA was exposed to a 0.6 M NaCl 70 µm thin film for 48 hours under a wet/dry cycle at 50°C. The cycle was 4 hours at 25% RH and 8 hours at 95% RH at a higher temperature of 50°C.

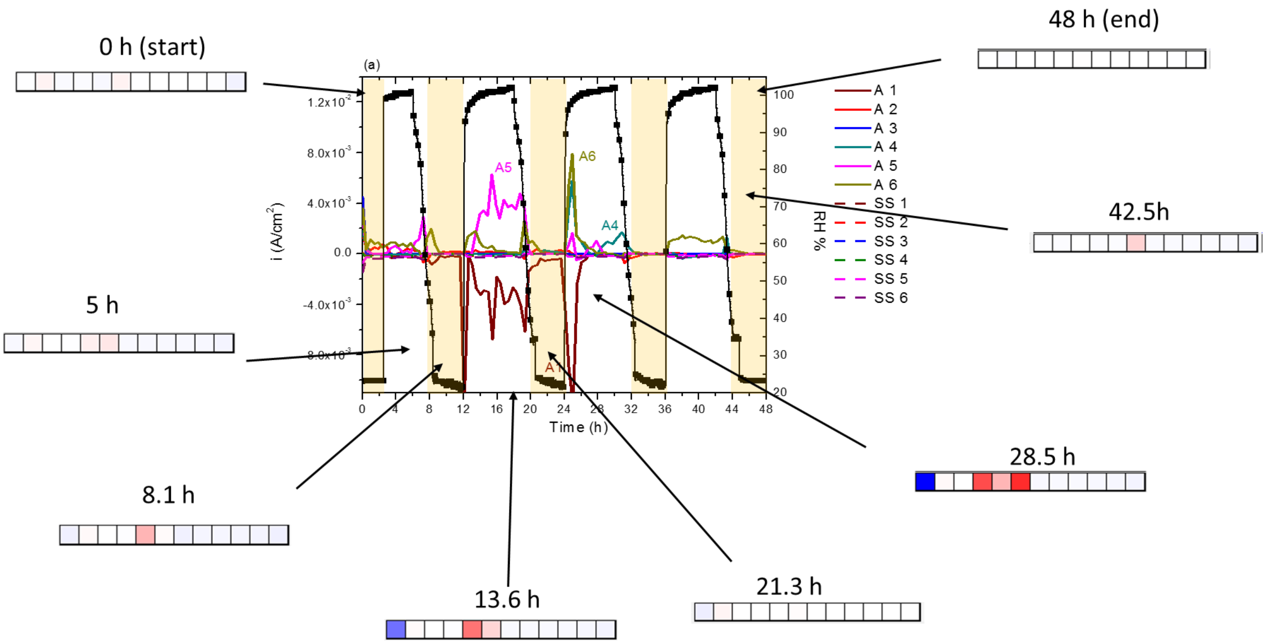

Figure 5.23. Net ZRA galvanic current density recorded over time for the flat galvanic geometric array and the corresponding color maps. The CMEA was exposed to a 0.6 M NaCl 70 µm thin film for 48 hours under a wet/dry cycle at 50°C. The cycle was 4 hours at 25% RH and 8 hours at 95% RH at a higher temperature of 50°C. Red indicates positive values (net anodic current), blue indicates negative values (net cathodic current) evident of galvanic coupling and white indicates zero current (electrodes with a net galvanic current close to zero).

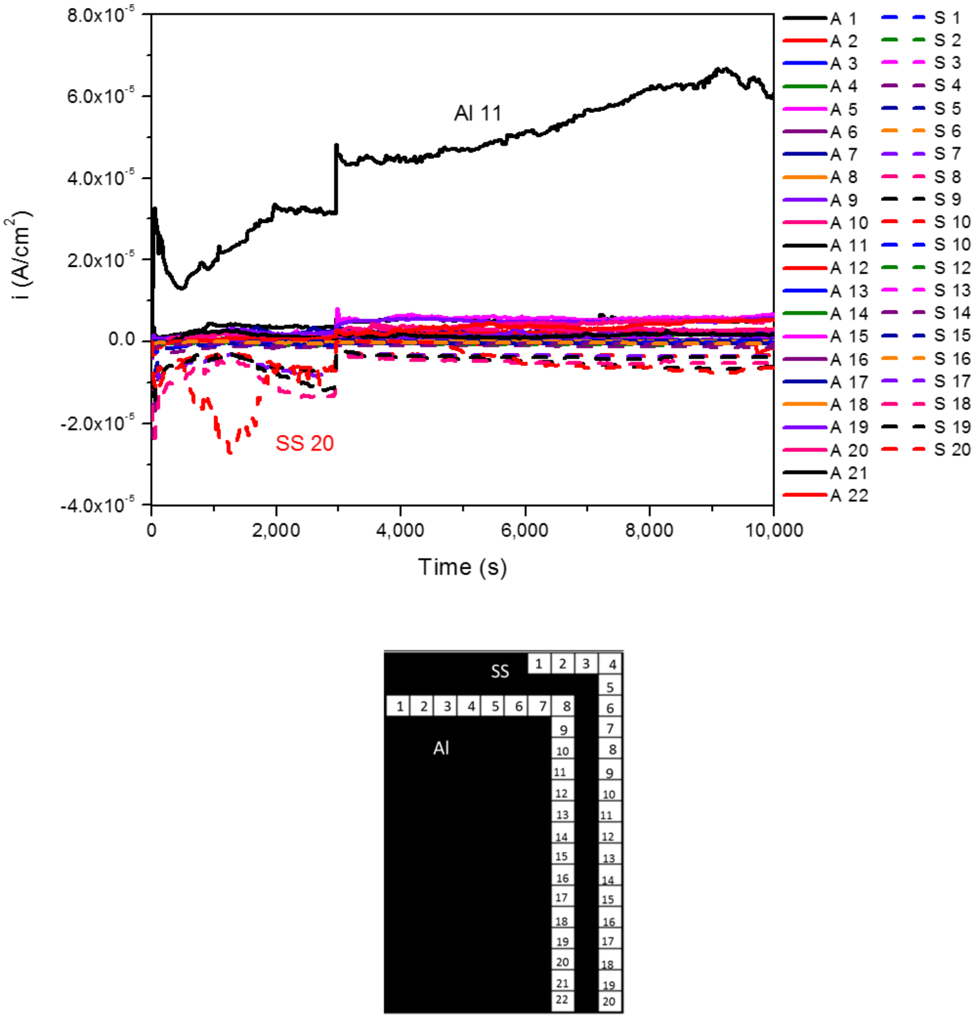

Figure 5.24. Net ZRA galvanic current density over 10000 s for the CMEA arranged in a fastener geometry where solid lines represent the current for AA7050 electrodes and dotted lines represent the Type 316 stainless steel electrodes. The key at the bottom shows the position of each wire in the array. The CMEA was exposed in full immersion 0.6 M NaCl with a gap of ~100 μm between the AA7050 and the steel fastener.

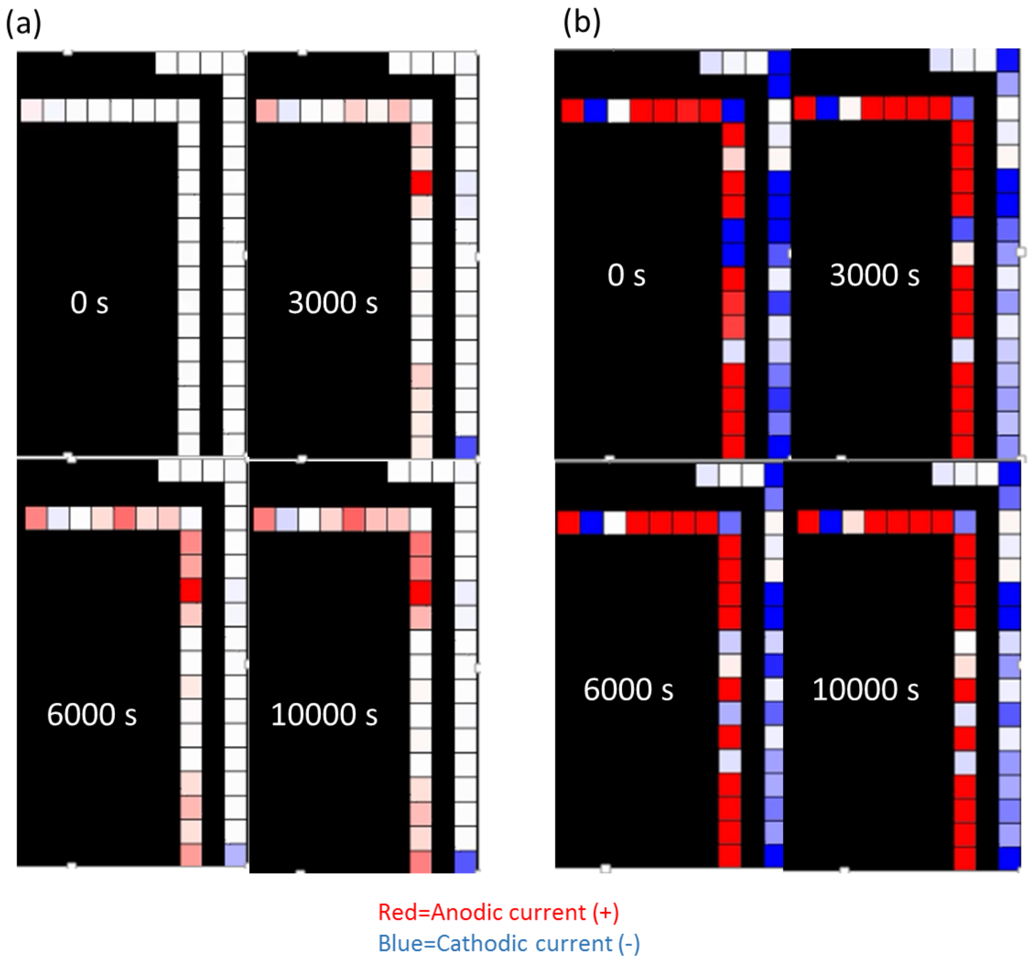

Figure 5.25. Color maps of the CMEA arranged in a fastener geometry over the 10000 s full immersion in 0.6 M NaCl with a small gap of (~100 µm) between the AA7050 and the steel fastener. (a) shows the color maps at a higher current scale then (b). Red indicates positive values (net anodic), blue indicates negative values (net cathodic) evident of galvanic coupling and white indicates zero current (electrodes with a net galvanic current close to zero).

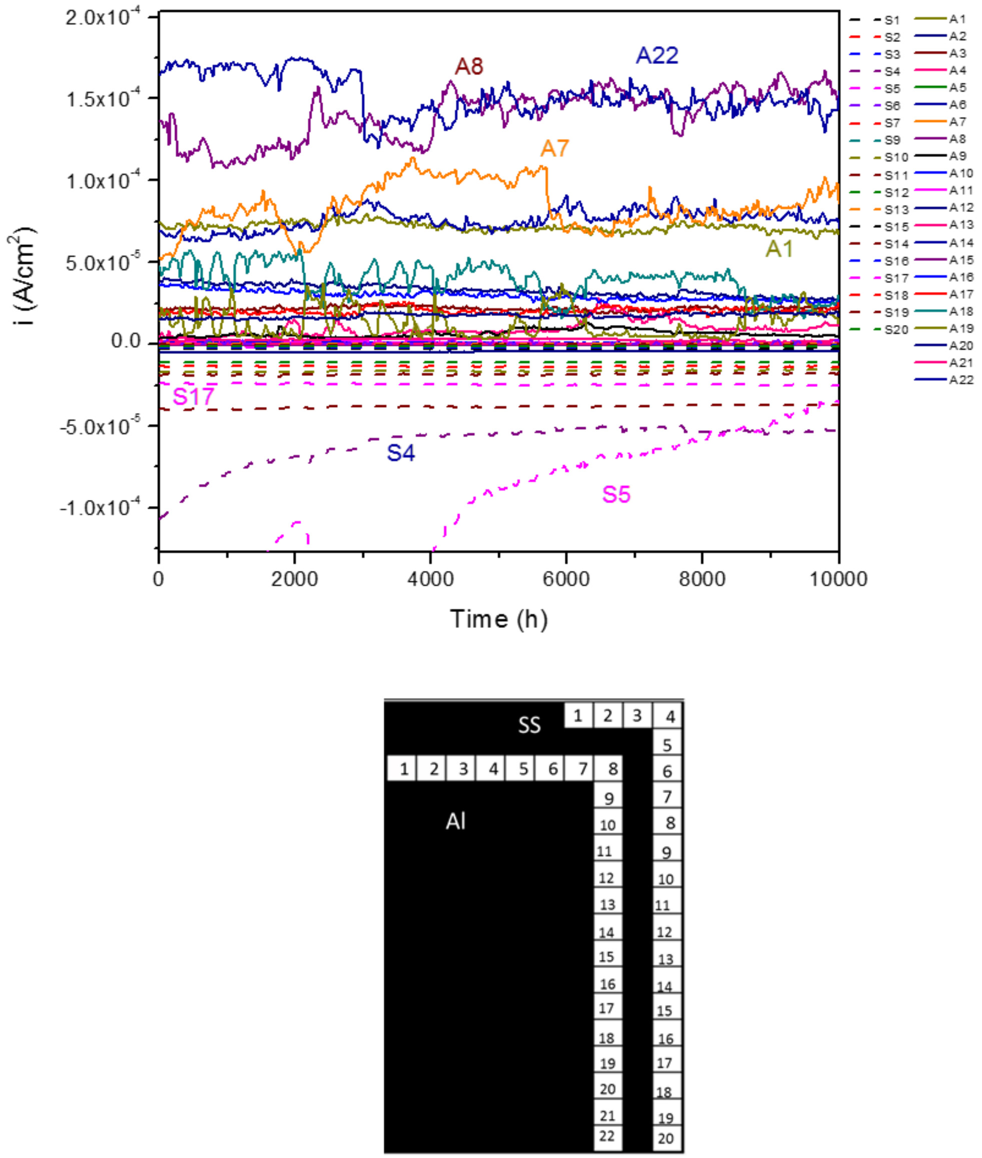

Figure 5.26. Net ZRA galvanic current density over 10000 s for the CMEA arranged in a fastener geometry where solid lines represent the current for AA7050 electrodes and dotted lines represent the Type 316 stainless steel electrodes. The key at the bottom shows the position of each wire in the array. The CMEA was exposed under a 70 µm thin film of 0.6 M NaCl at 98% RH for 10000 s with a gap of ~100 µm between the AA7050 and the steel fastener.

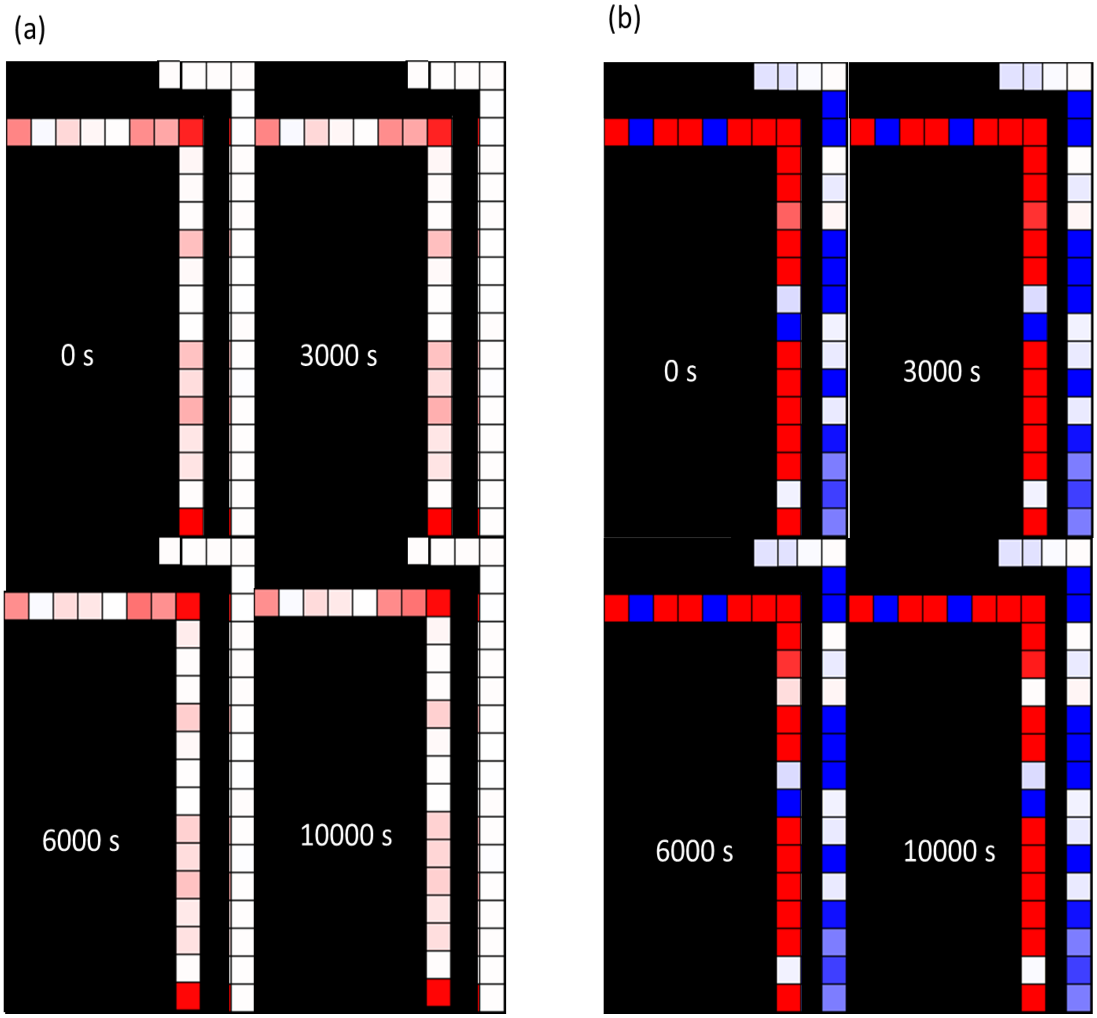

Figure 5.27. Color maps of the CMEA arranged in a fastener geometry over the 10000 s exposed under a 70 µm thin film of 0.6 M NaCl at 98% RH with a gap of ~100 µm between the AA7050 and the steel fastener. (a) shows the color maps at a higher current scale then (b). Red indicates positive values (net anodic), blue indicates negative values (net cathodic) evident of galvanic coupling and white indicates zero current (electrodes with a net galvanic current close to zero).

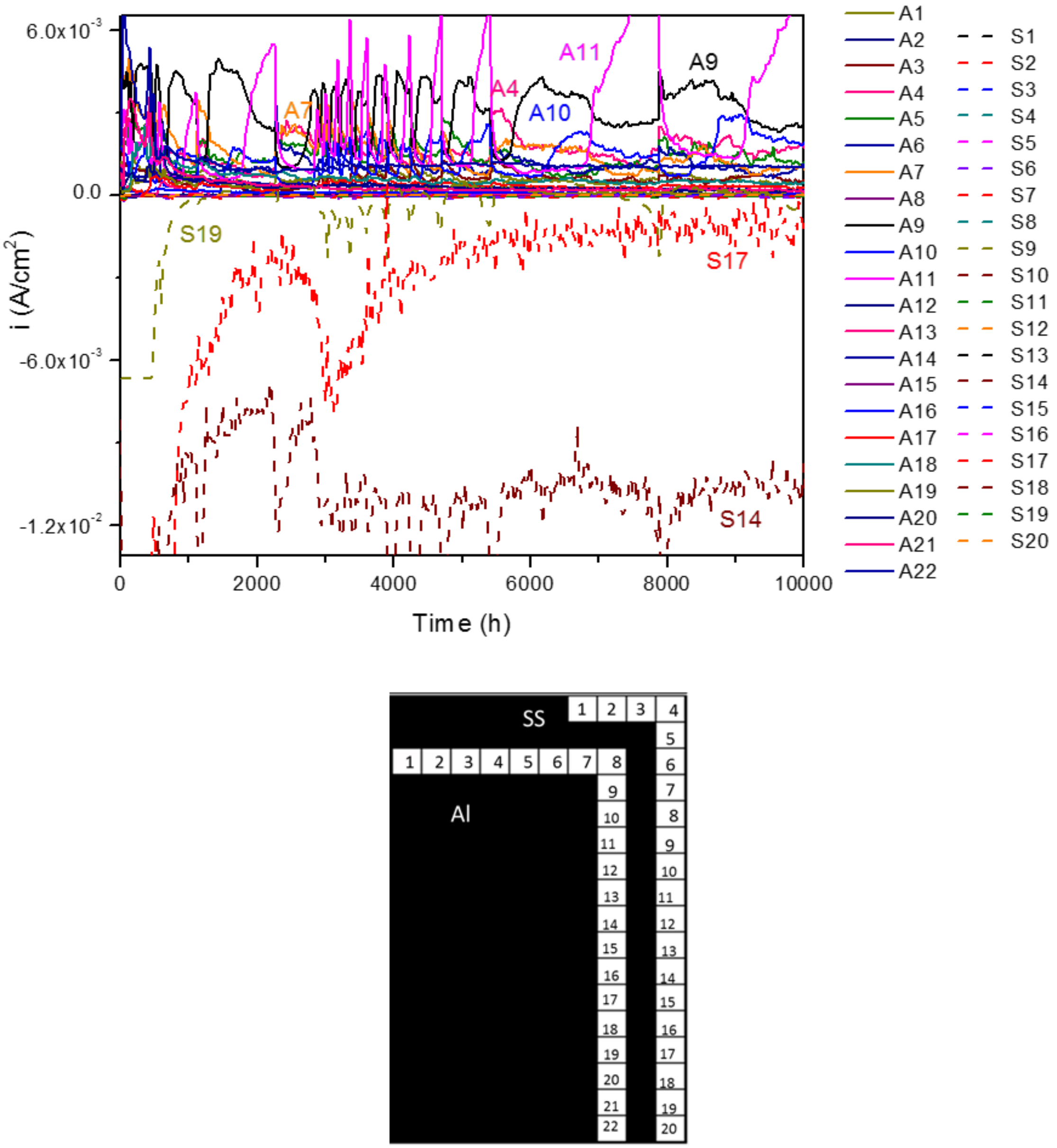

Figure 5.28. Net ZRA galvanic current density over 10000 s for the CMEA arranged in a fastener geometry where solid lines represent the current for AA7050 electrodes and dotted lines represent the Type 316 stainless steel electrodes. The key at the bottom shows the position of each wire in the array. The CMEA was exposed under a 500 µm thin film of 0.6 M NaCl at 98% RH for 10,000 s with a gap of ~100 µm between the AA7050 and the steel fastener.

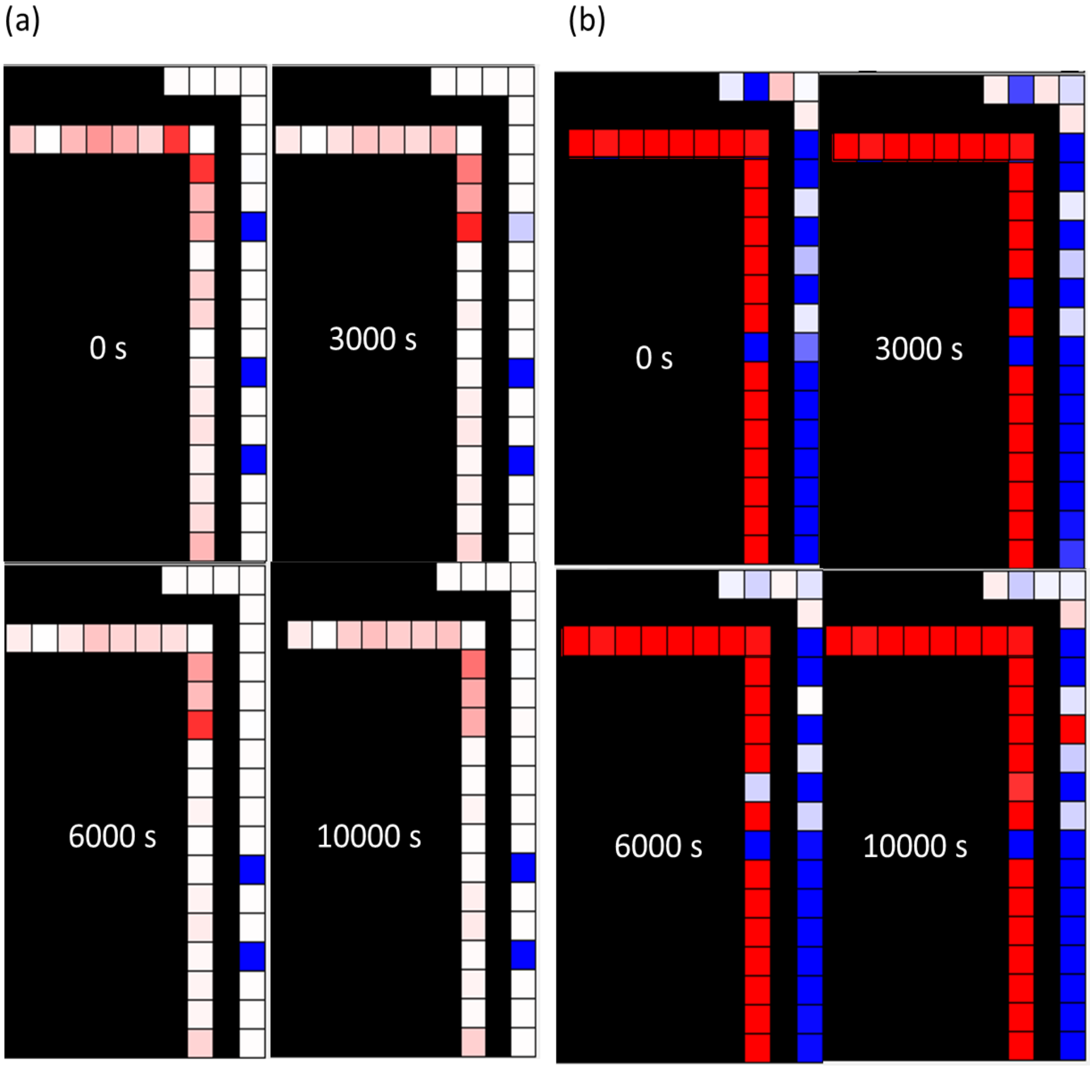

Figure 5.29. Color maps of the CMEA arranged in a fastener geometry after over the 10000 s exposed under a 500 µm thin film of 0.6 M NaCl at 98% RH with a gap of ~100 µm between the AA7050 and the steel fastener.(a) shows the color maps at a higher current scale then (b). Red indicates positive values (net anodic), blue indicates negative values (net cathodic) evident of galvanic coupling and white indicates zero current (electrodes with a net galvanic current close to zero).

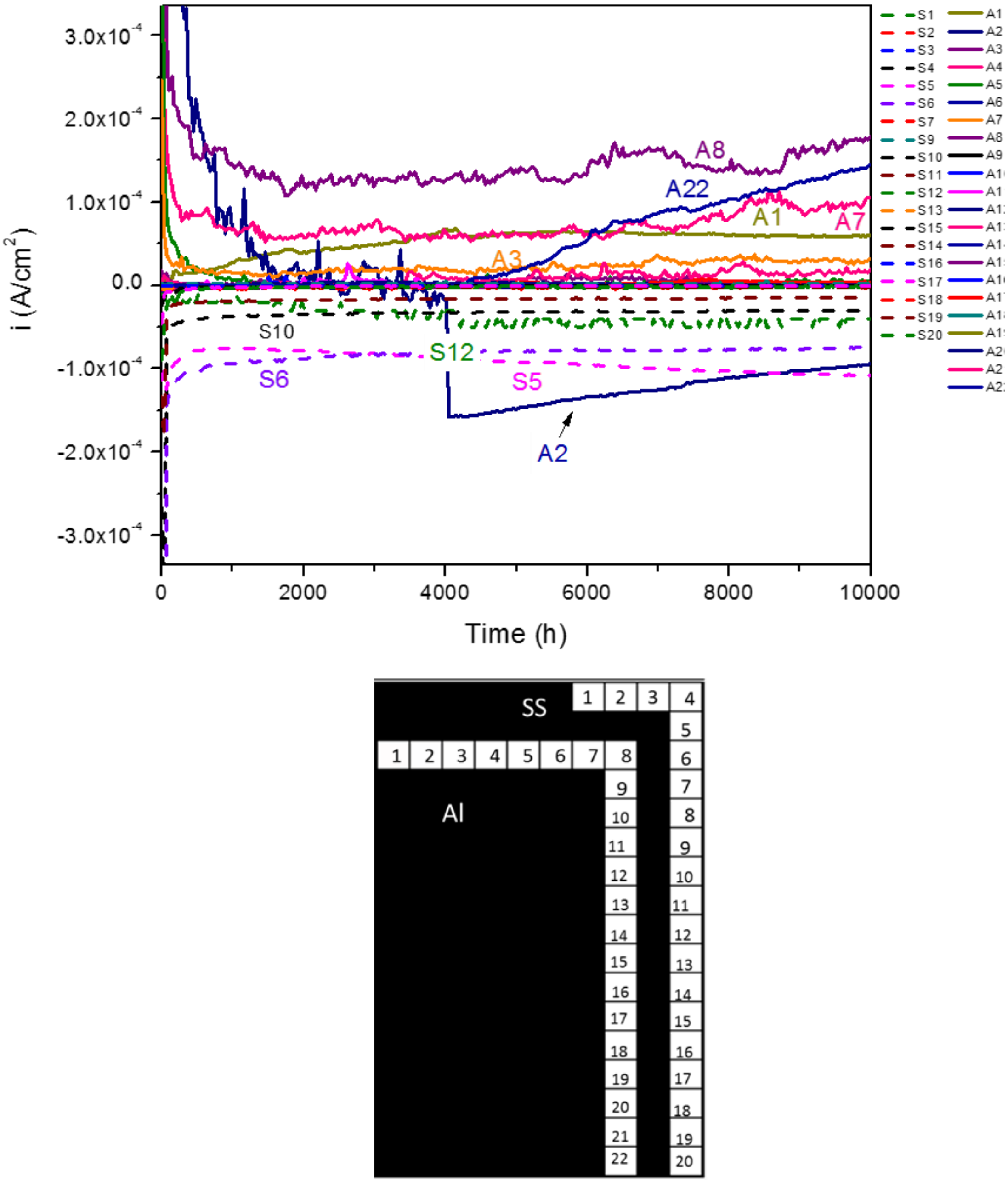

Figure 5.30. Net ZRA galvanic current density recorded over 10000 s for the CMEA arranged in a fastener geometry where solid lines represent the current for AA7050 electrodes and dotted lines represent the Type 316 stainless steel electrodes. The key at the bottom shows the position of each wire in the array. The CMEA was exposed under a 70 µm thin film of 0.6 M NaCl at 98% RH for 10,000 s with a large gap of ~500 µm between the AA7050 and the steel fastener.

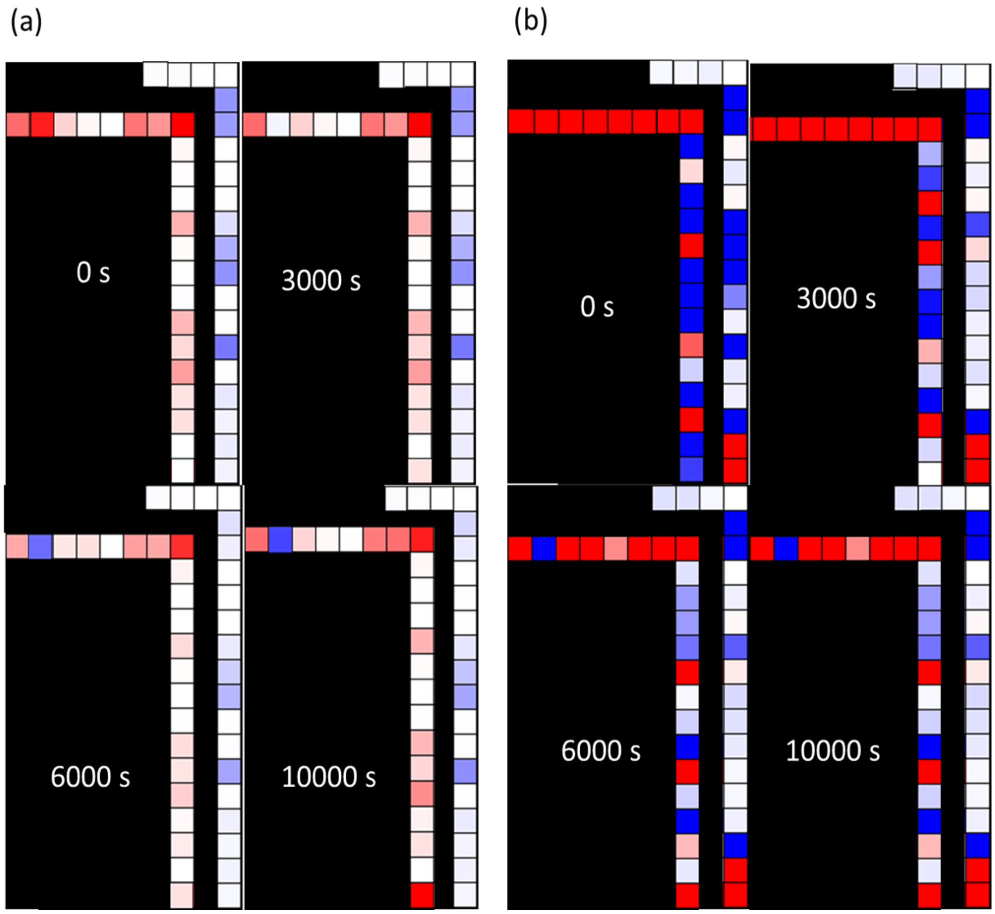

Figure 5.31. Color maps of the CMEA arranged in a fastener geometry after over the 10000 s exposed under a 70 µm thin film of 0.6 M NaCl at 98% RH with a large gap of ~500 µm between the AA7050 and the steel fastener. (a) shows the color maps at a higher current scale then (b). Red indicates positive values (net anodic), blue indicates negative values (net cathodic) evident of galvanic coupling and white indicates zero current (electrodes with a net galvanic current close to zero).

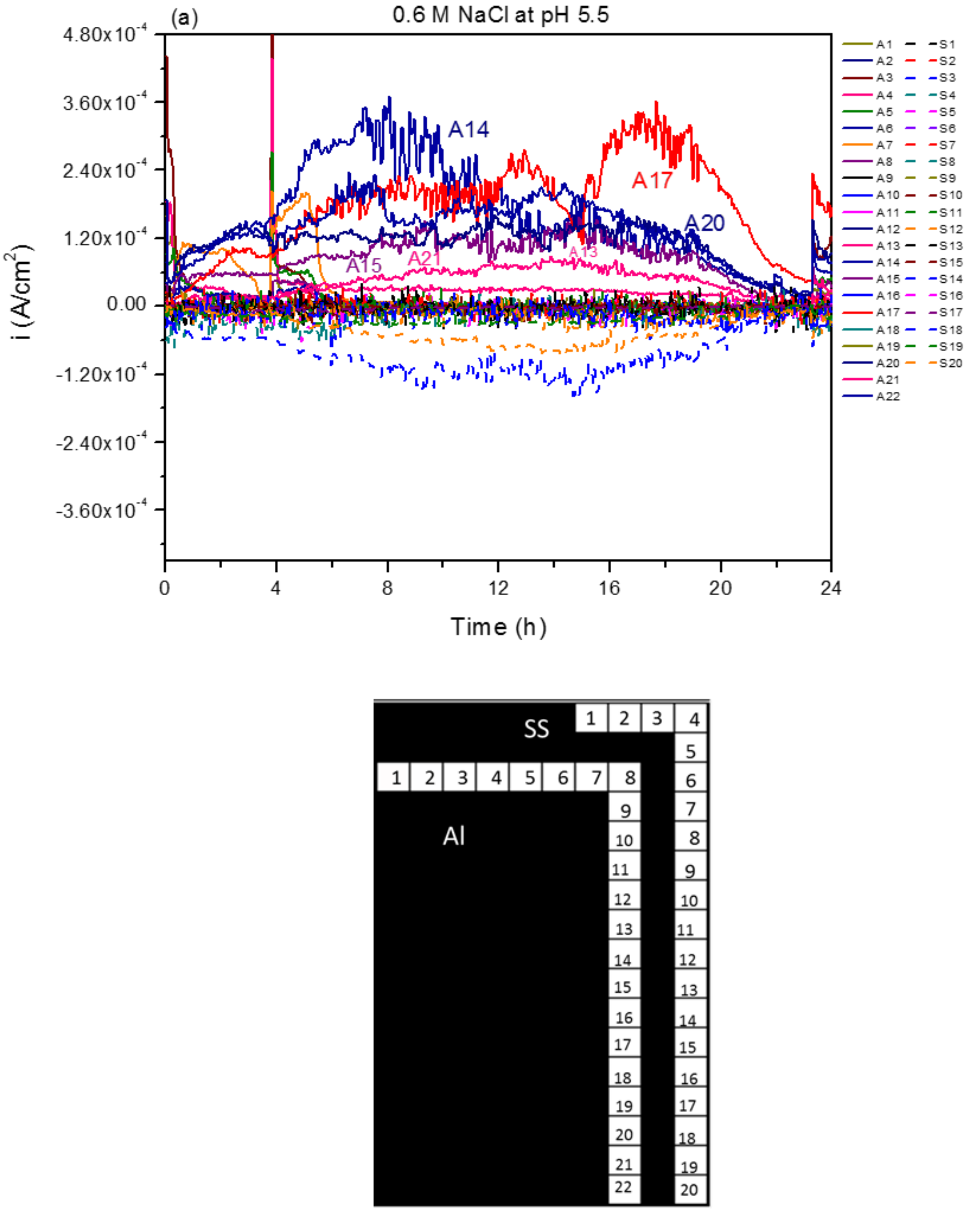

Figure 5.32. Net ZRA galvanic current density recorded over 24 h for the CMEA arranged in a fastener geometry where solid lines represent the current for AA7050 electrodes and dotted lines represent the Type 316 stainless steel electrodes. The key at the bottom shows the position of each wire in the array. The CMEA was exposed under a 70 µm thin film of 0.6 M NaCl at 98% RH for 10000 s with a gap of ~100 µm between the AA7050 and the steel fastener.

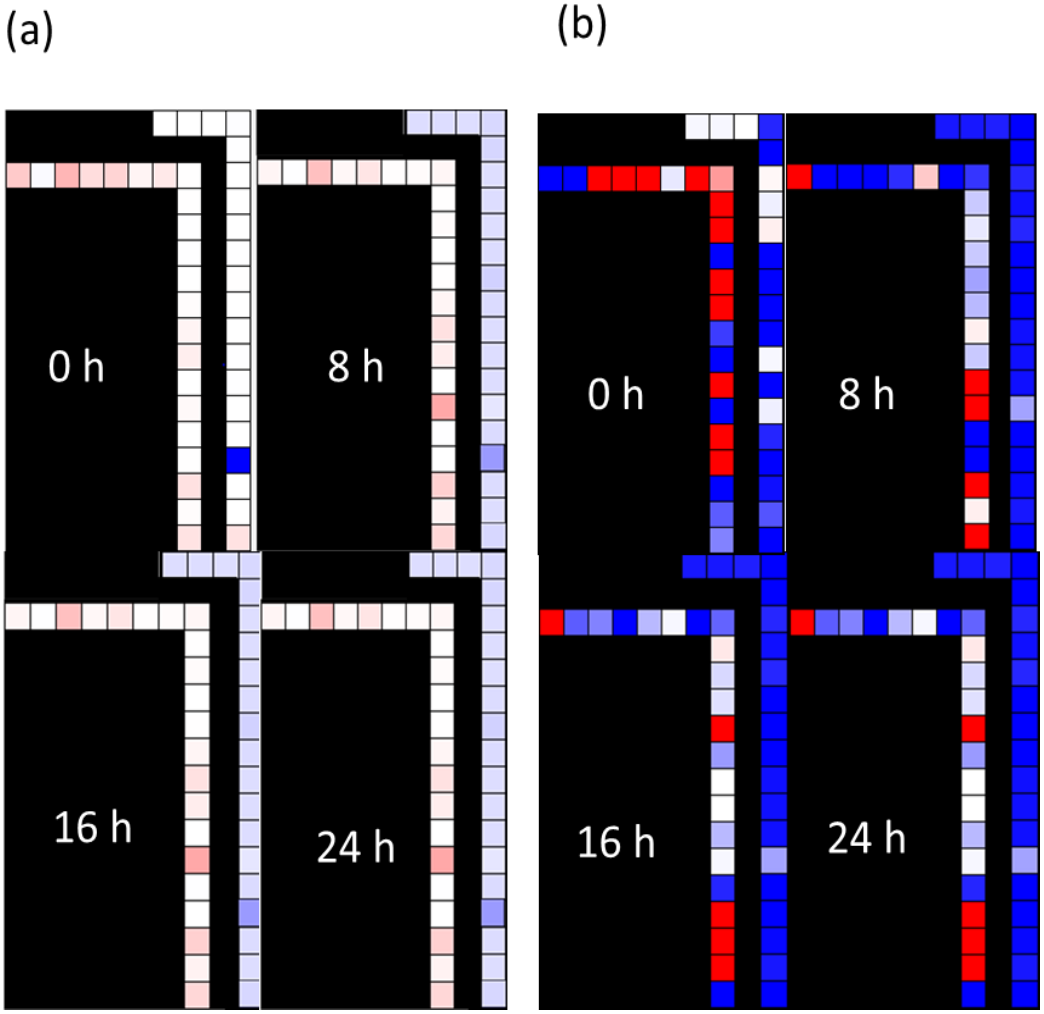

Figure 5.33. Color maps of the CMEA arranged in a fastener geometry after over the 24 h exposed under a 70 µm thin film of 0.6 M NaCl at 98% RH for 10000 s with a gap of ~100 µm between the AA7050 and the steel fastener. (a) shows the color maps at a higher current scale then (b). Red indicates positive values (net anodic), blue indicates negative values (net cathodic) evident of galvanic coupling and white indicates zero current (electrodes with a net galvanic current close to zero).

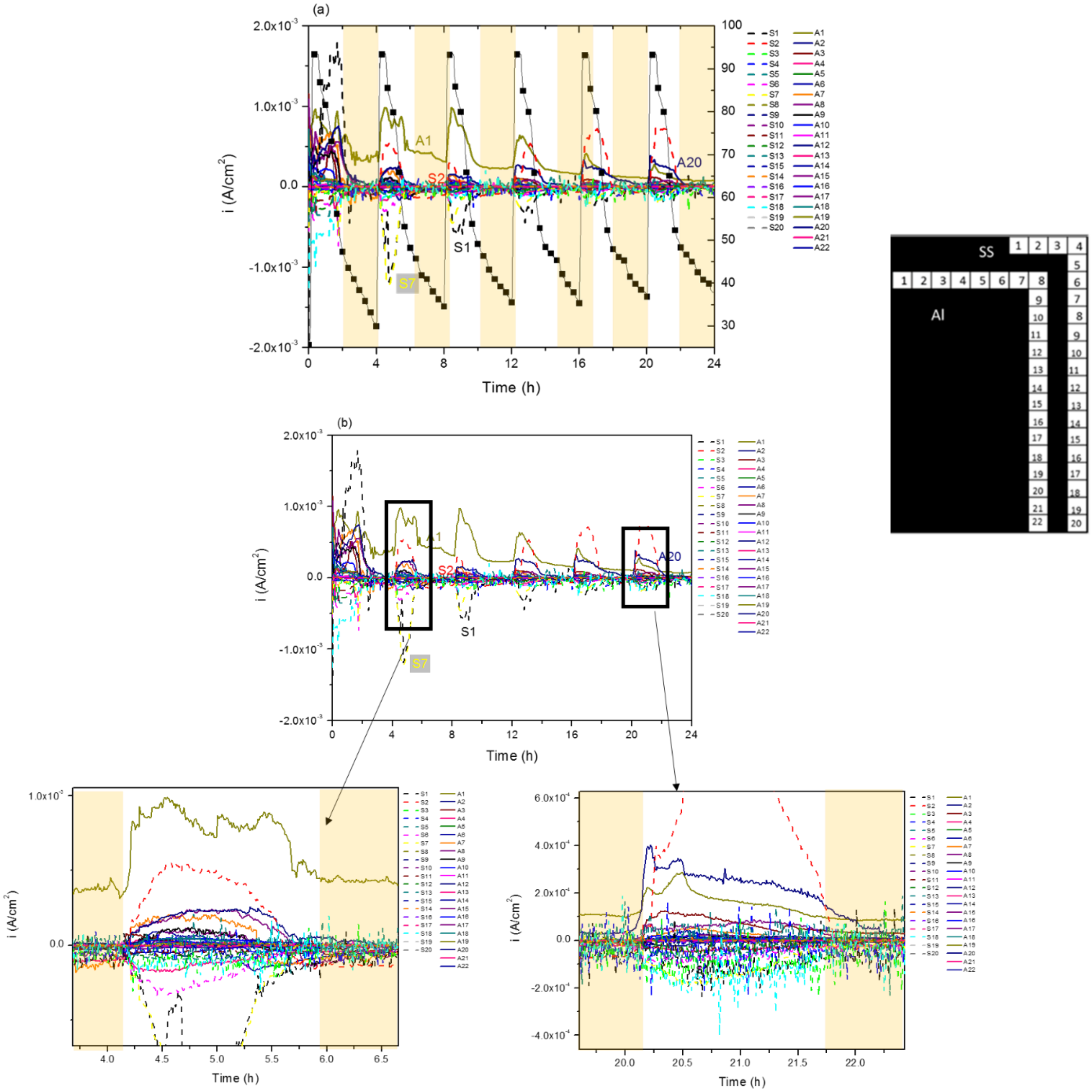

Figure 5.34. (a) Net ZRA current density recorded over time for the CMEA arranged in a fastener geometry where solid lines represent the current for AA7050 electrodes and dotted lines represent the Type 316 stainless steel electrodes. (b) CMEA net current without the RH cycle data. The key at the bottom shows the position of each wire in the array. The CMEA was exposed to a 0.6 M NaCl 70 µm thin film for 24 hours under a wet/dry cycle at 30°C with a small gap of ~100 µm between the AA7050 and the steel fastener. The cycle was 30 minutes at 95% RH and 3.5 hours at 30% RH at a temperature of 30°C.

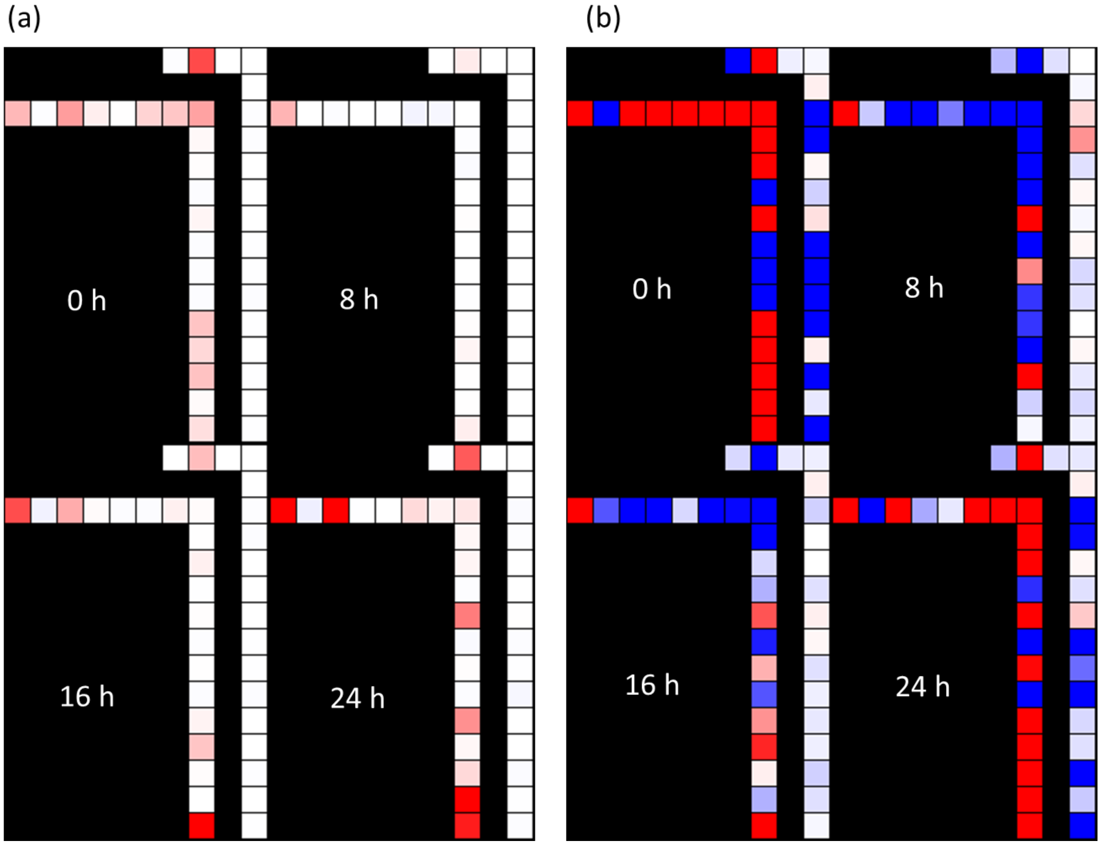

Figure 5.35. Color maps of the CMEA arranged in a fastener geometry after over the 24 h exposed under a 70 µm thin film of 0.6 M NaCl at 98% RH during wet/dry cycle at 30°C with a gap of ~100 µm between the AA7050 and the steel fastener. (a) shows the color maps at a higher current scale then (b). Red indicates positive values (net anodic), blue indicates negative values (net cathodic) evident of galvanic coupling and white indicates zero current (electrodes with a net galvanic current close to zero).

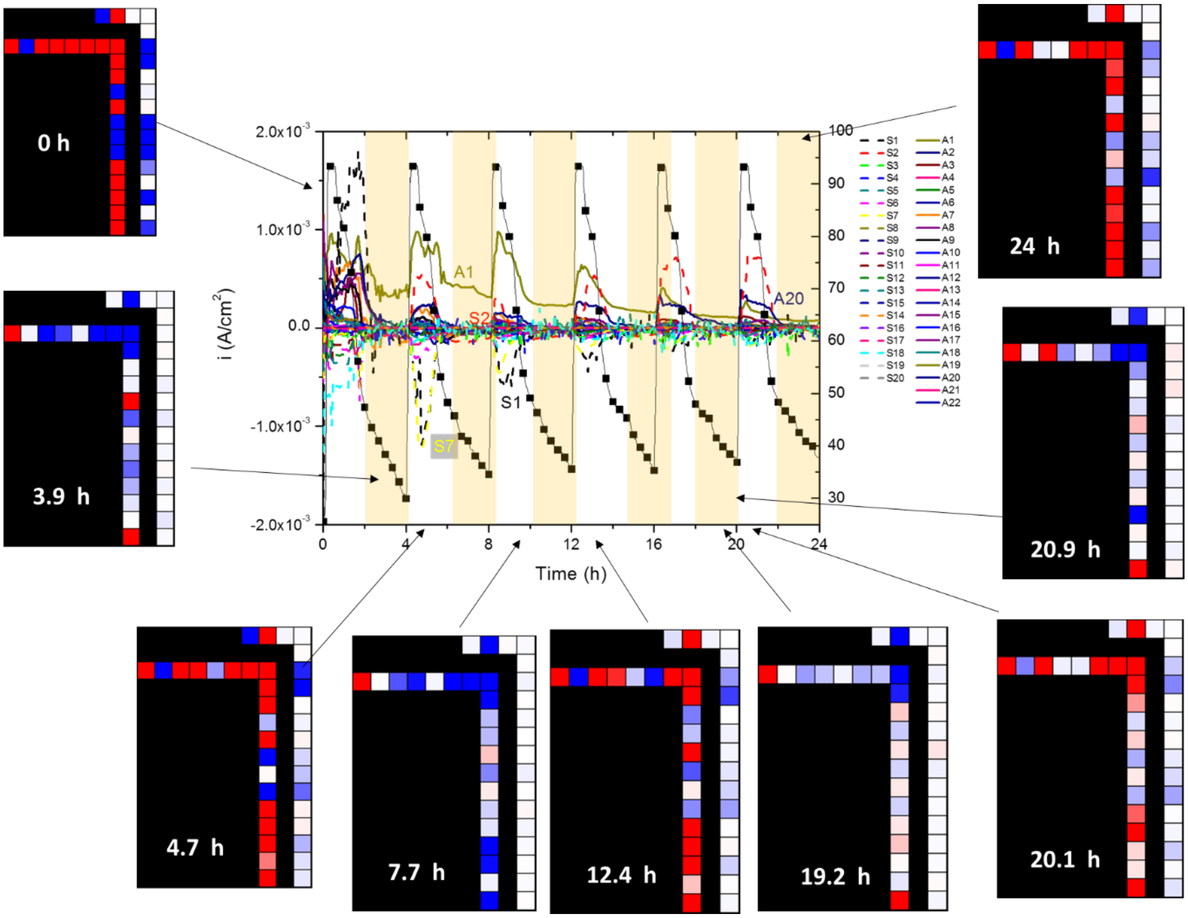

Figure 5.36. Net ZRA current density recorded over time for the the CMEA arranged in a fastener geometry and the corresponding color maps. The CMEA was exposed to a 0.6 M NaCl 70 µm thin film for 24 hours under a wet/dry cycle at 30°C with a gap of ~100 µm between the AA7050 and the steel fastener. The cycle was 30 minutes at 95% RH and 3 hours at 30% RH at a temperature of 30°C. Red indicates positive values (net anodic), blue indicates negative values (net cathodic) evident of galvanic coupling and white indicates zero current (electrodes with a net galvanic current close to zero).

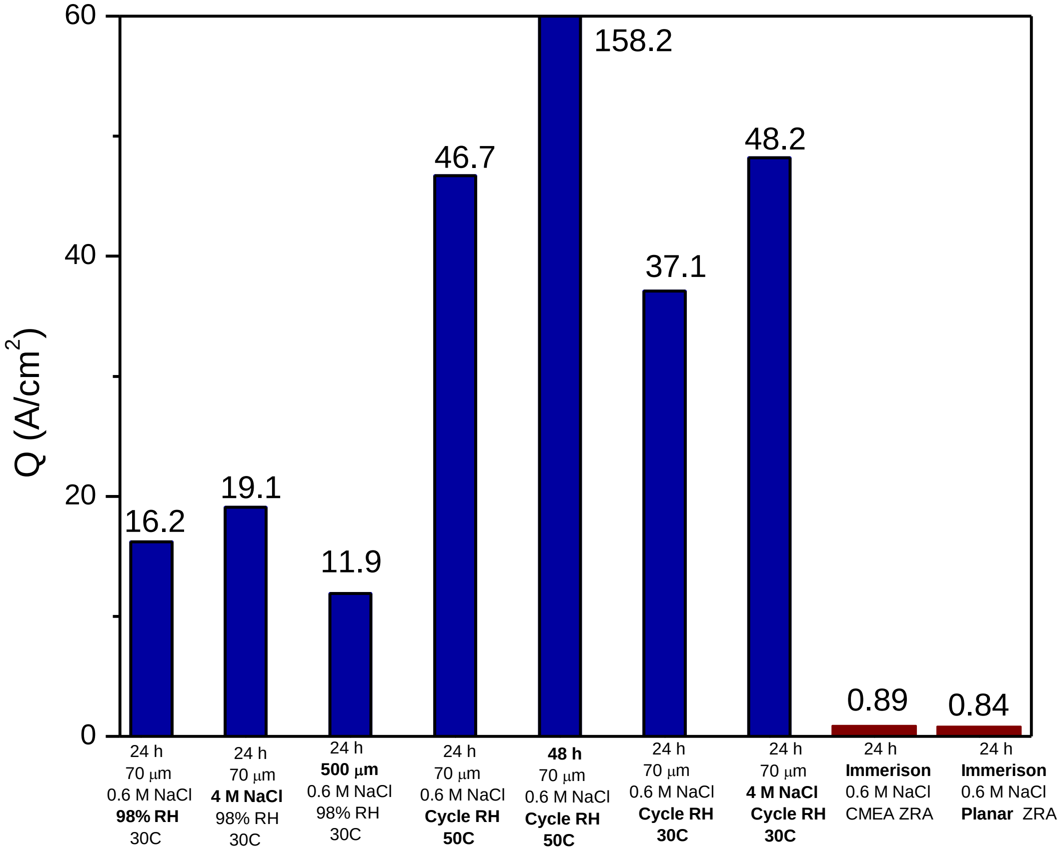

Figure 5.37. Summary bar plot of charge density of each of the geometric flat galvanic array exposures compared to full immersion ZRA results.

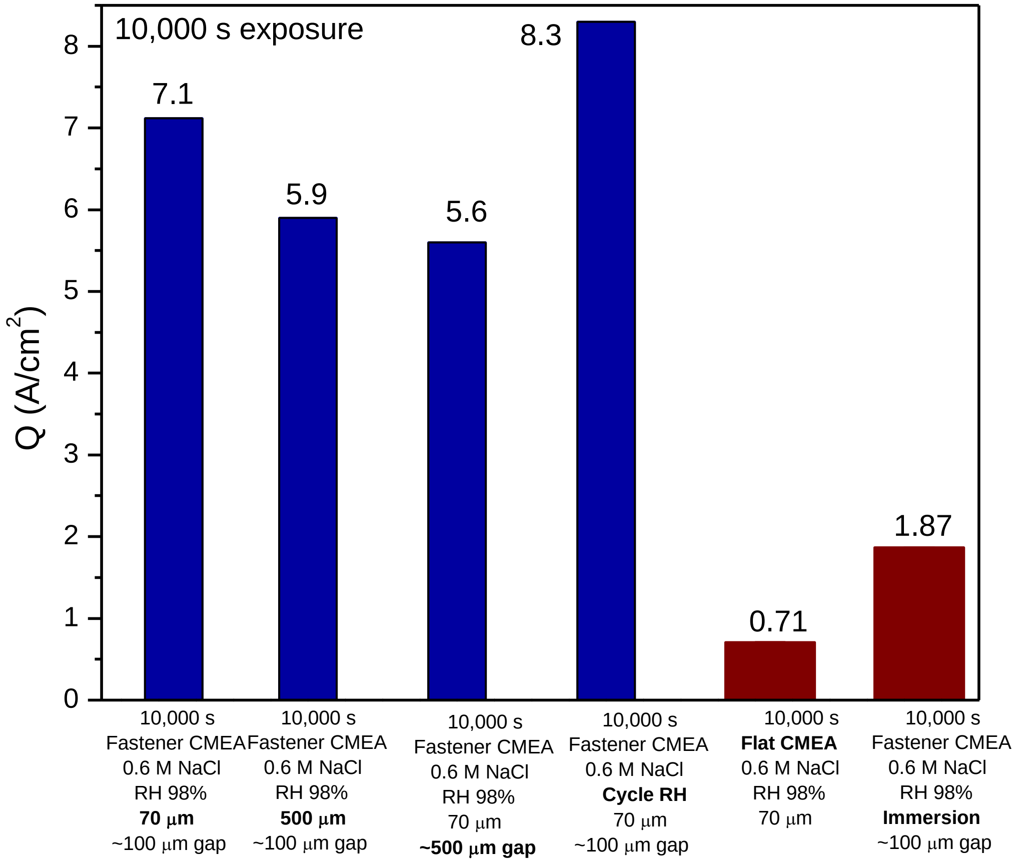

Figure 5.38. Summary bar plot of charge density of each of the CMEA arranged in a fastener geometry exposures compare to full immersion exposures.

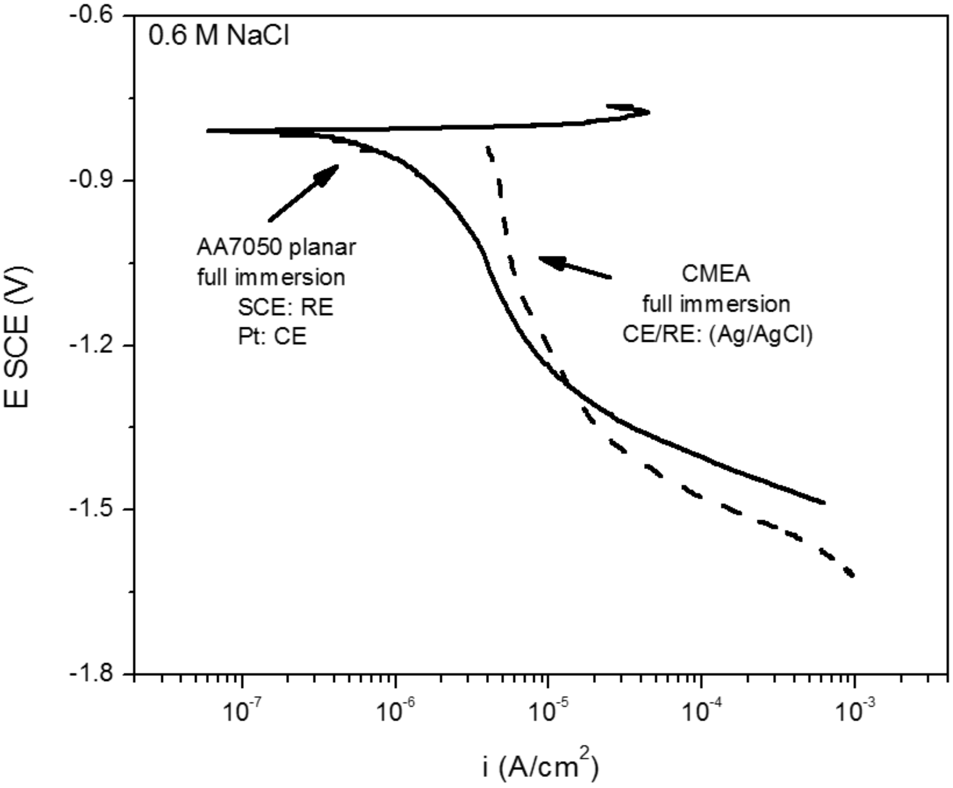

Figure 5.39. Cathodic polarization data in 0.6 M NaCl on an AA7050-T7451 planar electrode (area=1cm^2) using SCE as the RE and Pt mesh as the CE (solid line) compared to a single AA7050 electrode (area=0.0004 cm^2) in the CMEA consisting of 20 AA7050-T7451 electrodes using a flush mounted electrode Ag/AgCl functioning as the CE and RE.

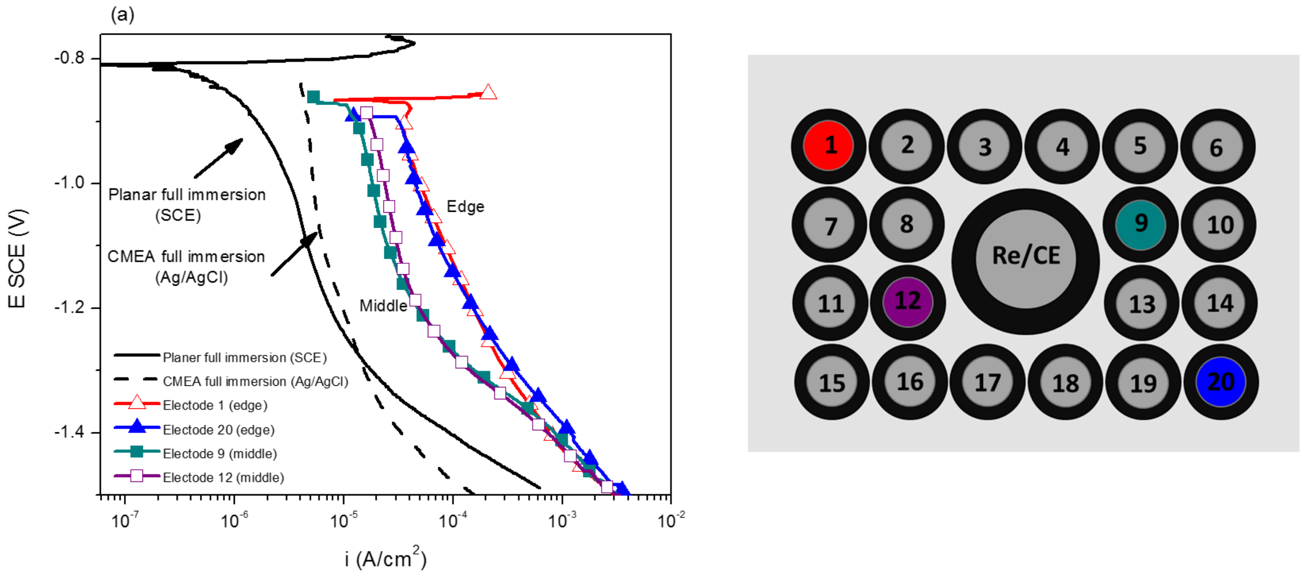

Figure 5.40. Cathodic polarization data of AA7050-T7451 in the CMEA consisting of 20 AA7050-T7451 under a 70 µm droplet of 0.6 M NaCl pH 5.5. The black line is full immersion, triangles are electrodes on the edge of the CMEA and squares are electrodes in the middle of the CMEA. The black line is full immersion, triangles are wires on the edge of the CMEA and squares are wires in the middle of the CMEA.

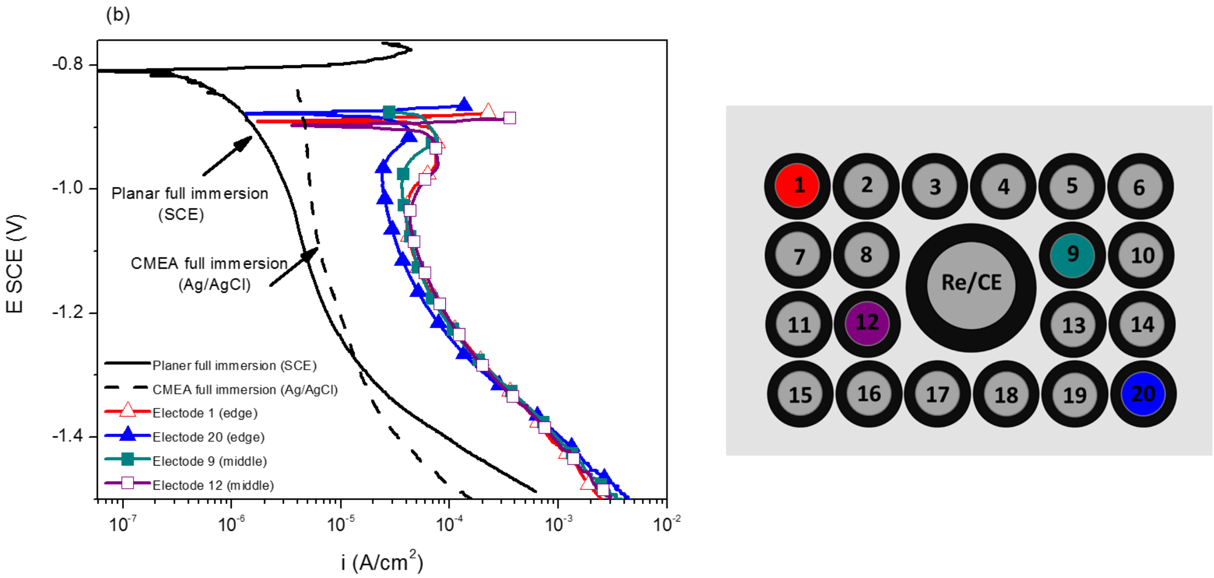

Figure 5.41. Cathodic polarization data for AA7050-T7451 on the CMEA consisting of 20 AA7050-T7451 under a 70 µm droplet of 0.6 M NaCl pH 5.5. The black line is full immersion, triangles are flush mounted electrodes on the edge of the CMEA and squares are electrodes in the middle of the CMEA.

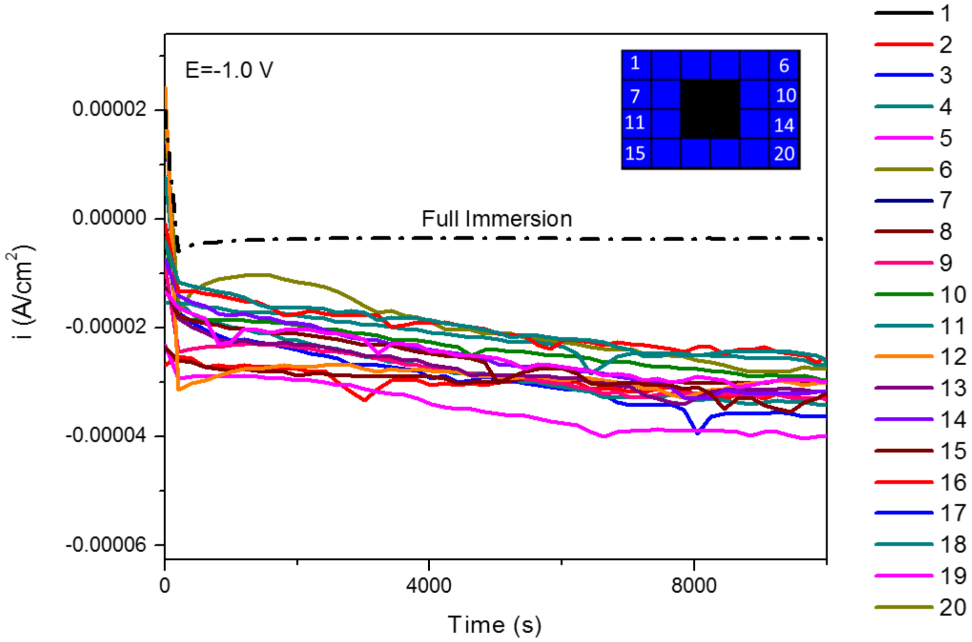

Figure 5.42. Potentiostatic net current density of the CMEA consisting of 20 AA7050-T7451 electrodes over 10000 s at E=-1.0 V SCE under a 70 µm droplet of 0.6 M NaCl at 98% RH.

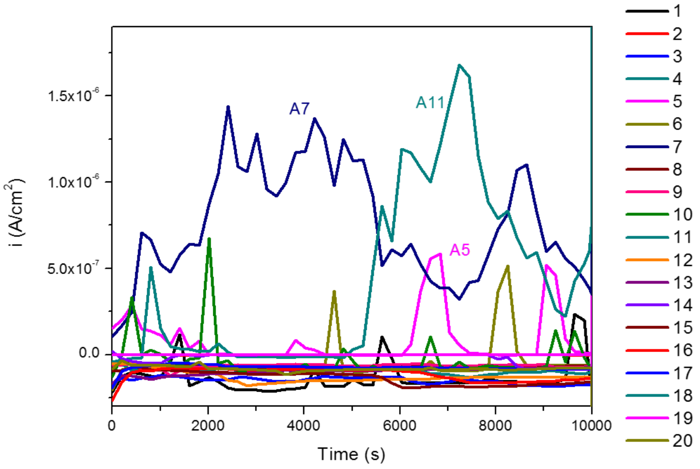

Electrode	Q (C/cm^2)	Electrode	Q (C/cm^2)
A 1	-0.013	A 11	0.044
A 2	-0.00032	A 12	-0.014
A 3	-0.016	A 13	-0.011
A 4	-0.0099	A 14	-0.0022
A 5	0.011	A 15	-0.015
A 6	-0.0053	A 16	-0.012
A 7	0.086	A 17	-0.0082
A 8	-0.0076	A 18	-0.012
A 9	-0.0072	A 19	-0.0023
A 10	-0.0036	A 20	-0.0091
$\sum Q_a=\sum Q_c$	0.14=-0.14		

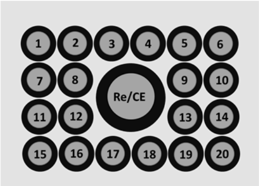

Figure 5.43. Net ZRA current recorded over 10000 s for the AA7050-T7451 CMEA consisting of 20 AA7050-T7451 electrodes. The key at the bottom shows the position of each wire in the array. The CMEA was exposed under a 70 μm thin film of 0.6 M NaCl at 98% RH for 10000 s.

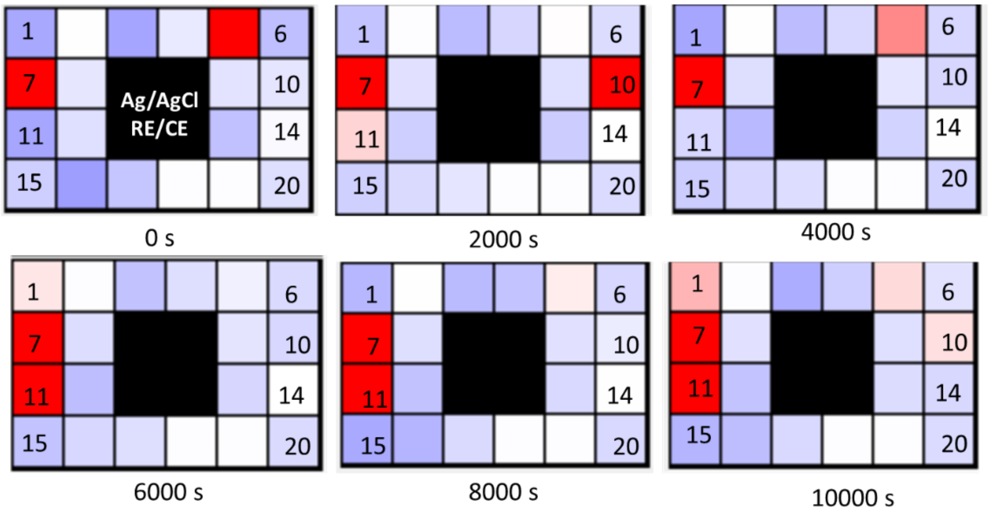

0 s
2000 s
4000 s
6000 s
8000 s
10000 s

Figure 5.44. Color maps during the 10000 s exposure under a 70 µm thin film of 0.6 M NaCl at 98% RH. Red indicates positive values (net anodic), blue indicates negative values (net cathodic) evident of galvanic coupling and white indicates zero current (electrodes with a net galvanic current close to zero).

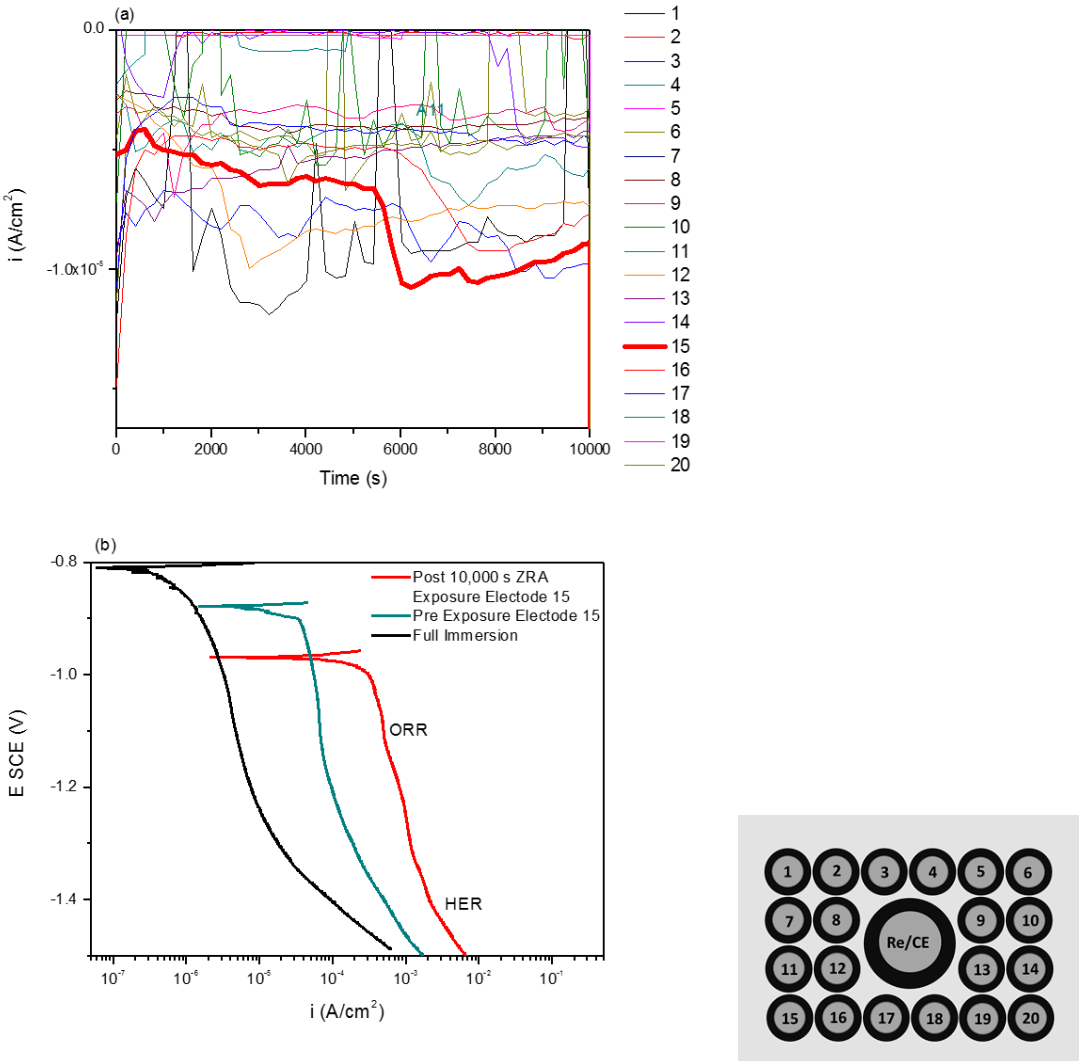

Figure 5.45(a) Zoomed in region of the cathodic electrodes for the ZRA recording of current density over 10000 s of the CMEA consisting of 20 AA7050-T7451 electrodes. The CMEA was exposed under a 70 µm thin film of 0.6 M NaCl at 98% RH for 10000 s. (b) Cathodic polarization of AA7050-T7541. The black indicates a planar AA7050 electrode under full immersion conditions, the dark green line indicates Al electrode 15 prior to the ZRA and the red line indicates Al electrode 15 after 24 h of ZRA measurements.

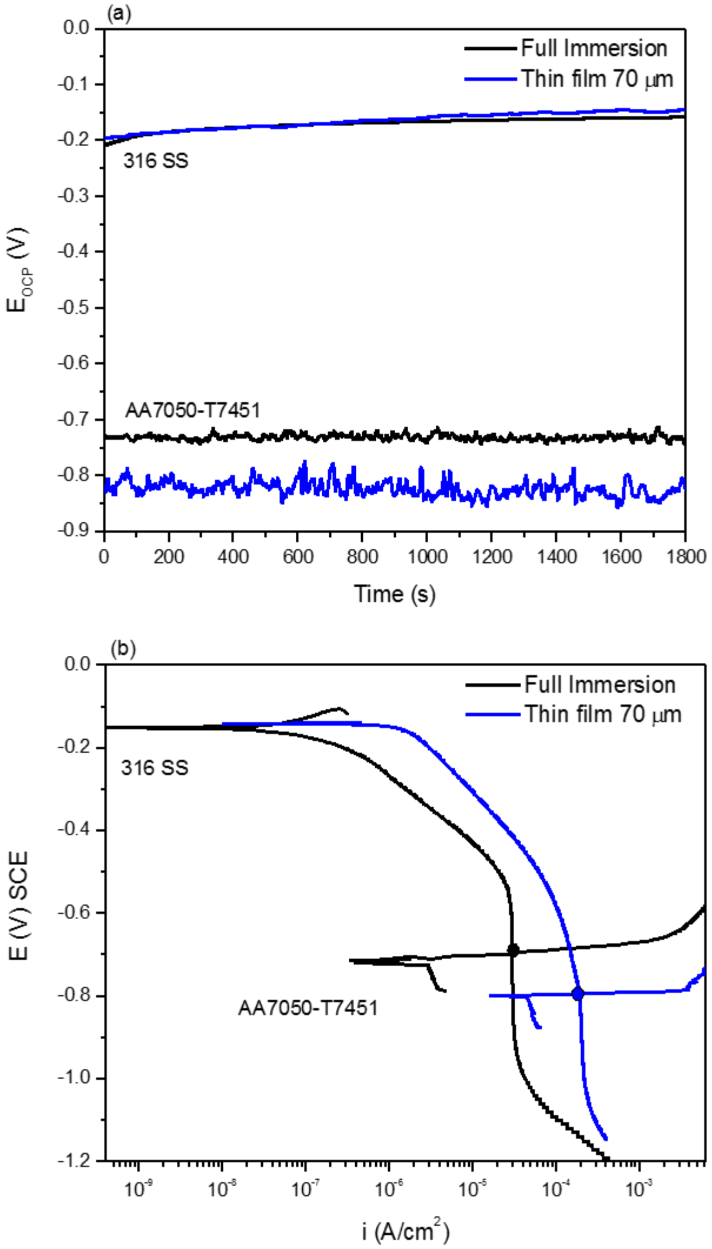

Figure 5.46. (a) Measured OCP for 1800 s (b) Anodic and cathodic potentiodynamic polarization of one AA7050 electrode and one Type 316 stainless steel electrode from the dissimilar metal galvanic couple CMEA consisting of 10 AA7050-T7451 electrodes coupled with 10 Type 316 stainless steel electrodes. A sintered Ag/AgCl electrode was utilized as both the reference and counter electrodes for the OCP and potentiodynamic polarization.

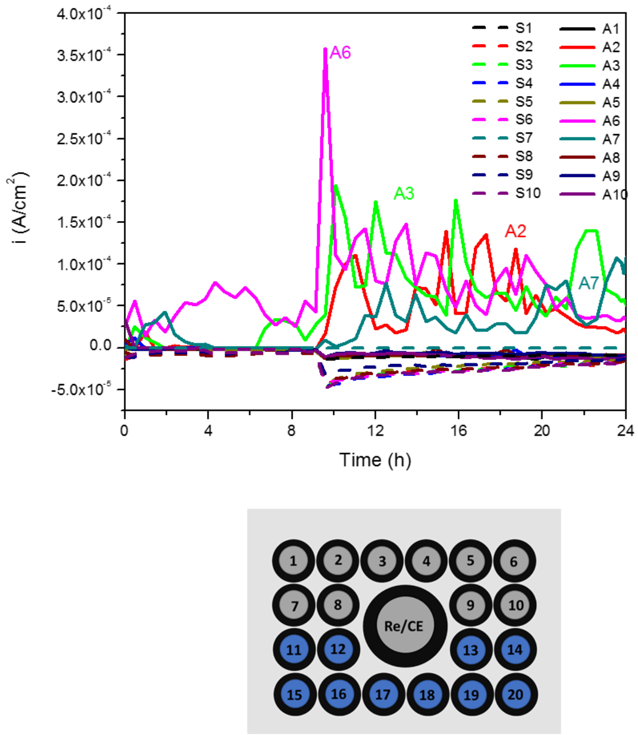

Electrode	Q (C/cm^2)	Electrode	Q (C/cm^2)
A 1	-0.57	S 1	-0.73
A 2	2.81	S 2	-1.61
A 3	5.12	S 3	-1.65
A 4	-0.51	S 4	-1.75
A 5	-0.56	S 5	-1.37
A 6	6.22	S 6	-1.72
A 7	2.41	S 7	-0.015
A 8	-0.55	S 8	-1.62
A 9	-0.44	S 9	-1.32
A 10	-0.58	S 10	-1.72
$\sum Q_a = \sum Q_c$	16.71=-16.69		

Figure 5.47. Net current recording of ZRA galvanic current density over 24 h of the CMEA consisting of 10 AA7050-T7451 electrodes coupled with 10 Type 316 stainless steel electrodes. The CMEA was tested in a controlled relative humidity chamber at 98 % RH under a continuous thin film of 0.6 M NaCl with height 70 μm.

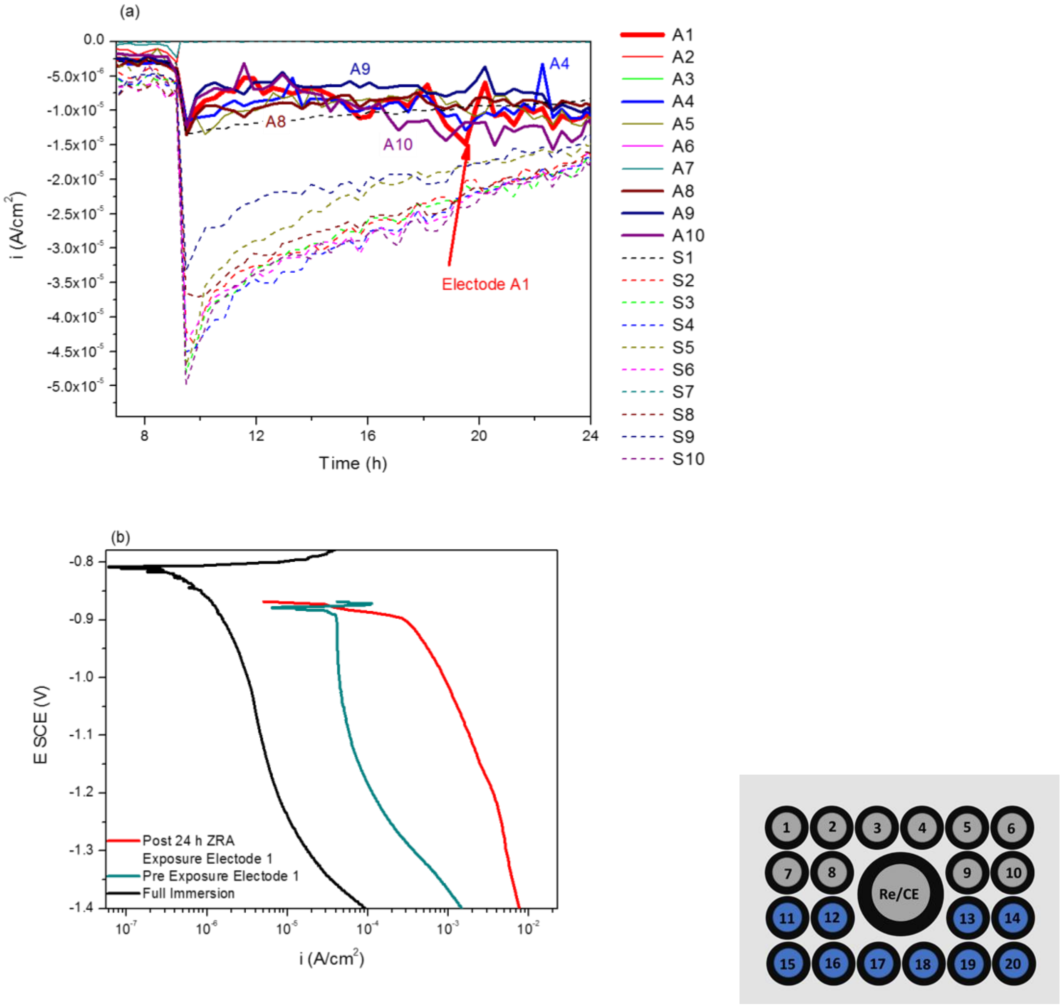

Figure 5.48. (a) Zoomed in region of the cathodic electrodes for the ZRA recording of current density over 24 h of the CMEA consisting of 10 AA7050-T7451 electrodes coupled with 10 Type 316 stainless steel electrodes with a sintered Ag/AgCl electrode as the reference and counter electrodes. (b) Cathodic polarization of AA7050-T7541. The black indicates a planar AA7050 electrode under full immersion conditions, the dark green line indicates Al electrode 1 prior to the ZRA and the red line indicates Al electrode 1 after 24 h of ZRA measurements.

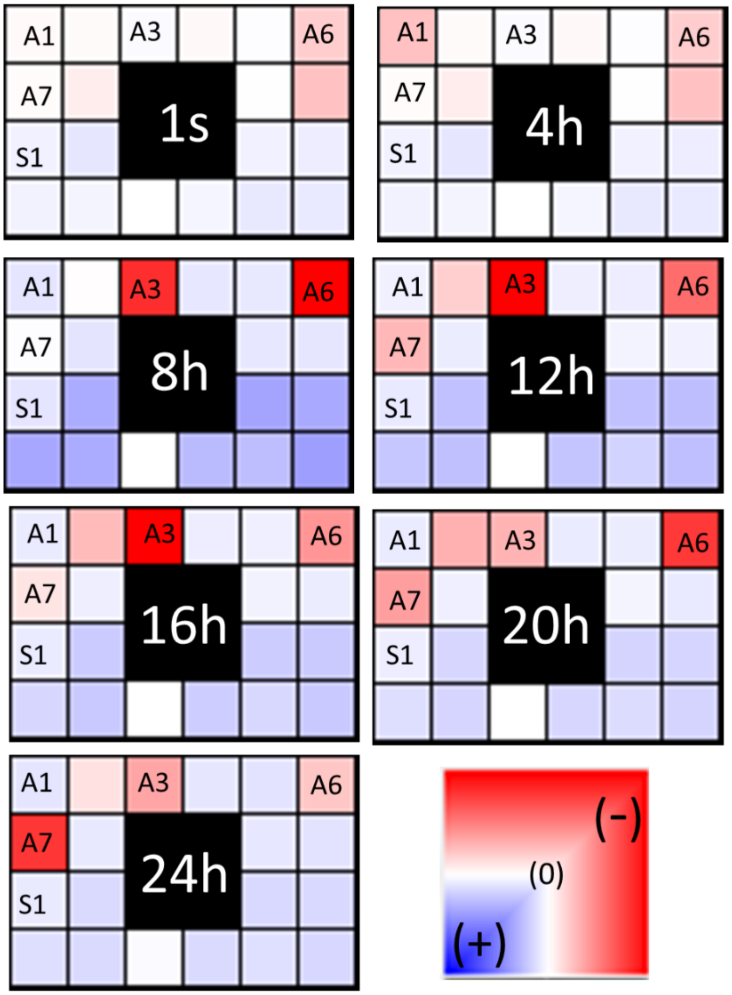

Figure 5.49. Color maps of the dissimilar metal AA7050-T7451 and Type 316 stainless steel CMEA after every 4h where red indicates positive values (net anodic), blue indicates negative values (net cathodic) evident of galvanic coupling and white indicates zero current (electrodes with a net galvanic current close to zero)

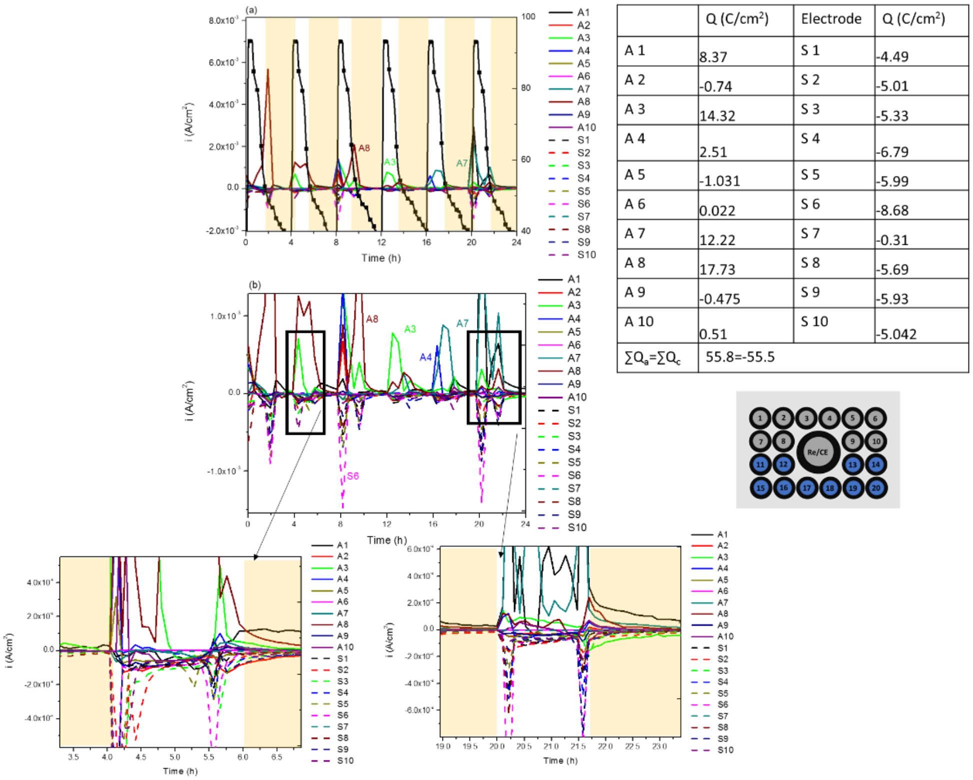

	Q (C/cm²)	Electrode	Q (C/cm²)
A 1	8.37	S 1	-4.49
A 2	-0.74	S 2	-5.01
A 3	14.32	S 3	-5.33
A 4	2.51	S 4	-6.79
A 5	-1.031	S 5	-5.99
A 6	0.022	S 6	-8.68
A 7	12.22	S 7	-0.31
A 8	17.73	S 8	-5.69
A 9	-0.475	S 9	-5.93
A 10	0.51	S 10	-5.042
$\sum Q_a = \sum Q_c$	55.8=-55.5		

Figure 5.50. Net current recording of ZRA galvanic current density over 24 h of the CMEA consisting of 10 AA7050-T7451 electrodes coupled with 10 Type 316 stainless steel electrodes. The CMEA was tested under a continuous thin film of 0.6 M NaCl with height 70 µm in a controlled relative humidity chamber during a wet/dry cycle of 30 minutes at 95% RH and 3 hours at 30% RH at a temperature of 30°C.

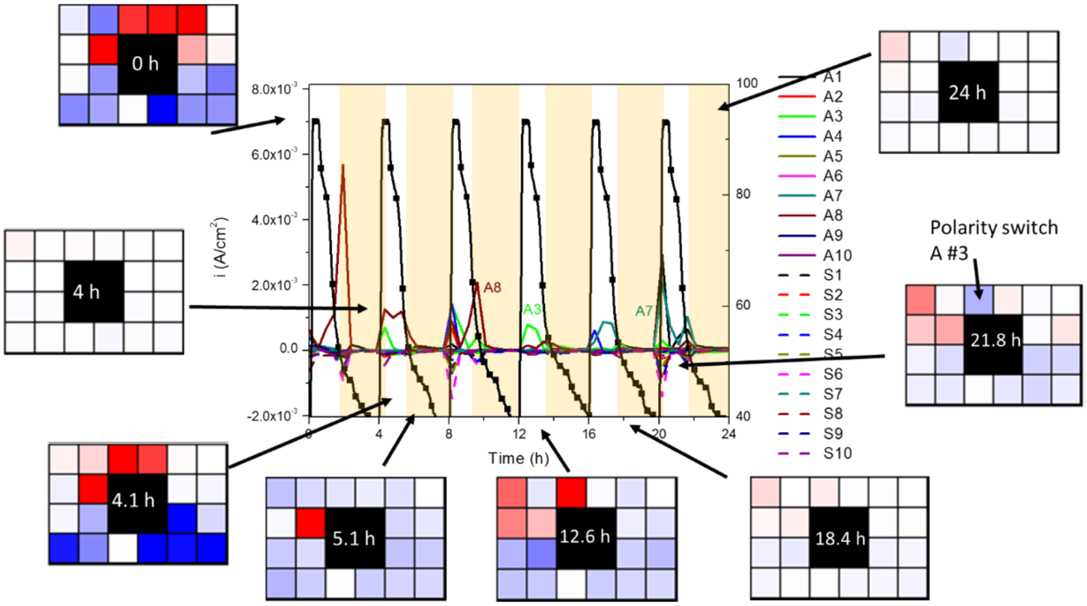

Figure 5.51. Net ZRA current recorded over time for the flat galvanic geometric array and the corresponding color maps. The CMEA was exposed to a 0.6 M NaCl 70 µm thin film for 24 hours under a wet/dry cycle at 30°C The cycle was 30 minutes at 95% RH and 3 hours at 30% RH at a temperature of 30°C. Red indicates positive values (net anodic), blue indicates negative values (net cathodic) evident of galvanic coupling and white indicates zero current (electrodes with a net galvanic current close to zero).

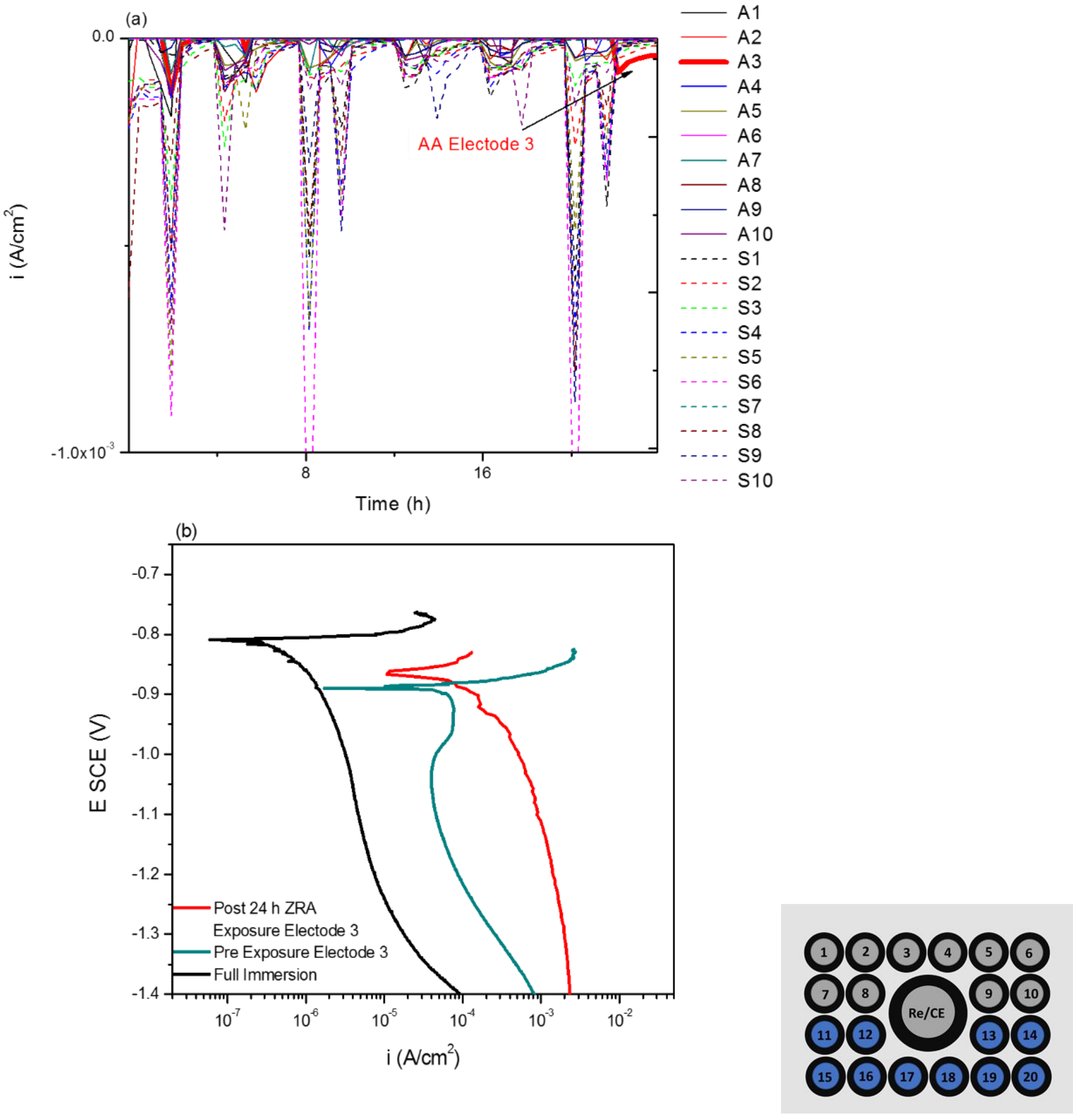

Figure 5.52. (a) Zoomed in region of the cathodic electrodes for the ZRA recording of current density over 24 h of the CMEA consisting of 10 AA7050-T7451 electrodes coupled with 10 Type 316 stainless steel electrodes with a sintered Ag/AgCl electrode as the reference and counter electrodes during a wet/dry cycle. (b) Cathodic polarization of AA7050-T7541. The black indicates a planar AA7050 electrode under full immersion conditions, the dark green line indicates Al electrode 3 prior to the ZRA and the red line indicates Al electrode 3 after 24 h of ZRA measurements.

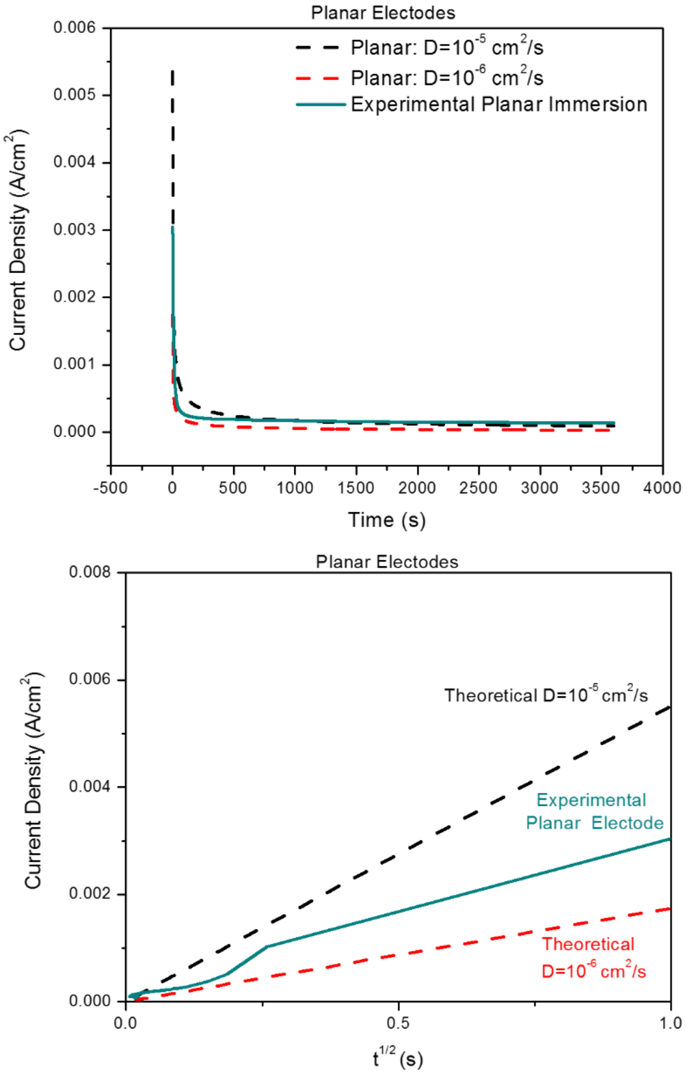

Figure 5.53. (a) Constant potential current density (E=-0.8 V SCE) (b) time dependence of stepped constant potential in the ORR regime for a theoretical planar electrode with diffusion coefficients of D=10^{-6} cm^2/s and D=10^{-5} cm^2/s compared to experimental planar Cu electrode. Constant potential was held at E=-0.8 V SCE for 3600 s.

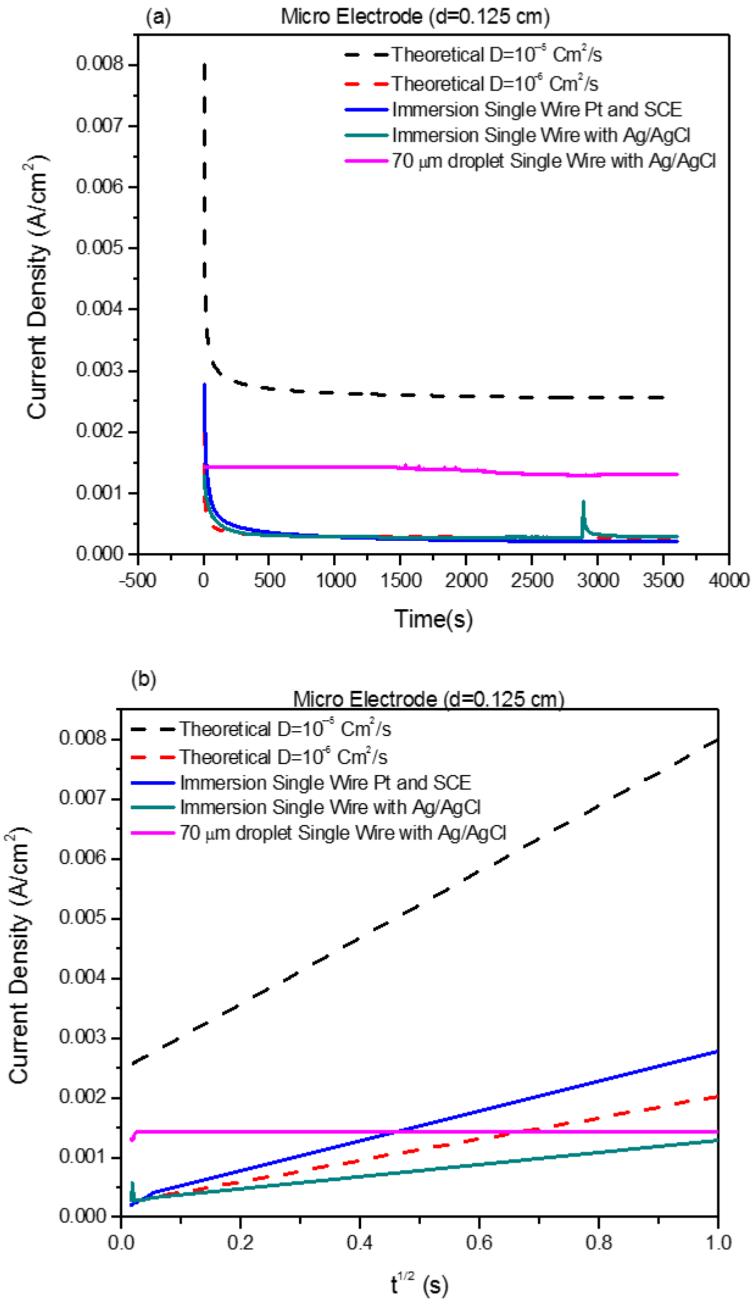

Figure 5.54. (a) Constant potential current density (E=-0.8 V SCE) (b) time dependence of stepped constant potential in the ORR regime for a theoretical micro-electrode with diffusion coefficients of D=10^{-6} cm^2/s and D=10^{-5} cm^2/s compared to experimental Cu micro-electrode. Constant potential was held at E=-0.8 V SCE for 3600 s.

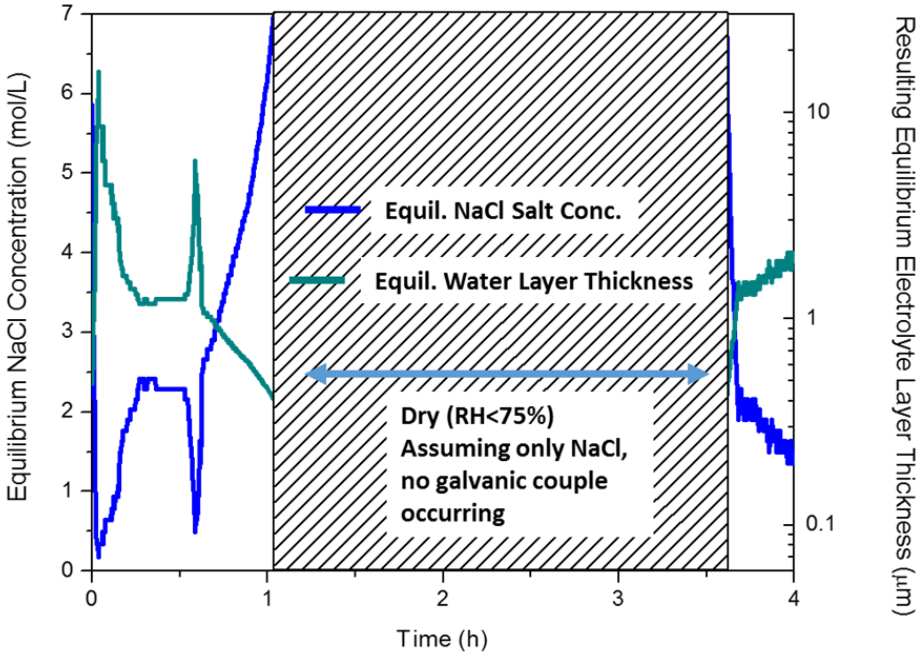

Figure 5.55. A single wet to dry RH cycle used in the CMEA exposures and resulting electrolyte layer thickness for NaCl equivalent surface deposition on the CMEA surface. This cycle was repeated for 24 h.

6 Assessment on the Effect of Soluble Chromate Inhibitor on the Macro and Meso-scale Corrosion Behavior and Damage Morphology of AA7050-T7451 Coupled to Type 316 Stainless Steel

6.1 Abstract

The damage morphology on AA7050-T7451 plate in chromate containing environments was studied utilizing a simulated fastener arrangement and characterized utilizing x-ray tomography. Constant potential holds near the galvanic couple potential provided additional characterization of the damage morphologies. Exposures were conducted in NaCl with the addition of three different chromate concentrations of 0.0001 M, 0.001 M and 0.01 M Na2CrO4. Both X-ray tomography of fasteners and potentiostatic polarization of planar electrodes showed that while the pit density was significantly reduced with the addition of soluble chromate. However, aggressive environments, such as galvanic coupling leads to fewer fissures whilst sometimes leading to surviving fissures 30-40 times deeper in concentrated chromate environments relative to chromate-free environments. The effect of, chromate, on the anodic kinetics of AA7050-T7451, Al-Zn-Mg-Zr (Cu-free 7000) and on the cathodic oxygen reduction reaction (ORR) of Type 316 stainless steel, pure Cu, Cu-replated on AA7050-T74751, and Al_2CuMg (*S* phase) was subsequently utilized to understand these findings. Electrochemistry showed that additions of sodium chromate reduced ORR cathodic kinetics by at least one order of magnitude on Type 316 stainless steel and S phase and by less than one order of magnitude on pure Cu. However, additions of sodium chromate did not inhibit cathodic kinetics on replated Cu on AA7050-T77451. In 0.5 M NaCl environments, pitting potentials were raised on AA7050-T7451 with additions of chromate and S-phase dissolution was inhibited. Anodic kinetics were decreased by at least one order of magnitude with the addition of chromate. Moreover, on AA7050-T7451 and Al-Zn-Mg-Zr, the best corrosion inhibition was observed in 0.5 M NaCl + 0.001 M Na_2CrO_4 and the worst was observed in the environment with the most concentrated amount of chromate: 0.5 M NaCl + 0.01 M Na_2CrO_4. These results support the notion that pit density is reduced.

6.2 Background and Introduction

It is well documented that chromate conversion coatings (CCC) and anodization of Al precipitation age hardened alloys, such as AA2024 and AA7075, improve corrosion resistance.[119,120,126,128,129] A typical coating system contains many layers, a surface treatment, the CCC, a primer and a topcoat. The CCC is typically a very thin layer (10-60 nm) that provides corrosion protection and improved adhesion between the next layers. The second layer, the primer, is comprised of a pigmented organic resin matrix. The primer is the reservoir which houses the soluble chromate. [8,121] Finally a top coat is applied which serves as a main barrier against environmental influences. [123] The topcoat is typically a UV resistant polyurethane that provides resistance to photonic degradation.[8] Barrier coatings are used to suppress the cathodic reaction by limiting diffusion of the electrolyte, oxygen and water to the substrate. [120,132] Ionic inhibitors released from coatings and pretreatments are a key approach to inhibit corrosion. [121] In this work, the NaCl based solutions will be tested with selected additions of the inhibitor species as a oxyanion circumventing the storage/release stages to probe the influence of chromate inhibitor on corrosion damage evolution involving a fissure in AA7050-T7451 galvanically coupled to SS.

In this study, the function of the inhibitor on bare AA7050 was be isolated to study the effect of soluble Cr^{6+} additions to testing solutions. Cr^{6+} compounds protect aluminum and other light alloys used in the aircraft and aerospace industry and forms protective coatings on high-strength steel fasteners used in both the aerospace and automotive industries. However, due to the fact that chromate is known to be a carcinogen, OSHA has many strict Cr(VI) exposure limits and therefore many efforts have been made to find a new non-toxic replacement. One major non-chromate method is the use of cationic and anionic inhibitors that are structurally analogues to hexavalent chromate such as molybdates, tungstates and vanadates. [120,122,213] However, many legacy structural components still rely on chromate for corrosion inhibition.

The inhibition of corrosion of aluminum alloys by chromate and CCCs has been extensively reported.[65,78,118,119,121,123,124,127,132,214-216] The properties of chromate allow for very different behaviors for oxy- and hydroxy- compounds of the Cr^{6+} and the Cr^{3+}.[217.] The tetrahedral,

d^0 hexavalent oxyanion compounds of chromium including chromate, dichromate, bichromate, and chromic acid, dissolve as stable complexes in water, transport easily, and adsorb on oxide surfaces. [124] As stated above, hexavalent chromate is reduced to the trivalent state forming a chromium (III) hydroxide following the overall or full cell reaction given in Equation 6.1[60,118,123-125]

$$2Al + Cr_2O_7^{-2} + H^+ + H_2O = Al_2O_3 + 2Cr(OH)_3 \qquad \text{Equation 6.1}$$

In general, the mechanism for chromate inhibition of Al alloy dissolution is that chromate is a very soluble, higher valent, oxidizing ion with a lower valent form that is insoluble and creates an extremely protective film.[118,216] Bulk Cr^{3+} hydroxides form by sol-gel polymerization, giving rise to well hydrated amorphous materials. [132] CCCs form on aluminum through reduction of Cr^{6+} in solution. CCC consists of a mixture of regions of Cr^{3+} hydroxide at sites where chromate was reduced along with regions of Al_2O_3. Cr^{6+} and Cr^{3+} may co-exist within the CCC in several specific forms. [125] Cr^{6+} and Cr^{3+} may co-exist within the CCC in several specific forms. [125] Cr^{6+} reduced on the bare aluminum surface can lead to a Cr^{3+} rich barrier oxide.

Passivating inhibitors such as chromate operate under site specific conditions.[60,65,118,119,122-125,128,132,215] Chromate dissolves or is solubilized in a +6 valence state oxyanions in aqueous solution. One hypothesized method on the inhibition of corrosion is that chromate is reduced to its more stable Cr^{3+} oxide or hydroxide at active anodic sites which creates a soluble barrier that protects the underlying substrate from local attack. Chromate can be reduced to a Cr^{3+} oxide that is stable over a much wider range of pH compared to aluminum oxide. [218] In aqueous chloride containing solutions, chromate has been found to be an excellent corrosion inhibitor which has been hypothesized to be attributed to its ability to stabilize barrier oxides thorough electrochemical reduction and incorporation into the oxide film or through competition adsorption with Cl^- as an adsorbing ion without a 3D oxide. [219] Pride found that CrO_4^{-2} inhibitor decreased the metastable pit nucleation rate at a given potential and Cl^- concentration, which minimized the change for pit stabilization. [220] Kaesche found that for 99.99% Al in mixed chloride-chromate solution ranging from 10^{-6} to 10^{-2} M, the pitting potential began to be ennobled when the chloride to chromate ratio was below 10:1 to 1:1. [221] Pride also found that CrO_4^{-2} lowered pit growth rates and reduced the metastable pit nucleation rate. [220]

Chromates are also excellent inhibitors of oxygen reduction near neutral and alkaline solutions. [132] In neutral or alkaline environment chromates can stifle corrosion by suppression of the cathodic reaction. [60,124,125] It was observed on cathodic polarization scans of AA2024-T3 that the ORR rate was reduced by about an order of magnitude with the addition of 10^{-5} M sodium dichromate. [132,222] Anodic inhibition of Al alloys by soluble chromate has been shown to occur as well. [123]

6.2.1 Impact of Chromate on Corrosion Damage Evolution of Aluminum Alloys

Young studied the stages of damage evolution with on bare AA2024-T3 around Cd plated SS fasteners during exposure in marine atmosphere and found crack initiation and propagation in the rivet holes after exposure. [223] The damage evolution from the Al and fastener corrosion did not occur by a single continuous corrosion mode. The damage evolution was found to evolve through several stages and transitions among corrosion modes. In addition to classic galvanic corrosion, galvanic action had a significant effect on crevice corrosion, IGC and SCC. [11] Previous work on bare AA7050 show that corrosion fissures occur in the forms of elongated fissures in the L direction, hemispherical pits and IGC. [140,188]

Frankel studied the effect of Cu content on chromate conversation coatings on AA7000-T6 panels and reported one breakdown potential which was slightly higher than the second breakdown on the bare alloy. They discovered that alloyed Cu is beneficial to CCC protection for coatings formed on polished AA7000-T6 but that Cu is detrimental if it is enriched on the surface prior to CCC formation. [215] These effects have not been studied in the T7 temper.

Galvanic attack was studied on coated AA2024-T3 in laboratory and field exposures. In this study AA2024-T3 panels with different scribed coatings with and without galvanic connections to Type 316 stainless steel fasteners were exposed in the field and to ASTM B117. The panels were given a CCC and then painted with a chromate epoxy primer. During field exposures, it was found that current transients associated with galvanic corrosion depended strongly on the electrolyte corresponding to changes in RH, water drop evaporations, condensation and precipitation. It was observed that field exposures had much lower galvanic charge than in an ASTM B117 chamber.[224] The CCC panels without a SS fastener, did not exhibit any corrosion attack after 460 days of field exposure. However, CCC panels with SS fasteners displayed corrosion damage even in short periods of field exposure despite the presence of chromate. The chromate coating system was not effective when corrosion attack was mainly driven by the bare stainless steel fasteners. The SS fasteners were distant from any released chromate and did not benefit from CrO_4^{-2} inhibition of cathodic reactions. [224]

The effect of pretreatment on galvanic attack of coated Al alloy panels was also studied. [225]The substrates for the galvanic samples were AA7075-T6 panels containing 4 through holes with five different pretreatments. All the pretreated panels were coated with the same chromate-containing epoxy primer and polyurethane top coat. The holes were created before surface pretreatment and were not intentionally treated. However, the inside surfaces were exposed during processing and eventually were unevenly coated with topcoat. A flaw in the study was that corrosion in the rivet hole was not analyzed. It was discovered that with a trivalent chromium pretreatment and chromate conversation coating pretreatment, the Al panels exhibited narrow but deep corrosion attack with the fastest pit growth compared to the other pretreatments which produced wide general corrosion attack. These findings point out that chromate might produce one dominant pit that might be a more severe sites for fatigue or stress corrosion cracking than with no chromate.

6.2.2 Objective

The objective of this work is to investigate the macro and meso-scale effects of chromate as an inhibitor on the damage morphology and corrosion electrochemistry when AA7050-T7451 is coupled to Type 316 stainless steel. The use of corrosion inhibitors such as chromate is hypothesized to significantly slow both the development of corrosion damage and fatigue crack growth rate in aerospace aluminum alloys. [226] However, no work has studied these effects inside a fastener hole. This work will quantitatively study the corrosion damage initiation and morphology with the use of soluble chromate in solution as an inhibitor in NaCl environments and elucidate the controlling electrochemical factors altered by the anionic inhibitor and the remaining damage morphology. This work seeks to understand the damage morphology occurring when soluble chromate chemical species is used as an aqueous phase.

6.2.3 Hypothesis

It is hypothesized that chromate as an inhibitor will significantly slow the development of corrosion damage in AA7050-T7451 in. Based on preliminary results, it is hypothesized that the damage morphology when chromate is used will produce discrete deep pitting inside a fastener hole that may affect the fatigue properties of AA7050-T7451 when coupled to stainless steel.

6.3 Experimental Methods

6.3.1 Materials

The Al alloy used in this study was machined from AA7050-T7451 plate of 50 mm thickness provided by Alcoa. The microstructure has elongated grains in both the longitudinal (L) and long transverse (T) directions and are thinned in the short transverse (S), forming a pancake-like microstructure. The grains in the L-direction ranged from 22-1250 µm in length, while the grains in the T and S-directions ranged from 15-265 µm and 12-112 µm, respectively.

The Al-Zn-Mg-Zr was cast at the Kroehling Advanced Materials Foundry (Virginia Tech Foundry Institute for Research and Education). The molten alloys were cooled in a sand mold and a thermocouple was used to determine cooling rates. Optical emission spectroscopy (OES) was used to determine the final composition. The alloy was OA at 121°C for 121 h. Cu was replated on AA7050-T7451 by potentiostatically holding for 600 sec at -1 V SCE in 0.1 M $CuSO_4$ +H_2SO_4 pH 3. This produced a 100 nm layer of Cu on the aluminum alloy surface.

Coupons were freshly ground with successively finer grit SiC abrasive paper (LECO wet/dry 600, 800, 1200 grit) using water lubrication. To prevent corrosion during polishing, final polishing was conducted without water in a 1:3 mixture of glycerol (Fisher Chemical, Certified ACS, ≥99.5 %) to denatured ethanol (UltraPure, ACS/USP grade, 190 proof). Alumina powders (Electron Microscopy Sciences 3.0 µm Al_2O_3, 1.0 µm Type DX α-Al_2O_3, and 0.05 µm Type DX γ-Al_2O_3) were mixed with the glycerol/ethanol lubricant to make slurries. Residual polishing compounds were removed using a clean polishing pad saturated in ethanol prior to ultrasonication in ethanol for 30 seconds, and blown dry with clean, compressed air.

6.3.2 Soluble Chromate in Sodium Chloride Solution

Sodium chromate (Na_2CrO_4) was added to 0.5 M NaCl and 4.0 M NaCl solutions. Three concentrations of Na_2CrO_4 were studied in this work: 0.0001 M (pH 7.8), 0.001 M (pH 8.3) and 0.01 M (pH 8.8). The pH of the solutions were not adjusted, only measured. Selected tests were conducted in 0.5 M NaCl + Na_2CrO_4 adjusted to pH 5.5 with H_2SO_4. The concentrations of Na_2CrO_4 were chosen based on previous work conducted on leaching of chromate into solution.[123,227] Chromate-containing solutions were compared to inhibitor-free 0.5 M NaCl and 4 M NaCl and in select exposures compared to simulated rivet environments of 0.5 M NaCl + $NaAlO_2$ at pH 8. In selected tests, the pH of 0.5 M NaCl was adjusted to pH 8 to match the natural pH of Na_2CrO_4.

6.3.3 Metallurgical Assessment of Damage Morphologies of AA7050 with Chromate Inhibitor

6.3.3.1 Electrochemical Methods to Assess Damage Morphology

All testing, unless noted otherwise, was performed using a three-electrode flat cell with a platinum niobium mesh counter electrode and a saturated calomel reference electrode (SCE). Hydrogen was collected using an electrolyte-filled burette with an inverted funnel attached and centered over the sample. The area exposed was 1 cm^2. Samples were cleaned in dilute nitric acid according to ASTM Standard G-1 to remove corrosion products before determining mass loss. All experimental procedures were conducted after 1 h at open circuit, unless noted otherwise.

Zero resistance ammeter was used to measure the galvanic coupling current between Type 316 stainless steel and AA7050-T7451. The exposures were conducted using a flat cell with planar electrodes where SL AA7050-T7451 exposed was the working electrode (i.e. anode) and Type 316 stainless steel was the counter electrode (i.e. cathode). ZRA was conducted for 504 h in 0.5 M NaCl with additions of 0.0001 M, 0.001 M and 0.01 M Na_2CrO_4.

Potentiostatic polarization was conducted on AA7050-T7451 coupons near the galvanic couple potential at -0.73 and -0.76 V SCE for 144 h. Furthermore, to assess the effect of chromate on the damage morphology at aggressive potentials, potentiostatic polarization above the pitting potential at -0.6 V SCE for 1 h was conducted.

6.3.3.2 Post-Mortem Analysis and Mass Loss Measurements

Post-mortem analysis was conducted using an FEI Quanta 650 scanning electron microscope, Hirox KH 7700 optical microscope, and Nikon inverted optical microscope. Damage morphologies and corrosion fissure depths were characterized on the surface and in cross-section. Mass loss measurements were obtained for each exposure.

Under anodic polarization, the total charge associated with anodic dissolution is theoretically described by Equation 6.2,

$$\boldsymbol{Q_{\Delta m} = Q_{H2} + Q_{i\,net\,anodic}} \qquad \text{Equation 6.2}$$

$Q_{\Delta m}$ is the anodic charge density associated with metal dissolution which can be determined from gravimetric mass loss after cleaning, Q_{H2} is the cathodic charge density associated with hydrogen evolution at the surface that is not reflected in $Q_{i\ net\ anodic}$, $Q_{i\ net\ anodic}$ is the net anodic charge density monitored by the potentiostat. $Q_{\Delta m}$ was calculated using the gravimetric mass loss from exposure using Equation 6.3.

$$Q_{\Delta m} = \frac{\Delta m * F}{E.W. * A} \qquad \text{Equation 6.3}$$

E.W. is the equivalent weight of AA7050, n the number of e^- transferred, Δm is change in mass, F is Faradays constant and A is the area of the electrode

The equivalent weight, given by Equation 6.4, of AA7050 (Al-Zn-Mg-Cu) was calculated according to ASTM G102 assuming both incongruent, Cu is not dissolving (9.54 g/equiv), and congruent dissolution (9.77 g/equiv). In this equation f_{i},, n_{i},, a_i are mass fraction, number of electrons exchanged to complete a given half-cell and atomic weight of the ith alloying element, respectively.

$$\mathrm{E.W.} = \sum \frac{a_i}{f_i n_i}$$

Equation 6.4

The hydrogen collected for select exposures was converted to the corresponding cathodic charge density using the idea gas law and Faradays law using Equation 6.5

$$Q_{H2} = \frac{zPVF}{ART}$$

Equation 6.5

Where z is 2 for hydrogen evolution, P is the pressure inside the burette (1 atm), V is the volume of gas in the burette, F is Faradays law, A is the exposed area of the electrode, R is the idea gas constant, and T is temperature.

The net charge density from the measured current was determined by integrating the current density over time at each potential.

The pitting index (PI) was calculated using Equation 6.6 where p is the deepest pit penetration obtained from metallography and d is the average penetration from mass loss, divided by the total exposed area. PI gave indication to the severity of pitting observed.

$$\mathrm{PI} = \frac{p}{d}$$

Equation 6.6

6.3.4 Characterization of Damage Morphology Using *Ex-situ* X-ray Tomography in AA7050-T7451 Simulated Rivets

The X-ray fastener geometry was a 1 mm diameter cylindrical AA 7050-T7451 pin with a 250 µm rivet hole embedded with a 304 stainless steel wire. The rivet hole was 400- 500 µm deep. The gaps between the stainless steel wire and the AA 7050-T7451 varied from 1 µm to 50 µm, depending on the 360° location and the tilt of the pin. The area ratio inside the hole of AA 7050-T7451 to stainless steel was 0.89:0.87. The entire pin was encapsulated with a plastic tube that containing filter paper with saturated potassium sulfate (K_2SO_4), fixing the relative humidity to approximately 98%. The plastic was sealed with an Al stopper at the top. A schematic of the simulated fastener is shown in Figure 6.1. Three pin samples with three different chromate concentrations of 0.5 M NaCl + 0.0001 M Na_2CrO_4 (pH 7.8), 0.5 M NaCl + 0.001 M Na_2CrO_4 (pH 8.3) and 0.5 M NaCl + 0.01 M Na_2CrO_4 at (pH 8.8) were exposed under a 0.4 µL droplet for 62 h. The electrolyte concentrations of the droplet on the surface of the pin equilibrated to the droplet's equilibrium concentration of 0.5 M NaCl and 0.5 M $MgCl_2$ at 98% RH. The steel rivet was removed and e*x-situ* x-ray tomography was performed with an XRadia MicroXCT-200 at 10x magnification and 80 kV voltage. The voxel size was 4.2 x 4.2 x 4.2 with 3 µm resolution.

6.3.5 Poteniodynamic Polarization to Assess the Galvanic Couple Potential of AA7050-T7451 coupled to Type 316 Stainless Steel with Chromate as an Inhibitor

All testing, unless noted otherwise, was performed using a three-electrode flat cell with a platinum mesh counter electrode and a saturated calomel reference electrode (SCE). The area exposed was 1 cm^2. Samples were cleaned in dilute nitric acid as according to ASTM standard G-1 to remove corrosion products for determination of mass loss. All experimental procedures were conducted after 1 h at open circuit potential, unless noted otherwise.

Potentiodynamic polarization was conducted on AA7050-T7451, Type 316 stainless steel, pure Cu, Al-Zn-Mg-Zr, replated Cu on AA7050-T7451 and in some cases Al_2CuMg (*S* phase) coupons in various environments to understand the effect of chromate in solution on the galvanic couple potential and current contributions. Anodic and cathodic potentiodynamic polarization was conducted with a scan rate of 1 mV/s.

6.3.6 Assessment of Current Distributions using Coupled Multielectode Array with Chromate as an Inhibitor

Figure 6.2 shows schematic representations of the coupled multielectode array (CMEA) geometrical configurations used in this work where (a) shows a geometric flat galvanic array containing 6 AA7050 electrodes and 6 Type 316 stainless steel electrodes embedded in an AA7050-T7451 plate (b) shows a AA7050-T7451 rectangular panel with twenty holes surrounding one larger hole in the center. 10 AA7050-T7451 wires and 10 Type 316 stainless steel wires with 0.25 mm diameter were embedded in the drilled panel. A sintered Ag/AgCl electrode with 0.8 mm diameter was embedded in the larger hole in the center of the panel (c) shows a simulated fastener arrangement representing a cross-section at a fastener plate assembly where 22 AA-7050 electrodes were embedded in an AA7050 panel and 20 type 316 stainless steel electrodes were embedded in an Type 316 stainless steel panel (the ends of each wire, i.e. the individual flush mounted electrodes, are shown here facing outwards to illustrate the placement of electrodes. In all cases, the electrodes were separately addressable and constructed from electrically isolated wires of 25 µm diameter with a spacing of ~125 µm.

CMEAs were tested in a controlled relative humidly (RH) chamber set to 98%. The CMEA epoxy was masked using polyamide electrochemical tape to fix the thickness of a thin water layer to 70 µm. The electrolyte used in this study was 0.6 M NaCl pH 5.5. The individual wires used to build an CMEA need to be electrically isolated using an insulating varnish and the exposed ends that form the electrodes can be flush mounted into epoxy resin or embedded in a panel of the material of interest. The latter was used in this study due to the higher wettability of Al and its oxides; this was particularly important for the fastener geometry which required the electrolyte solution to wick in and completely fill the crevice. CMEAs can be composed of a combination of different electrode materials to simulate compositional or structural non-uniformities in complex alloys or could be composed of nominally identical electrodes to simulate larger planar electrodes. The most valuable and key advantage of this technique is the aptitude of temporal and spatial measurements of electrochemical processes concurrently and instantaneously enabling the determination of real-time processes taking place on an electrode surface

A Scribner Associates, Inc. model MMA910B was used and capable of providing a graphical interface to display the array and data acquisition of each microelectrode current. The instrument is capable of galvanically coupling and measuring up to 100 working electrode current channels and contains an individual zero resistance ammeter (ZRA) dedicated to each current channel with a measureable current range of 3.3 nA to 100 uA per channel. Furthermore, the applied potentiostatic or potentiodynamic potential can be controlled in ten groups of ten electrodes such that specific groups of electrodes can be controlled at a desired potential. Current distribution maps are produced where red denotes anodic current (+) and blue denotes cathodic current (-). Charge conservation for microelectrode array experiments can be validated in accordance with mixed potential theory where the sum of anodic current is equal to the sum of cathodic current.

6.4 Results

6.4.1 Evaluation of Corrosion Damage Morphology of AA7050-T7451 with Soluble Chromate Inhibitor in Solution

6.4.1.1 Assessment of Galvanic Couple Potential Corrosion Damage Morphology when AA7050-T7451 is Coupled to Type 316 stainless Steel via Zero Resistance Ammeter

ZRA laboratory testing was used to monitor both galvanic current and galvanic potential over 504 h when AA7050-T7451 is coupled to Type 316 stainless steel. The electrolytes considered were, 0.5 M NaCl with additions of 0.0001 M (pH 7.8), 0.001 M (pH 8.3) and 0.01 M (pH 8.8) Na_2CrO_4. Figure 6.3 shows the measured galvanic potential and current in these environments. The galvanic couple potential was the most negative in the 0.01 M Na_2CrO_4 environment and the most positive for inhibitor-free 0.5 M NaCl and 0.001 M Na_2CrO_4. Additionally, the galvanic potential decreased over the course of the 504 h exposure in the 0.0001 M and 0.01 M Na_2CrO_4 environments. The average current density in the 0.5 M NaCl inhibitor-free, 0.0001 M, 0.001 M, and 0.01 M Na_2CrO_4 was observed to be approximately 0.004, 0.001, 0.002 and 0.003 A/cm^2. The environment with the lowest current density was 0.0001 M Na_2CrO_4 followed by 0.001 M Na_2CrO_4, 0.01 M Na_2CrO_4, and 0.5 M NaCl. The charge density over 504 h in 0.5 M NaCl inhibitor-free, 0.0001, 0.001, and 0.01 M Na_2CrO_4, environments was 9.1, 0.03, 2.9 and 6.2 C/cm^2, respectively. In the chromate-containing environments, the least corrosion inhibition was observed in 0.01 M Na_2CrO_4 and the best corrosion inhibition was observed in the 0.001 M Na_2CrO_4.

The surface damage morphology of AA7050-T7451 can be observed in Figure 6.4. In 0.5 M NaCl inhibitor-free environment, the AA7050-T7451 surface contained 100-150 pits small pits in the L-direction. The surface was covered with a bronze-like film, which was determined by cyclic voltammetry to be Cu. In environments of 0.5 M NaCl + Na_2CrO_4, the corrosion pit density was tremendously suppressed for all 3 concentrations. Only 3-5 pits were observed on the surface of AA7050-T7841. AA7050 exposed to 0.5 M NaCl + 0.01 Na_2CrO_4 experienced the most surface damage relative to the less concentrated environments. Scanning electron micrographs on the surface of AA7050-T7451 showed that damage morphology of the samples that were in Na_2CrO_4 were similar to the damage morphology observed in the inhibitor-free exposure. The corrosion damage morphology formed as wide fissures orientated in the L-direction (Figure 6.5). In inhibitor-free 0.5 M NaCl, many pits formed and coalesced together to form larger pits. In 0.0001 M Na_2CrO_4, 5 small pits formed. In the 0.001 M and 0.01 M Na_2CrO_4, 2 small pits were formed on each. However, no information on pit depth was determined from micrographs. Figure 6.6 shows the cross-sectioned micrographs around one of AA7050-T7451. The deepest pit, 347 µm, formed in the 0.01 M Na_2CrO_4. The average pit depth in the inhibitor-free 0.5 M NaCl, 0.0001 M Na_2CrO_4 and 0.001 M Na_2CrO_4 environments were 132 µm, 128 µm and 166 µm, respectively. The results of the 504 ZRA exposure are summarized in Table 6.1. Long term ZRA exposure presented that the least amount of corrosion inhibition was observed in 0.5 M NaCl + 0.01 M Na_2CrO_4 and the best in 0.5 M NaCl + 0.001 M Na_2CrO_4. In the most concentrated chromate environment, the pit depth was 2.5 times deeper than the pit produced in the inhibitor-free environments.

6.4.1.2 Assessment of Damage Morphology at Anodic Potentials Near and Above the Galvanic Couple Potential of AA7050-T7451 and Type 316 Stainless Steel

Potentiostatic polarization was conducted at the galvanic couple potential (-0.73) for AA7050-T7451 coupled to Type 316 stainless steel for 144 h in chromate-containing environments of 0.5 M NaCl with additions of 0.0001 M, 0.001 M, and 0.01 M Na_2CrO_4 and compared to 0.5 M NaCl (pH 5.5), 0.5 M NaCl + $NaAlO_2$ (pH 8) and 0.5 M NaCl + NaOH (pH 8). Cu-replated on AA7050 was exposed to 0.5 M NaCl + 0.01 M Na_2CrO_4. The current density and charge density plots over the 144 h exposure can be observed in Figure 6.7. The environments that produced the highest charge densities were the 0.5 M NaCl + 0.01 M Na_2CrO_4 at pH 8.8 and Cu-replated on AA7050-T7451 in 0.5 M NaCl + 0.01 M Na_2CrO_4 at pH 8.8. In 0.0001 M Na_2CrO_4 corrosion kinetics were not inhibited relative to 0.5 M NaCl at pH 5 and pH 8. However, in 0.001

M Na_2CrO_4 corrosion kinetics were reduced by approximately one order of magnitude. The charge density of the inhibitor-free exposures 0.5 M NaCl at pH 5.5, 0.5 M NaCl + $NaAlO_2$ at pH 8 and 0.5 M NaCl + NaOH at pH 8 were 9.9 C/cm^2, 45.5 and 4.7 C/cm^2, respectively. The charge density in chromate environments of 0.001 M, 0.001 M and 0.01 M Na_2CrO_4 were 9.7 C/cm^2, 1.9 C/cm^2 and 142.2 C/cm^2, respectively. On Cu-replated on AA7050-T7451 exposed in 0.001 M Na_2CrO_4, the charge density was 71.8. Therefore, the most concentrated chromate environments, 0.01 M Na_2CrO_4, the andic charge density increased by 14-fold. In 0.001 M Na_2CrO_4 the anodic charge density was reduced by 5-fold. However, in 0.001 M Na_2CrO_4 it was found that when Cu-replated on AA7050-T7451 the anodic chare density increased by 37 times. This suggests in chromate environments, Cu-replated on AA7050-T7451 is detrimental to the corrosion of AA7050-T74514.

The damage morphologies of these samples were analyzed with scanning electron microscopy on the surface and in cross-section with optical microscopy. Figure 6.8 shows images of the SL surface of AA7050-T7451 and Figure 6.9 shows the secondary electron images of the SL surface of AA7050-T7451. In inhibitor-free environments, hundreds of small pits were observed. In the environment containing the least amount of Cr, 0.0001 M Na_2CrO_4 approximately 20 pits were visible. In the 0.001 M Na_2CrO_4 at pH no pitting were observed. In the most concentrated chromate environment, 0.01 M Na_2CrO_4, approximately 42 deep trench-like pits prevailed. On Cu-replated on AA7050-T7451 in 0.001 M Na_2CrO_4 18 deep trench-like pits were observed.

Figure 6.10 shows the cross-sectioned optical micrographs of AA7050-T7451 LS. The deepest pits formed on replated Cu on AA7050-T7451 in 0.001 M Na_2CrO_4 and AA7050-T7451 in 0.01 M Na_2CrO_4. The average pit depth was 427.5 µm and 627 µm deep, respectively. In the chromate-containing environments 0.0001 M, 0.001 M and 0.01 M Na_2CrO_4 the average pit depth was 127, 0, and 627 µm, respectively. In chromate-free environments, the deepest pits were observed in 0.5 M NaCl + $NaAlO_2$ (pH 8) followed by 0.5 M NaCl + NaOH (pH 8), and 0.5 M NaCl (pH 5). These results are summarized in Table 6.2.

AA7050-T7451 coupons were also exposed at an applied potential slightly below the pitting potential (-0.76 V) for 144 h. The exposure environments were chromate-containing solutions of 0.5 M NaCl with additions of 0.01 M, 0.001 M and 0.0001 M Na_2CrO_4 and co pared to inhibitor-free 0.5 M NaCl (pH 5.5). Figure 6.11 shows the current and charge densities for the potentiostatic polarization exposure. The highest current density was observed in 0.5 M NaCl + 0.01 M Na_2CrO_4, the most concentrated chromate environment. The lowest current density was observed in 0.5 M NaCl + 0.001 M Na_2CrO_4. The total charge density over 144 h 0.01 M, 0.001 M, 0.0001 M Na_2CrO_4 and inhibitor-free 0.5 M NaCl (pH 5.5) were 6.9, 0.05, 0.2 and 3.9 C/cm^2, respectively. The charge density in the exposure with the most concentrated chromate was 3 C/cm^2 larger than inhibitor-free 0.5 M NaCl. The charge density was reduced by 138% in 0.001 M Na_2CrO_4 exposure. The surface damage morphology and pit density can be observed in Figure 6.12. The inhibitor-free 0.5 M NaCl showed numerous mico-pits on the Cu covered surface while the chromate containing environments showed discrete pitting, with the largest observed in the 0.5 M NaCl + 0.01 M Na_2CrO_4 exposure. Scanning electron microscopy revealed that in the inhibitor-free 0.5 M NaCl environment the pits were approximately 100 µm in width. In the chromate-containing environments 0.0001 M, 0.001 M and 0.01 M Na_2CrO_4 the average pit width was 200, 60 and 300 µm (Figure 6.13). The average pit depth was determined with optical microscopy and can be observed in Figure 6.14. The inhibitor-free 0.5 M NaCl environment formed pits that were on average, 12 µm in depth. In the chromate-containing environments 0.0001 M, 0.001 M and 0.01 M Na_2CrO_4 the average pit width was 104, 12 and 227 µm, respectively. High magnification micrographs of the damage morphology can be observed in Figure 6.15.

AA7050-T7451 coupons were also exposed to a an anodic potential approximately 10 mV above the pitting potential for 1 h in 0.5 M NaCl (pH 5.5) with additions of 0.0001, 0.001 M and 0.01 M Na_2CrO_4. The current density was the highest in 0.5 M NaCl and the lowest in 0.5 M NaCl + 0.001 M Na_2CrO_4. While the inhibitor was in general inadequate at these this high anodic potential, Na_2CrO_4 was found to reduce the current density by at least 0.04 and by as much as 0.06 A/cm^2 (Figure 6.16). The total charge density over 1 h in 0.01 M, 0.001 M, 0.0001 M and inhibitor-free 0.5 M NaCl were 136, 96.8, 133 C and 274 C/cm^2, respectively. The surface of the AA7050-T7451 post-exposure can be observed in Figure 6.17. It was observed that in 0.5 M NaCl severe pitting and surface recession occurred. In the chromate-containing environments, high corrosion pit densities were observed at all concentrations. The AA7050-T7451 coupon exposed to 0.5 M NaCl + 0.01M Na_2CrO_4 slightly deeper pitting relative to the other chromate-containing environments. Figure 6.18 shows scanning electron micrographs on surface of the AA7050-T7451. It can be observed that while corrosion fissures occurred in all environments, they were less severe in the chromate-containing environments, specifically in the 0.5 M NaCl + 0.001 M Na_2CrO_4. The inhibitor-free 0.5 M NaCl environment produced pits that were 346 µm in depth. In chromate containing environments 0.0001 M, 0.001 M and 0.01 M Na_2CrO_4 the pit depth was 288, 258 and 287 µm, respectively. Cross-sectional micrographs of the damage morphology can be observed in Figure 6.19.

6.4.1.3 Assessment of 3D Corrosion Damage Morphology Utilizing Ex-situ X-ray Tomography

AA7050-T7841 simulated stainless steel fasteners were exposed to droplets and assessed with x-ray tomography. Chromate-containing droplets of 4 M NaCl + 0.0001 M Na_2CrO_4 (pH 7.7), 4 M NaCl + 0.001 M Na_2CrO_4 (pH 8.3) and 4 M NaCl + 0.01 M Na_2CrO_4 (pH 8.8) were placed on the surface of the simulated fasteners. Chromate-containing exposures were compared to previous work on geometrically-similar simulated fasteners under a droplet of inhibitor-free 4 M NaCl exposure, conducted in *operando* at the Diamond Light Source in Oxfordshire, U.K.[139,140,188] Typical 2D horizontal slices through an x-ray tomogram for the simulated fasteners exposed to 4 M NaCl with additions of 0.0001 , 0.001 and 0.01 M Na_2CrO_4 can be observed in Figure 6.20, relative to inhibitor-free 4 M NaCl. This shows a horizontal section in the LT plane at different depths into the fastener from the top of the cylindrical AA7050 test piece, where the large grey disk is the AA7050 and light spots are constituent particles. The large dark grey circle is the rivet hole where the stainless steel wire was simulating a rivet. The dark corrosion fissures (showed with color) were observed in AA7050 around the rivet hole and extended from 1-500 µm in depth.

The corrosion damage was identified by phase contrast and verified using scanning electron microscopy.

In previous work, it was found that in inhibitor-free 4 M NaCl after 62 hours, four separate fissures grew throughout the 500 µm rivet hole. [139,140,188] One largest fissure formed at the mouth and the other three fissures formed near the bottom of the rivet. In 4 M NaCl the corrosion fissures, did not seem to follow bands of constituent clusters, instead corroding intragranually. The 4 M NaCl exposure corroded 0.91% of the AA7050-T7451 pin. A 3D reconstruction of the corrosion fissure damage after the 4 M NaCl inhibitor-free exposure can be seen in Figure 6.21. [139,140,188]

In the least concentrated chromate-containing environment of 4 M NaCl + 0.0001 M Na_2CrO_4, approximately 9 small fissures in the top half of the rivet hole were formed. These pits all formed on one side of the rivet and were at most, 100 µm in length. The 3D reconstruction can be observed in Figure 6.22. The stainless steel rivet is shown in blue and the 3D-shaped volume is representing the corrosion damage in red. In the middle chromate concentration (0.001 M) one small fissure developed in the middle of the 400 µm rivet hole (Figure 6.23). The corrosion fissure was approximately 55 µm in depth. This exposure produced the least amount of corrosion damage. The most concentrated chromate-containing exposure (0.01 M)produced the most severe damage in the form of one large fissure at the bottom of rivet hole which was approximately 150 µm deep (Figure 6.24).

For each exposure the fissure area and depth were tracked over time. The area was quantified using Image J contrast analysis. At every slice, the image was individually adjusted via threshold subtracting the ring artifacts at each slice, as they appeared in different locations throughout the pins. Each fissure was then individualized per 10 slices for each of the 570 slices in the 4 M NaCl + Na_2CrO_4 exposures to ensure the fissure area was actually damage and not reconstruction artifacts. This was the only way to complete this task because of the similar greyscale value. The damage morphology of the first fissure in the 4 M NaCl inhibitor-free exposure and each of three chromate exposures can be observed in Figure 6.25. The damage morphology seen in this figure shows one 2D slice after threshold and binary image processing.

The 2D area of damage in each of the 2D slices observed above were plotted as a function of rivet depth in Figure 6.26. The red bars shows the corrosion damage in chromate-containing exposures and the white bars behind the chromate bars indicate the *operando* 4 M NaCl inhibitor-free corrosion damage. The total volume lost as a result of corrosion in the 4 M NaCl exposure was 3.3 x 10^5 μm^3. The area corrosion total volume lost in the 0.0001 M, 0.001 M, and 0.01 M Na_2CrO_4 was 1.3 x 10^5, 7.7 x 10^3 and 2.8 x 10^5 μm^3, respectively. In 4 M NaCl + 0.01 M Na_2CrO_4, while only one corrosion fissure formed, the volume lost as a result of corrosion was almost as large as the sum of the four fissure observed in the control (4 M NaCl). Additions of 0.001 M and 0.0001 M Na_2CrO_4 reduced the volume lost as a result of corrosion by two orders of magnitude after a 62 h exposure.

The volume lost as a result of corrosion from the *operando* exposure was calculated for various exposure times. The volume was an important parameter, as it enabled determination of the required anodic charge to produce the damage observed. The anodic charge associated with cumulative damage, Q_A , can be found using Equation 6.7.

$$Q_A = \frac{V_{XCT} * F * \rho}{E.W.} \qquad \text{Equation 6.7}$$

Where V_{XCT} is the volume lost as a result of corrosion found according to XCT, F is Faraday's constant, ρ is the density of AA7050 (2.83 g/cm^2), and E.W. is the equivalent weight of AA7050, which was calculated to be 9.77 g/eq, assuming congruent dissolution. The charge over the 62 h exposure can be seen in Figure 6.27. The charge of the inhibitor-free 4 M NaCl exposure is indicated by the dark blue bar compared with the red bars for each of the different chromate containing environments. The total anodic charge, determined from volume lost, in the 4 M NaCl exposure was 1.46 x 10^{-2} C/cm^2. The area corrosion total volume loss in the 4 M NaCl + 0.0001 M Na_2CrO_4, 4 M NaCl + 0.001 M Na_2CrO_4 and 4 M NaCl + 0.01 M Na_2CrO_4 was 3.4 x 10^{-3}, 1.9 x 10^{-4} C/cm^2 and 7.3 x 10^{-3} C/cm^2. In general, chromate reduced corrosion by 10 fold. The most significant improvement was observed 0.001 M Na_2CrO_4. In this exposure, none of the chromate containing exposure produced fissures that were deeper than the inhibitor-free exposure. . The deepest pit in each exposure correlated with the anodic charge density (Figure 6.28). This showed that the chromate containing exposure produced a lower anodic charge than inhibitor-free exposure whist producing narrow deep pits.

EBSD was conducted on the surface of simulated rivet prior to exposure enabling correlation between damage morphology grain shape, and size (Figure 6.29). The simulated rivet that was exposed in 0.001 M Na_2CrO_4 had many small, recrystallized, deformation-free grains while the simulated rivet that was exposed to 0.0001 M and 0.01 M Na_2CrO_4 contained large, deformed grains. The simulated rivet with the small, recrystallized, deformation-free grains contained the least corrosion damage.

6.4.2 Assessment of Anodic and Cathodic Kinetics in Chromate-Containing NaCl Solutions

6.4.2.1 Effect of Soluble Chromate on Cathodic Kinetics of Type 316 Stainless steel, pure Cu and Cu-replated on AA7050-T7451, and S phase

Cathodic Electrochemistry in 0.5 M NaCl pH unadjusted (pH 5.5)

OCP and cathodic potentiodynamic polarization conducted in the solution with the lowest chromate concentration, 0.5 M NaCl + 0.0001 M Na_2CrO_4 (pH 8.3) are shown in Figure 6.30. It was observed that chromate had little effect on the OCP of Cu and replated Cu on AA7050-T7451. However, on Type 316 stainless steel, OCP was ennobled by 150 mV and only increased by 20 mV for pure Cu and 0 mV for Cu-replated on AA7050. Cathodic potentiodynamic polarization in 0.5 M NaCl showed that additions of 0.0001 M Na_2CrO_4 reduced ORR cathodic kinetics of Type 316 stainless steel from 10^{-5} to 10^{-6} A/cm^2. However, pure Cu showed little decrease in ORR cathodic kinetics and replated Cu on AA7050 showed no change in cathodic kinetics. Higher Na_2CrO_4 concentrations of 0.001 M Na_2CrO_4 pH 8.3 (Figure 6.31) and 0.01 M Na_2CrO_4 pH 8.8 (Figure 6.32) exhibited similar trends where cathodic kinetics were decreased on the Type 316 stainless steel and small changes were observed in pure Cu and Cu-replated on AA7050-T7451.

Figure 6.33 shows summary plots of cathodic potentiodynamic polarization on Type 316 stainless steel, pure Cu and Cu-replated on AA7050-T7451 in 0.5 M NaCl as a function of Na_2CrO_4 concentration. In addition cathodic polarization in inhibitor-free 0.5 M NaCl + NaOH at pH 8 was added to assess the effect of pH on the cathodic kinetics. It can be observed that the changed change from 5.5 to 8 made small change in ORR kinetics. In general, 0.5 M NaCl at pH 8 slightly increased cathodic kinetics relative to 0.5 M NaCl at pH 5. The OCP of Cu-replated on AA7050-T7451 showed no change with additions of Na_2CrO_4. On Type 316 stainless steel, the most potent effect on the cathodic kinetics was found in the environment with the highest concentration of Na_2CrO_4 (0.01 M Na_2CrO_4). Interestingly, in 0.01 M Na_2CrO_4, while the ORR kinetics were reduced, the OCP in this concentration was the in inhibitor-free 0.5 M NaCl. The limiting current density, $i_{L,}$ of Type 316 stainless steel in 0.5 M NaCl with additions of 0 M, 0.0001 M, 0.001 M, and 0.01 M Na_2CrO_4 were $3x10^{-5}$, $8.5x10^{-6}$, $6.4x10^{-6}$ and $2.4x10^{-6}$ A/cm^2, respectively. Cathodic kinetics of pure Cu were not reduced with additions of 0.0001 M Na_2CrO_4. However, additions of 0.001 M and 0.01 M Na_2CrO_4 slightly reduced ORR kinetics by 2% and 4%, respectively. Interestingly, on AA7050-T7451 coupons with replated Cu, additions of Na_2CrO_4 proved to only slightly increase ORR by 1%.

The effect of Na_2CrO_4 on cathodic kinetics on the secondary phase Al_2CuMg (*S* phase) was also studied (Figure 6.34). On S phase all three chromate-containing environments significantly reduced cathodic kinetics. Moreover, minimal differences were observed between 0.01 M and 0.0001 M Na_2CrO_4. The OCP was ennobled by 32 mV relative to inhibitor-free environments.

Cathodic Electrochemistry in 4 M NaCl pH unadjusted (pH 5.5)

In a more concentrated Cl^- environment, 4 M NaCl, the effect of Na_2CrO_4 as an inhibitor showed differences. Figure 6.35 shows that in 4 M NaCl + 0.0001 M Na_2CrO_4 the most potent effect was on pure Cu. The OCP of pure Cu increased by 230 mV and ORR was reduced by one order of magnitude. 4 M NaCl environments with more concentrated amounts of Na_2CrO_4 showed similar trends. Figure 6.36 and Figure 6.37 shows the OCP and cathodic polarization in 4 M NaCl with additions of 0.001 M and 0.01 M Na_2CrO_4. Interestingly, on Type 316 stainless steel, in all three concentrations of Na_2CrO_4, the OCP initially was higher than inhibitor-free environments. However after 1000 seconds, the OCP in Na_2CrO_4 environments became lower than the OCP of inhibitor-free environments. In more concentrated chloride solutions, all three materials depicted that while chromate had an effect the cathodic kinetics, the amount of Na_2CrO_4 had very little effect. In other words, concentrations of 0.001 M Na_2CrO_4 had similar effects to 0.01 M Na_2CrO_4 on cathodic kinetics. Similar to less concentrated chloride environments (0.5 M NaCl), addition of Na_2CrO_4 reduced ORR on the stainless steel and pure Cu. However, additions of Na_2CrO_4 increased ORR kinetics on replated Cu on AA7050-T7451. The summary on the effect of 4 M NaCl chloride environments on the cathodic kinetics of Type 316 stainless steel, pure cu, and replated Cu can be observed in Figure 6.38.

In summary, in both 0.5 M NaCl and 4 M NaCl additions of 0.0001 M, 0.001 M and 0.01 M Na_2CrO_4 sustainably reduced ORR kinetics on Type 316 stainless steel and slightly on pure Cu. In the 0.5 M NaCl environment additions of 0.01 M NaCl had the most potent effect, however in 4 M NaCl, all three concentrations had a similar effect. In all environments containing Na_2CrO_4, replated Cu on AA7050-T7451 showed a slight increase in ORR kinetics. Figure 6.39 shows the effect of Cl^- concentration on cathodic polarization of Type 316 stainless steel. It was observed that on Type 316 stainless steel the OCP was more negative in 4 M NaCl relative to 0.5 M NaCl. Furthermore, ORR rates were similar in the 4 M NaCl and 0.5 M NaCl environments.

6.4.2.2 Effect of Soluble Chromate on Anodic Kinetics and the Galvanic Corrosion Potential of AA7050-T7451 and Al-Zn-Mg-Zr Alloys Coupled to Type 316 Stainless Steel

Galvanic Cathodic and Anodic Electrochemistry in 0.5 M NaCl pH unadjusted (pH 5.5)

In 0.5 M NaCl + 0.001 M Na_2CrO_4, i_{corr} decreased by one order of magnitude on AA7050-T7451 and less than order of magnitude on Al-Zn-Mg-Zr relative to inhibitor-free 0.5 M NaCl (Figure 6.40). In inhibitor-free 0.5 M NaCl, the OCP of AA7050-T7451 near the pitting potential. However with additions of chromate, the pitting potential was raised above the OCP. From a galvanic corrosion perspective, the galvanic couple current, i_{couple}, between, AA7050 and Type 316 stainless steel was reduced by 5-fold. The galvanic couple current between Al-Zn-Mg-Zr was reduced by 4% with the chromate. In the 0.5 M NaCl with 0.001 M Na_2CrO_4, i_{corr} was reduced by one order of magnitude on AA7050-T7451 and Al-Zn-Mg-Zr, relative to inhibitor-free 0.5 M NaCl (Figure 6.41). Furthermore, the galvanic couple current between Type 316 stainless steel and AA7050-T7451 or Al-Zn-Mg-Zr decreased by 3.5%. The galvanic couple potential increased by 80 mV and 70 mV for AA7050-T7451 and Al-Zn-Mg-Zr, respectively, coupled to Type 316 stainless steel. Lastly, the in 0.5 M NaCl environment, with the most chromate added, 0.01 M Na_2CrO_4, i_{corr} was reduced by over two orders of magnitude on AA7050-T7451 and one order of magnitude on Al-Zn-Mg-Zr, relative to inhibitor-free 0.5 M NaCl (Figure 6.42). However, the OCP slightly decreased by 29 mV on AA7050-T7451 and increased by 161 mV on Al-Zn-Mg-Zr. The pitting potential of AA7050-T7451 and Al-Zn-Mg-Zr were both raised above the OCP. The galvanic couple potential was ennobled by 130 mV and 80 mV for AA7050-T7451 and Al-Zn-Mg-Zr, respectively, when coupled with Type 316 stainless steel.

In general, in 0.5 M NaCl, the anodic kinetics of AA7050-T7451 and Al-Zn-Mg-Zr were reduced with additions of Na_2CrO_4, as shown in Figure 6.43. The most substantial effect was observed by the increase in potential difference from the OCP with concentrations of 0.001 M and 0.01 M $Na2_2CrO_4$. The pitting potential was significantly increased with additions of Na_2CrO_4. The pitting potential of AA7050-T7451 and Al-Zn-Mg-Zr was the highest in the 0.001 M Na_2CrO_4 environments, followed by 0.0001 M and lastly 0.01 M Na_2CrO_4. In summary, on AA7050-T7451 and Al-Zn-Mg-Zr the best corrosion inhibition was observed in environments of 0.5 M NaCl + 0.001 M Na_2CrO_4 and the worst corrosion inhibition was observed in the environment with the most concentrated amount of Na_2CrO_4, 0.5 M NaCl + 0.01 M Na_2CrO_4. However, all concentrations of chromate were observed to reduce anodic kinetics relative to inhibitor-free 0.5 M NaCl. In general, the corrosion inhibition was most significant on AA7050-T7451 compared to the Cu-free Al-Zn-Mg-Zr alloys. On S phase, anodic kinetics were significantly reduced. The most significant improvement on the pitting potential was observed in 0.01 M Na_2CrO_4 (Figure 6.44).

0.001 M and 0.001 M had similar anodic kinetics. Anodic kinetics of S-phase were reduced by almost 2 order of magnitude.

All three materials, in all concentrations of chromate were observed to reduce anodic kinetics relative to inhibitor-free 0.5 M NaCl. Anodic kinetics were most significantly improved in AA7050-T7451 and S phase.

Cathodic and Anodic Electrochemistry in 4 M NaCl pH unadjusted (pH 5.5)

It was observed that in 4 M NaCl environments, in general, corrosion potentials increased with additions of Na_2CrO_4. However, while corrosion potential was raised, the difference in potential between the OCP and the pitting potential was minimal in 4 M NaCl. Figure 6.45 shows that on AA7050-T7451 in 4 M NaCl + 0.0001 M Na_2CrO_4 while the OCP decreased by 30 mV, I_{corr} also was reduced by over 20% relative inhibitor-free 4 M NaCl. However, on Al-Zn-Mg-Zr in 4 M NaCl + 0.0001 M Na_2CrO_4, the OCP increased by 6 mV and I_{corr} was not affected when compared to inhibitor-free 4 M NaCl. The galvanic couple potential was ennobled by 5 mV and 3 mV on AA7050-T7451 and Al-Zn-Mg-Zr coupled to Type 316 stainless steel. In 4 M NaCl + 0.001 M Na_2CrO_4 (Figure 6.46) Na_2CrO_4 had a stronger effect on the anodic kinetics than in the 0.0001 M Na_2CrO_4 environment. It was observed that on AA7050-T7451, the OCP decreased by 30 mV and I_{corr} was reduced by one order of magnitude relative to inhibitor-free 4 M NaCl. It was observed that on Al-Zn-Mg-Zr in 4 M NaCl + 0.001 M Na_2CrO_4, the OCP was ennobled by 120 mV and I_{corr} was reduced by two orders of magnitude when compared to inhibitor-free 4 M NaCl. The galvanic couple potential was reduced by 3 mV and 21 mV for AA7050-T7451 and Al-Zn-Mg-Zr coupled to Type 316 stainless steel. In the most concentrated chromate environment, 4 M NaCl + 0.01 M Na_2CrO_4, showed that Na_2CrO_4 had similar effects on the anodic kinetics as 0.001 M Na_2CrO_4 (Figure 6.47). The anodic kinetics of Al-Zn-Mg-Zr were more inhibited AA7050-T7451. On AA7050-T7451 and Al-Zn-Mg-Zr the OCP was ennobled by 46 mV and 140 mV. The galvanic couple potential increased by 7 and 3 mV for AA7050-T7451 and Al-Zn-Mg-Zr coupled to Type 316 stainless steel.

Figure 6.48 shows that the pitting potential of AA7050-T7451 substantially increased with additions of Na_2CrO_4. However, on Al-Zn-Mg-Zr, the pitting potential was only mildly increased. It was observed that the pitting potential of AA7050-T7451 and Al-Zn-Mg-Zr was the highest in the 0.01 M and 0.001 M, followed by 0.0001 M Na_2CrO_4. In summary, on AA7050-T7451 and Al-Zn-Mg-Zr the equivalent and most improved inhibition was observed in environments of 4 M NaCl + 0.01 M Na_2CrO_4 and 4 M NaCl + 0.001 M Na_2CrO_4, while the least amount of corrosion inhibition was observed in the environment with the least concentrated chromate: 4 M NaCl + 0.0001 M Na_2CrO_4.

The effect of chromate as a function of Cl^- concentration can be observed in Figure 6.49. In 0.5 M NaCl the pitting potential was substantially raised above the OCP. The pitting potential of AA7050-T7451 was reduced by 100 mV in the more concentrated Cl^- environments. In 4 M NaCl, the pitting potential was near OCP indicating localized corrosion may occur at OCP. This can be attributed to chloride attack on the chromium hydroxide in these Cl^- concentrated solutions. However, inhibition was still observed in the 4 M NaCl following additions of chromate.

Na_2CrO_4 changes the pH the solution to 7.8-8.8, depending on the concentration. Cathodic and anodic potentiodynamic polarization was conducted in 0.5 M NaCl + 0.001 M Na_2CrO_4 with the addition of H_2SO_4 to adjust the pH to 5.5 (Figure 6.50). The pH change was observed to negligibly effect both the anodic and cathodic kinetics

6.4.2.3 Effect of Time at OCP on Corrosion Kinetics on AA7050-T7451 and Stainless Steel 316

Cyclic anodic polarization in 0.5 M NaCl + 0.001 Na_2CrO_4 (pH 8.3) on AA7050-T7451 after 24 h at OCP showed reduced ORR cathodic kinetics by two orders of magnitude relative to the anodic polarization behavior examined without an OCP (Figure 6.51). The OCP was ennobled by 200 mV. While no change was observed in the width of the passive region, I_{pass} was reduced with the longer OCP. It was observed that in 0.5 M NaCl chromate-free environment with 1 h at OCP the passive current density was 2.9×10^{-6} A/cm^2. The passive current densities in chromate-containing environments after no OCP, 1 h, and 24 h OCP were 1.1×10^{-6}, 3.5×10^{-7} and $5.7 \times 10^{-}$

^{8} A/cm^2, respectively. The pitting potential of AA7050-T7451 increased by 150 mV after 24 h at OCP. Moreover, cyclic polarization showed that the repassivation potential following all OCP times and environments were the same as the bulk material. Anodic polarization was indicative of a thicker chromium hydroxide layer forming on the surface of AA7050-T7451. After 24 h OCP, cathodic polarization showed a decrease in the limiting current density by one order of magnitude relative to that of 1 h at OCP.

6.4.2.4 Assessment of Electrochemical Framework on Dissected AA7050 Matrix and Secondary Phases in Soluble Chromate Solutions

Anodic polarization scans of different secondary phases in AA7050-T7451 including pure Al, AA7050 SHT, $MgZn_2$, $Mg(ZnCuAl)_2$, and the Cu-free Al-Zn-Mg-Zr alloy in 0.5 M NaCl + 0.001 M Na_2CrO_4 (pH 8.3) are shown in Figure 6.52. The highlighted region shows the window of corrosion susceptibility, ΔE. The electrochemical IGC behavior can be inferred by the potential window (ΔE) between the pitting potential of the matrix and the $MgZn(CuAl)_2$ phases. ΔE can suggest the type of damage expected. In 0.5 M NaCl + 0.001 M Na_2CrO_4 ΔE between $MgZn_2$ and bulk A7050-T7451 was 200 mV and in inhibitor-free 0.5 M NaCl, ΔE was 320 mV. Therefore, 0.001 M Na_2CrO_4 reduced the potential window of corrosion susceptibility by 120 mV. In previous work, it was shown that Al and Cu have high solubility in $MgZn_2$ and therefore $MgZn_2$ particles may become enriched with Cu and/or Al. [32] If $MgZn_2$ becomes enriched with Cu only, ΔE becomes more narrow (90 mV). If $MgZn_2$ becomes enriched with both Cu and Al, ΔE was found to be 139 mV. In inhibitor-free 0.5 M NaCl, if $MgZn_2$ becomes enriched with Cu, ΔE was 130 mV. Lastly, when enriched with both Cu and Al the potential window increases to 240 mV. Anodic polarizations on the different phases in AA7050-T7451 showed that soluble chromate in solution was observed to decrease the window of corrosion susceptibility by 37%.

6.4.3 Galvanic Couple Current and Potential Interactions between Type 316 Stainless Steel and AA 7050-T7451 under Droplets and Thin Films Analyzed by Coupled Microelectrode Arrays

CMEAs were used understand the effect of chromate on current distributions. Figure 6.53 show the current density over time for the flat galvanic geometric CMEA where 6 AA7050 electrodes and 6 Type 316 stainless steel electrodes were embedded in an AA7050-T7451 plate under a 70 µm thin film of 0.6 M NaCl + 0.001 M Na_2CrO_4 compared to a exposure with a droplet of 0.6 M NaCl. The current density of each electrode was significantly reduced with the addition of Na_2CrO_4. It can be observed that electrode currents were high for 8 h. After 8 h the anodic current densities of the electrode decreased with the exception of one electrode: A4. Table 6.5 shows the compiled charge density of each individual wire. The sum of the net anodic charge density of the CMEA exposure was 0.77 C/cm^2. The net anodic charge density in inhibitor-free 0.6 M NaCl was 16.29 C/cm^2. Furthermore, no polarity switches were observed, suggesting no Cu was replated on the surface of AA7050-T7451 electrodes. Figure 6.54 shows the color maps for the flat galvanic geometric CMEA. The darker color indicates higher magnitude current. Much stronger current was observed in inhibitor-free 0.5 M NaCl whereas in the chromate-containing environment it can be observed that the current weakened over the 24 h exposure. The CMEA exposure showed that the charge density was reduced by 20-fold.

The galvanic couple potential under a 70 µm thin film of chromate-containing solution was determined by overlaying the potentiodynamic polarizations of AA7050-T7451 and Type 316 stainless steel using the dissimilar galvanic couple CMEA consisting of an AA7050-T7451 panel with 10 embedded AA7050-T7451 electrodes, 10 Type 316 stainless steel electrodes and a sintered Ag/AgCl electrode used as the RE and CE. Figure 6.55 shows the measured OCP and cathodic and anodic potentiodynamic polarizations under full immersion and a 70 µm thin film of 0.6 M NaCl relative to polarizations under a 70 µm thin film of 0.6 M NaCl + 0.001 M Na_2CrO_4. Under inhibitor-free thin film conditions, the OCP of stainless was not changed. However, the OCP of AA7050-T7451 was lowered by 80 mV. Thin film conditions effected both the galvanic couple potential and current. The galvanic couple potential was lowered from -0.69 V SCE to -0.80 V SCE from full immersion to thin film conditions. With the addition of chromate cathodic ORR kinetics of Type 316 stainless steel increased marginally under thin film conditions. However, a more substantial effect was observed on the anodic kinetics of AA7050-T7451. In the chromate-containing thin film, the pitting potential of AA7050-T7451 was ennobled by 83 mV. Anodic inhibition under chromate-containing thin films can be attributed to the pitting potential being raised above the OCP. The galvanic couple potential in full immersion conditions, under a 70 µm thin film of 0.6 M NaCl and under a 70 µm thin film of 0.6 M NaCl+ 0.001 M Na_2CrO_4 were -0.68, -0.79, and -0.71 V SCE, respectively. Moreover, the galvanic current in these three environments were 2.9 x 10^{-5}, 1.8 x $10^{-}4$, and 9.0 x 10^{-5}A/cm^{2}, respectively.

Figure 6.56 shows the current density over time for the dissimilar metal galvanic CMEA with a AA7050-T7451 rectangular panel with 10 AA7050-T7451 electrodes and 10 Type 316 stainless steel surrounding a sintered Ag/AgCl electrode under a 70 µm thin film of 0.6 M NaCl + 0.001 M Na_2CrO_4 at pH 8.3 as compared to inhibitor-free 0.6 M NaCl. The addition of soluble chromate inhibited the anodic and cathodic currents. Under a chromate-containing thin film, one strong anode, A8, persisted after approximately 4 hours. The total charge density under a 70 µm thin film of 0.6 M NaCl + 0.001 M Na_2CrO_4 at pH 8.3 was 0.74 C/cm$^{2.}$ In a thin film with no chromate (0.6 M NaCl) the charge density was 16.71 C/cm^{2}. Figure 6.57 shows the color maps for this exposure. The darker color indicates higher magnitude current. Much stronger current was observed in the inhibitor-free exposure. In the chromate-containing exposure, inhibition occurred after 10,000 seconds of exposure. Furthermore, there is indication of Cu-replating on the surface on AA7050-T7451 in the inhibitor-free exposure, this did occur in the chromate-containing environment. Table 6.6 summarizes the charge density of each of the electrodes. Immediately after the 24 h ZRA, the CMEA was connected to a potentiostat and a cathodic scan was conducted on a single AA7050-T7451 electrode that showed faster cathodic kinetics, relative to other AA7050-T7451 electrodes. Figure 6.58 shows the cathodic polarization of AA7050-T7451 electrode 1 after exposure under a thin film of 0.6 M NaCl and 0.6 M NaCl + 0.001 M Na_2CrO_4. Interestingly, in 0.6 M NaCl after the 24 h thin film ZRA exposure, the ORR cathodic kinetics of the AA7050 electrode were increased by an order of magnitude. However, after the 24 h under a 0.6 M NaCl + 0.001 M Na_2CrO_4 thin film, the ORR cathodic kinetics of AA7050 were reduced. This can be attributed to $Cr(OH)_3$ formation on the surface, reducing ORR cathodic kinetics.

Figure 6.59 shows the current density over a 24 h exposure for the CMEA arranged in fastener geometry with 22 AA7050-T7451 electrodes and 20 Type 316 stainless under a 70 µm thin film of 0.6 M NaCl + 0.001 M Na_2CrO_4 and inhibitor-free 0.6 M NaCl at pH 5.5. In the chromate-containing environment, the currents were inhibited after approximately 3 h of exposure. One strong cathode at the bottom of the crevice become a hotspot for ORR, while 2 electrodes dominated the anodic reactions. The total charge under a 70 µm thin film of 0.6 M NaCl + 0.001 M Na_2CrO_4 was 1.32 C/cm^2. In a thin film, containing no chromate (0.6 M NaCl) the charge density was 59.12 C/cm^2. Figure 6.60 shows the color maps for the exposures in the fastener-type CMEA. It can be observed that kinetics were inhibited in the chromate-containing exposure. Furthermore, in both the chromate and inhibitor-free environments the highest anodic and cathodic reactions were occurring inside the crevice towards the end of the 24 h exposure. In the 0.5 M NaCl inhibitor-free exposure, the mouth of the AA7050-T7451 became a cathodic region for ORR to occur after 35,000 s. This trend was not observed in the chromate environment.

6.5 Discussion

6.5.1 X-ray Tomography: Q_{anodic} Limited by $Q_{cathodic}$

XCT on AA7050-T7451 fasteners under NaCl chromate-containing droplets showed that chromate, in general, reduced the total metal volume loss and furthermore reduced the number of corrosion sites when compared to the inhibitor-free exposure (Figure 6.22-Figure 6.25). In the previous work, inhibitor-free exposures showed that multiple corrosion fissures were growing simultaneously over time, indicating that corrosion fissure growth was not cathodically limited.[166] This was attributed the presence of strong cathodes such as the stainless steel fastener and replated-Cu on AA7050-T7451 supporting ORR. In this work, it was evident that true anodic charge density associated with the metal volume loss was less with chromate in solution than in the inhibitor-free exposure. This can be attributed to a lack of replated-Cu and therefore, an absence of ORR at high rates to support the growth of new fissures. Constant potential holds at the galvanic couple potential showed that after exposure in chromate–containing environments, Cu-replating was not visible (Figure 6.8). Cyclic voltammetry was conducted on post-exposure AA7050 samples to assess the surface coverage of Cu on AA7050-T7451. Figure 6.61 shows that after exposure in inhibitor-free 0.5 M NaCl at pH 8, a Cu oxidation peak was observed. An important note is that this peak was not observed after exposure in 0.5 M NaCl + 0.001 M Na_2CrO_4 at pH 8. The dearth of anodic charge associated with metal volume loss in chromate-containing environments can be speculated to be a result of the lack of the Cu-replating mechanism. Cu-replating does not occur readily in chromate-containing through the inhibition of corrosion of Al_2CuMg. Figure 6.62 showed that the ORR cathodic reaction rate was reduced by over an order of magnitude in the presence of chromate. Therefore, it is more difficult for Al_2CuMg to undergo dealloying in chromate-containing environments and thus, little Cu will be leached into solution to replate on the surface of AA7050-T7451.

6.5.2 Effect of Chromate on Anodic Kinetics and Pitting Potentials

Electrochemistry in this work agrees with the findings of other authors that soluble chromate in solution suppresses corrosion kinetics (Figure 6.33 and Figure 6.43). [118,123,124,215,225] The pitting potentials of AA7050-T7451, Al-Zn-Mg-Zr and Al_2CuMg were raised in 0.0001 M and 0.001 M Na_2CrO_4 (Figure 6.63) However, in 0.01 M Na_2CrO_4 the pitting potential of AA7050-T7451 and Al-Zn-Mg-Zr did not experience significant ennoblement. *S* phase experienced the most significant pitting potential or critically dealloying potential ennoblement in all three chromate concentrations. Ennoblement of the pitting potential indicates fewer corrosion sites but does not necessarily indicate a lower anodic charge density. This suggests that Cu replating is likely inhibited through inhibition of Al_2CuMg corrosion.

6.5.3 Effect of Chromate on ORR Cathodic Kinetics

The ORR current density for Type 316 stainless steel, Cu, Cu replated on AA7050 and Al_2CuMg (*S* phase) are plotted as a function of Na_2CrO_4 concentration in Figure 6.62. The limiting current density on Type 316 stainless steel and Al_2CuMg was significantly reduced with increasing chromate. Pure Cu experienced less ORR kinetic inhibition. Interestingly, for Cu-replated on AA7050-T7451, the ORR current density increased with the additions of chromate. An important result observed in the electrochemistry was that pure Cu and Cu-replated on AA7050-T7451 were not significantly inhibited by the addition of chromate. This may be attributed to difference in contribution of the chromate reduction reaction to the net cathodic kinetics of the different metals and surfaces. The rate of ORR kinetics on Al is much lower than that of Cu and other Cu-containing constituent particles. Therefore any small contribution to the net cathodic current density of chromate would be more substantial on Al then on Cu or Cu replated on AA7050-T7451. Chromate was shown to inhibit corrosion on S phase. Inhibition of Cu release through passivation of Al_2CuMg would lower cathodic reaction rates. However, any Cu replated on the AA7050-T7451 surface during corrosion in Cl^- or alkaline treatments would raise cathodic reactions rates when Cu is negatively polarized to the OCP of AA7050-T7451. However in all studies presented here involving potentiodynamic scans, the potentiostat was the counter electrode and supplied cathodic reactions therefore any role of microstructure in supporting cathodic reactions was minimized.

The CMEAs (Figure 6.53-Figure 6.57) showed that soluble chromate inhibited open circuit corrosion even though mass transport O_2 kinetics were not altered. The control samples in NaCl with no added inhibitor indicated that certain AA7050 electrodes switched from anodes to cathode after some time. This was attributed to Cu enrichment or Cu-replating on the surface. However, polarity switches were not observed in any of the chromate-containing CMEA exposures. In this work and previous work [124], it was shown that chromate inhibits the corrosion of Al_2CuMg which reduces the possible formation of porous Cu rich phases and Cu-replating on the surface. Therefore, inhibition of Cu release through passivation of Al_2CuMg would lower cathodic reaction rates. However, any Cu-replated on the AA7050-T7451 surface during corrosion in Cl^- or alkaline treatments would raise cathodic reactions rates when Cu is negatively polarized to the OCP of AA7050-T7451.

6.5.4 Role of Fissure Acidity and H_2CrO_4 on Corrosion Fissure Growth

ZRA (Figure 6.6), potentiostatic polarization (Figure 6.10), and x-ray tomography (Figure 6.22-Figure 6.24) showed that while chromate reduced the ORR kinetics and ennobled the pitting potential of Type 316 stainless steel and AA7050-T7451, the damage morphology may be affected in complicated ways. However, it was observed that aggressive environments, such as high anodic potentials or galvanic coupling, induced deep pitting in concentrated chromate environments (Figure 6.10). XCT showed that one deep pit formed in 0.01 M Na_2CrO_4 at the bottom of the rivet hole (Figure 6.26) while one small pit formed inside the rivet hole in 0.001 M Na_2CrO_4 (Figure 6.23). The XCT also showed that the large corrosion pit that formed in 0.01 M Na_2CrO_4 was nearly as large as the sum of all the corrosion sites formed in the inhibitor free exposure (Figure 6.27 and Figure 6.26). Table 6.2 summarizes the constant potential hold exposures. In 0.01 M Na_2CrO_4, the corrosion pits that formed were over seven times deeper than in the inhibitor free exposure. AA7050-T7451 coupons that deliberately had Cu-replated exposed in 0.001 M Na_2CrO_4 formed deep corrosion fissures that were 6 times larger than observed in the equivalent exposure with no Cu-replated on AA7050. This suggests that chromate may inhibit corrosion on AA7050-T7451. However, when Cu is replated on the surface, this condition led to detrimental corrosion effects (Figure 6.10).

Cr^{+6} is hydrolyzed in aqueous solutions and exists as an oxyanion in all but the most acidic conditions. [132] Figure 6.64 shows the predominance diagram for chromate as a function of pH based on standard free enthalpies given by Pourbaix [218] The predominant species at pH levels between 1 and 6 is $HCrO_4^-$ and above pH 6, CrO_4^{-2} is stable. The dichromate ion ($Cr_2O_7^{-2}$) forms when the concentration of chromium exceed 1 g/L. Even if pH is maintained constant for a particular experiment, effects are still unknown due to the distribution of Cr^{6+} between the mononuclear ($HCrO_4^-$) and the dichromate ion ($Cr_2O_7^{-2}$) varies with concentration.[132,228] While corrosion inhibition is detected in chromate solutions with widely varying pH, a possible exception to this is the fully protonated H_2CrO_4 which exists in strongly acidic solutions. [132] Evidence suggests H_2CrO_4 is present in active pits, but does not inhibit corrosion because it is not charged and cannot compete with Cl^- and adsorb or interact with the corroding surface.[229] Therefore it can be stipulated that in aggressive environments, when halide is present and pitting does occurs, the pH local to the fissure becomes acidic. Under this condition, $HCrO_4$ and H_2CrO_4 may form and would not contribute strongly to the corrosion inhibition. The predominance diagram in Figure 6.64 also showed that $Cr_2O_7^{-2}$ forms between a pH level 1 and 6. Previous work by Frankel determined that in dichromate-containing chloride solutions, the corrosion and repassivation potentials shifted in the noble direction, and rather large metastable pits formed at open circuit. These metastable pits act as sites for initiation of further pitting at higher applied potentials. These explanations may lead to fast growing pits supported by many cathodic hotspots, such as locations where Al_2CuMg is deployed and subsequent Cu is replated, around the pit. In the case of one deep corrosion pit, the entirety of the cathodic reaction occurring was supplying the anodic current for the single fissure resulting in deeper pit propagating. In many cases, the corrosion metal volume loss was equal or more significant than the sum of all the corrosion pits in exposure with no inhibitor (Table 6.2).

6.5.5 Leaching Rate vs Chromate Concentration Used

Kelly et all studied the effect of soluble chromate additions vs CCCs in small volume cells. They determined that under conditions where a thin water layer exists on the surface in high humidity the accumulation rate was 1 mM/h. Therefore, after 10 h, a chromate concentration of 10 mM would be expected. [125] In this work, concentrations of 0.1, 1 and 10 mM were chosen to represent the amount of chromate present in solution when a CCC is under thin film corrosion conditions for 0.1, 1 and 10 h of exposure. The predominance diagram showed that in environments with a high concentration of chromate (above 1 g/L), $Cr_2O_7^{-2}$ forms between pH 1-6. Under these conditions, it was apparent that large pits formed on the surface of AA7050-T7451.

6.6 Conclusions

- Additions of Na_2CrO_4 reduced cathodic kinetics by one order of magnitude for Type 316 stainless steel and by less than one order of magnitude on pure Cu. However, additions of Na_2CrO_4 slightly increased cathodic kinetics of replated Cu on AA7050-T77451.
- In 0.5 M NaCl, the most potent effect on the cathodic kinetics were found in environments with 0.01 M Na_2CrO_4. In environments with higher chloride concentration (4 M NaCl), additions of chromate in general reduced ORR kinetics.
- In 0.5 M NaCl environments, anodic kinetics were reduced by at least one order of magnitude with the addition of Na_2CrO_4. This can be attributed to chromate raising the pitting potential above the OCP. Moreover, on AA7050-T7451 and Al-Zn-Mg-Zr, the best corrosion inhibition was observed in 0.5 M NaCl + 0.001 M Na_2CrO_4 and the least significant corrosion inhibition was observed the most concentrated solution of Na_2CrO_4, (0.01 M Na_2CrO_4). Inhibition was most significant on AA7050-T7451 compared to the Cu-free Al-Zn-Mg-Zr alloys.

- In 4 M NaCl on AA7050-T7451 and Al-Zn-Mg-Zr, equivalent and improved anodic inhibition was observed with additions of 0.01 M and 0.001 M Na_2CrO_4. The lowest anodic inhibition was observed in the environment with the least amount of Na_2CrO_4 (0.0001 M Na_2CrO_4)
- Anodic polarizations on the different phases present in AA7050-T7451 showed that soluble chromate in solution was observed to decrease the potential window between AA7050-T7451 and the $MgZn_2$ phase by 37%.
- Damage morphology studies showed that while the pit density was significantly reduced with the addition of soluble chromate, it was observed that aggressive environments (i.e. high anodic potentials or galvanic coupling) induced deep and narrow pitting up to seven times deeper in chromate environments than chromate-free environments.
- The addition of chromate was determined to inhibit the corrosion of Al_2CuMg, reducing the possible formation of porous Cu-rich phases and Cu-replating on the surface. Therefore, inhibition of Cu release through passivation of Al_2CuMg would lower the overall cathodic reaction rates.

6.7 Tables

Table 6.1 ZRA exposure data summary for AA7050-T7451 coupled with Type 316 stainless steel after 504 h exposure in inhibitor-free 0.5 M NaCl at pH 5.5, 0.5 M NaCl + 0.0001 Na_2CrO_4 at pH 7.8, 0.5 M NaCl + 0.001 Na_2CrO_4 at pH 8.38, 0.5 M NaCl + 0.01 Na_2CrO_4 at pH 8.88 Q_{net} is the charge consumed by the potentiostat, $Q_{\Delta m}$ is the anodic charge consumed from metal dissolution determined from gravimetric mass loss, average L is the average corrosion fissure length determined by sectioning and PI is the pitting index.

ZRA 504 h					
Solution	Q_{net} (C/cm^2)	$Q_{\Delta m}$ (C/cm^2)	Average L (µm)	PI	Damage Morphology
0.5 M NaCl pH 5.5	9.5	10.8	132..3	11	Large pits, clustered together, round and long pits
0.5 M NaCl + 0.0001 M Na_2CrO_4 pH 7.8	0.03	1.5	128.2	3	Very small 5-6 pits
0.5 M NaCl + 0.001 M Na_2CrO_4 pH 8.3	2.8	3.5	166.8	2	Very small 1-2 pits
0.5 M NaCl + 0.01 M Na_2CrO_4 pH 8.8	6.2	8.7	347.4	2	Large 3-5 pits

Table 6.2. Potentiostatic exposure data summary for AA7050-T7451 at the galvanic couple potential, E=-0.73, for 144 h in inhibitor-free 0.5 M NaCl at pH 5.5, 0.5 M NaCl + $NaAlO_2$ at pH 8, 0.5 M NaCl + NaOH at pH 8 relative to chromate-containing environments of 0.5 M NaCl + 0.0001 Na_2CrO_4 at pH 7.8 and 0.5 M NaCl + 0.01 Na_2CrO_4 at pH 8.8. Q_{net} is the charge consumed by the potentiostat, $Q_{\Delta m}$ is the anodic charge consumed from metal dissolution determined from gravimetric mass loss, L is the average corrosion fissure length determined by sectioning and PI is the pitting index.

144 h E=-0.73 V

Solution	Q (C/cm^2)	$Q_{\Delta m}$ (C/cm^2)	Average L (µm)	PI	Damage Morphology
0.5 M NaCl pH 5.5	9.9	10.7	84.1	16	High pit density, shallow pits
0.5 M NaCl + $NaAlO_2$ pH 8	45.5	47.1	247.5	68	High pit density, deep pits
0.5 M NaCl + NaOH pH 8	4.7	5.3	213.8	34	High pit density, deeper pits
Cu-replated on AA 0.5 M NaCl + 0.01 M Na_2CrO_4 pH 8.8	71.8	78.1	493.5	21	Low pit density, deep pits
0.5 M NaCl + 0.0001 M Na_2CrO_4 pH 7.8	9.7	11.2	127.3	14	Low pit density, shallow/deep pits
0.5 M NaCl + 0.001 M Na_2CrO_4 pH 8.3	1.9	2.3	0	Na	
0.5 M NaCl + 0.01 M Na_2CrO_4 pH 8.8	142.2	148.1	627.1	25	Medium pit density, deep pits

Table 6.3. Potentiostatic exposure data summary for AA7050-T7451 coupled to Type 316 stainless steel in inhibitor-free for 144 h (-0.76 V DCE) in 0.5 M NaCl at pH 5.5, 0.5 M NaCl + 0.0001 Na_2CrO_4 at pH 7.8, 0.5 M NaCl + 0.001 Na_2CrO_4 at pH 8.3, and 0.5 M NaCl + 0.01 Na_2CrO_4 at pH 8.8. Q_{net} is the charge consumed by the potentiostat, $Q_{\Delta m}$ is the anodic charge consumed from metal dissolution determined from gravimetric mass loss, L is the average corrosion fissure length determined by sectioning and PI is the pitting index.

144 h E=-0.76 V

Solution	Q (C/cm^2)	$Q_{\Delta m}$ (C/cm^2)	Average L (µm)	PI	Damage Morphology
0.5 M NaCl pH 5.5	6.8	5.9	12.1	3.2	Numerous tiny pits
0.5 M NaCl + 0.0001 M Na_2CrO_4 pH 7.8	0.05	0.1	104.2	2.1	One medium pit
0.5 M NaCl + 0.001 M Na_2CrO_4 pH 8.3	0.1	1.2	7.2	NA	One very small pit
0.5 M NaCl + 0.01 M Na_2CrO_4 pH 8.8	4.8	5.1	227.1	1.1	One deep pit

Table 6.4. Potentiostatic exposure data summary for AA7050-T7451 coupled with Type 316 stainless Steel for 1 h (-0.6 V) in inhibitor-free 0.5 M NaCl at pH 5.5, 0.5 M NaCl + 0.0001 Na_2CrO_4 at pH 7.8, 0.5 M NaCl + 0.001 Na_2CrO_4 at pH 8.3, and 0.5 M NaCl + 0.01 Na_2CrO_4 at pH 8.8. Q_{net} is the charge consumed from by the potentiostat, $Q_{\Delta m}$ is the anodic charge consumed from metal dissolution determined from gravimetric mass loss, average L is the average corrosion fissure length determined by sectioning and PI is the pitting index.

1 h E=-0.6 V					
Solution	Q (C/cm^2)	$Q_{\Delta m}$ (C/cm^2)	Average L (µm)	PI	Damage Morphology
0.5 M NaCl pH 5.5	274.3	283.3	346.2	67	Many large pits
0.5 M NaCl + 0.0001 M Na_2CrO_4 pH 7.8	136.4	148.1	288.4	52	Many large pits
0.5 M NaCl + 0.001 M Na_2CrO_4 pH 8.3	96.8.5	112.5	258.8	38	Many medium pits
0.5 M NaCl + 0.01 M Na_2CrO_4 pH 8.8	133.6	142.5	287.3	52	Many large pits

Table 6.5. Charge density for each electrode over 24 h on the flat galvanic geometric CMEA where 6 AA7050 electrodes and 6 Type 316 stainless steel electrodes were embedded in an AA7050-T7451 plate with a 70 µm thin film of 0.6 M NaCl +0.001 M Na_2CrO_4 at pH 8.3.

Electrode	**Q (C/cm^2)**	**Electrode**	**Q (C/cm^2)**
A 1	0.0073	SS 1	-0.039
A 2	0.071	SS 2	-0.11
A 3	0.011	SS 3	-0.088
A 4	0.46	SS 4	-0.11
A 5	-0.018	SS 5	-0.33
A 6	-.021	SS 6	-0.091
$\sum Q_a = \sum Q_c$	0.77=-0.77		

Table 6.6. Charge density for each electrode over 24 h on the flat galvanic geometric CMEA where 6 AA7050 electrodes and 6 Type 316 stainless steel electrodes were embedded in an AA7050-T7451 plate with a 70 µm thin film of 0.6 M NaCl +0.001 M Na_2CrO_4 at pH 8.3.

Electrode	**Q (A/cm^2)**	**Electrode**	**Q (A/cm^2)**
A1	-0.0032	S1	-0.014
A2	-0.0021	S2	-0.076
A3	-0.013	S3	-0.052
A4	-0.0031	S4	-0.043
A5	-0.021	S5	-0.083
A6	0.015	S6	-0.065
A7	0.059	S7	-0.39
A8	0.051	S8	-0.041
A9	-0.019	S9	-0.037
A10	0.023	S10	-0.051
$\sum Q_a = \sum Q_c$	0.86=-0.90		

6.8 Figures

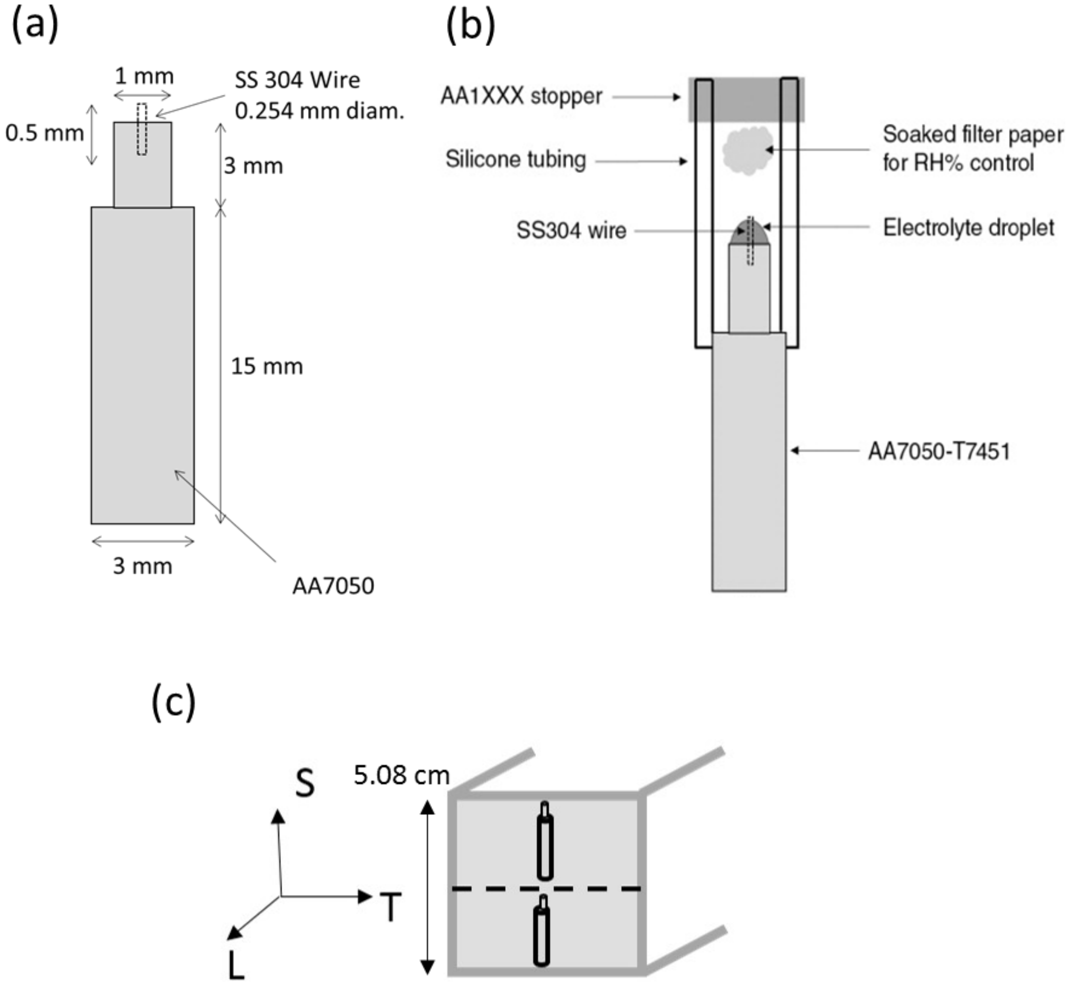

Figure 6.1. (a) Schematic of simulated rivet geometry consisting of an AA7050-T7451 pin and stainless steel wire. (b) Experimental setup of a simulated rivet encapsulated with the Si tubing capped with the AA1xxx stopper. The soaked filter paper was used to control the RH. (c) Schematic showing the location where the samples came from relative to the LT plane, with the long axis in the S orientation.

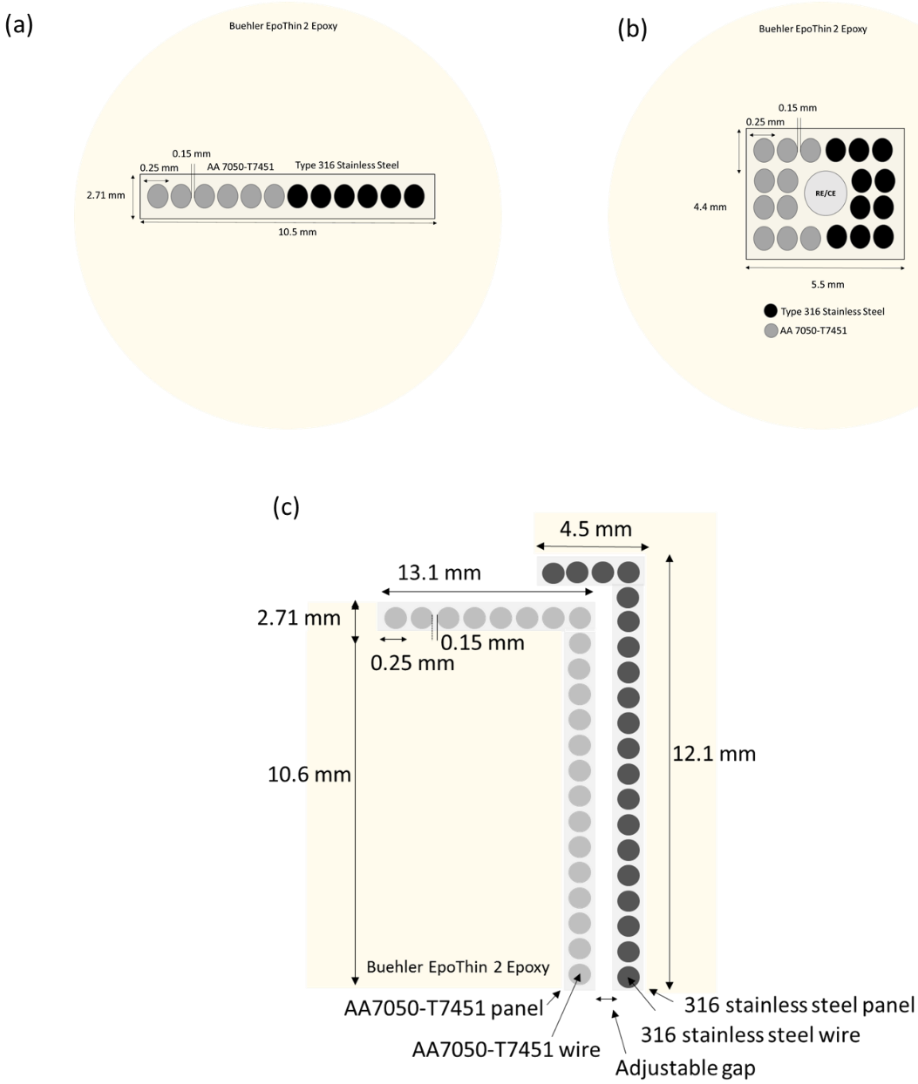

Figure 6.2. CMEA schematic of the (a) flat galvanic geometric array where 6 AA7050 electrodes and 6 Type 316 electrodes were embedded in an AA7050-T7451 panel in a flat arrangement (b) AA7050-T7451 rectangular panel with twenty holes surrounding one larger hole in the center.10 AA7050-T7451 electrodes and 10 Type 316 stainless steel electrodes with a sintered Ag/AgCl electrode was embedded in the larger hole in the center of the panel. (c) galvanic fastener geometric array where 22 AA7050 electrodes were embedded in an AA7050 panel and 20 Type 316 stainless electrodes were embedded in an stainless steel panel and arranged in a geometry representing a fastener with an adjustable gap between a Type 316 stainless rivet and 7050-T7451 plate where the separately addressable electrodes in each panel are facing each other (note: the electrodes in the schematic have been deliberately turned outwards so that each electrode can be seen).

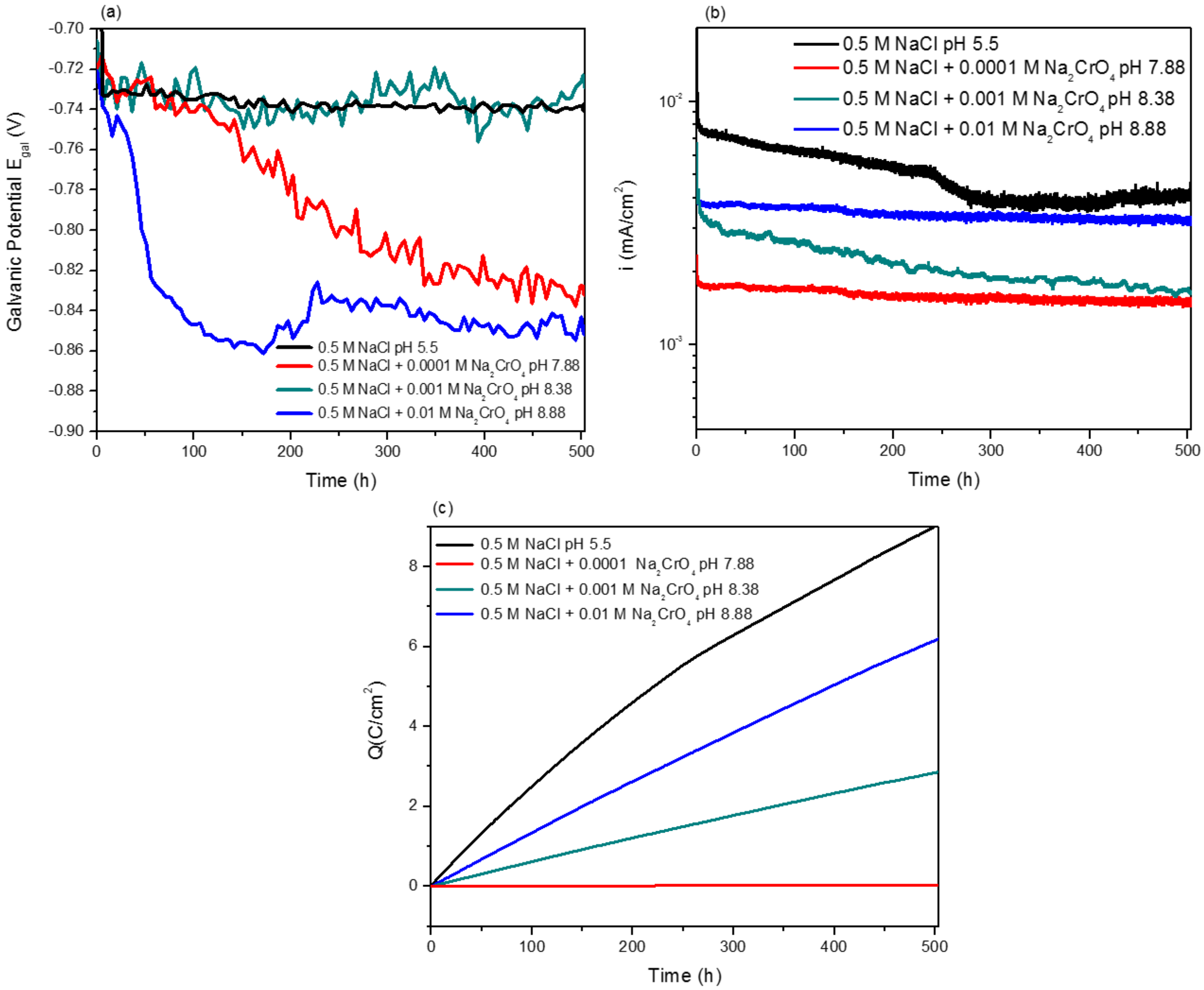

Figure 6.3. Galvanic couple (a) potential and (b) current density(c) anodic charge density of AA 7050-T7451 coupled to 316 SS obtained using zero resistance ammeter for 504 h in 0.5 M NaCl + 0.01 M Na_2CrO_4 at pH 8.8, 0.5 M NaCl + 0.001 M Na_2CrO_4 pH at pH 8.3 0.5 M NaCl + 0.0001 M Na_2CrO_4 pH at pH 7.8 and inhibitor-free 0.5 M NaCl at pH 5.5

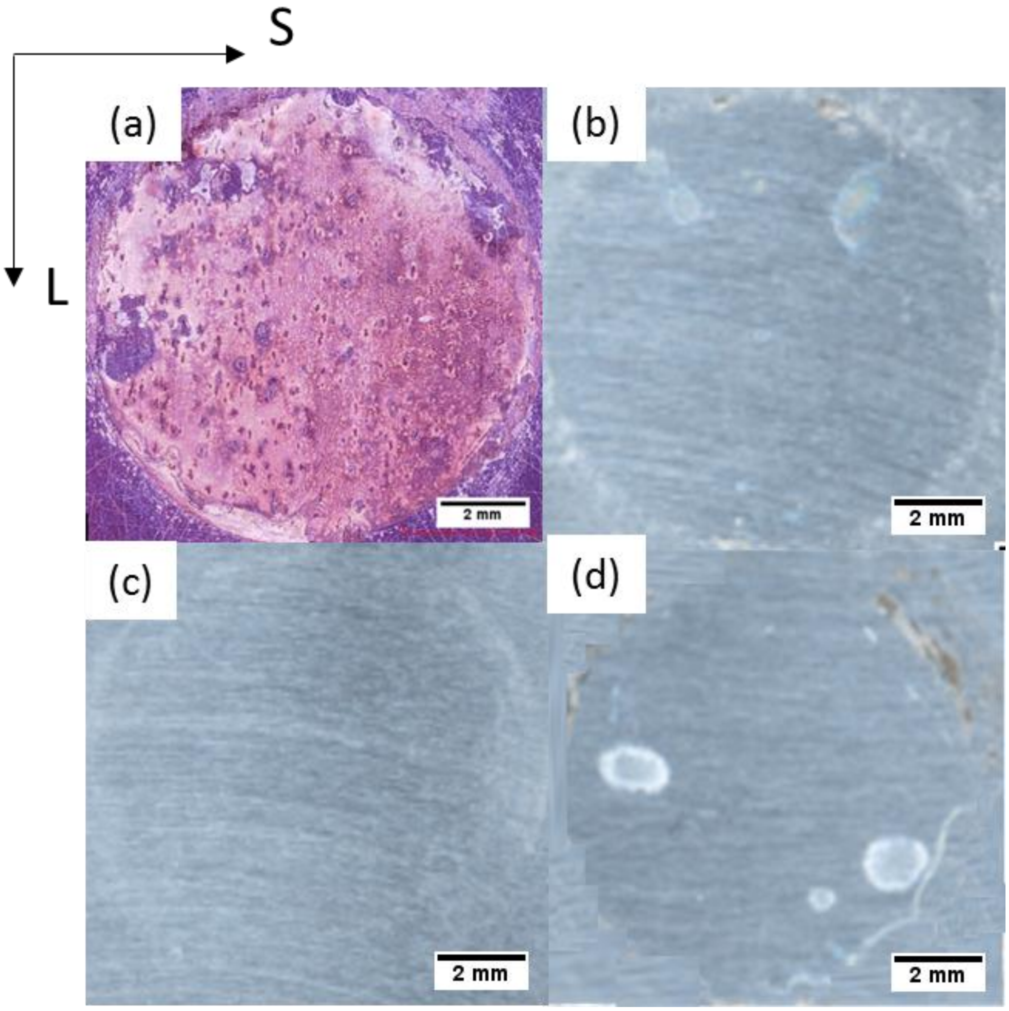

Figure 6.4. Scanned images of the SL surface AA7050-T7451 after 504 h ZRA exposure in (a) inhibitor-free 0.5 M NaCl at pH 5.5 (b) 0.5 M NaCl + 0.0001 Na_2CrO_4 at pH 7.8 (c) 0.5 M NaCl + 0.001 Na_2CrO_4 at pH 8.3 (d) 0.5 M NaCl + 0.01 Na_2CrO_4 at pH 8.8.

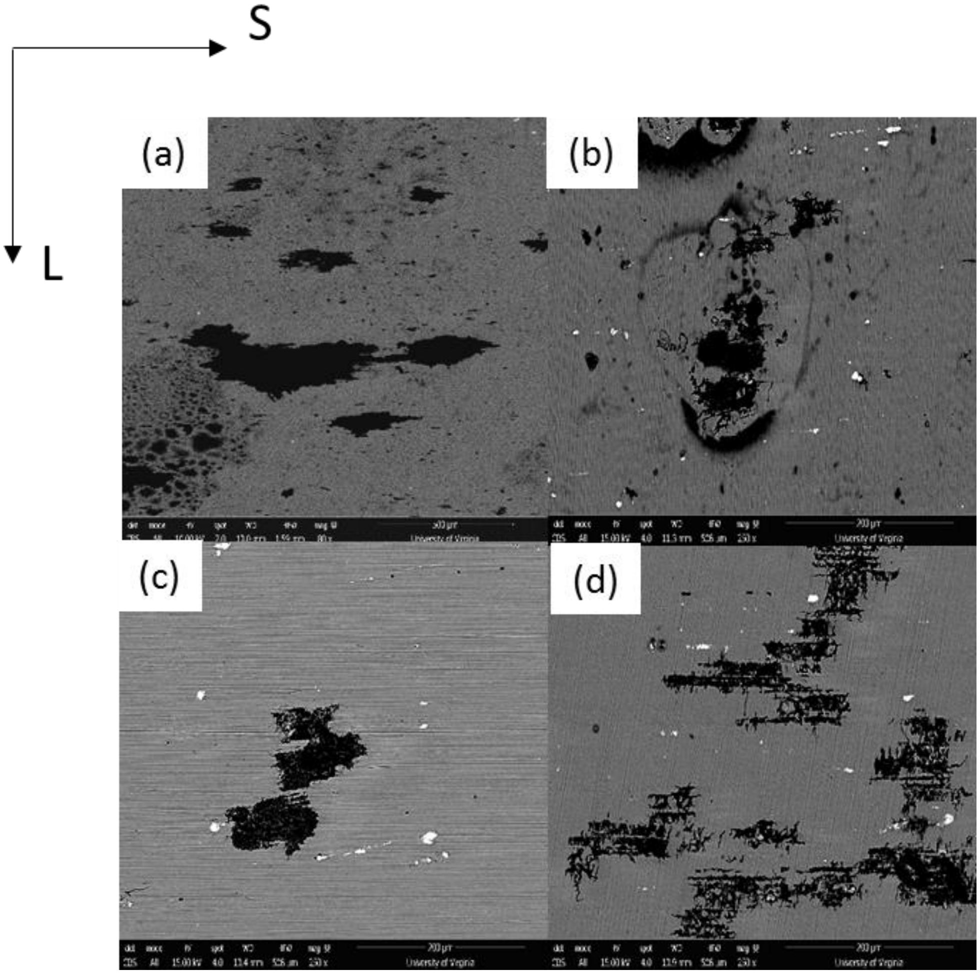

Figure 6.5. SEM micrographs of the surface of AA7050-T7451 SL after 504 h ZRA exposures in (a) inhibitor-free 0.5 M NaCl at pH 5.5 (b) 0.5 M NaCl + 0.0001 Na_2CrO_4 at pH 7.8 (c) 0.5 M NaCl + 0.001 Na_2CrO_4 at pH 8.3 (d) 0.5 M NaCl + 0.01 Na_2CrO_4 at pH 8.8.

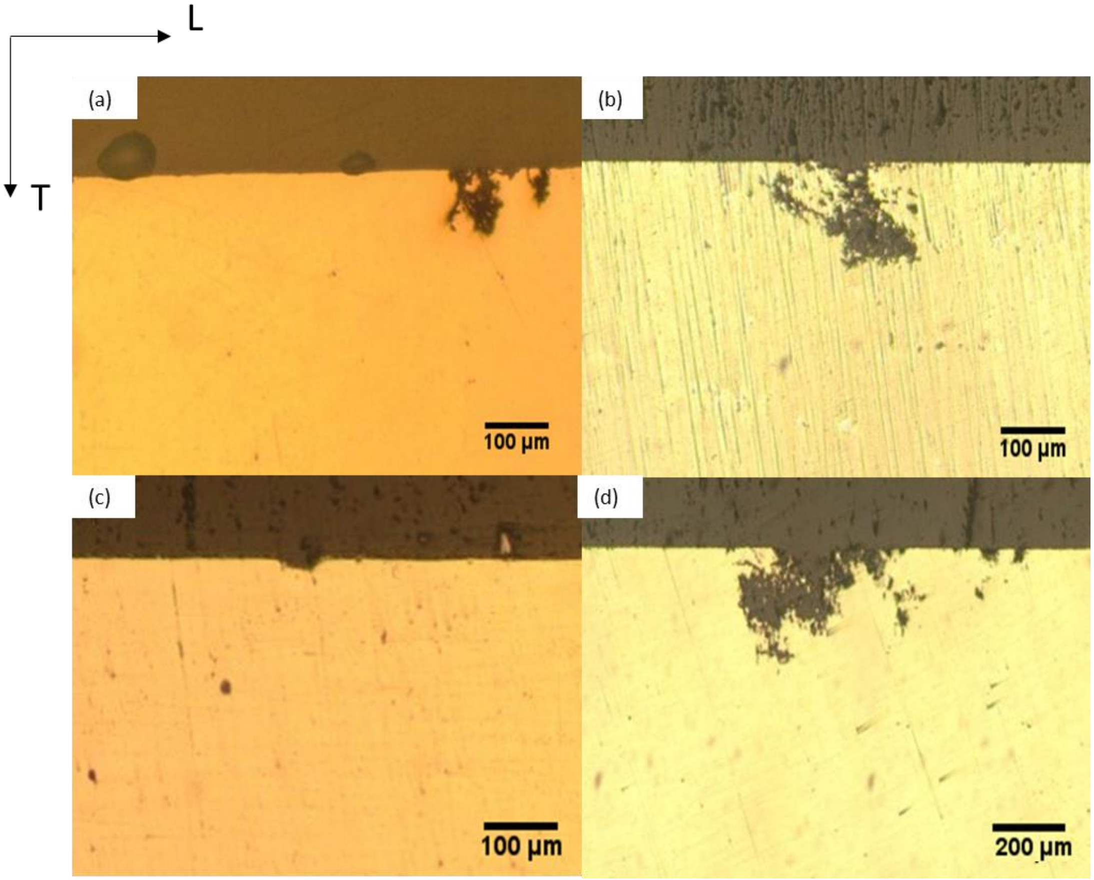

Figure 6.6. Cross-sectioned optical micrographs of AA7050-T7451 after 504 h ZRA exposures in (a) inhibitor-free 0.5 M NaCl at pH 5.5 (b) 0.5 M NaCl + 0.0001 Na_2CrO_4 at pH 7.8 (c) 0.5 M NaCl + 0.001 Na_2CrO_4 at pH 8.3 (d) 0.5 M NaCl + 0.01 Na_2CrO_4 at pH 8.8.

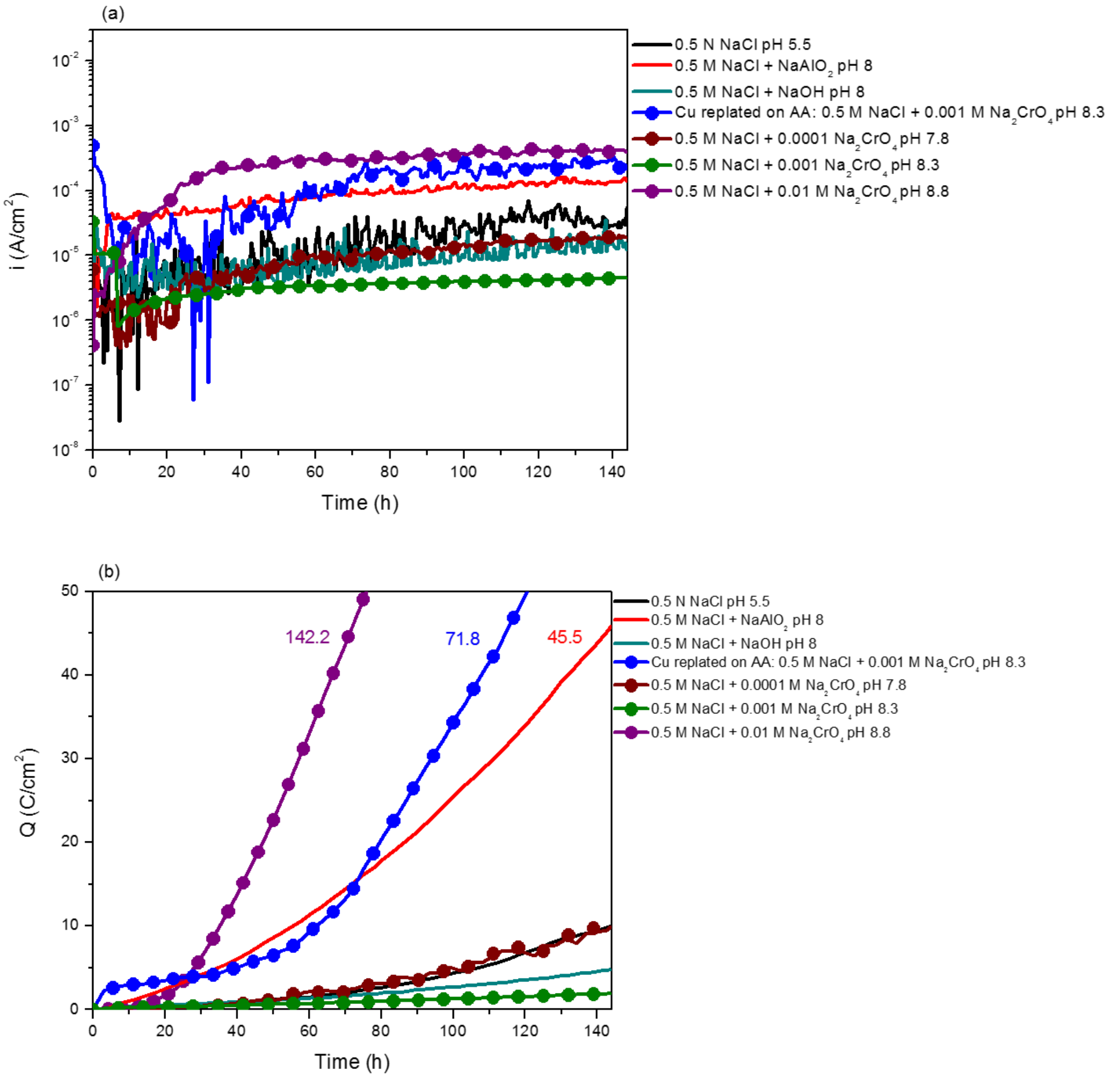

Figure 6.7. Potentiostatic polarization for 144 h (-0.73 V SCE) on AA7050-T7451 and the resulting (a) current density and (b) corresponding charge density in simulated rivet solutions of inhibitor-free 0.5 M NaCl at pH 5.5, 0.5 M NaCl + $NaAlO_2$ at pH 8, 0.5M NaCl + NaOH at pH 8, compared with chromate-containing solutions of 0.5 M NaCl + 0.0001 Na_2CrO_4 at pH 7.8 and, 0.5 M NaCl + 0.001 Na_2CrO_4 at pH 8.3, 0.5 M NaCl + 0.01 Na_2CrO_4 at pH 8.88.

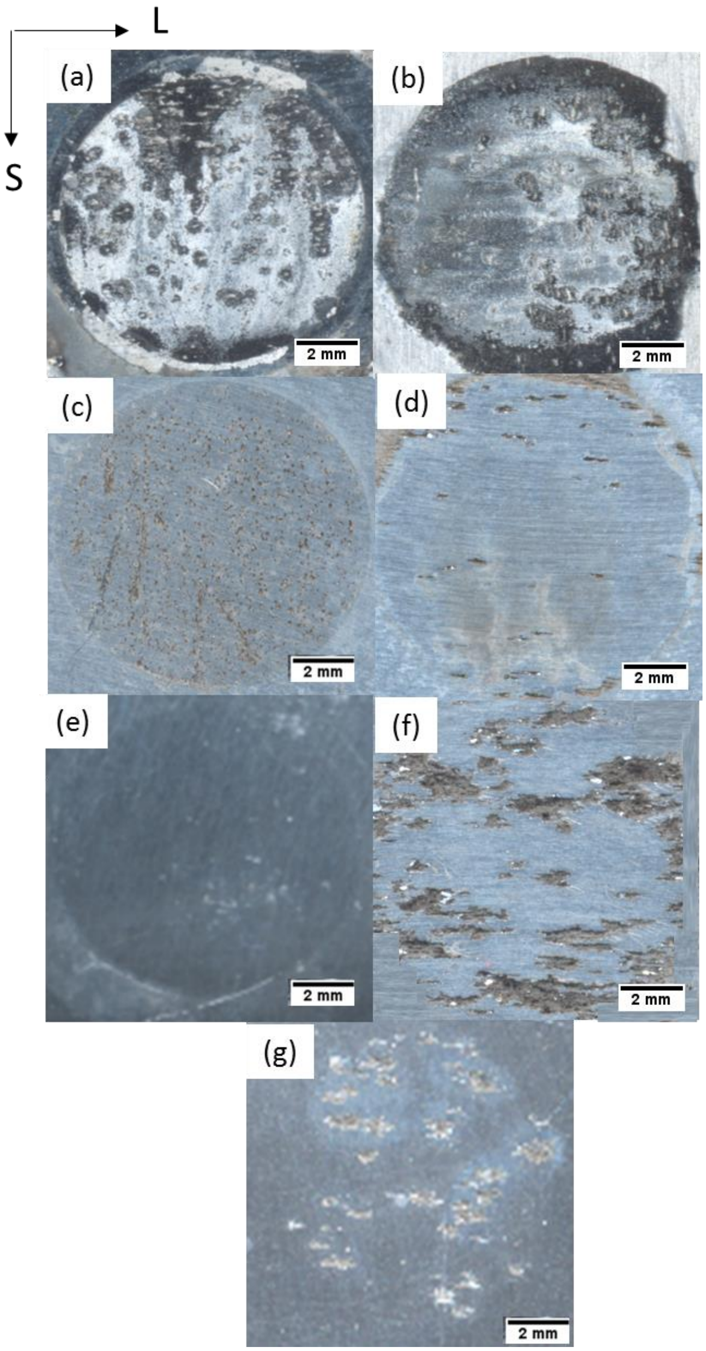

Figure 6.8. Scanned images of the SL surface of AA7050-T7451 after 144 h potentiostatic hold (-0.73 V SCE) exposures in (a) 0.5 M NaCl at pH 5.5 (b) 0.5 M NaCl + $NaAlO_2$ at pH 8 (c) 0.5 M NaCl + NaOH at pH 8 (d) 0.5 M NaCl + 0.0001 Na_2CrO_4 at pH 7.3 (e) 0.5 M NaCl + 0.001 Na_2CrO_4 at pH 8.3 (f) 0.5 M NaCl + 0.01 Na_2CrO_4 at pH 8.88 and (g) replated Cu on AA7050 in 0.5 M NaCl + 0.001 Na_2CrO_4 at pH 8.3.

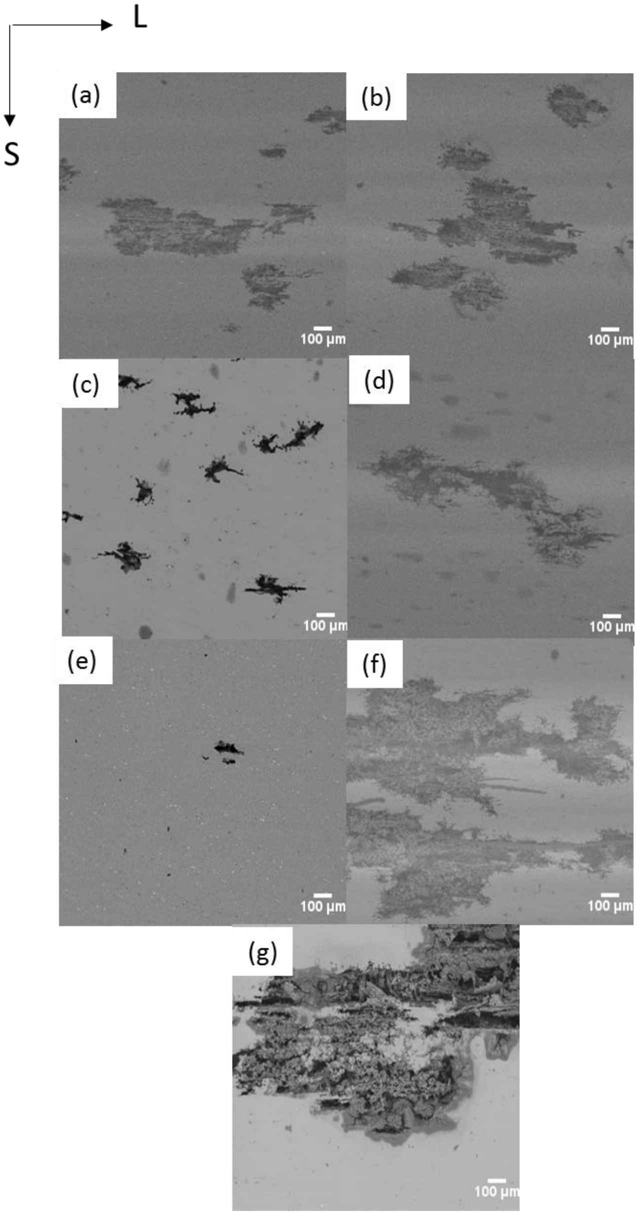

Figure 6.9. Scanned electron micrographs of the SL surface of AA7050-T7451 after 144 h potentiostatic (-0.73 V SCE) exposures in (a) 0.5 M NaCl at pH 5.5 (b) 0.5 M NaCl + $NaAlO_2$ at pH 8 (c) 0.5 M NaCl + NaOH at pH 8 (d) 0.5 M NaCl + 0.0001 Na_2CrO_4 at pH 7.3 (e) 0.5 M NaCl + 0.001 Na_2CrO_4 at pH 8.3 (f) 0.5 M NaCl + 0.01 Na_2CrO_4 at pH 8.88 and (g) replated Cu on AA7050 in 0.5 M NaCl + 0.001 Na_2CrO_4 at pH 8.3.

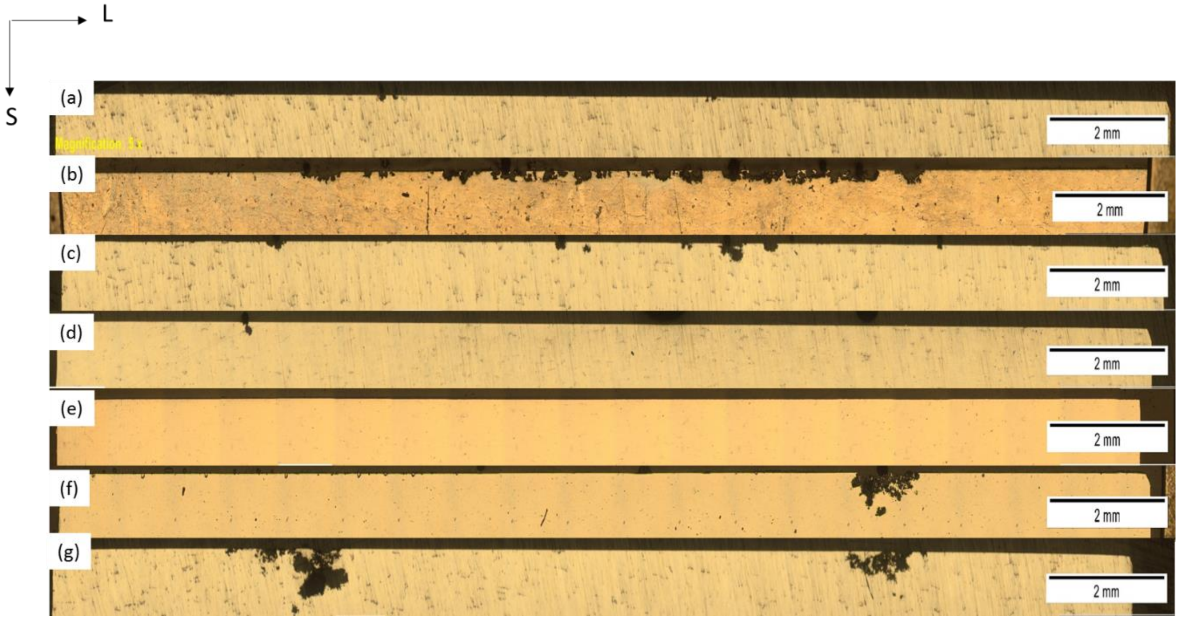

Figure 6.10. Cross-sectional optical micrograph of AA7050-T7451 SL after 144 h potentiostatic hold at E=-0.73 V SCE in (a) 0.5 M NaCl at pH 5.5 (b) 0.5 M NaCl + $NaAlO_2$ at pH 8 (c) 0.5 M NaCl + NaOH at pH 8 (d) 0.5 M NaCl + 0.0001 Na_2CrO_4 at pH 7.3 (e) 0.5 M NaCl + 0.001 Na_2CrO_4 at pH 8.3 (f) 0.5 M NaCl + 0.01 Na_2CrO_4 at pH 8.88 and (g) replated Cu on AA7050 in 0.5 M NaCl + 0.001 Na_2CrO_4 at pH 8.3.

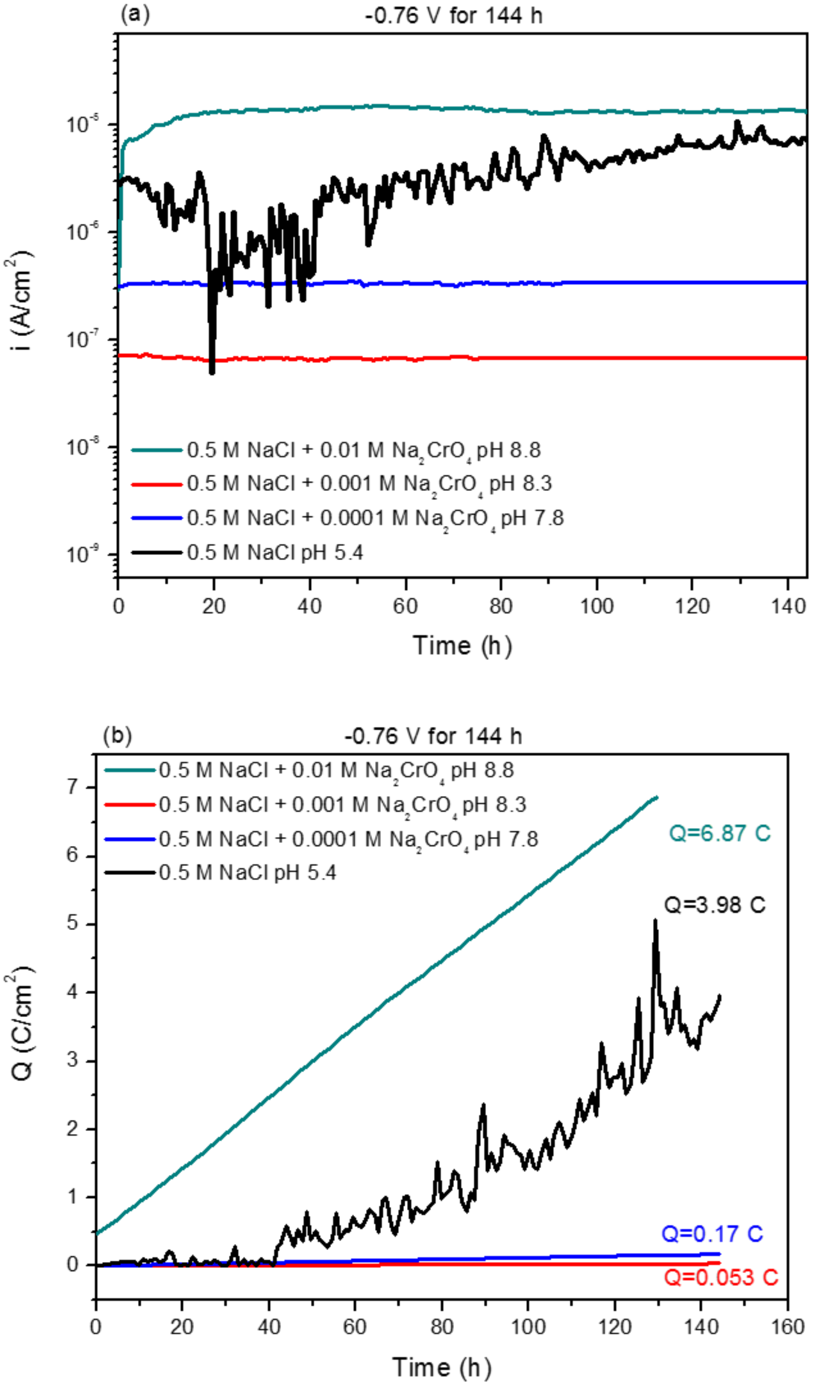

Figure 6.11. Potentiostatic polarization for 144 h (-0.76 V SCE) on AA7050-T7451 and the resulting (a) current density and (b) charge density in chromate-containing solutions of 0.5 M NaCl + 0.0001 Na$_2$CrO$_4$ at pH 7.8, 0.5 M NaCl + 0.001 Na$_2$CrO$_4$ at pH 8.3 , 0.5 M NaCl + 0.01 Na$_2$CrO$_4$ at pH 8.88, and inhibtor-free 0.5 M NaCl at pH 5.5.

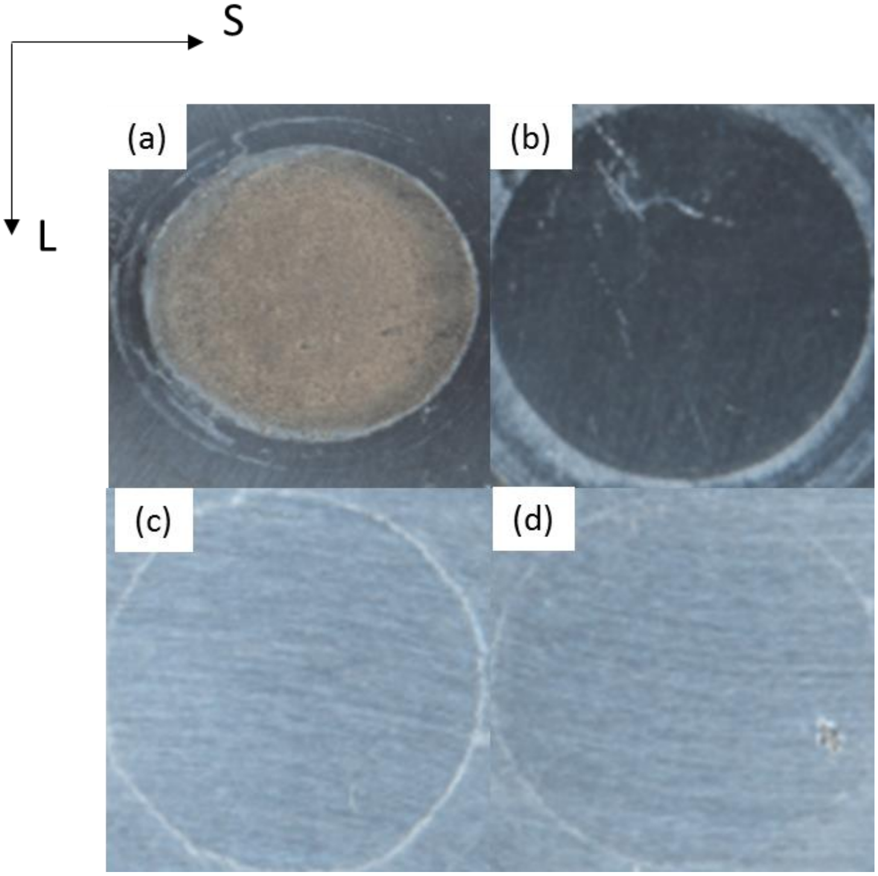

Figure 6.12. Scanned images of the SL surface of AA7050-T7451 after 144 h potentiostatic hold at (-0.76 V SCE) exposures in (a) 0.5 M NaCl at pH 5.5 (b) 0.5 M NaCl + 0.0001 Na_2CrO_4 at pH 7.8 and (c) 0.5 M NaCl + 0.001 Na_2CrO_4 at pH 8.3 and, (d) 0.5 M NaCl + 0.01 Na_2CrO_4 at pH 8.8.

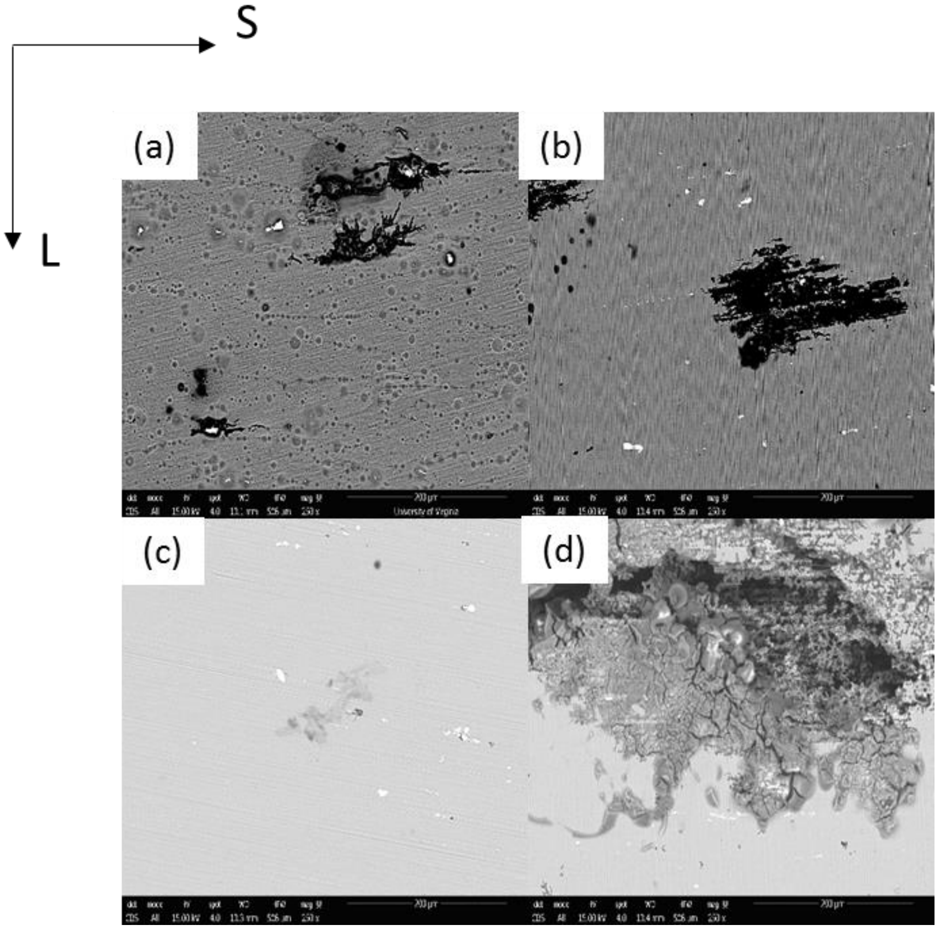

Figure 6.13. Scanning electron micrograph of the SL surface of AA7050-T7451 after 144 h potentiostatic hold (-0.76 V SCE) in (a) 0.5 M NaCl at pH 5.5 (b) 0.5 M NaCl + 0.0001 Na_2CrO_4 at pH 7.8 and (c) 0.5 M NaCl + 0.001 Na_2CrO_4 at pH 8.3 (d) 0.5 M NaCl + 0.01 Na_2CrO_4 at pH 8.8.

Figure 6.14. Cross-sectional optical micrograph of AA7050-T7451 after 144 h potentiostatic hold (-0.76 V SCE) in (a) 0.5 M NaCl at pH 5.5 (b) 0.5 M NaCl + 0.0001 M Na_2CrO_4 at pH 7.8 and (c) 0.5 M NaCl + 0.001 Na_2CrO_4 at pH 8.3 (d) 0.5 M NaCl + 0.01 M Na_2CrO_4 at pH 8.8.

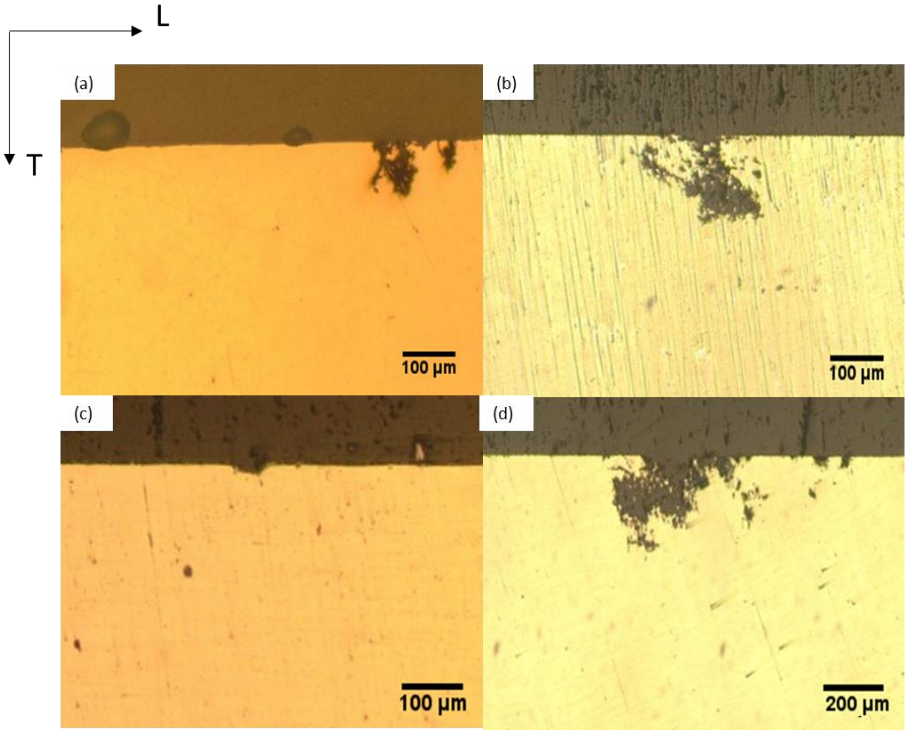

Figure 6.15. High magnification cross-sectional optical micrograph of AA7050-T7451 after 144 h potentiostatic hold (-0.76 V SCE) in (a) 0.5 M NaCl at pH 5.5 (b) 0.5 M NaCl + 0.0001 Na_2CrO_4 at pH 7.8 and (c) 0.5 M NaCl + 0.001 Na_2CrO_4 at pH 8.3 (d) 0.5 M NaCl + 0.01 Na_2CrO_4 at pH 8.8.

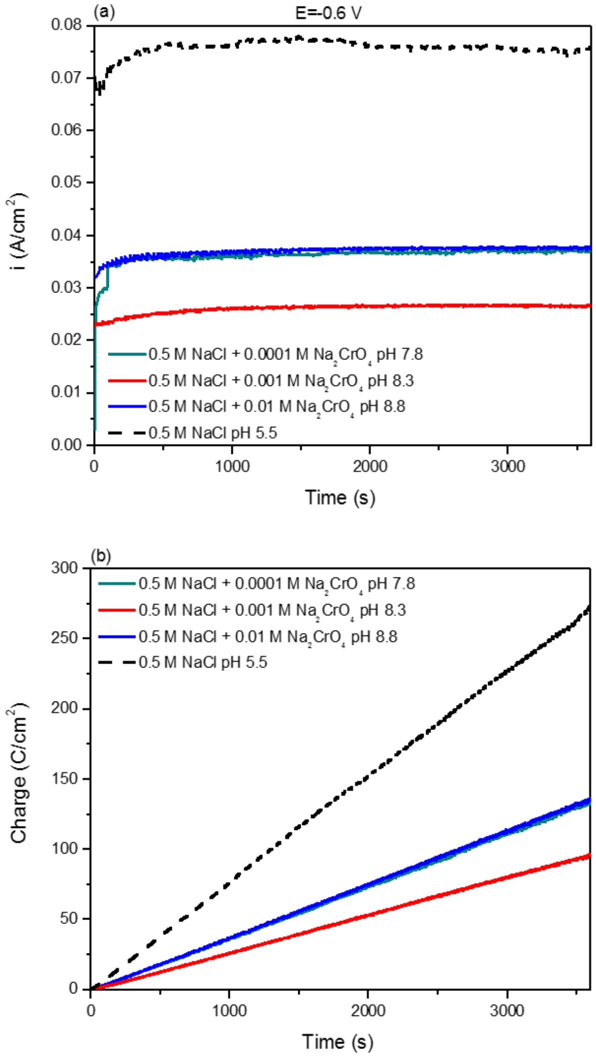

Figure 6.16. Potentiostatic polarization for 1 h (-0.6 V SCE) on AA7050-T7451 and the resulting (a) current density and (b) charge density in chromate-containing solutions of 0.5 M NaCl + 0.0001 Na_2CrO_4 at pH 7.8, 0.5 M NaCl + 0.001 Na_2CrO_4 at pH 8.3 , 0.5 M NaCl + 0.01 Na_2CrO_4 at pH 8.8, and inhibtor-free 0.5 M NaCl at pH 5.5.

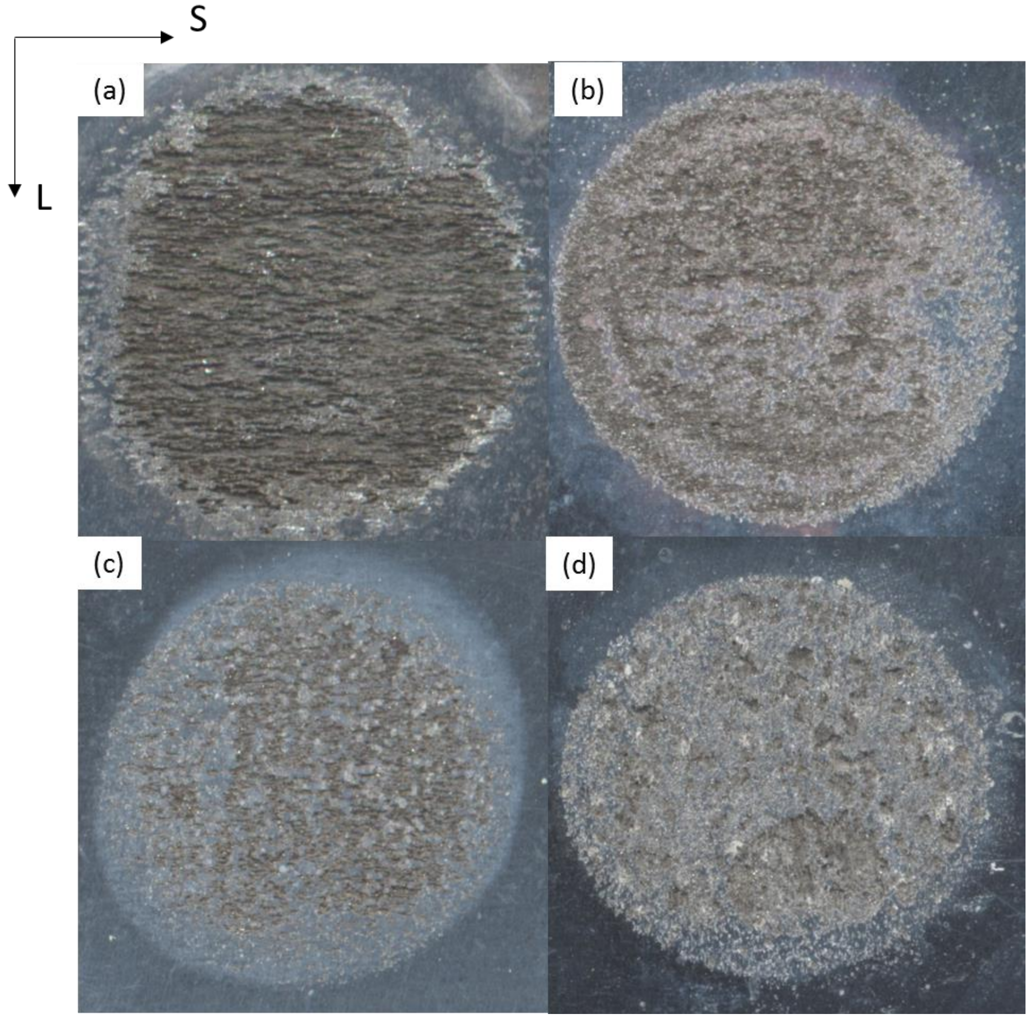

Figure 6.17. Scanned images of the SL surface of AA7050-T7451 after 1 h potentiostatic hold (-0.6 V SCE) exposures in (a) 0.5 M NaCl at pH 5.5 (b) 0.5 M NaCl + 0.0001 Na_2CrO_4 at pH 7.8 and (c) 0.5 M NaCl + 0.001 Na_2CrO_4 at pH 8.3, and (d) 0.5 M NaCl + 0.01 Na_2CrO_4 at pH 8.8.

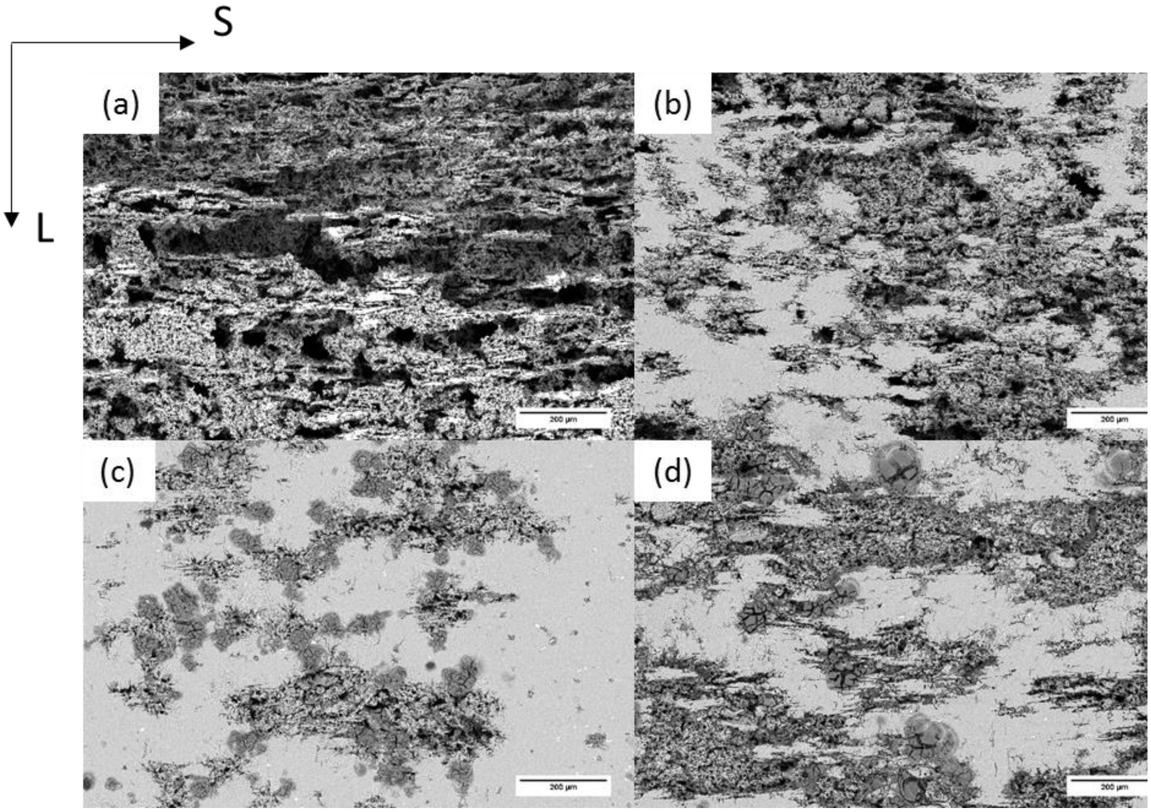

Figure 6.18. Scanning electron micrograph of the SL surface of AA7050-T7451 after 1 h potentiostatic hold (-0.6 V SCE) exposures in (a) 0.5 M NaCl at pH 5.5 (b) 0.5 M NaCl + 0.0001 Na_2CrO_4 at pH 7.8 and (c) 0.5 M NaCl + 0.001 Na_2CrO_4 at pH 8.3, and (d) 0.5 M NaCl + 0.01 Na_2CrO_4 at pH 8.8.

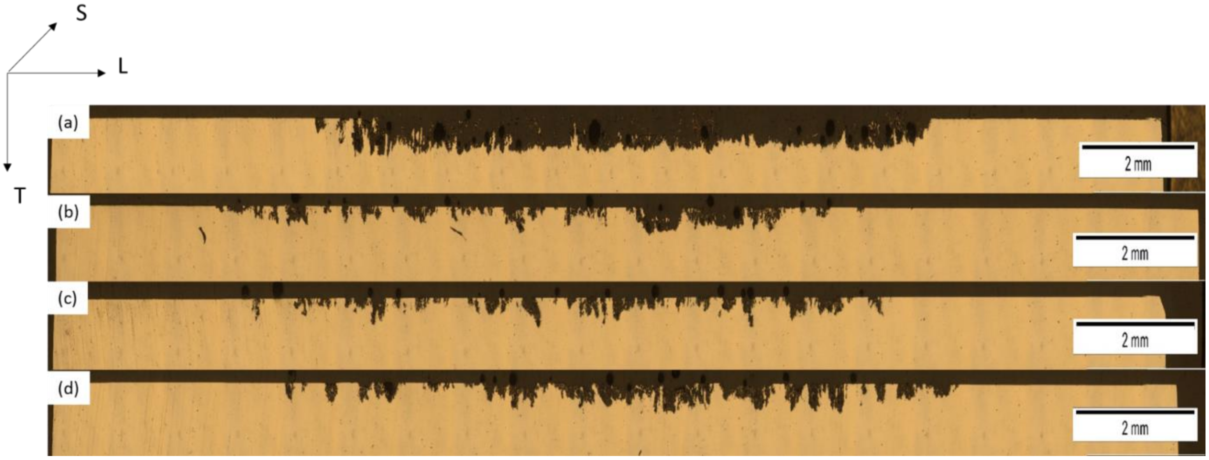

Figure 6.19. Cross-sectional optical micrograph of AA7050-T7451 after 1 h potentiostatic hold at (-0.6 V SCE) in (a) 0.5 M NaCl at pH 5.5 (b) 0.5 M NaCl + 0.0001 Na_2CrO_4 at pH 7.8 and (c) 0.5 M NaCl + 0.001 Na_2CrO_4 at pH 8.3, and (d) 0.5 M NaCl + 0.01 Na_2CrO_4 at pH 8.8.

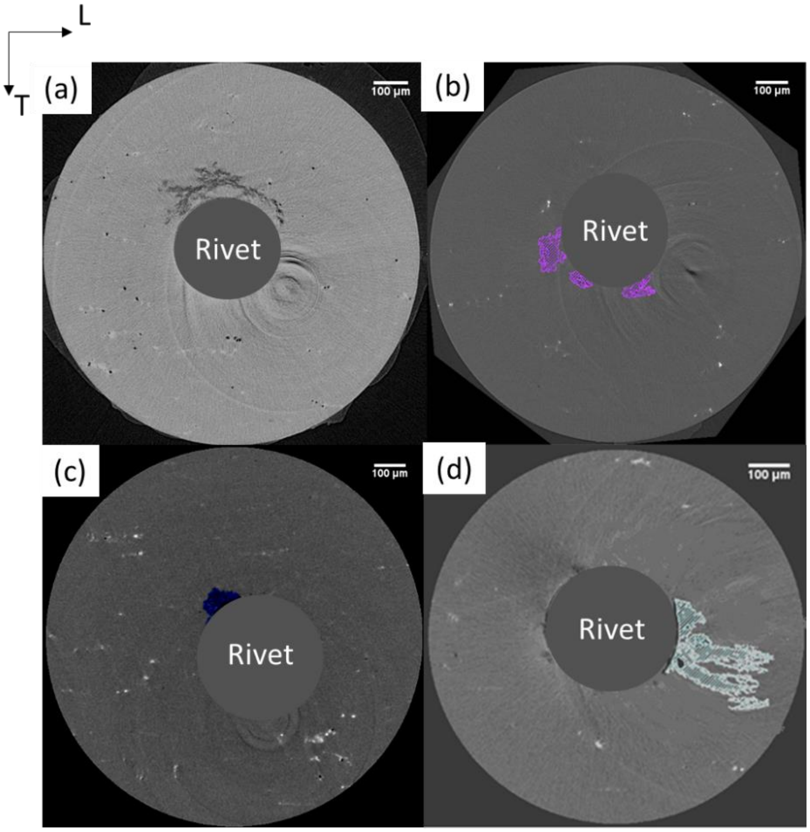

Figure 6.20. X-ray tomograms of a selected 2D vertical projection for the (a) *operando* 4 M NaCl at a depth of 84 µm (control) (b) *ex-situ* 4 M NaCl + 0.0001 M Na_2CrO_4 at depth 126 µm (b) *ex-situ* 4 M NaCl + 0.001 M Na_2CrO_4 at depth 205 µm and (c) *ex-situ* 4 M NaCl + 0.001 M Na_2CrO_4 at depth 395 µm.

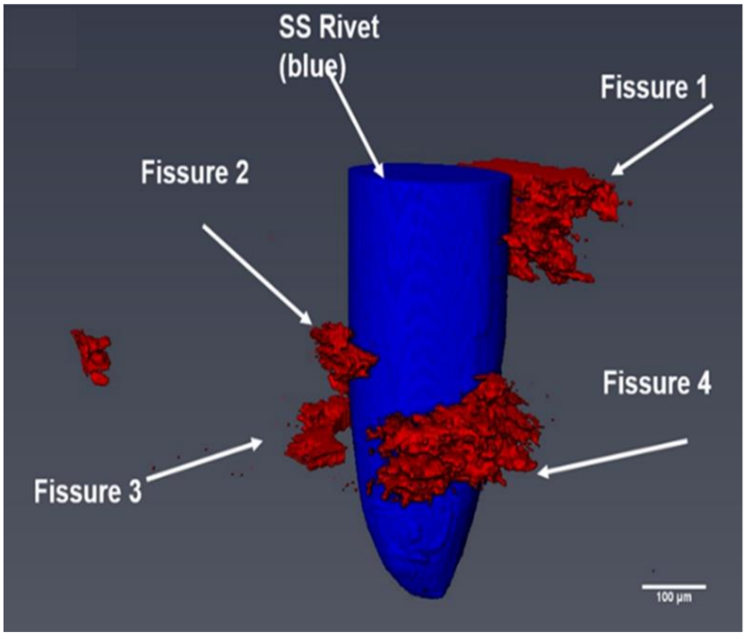

Figure 6.21. The reconstructed 3D representation of corrosion damage for the inhibitor-free 4M NaCl droplet exposure after 62 h with the AA7050 transparent showing the SS rivet (blue) and the 3D-shaped volume (red) representing the corrosion damage in the form of fissures.

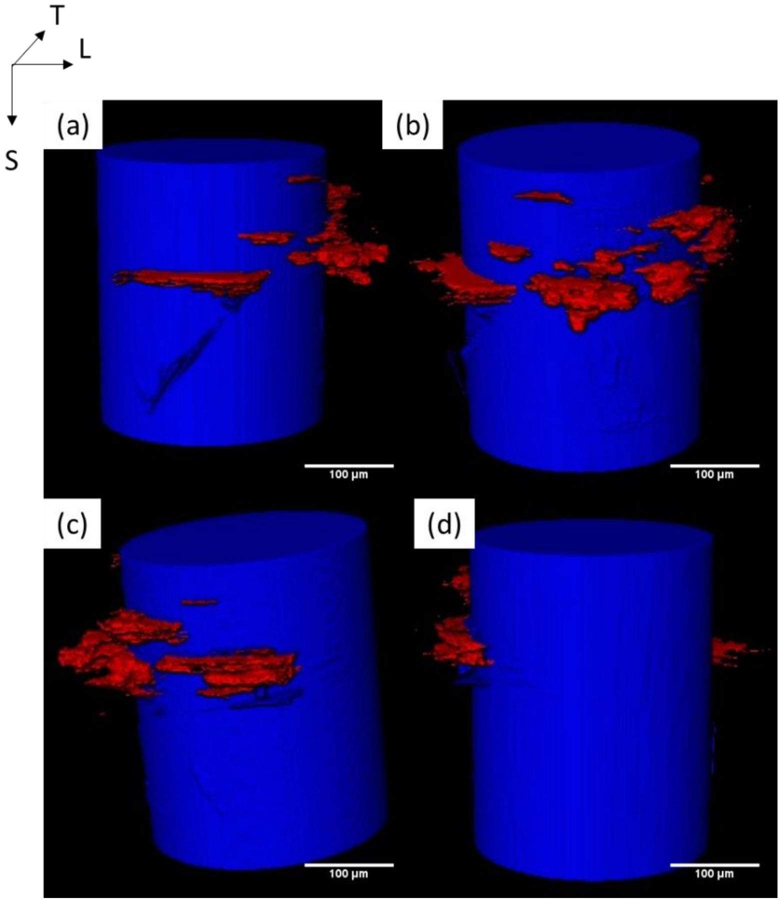

Figure 6.22. The reconstructed 3D representation of corrosion damage for the 4 M NaCl + 0.0001 Na_2CrO_4 at pH 7.8 droplet exposure after 62 h with the AA7050-T7451 transparent showing the stainless steel rivet (blue) and the 3D-shaped volume (red) representing the corrosion damage in the form of fissures rotated (a) 0° (b) 72° (c) 216° and (d) 288°

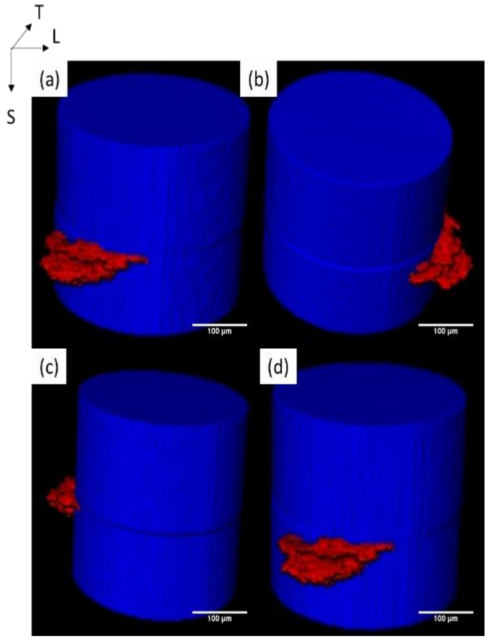

Figure 6.23. The reconstructed 3D representation of corrosion damage for the 4 M NaCl + 0.001 Na_2CrO_4 at pH 8.3 droplet exposure after 62 h with the AA7050-T7451 transparent showing the stainless steel rivet (blue) and the 3D-shaped volume (red) representing the corrosion damage in the form of fissures rotated (a) 0° (b) 72° (c) 216° and (d) 288°.

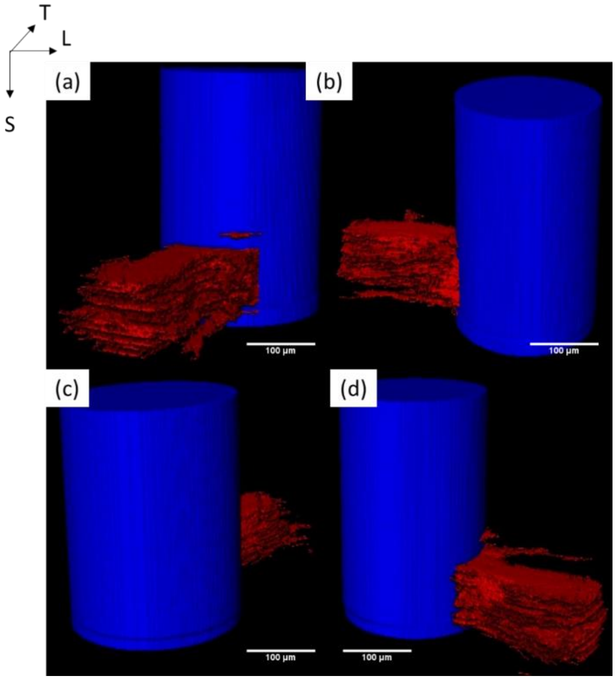

Figure 6.24. The reconstructed 3D representation of corrosion damage for the 4 M NaCl + 0.01 Na_2CrO_4 at pH 8.8 droplet exposure after 62 h with the AA7050-T7451 transparent showing the stainless steel rivet (blue) and the 3D-shaped volume (red) representing the corrosion damage in the form of fissures rotated (a) 0° (b) 72° (c) 216° and (d) 288°.

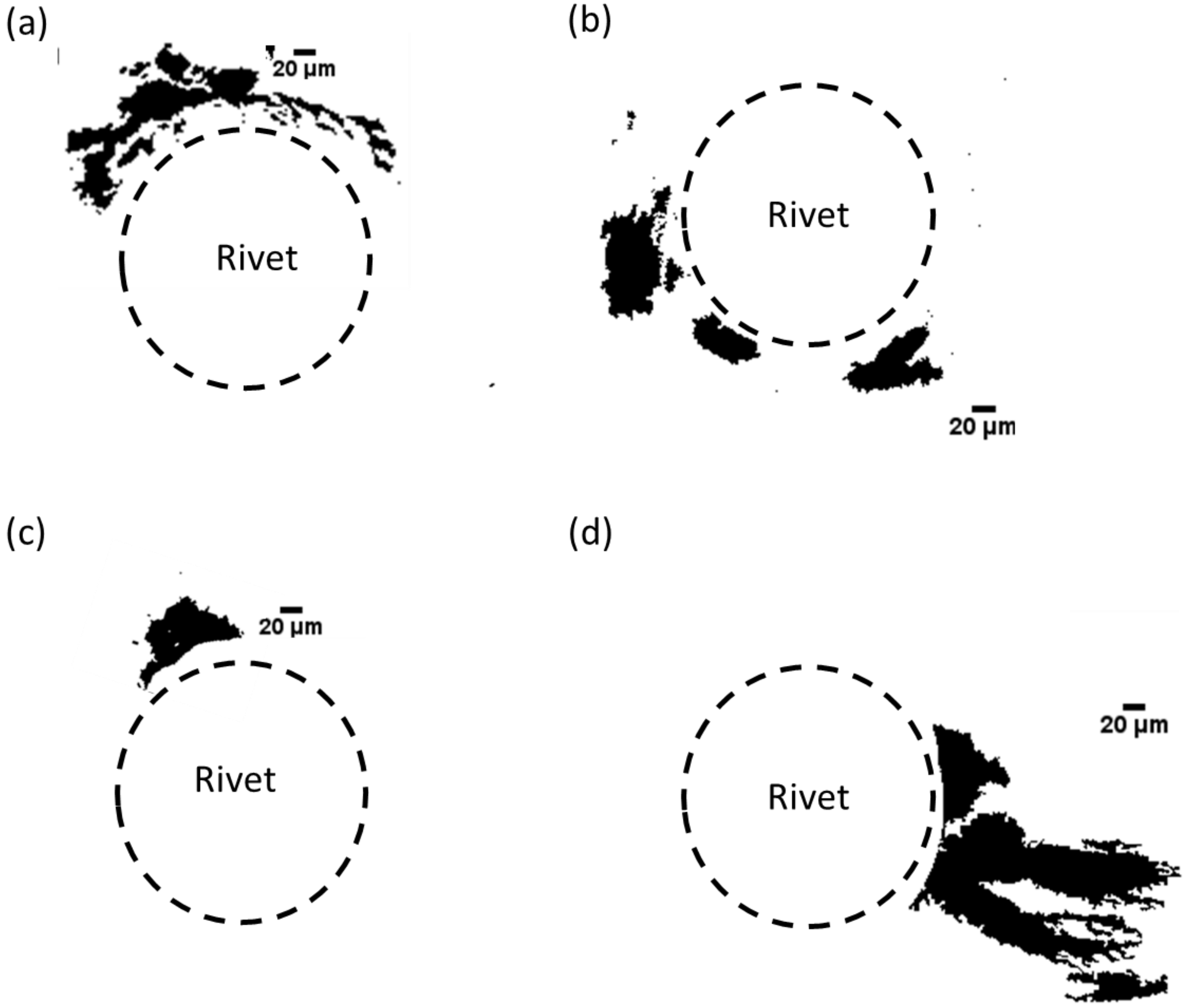

Figure 6.25. Corrosion fissure damage morphology from the 2D tomogram obtained from XCT exposures in (a) 4 M NaCl at pH 5.5 (b) 4 M NaCl + 0.0001 M Na_2CrO_4 at pH 7.8 (c) 4 M NaCl + 0.001 M Na_2CrO_4 at pH 8.3 (d) 4 M NaCl + 0.01 M Na_2CrO_4 at pH 8.8.

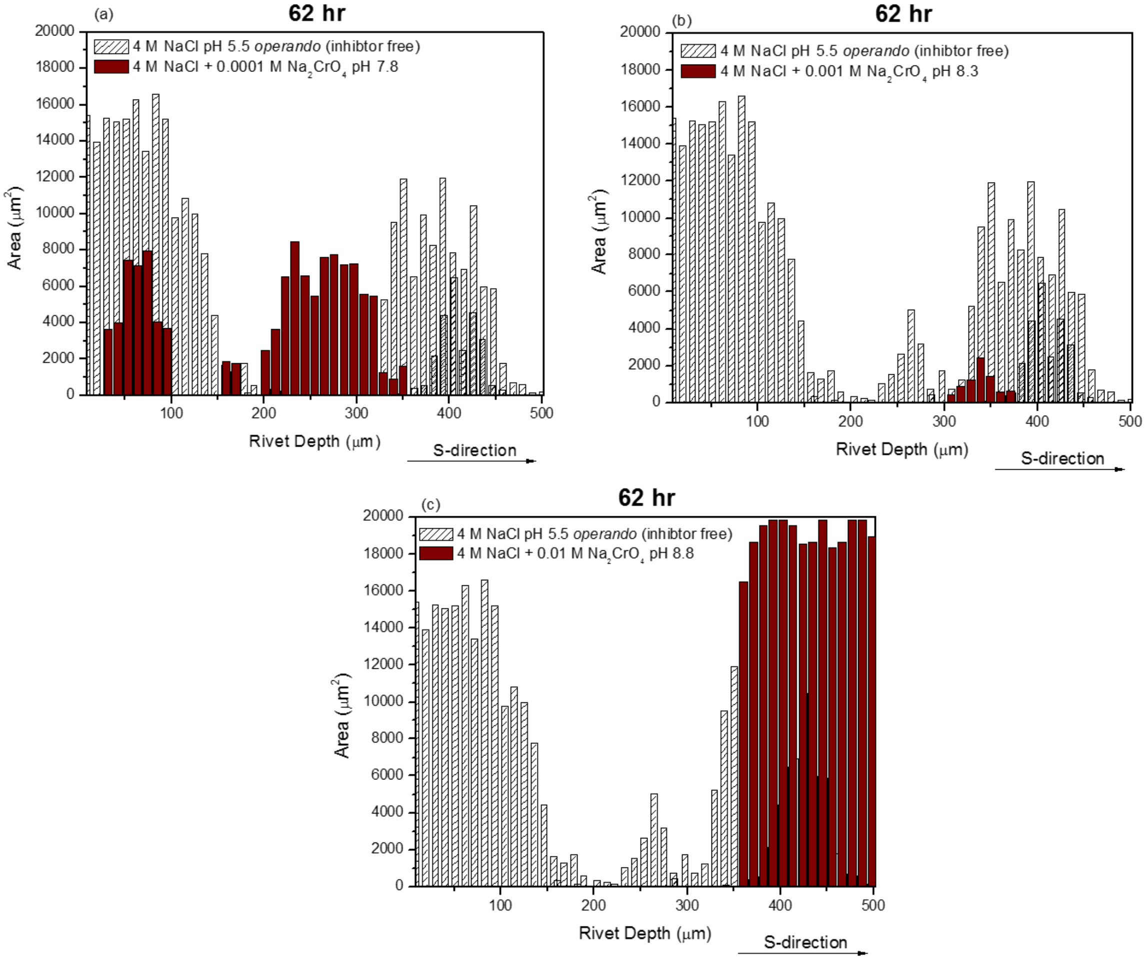

Figure 6.26. Corrosion 2D area for the fissures observed in the AA7050-T7451 simulated fastener in (a) 4 M NaCl + 0.0001 M Na_2CrO_4 at pH 7.8 (b) 4 M NaCl + 0.001 M Na_2CrO_4 at pH 8.3 (c) 4 M NaCl + 0.01 M Na_2CrO_4 at pH 8.8. The white bars represent the inhibitor-free exposure while the red bars represent the chromate-containing exposures.

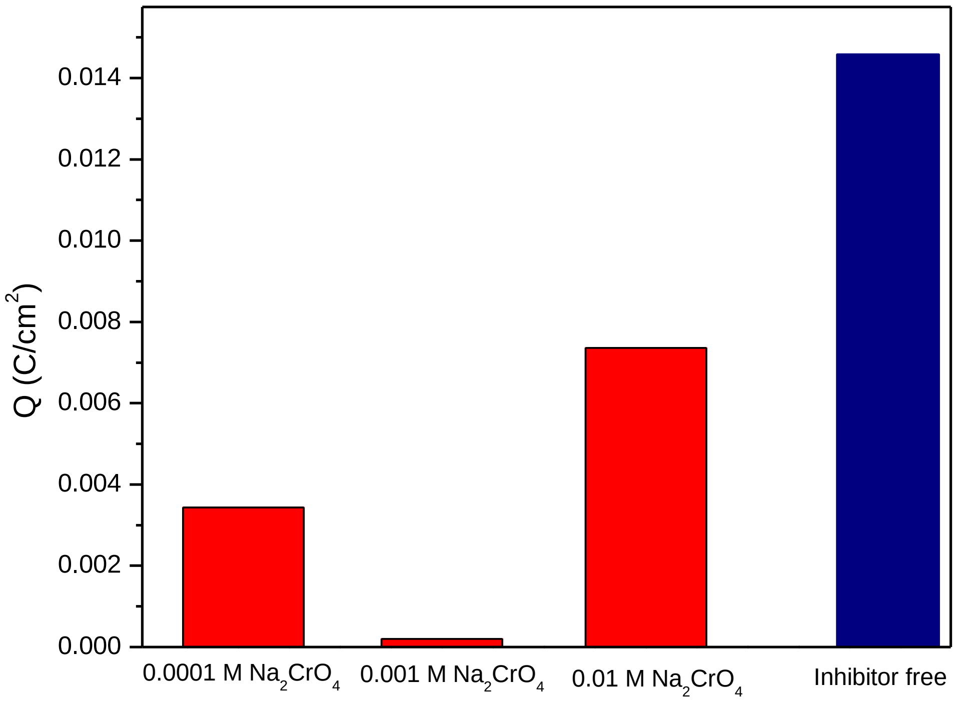

Figure 6.27. Anodic charge density bar plot after 62 h for each of the chromate-containing exposure: 4 M NaCl + 0.0001 M Na_2CrO_4 at pH 7.8, 4 M NaCl + 0.001 M Na_2CrO_4 at pH 8.3 and 4 M NaCl + 0.01 M Na_2CrO_4 at pH 8.8 compared with inhibitor-free 4 M NaCl depicted in blue.

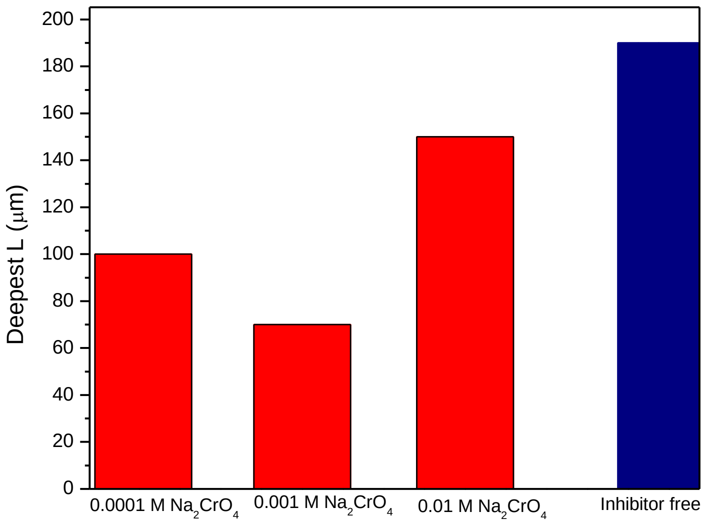

Figure 6.28. Deepest pit depth bar plots after 62 h for each of the chromate containing exposures of 4 M NaCl + 0.0001 M Na2CrO4 at pH 7.8, 4 M NaCl + 0.001 M Na2CrO4 at pH 8.3 and 4 M NaCl + 0.01 M Na2CrO4 at pH 8.8 compared with inhibitor free 4 M NaCl depicted in blue.

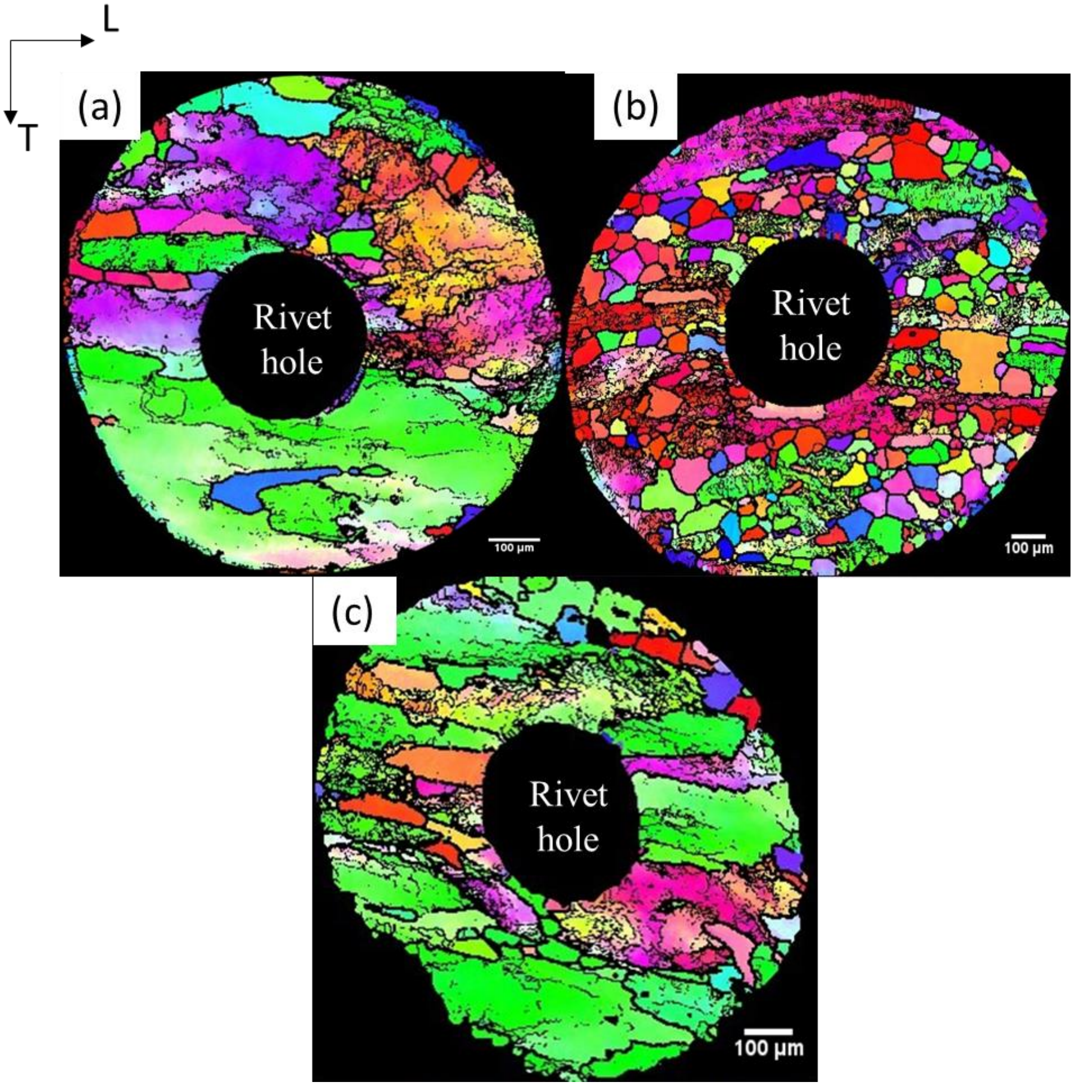

Figure 6.29. EBSD map on the surface of AA7050-T7451 LT simulated fasteners pre-exposure for t(a) 4 M NaCl + 0.0001 M Na_2CrO_4 at pH 7.8 (b) 4 M NaCl + 0.001 M Na_2CrO_4 at pH 8.3 and (c) 4 M NaCl + 0.01 M Na_2CrO_4 at pH 8.8.

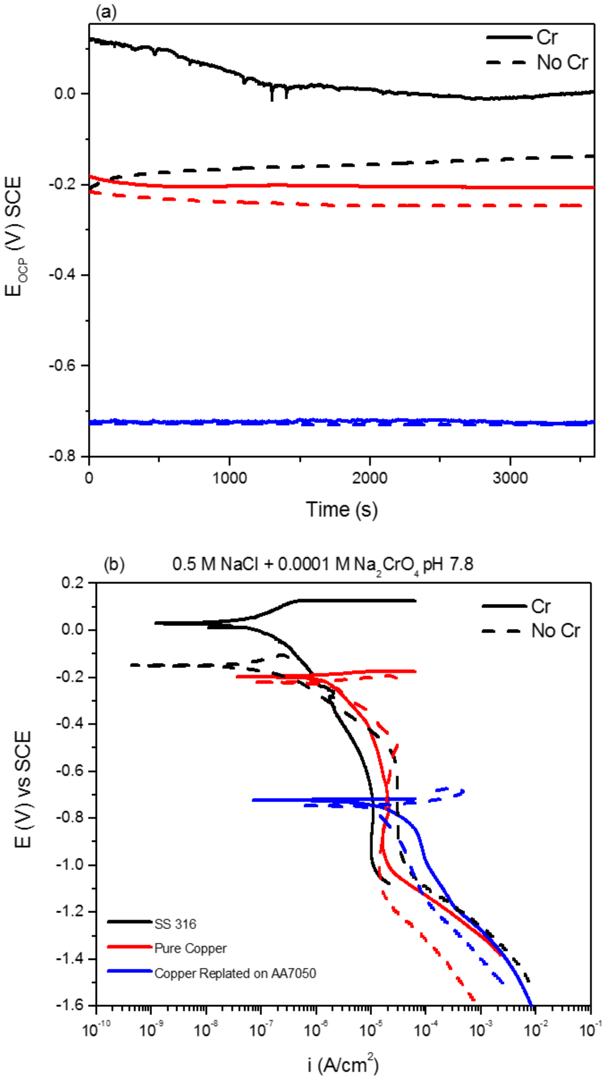

Figure 6.30. (a) OCP over 1 h (b) cathodic potentiodynamic polarization of Type 316 stainless steel, pure Cu and Cu-replated on AA7050-T7451 in 0.5 M NaCl + 0.0001 M Na_2CrO_4 pH at pH 7.8 (solid lines) and inhibitor-free 0.5 M NaCl at pH 5.5 (dashed lines).

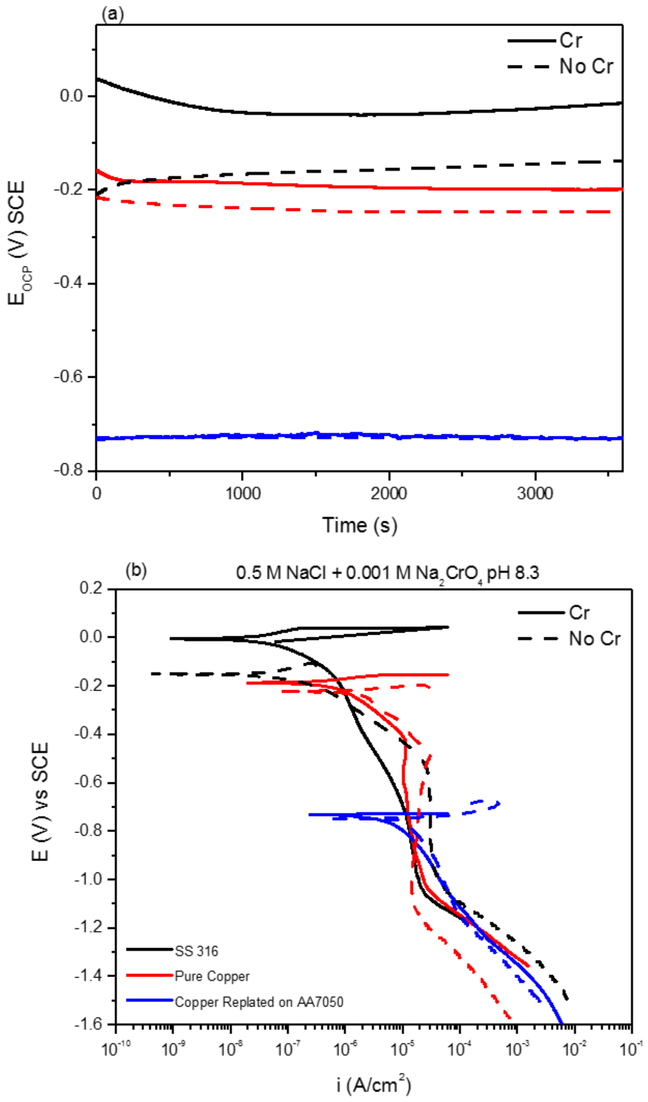

Figure 6.31. (a) OCP over 1 h (b) cathodic potentiodynamic polarization of Type 316 stainless steel, pure Cu and Cu-replated on AA7050-T7451 in 0.5 M NaCl + 0.001 M Na_2CrO_4 pH at pH 8.3 (solid lines) and inhibitor-free 0.5 M NaCl at pH 5.5 (dashed lines).

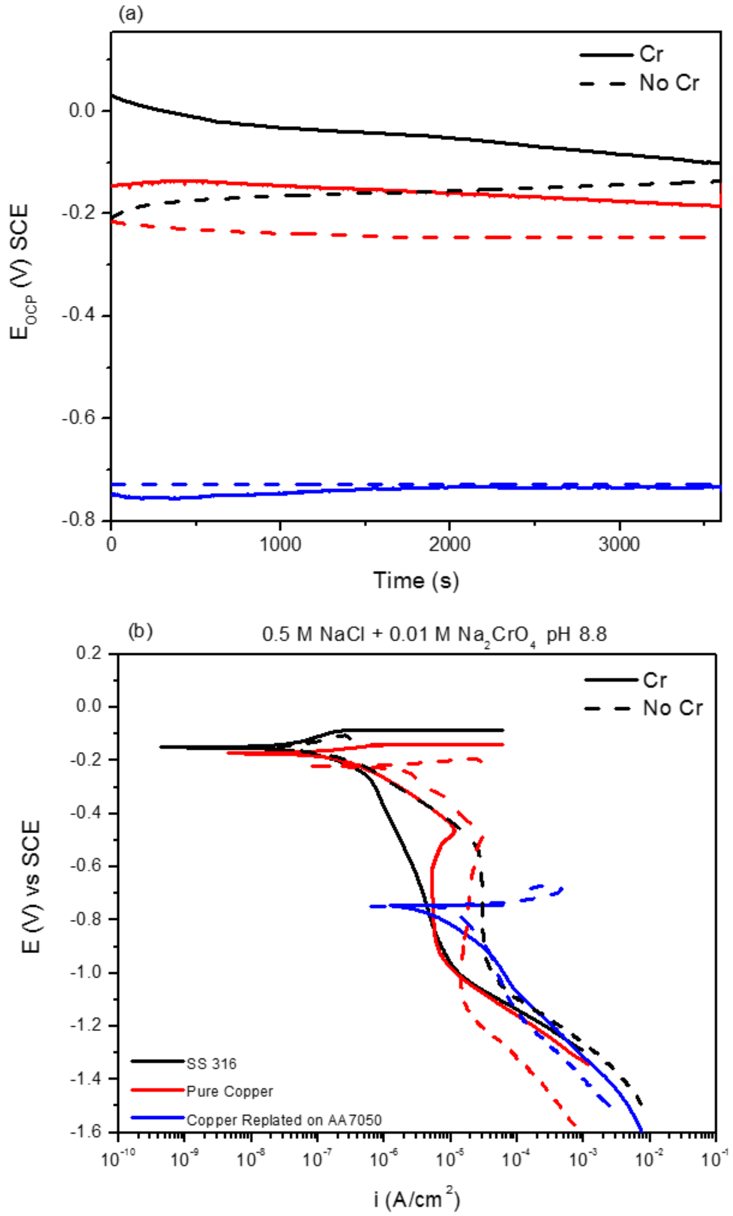

Figure 6.32. OCP over 1 h (b) cathodic potentiodynamic polarization of Type 316 stainless steel, pure Cu and Cu-replated on AA7050-T7451n 0.5 M NaCl + 0.01 M Na_2CrO_4 pH at pH 8.8 (solid lines) and inhibitor-free 0.5 M NaCl at pH 5.5 (dashed lines).

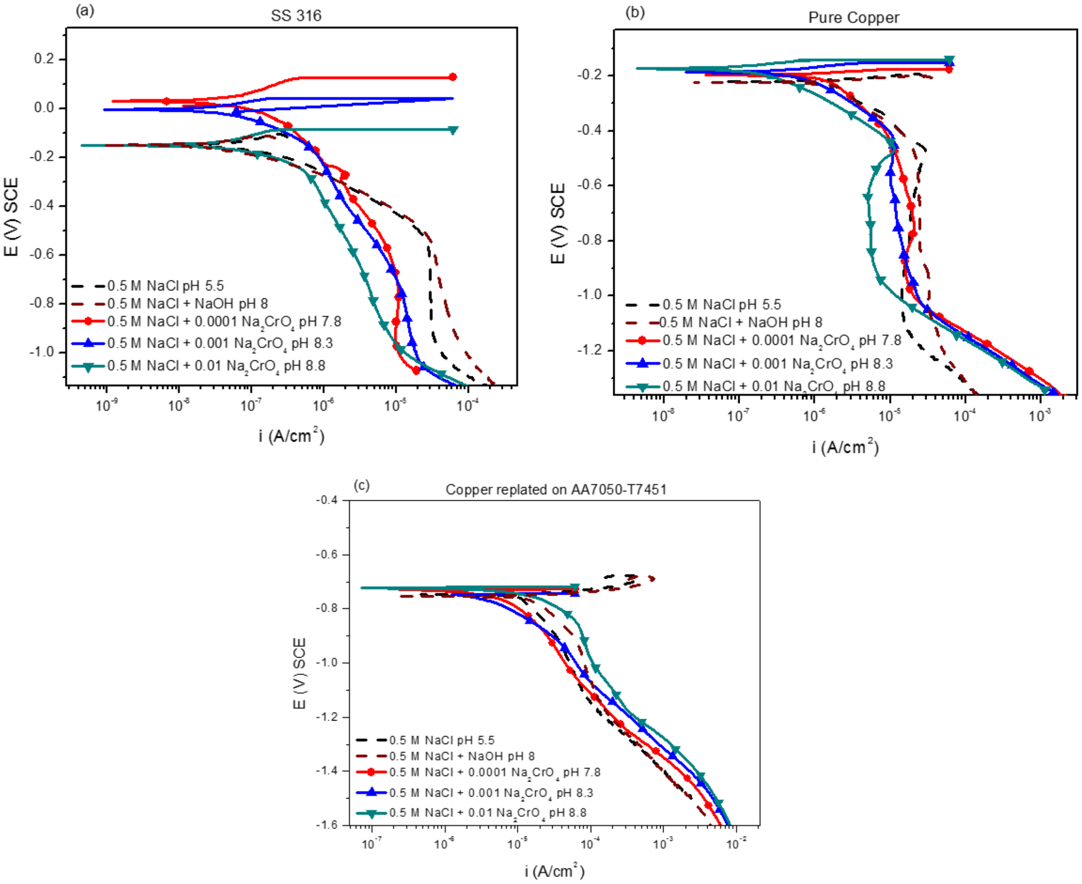

Figure 6.33. Cathodic potentiodynamic polarization in inhibitor-free 0.5 M NaCl at pH 5.5 0.5 M NaCl + NaOH at pH8, 0.5 M NaCl + 0.0001 Na_2CrO_4 at pH 7.8 , 0.5 M NaCl + 0.001 Na_2CrO_4 at pH 8.3 and 0.5 M NaCl + 0.01 Na_2CrO_4 at pH 8.8 on (a) Type 316 stainless steel (b) pure Cu and (c) Cu-replated on AA7050-T7451.

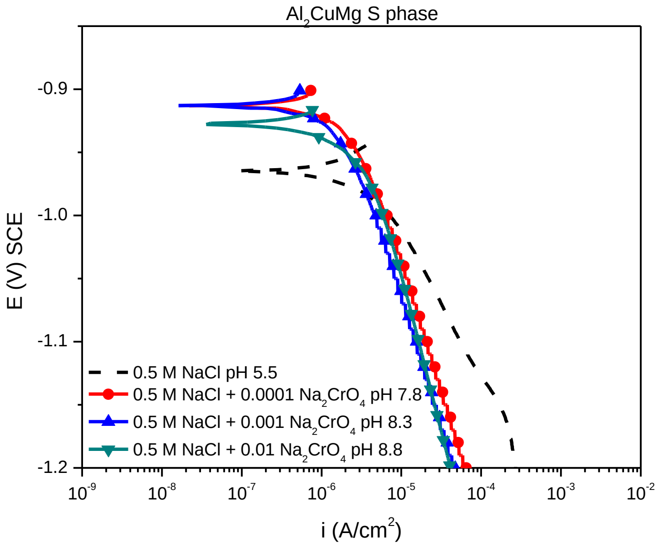

Figure 6.34. Cathodic potentiodynamic polarization in inhibitor-free 0.5 M NaCl at pH 5.5, 0.5 M NaCl + NaOH at pH 8, 0.5 M NaCl + NaOH at pH 8, 0.5 M NaCl + 0.0001 Na_2CrO_4 at pH 7.8 , 0.5 M NaCl + 0.001 Na_2CrO_4 at pH 8.3 and 0.5 M NaCl + 0.01 Na_2CrO_4 at pH 8.8 on *S* phsae (Al_2CuMg).

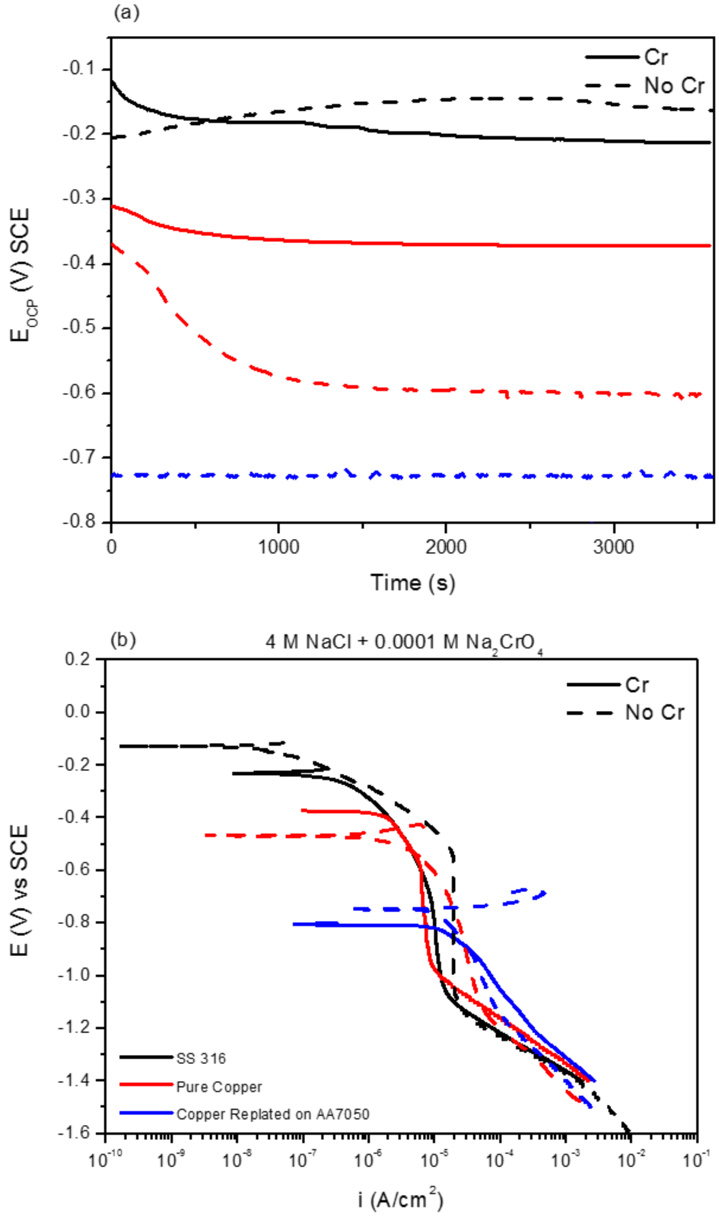

Figure 6.35. (a) OCP over 1 h (b) cathodic potentiodynamic polarization of Type 316 stainless steel, pure Cu and Cu-replated on AA7050-T7451 in 4 M NaCl + 0.0001 M Na_2CrO_4 pH at pH 7.8 (solid lines) and inhibitor0free 4 M NaCl at pH 5.5 (dashed lines).

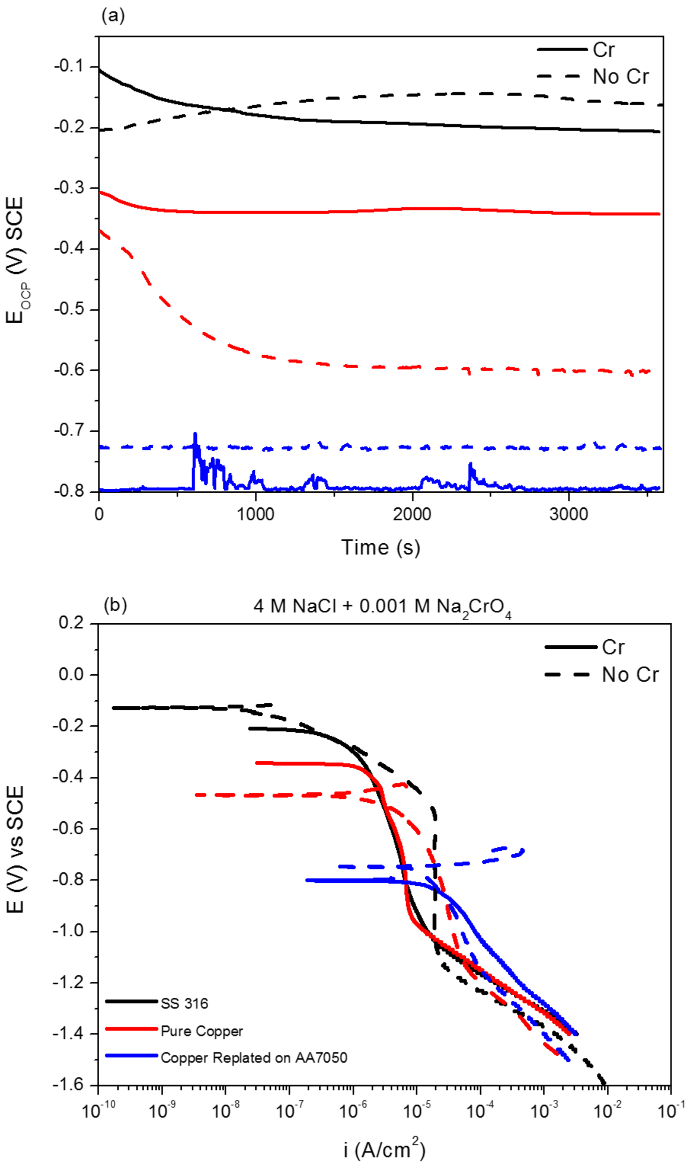

Figure 6.36. (a) OCP over 1 h (b) cathodic potentiodynamic polarization of Type 316 stainless steel, pure Cu and Cu-replated on AA7050-T7451 in 4 M NaCl + 0.001 M Na_2CrO_4 pH at pH 8.3 (solid lines) and inhibitor-free 4 M NaCl at pH 5.5 (dashed lines).

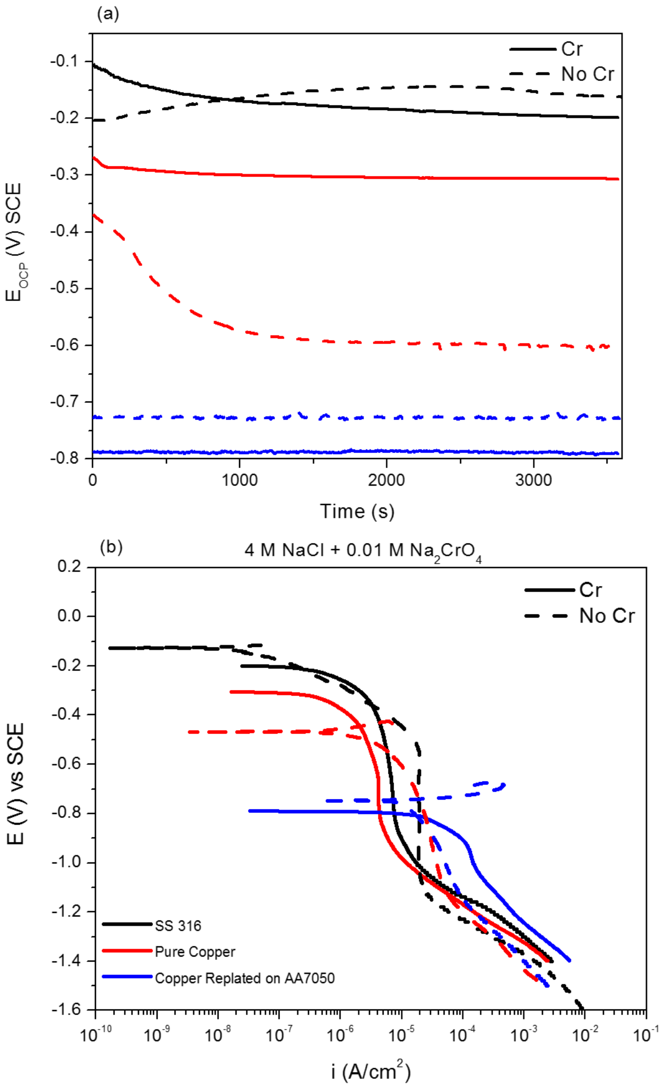

Figure 6.37. OCP over 1 h (b) cathodic potentiodynamic polarization of Type 316 stainless steel, pure Cu and Cu-replated on AA7050-T7451 on 4 M NaCl + 0.01 M Na_2CrO_4 pH at pH 8.8 (solid lines) and inhibitor-free 4 M NaCl at pH 5.5 (dashed lines).

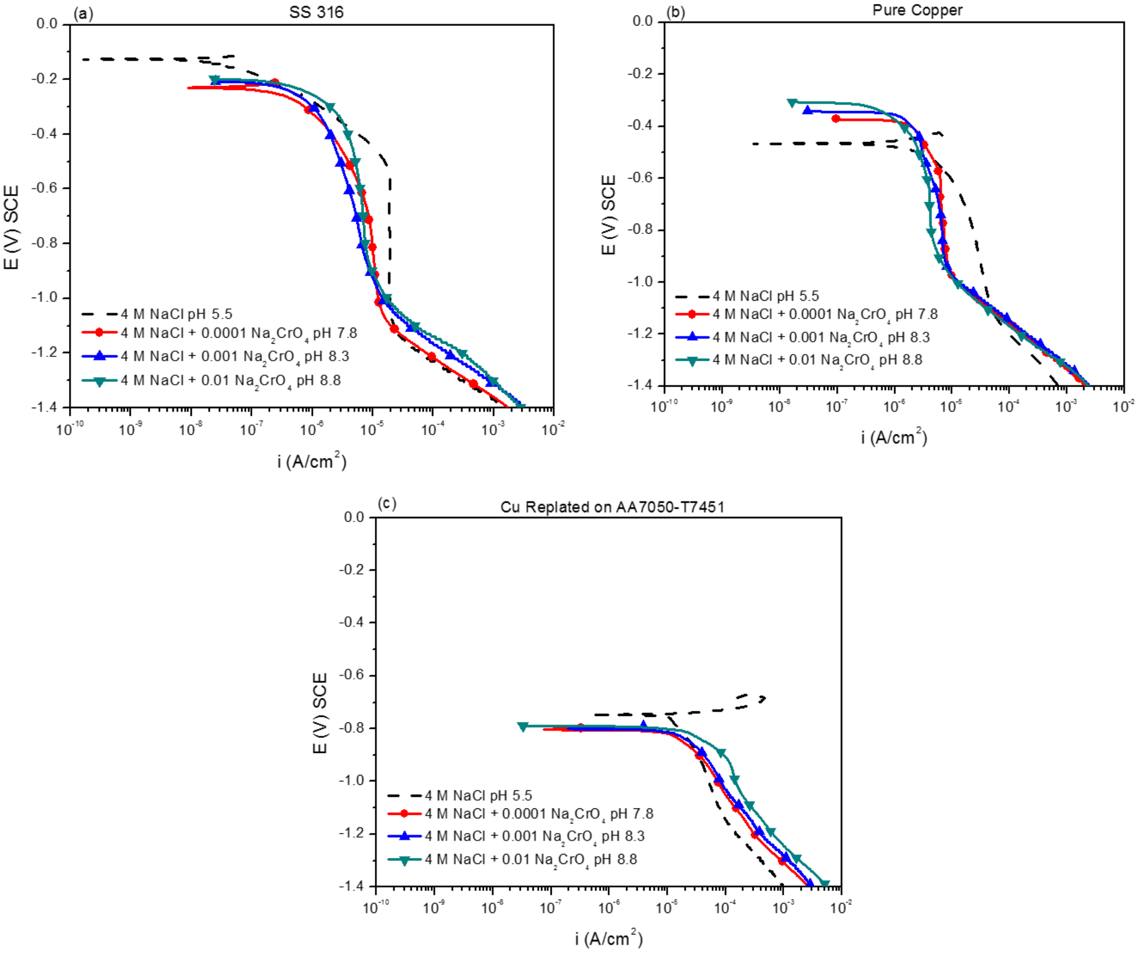

Figure 6.38. Cathodic potentiodynamic polarization in inhibitor-free 4 M NaCl at pH 5.5, 4 M NaCl + 0.0001 Na_2CrO_4 at pH 7.8 , 4 M NaCl + 0.001 Na_2CrO_4 at pH 8.3 and 4 M NaCl + 0.01 Na_2CrO_4 at pH 8.8 on (a) Type 316 stainless steel (b) pure Cu and (c) Cu-replated on AA7050-T7451.

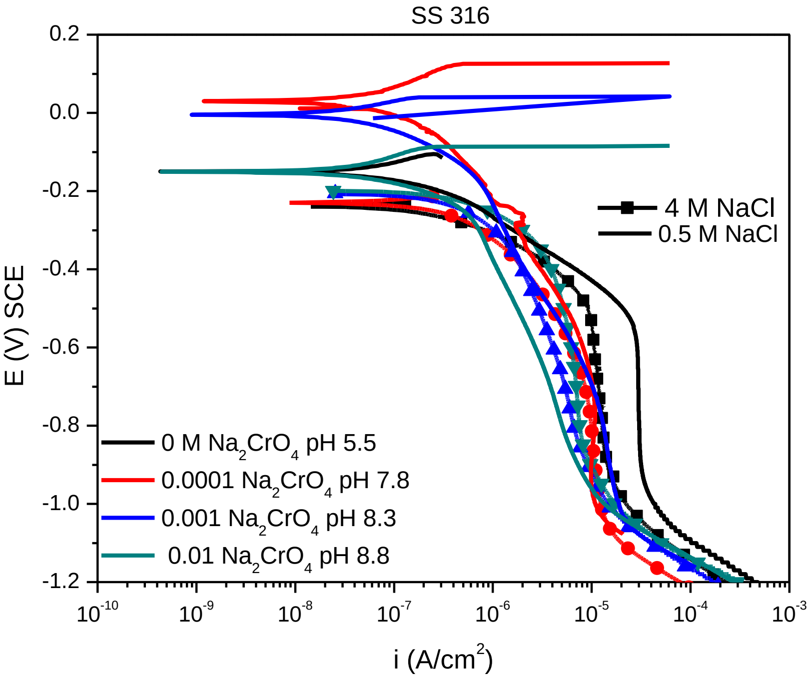

Figure 6.39. Cathodic potentiodynamic polarization on Type 316 stainless steel in 0.5 M NaCl and 4 M NaCl with additions of 0.0001, 0.001 and 0.01 M Na_2CrO_4.

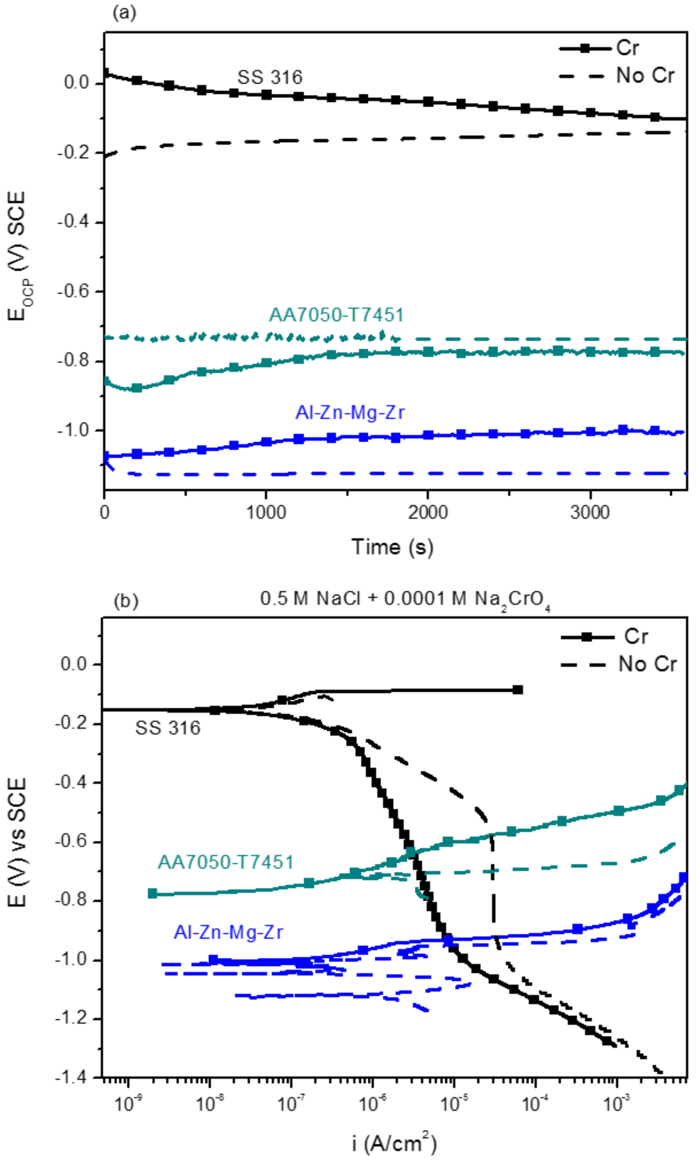

Figure 6.40. (a) OCP over 1 h (b) anodic potentiodynamic polarization of AA7050-T7451 and Al-Zn-Mg-Zr with cathodic polarization on Type 316 stainless steel in 0.5 M NaCl + 0.0001 M Na_2CrO_4 at pH 7.8 (solid lines) and inhibitor-free 0.5 M NaCl at pH 5.5 (dashed lines).

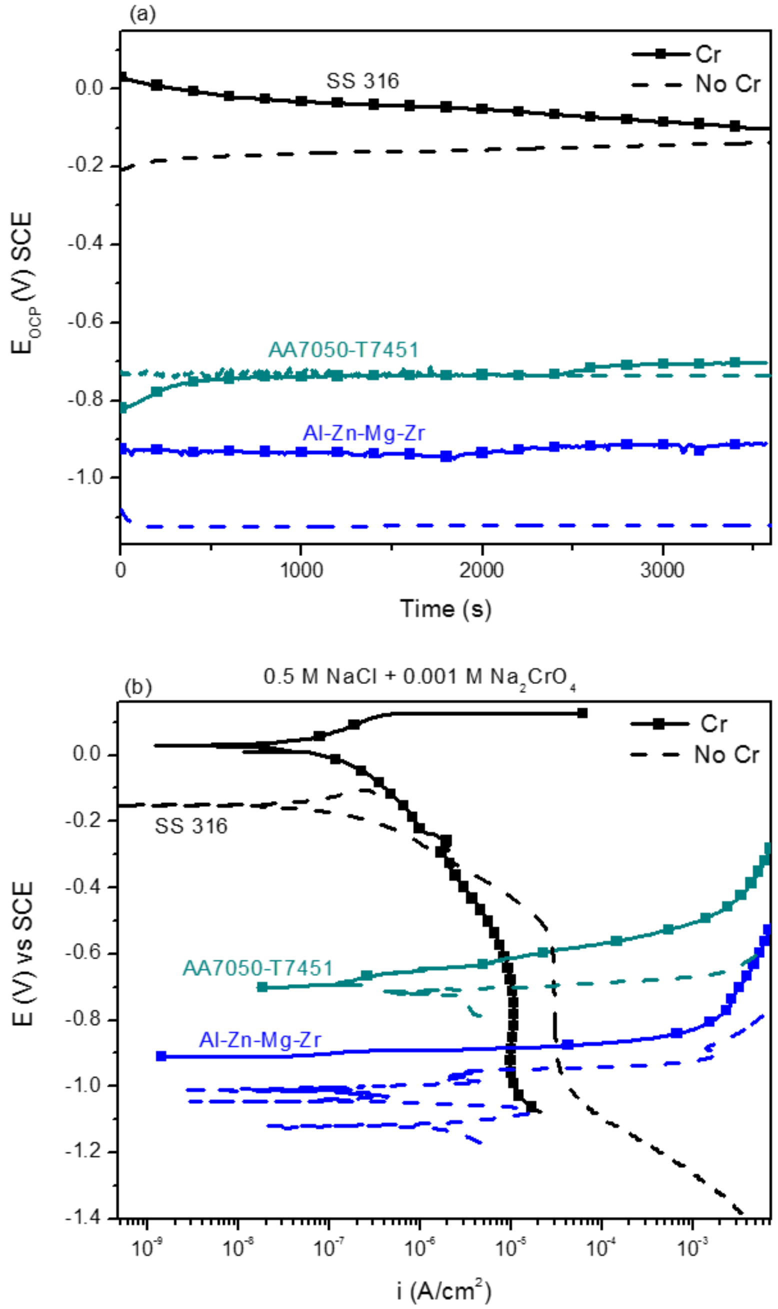

Figure 6.41. (a) OCP over 1 h (b) anodic potentiodynamic polarization of AA7050-T7451 and Al-Zn-Mg-Zr with cathodic polarization on Type 316 stainless steel in 0.5 M NaCl + 0.001 M Na_2CrO_4 at pH 8.3 (solid lines) and inhibitor-free 0.5 M NaCl at pH 5.5 (dashed lines).

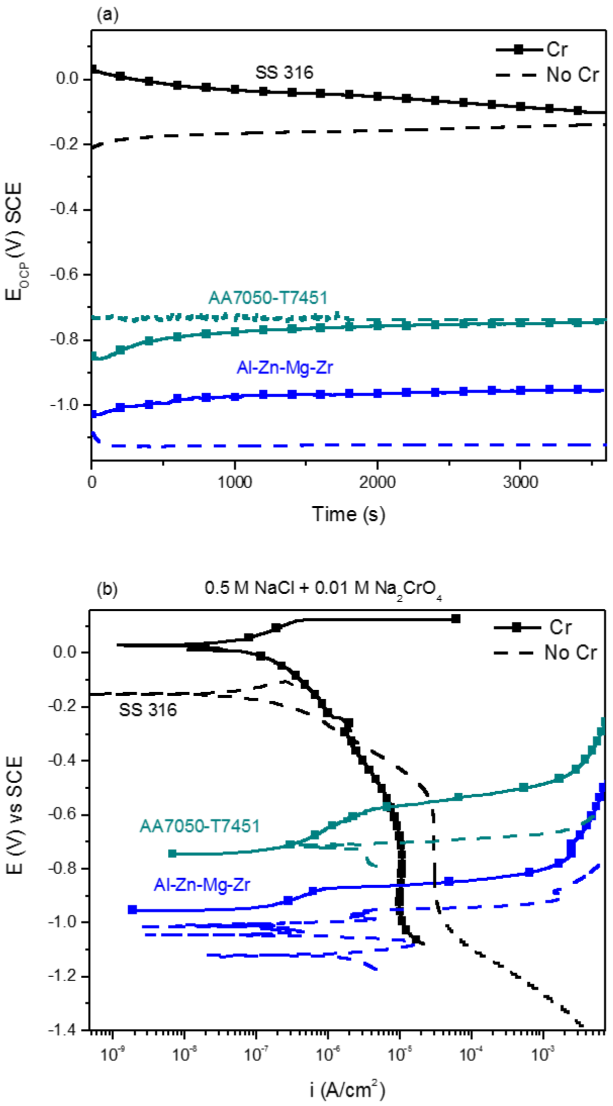

Figure 6.42. (a) OCP over 1 h (b) anodic potentiodynamic polarization of AA7050-T7451 and Al-Zn-Mg-Zr with cathodic polarization on Type 316 stainless steel in 0.5 M NaCl + 0.01 M Na_2CrO_4 at pH 8.8 (solid lines) and inhibitor-free 0.5 M NaCl at pH 5.5 (dashed lines).

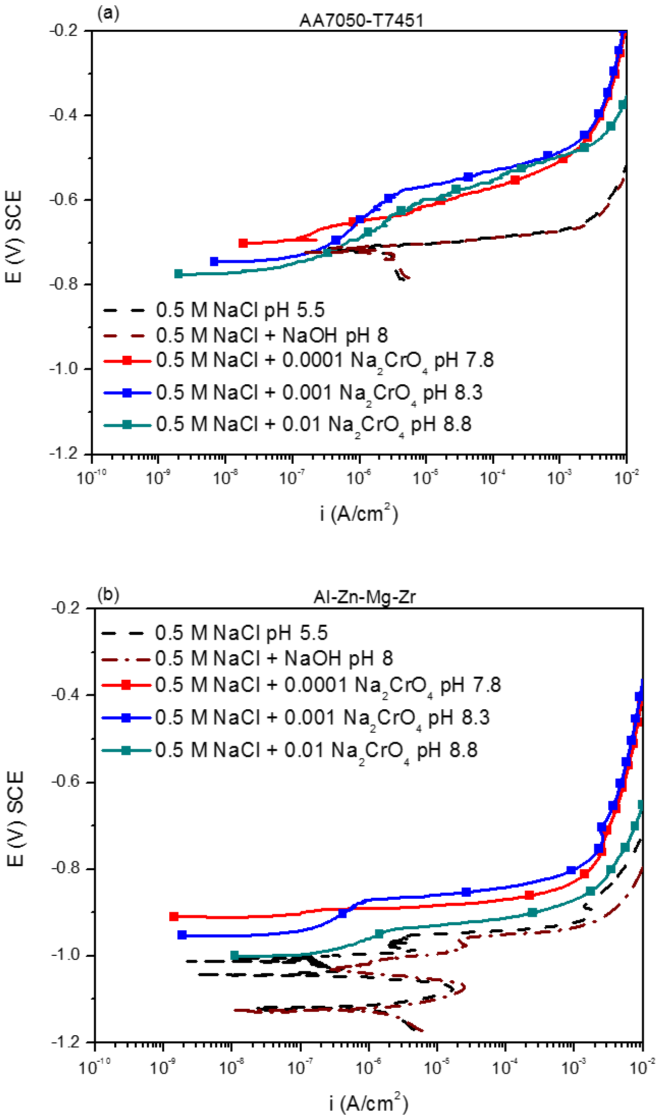

Figure 6.43. Anodic potentiodynamic polarization in inhibitor-free 0.5 M NaCl M NaCl at pH 5.5 and 0.5 M NaCl + NaOH at pH 8 compared to chromate-containing 0.5 M NaCl + 0.0001 Na_2CrO_4 at pH 7.8 , 0.5 M NaCl + 0.001 Na_2CrO_4 at pH 8.3, and 0.5 M NaCl + 0.01 Na_2CrO_4 at pH 8.8 on (a) AA7050-T7451 and (b) Al-Zn-Mg-Zr.

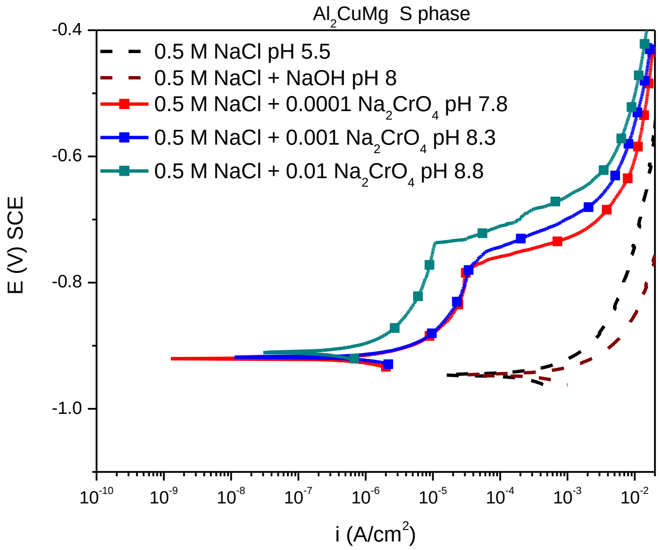

Figure 6.44. Anodic potentiodynamic polarization of Al_2CuMg S phase in 0.5 M NaCl pH 5, 0.5 M NaCl + NaOH at pH8, 0.5 M NaCl + 0.0001 M Na_2CrO_4 at pH 7.8, 0.5 M NaCl + 0.001 M Na_2CrO_4 at pH 8.3, and 0.5 M NaCl + 0.01 M Na_2CrO_4 at pH 8.8

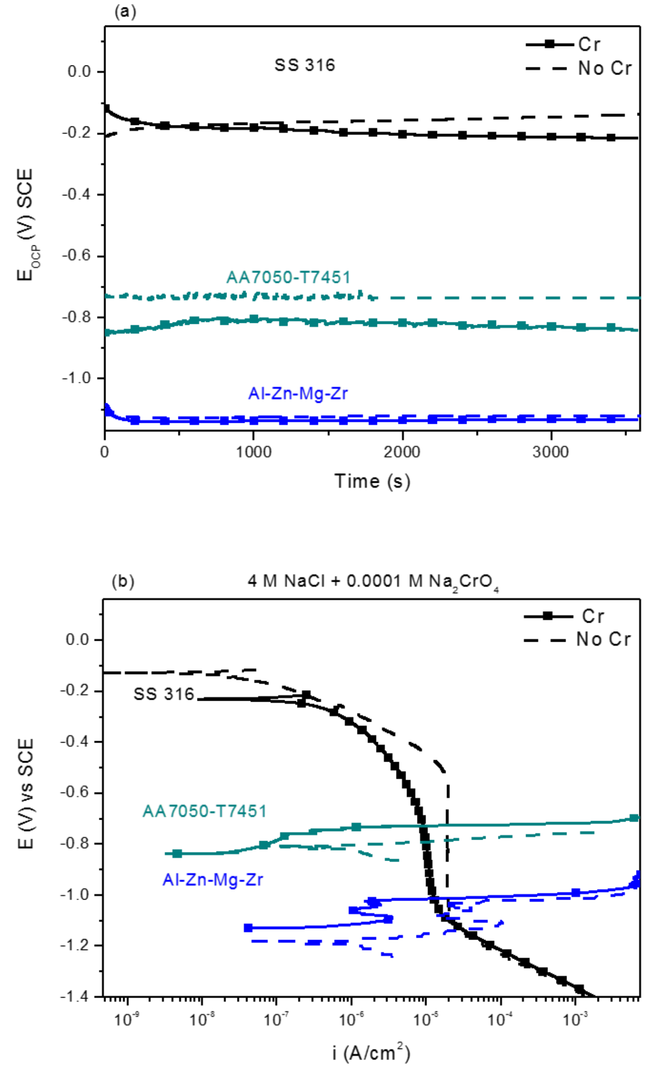

Figure 6.45. (a) OCP over 1 h (b) anodic potentiodynamic polarization of AA7050-T7451 and Al-Zn-Mg-Zr with cathodic polarization on Type 316 stainless steel in 4 M NaCl + 0.0001 M Na_2CrO_4 at pH 7.8 (solid lines) and inhibitor-free 4 M NaCl at pH 5.5 (dashed lines).

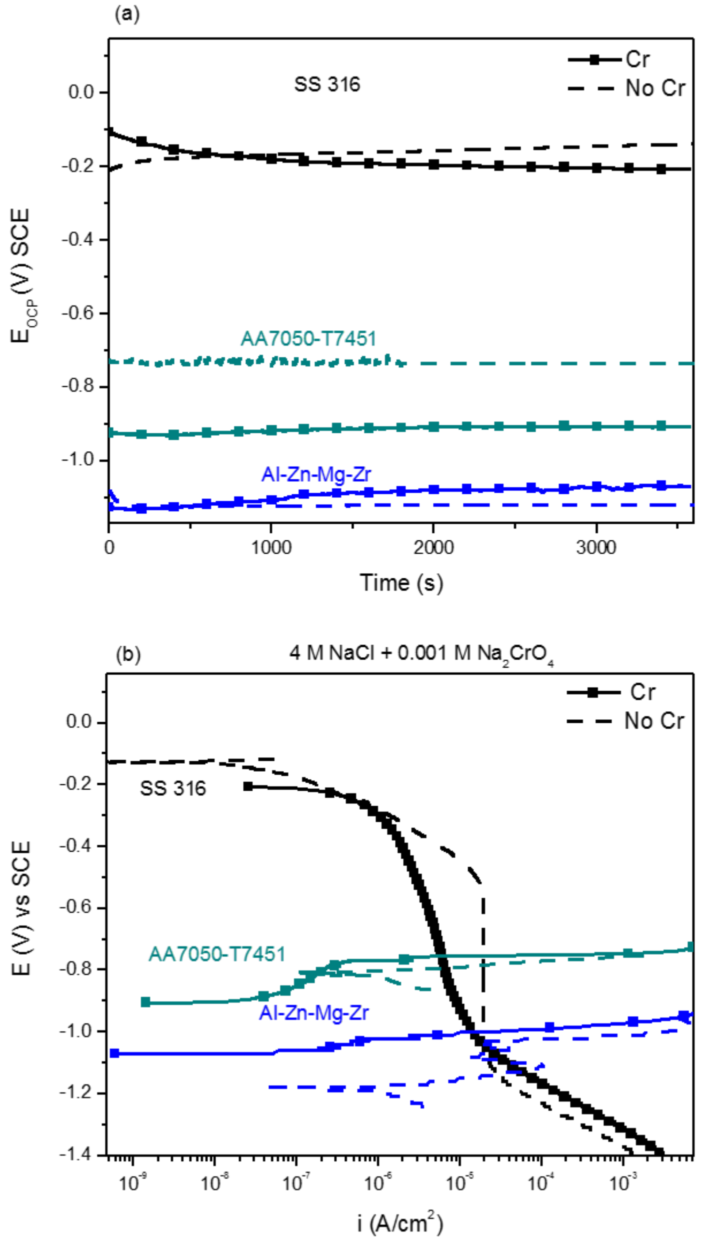

Figure 6.46. (a) OCP over 1 h (b) anodic potentiodynamic polarization of AA7050-T7451 and Al-Zn-Mg-Zr with cathodic polarization on Type 316 stainless steel in 4 M NaCl + 0.001 M Na_2CrO_4 at pH 8.3 (solid lines) and inhibitor-free 4 M NaCl at pH 5.5 (dashed lines).

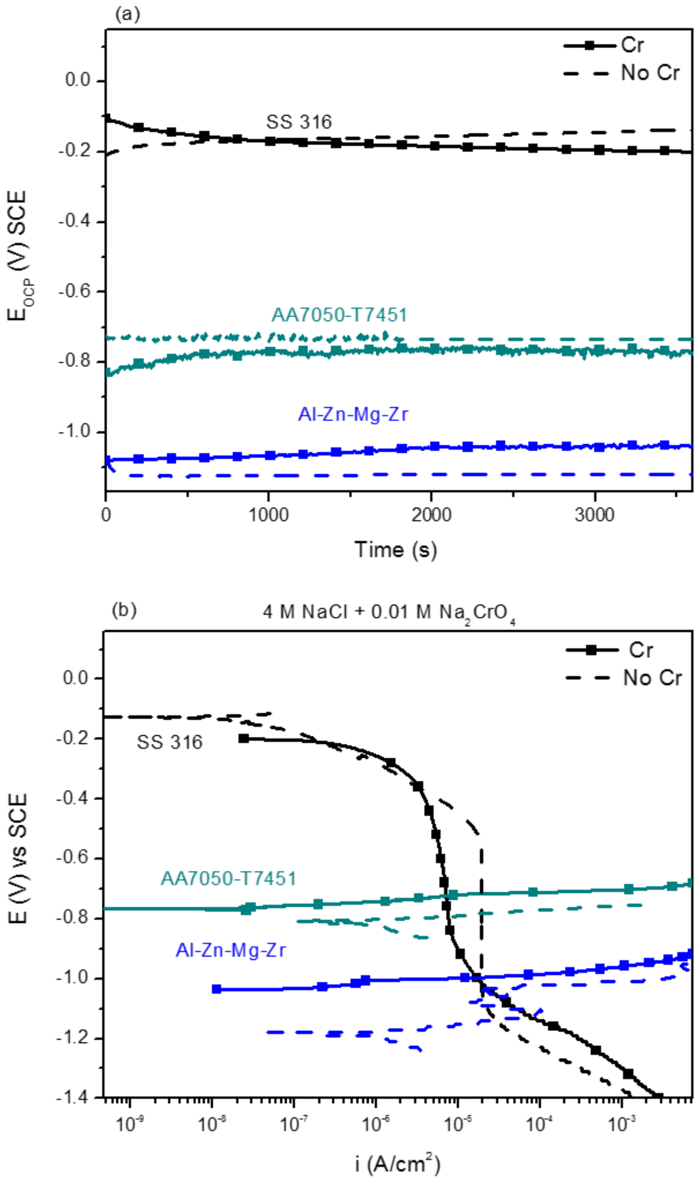

Figure 6.47. (a) OCP over 1 h (b) anodic potentiodynamic polarization of AA7050-T7451 and Al-Zn-Mg-Zr with cathodic polarization on Type 316 stainless steel in 4 M NaCl + 0.01 M Na_2CrO_4 at pH 8.8 (solid lines) and inhibitor-free 4 M NaCl at pH 5.5 (dashed lines).

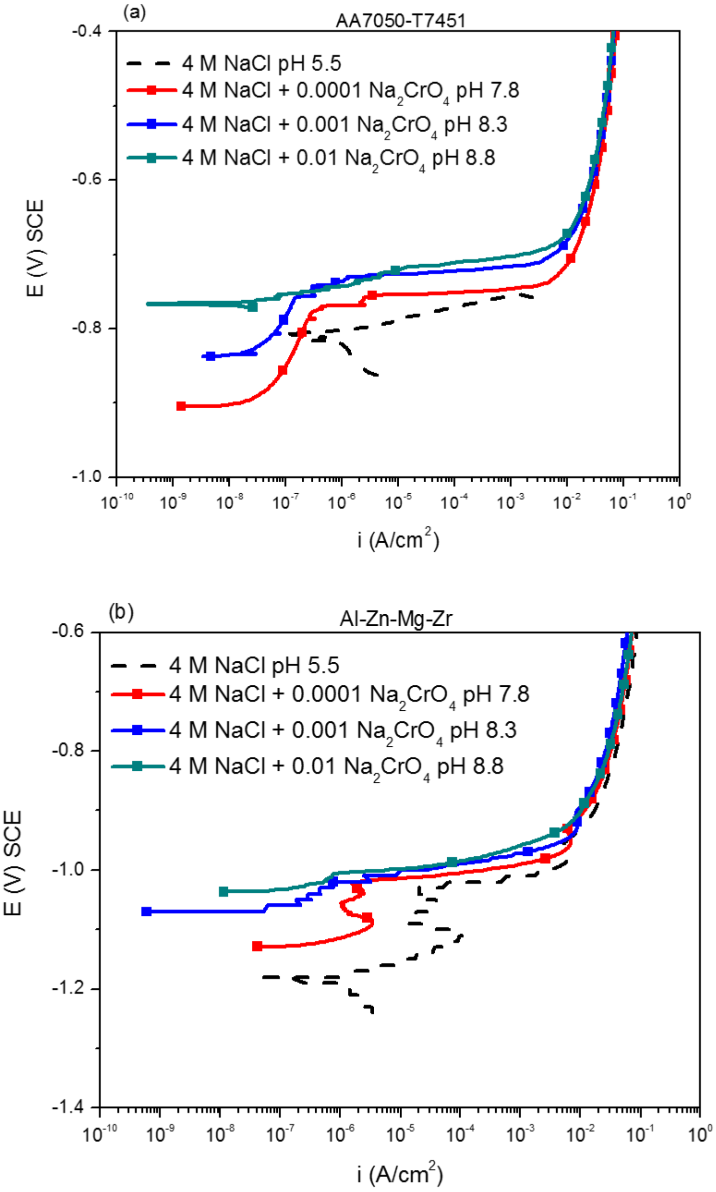

Figure 6.48. Anodic potentiodynamic polarization in inhibitor-free 4 M NaCl M NaCl at pH 5.5, 4 M NaCl + 0.0001 Na_2CrO_4 at pH 7.8 , 4 M NaCl + 0.001 Na_2CrO_4 at pH 8.3 and 4 M NaCl + 0.01 Na_2CrO_4 at pH 8.8 on (a) AA7050-T7451 and (b) Al-Zn-Mg-Zr.

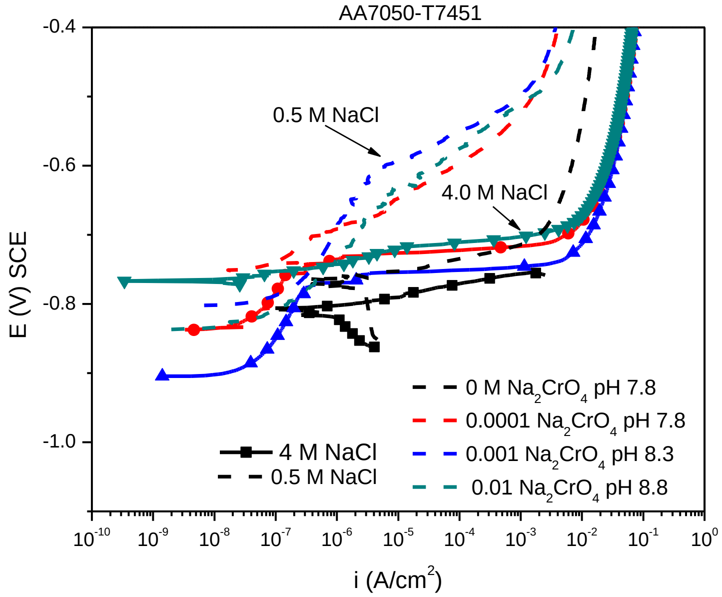

Figure 6.49. Anodic potentiodynamic polarization in AA7050-T7451 in 0.5 M NaCl and 4 M NaCl with additions of 0.0001, 0.001 and 0.01 M M Na_2CrO_4.

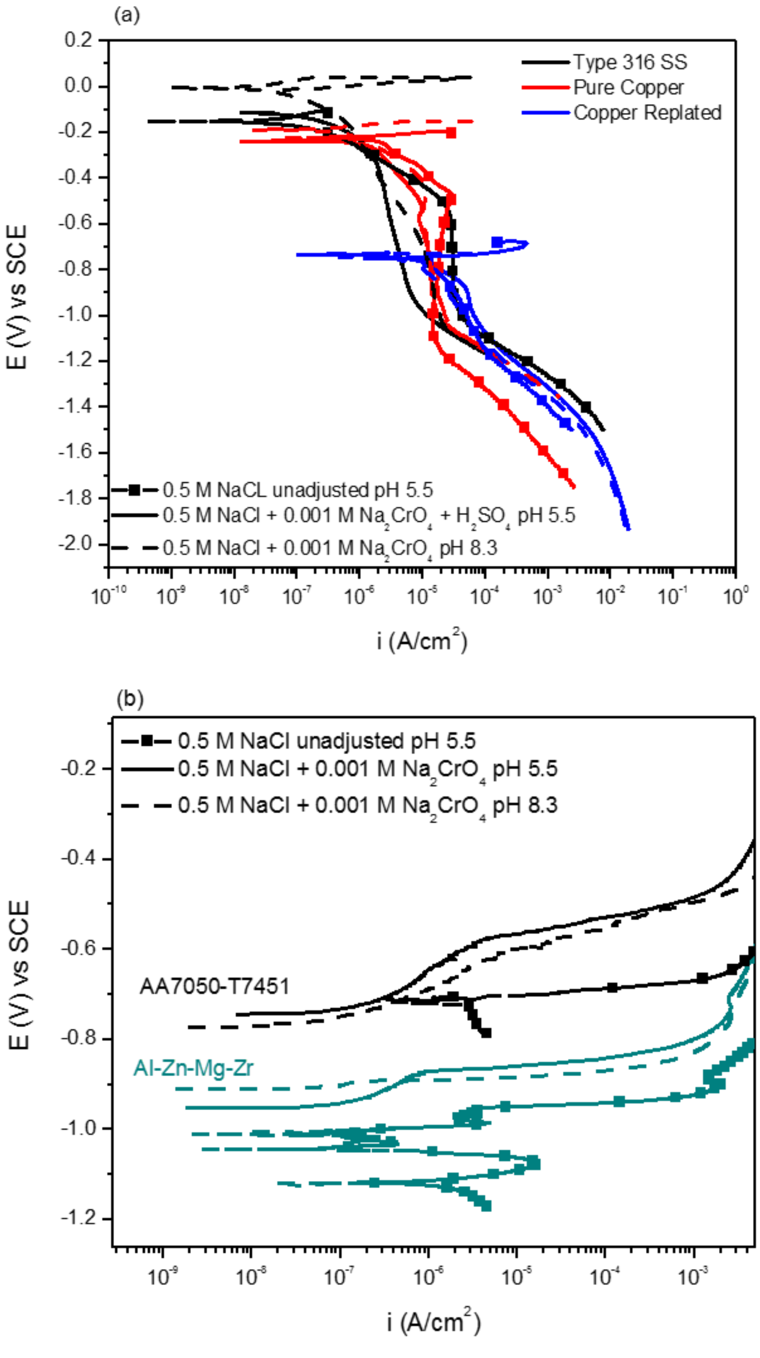

Figure 6.50. (a) cathodic potentiodynamic on Type 316 stainless steel, pure copper, Cu-replated and (b) anodic potentiodynamic polarization of AA7050-T7451 and Al-Zn-Mg-Zr in 0.5 M NaCl + 0.001 M Na_2CrO_4 + H_2SO_4 at pH 5.5 relative to 0.5 M NaCl at pH 5.5, and 0.5 M NaCl + 0.001 M Na_2CrO_4 at pH 8.3.

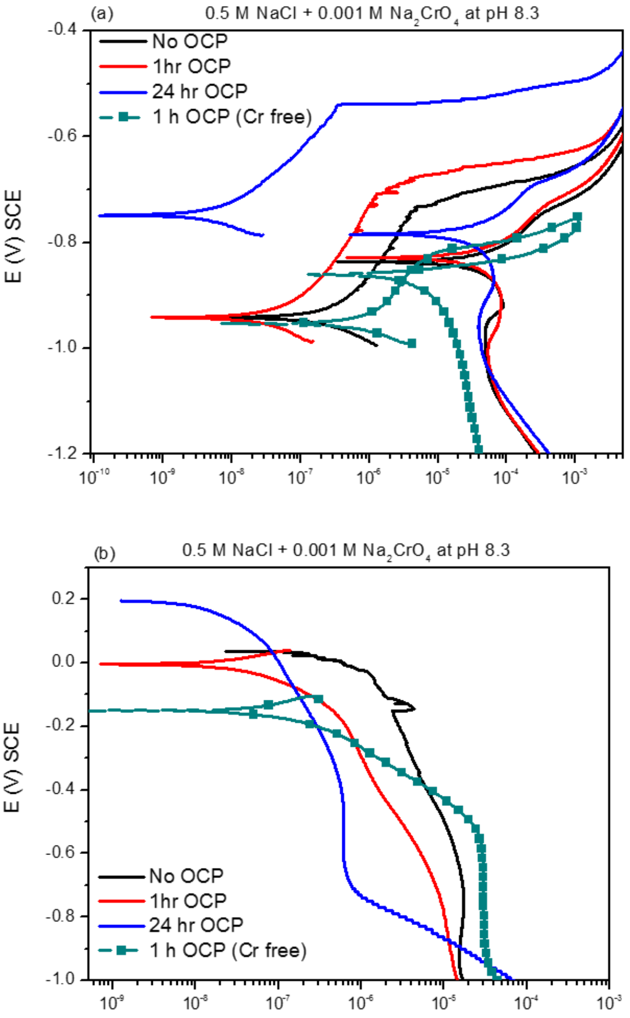

Figure 6.51. (a) Anodic cyclic and (b) cathodic potentiodynamic polarization on AA7050-T7451 in 0.5 M NaCl + 0.001 M Na_2CrO_4 at pH 8.3 after 0 h, 1 h, and 24 h at the open circuit potential prior to cyclic polarization.

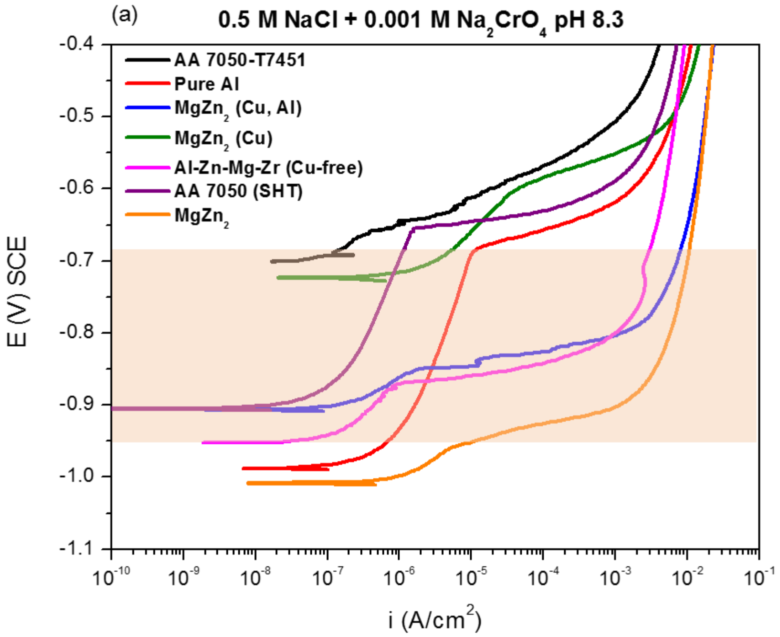

Figure 6.52. Anodic polarization scans of different phases in AA7050-T7451 including pure Al, AA7050 SHT, $MgZn_2$, $Mg(ZnCuAl)_2$ and the Cu-free Al-Zn-Mg-Zr alloy in (a) 0.5 M NaCl + 0.001 M Na_2CrO_4 at pH 8. The highlighted region show the window for IGC susceptibility, ΔE.

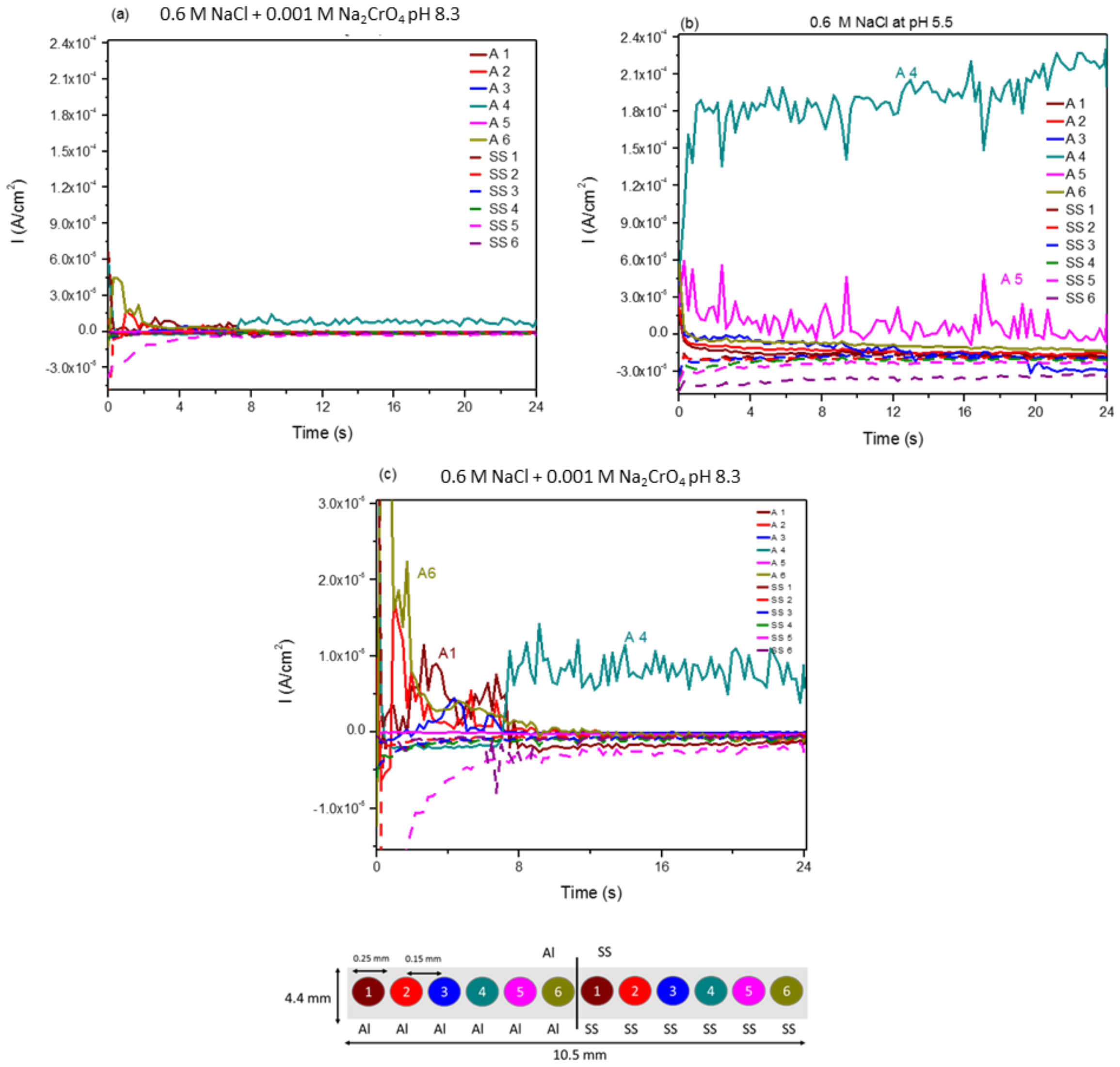

Figure 6.53. Current density over 24 h on the flat galvanic geometric CMEA where 6 AA7050 electrodes and 6 Type 316 stainless steel electrodes were embedded in an AA7050-T7451 plate and exposed under a 70 µm thin film (98% RH) of (a) 0.6 M NaCl + 0.001 M Na$_2$CrO$_4$ at pH 8.3 (b) inhibitor-free 0.6 M NaCl at pH 5.5 (c) zoomed in region of (a)

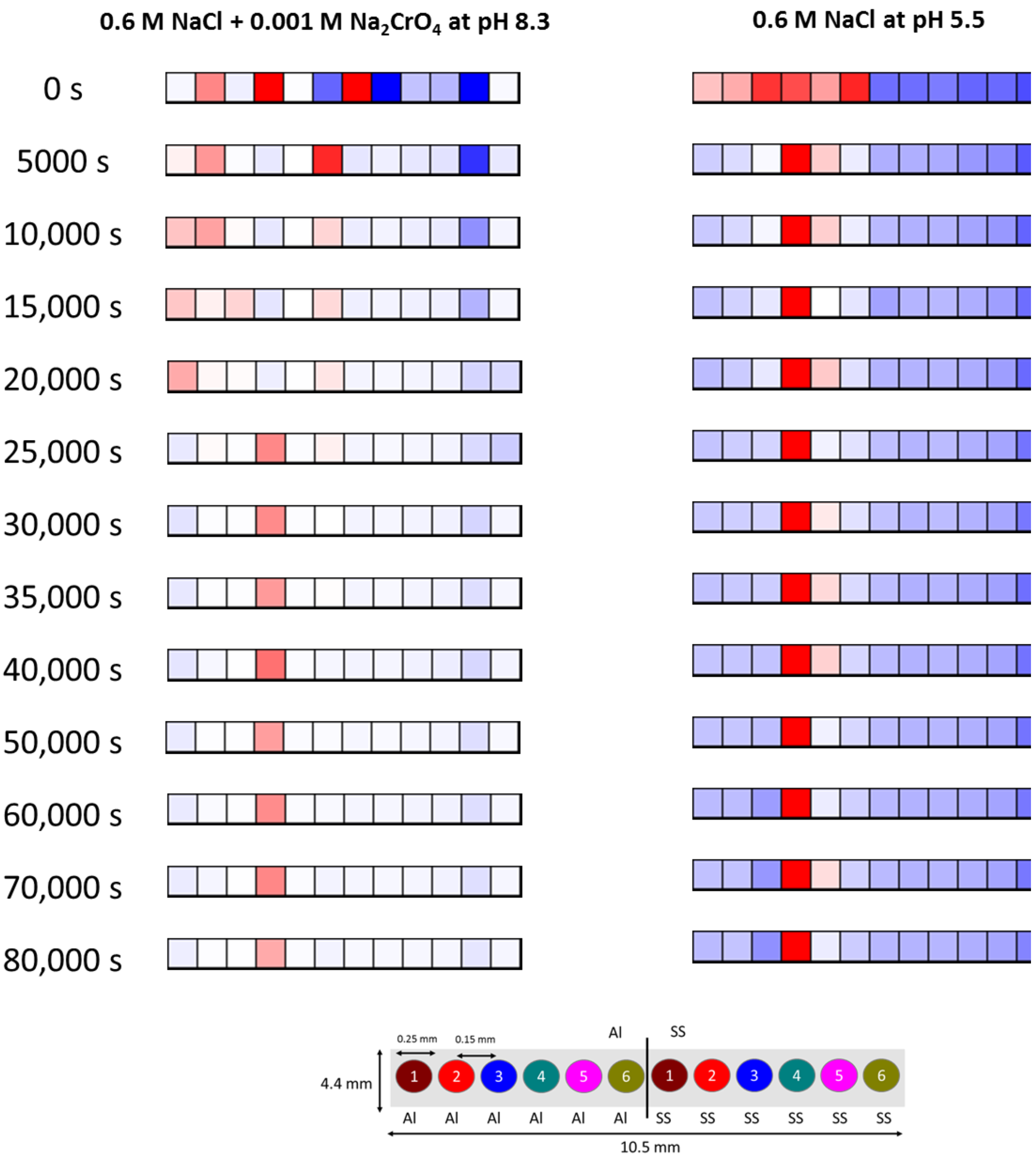

Figure 6.54. CMEA electrode color map over 24 h on the flat galvanic geometric CMEA where 6 AA7050 electrodes and 6 Type 316 stainless steel electrodes were embedded in an AA7050-T7451 plate exposed under a 70 µm thin film (98% RH) of 0.6 M NaCl + 0.001 M Na_2CrO_4 at pH 8.3 and inhibitor-free 0.6 M NaCl at pH 5.5. The red indicated positive current, blue indicates negative current and white indicates zero net current.

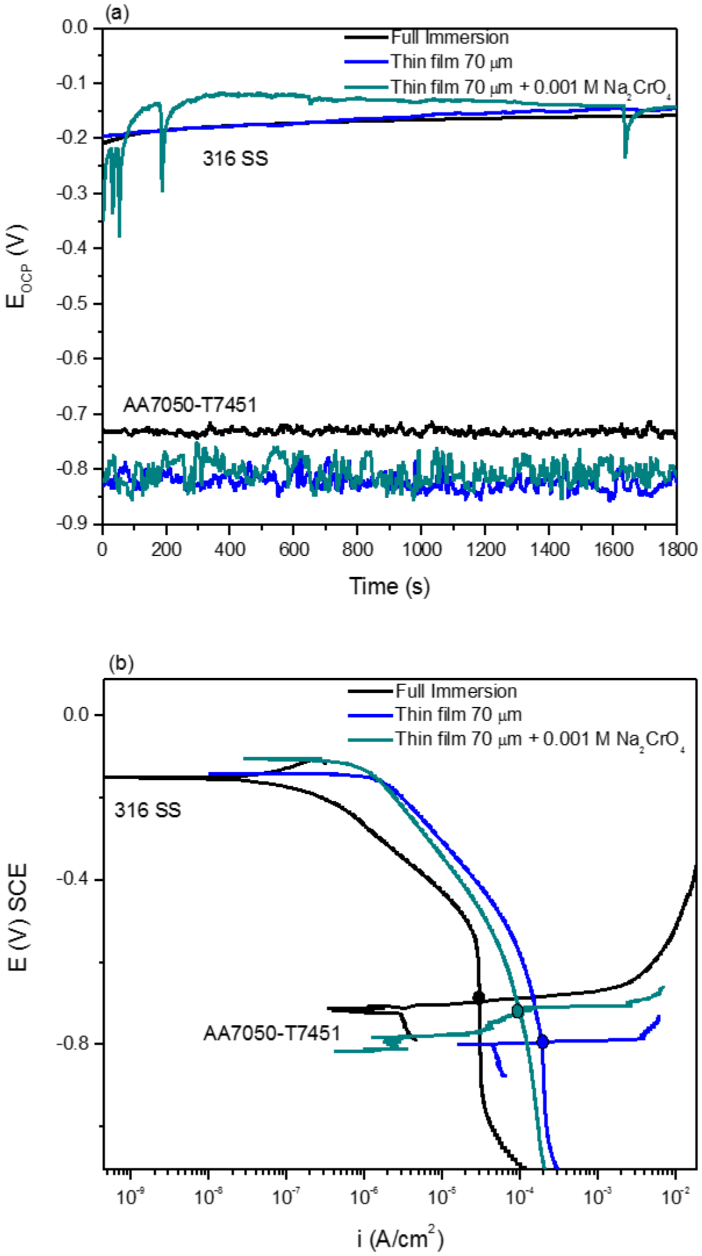

Figure 6.55. (a) OCP over 1800 s (b) cathodic and anodic potentiodynamic polarization on Type 316 stainless steel and AA7050-T7451 on a single electrode from the CMEA consisting of 10 AA7050-T7451 electrode and 10 Type 316 stainless steel electrode in 0.6 M NaCl full immersion (black), under a 70 μm thin film of 0.6 M NaCl (98% RH) and under a 70 μm thin film of 0.6 M NaCl + 0.001 M Na_2CrO_4 at (98% RH).

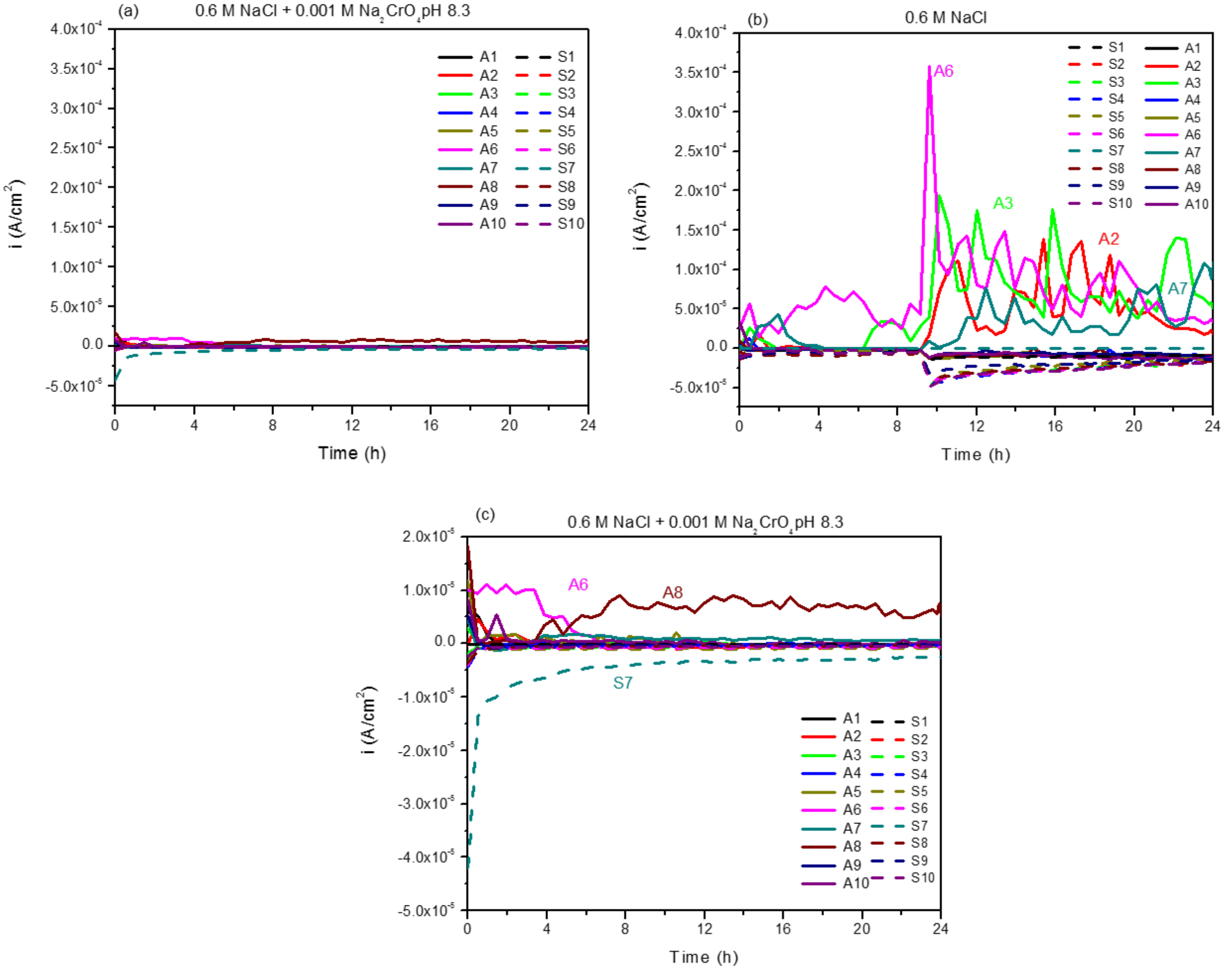

Figure 6.56. Current density over 24 h on the CMEA with a AA7050-T7451 rectangular panel with 10 AA7050-T7451 electrodes and 10 Type 316 stainless steel surrounding a sintered Ag/AgCl electrode embedded in an AA7050 panel exposed under a 70 µm thin film of (a) 0.6 M NaCl + 0.001 M Na_2CrO_4 at pH 8.3 (b) inhibitor-free 0.6 M NaCl at pH 5.5 (c) zoomed in region of (a).

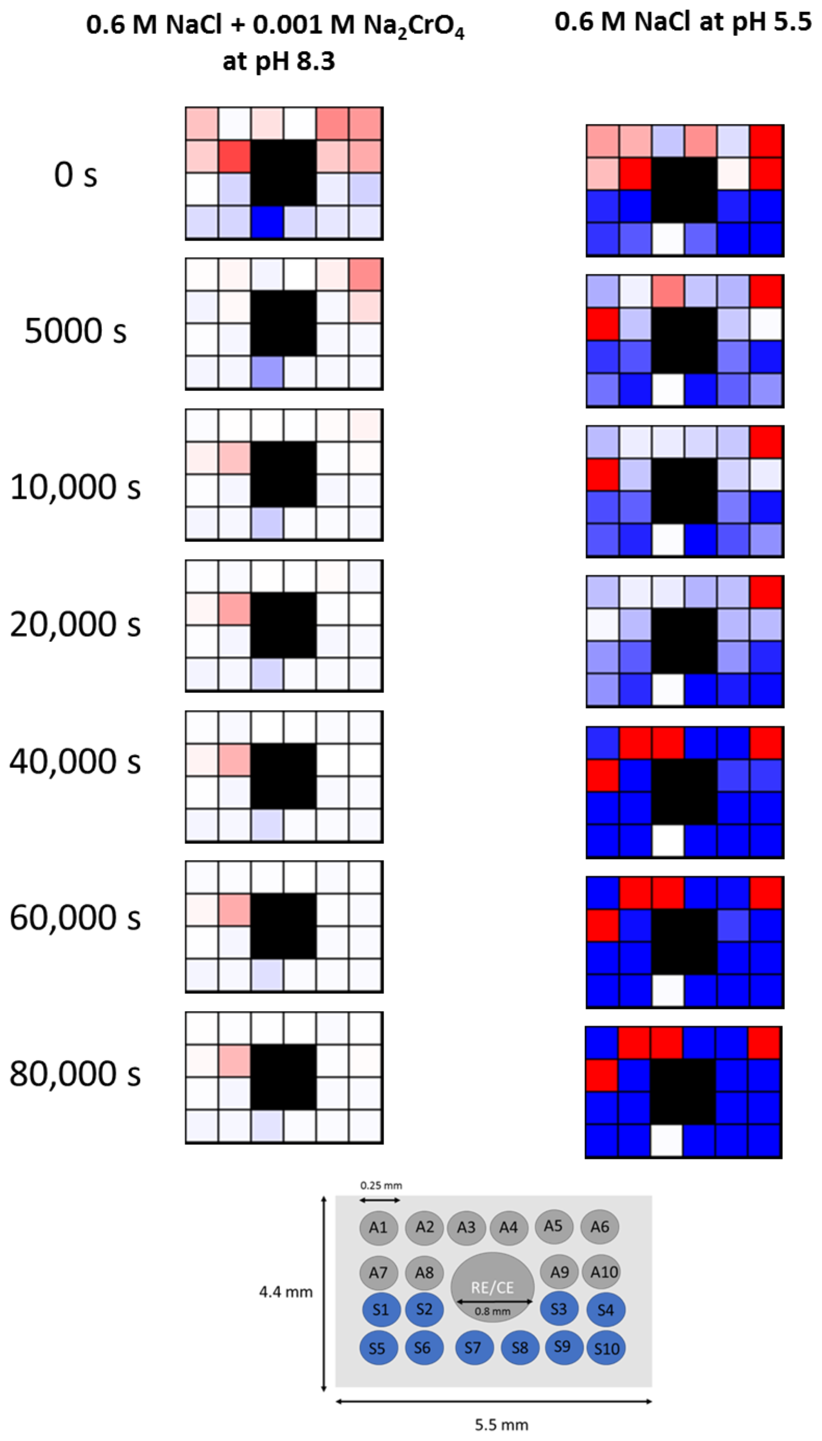

Figure 6.57. CMEA electrode color map over 24 h on the CMEA with a AA7050-T7451 rectangular panel with 10 AA7050-T7451 electrodes and 10 Type 316 stainless steel surrounding a sintered Ag/AgCl electrode embedded in an AA7050 panel exposed under a 70 μm thin film plate of 0.6 M NaCl + 0.001 M Na2CrO4 at pH 8.3 and inhibitor-free 0.6 M NaCl at pH 5.5. The red indicated positive current, blue indicates negative current and white indicates zero net current.

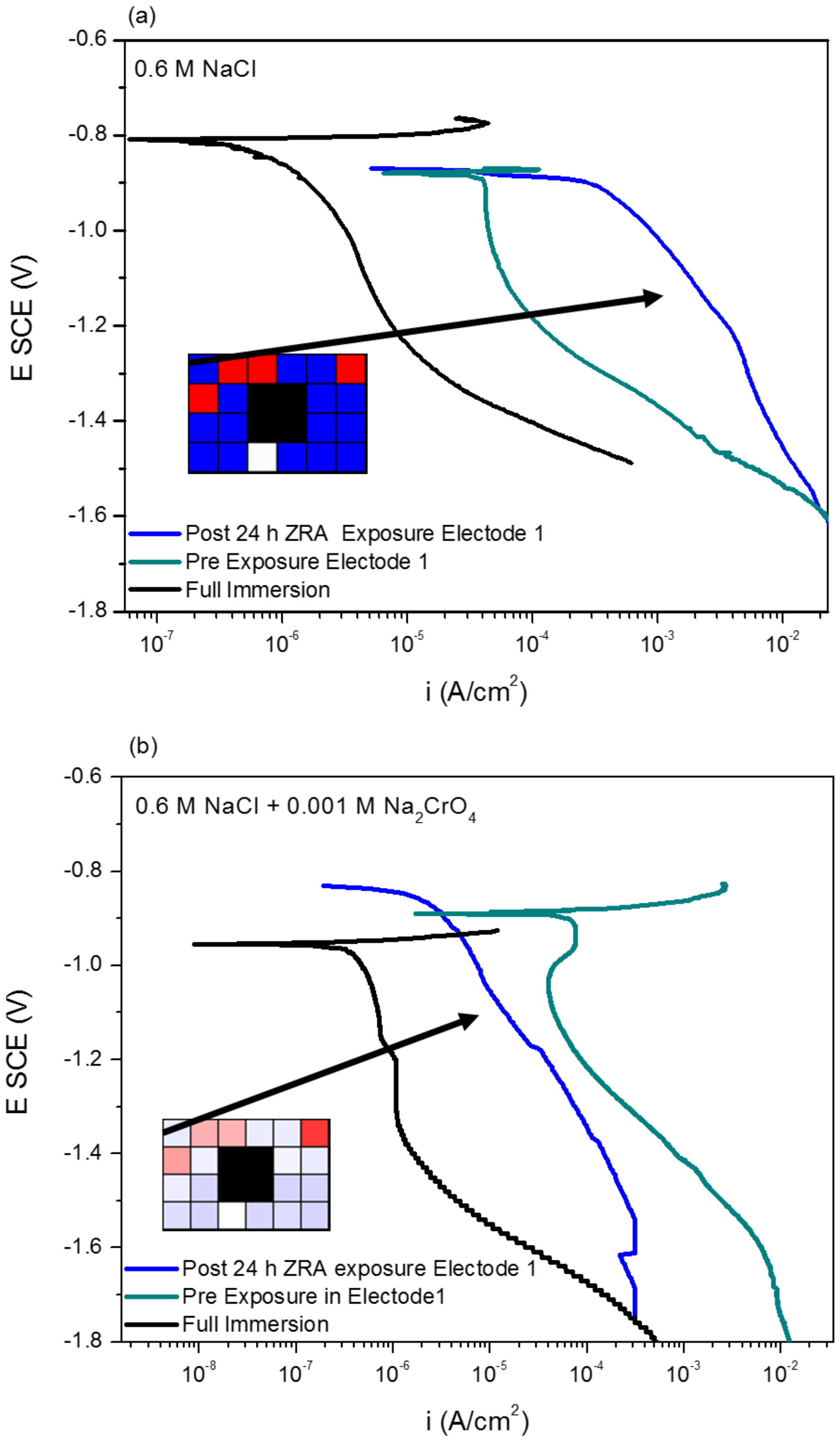

Figure 6.58. Cathodic polarization on CMEA of AA7050-T7451 and Type 316 stainless steel after 24 h ZRA thin film (70 µm) exposure in (a) 0.6 M NaCl and (b) 0.6 M NaCl + 0.001Na$_2$CrO$_4$. The blue indicates the cathodic scan after the exposure, the dark green line indicates a cathodic scan before the exposure and the black indicates a full immersion exposure.

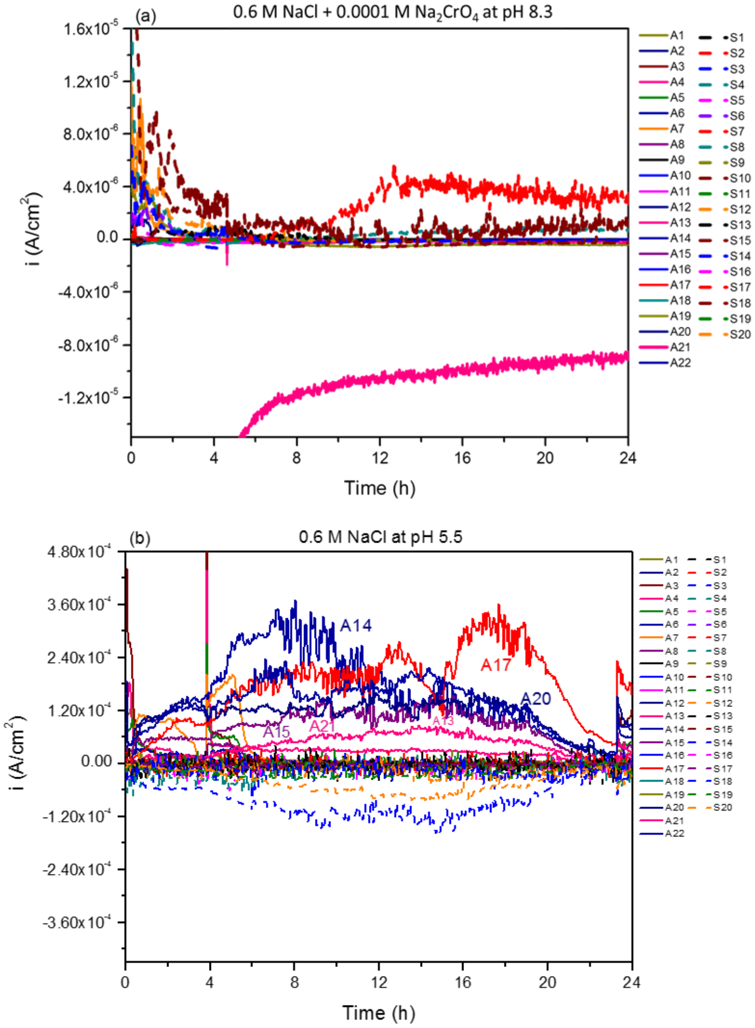

Figure 6.59. Current density over 24 h CMEA arranged in a fastener geometry with 22 AA7050-T7451 electrodes and 20 Type 316 stainless exposed under a 70 µm thin film of (a) 0.6 M NaCl + 0.001 M Na$_2$CrO$_4$ at pH 8.3 and (b) inhibitor-free 0.6 M NaCl at pH 5.5.

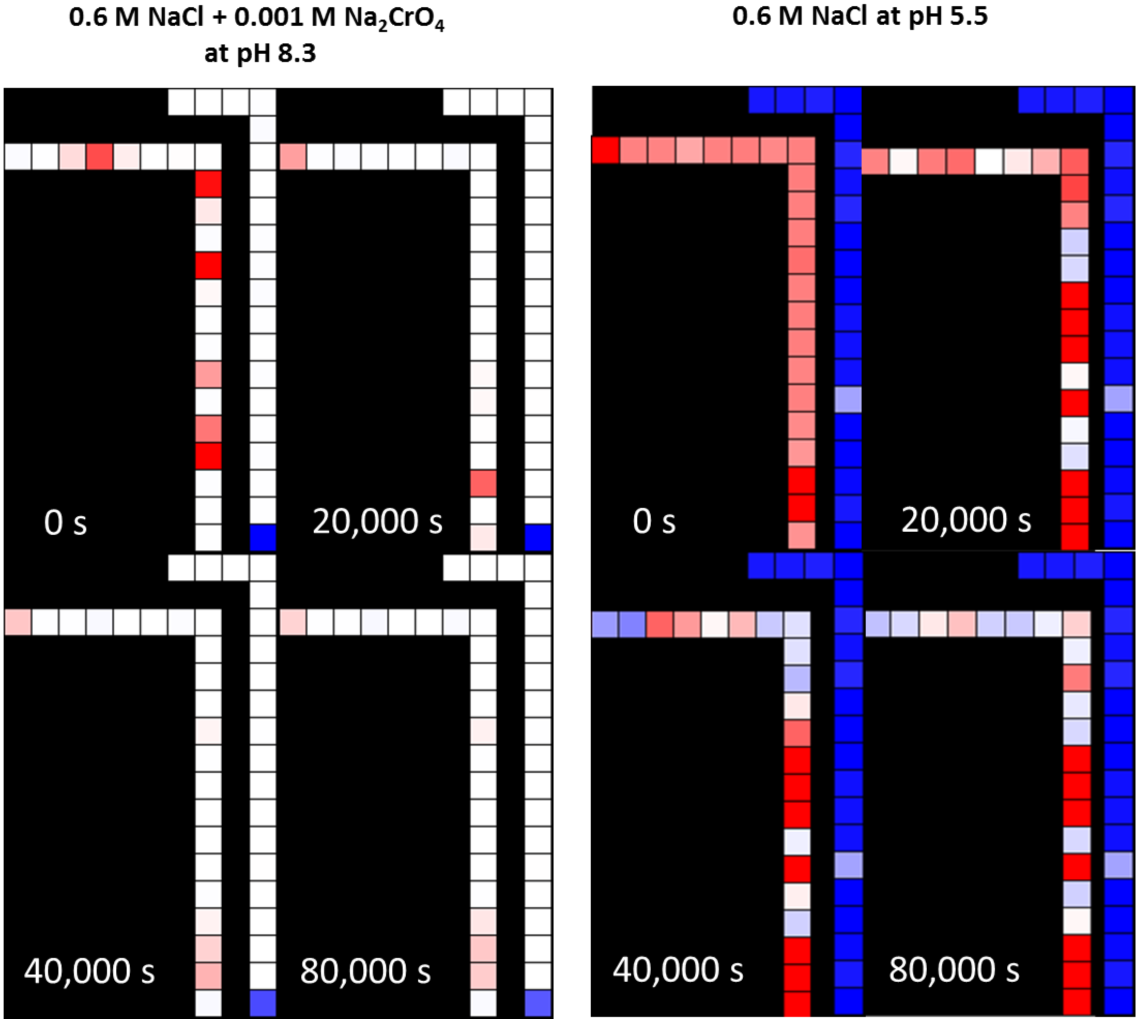

Figure 6.60. CMEA electrode color map over 24 h on the CMEA arranged in fastener geometry with 22 AA7050-T7451 electrodes and 20 Type 316 stainless exposed under a 70 µm thin film of 0.6 M NaCl + 0.001 M Na_2CrO_4 at pH 8.3 and inhibitor-free 0.6 M NaCl at pH 5.5. The red indicated positive current, blue indicates negative current and white indicates zero net current.

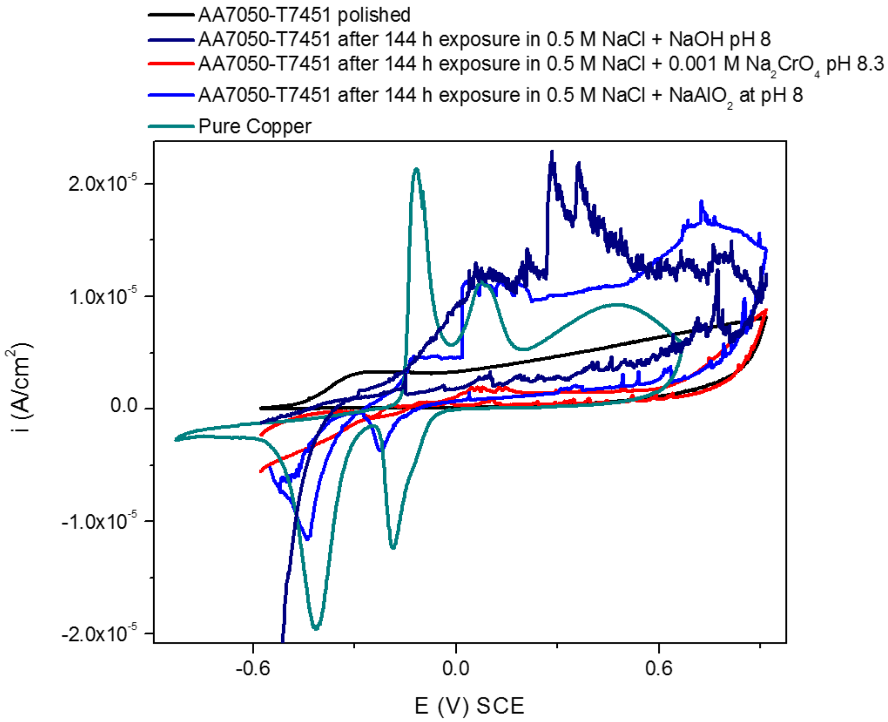

Figure 6.61. Cyclic voltammogram of pure Cu, AA7050-T7451 polished compared to AA7050-T7451 after potentiostatic polarization (-0.73 V) for 144 h in 0.5 M NaCl + $NaAlO_2$ pH 8, 0.5 M NaCl + NaOH (pH 8) and 0.5 M NaCl + 0.001 M Na_2CrO_4 in deaerated pH 8.4 borate buffer.

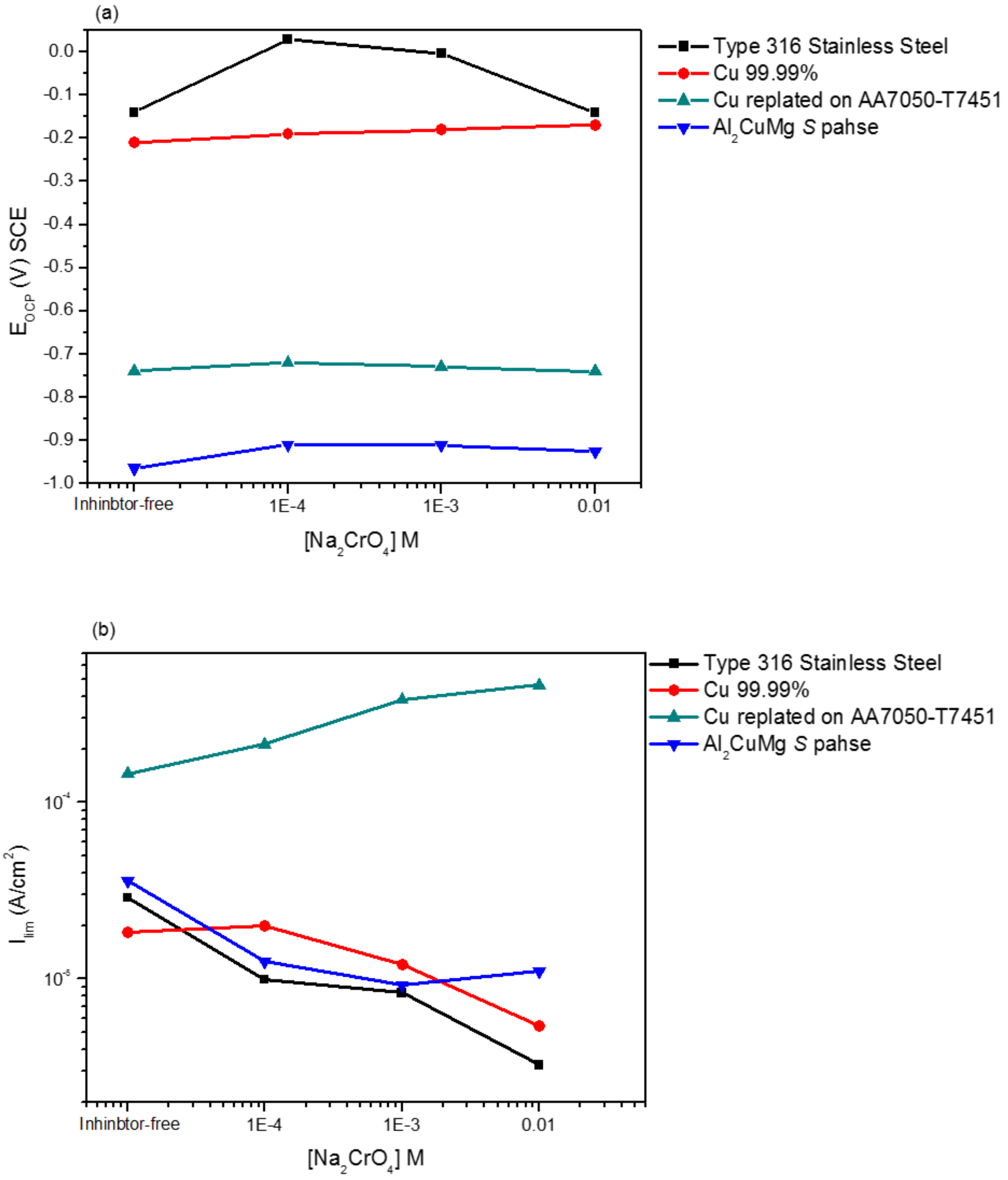

Figure 6.62. (a) OCP and (b) limiting current density (l_{lim}) from cathodic potentiodynamic polarization as a function of Na_2CrO_4 concentration on Type 316 stainless steel, Cu 99.99%, replated Cu on AA7050-T7451 and Al_2CuMg *S* phase.

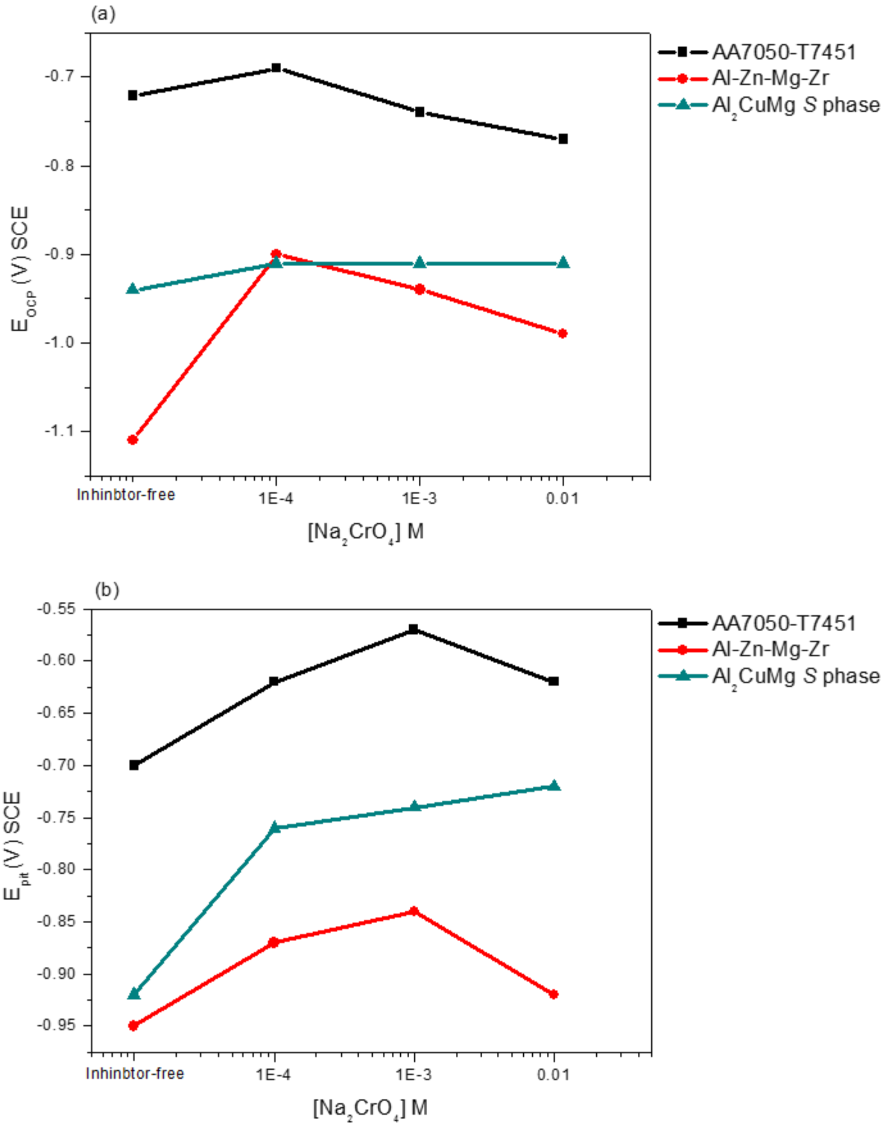

Figure 6.63. (a) OCP and (b) E_{pit} from cathodic potentiodynamic polarization as a function of Na_2CrO_4 on AA7050-T7451, Al-Zn-Mg-Zr, and Al_2CuMg *S* phase.

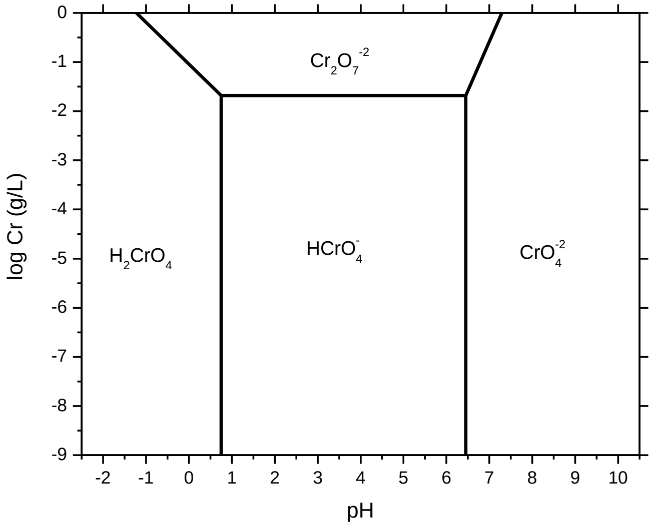

Figure 6.64. Predominance diagram of chromate as a function of pH based on standard free enthalpies given by Pourbaix [218]

7 Thesis Conclusions and Suggested Future Work

7.1 Conclusions

This dissertation further developed an understanding of how the environmental, microstructural, physical and electrochemical factors govern the three dimensional corrosion damage evolution at the sub-meso and micro/nano-scales on AA7050-T7451 coupled with Type 316 stainless steel. A mechanistic understanding was characterized by systematic variation in relevant environmental, geometric, metallurgical and physical parameters such that corrosion damage morphology (fissures, hemispherical pits, intergranular corrosion or combinations) could be predictable for a given set of corrosive conditions.

Operando x-ray tomography on a simulated fastener of AA7050-T7451 and Type 316 stainless revealed multiple corrosion fissures grew simultaneously over the period of exposure in in NaCl and $MgCl_2$. Fissures did not follow obvious clusters of constituent particles suggesting the presence of a newly developed strong cathode such as Cu-replating and a fixed strong cathode attributed to the stainless steel dissimilar metal. EBSD on the surface of the pins followed obvious grains. Detailed examination was undertaken to understand the precise macro and micro cathodes controlling the galvanic corrosion between AA 7050-T7451 and Type 316 stainless central to damage, enabling targeted suppression of certain cathodes to mitigate corrosion damage. It was determined that the Cu-replating may have a greater contribution to the total cathodic charge than the stainless steel rivet. This was an interesting observation as no corrosion sites grew when the stainless steel was removed before exposure. This indicated that the stainless steel provides the key driving force for AA7050-T7451 to corrode and furthermore enable Cu to replate on the surface over the lifetime of corrosion growth.

Environmental and therefore corrosion electrochemical-material combinations were considered in accompanying lab studies which produced severe morphologies that were compared to the field data and other rescaled rivet studies. Guided electrochemical testing using anodic and cathodic polarization methods were developed over a range of relevant potentials for likely corrosion susceptibility in rivet specific environments. Investigation of methods used to study galvanic corrosion were compared to tear-down field damage. Zero resistance ammeter resulted in the closest correlation between the simulated fastener corrosion morphology and actual service corrosion from the perspective of the damage morphology. It was also found that various corrosion damage morphologies can be developed in AA7050-T7451 associated with the galvanic conditions specific to a fastener and based on test method and environment. For instance, intergranular corrosion was found to prevail in acidic environments and further intensified with the addition of Al ions in solution. Intra-granular corrosion pits were found to be developed in neutral and alkaline NaCl environments. Deep elongated fissures in grains oriented in the L-direction were often produced in alkaline NaCl environments with the addition of Al ions, which was attributed to Cu-replating on AA7050-T7451. The corrosion damage morphologies that were developed in specific cases are significant as they may each affect the fatigue transition differently.

The metallurgical factors and electrochemical framework controlling intergranular and intragranular corrosion path was also established in this work. AA7050-T7451 is made up of many different regions with a variety of compositions. This includes the matrix, constituent particles, solute depleted zones and precipitate free zones and each of these regions has a different chemical composition and different critical potentials. It is rationalized that difference in critical potential associated with these microstructural regions combine with Ecouple within a region accounts for IGC. TEM showed that Cu and Al were often being incorporated into the strengthening precipitate $MgZn_2$. Furthermore, Cu depletion was observed in the region adjacent to the grain boundary. It was determined that the window of susceptibility decreased with incorporation of Cu and/or Al into the $MgZn_{2.}$ However, an IGC framework was proposed as Cu^{2+} in solution was found to raise the pitting potential of the solute depleted grain boundary region closing the window for IGC to occur.$Cu^{2+\ is}$ often found in bulk solution in alkaline and neutral environments that promote Cu-replating. This also suggests that pitting can be attributed to the course secondary phases in AA7050-T7451. EBSD showed that unrecrystallized grains containing low-angle boundaries may be more susceptible to intragranular corrosion damage. This may be attributed to unrecrystallized grains collecting Cu in the precipitates upon the over-aging heat treatment of the AA7050 (T7451) with associated Cu depletion.

In this work, galvanic current interactions and cathodic and anodic reaction rate measurements under droplets and thin films were conducted using coupled multi-electrode arrays constructed of AA7050-T7451 and Type 316 stainless steel. It was found that under a NaCl thin film of 70 µm AA7050-T7451 anodic corrosion kinetics and Type 316 stainless cathodic kinetics were increased by at least one order of magnitude when compared to full immersion kinetics. Furthermore coupled multi-electrode arrays constructed in a fastener geometry revealed that anodic currents were often higher at the mouth of the crevice and inside the crevice. In many of the exposures, AA7050 anodic sites were often found to abruptly switch to cathodic sites. This suggested that that dealloyed S-phase (Al_2CuMg) and/or Cu-replating on the surface was the cause of the increased cathodic kinetics of AA7050-T7451 electrodes. It was observed that when AA7050-T7451 was coupled to stainless steel, the AA7050-T7451 electrodes were still significant cathodes supporting ORR. In some cases AA7050-T7451 electrodes contributed 90% of the total net cathodic reaction. This enabled and supported growth of corrosion fissures. The CMEA were tested under atmospheric wet/dry cycle conditions. Wet/dry cycling resulting in a 4-fold increase in current density. Cyclic exposures increased corrosion kinetics due to strong spikes in current on the onset of wetting/drying as the water layer was more concentrated. In a separate study, a CMEA was constructed with an embedded sintered Ag/AgCl electrode as both the counter and reference electrode. The Ag/AgCl electrode is a preferred non-polarizable electrode which can function as a reference electrode and counter electrode. It was found that cathodic ORR reaction rates increased by at least one order of magnitude in atmospheric thin film or droplet environments as compared to bulk full immersion conditions. Furthermore, under droplet conditions it was observed the electrodes on the edge of the droplet had increased cathodic kinetics as compared to electrodes under the center of the droplet while a thin continuous film exhibited equal cathodic kinetics as a function of position. Anodes were dictated by local sites where AA7050 initiated pitting. It is speculated that SS enables initiation but propagation largely is supported by replated-Cu.

The effect of chromate as an inhibitor on corrosion kinetics and damage morphology of AA7050-T7451 was also studied. It was found that additions of sodium chromate reduced cathodic kinetics by one order of magnitude for Type 316 stainless steel and by less than one order of magnitude on pure Cu. However, additions of sodium chromate slightly increased cathodic kinetics of replated-Cu on AA7050-T77451, which is detrimental to corrosion inhibition. Damage morphology studies showed that while the fissure density was reduced with the addition of soluble chromate, aggressive environments created by application of high anodic potentials or galvanic coupling to stainless steel, induced deep fissure formation. In one case, fissures were over 7 times deeper in more concentrated chromate environments than chromate free environments. The addition of 1 mM Na2CrO4 inhibited corrosion pitting on AA7050-T7451. The addition of chromate was determined to inhibit the corrosion of Al_2CuMg, which reduces the possible formation of porous Cu-rich phases and Cu-replating on the surface. Therefore, inhibition of Cu release through passivation of Al_2CuMg would lower cathodic reaction rates.

7.2 Future Work

- Characterization of physical geometric effects of AA7050-T7451 and Type 316 stainless steel fasteners such as gap width, crevice length and external cathode area. Furthermore, obtain polarization data from inside a crevice. This can accomplished by constructing an improved coupled multi-electrode array design that enables precise gap adjustments and the use of a sintered Ag/AgCl embedded inside the crevice.
- Damage morphology characterization of AA7050-T7451 under various atmospheric and accelerated testing environmental conditions, such as salt spray as a function of water layer thickness and cyclic exposures.
- Further study the effect of Cu^{2+} ions in solution on the damage morphology of AA7050-T7451.
- Clarify on the effect of cathode capacity by studying the corrosion damage morphology and electrochemistry of AA7050-T7451 coupled with a “good” cathode and a “bad” cathode. Decouple effects of cathodes on initiation vs assessment of propagation.

- Further investigate the effect of chromate inhibitor on AA7050-T7451. Specifically understand whether corrosion inhibition is established through cathodic inhibition or anodic inhibition. Moreover, a more systematic approach on understanding why Cu-replating on AA7050-T7451 is detrimental to corrosion inhibition with chromate.
- Effect of chromate as an inhibitor in rivet specific environments, such as NaCl and $MgCl_2$ environments adjusted to different pH values and with the addition of Al ions in solution.
- Effect of environmentally friendly inhibitors such as permanganate, cerium or molybdate on the corrosion damage morphology of AA7050-T7451.
- Characterization of damage morphology on full scale Type 316 fasteners in AA7050-T7451 panels.

8 References

1. A. Turnbull, "Current understanding of environment-induced cracking of steam turbine steels," Corrosion 64, 5 (2008): p. 420-438.
2. G. Shoales, *Procedures For Aircraft Structural Teardown Analysis: Development Of A Best Practices Handbook*, in *ICAF 2009, Bridging the Gap between Theory and Operational Practice*, M.J. Bos, Editor. 2009, Springer Netherlands. p. 330-353.
3. R.P. Gangloff and M.B. Ives, Environment-induced Cracking of Metals: Proceedings of the First International Conference on Environment-Induced Cracking of Metals, Held in Conjunction with the First World Materials Congress, October 2-7, 1988, The American Club, Kohler, Wisconsin, USA: National Association of Corrosion Engineers, 1990.
4. J.T. Burns, J.M. Larsen, and R.P. Gangloff, "Driving forces for localized corrosion-to-fatigue crack transition in Al–Zn–Mg–Cu," Fatigue & Fracture of Engineering Materials & Structures 34, 10 (2011): p. 745-773.
5. J.T. Burns, S. Kim, and R.P. Gangloff, "Effect of corrosion severity on fatigue evolution in Al–Zn–Mg–Cu," Corros Sci 52, 2 (2010): p. 498-508.
6. K. Jones and D.W. Hoeppner, "Pit-to-crack transition in pre-corroded 7075-T6 aluminum alloy under cyclic loading," Corros Sci 47, 9 (2005): p. 2185-2198.
7. S.K. Bhaumik, M. Sujata, and M.A. Venkataswamy, "Fatigue failure of aircraft components," Engineering Failure Analysis 15, 6 (2008): p. 675-694.
8. J.R. Davis, Corrosion of aluminum and aluminum alloys (Materials Park, OH: ASM International, 1999). p. vii, 313 p.
9. J. Zhang, M. Przystupa, and A. Luévano, "Characterizations of pore and constituent particle populations in 7050-T7451 aluminum plate alloys," Metall and Mat Trans A 29, 3 (1998): p. 727-737.
10. R.T. Foley, "Localized Corrosion of Aluminum Alloys—A Review," Corrosion 42, 5 (1986): p. 277-288.
11. P.S. Young and J.H. Payer, "Stages of Damage Evolution for Al 2024-T3 Around Fasteners in Marine Atmosphere," Corrosion 71, 10 (2015): p. 1278-1293.
12. N. Holroyd, "Environment-induced cracking of high-strength aluminum alloys," Environment-Induced Cracking of Metals (Houston, TX: NACE International, 1990) (1990): p. 311.
13. S.P. Knight, N. Birbilis, B.C. Muddle, A.R. Trueman, and S.P. Lynch, "Correlations between intergranular stress corrosion cracking, grain-boundary microchemistry, and grain-boundary electrochemistry for Al-Zn-Mg-Cu alloys," Corros Sci 52, 12 (2010): p. 4073-4080.
14. S. Maitra and G. English, "Mechanism of localized corrosion of 7075 alloy plate," Metallurgical Transactions A 12, 3 (1981): p. 535-541.
15. S.-S. Wang, G. Frankel, J.-T. Jiang, J.-F. Chen, S.-L. Dai, and L. Zhen, "Mechanism of localized breakdown of 7000 series aluminum alloys," J Electrochem Soc 160, 10 (2013): p. C493-C502.
16. *Standard Test Method for Exfoliation Corrosion Susceptibility in 2XXX and 7XXX Series Aluminum Alloys (EXCO Test)*. 2013, ASTM International.

17. *Standard Test Method for Determination of Hydrogen Peroxide and Combined Organic Peroxides in Atmospheric Water Samples by Peroxidase Enzyme Fluorescence Method*. 2013, ASTM International.
18. D.A. Jones, Principles and Prevention of Corrosion. 2nd ed (Upper Saddle River, NJ: Prentice Hall, 1996). p. xvi, 572 p.
19. N.D. Greene and M.G. Fontana, "A Critical Analysis of Pitting Corrosion★," Corrosion 15, 1 (1959): p. 41-47.
20. I.L. Rosenfeld and I.K. Marshakov, "Mechanism of Crevice Corrosion," Corrosion 20, 4 (1964): p. 115t-125t.
21. R.G. Buchheit, J.P. Moran, and G.E. Stoner, "Localized Corrosion Behavior of Alloy 2090—The Role of Microstructural Heterogeneity," Corrosion 46, 8 (1990): p. 610-617.
22. N. Birbilis and R.G. Buchheit, "Investigation and discussion of characteristics for intermetallic phases common to aluminum alloys as a function of solution pH," J Electrochem Soc 155, 3 (2008): p. C117-C126.
23. N. Birbilis and R.G. Buchheit, "Electrochemical characteristics of intermetallic phases in aluminum alloys - An experimental survey and discussion," J Electrochem Soc 152, 4 (2005): p. B140-B151.
24. R. Buchheit, "A compilation of corrosion potentials reported for intermetallic phases in aluminum alloys," J Electrochem Soc 142, 11 (1995): p. 3994-3996.
25. J. Hirsch, B. Skrotzki, and G. Gottstein, Aluminum Alloys: Their Physical and Mechanical Properties (Wienheim, Germany: Wiley-VCH, 2008.
26. M. Dixit, R.S. Mishra, and K.K. Sankaran, "Structure-property correlations in Al 7050 and Al 7055 high-strength aluminum alloys," Mat Sci Eng a-Struct 478, 1-2 (2008): p. 163-172.
27. T. Ramgopal, P.I. Gouma, and G.S. Frankel, "Role of grain-boundary precipitates and solute-depleted zone on the intergranular corrosion of aluminum alloy 7150," Corrosion 58, 8 (2002): p. 687-697.
28. K. Jones and D.W. Hoeppner, "The interaction between pitting corrosion, grain boundaries, and constituent particles during corrosion fatigue of 7075-T6 aluminum alloy," International Journal of Fatigue 31, 4 (2009): p. 686-692.
29. X. Fan, D. Jiang, L. Zhong, T. Wang, and S. Ren, "Influence of microstructure on the crack propagation and corrosion resistance of Al–Zn–Mg–Cu alloy 7150," Materials Characterization 58, 1 (2007): p. 24-28.
30. E. McCafferty, Introduction to Corrosion Science (New York: Springer, 2010). p. xvi, 575 p.
31. R. Buchheit, M. Martinez, and L. Montes, "Evidence for Cu Ion Formation by Dissolution and Dealloying the Al2CuMg Intermetallic Compound in Rotating Ring-Disk Collection Experiments," J Electrochem Soc 147, 1 (2000): p. 119-124.
32. T. Ramgopal, P. Schmutz, and G.S. Frankel, "Electrochemical behavior of thin film analogs of Mg(Zn,Cu,Al)(2)," J Electrochem Soc 148, 9 (2001): p. B348-B356.
33. M. Vukmirovic, N. Dimitrov, and K. Sieradzki, "Dealloying and Corrosion of Al Alloy 2024 T 3," J Electrochem Soc 149, 9 (2002): p. B428-B439.
34. G. Sha and A. Cerezo, "Early-stage precipitation in Al–Zn–Mg–Cu alloy (7050)," Acta Materialia 52, 15 (2004): p. 4503-4516.

35. V. Hansen, O. Karlsen, Y. Langsrud, and J. Gjønnes, "Precipitates, zones and transitions during aging of Al-Zn-Mg-Zr 7000 series alloy," Mater Sci Tech-Lond 20, 2 (2004): p. 185-193.
36. F. Song, X. Zhang, S. Liu, N. Han, and D. Li, "Anisotropy of localized corrosion in 7050–T7451 Al alloy thick plate," Transactions of Nonferrous Metals Society of China 23, 9 (2013): p. 2483-2490.
37. A.F. Oliveira Jr, M.C. de Barros, K.R. Cardoso, and D.N. Travessa, "The effect of RRA on the strength and SCC resistance on AA7050 and AA7150 aluminium alloys," Materials Science and Engineering: A 379, 1–2 (2004): p. 321-326.
38. D.K. Xu, N. Birbilis, D. Lashansky, P.A. Rometsch, and B.C. Muddle, "Effect of solution treatment on the corrosion behaviour of aluminium alloy AA7150: Optimisation for corrosion resistance," Corros Sci 53, 1 (2011): p. 217-225.
39. B.-L. Ou, J.-G. Yang, and M.-Y. Wei, "Effect of Homogenization and Aging Treatment on Mechanical Properties and Stress-Corrosion Cracking of 7050 Alloys," Metall and Mat Trans A 38, 8 (2007): p. 1760-1773.
40. J.S. Robinson, R.L. Cudd, D.A. Tanner, and G.P. Dolan, "Quench sensitivity and tensile property inhomogeneity in 7010 forgings," Journal of Materials Processing Technology 119, 1–3 (2001): p. 261-267.
41. J.D. Robson and P.B. Prangnell, "Dispersoid precipitation and process modelling in zirconium containing commercial aluminium alloys," Acta Materialia 49, 4 (2001): p. 599-613.
42. G.O. Ilevbare, O. Schneider, R.G. Kelly, and J.R. Scully, "In situ confocal laser scanning microscopy of AA 2024-T3 corrosion metrology - I. Localized corrosion of particles," J Electrochem Soc 151, 8 (2004): p. B453-B464.
43. G.S. Chen, M. Gao, and R.P. Wei, "Microconstituent-Induced Pitting Corrosion in Aluminum Alloy 2024-T3," Corrosion 52, 1 (1996): p. 8-15.
44. Q.J. Meng and G.S. Frankel, "Effect of Cu content on corrosion behavior of 7xxx series aluminum alloys," J Electrochem Soc 151, 5 (2004): p. B271-B283.
45. N. Dimitrov, J. Mann, and K. Sieradzki, "Copper redistribution during corrosion of aluminum alloys," J Electrochem Soc 146, 1 (1999): p. 98-102.
46. G.O. Ilevbare and J.R. Scully, "Erratum: “Mass-Transport-Limited Oxygen Reduction Reaction on AA2024-T3 and Selected Intermetallic Compounds in Chromate-Containing Solutions” (Vol. 57, No. 2, pp. 134–152)," Corrosion 57, 5 (2001): p. 480-480.
47. D. Dumont, A. Deschamps, and Y. Brechet, "On the relationship between microstructure, strength and toughness in AA7050 aluminum alloy," Materials Science and Engineering: A 356, 1–2 (2003): p. 326-336.
48. R. Wei, C.-M. Liao, and M. Gao, "A transmission electron microscopy study of constituent-particle-induced corrosion in 7075-T6 and 2024-T3 aluminum alloys," Metall and Mat Trans A 29, 4 (1998): p. 1153-1160.
49. J.C. Lin, H.L. Liao, W.D. Jehng, C.H. Chang, and S.L. Lee, "Effect of heat treatments on the tensile strength and SCC-resistance of AA7050 in an alkaline saline solution," Corros Sci 48, 10 (2006): p. 3139-3156.

50. P.-y. Li, B.-q. Xiong, Y.-a. Zhang, and Z.-h. Li, "Temperature variation and solution treatment of high strength AA7050," Transactions of Nonferrous Metals Society of China 22, 3 (2012): p. 546-554.
51. Z.-h. Li, B.-q. Xiong, Y.-a. Zhang, B.-h. Zhu, F. Wang, and H.-w. Liu, "Microstructural evolution of aluminum alloy 7B04 thick plate by various thermal treatments," Transactions of Nonferrous Metals Society of China 18, 1 (2008): p. 40-45.
52. D.A. Little, B.J. Connolly, and J.R. Scully, "An electrochemical framework to explain the intergranular stress corrosion behavior in two Al–Cu–Mg–Ag alloys as a function of aging," Corros Sci 49, 2 (2007): p. 347-372.
53. J. Wloka, T. Hack, and S. Virtanen, "Influence of temper and surface condition on the exfoliation behaviour of high strength Al–Zn–Mg–Cu alloys," Corros Sci 49, 3 (2007): p. 1437-1449.
54. I.L. Muller and J.R. Galvele, "Pitting potential of high purity binary aluminium alloys—I. Al ▪ Cu alloys. Pitting and intergranular corrosion," Corros Sci 17, 3 (1977): p. 179-193.
55. R. Buchheit, R. Grant, P. Hlava, B. McKenzie, and G. Zender, "Local Dissolution Phenomena Associated with S Phase (Al2CuMg) Particles in Aluminum Alloy 2024-T3," J Electrochem Soc 144, 8 (1997): p. 2621-2628.
56. N. Dimitrov, J. Mann, M. Vukmirovic, and K. Sieradzki, "Dealloying of Al2CuMg in alkaline media," J Electrochem Soc 147, 9 (2000): p. 3283-3285.
57. A. Bigot, F. Danoix, P. Auger, D. Blavette, and A. Reeves. *Tomographic atom probe study of age hardening precipitation in industrial AlZnMgCu (7050) alloy*. in *Materials Science Forum*. 1996: Trans Tech Publ.
58. G. Thomas, "The Aging Characteristics of Aluminum Alloys. Electron Transmission Studies of Al-Mg-Si Alloys," J inst. of Metals 90, UCRL-9582 (1961).
59. N.Q. Chinh, Z. Kovács, L. Reich, F. Szekely, J. Illy, and J. Lendvai. *Precipitation and work hardening in high strength AlZnMg (Cu, Zr) alloys*. in *Materials science forum*. 1996: Trans Tech Publ.
60. G. Ilevbare and J. Scully, "Oxygen reduction reaction kinetics on chromate conversion coated Al-Cu, Al-Cu-Mg, and Al-Cu-Mn-Fe intermetallic compounds," J Electrochem Soc 148, 5 (2001): p. B196-B207.
61. D. Jung, I. Dumler, and M. Metzger, "Electronmicroscopic Examination of Corroded Aluminum-Copper Alloy Foils," J Electrochem Soc 132, 10 (1985): p. 2308-2312.
62. N. Murer, N. Missert, and R. Buchheit, "Finite Element Modeling of the Galvanic Corrosion of Aluminum at Engineered Copper Particles," J Electrochem Soc 159, 6 (2012): p. C265-C276.
63. H. Obispo, L. Murr, R. Arrowood, and E. Trillo, "Copper Deposition During the Corrosion of Aluminum Alloy 2024 in Sodium Chloride Solutions," Journal of Materials Science 35, 14 (2000): p. 3479-3495.
64. D.K. Xu, N. Birbilis, and P.A. Rometsch, "Effect of S-Phase Dissolution on the Corrosion and Stress Corrosion Cracking of an As-Rolled Al-Zn-Mg-Cu Alloy," Corrosion 68, 3 (2012): p. 035001-035001-035001-035010.
65. W.J. Clark, J.D. Ramsey, R.L. McCreery, and G.S. Frankel, "A galvanic corrosion approach to investigating chromate effects on aluminum alloy 2024-T3," J Electrochem Soc 149, 5 (2002): p. B179-B185.

66. D. Jones and B. Wilde, "Galvanic reactions during localized corrosion on stainless steel," Corros Sci 18, 7 (1978): p. 631-643.
67. A. Pardo, E. Otero, M. Merino, M. López, M. Utrilla, and F. Moreno, "Influence of pH and chloride concentration on the pitting and crevice corrosion behavior of high-alloy stainless steels," Corrosion 56, 4 (2000): p. 411-418.
68. M. Pryor and D. Keir, "Galvanic Corrosion II. Effect of pH and Dissolved Oxygen Concentration on the Aluminum-Steel Couple," J Electrochem Soc 105, 11 (1958): p. 629-635.
69. A. Alavi and R.A. Cottis, "The determination of pH, potential and chloride concentration in corroding crevices on 304 stainless steel and 7475 aluminium alloy," Corros Sci 27, 5 (1987): p. 443-451.
70. C. Liu, University of Virginia. 2016, Unpublished data.
71. R. Ambat, A.J. Davenport, G.M. Scamans, and A. Afseth, "Effect of iron-containing intermetallic particles on the corrosion behaviour of aluminium," Corros Sci 48, 11 (2006): p. 3455-3471.
72. Y. Xu and H.W. Pickering, "The initial potential and current distributions of the crevice corrosion process," J Electrochem Soc 140, 3 (1993): p. 658-668.
73. Z. Chen, F. Cui, and R. Kelly, "Calculations of the cathodic current delivery capacity and stability of crevice corrosion under atmospheric environments," J Electrochem Soc 155, 7 (2008): p. C360-C368.
74. M. Stratmann and H. Streckel, "On the atmospheric corrosion of metals which are covered with thin electrolyte layers—I. Verification of the experimental technique," Corros Sci 30, 6-7 (1990): p. 681-696.
75. M. Stratmann, H. Streckel, K.T. Kim, and S. Crockett, "On the atmospheric corrosion of metals which are covered with thin electrolyte layers-iii. the measurement of polarisation curves on metal surfaces which are covered by thin electrolyte layers," Corros Sci 30, 6 (1990): p. 715-734.
76. F. Mansfeld, "Electrochemical techniques for monitoring of atmospheric corrosion phenomena," Corrosion Inhibitors, Fifth. 1, (1980): p. 191-216.
77. V.S. Agarwala and G.M. Ugiansky, New methods for corrosion testing of aluminum alloys. Stp (Philadelphia, PA: ASTM, 1992). p. ix, 219 p.
78. G. Bierwagen, R. Brown, D. Battocchi, and S. Hayes, "Active metal-based corrosion protective coating systems for aircraft requiring no-chromate pretreatment," Progress in Organic Coatings 68, 1–2 (2010): p. 48-61.
79. G.A. El-Mahdy and K.B. Kim, "AC impedance study on the atmospheric corrosion of aluminum under periodic wet–dry conditions," Electrochimica Acta 49, 12 (2004): p. 1937-1948.
80. Y.Y. Shi, Z. Zhang, J.X. Su, and J.Q. Zhang, "EIS study on 2024-T3 aluminum alloy corrosion in simulated acid rain under cyclic wet-dry conditions," Materials and Corrosion 56, 10 (2005): p. 701-706.
81. J. Davalos, M. Gracia, J.F. Marco, and J.R. Gancedo, "Corrosion of weathering steel and iron under wet-dry cycling conditions: Influence of the rise of temperature during the dry period," Hyperfine Interact 69, 1 (1992): p. 871-874.

82. M. Stratmann, "The investigation of the corrosion properties of metals, covered with adsorbed electrolyte layers—A new experimental technique," Corros Sci 27, 8 (1987): p. 869-872.
83. S. Hœrlé, F. Mazaudier, P. Dillmann, and G. Santarini, "Advances in understanding atmospheric corrosion of iron. II. Mechanistic modelling of wet–dry cycles," Corros Sci 46, 6 (2004): p. 1431-1465.
84. A.K. Neufeld, I.S. Cole, A.M. Bond, and S.A. Furman, "The initiation mechanism of corrosion of zinc by sodium chloride particle deposition," Corros Sci 44, 3 (2002): p. 555-572.
85. S. Oesch and M. Faller, "Environmental effects on materials: The effect of the air pollutants SO2, NO2, NO and O3 on the corrosion of copper, zinc and aluminium. A short literature survey and results of laboratory exposures," Corros Sci 39, 9 (1997): p. 1505-1530.
86. K. Van der Walde, J. Brockenbrough, B. Craig, and B. Hillberry, "Multiple fatigue crack growth in pre-corroded 2024-T3 aluminum," International Journal of Fatigue 27, 10 (2005): p. 1509-1518.
87. P. Pao, C. Feng, and S. Gill, "Corrosion fatigue crack initiation in aluminum alloys 7075 and 7050," Corrosion 56, 10 (2000): p. 1022-1031.
88. S. Kim, J.T. Burns, and R.P. Gangloff, "Fatigue crack formation and growth from localized corrosion in Al–Zn–Mg–Cu," Eng Fract Mech 76, 5 (2009): p. 651-667.
89. D.A. Horner, B.J. Connolly, S. Zhou, L. Crocker, and A. Turnbull, "Novel images of the evolution of stress corrosion cracks from corrosion pits," Corros Sci 53, 11 (2011): p. 3466-3485.
90. R. Davies, G. Nordmark, and J. Walsh, *Design mechanical properties, fracture toughness, fatigue properties, exfoliation and stress-corrosion resistance of 7050 sheet, plate, hand forgings, die forgings and extrusions*. 1975, DTIC Document.
91. B.J. Connolly, D.A. Horner, S.J. Fox, A.J. Davenport, C. Padovani, S. Zhou, A. Turnbull, M. Preuss, N.P. Stevens, T.J. Marrow, J.Y. Buffiere, E. Boller, A. Groso, and M. Stampanoni, "X-ray microtomography studies of localised corrosion and transitions to stress corrosion cracking," Mater Sci Tech-Lond 22, 9 (2006): p. 1076-1085.
92. R.J. Bucci, "Selecting Aluminum-Alloys to Resist Failure by Fracture Mechanisms," Eng Fract Mech 12, 3 (1979): p. 407-441.
93. S. Barter, P. Sharp, G. Holden, and G. Clark, "Initiation and early growth of fatigue cracks in an aerospace aluminium alloy," Fatigue & Fracture of Engineering Materials & Structures 25, 2 (2002): p. 111-125.
94. P. Pao, S. Gill, and C. Feng, "On fatigue crack initiation from corrosion pits in 7075-T7351 aluminum alloy," Scripta Materialia 43, 5 (2000): p. 391-396.
95. K. Van der Walde and B. Hillberry, "Initiation and shape development of corrosion-nucleated fatigue cracking," International Journal of Fatigue 29, 7 (2007): p. 1269-1281.
96. J. Burns, J. Larsen, and R. Gangloff, "Driving forces for localized corrosion-to-fatigue crack transition in Al–Zn–Mg–Cu," Fatigue & Fracture of Engineering Materials & Structures 34, 10 (2011): p. 745-773.

97. J. Rajasankar, N.R. Iyer, and S. Gopinath, "Probabilistic modelling of fatigue crack initiation from pits and pit clusters in aluminium alloys," Corrosion Engineering, Science and Technology 42, 3 (2007): p. 260-265.

98. G.S. Chen, K.C. Wan, M. Gao, R.P. Wei, and T.H. Flournoy, "Transition from pitting to fatigue crack growth—modeling of corrosion fatigue crack nucleation in a 2024-T3 aluminum alloy," Materials Science and Engineering: A 219, 1 (1996): p. 126-132.

99. Y. Kondo, "Prediction of fatigue crack initiation life based on pit growth," Corrosion 45, 1 (1989): p. 7-11.

100. K.K. Sankaran, R. Perez, and K.V. Jata, "Effects of pitting corrosion on the fatigue behavior of aluminum alloy 7075-T6: modeling and experimental studies," Materials Science and Engineering: A 297, 1 (2001): p. 223-229.

101. V. Sabelkin, V. Perel, H. Misak, E. Hunt, and S. Mall, "Investigation into crack initiation from corrosion pit in 7075-T6 under ambient laboratory and saltwater environments," Eng Fract Mech 134, (2015): p. 111-123.

102. J.R. Donahue and J.T. Burns, "Effect of chloride concentration on the corrosion–fatigue crack behavior of an age-hardenable martensitic stainless steel," International Journal of Fatigue 91, (2016): p. 79-99.

103. A. Turnbull, "The environmentally small/short crack growth effect: current understanding," Corrosion Reviews 30, 1-2 (2012): p. 1-17.

104. J.T. Burns, J.M. Larsen, and R.P. Gangloff, "Effect of initiation feature on microstructure-scale fatigue crack propagation in Al–Zn–Mg–Cu," International Journal of Fatigue 42, (2012): p. 104-121.

105. J. Bozek, J. Hochhalter, M. Veilleux, M. Liu, G. Heber, S. Sintay, A. Rollett, D. Littlewood, A. Maniatty, and H. Weiland, "A geometric approach to modeling microstructurally small fatigue crack formation: I. Probabilistic simulation of constituent particle cracking in AA 7075-T651," Modelling and Simulation in Materials Science and Engineering 16, 6 (2008): p. 065007.

106. E. De Los Rios, X. Xin, and A. Navarro. *Modelling microstructurally sensitive fatigue short crack growth*. in *Proceedings of the Royal Society of London A: Mathematical, Physical and Engineering Sciences*. 1994: The Royal Society.

107. R. Ritchie and J. Lankford, "Small fatigue cracks: a statement of the problem and potential solutions," Materials Science and Engineering 84, (1986): p. 11-16.

108. T. Prosek, A. Iversen, C. Taxén, and D. Thierry, "Low-Temperature Stress Corrosion Cracking of Stainless Steels in the Atmosphere in the Presence of Chloride Deposits," Corrosion 65, 2 (2009): p. 105-117.

109. J.F. Li, B. Maier, and G.S. Frankel, "Corrosion of an Al–Mg–Si alloy under MgCl2 solution droplets," Corros Sci 53, 6 (2011): p. 2142-2151.

110. N. Tomashov, "Development of the electrochemical theory of metallic corrosion," Corrosion 20, 1 (1964): p. 7t-14t.

111. A. Cox and S.B. Lyon, "An electrochemical study of the atmospheric corrosion of mild steel-I. Experimental method," Corros Sci 36, 7 (1994): p. 1167-1176.

112. F. Mansfeld and S. Tsai, "Laboratory studies of atmospheric corrosion—I. Weight loss and electrochemical measurements," Corros Sci 20, 7 (1980): p. 853-872.

113. M. Stratmann and H. Streckel, "On the atmospheric corrosion of metals which are covered with thin electrolyte layers—I. Verification of the experimental technique," Corros Sci 30, 6 (1990): p. 681-696.
114. G.A. El-Mahdy, A. Nishikata, and T. Tsuru, "AC impedance study on corrosion of 55%Al–Zn alloy-coated steel under thin electrolyte layers," Corros Sci 42, 9 (2000): p. 1509-1521.
115. S.H. Zhang and S.B. Lyon, "The electrochemistry of iron, zinc and copper in thin layer electrolytes," Corros Sci 35, 1 (1993): p. 713-718.
116. A. Nishikata, Y. Ichihara, Y. Hayashi, and T. Tsuru, "Influence of electrolyte layer thickness and pH on the initial stage of the atmospheric corrosion of iron," J Electrochem Soc 144, 4 (1997): p. 1244-1252.
117. S.C. Morton and G.S. Frankel, "Atmospheric pitting corrosion of AA7075-T6 under evaporating droplets with and without inhibitors," Materials and Corrosion 65, 4 (2014): p. 351-361.
118. J. Zhao, L. Xia, A. Sehgal, D. Lu, R.L. McCreery, and G.S. Frankel, "Effects of chromate and chromate conversion coatings on corrosion of aluminum alloy 2024-T3," Surface and Coatings Technology 140, 1 (2001): p. 51-57.
119. Q. Yu, C. Reddy, C. Moffitt, D. Wieliczka, R. Johnson, J. Deffeyes, and H. Yasuda, "Improved corrosion protection of aluminum alloys by system approach interface engineering: Part 2-AA2024-T3," Corrosion 56, 9 (2000): p. 887-900.
120. R.L. Twite and G.P. Bierwagen, "Review of alternatives to chromate for corrosion protection of aluminum aerospace alloys," Progress in Organic Coatings 33, 2 (1998): p. 91-100.
121. J. Sinko, "Challenges of chromate inhibitor pigments replacement in organic coatings," Progress in Organic Coatings 42, 3 (2001): p. 267-282.
122. M. Jakab, F. Presuel-Moreno, and J. Scully, "Critical concentrations associated with cobalt, cerium, and molybdenum inhibition of AA2024-T3 corrosion: delivery from Al-Co-Ce (-Mo) alloys," Corrosion 61, 3 (2005): p. 246-263.
123. G.O. Ilevbare, J.R. Scully, J. Yuan, and R.G. Kelly, "Inhibition of Pitting Corrosion on Aluminum Alloy 2024-T3: Effect of Soluble Chromate Additions vs Chromate Conversion Coating," Corrosion 56, 3 (2000): p. 227-242.
124. G.O. Ilevbare and J.R. Scully, "Mass-Transport-Limited Oxygen Reduction Reaction on AA2024-T3 and Selected Intermetallic Compounds in Chromate-Containing Solutions," Corrosion 57, 2 (2001): p. 134-152.
125. G. Ilevbare, J. Scully, J. Yuan, and R. Kelly, "Inhibition of pitting corrosion on aluminum alloy 2024-T3: effect of soluble chromate additions vs chromate conversion coating," Corrosion 56, 3 (2000): p. 227-242.
126. M. Bethencourt, F. Botana, J. Calvino, M. Marcos, and M. Rodriguez-Chacon, "Lanthanide compounds as environmentally-friendly corrosion inhibitors of aluminium alloys: a review," Corros Sci 40, 11 (1998): p. 1803-1819.
127. E. Akiyama, A. Markworth, J. McCoy, G. Frankel, L. Xia, and R. McCreery, "Storage and release of soluble hexavalent chromium from chromate conversion coatings on Al alloys: Kinetics of release," J Electrochem Soc 150, 2 (2003): p. B83-B91.

128. M. Iannuzzi and G. Frankel, "Inhibition of aluminum alloy 2024 corrosion by vanadates: an in situ atomic force microscopy scratching investigation," Corrosion 63, 7 (2007): p. 672-688.
129. R.S. Neves, D.P.B. Silva, and A.J. Motheo, "Corrosion Protection of AA7075 Aluminium Alloy by Trimethoxy-Silanes Self-Assembled Monolayers," ISRN Electrochemistry 2013, (2013): p. 9.
130. G.P. BIERWAGEN, D.E. TALLMAN, M. NANNA, D. BATTOCCHI, A. STAMNESS, and V.J. GELLING. *New developments in Cr-free primers for aerospace alloys*. in *Papers presented at the meeting-American Chemical Society. Division of Polymer Chemistry*. 2004: American Chemical Society.
131. S. Lim, nbsp, Taek, I. Eun, Sang, S. Nam, and Woo, "Control of Equilibrium Phases (M,T,S) in the Modified Aluminum Alloy 7175 for Thick Forging Applications," MATERIALS TRANSACTIONS 44, 1 (2003): p. 181-187.
132. M.W. Kendig and R.G. Buchheit, "Corrosion Inhibition of Aluminum and Aluminum Alloys by Soluble Chromates, Chromate Coatings, and Chromate-Free Coatings," Corrosion 59, 5 (2003): p. 379-400.
133. S.J. Findlay and N.D. Harrison, "Why aircraft fail," Materials Today 5, 11 (2002): p. 18-25.
134. D.A. Little, M.A. Jakab, and J.R. Scully, "Effect of Surface Pretreatment on the Underpaint Corrosion of AA2024-T3 at Various Temperatures," Corrosion 62, 4 (2006): p. 300-315.
135. F. Eckermann, T. Suter, P.J. Uggowitzer, A. Afseth, A.J. Davenport, B.J. Connolly, M.H. Larsen, F. De Carlo, and P. Schmutz, "In situ monitoring of corrosion processes within the bulk of AlMgSi alloys using X-ray microtomography," Corros Sci 50, 12 (2008): p. 3455-3466.
136. F. Eckermann, T. Suter, P.J. Uggowitzer, A. Afseth, M. Stampanoni, F. Marone, and P. Schmutz, "In Situ Microtomographically Monitored and Electrochemically Controlled Corrosion Initiation and Propagation in AlMgSi Alloy AA6016," J Electrochem Soc 156, 1 (2009): p. C1-C7.
137. T. Marrow, L. Babout, B. Connolly, D. Engelberg, G. Johnson, J. Buffiere, P. Withers, and R. Newman, "High-resolution, in-situ, tomographic observations of stress corrosion cracking," EICM 2, Prediction, industrial developments and evaluation (2004).
138. L. Salvo, P. Cloetens, E. Maire, S. Zabler, J.J. Blandin, J.Y. Buffiere, W. Ludwig, E. Boller, D. Bellet, and C. Josserond, "X-ray micro-tomography an attractive characterisation technique in materials science," Nucl Instrum Meth B 200, (2003): p. 273-286.
139. V. Rafla, A. Davenport, and J.R. Scully, "Determination of Cathodic and Anodic Charge from Operando X-Ray Tomography Observation of Galvanic Corrosion of Aluminum Alloy 7050-T7451 and 304 Stainless Steel in a Simulated Fastener," Corrosion 71, 11 (2015): p. 1300-1303.
140. V. Rafla, A.D. King, S. Glanvill, A. Parsons, A. Davenport, and J.R. Scully, "Operando Observation of Galvanic Corrosion Between Aluminum Alloy 7050-T7451 and 304 Stainless Steel in a Simulated Fastener Arrangement Using X-Ray Tomography," Corrosion 71, 10 (2015): p. 1171-1176.
141. J. Baruchel, J.-Y. Buffiere, and E. Maire, "X-ray tomography in material science," (2000).

142. S.P. Knight, M. Salagaras, A.M. Wythe, F. De Carlo, A.J. Davenport, and A.R. Trueman, "In situ X-ray tomography of intergranular corrosion of 2024 and 7050 aluminium alloys," Corros Sci 52, 12 (2010): p. 3855-3860.

143. X. Zhao, G.S. Frankel, B. Zoofan, and S.I. Rokhlin, "In Situ X-Ray Radiographic Study of Intergranular Corrosion in Aluminum Alloys," Corrosion 59, 11 (2003): p. 1012-1018.

144. C.M. Liao, J.M. Olive, M. Gao, and R.P. Wei, "In-Situ Monitoring of Pitting Corrosion in Aluminum Alloy 2024," Corrosion 54, 6 (1998): p. 451-458.

145. S.M. Ghahari, A.J. Davenport, T. Rayment, T. Suter, J.-P. Tinnes, C. Padovani, J.A. Hammons, M. Stampanoni, F. Marone, and R. Mokso, "In situ synchrotron X-ray micro-tomography study of pitting corrosion in stainless steel," Corrosion Science 53, 9 (2011): p. 2684-2687.

146. A.J. Davenport, C. Padovani, B.J. Connolly, N.P. Stevens, T.A. Beale, A. Groso, and M. Stampanoni, "Synchrotron X-ray microtomography study of the role of Y in corrosion of magnesium alloy WE43," Electrochemical and solid-state letters 10, 2 (2007): p. C5-C8.

147. W.S. Rasband, ImageJ, U. S. National Institutes of Health,ethesda, Maryland, USA, http://imagej.nih.gov/ij/, 1997-2014.

148. C. Liu and R. Kelly, "The Use of Finite Element Methods (FEM) in the Modeling of Localized Corrosion," The Electrochemical Society Interface 23, 4 (2014): p. 47-51.

149. J.C. Russ, Image Processing Handbook, Fourth Edition: CRC Press, Inc., 2002). p. 744.

150. S. Policastro, C.M. Hangarter, and F.J. Martin. *Investigating the Role of Electrolyte Composition and Oxide Structure in Galvanic Corrosion Susceptibility Under Atmospheric Electrolytes*. in *Meeting Abstracts*. 2014: The Electrochemical Society.

151. M. Jakab, F. Presuel-Moreno, and J. Scully, "Effect of molybdate, cerium, and cobalt ions on the oxygen reduction reaction on AA2024-T3 and selected intermetallics experimental and modeling studies," J Electrochem Soc 153, 7 (2006): p. B244-B252.

152. M.A. Jakab, F. Presuel-Moreno, and J.R. Scully, "Critical Concentrations Associated with Cobalt, Cerium, and Molybdenum Inhibition of AA2024-T3 Corrosion: Delivery from Al-Co-Ce(-Mo) Alloys," Corrosion 61, 3 (2005): p. 246-263.

153. F. Presuel-Moreno, M. Jakab, and J. Scully, "Inhibition of the oxygen reduction reaction on copper with cobalt, cerium, and molybdate ions," J Electrochem Soc 152, 9 (2005): p. B376-B387.

154. J. Scully and M.A. Jakab, "Design of Cathodic Inhibitors for AA2024-T3 Guided by Understanding Heterogeneous Cathodic Reaction Kinetics," ECS Transactions 1, 9 (2006): p. 47-63.

155. C. Liu and R.G. Kelly, *Combined Numerical and Experimental Approach to Study pH and Conductivity Effects on Electrochemical Distributions in Galvanic Coupling in Airframe Components*. 2015, Univerisity of Virginia: Charlottesville.

156. R. Kelly and K. Stewart, "Combining the ohmic drop and critical crevice solution approaches to rationalize intermediate attack in crevice corrosion," Passivity of Metals and Semiconductors VIII, eds. MB Ives, BR MacDougall, JA Bardwell, PV (2001): p. 99-42.

157. M.O. Speidel, "Current understanding of stress corrosion crack growth in aluminum alloys," Paper from" The Theory of Stress Corrosion Cracking in Alloys". 1971. NATO, Brussels, Belgium. 289-344. (1971).

158. K. Sotoudeh, T.H. Nguyen, R.T. Foley, and B.F. Brown, "The Chemical Nature of Aluminum Corrosion: I Corrosion of Aluminum Surfaces by Aluminum Salts," Corrosion 37, 6 (1981): p. 358-362.
159. A.H. Le, B.F. Brown, and R.T. Foley, "The Chemical Nature of Aluminum Corrosion: IV. Some Anion Effects on SCC of AA 7075-T651," Corrosion 36, 12 (1980): p. 673-679.
160. Z. Szklarska-Smialowska, Pitting corrosion of metals: National Association of Corrosion Engineers, 1986.
161. M.J. Robinson and N.C. Jackson, "The influence of grain structure and intergranularcorrosion rate on exfoliation and stress corrosion crackingof high strength Al–Cu–Mg alloys," Corros Sci 41, 5 (1999): p. 1013-1028.
162. S. Lee and B.W. Lifka, *Modification of the EXCO Test Method for Exfoliation Corrosion Susceptibility in 7XXX, 2XXX, and Aluminum-Lithium Alloys*, in *New Methods for Corrosion Testing of Aluminum Alloys*. 1992, ASTM International.
163. T. Marlaud, B. Malki, C. Henon, A. Deschamps, and B. Baroux, "Relationship between alloy composition, microstructure and exfoliation corrosion in Al–Zn–Mg–Cu alloys," Corros Sci 53, 10 (2011): p. 3139-3149.
164. V. Sinyavskii, V. Ulanova, and V. Kalinin, "On the mechanism of intergranular corrosion of aluminum alloys," Protection of metals 40, 5 (2004): p. 481-490.
165. B. F. M. R. Facility, "Subtropical Exposure Testing Facility," Issue (2014).
166. V.N. Rafla, A.D. King, S. Glanvill, A. Davenport, and J.R. Scully, "Operando Assessment of Galvanic Corrosion Between Al-Zn-Mg-Cu Alloy and a Stainless Steel Fastener Using X-ray Tomography," Corrosion (2017).
167. V. Rafla, A.D. King, S. Glanvill, A. Parsons, A.J. Davenport, and J.R. Scully, "Operando Observation of Galvanic Corrosion between AA7050-T7451 and 304 Stainless Steel in a Simulated Fastener Arrangement using X-ray Tomography," Corrosion (2015).
168. X. Zhang, W. Liu, S. Liu, and M. Zhou, "Effect of processing parameters on quench sensitivity of an AA7050 sheet," Materials Science and Engineering: A 528, 3 (2011): p. 795-802.
169. W. Gruhl, "The stress-corrosion behavior of high-strength Al-Zn-Mg alloys," Aluminium alloys in the aircraft industries (1978): p. 171-174.
170. M. Dixit, R. Mishra, and K. Sankaran, "Structure–property correlations in Al 7050 and Al 7055 high-strength aluminum alloys," Materials Science and Engineering: A 478, 1 (2008): p. 163-172.
171. M. Conserva and P. Fiorini, "Interpretation of quench-sensitivity in Al-Zn-Mg-Cu alloys," Metallurgical and Materials Transactions B 4, 3 (1973): p. 857-862.
172. F.-S. Lin and E.A. Starke, "The effect of copper content and degree of recrystallization on the fatigue resistance of 7XXX type aluminum alloys I. Low cycle corrosion fatigue," Materials Science and Engineering 39, 1 (1979): p. 27-41.
173. M. Zeren, "Effect of copper and silicon content on mechanical properties in Al–Cu–Si–Mg alloys," Journal of Materials Processing Technology 169, 2 (2005): p. 292-298.
174. F.-S. Lin and E. Starke, "The effect of copper content and degree of recrystallization on the fatigue resistance of 7XXX-type aluminum alloys II. Fatigue crack propagation," Materials Science and Engineering 43, 1 (1980): p. 65-76.

175. T. Srivatsan, S. Anand, D. Veeraghavan, and V. Vasudevan, "The tensile response and fracture behavior of an Al-Zn-Mg-Cu alloy: Influence of temperature," Journal of materials engineering and performance 6, 3 (1997): p. 349-358.
176. E. Starke and J. Staley, "Application of modern aluminum alloys to aircraft," Progress in Aerospace Sciences 32, 2-3 (1996): p. 131-172.
177. J. Kaufman and J. Santner, "Fracture properties of aluminum alloys," Application of fracture mechanics for selection of metallic structural materials.(A 83-25317 10-26) Metals Park, OH, American Society for Metals, 1982 (1982): p. 169-211.
178. N. Deshpande, A. Gokhale, D. Denzer, and J. Liu, "Relationship between fracture toughness, fracture path, and microstructure of 7050 aluminum alloy: Part I. Quantitative characterization," Metall and Mat Trans A 29, 4 (1998): p. 1191-1201.
179. A.K. Vasudevan and R. Doherty, "Grain boundary ductile fracture in precipitation hardened aluminum alloys," Acta metallurgica 35, 6 (1987): p. 1193-1219.
180. R. Becker, A. Needleman, S. Suresh, V. Tvergaard, and A. Vasudevan, "An analysis of ductile failure by grain boundary void growth," Acta metallurgica 37, 1 (1989): p. 99-120.
181. J. Chen, T. Sun, R. Viswanadham, and J. Green, "Grain boundary segregation of an Al-Zn-Mg ternary alloy," Metallurgical Transactions A 8, 12 (1977): p. 1935-1940.
182. Y. Murakami, "Stress Corrosion Cracking in Aluminum Alloys," CORROSION ENGINEERING 26, 5 (1977): p. 245-255.
183. R. Buchheit, J. Moran, and G. Stoner, "Electrochemical behavior of the T1 (Al2CuLi) intermetallic compound and its role in localized corrosion of Al-2% Li-3% Cu alloys," Corrosion 50, 2 (1994): p. 120-130.
184. T.-g. Zhai, A.J. Wilkinson, and J.W. Martin, "A crystallographic mechanism for fatigue crack propagation through grain boundaries," Acta Materialia 48, 20 (2000): p. 4917-4927.
185. M.A. Przystupa, R.J. Bucci, P.E. Magnusen, and A.J. Hinkle, "Microstructure based fatigue life predictions for thick plate 7050-T7451 airframe alloys," International Journal of Fatigue 19, 93 (1997): p. 285-288.
186. P.S. Pao, C.R. Feng, and S.J. Gill, "Corrosion fatigue crack initiation in aluminum alloys 7075 and 7050," Corrosion 56, 10 (2000): p. 1022-1031.
187. J.-C. Lin, H.-L. Liao, W.-D. Jehng, C.-H. Chang, and S.-L. Lee, "Effect of heat treatments on the tensile strength and SCC-resistance of AA7050 in an alkaline saline solution," Corros Sci 48, 10 (2006): p. 3139-3156.
188. V. Rafla, A. King, S. Glanvill, A. Davenport, and J. Scully, "Operando Assessment of Galvanic Corrosion between Al-Zn-Mg-Cu Alloy and a Stainless Steel Fastener using X-ray Tomography," Corrosion (2017).
189. K.D. Ralston, N. Birbilis, M.K. Cavanaugh, M. Weyland, B.C. Muddle, and R.K.W. Marceau, "Role of nanostructure in pitting of Al–Cu–Mg alloys," Electrochimica Acta 55, 27 (2010): p. 7834-7842.
190. M. Woldemedhin, M. Shedd, and R. Kelly, "Evaluation of the maximum pit size model on stainless steels under thin film electrolyte conditions," J Electrochem Soc 161, 8 (2014): p. E3216-E3224.
191. E. Schindelholz and R.G. Kelly, "Wetting phenomena and time of wetness in atmospheric corrosion: a review," (2012).

192. A. Nishikata, Y. Ichihara, and T. Tsuru, "Electrochemical impedance spectroscopy of metals covered with a thin electrolyte layer," Electrochimica Acta 41, 7 (1996): p. 1057-1062.
193. D. Mizuno and R. Kelly, "Galvanically induced intergranular corrosion of AA5083-H131 under atmospheric exposure conditions: part 1—experimental characterization," Corrosion 69, 6 (2013): p. 580-592.
194. J. Li, B. Maier, and G. Frankel, "Corrosion of an Al–Mg–Si alloy under MgCl2 solution droplets," Corros Sci 53, 6 (2011): p. 2142-2151.
195. P. Khullar, J.V. Badilla, and R.G. Kelly, "Cathodic Control of Intergranular Corrosion Propagation in Al-Mg Alloys Under Thin Film Conditions," Corrosion 72, 10 (2016): p. 1223-1225.
196. P. Khullar, J. Badilla, and R. Kelly, "The Use of a Sintered Ag/AgCl Electrode as Both Reference and Counter Electrode for Electrochemical Measurements in Thin Film Electrolytes," ECS Electrochemistry Letters 4, 10 (2015): p. C31-C33.
197. Y.L. Cheng, Z. Zhang, F.H. Cao, J.F. Li, J.Q. Zhang, J.M. Wang, and C.N. Cao, "A study of the corrosion of aluminum alloy 2024-T3 under thin electrolyte layers," Corros Sci 46, 7 (2004): p. 1649-1667.
198. S. Yee, R. Oriani, and M. Stratmann, "Application of a Kelvin microprobe to the corrosion of metals in humid atmospheres," J Electrochem Soc 138, 1 (1991): p. 55-61.
199. S. Song and Z. Chen, "Initial corrosion of pure zinc under NaCl electrolyte droplet using a Zn-Pt-Pt three-electrode system," Int. J. Electrochem. Sci 8, (2013): p. 6851-6863.
200. H. Zhou, X. Li, J. Ma, C. Dong, and Y. Huang, "Dependence of the corrosion behavior of aluminum alloy 7075 on the thin electrolyte layers," Materials Science and Engineering: B 162, 1 (2009): p. 1-8.
201. Y. Cheng, Z. Zhang, F. Cao, J. Li, J. Zhang, J. Wang, and C. Cao, "A study of the corrosion of aluminum alloy 2024-T3 under thin electrolyte layers," Corros Sci 46, 7 (2004): p. 1649-1667.
202. S. Zhang and S. Lyon, "Anodic processes on iron covered by thin, dilute electrolyte layers (I)—Anodic polarisation," Corros Sci 36, 8 (1994): p. 1289-1307.
203. C.M. Hangarter and S.A. Policastro, "Electrochemical Characterization of Galvanic Couples Under Saline Droplets in a Simulated Atmospheric Environment," Corrosion 73, 3 (2016): p. 268-280.
204. C. Liu, J. Srinivasan, and R. Kelly, "Editors' Choice—Electrolyte Film Thickness Effects on the Cathodic Current Availability in a Galvanic Couple," J Electrochem Soc 164, 13 (2017): p. C845-C855.
205. C. Glover, V. Rafla, M. Hutchison, and J.R. Scully, "Progress in Development of Electrochemical Methods in Corrosion Science and Engineering," STP: Selected Technical Papers: Symposium on Advances in Electrochemical Techniques for Corrosion Monitoring and Laboratory Corrosion Measurements (2018).
206. A. King, J.S. Lee, and J. Scully, "Galvanic couple current and potential distribution between a Mg electrode and 2024-T351 under droplets analyzed by microelectrode arrays," J Electrochem Soc 162, 1 (2015): p. C12-C23.

207. H. Cong and J.R. Scully, "Use of coupled multielectrode arrays to elucidate the pH dependence of copper pitting in potable water," J Electrochem Soc 157, 1 (2010): p. C36-C46.
208. N.D. Budiansky, F. Bocher, H. Cong, M. Hurley, and J.R. Scully, "Use of coupled multi-electrode arrays to advance the understanding of selected corrosion phenomena," Corrosion 63, 6 (2007): p. 537-554.
209. N. Budiansky, J. Hudson, and J. Scully, "Origins of persistent interaction among localized corrosion sites on stainless steel," J Electrochem Soc 151, 4 (2004): p. B233-B243.
210. T. Kosec, M. Hren, and A. Legat, "Monitoring copper corrosion in bentonite by means of a coupled multi-electrode array," Corrosion Engineering, Science and Technology 52, sup1 (2017): p. 70-77.
211. E. Schindelholz, B. Risteen, and R.G. Kelly. *Atmospheric Corrosion of Plain Carbon Steel Below the Deliquescence Point of Sodium Chloride*. in *Meeting Abstracts*. 2013: The Electrochemical Society.
212. M. Jakab and J. Scully, "On-demand release of corrosion-inhibiting ions from amorphous Al–Co–Ce alloys," Nature materials 4, 9 (2005): p. 667.
213. W. Robertson, "Molybdate and tungstate as corrosion inhibitors and the mechanism of inhibition," J Electrochem Soc 98, 3 (1951): p. 94-100.
214. R. Twite and G. Bierwagen, "Review of alternatives to chromate for corrosion protection of aluminum aerospace alloys," Progress in Organic Coatings 33, 2 (1998): p. 91-100.
215. Q. Meng and G.S. Frankel, "Effect of Copper Content on Chromate Conversion Coating Protection of 7xxx-T6 Aluminum Alloys," Corrosion 60, 10 (2004): p. 897-905.
216. M.W. Kendig, A.J. Davenport, and H.S. Isaacs, "The mechanism of corrosion inhibition by chromate conversion coatings from x-ray absorption near edge spectroscopy (Xanes)," Corros Sci 34, 1 (1993): p. 41-49.
217. F.A. Cotton and G. Wilkinson, Advanced inorganic chemistry. 5th ed (New York: Wiley, 1988). p. xvii, 1455 p.
218. M. Pourbaix, Atlas of electrochemical equilibria in aqueous solutions. Vol. 1: Pergamon, 1966.
219. B.D. Chambers, S.R. Taylor, and M.W. Kendig, "Rapid Discovery of Corrosion Inhibitors and Synergistic Combinations Using High-Throughput Screening Methods," Corrosion 61, 5 (2005): p. 480-489.
220. S. Pride, J. Scully, and J. Hudson, "Metastable pitting of aluminum and criteria for the transition to stable pit growth," J Electrochem Soc 141, 11 (1994): p. 3028-3040.
221. H. Kaesche, "Pitting corrosion of aluminum and intergranular corrosion of Al alloys," Localized Corrosion 3, (1971): p. 516.
222. A. Sehgal, G. Frankel, B. Zoofan, and S. Rokhlin, "Pit growth study in Al alloys by the foil penetration technique," J Electrochem Soc 147, 1 (2000): p. 140-148.
223. P.S. Young, *Modeling and Analysis for Atmospheric Galvanic Corrosion of Fasteners in Aluminum*. 2015, University of Akron.
224. Z. Feng, G.S. Frankel, W.H. Abbott, and C.A. Matzdorf, "Galvanic Attack of Coated Al Alloy Panels in Laboratory and Field Exposure," Corrosion 72, 3 (2015): p. 342-355.

225. C. Matzdorf, W. Nickerson, B.C. Rincon Troconis, G. Frankel, L. Li, and R. Buchheit, "Galvanic Test Panels for Accelerated Corrosion Testing of Coated Al Alloys: Part 1—Concept," Corrosion 69, 12 (2013): p. 1240-1246.
226. M. Kendig and R. Buchheit, "Corrosion inhibition of aluminum and aluminum alloys by soluble chromates, chromate coatings, and chromate-free coatings," Corrosion 59, 5 (2003): p. 379-400.
227. B. Kannan and J.R. Scully, "Performance of a Magnesium-Rich Primer on Pretreated AA2024-T351 in Selected Laboratory and Field Environments: Conversion Coating Pretreatments," Corrosion 72, 11 (2016): p. 1363-1384.
228. J.D. Ramsey, L. Xia, M.W. Kendig, and R.L. McCreery, "Raman spectroscopic analysis of the speciation of dilute chromate solutions," Corros Sci 43, 8 (2001): p. 1557-1572.
229. G.S. Frankel, *Mechanism of Al alloy corrosion and the role of chromate inhibitors*. 2001, OHIO STATE UNIV COLUMBUS FONTANA CORROSION CENTER.